

Dissertation

Paul Larin

**Measurement of the Timelike Electromagnetic
Form Factors of the Neutron at the BESIII
Experiment with the Process $e^+e^- \rightarrow \bar{n}n$**

**Measurement of the Timelike
Electromagnetic Form Factors of the
Neutron at the BESIII Experiment with
the Process $e^+e^- \rightarrow \bar{n}n$**

Dissertation

zur Erlangung des Grades

”Doktor der Naturwissenschaften”

am Fachbereich Physik, Mathematik und Informatik
der Johannes Gutenberg-Universität
in Mainz

Paul Larin

geb. in Kujbyshev, Russland

Mainz, September 2019

Paul Larin: *Measurement of the timelike electromagnetic form factors of the neutron at the BESIII experiment with the process $e^+ e^- \rightarrow \bar{n} n$*

1. Berichterstatter: Prof. Dr. Frank E. Maas
 2. Berichterstatter: Prof. Dr. Marc Vanderhaeghen
- Tag der mündlichen Prüfung: 10. Juli 2020

Abstract

The investigation of the fundamental properties of the nucleon is one of the most important topics in modern hadron physics. The precise knowledge of its internal structure in terms of quark and gluon degrees of freedom, accessible through the electromagnetic probe, is crucial for the understanding of the strong interaction. This structure can be studied through the measurement of the electromagnetic form factor (FF). Starting with the groundbreaking work of Hofstadter, many experiments successfully extended the picture of the spatial electromagnetic distribution densities of protons and neutrons in the spacelike region with a negative momentum transfer $q^2 < 0$. In contrast, the experimental situation of the FF in the timelike region ($q^2 > 0$) is less clear. In particular, the investigation on the timelike FF of the neutron has been done only by three experiments up to date. Moreover, limited statistics permitted to determine only the effective FF. While in the case of the proton, at least several experiments measured the magnetic FF and the electromagnetic FF ratio, the neutron FF remains mainly unknown.

In this thesis, the first measurement of the magnetic FF $|G_M^n(q^2)|$ and the electromagnetic FF ratio of the neutron $|G_E^n(q^2)|/|G_M^n(q^2)|$, determined at five center-of-mass energies from the final state angular distribution in the reaction $e^+e^- \rightarrow \bar{n}n$, is reported. The analyzed data set covers the center-of-mass energy range between 2.00 and 3.08 GeV with a total integrated luminosity of 651 pb^{-1} and was collected at the BESIII experiment at the BEPCII collider in Beijing, China. The Born cross section and the effective FF are analyzed from 18 data sets, using Monte Carlo simulation with dedicated event generators for the determination of the selection efficiency. Corrections of the selection efficiency determined from the Monte Carlo simulation are obtained with data-driven methods. Radiative QED corrections are implemented.

The results from this work are a significant addition to the database, extending the knowledge of the electromagnetic FF of the neutron in a wide momentum transfer region and therefore contribute to the understanding of the nucleon in the framework of strong interaction. They will serve as a new reference in every physics context where FFs are needed as input, for example helping to distinguish between a variety of phenomenological and theory-inspired parametrizations for the electromagnetic structure of the nucleon, or serving as input parameters for a new generation of Monte Carlo based event generators.

Zusammenfassung

Die Untersuchung der fundamentalen Eigenschaften des Nukleons ist eine der wichtigsten Herausforderungen der modernen Hadronenphysik. Die Kenntnis der inneren Struktur des Nukleons in Bezug auf die quarkonischen und gluonischen Freiheitsgrade ist Voraussetzung für das Verständnis der starken Wechselwirkung. Das Studium der Struktur durch die Messung des elektromagnetischen Formfaktors (FF) ist möglich mit Hilfe der elektromagnetischen Probe. Seit den richtungsweisenden Resultaten von Hofstadter haben viele Experimente erfolgreich das heutige Bild der elektromagnetischen Ladungsverteilung geprägt. Insbesondere wurden die FF vom Proton und vom Neutron im raumartigen Impulsübertragungsbereich mit negativem Impulsübertrag $q^2 < 0$ in zahlreichen Experimenten vermessen. Im Gegensatz dazu gibt es nur wenige experimentelle Ergebnisse im zeitartigen Bereich ($q^2 > 0$). Bis heute haben nur drei Experimente und wegen geringer Statistik nur den effektiven zeitartigen FF des Neutrons vermessen. Folglich und im Gegensatz zur Situation für das Proton, ist die Datenlage für das Neutrons sehr begrenzt.

In dieser Arbeit wird die erste Messung des magnetischen FF $|G_M^n(q^2)|$ und des elektromagnetischen Formfaktorverhältnisses $|G_E^n(q^2)|/|G_M^n(q^2)|$ des Neutrons im zeitartigen Bereich vorgestellt. Dabei wird die Winkelverteilung des Endzustandes im Prozess $e^+e^- \rightarrow \bar{n}n$ bei fünf Schwerpunktsenergien analysiert. Die Analyse beruht auf einem Datensatz des BESIII Experiments am BEPCII Kollider in Beijing, China, und deckt die Schwerpunktsenergie zwischen 2.0 und 3.08 GeV mit einer Gesamtluminosität von 651 pb^{-1} ab. Der Born-Wirkungsquerschnitt und der daraus bestimmte effektive Formfaktor werden bei 18 Schwerpunktsenergien vermessen, wobei Monte Carlo Simulationen dedizierter Ereignisgeneratoren zur Bestimmung der Selektionseffizienz verwendet werden. Wegen Ungenauigkeiten in der Simulation des Prozesses werden die Monte Carlo-Simulationen mit Hilfe Daten-getriebener Methoden korrigiert. QED-Strahlungskorrekturen werden mit Hilfe der Simulation vom Ereignisgenerator angebracht.

Die hier präsentierten Ergebnisse stellen die Datenlage für den zeitartigen Formfaktor des Neutrons zum ersten Mal auf solide Füße und helfen beim Verständnis des Nukleons im Rahmen der starken Wechselwirkung. Sie werden in Zukunft als Referenz dienen und zum Beispiel dabei helfen eine bessere Kategorisierung zwischen der Vielzahl phänomenologischer und Theorie-inspirierter Parametrisierungen für die elektromagnetische Struktur des Nukleons zu ermöglichen oder als Parameter für eine neue Generation von Monte Carlo Ereignisgeneratoren einfließen.

Table of Contents

1	Introduction	1
2	The Electromagnetic Form Factor of the Nucleon	5
2.1	The Standard Model of particle physics	5
2.2	The nucleon structure	8
2.2.1	Historical perspective	8
2.2.2	The hadronic current and the nucleon form factor	11
2.2.3	Asymptotic properties and boundary conditions	18
2.3	Overview on the nucleon form factor measurement	20
2.3.1	Proton form factor from Rosenbluth separation	21
2.3.2	Proton form factor from polarization transfer	23
2.3.3	Proton form factor from annihilation	24
2.3.4	Neutron form factors from electron scattering	28
2.3.5	Neutron form factor ratio from electron scattering	31
2.3.6	Neutron form factor from annihilation	32
2.4	Parametrization of the electromagnetic form factor	34
2.4.1	Dipole behavior	34
2.4.2	Perturbative QCD	35
2.4.3	Dispersion-theoretical approach	36
2.4.4	Relativistic constituent quark model	38
2.4.5	Lattice QCD simulation	38
2.4.6	Chiral effective field theory	39
2.4.7	Soft collinear effective theory approach	41
2.4.8	Vector Meson Dominance	42
3	The BESIII Experiment	45
3.1	Beijing Electron Positron Collider II	45
3.2	Beijing Electron Spectrometer III	47
3.2.1	Beam pipe and interaction region	48

3.2.2	Momentum measurement with the tracking system	49
3.2.3	The time-of-flight measurement	52
3.2.4	Electromagnetic calorimetry	57
3.2.5	Muon detection system	62
3.2.6	Trigger system	65
3.3	Software framework	72
3.3.1	BESIII Offline Software System	72
3.3.2	Detector response simulation with the Geant4	74
3.3.3	CERN ROOT for statistical treatment and visualization of data . . .	75
3.3.4	Fitting and toy Monte Carlo studies with RooFit	75
3.4	The data set of the BESIII experiment	76
4	The Monte Carlo Simulation	79
4.1	Monte Carlo event generators for the physics simulation	80
4.2	The signal Monte Carlo simulation	82
4.2.1	The initial form factor parametrization	83
4.2.2	The iterative optimization of the form factor model	86
4.3	The simulation of the dominant physics background	89
4.4	The simulation for the efficiency correction	90
5	The Event Selection for the Signal Process $e^+e^- \rightarrow \bar{n}n$	91
5.1	The detector response of the signal events	91
5.2	Concept of the data analysis	99
5.3	The signal selection with the category C approach	101
5.3.1	Pre-selection	101
5.3.2	The selection of the antineutron	102
5.3.3	The selection of the neutron	105
5.3.4	Additional selection criteria for background rejection	106
5.4	The summary of all selection criteria	109
6	The Evaluation of the Background Contamination	111
6.1	Remaining background in the selected events	111
6.2	Evaluation of the background contamination	115
6.2.1	The beam related and the cosmic ray background	115
6.2.2	The hadronic background	118
7	The Extraction of the Signal Events	121
7.1	The modeling of the signal component	121

7.2	The modeling of the background component	123
7.2.1	The beam related and the cosmic ray component	123
7.2.2	The hadronic background component	124
7.3	The fit of the combined model to the BESIII data set	127
7.4	The summary of the extracted signal from collider data	132
8	The Reconstruction Efficiency	135
8.1	Reconstruction efficiency from signal MC simulation	135
8.2	Efficiency correction C_{dm}	137
8.2.1	The selection of $J/\psi \rightarrow p\bar{n}\pi^-$ and $J/\psi \rightarrow \bar{p}n\pi^+$ control channels . .	137
8.2.2	The selection of \bar{n} and n showers from $J/\psi \rightarrow p\bar{n}\pi^-$ and $J/\psi \rightarrow \bar{p}n\pi^+$	140
8.2.3	The calculation of C_{dm}	144
8.3	Efficiency correction due to the selection criterion S_8	149
8.3.1	Stability plateau for the cut determination	149
8.3.2	The extraction of C_{ee}^{data} from the collider data using $e^+e^- \rightarrow \bar{p}p$. . .	150
8.3.3	The fit to the C_{ee}^{data} values for the extraction of C_{ee}	151
8.4	Efficiency correction due to the selection criterion S_9	153
8.5	The efficiency correction C_{trg} due to the BESIII trigger	155
8.5.1	The energy deposition related trigger response function	156
8.5.2	Modification of the signal MC simulation $e^+e^- \rightarrow \bar{n}n$	161
8.5.3	The calculation of C_{trg} for the signal channel $e^+e^- \rightarrow \bar{n}n$	162
8.6	Efficiency correction C_{mod} due to the form factor model	164
8.7	The radiative correction factor $(1 + \delta)$	165
8.8	Summary of the signal efficiency and its corrections	167
9	The Extraction of the Results	169
9.1	The individual results for $\sigma_{\text{Born}}^{\text{ind}}(s)$ and $ G_{\text{eff}}^{\text{ind}}(s) $	169
9.2	The combined results for $\sigma_{\text{Born}}^{\text{n}}(s)$ and $ G_{\text{eff}}^{\text{n}}(s) $	173
9.3	Extraction of individual results for $G_{\text{M}}^{\text{ind}}(s)$ and $R_{\text{em}}^{\text{ind}}(s)$	175
9.4	Extraction of the combined results for $G_{\text{M}}^{\text{n}}(s)$ and $R_{\text{em}}^{\text{n}}(s)$	182
10	Systematic Uncertainties	193
10.1	Systematic uncertainty of the Born cross section	193
10.1.1	The luminosity measurement	193
10.1.2	The signal selection	194
10.1.3	The signal yield extraction	194
10.1.4	The model dependence of the angular distribution $\cos\theta_{\bar{n}}$	196

10.1.5	The trigger efficiency	198
10.1.6	The radiative corrections	199
10.1.7	Summary of the systematic uncertainties on σ_{Born} and $ G_{\text{eff}} $	200
10.2	Systematic uncertainty on the form factor ratio	202
10.2.1	The differential signal selection	202
10.2.2	The differential signal yield extraction	206
10.2.3	The bin width of the angular distribution	207
10.2.4	The range of the angular fit	208
10.2.5	The signal MC form factor parametrization	209
10.2.6	Summary of the systematic uncertainties on $R_{\text{em}}^{\text{ind}}(s)$	211
10.3	Systematic uncertainty of the magnetic form factor	212
10.4	Combined systematic uncertainties on R_{em} and G_{M}	213
11	The Discussion of the Final Results	217
11.1	The Born cross section results	217
11.2	The effective form factor results	221
11.3	The magnetic form factor results	224
11.4	The form factor ratio results	228
11.5	Comparison of the results with the spacelike region	229
11.6	Asymptotic behavior between the SL and TL region	231
12	Conclusion	233
Appendix A	Additional Details for the Analysis Performed by the Author	239
Appendix B	External Contributions to the Final Results from this Analysis	291
Appendix C	The Time-of-Flight Measurement for Neutral Particles at BESIII	331
	List of Figures	341
	List of Tables	353
	Bibliography	359
	Curriculum Vitae	371

Chapter 1

Introduction

The nucleon structure is a central element for the understanding of the strong interaction, one of the four fundamental forces in physics. Nucleons, both proton and neutron, are bound systems of three quarks each and, therefore non-elemental, extended particles, as impressively shown in 1956 by Hofstadter in his pioneering experiment on elastic electron scattering of hydrogen and helium [1] at the High Energy Physics Laboratory at Stanford University. The nucleon electromagnetic form factors (FFs) originate from electromagnetic currents in the nucleon, parametrize the inner structure and display the difference to a point-like particle, e.g., an electron. Being among the most basic observables of the nucleon they are a key for a deeper understanding of the Quantum chromodynamics (QCD). A quantitative experimental access to these observables is possible via the electromagnetic probe; in the spacelike (SL) momentum transfer region characterized through a lepton scattering via the intermediate photon on the nucleon. The timelike (TL) momentum transfer domain is characterized through a virtual photon produced after an lepton-antilepton annihilation into a nucleon-antinucleon pair or the reversed process. Here, the virtual photon carries hadronic contributions to the vacuum polarization which become real, if the photon energy exceeds the production threshold for a specific hadron-antihadron pair. The reason for the importance of the nucleon electromagnetic form factors arises from the associated matrix element for elastic scattering or annihilation, the simplest involving nucleon structure. This lets the nucleon electromagnetic FFs serve as a testing ground for the understanding of the underlying theoretical description of the internal structure of the nucleon and its dynamics.

In the SL region, the electromagnetic FFs of the nucleon are associated with the spatial electric and magnetic charge distribution of the nucleon. First results on the FFs of the proton in the SL region have been reported by the team of researchers around Hofstadter in 1955 [2], shortly followed by results on the neutron in 1958 [3]. Since then, many experiments improved the knowledge of the FFs over a large four momentum transfer $Q^2 = 0$ region, the precision of the results and added new approaches for their measurement. At the same time a lot of work has been invested in the field of theoretical description of the nucleon and its interaction with an electromagnetic probe. Recent summaries and reviews on results in the SL region can be found in the References [4] - [8]. Even with a rising amount of high precision results for proton and neutron electromagnetic FF in the SL region, many questions are still left unanswered. With new advancements in the precision of the results, new phenomena of the FF have been uncovered and further questions arose. Results on the ratio between the electric $G_E^p(Q^2)$ and magnetic $G_M^p(Q^2)$ FF of the proton in the SL region from two different measurement methods, the Rosenbluth separation and the polarization transfer, show significant differences [9], today considered to arise from the contribution of a two-photon exchange. The long living assumption on the equality of the proton electric and magnetic FF could be proven wrong by JLab experiments [10]. Another prominent example of the incomplete understanding in this field of research is the "puzzle of the proton charge radius", the first derivative of the electric FF at Q^2 close to zero, where two significantly different sets of results are extracted when using electrons and muons as the electromagnetic probe [11].

In the TL momentum transfer region, the situation on the FF results is different. While several experiments measured the FFs of the proton and their ratio by electron-positron and proton-antiproton annihilations [12] - [21], the experimental situation on the neutron FFs is poor. The FENICE experiment published the first results on the TL FF of the neutron in 1994 [22] - [24], assuming that the electric FF is equal zero, followed by a publication from the DM2 experiment [25]. Recent results have been released by the SND collaboration in 2014, adding data for the effective form factor (implying for the extraction the identity of the electric and magnetic FF $G_E^n(q^2) = G_M^n(q^2)$, with $q^2 = -Q^2$) close to the production threshold at two times the mass of the neutron [26]. Since no free neutron target exists, the neutron FF in the TL region can only be measured by the channel $e^+e^- \rightarrow \bar{n}n$, leading to a limited experimental access. Additionally, the analysis is challenging because of the requirement of reconstruction of two neutral hadrons, requiring advanced and non-standard analysis techniques as well as limiting the selection efficiency.

The results presented in this thesis are based on the analysis of recently collected data at the BESIII experiment with center-of-mass energies between $\sqrt{s} = 2.00$ to 3.08 GeV [27]. This data set contains several large luminosity samples close to the signal production threshold and opens the possibility for the disentanglement of the electric and magnetic FF contributions. For the first time, the magnetic FF and the electromagnetic FF ratio are measured for the neutron in the TL region. Additionally, the range and precision on the results of the effective FF of the neutron in the TL region are improved drastically.

This thesis is organized as follows. **Chapter 2** gives a brief overview on the topic of the electromagnetic form factors, its classification within the field of particle physics and the Standard Model, lists the experimental techniques for the FF measurement, and presents the existing results from other experiments. In **Chapter 3**, a detailed description of the BESIII experiment is given, where the data for this analysis was taken. In **Chapter 4**, a description of the Monte Carlo simulation used in this thesis is presented. **Chapter 5** shows the event selection for the signal process $e^+e^- \rightarrow \bar{n}n$. In **Chapter 6** the background estimation after the event selection is discussed. Following, the signal yield extraction through a fit to the opening angle between neutron and antineutron is shown in **Chapter 7**. In **Chapter 8** the signal reconstruction efficiency and the applied corrections are presented. The results of the Born cross section of the signal process, together with the corresponding effective form factor of the neutron, as well as for the first time the results on the magnetic form factor $G_M^n(q^2)$ and the electromagnetic ratio $R_{em}^n(q^2) = |G_E^n(q^2)|/|G_M^n(q^2)|$ are shown in **Chapter 9**. Following, in **Chapter 10** the contributions for the systematical uncertainties are studied. In **Chapter 11** the results are summarized and discussed. Additionally, the results from this thesis are combined with two different, independent approaches (shown in Appendix B), and compared to the existing world data. **Chapter 12** closes the main part of this thesis with a conclusion and finally a classification into the recent knowledge of TL FFs is given.

This analysis is a combined effort including three different signal process selections, performed on sub-data sets. While the results shown in the main part of this thesis are achieved by the author, most methods have been developed in a collaboration with Samer Ahmed, Xiaorong Zhou, and Jifeng Hu. Furthermore, several side studies have been performed by one of the named scientists, which will be indicated accordingly in the text.

Chapter 2

The Electromagnetic Form Factor of the Nucleon

In this chapter the topic of this thesis is embedded into the theoretical context in the field of the particle physics and a review of the up-to-date knowledge on the nucleon structure is given. The electromagnetic FF of the nucleon is introduced in Section 2.2. Section 2.3 is dedicated to the measurement of the FF in the SL and TL momentum transfer domain and to the existing results available for both, the proton and the neutron. In the last section of this chapter various parametrizations of the electromagnetic FF are introduced.

1.1 The Standard Model of particle physics

Physics, translated from Greek "physica" and meaning literally "the natural thing/natural science", is a discipline of science with the attempt to understand the laws of nature. In early days more an abstract and philosophical than an experimental approach, it developed over the centuries to the branch of science for study of matter and its interaction, space, time and energy. The idea of matter built from elementary particles goes back to ancient Greek philosophers, trying to develop a deeper understanding of nature. Democritus as one of these early natural philosophers, living between 460 to 360 BC, developed the atomic theory, a first approach to model a theory of matter. Almost two thousand years later Copernicus' famous heliocentric model had a great impact on science and philosophy. Galileo Galilei introduced his celestial theory and paved the way for Kepler's description of the planetary motion. Newton formulated the laws of mechanics, for many generations after him the basic ground principles of nature, following by other milestones

like Maxwell's theory of electromagnetism. With Planck's contribution to the development of the quantum theory and Einstein's theory for special and general relativity the modern era of physics began. This led to an modern description of matter and the discoveries of the proton in 1917 and the neutron in 1932. The discovery of elementary particles culminated in the description of fundamental forces in the quantum field theories and the Standard Model (SM) of particle physics.

The SM of particle physics unifies the description of known matter and its interaction through three of the fundamental forces, the electromagnetic, the weak and the strong interaction [28]. The unification with the general description of gravity, formulated in Einstein's general relativity theory, is recently one of the most important goals for physicists, but could not be achieved until now. The SM was developed in the second half of the 20th century, proposed first by Glashow, Weinberg and Salam and constantly expanded with new discoveries. In the SM, elementary particles are divided into two groups: gauge bosons, which are invariant under certain symmetry transformations of the underlying gauge type field theory, as the carriers of the fundamental forces, and the fermionic elementary building blocks of matter, quarks and leptons. A representation of all included components in the SM is shown in Figure 2.1 (top). Elementary particles can couple to one or more gauge bosons and therefore interact through fundamental forces. Their interactions are shown schematically in Figure 2.1 (bottom). The SM further divides the fermionic spin- $\frac{1}{2}$ particles into three generation, dependant on their masses. The six fundamental quarks u, d, c, s, t and b carry charges of all three fundamental forces described by the SM, and are therefore affected by them. The charged leptons e, μ and τ couple to the weak and electromagnetic force, their neutral partners ν_e , ν_μ and ν_τ couple only to the weak force. The photon γ carries the electromagnetic force, the 8 gluons are the the carrier of the strong force, while both are massless. The charged W^\pm and the neutral Z^0 bosons are massive and the exchange particles of the weak interaction. Finally, the Higgs boson H describes the origin of masses of the elementary particles through the Higgs-Mechanism. A specific characteristic of the gluons and the Higgs boson is the self-coupling.

Over the years, Standard Model predictions for the energy range above some GeV have been confirmed by various experiments. Taking as an example, the predicted existence of the weak interaction gauge bosons W^\pm and Z^0 which could be confirmed in 1983 [29] [30] and the discovery of the top quark t in 1995 [31] - each honored by a Nobel Prize. Another good example for the extraordinary success of the SM in terms of completeness is the discovery of the Higgs boson in 2012 [32], proposed in 1964 to explain the mass of W^\pm

and Z^0 bosons without breaking the the gauge symmetry, also followed by a Nobel Prize win. With all these milestone achievements, there are still open questions and difficulties within the Standard Model.

Embedded in the SM, the quantum chromodynamics describes the strong interaction between the elementary particles. Although very successful to explain various experimental results, the most basic property of the theory, the confinement of the elementary quarks and gluons into hadrons is not described in detail within the theory. Therefore, one open question in the SM is the quantitative understanding of the nucleon structure, with the electromagnetic FF being the characterizing observable, accessible via electromagnetic probes. This work focuses on the experimental determination of the electromagnetic form factor of the neutron in the timelike momentum range.

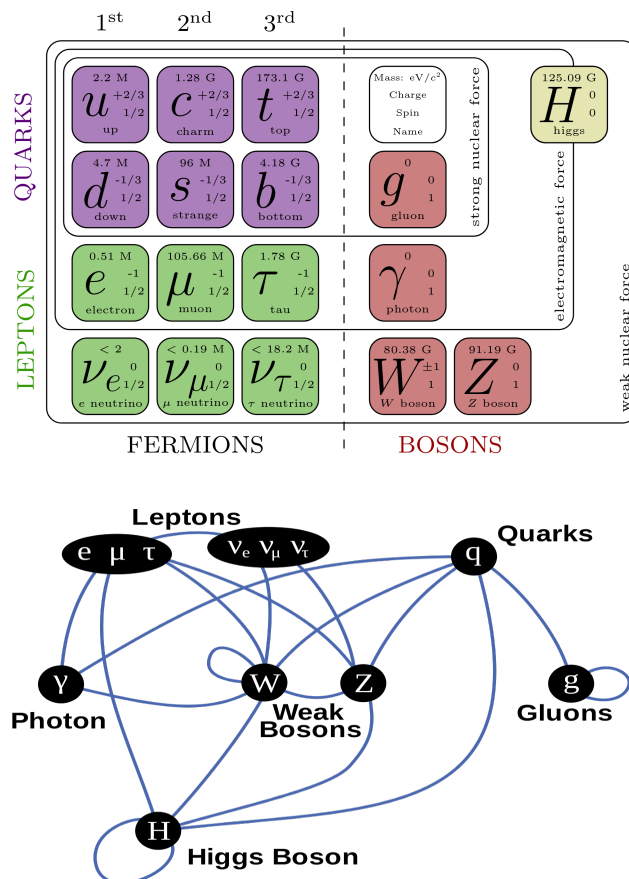


Fig. 2.1: (Top) The Standard Model of elementary particles with the three generations of matter, gauge bosons and the Higgs boson. (Original image from <https://github.com/mlubej/standard-model>). (Bottom) Summary of interactions between particles described by the Standard Model. (Original image from https://en.wikipedia.org/wiki/Mathematical_formulation_of_the_Standard_Model).

2.2 The nucleon structure

The nucleon, either a proton or a neutron, belongs to the class of baryons, composite subatomic particles consisting of an odd number of valence quarks. It is the main building block of every atomic nucleus and therefore represents the fundamental ingredient of the visible matter in the universe. Given the effort invested since almost one hundred years of scientific research, its internal structure is still not fully understood yet. One of the most useful tools for the investigation of the nucleon structure is an electromagnetic probe. In the spacelike (SL) region, the elastic electron scattering on the nucleon provides the best characteristics for the experiment. The point-like nature of the electron simplifies the analysis, while the weak electromagnetic coupling constant α_{EM} only disturbs the baryonic system lightly, which makes a perturbative approach for the theoretical description applicable. These arguments also apply to the timelike (TL) region, where the FF study can be performed via the e^+e^- annihilation and a sub-sequential baryon-antibaryon pair production or via the time-reversed process, since these reactions proceed in the SL and TL region in the lowest order through an exchange of a virtual photon. From the experimental view, for example deviations on the proton form factor ratio between the Rosenbluth approach and the polarization transfer method in the SL region can't be fully explained yet [33], while the poor situation in the experimental data in the TL region don't allow a final conclusion between the PS170 and the BaBar results [34]. The situation for the neutron is even worse, since in the TL region no data at all are available for the electric FF and the FF ratio, while the magnetic FF only has been studied under a hypothesis and in a limited energy range by the FENICE experiment [35].

2.2.1 Historical perspective

In this section, a short overview of the historical development in the field of nucleon structure, based on the review as presented in [5], is given. In the early 20th century, Ernest Rutherford performed elastic scattering experiments of α -particles on a gold foil [36]. His research led to the discovery of the proton in 1917. It was also Rutherford who firstly proposed the neutron, which was discovered in 1932 by Chadwick [37], [38]. Scattering experiments at this time have been analyzed with respect to the Rutherford cross section which describes the elastic scattering of two Dirac particles:

$$\left(\frac{d\sigma}{d\Omega}\right)_{\text{Ruth}} = \left(\frac{Z_1 Z_2 \alpha_{em} (\hbar c)}{4E_{\text{kin}} \sin^2 \frac{\theta}{2}}\right)^2 \quad (2.1)$$

with the atomic numbers of target material and the used projectiles Z_i , the fine-structure constant $\alpha_{\text{em}} = \frac{e^2}{4\pi}$, the scattering angle of the projectile θ , the non-relativistic kinetic energy of the projectile E_{kin} (in MeV) and the product from the reduced Planck constant and the speed of light $\hbar c \sim 197 \text{ MeV} \times \text{fm}$.

For the description of scattering of two point-like particles, taking into account a spin of $\frac{1}{2}$ for one of them, Mott modified the Rutherford cross section formula in the following way:

$$\left(\frac{d\sigma}{d\Omega}\right)_{\text{Mott}} = \left(\frac{d\sigma}{d\Omega}\right)_{\text{Ruth}} \times \left[1 - \left(\frac{v}{c}\right)^2 \sin^2 \frac{\theta}{2}\right] \quad (2.2)$$

where v is the projectile's speed. In the non-relativistic case (spin is neglected due to $\frac{v}{c} \ll 1$), the Mott cross section transforms to the Rutherford formula. Further investigations on the atomic internal structure led to an experiment for the investigation of the proton's magnetic moment by Stern and Gerlach [39] in 1933, which extracted a value 2.8 times larger than would have been expected for a point-like spin- $\frac{1}{2}$ particle. 1940 the anomalous magnetic moment of the neutron was measured by Alvarez and Bloch to be 1.9 times the value for a point-like particle [40], leading to the conclusion, that both nucleons must have an extended charge distribution. In 1950 Rosenbluth published a model for the scattering of electrons on protons [41], denoted as the weak coupling model. Rosenbluth proposed this model for the proton as a neutron core with a surrounding positively charged meson cloud. Electrons with an sufficient incident energy are supposed to "notice" the effective charge e' and the effective anomalous magnetic moment κ of the proton.

In 1953 and again with elastic electron-proton scattering on a gold foil, Hofstadter et al. could show with their results a deviation from the hypothesis of point-like nucleon targets in the scattering behavior of the electrons [42]. Two years later Hofstadter and McAllister introduced for the first time the concept of form factors as an internal charge distribution $\rho(\vec{r})$ [2] in the cross section for elastic electron proton scattering. In a review paper in 1956 Hofstadter related these results to the Mott cross section and introduced the generalized form factor $|F(q^2)|^2$ as the deviation from the point-like particle [43]:

$$\sigma(\theta) = \sigma_{\text{Mott}} \left| \int \rho(\vec{r}) e^{i\vec{q}\cdot\vec{r}} d^3\vec{r} \right|^2 \hat{=} \sigma_{\text{Mott}} \cdot |F(q^2)|^2 \quad (2.3)$$

where $q = |\vec{q}|$, $\vec{q} = \vec{p}_{\text{Beam}} - \vec{p}_e$ is the momentum transfer, \vec{p}_{Beam} is the incident electron momentum, \vec{p}_e is the scattered electron momentum. This groundbreaking result on the extended structure of the proton quoted in Equation 2.3 is shown in Figure 2.2. Following,

Hofstadter et. al. introduced the Dirac and Pauli form factors $F_1(q^2)$ and $F_2(q^2)$ as the deviations of the effective magnetic moment from a point-like anomalous magnetic moment and the deviation of the effective charge from a point-like charged particle, respectively.

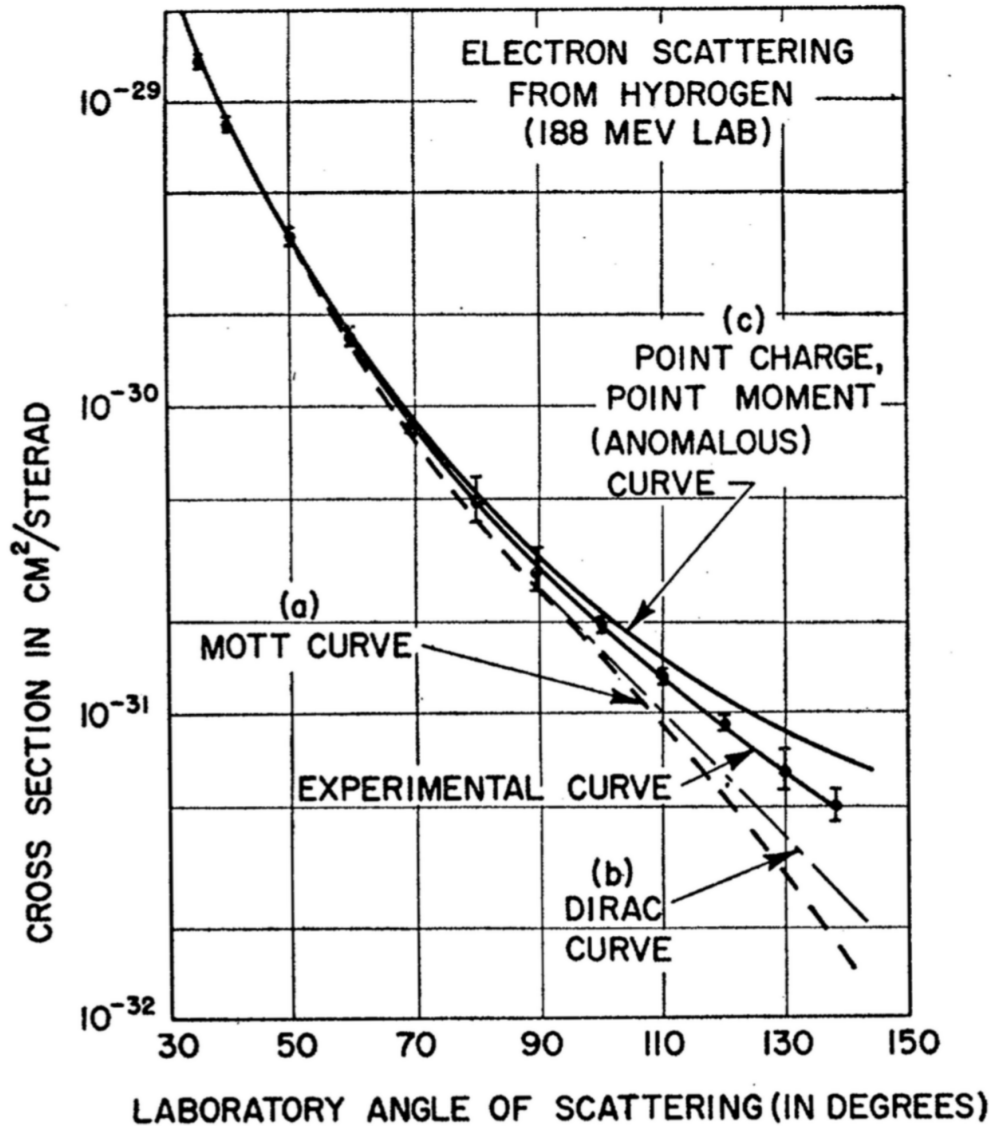


Fig. 2.2: Original results from Hofstadter [1]. "Electron-proton scattering from the proton with an incident energy of 188 Mev". The differential cross section for the electron-proton interaction is shown with respect to the scattering angle in the laboratory frame. The theoretical curves correspond to (a) a point-like spinless proton (Mott), (b) a point-like Dirac proton without an anomalous magnetic moment and (c) a point-like Dirac proton with an anomalous magnetic moment. The experimental data (dots with errors) support the extended structure of the proton associated with the electromagnetic form factors.

2.2.2 The hadronic current and the nucleon form factor

The extended structure of the nucleon can be studied with an electromagnetic probe. For this kind of investigation, typically elastic electron-nucleon scattering is used in the SL region, while a nucleon pair production after an electron-positron annihilation and the time-reversed process is used in the TL region. The Feynman diagram for the scattering process in the SL region is shown in Figure 2.3, with $l = e, \mu$ and $N = p, n$. In the leading order (Born approximation) the interaction is carried out through a single virtual photon. As described before, the interaction between point-like leptons and a virtual photon at the vertex can be calculated within the quantum electrodynamics (QED), while the interaction of the virtual photon with a nucleon can't be calculated precisely due to the lack of knowledge of the nucleon internal structure. A way to model the nucleon structure is the comparison between a measurement of two fundamental point-like particles and the mentioned processes involving a nucleon. The deviation takes into account the composite nature of the nucleon and can be expressed in terms of the electric and magnetic FF.

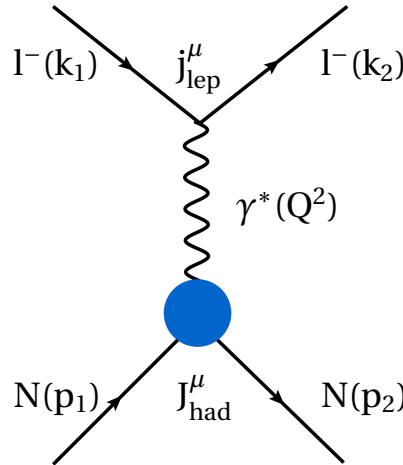


Fig. 2.3: Feynman diagram for lepton-nucleon scattering in leading order (Born approximation).

In the following, natural units ($\hbar = c = 1$) and the particle physics metric convention $(+, -, -, -)$ are used. For the understanding of the physical meaning of the electromagnetic FFs, the process of elastic lepton-nucleon scattering for the FF study in the SL region with the momentum transfer $Q^2 = -q^2 < 0$ (GeV) is discussed. The process is described via:

$$l^-(k_1) + N(p_1) \rightarrow l^-(k_2) + N(p_2) \quad (2.4)$$

where $k_1, k_2,$ and p_1, p_2 are the four momenta of the lepton and the nucleon before and after the interaction, respectively, using $p_i = (E_i, \vec{p}_i)$ and $k_i = (e_i, \vec{k}_i)$. The virtual photon

γ^* transfers the four momentum squared Q^2 , which can be described for a nucleon with mass m_N in rest ($\vec{p}_1 = 0, E_2 > m_N$) and E_2 as the energy of the recoiling nucleon as:

$$Q^2 = -q^2 = t = (k_1 - k_2)^2 = (p_1 - p_2)^2 = 2m_N E_2 - p_2^2 - p_1^2 = 2m_N E_2 - 2m_N^2 > 0 \quad (2.5)$$

The matrix element \mathcal{M} for such a process is a product of the leptonic and hadronic currents, j_{lep}^μ and J_{had}^μ , representing the interaction between the electron and the nucleon field:

$$-i\mathcal{M} = \frac{i}{q^2} j_{\text{lep}}^\mu J_{\text{had}}^\mu \quad (2.6)$$

The leptonic current j_μ can be expressed as:

$$j_{\text{lep}}^\mu = -ie\bar{u}(k_2)\gamma_\mu u(k_1) \quad (2.7)$$

with the in- and outgoing lepton Dirac spinors $u(k_1)$ and $\bar{u}(k_2)$, the lepton charge $-e$ and the in- and outgoing lepton four momenta k_1 and k_2 . The interaction vertex between the point-like lepton and the virtual photon is described through the Dirac gamma matrices $\gamma^\nu = \{\gamma^0, \gamma^1, \gamma^2, \gamma^3\}$. Considering the extended nucleon structure, the vertex Γ_{had}^μ has to be parametrized taking these deviations from a point-like particle into account. With the nucleon Dirac spinors $v(p_1)$ and $\bar{v}(p_2)$ for the nucleons initial and final state and the charge e , the nucleon current operator J_{had}^μ can be written as:

$$J_{\text{had}}^\mu = -ie\bar{v}(p_2)\Gamma_{\text{had}}^\mu v(p_1) \quad (2.8)$$

The strong interaction is invariant under Lorentz transformation, as well as under the parity and the charge conjugation [44]. The Lorentz invariance denotes a transformation behavior for J_{had}^μ analogous to j_{lep}^μ , implying a sole dependence on the in- and outgoing momenta p_1 and p_2 . The conservation of parity and charge fixes the number of contributions. Further, the nucleon current needs to satisfy the conservation of the electromagnetic current, all in total leading to a reduced description of the nucleon vertex Γ_{had}^μ including for spin- $\frac{1}{2}$ particles only two independent variables, the electromagnetic FFs $F_1(Q^2)$ and $F_2(Q^2)$. It has been shown in [45], [33] that the most general form for the hadronic current J_{had}^μ satisfies relativistic invariance and current conservation and can be expressed as:

$$J_{\text{had}}^\mu = -ie\bar{v}(p_2)\Gamma_{\text{had}}^\mu v(p_1) = ie\bar{v}(p_2) \left[F_1(Q^2)\gamma^\mu + F_2(Q^2)\frac{i\sigma^{\mu\nu}q_\nu}{2m_N} \right] v(p_1) \quad (2.9)$$

with $\sigma^{\mu\nu} = 1/2 [\gamma^\mu, \gamma^\nu]$. Taking into account the hermiticity of the hadronic current operator, which implies that the FFs $F_1(Q^2)$ and $F_2(Q^2)$ are real functions, the amplitude of the lepton-nucleon process can be written as:

$$-i\mathcal{M} = \frac{-ig^{\mu\nu}}{Q^2} [ie\bar{u}(k_2)\gamma^\mu u(k_1)] [-ie\bar{v}(p_2)\Gamma^\nu(p_1, p_2)v(p_1)] \quad (2.10)$$

with $g^{\mu\nu}$ as the metric tensor and $F_1(Q^2)$ and $F_2(Q^2)$ the helicity conserving Dirac- and the helicity flip Pauli form factor. Following the discussion, the differential cross section for unpolarized lepton-nucleon scattering in the laboratory frame can be written as:

$$\frac{d\sigma}{d\Omega_{\text{lab}}} = \left(\frac{d\sigma}{d\Omega}\right)_{\text{Mott}} \cdot \frac{E_1}{E_{\text{beam}}} \left[F_1^2(Q^2) + \tau \cdot \left(F_2^2(Q^2) + 2 \cdot (F_1(Q^2) + F_2(Q^2))^2 \tan^2 \frac{\theta_1}{2} \right) \right] \quad (2.11)$$

where $\frac{E_1}{E_{\text{beam}}} = (1 + \tau)^{-1}$ is the recoil factor with $\tau = Q^2/4m_N^2$ and θ_1 is the scattering angle of the outgoing lepton in the laboratory frame.

In many experiments a different parametrization of the nucleon electromagnetic FFs is used. This parametrization allows to decouple the electric and magnetic information encoded in the FFs. The Sachs FFs are linear combinations of the Dirac- and Pauli FFs, expressing the electric and magnetic FFs $G_E(Q^2)$ and $G_M(Q^2)$ as:

$$\begin{aligned} G_E(Q^2) &= F_1(Q^2) - \tau F_2(Q^2) \\ G_M(Q^2) &= F_1(Q^2) + F_2(Q^2) \end{aligned} \quad (2.12)$$

Considering this linear combination of the Dirac- and Pauli- FFs, the cross section in Equation 2.11 can be written in a compact form and is named after Rosenbluth:

$$\frac{d\sigma}{d\Omega_{\text{lab}}} = \left(\frac{d\sigma}{d\Omega}\right)_{\text{Mott}} \cdot \left[\frac{G_E^2(Q^2) + \tau G_M^2(Q^2)}{1 + \tau} + 2\tau G_E^2(Q^2) \tan^2 \frac{\theta}{2} \right] \quad (2.13)$$

In the TL momentum transfer region with $q^2 = -Q^2 > 0$ the electromagnetic FFs of the nucleon can be studied through the reaction shown in the lowest order in Figure 2.4:

$$l^-(k_1) + l^+(k_2) \rightarrow N(p_1) + \bar{N}(p_2) \quad (2.14)$$

or the corresponding time-reversed process:

$$N(p_1) + \bar{N}(p_2) \rightarrow l^-(k_1) + l^+(k_2) \quad (2.15)$$

In general, the leptonic side of the reaction isn't limited to electrons, but can also be realized with a muon-antimuon pair, but here only the case of an electron-positron annihilation will be discussed (a discussion of the reaction in Equation 2.15 can be found in Reference [46]). Since there are no free neutron targets available, the focus here lies on the electron-positron annihilation with a following nucleon-antinucleon production.

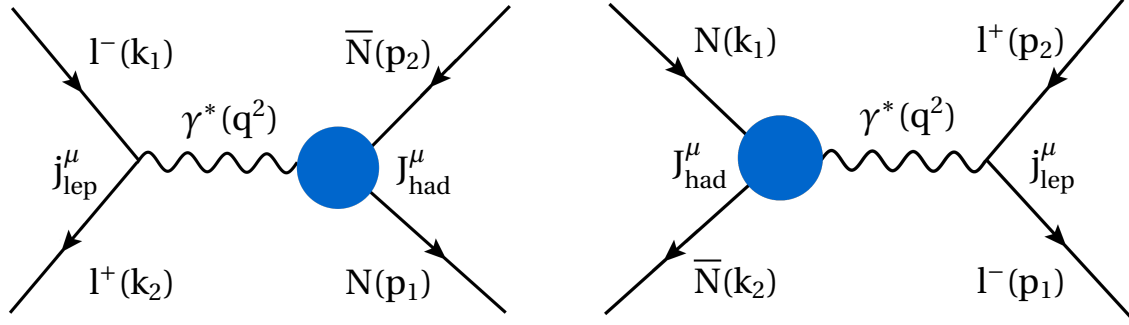


Fig. 2.4: Feynman diagram for (left) the lepton-antilepton annihilation with a following nucleon-antinucleon production and (right) the reversed process, both in leading order.

As for the SL region, the four momenta in brackets denote the in- and outgoing momenta of the involved particles. The momentum transfer squared follows the identity:

$$q^2 = (k_1 + k_2)^2 = s \quad (2.16)$$

The momentum transfer squared in Born approximation is equal to the center of mass energy of the electron-positron annihilation and is positive, as can be shown in the laboratory frame:

$$s = (k_1 + k_2)^2 = (p_1 + p_2)^2 = 2m_N^2 + 2p_1 p_2 > 4m_N^2 \quad (2.17)$$

The differential cross section for the process in Equation 2.14 in Born approximation and the center-of-mass system (CMS), where electron and positron have the momenta $p_{e^+} = -p_{e^-}$, can be written as following [47]:

$$\left(\frac{d\sigma}{d\Omega} \right)_{e^+e^- \rightarrow \bar{N}N} = \frac{\alpha_{em}^2 \beta C(q^2)}{4q^2} \left[|G_M^N(q^2)|^2 (1 + \cos^2 \theta) + |G_E^N(q^2)|^2 \frac{1}{\tau} \sin^2 \theta \right] \quad (2.18)$$

where θ is the angle between the electron and the nucleon (see for definition Figure 2.5), $\beta = \sqrt{1 - 4m_N^2/q^2}$ the velocity of the nucleon or the antinucleon, $\tau = q^2/4m_N^2$ as in Equation 2.11 but with an opposite sign, and $C(q^2)$ the so-called S-wave Sommerfeld-Gamow factor [48], which takes into account the QED coulomb interaction between

proton and antiproton, which is especially important at the nucleon pair production threshold:

$$C(y) = \begin{cases} \frac{y}{1-e^{-y}} & \text{for } p\bar{p} \\ 1 & \text{for } n\bar{n} \end{cases} \quad y = \frac{2m_p \alpha_{em} \pi}{q\beta} \quad (2.19)$$

The Sommerfeld-Gamow factor is the reason, that the cross section for the $e^+e^- \rightarrow p\bar{p}$ process differs from zero at threshold $q^2 = 4m_p^2$, while the corresponding cross section for $e^+e^- \rightarrow n\bar{n}$ is expected to be zero at the production threshold. Taking Equation 2.18 into account, a disentangled determination of the electric and magnetic FF $|G_E^N(q^2)|$ and $|G_M^N(q^2)|$ is possible through an analysis of the final state particles' angular dependence.

The total cross section, after integrating Equation 2.18 over the solid angle, is:

$$\sigma_{e^+e^- \rightarrow \bar{N}N} = \frac{4\pi\alpha_{em}^2\beta C(q^2)}{3q^2} \left[|G_M^N(q^2)|^2 + |G_E^N(q^2)|^2 \frac{1}{2\tau} \right] \quad (2.20)$$

Historically, the so-called effective form factor $|G_{\text{eff}}^N(q^2)|$ can be introduced, which helps to compare results between different experiments and describes in particular the deviation from the cross section for a point-like nucleon:

$$|G_{\text{eff}}^N(q^2)| = \sqrt{\frac{\sigma_{e^+e^- \rightarrow \bar{N}N}(q^2)}{\sigma_{e^+e^- \rightarrow \bar{N}N}^{\text{point}}(q^2)}} = \sqrt{\frac{2\tau |G_M^N(q^2)|^2 + |G_E^N(q^2)|^2}{2\tau + 1}} \quad (2.21)$$

with the point-like cross section defined as:

$$\sigma_{e^+e^- \rightarrow \bar{N}N}^{\text{point}}(q^2) = \frac{4\pi\alpha_{em}^2\beta C(q^2)}{3q^2} \left[1 + \frac{1}{2\tau} \right] \quad (2.22)$$

As described above, the Sommerfeld-Gamow factor leads to a non-vanishing point-like cross section for the proton pair production $e^+e^- \rightarrow p\bar{p}$ at threshold $q^2 = 4m_p^2$, while in the case of the neutron pair production $e^+e^- \rightarrow n\bar{n}$, the point-like cross section drops to zero:

$$\sigma_{e^+e^- \rightarrow p\bar{p}}^{\text{point}}(4m_p^2) = \frac{\pi^2\alpha_{em}^3}{2m_p^2} = 0.848 \text{ nb}, \quad \sigma_{e^+e^- \rightarrow n\bar{n}}^{\text{point}}(4m_n^2) = 0 \quad (2.23)$$

With the definition of the effective FF $|G_{\text{eff}}^N(q^2)|$ in Equation 2.21 and the point-like cross section in Equation 2.22, the integrated cross section can be expressed as:

$$\sigma_{e^+e^- \rightarrow \bar{N}N} = \sigma_{e^+e^- \rightarrow \bar{N}N}^{\text{point}}(q^2) \times |G_{\text{eff}}^N(q^2)|^2 \quad (2.24)$$

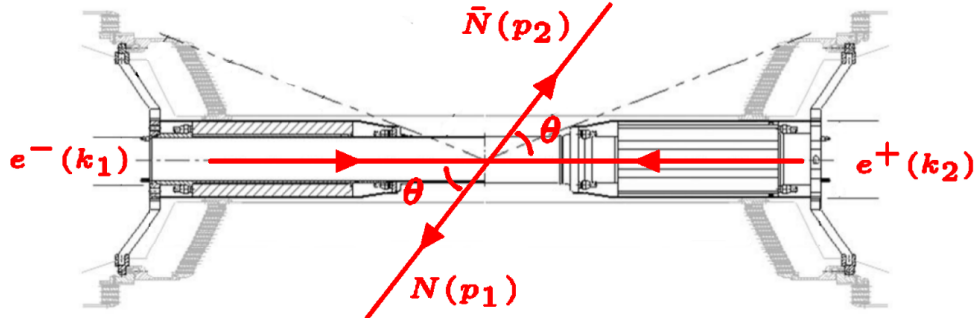


Fig. 2.5: The BESIII experiment beam pipe with the interaction point in the middle of the schematic drawing. The angle θ as defined in the Equation 2.18 in the CMS as the angle between the electron beam direction and the outgoing nucleon. For the extraction of the electromagnetic FFs, the theoretical description makes no difference between the nucleon or its anti-counterpart. In the data analysis part of this thesis, the angle θ is defined between the positron beam direction and the outgoing antineutron.

The electric and magnetic form factors,

$$G_E^N(q^2) = F_1^N(q^2) + \tau F_2^N(q^2) \quad G_M^N(q^2) = F_1^N(q^2) + F_2^N(q^2) \quad (2.25)$$

introduced in Equation 2.12, are by definition equal at threshold $q^2 = 4m_N^2$. While the identity $|G_E^N(4m_N^2)| = |G_M^N(4m_N^2)|$ is obviously only valid at the production threshold, most experiments published results for $|G_{\text{eff}}^N(q^2)| = |G_E^N(q^2)| = |G_M^N(q^2)|$ for momentum transfer squared values $q^2 > 4m_N^2$ above the production threshold. The effective FF $|G_{\text{eff}}^N(q^2)|$ is used to indicate the deviation of the experimentally measured cross section from a cross section for point-like nucleons. Additionally, it is used to compare the results between the time-reversed processes $l^+l^- \rightarrow \bar{N}N$ and $\bar{N}N \rightarrow l^+l^-$ with their different differential cross section shown in the Equations 2.20 and 2.44.

The Born cross section in Equation 2.20 is experimentally not accessible, since higher order processes always take place during a nucleon-antinucleon production. These radiative corrections need to be taken into account when extracting the Born cross section from the observed cross section in the experiment. This is possible via the introduction of a so-called radiative correction factor $(1 + \delta)$ which includes one or several corrections as shown in Figure 2.6:

$$\sigma_{e^+e^- \rightarrow \bar{N}N}^{\text{observed}} = (1 + \delta) \times \sigma_{e^+e^- \rightarrow \bar{N}N}^{\text{Born}} \quad (2.26)$$

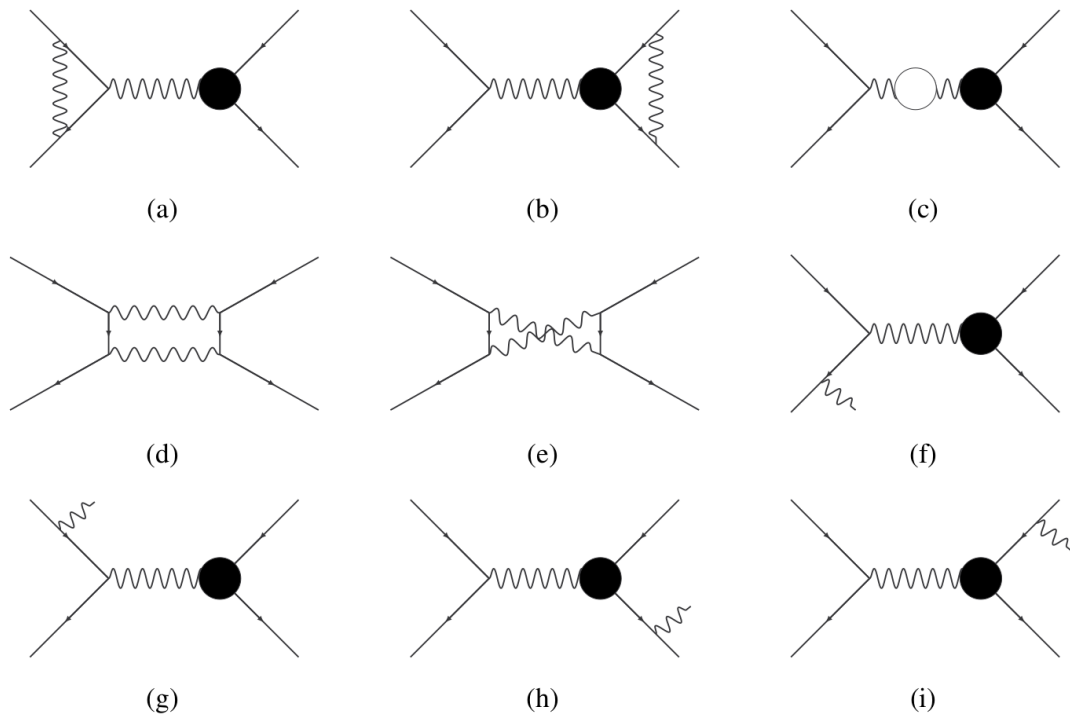


Fig. 2.6: Feynman diagrams for the first-order correction to $e^+e^- \rightarrow N\bar{N}$. (a) Virtual lepton vertex correction, (b) virtual hadron vertex correction, (c) vacuum polarization, (d) and (e) two-photon exchange, (f) and (g) initial state radiation, (h) and (i) final state radiation. The corrections (b), (h) and (i) don't contribute to the process $e^+e^- \rightarrow n\bar{n}$, due to the missing electric charge. (Original figures from [49]).

The radiative correction factor $(1 + \delta)$ needs to be calculated from theory. It takes into account several virtual and real corrections and can contain:

- Virtual corrections coming from the interference between the Born process, shown in Figure 2.3, and the processes shown in the Feynman diagrams for the (a) leptonic vertex, (b) hadronic vertex, (c) vacuum polarization, (d-e) two-photon exchange.
- Real photon corrections coming from bremsstrahlung and including the processes shown in the Feynman diagrams for (f-g) the initial state radiation, (h-i) the final state radiation, and their interferences.

Not all of these corrections apply in each physical process used for the nucleon FF investigation. The corrections shown in (h) and (i) aren't present in the case of the signal process $e^+e^- \rightarrow n\bar{n}$ in this thesis. The reason is the missing electrical charge of the neutron and antineutron.

2.2.3 Asymptotic properties and boundary conditions

In the limit of $Q^2 \rightarrow 0$ the Dirac and Pauli form factors are normalized to the charge and magnetic moment of the nucleons, denoted with μ_p for proton and μ_n for the neutron:

$$\begin{aligned} \lim_{Q^2 \rightarrow 0} F_1^p(Q^2) &= 1, & \lim_{Q^2 \rightarrow 0} F_2^p(Q^2) &= \mu_p - 1 \\ \lim_{Q^2 \rightarrow 0} F_1^n(Q^2) &= 0, & \lim_{Q^2 \rightarrow 0} F_2^n(Q^2) &= \mu_n \end{aligned} \quad (2.27)$$

with $\mu_p = 2.7928473508(85)\mu_N$ and $\mu_n = -1.91304272(45)\mu_N$ the nucleon magnetic moments in units of the nuclear magneton $\mu_N = e\hbar/2m_N$ [50] (page 119), which express the magnetic dipole moments of heavy particles, with e the electron charge magnitude. The normalization of the Sachs FFs, introduced in Equation 2.25, at $Q^2 \rightarrow 0$ is:

$$\begin{aligned} \lim_{Q^2 \rightarrow 0} G_E^p(Q^2) &= 1, & \lim_{Q^2 \rightarrow 0} G_M^p(Q^2) &= \mu_p \\ \lim_{Q^2 \rightarrow 0} G_E^n(Q^2) &= 0, & \lim_{Q^2 \rightarrow 0} G_M^n(Q^2) &= \mu_n \end{aligned} \quad (2.28)$$

In the TL region using the process in Equation 2.14, the nucleon FF can be only extracted for momentum transfers larger than the production threshold of the nucleon-antinucleon pair $q^2 \geq (2m_N)^2$. From Equation 2.25 and $\tau = 1$, which corresponds to $q^2 = (2m_N)^2$, for electric and magnetic FFs follows:

$$|G_E(4m_N^2)| = |G_M(4m_N^2)| \quad (2.29)$$

The region between $0 < q^2 < (2m_N)^2$ is called "unphysical", since below the nucleon pair production threshold. Nucleon FFs can be studied in this region by processes of the kind of $\bar{p}p \rightarrow \pi^0 l^+ l^-$ with l^\pm ($l = e, \mu$) leptons [51], or by the channel $\bar{p}p \rightarrow \pi^- l^+ l^-$. The possibility will be given, for example at the future PANDA experiment at the Fair facility.

In the SL region and in the so-called Breit frame (where the momentum of the electron is exactly reversed after the scattering process), the electric and magnetic FFs can be understood as the Fourier transform of the charge distribution and the magnetic moment distribution of the nucleon, respectively. In the $Q^2 \rightarrow 0$ limit the slopes of the FFs are the electric and magnetic charge radii by definition:

$$\langle r_E^2 \rangle = -6 \frac{dG_E(Q^2)}{dQ^2} \Big|_{Q^2=0}, \quad \langle r_M^2 \rangle = -6 \frac{dG_M(Q^2)}{\mu_{p,n} dQ^2} \Big|_{Q^2=0} \quad (2.30)$$

In the TL region, the physical meaning of the nucleon FF is less explicit. The classical paper in nucleon structure [46] states that in the TL momentum transfer, FFs can be related to the time evolution of the electromagnetic charges within the nucleon.

The nucleon electromagnetic form factors are functions of the 4-momentum transfer q^2 and defined for the whole region $-\infty < q^2 < \infty$, connected by dispersion relations. In the SL region the momentum transfer is negative $q^2 = -Q^2 < 0$. Taking into account the hermiticity of the current operator, the identity follows:

$$\langle N(p_2) | J_{\text{had}}^\mu | N(p_1) \rangle^* = \langle N(p_1) | J_{\text{had}}^{\mu\dagger} | N(p_2) \rangle = \langle N(p_1) | J_{\text{had}}^\mu | N(p_2) \rangle \quad (2.31)$$

with

$$\begin{aligned} \langle N(p_2) | J_{\text{had}}^\mu | N(p_1) \rangle^* &= ie\bar{N}(p_1) \left[F_1^*(Q^2)\gamma^\mu - F_2^*(Q^2)\frac{i\kappa\sigma^{\mu\nu}q_\nu}{2m_N} \right] N(p_2) \\ \langle N(p_1) | J_{\text{had}}^\mu | N(p_2) \rangle &= ie\bar{N}(p_1) \left[F_1(Q^2)\gamma^\mu + F_2(Q^2)\frac{i\kappa\sigma^{\mu\nu}q_\nu}{2m_N} \right] N(p_2) \end{aligned} \quad (2.32)$$

From Equation 2.31 and 2.32 it is obvious that:

$$F_{1,2}(q^2) = F_{1,2}^*(q^2) \quad (2.33)$$

and therefore it can be concluded, that SL FFs are real. FFs in the TL region fulfill the Schwarz reflection principle and are complex functions of q^2 [52].

The asymptotic behavior of the FFs can be calculated by means of dimensional counting rule or perturbative QCD [53], [54] in the limits of an infinite momentum transfer. In this limit the strong coupling constant α_s is small and can be treated perturbatively. The scaling behavior can be determined to:

$$\begin{aligned} \lim_{q^2 \rightarrow -\infty} F_1(q^2) &\sim (-q^2)^{-2}, & \lim_{q^2 \rightarrow -\infty} F_2(q^2) &\sim (-q^2)^{-3} \\ \lim_{q^2 \rightarrow -\infty} G_E(q^2) &\sim (-q^2)^{-2}, & \lim_{q^2 \rightarrow -\infty} G_M(q^2) &\sim (-q^2)^{-2} \end{aligned} \quad (2.34)$$

Taking the power-laws in Equation 2.34 and the analyticity of nucleon FFs, the Phragmén-Lindelöf theorem [55] can be applied, which implies that the asymptotic behavior from the SL region can be extended to the TL region, therefore it is possible to show that not only the scaling power is the same in TL and SL region, but also that the values for the FF in the TL region $G^{\text{TL}}(q^2)$ and in the SL region $G^{\text{SL}}(-q^2)$ must be the same in the limit of

$q^2 \rightarrow \infty$ [52], here e.g. for the magnetic FF G_M :

$$\lim_{q^2 \rightarrow -\infty} G_M(q^2) \sim \frac{G_M^{\text{SL}}}{(q^2)^2}, \quad \lim_{q^2 \rightarrow \infty} G_M(q^2) \sim \frac{G_M^{\text{TL}}}{(q^2)^2}, \quad \lim_{q^2 \rightarrow \infty} \frac{|G_M^{\text{TL}}(q^2)|}{|G_M^{\text{SL}}(-q^2)|} \rightarrow 1 \quad (2.35)$$

A direct conclusion from Equation 2.35 is that since the nucleon FFs are real function in the SL region, their limit in the TL region must also be real, which means that with diverging q^2 the real part vanishes slower than the imaginary part.

2.3 Overview of the nucleon form factor measurement

The nucleon electromagnetic FFs in the SL momentum transfer region can be experimentally accessed through lepton-nucleon scattering (Feynman diagram in Figure 2.3) and extracted via different methods: here the Rosenbluth separation and the polarization transfer methods, are discussed in detail. Results from these two methods show a large discrepancy in the proton FF ratio (shown in Figure 2.9), not simply explainable by well-known systematic sources. These unexpected results motivated a discussion on the impact of radiative corrections and the contribution of two photon exchange (TPE). The FFs of the proton are experimentally easier accessible because free proton targets are available, while the situation for the neutron FFs is more complicated due to the lack of free neutron targets. Instead, the deuteron or polarized ^3He targets are used in latter case, and the contribution from the proton is subtracted. In contrast to the SL momentum transfer region, nucleon FFs have been studied in the TL region with far less accuracy. This is due to the more complicated experimental situation, higher background contamination in the analyzed data and less total collected luminosity available for analysis. For the proton, results for the magnetic-, effective-, and electromagnetic FF ratio are available from electron-positron annihilation and the time reversed process. Further results are extracted with the Initial-State-Radiation (ISR) method. Results for the neutron exist exclusively as the effective FF (and the magnetic FF under some assumptions, discussed later), published by only three experiments so far, two of them using the process $e^+e^- \rightarrow \bar{n}n$, while one experiment extracts the effective FF of the neutron from the processes $e^+e^- \rightarrow \Lambda\bar{\Lambda}$ and $e^+e^- \rightarrow \Sigma^0\bar{\Sigma}^0$ under the minimal assumption of the U-spin invariance [56]:

$$G_{\text{eff}}^n(q^2) = \frac{3}{2}G_{\text{eff}}^\Lambda(q^2) - \frac{1}{2}G_{\text{eff}}^{\Sigma^0}(q^2) \quad (2.36)$$

In the following results for the nucleon FFs in SL and TL region are discussed.

2.3.1 Proton form factor from Rosenbluth separation

Historically, the first measurements of the Sachs FFs have been performed via elastic electron-proton scattering for the measurement of $G_E^p(Q^2)$ and $G_M^p(Q^2)$ with the Rosenbluth separation method [41], [43]. The differential Rosenbluth cross section describes the case of an unpolarized cross section and can be written in Born approximation as:

$$\frac{d\sigma(Q^2)}{d\Omega} = \left(\frac{d\sigma(Q^2)}{d\Omega} \right)_{\text{Mott}} \left(\frac{\epsilon G_E^2(Q^2) + \tau G_M^2(Q^2)}{\epsilon(1 + \tau)} \right), \quad \epsilon = \left(1 + 2(1 + \tau) \tan^2 \frac{\theta_e}{2} \right)^{-1} \quad (2.37)$$

with θ_e as the electron scattering angle, ϵ the virtual photon polarization and the Mott cross section as in Equation 2.2. In many experiments the "reduced cross section" is introduced:

$$\left(\frac{d\sigma(Q^2)}{d\Omega} \right)_R = \epsilon(1 + \tau) \left(\frac{d\sigma(Q^2)}{d\Omega} \right) / \left(\frac{d\sigma(Q^2)}{d\Omega} \right)_{\text{Mott}} = \tau G_M^2(Q^2) + \epsilon G_E^2(Q^2) \quad (2.38)$$

By measuring the reduced cross section for fixed Q^2 values under variation of ϵ allow to disentangle the electric and magnetic FFs. From a linear fit of $\left(\frac{d\sigma(Q^2)}{d\Omega} \right)_R$ to ϵ the electric FF $G_E(Q^2)$ is accessible through the slope, while the magnetic FF $G_M(Q^2)$ is proportional to the intercept at $\epsilon = 0$. Results from the Rosenbluth separation method show for both proton electromagnetic FFs an approximate dipole behavior:

$$G_E^p(Q^2) \sim \frac{G_M^p(Q^2)}{\mu_p} \sim G_D(Q^2), \quad \text{with } G_D(Q^2) = \frac{1}{\left(1 + \frac{Q^2}{0.71 \text{ (GeV)}^2} \right)^2} \quad (2.39)$$

An experimental drawback of the Rosenbluth separation method arises due to the fact that the reduced cross section in Equation 2.39 is dominated by $G_M(Q^2)$ while $G_E(Q^2)$ is suppressed with a factor $1/Q^2$. This leads to an increasing difficulty for the extraction of $G_E(Q^2)$ with rising Q^2 . Additionally, even at low Q^2 values the electric FF $G_E(Q^2)$ is suppressed by μ_p . Figure 2.8 shows the experimental results from the References [57] - [70] for $G_E^p(Q^2)$ and $G_M^p(Q^2)$ of the proton in the SL region divided by the dipole FF $G_D(Q^2)$ as defined in Equation 2.39. Additionally, results for $G_E^p(Q^2)$ and $G_M^p(Q^2)$ divided by the dipole FF $G_D(Q^2)$ and their ratio $R_{\text{em}}^p(Q^2) = G_E^p(Q^2)/G_M^p(Q^2)$ from a recent measurement at the A1 experiment in Mainz [71] are shown in Figure 2.7. The latter results are extracted from measured cross sections at more than 1400 individual Q^2 values between 0.004 to 1 GeV with a statistical precision below 0.2% for most of the measured energy points.

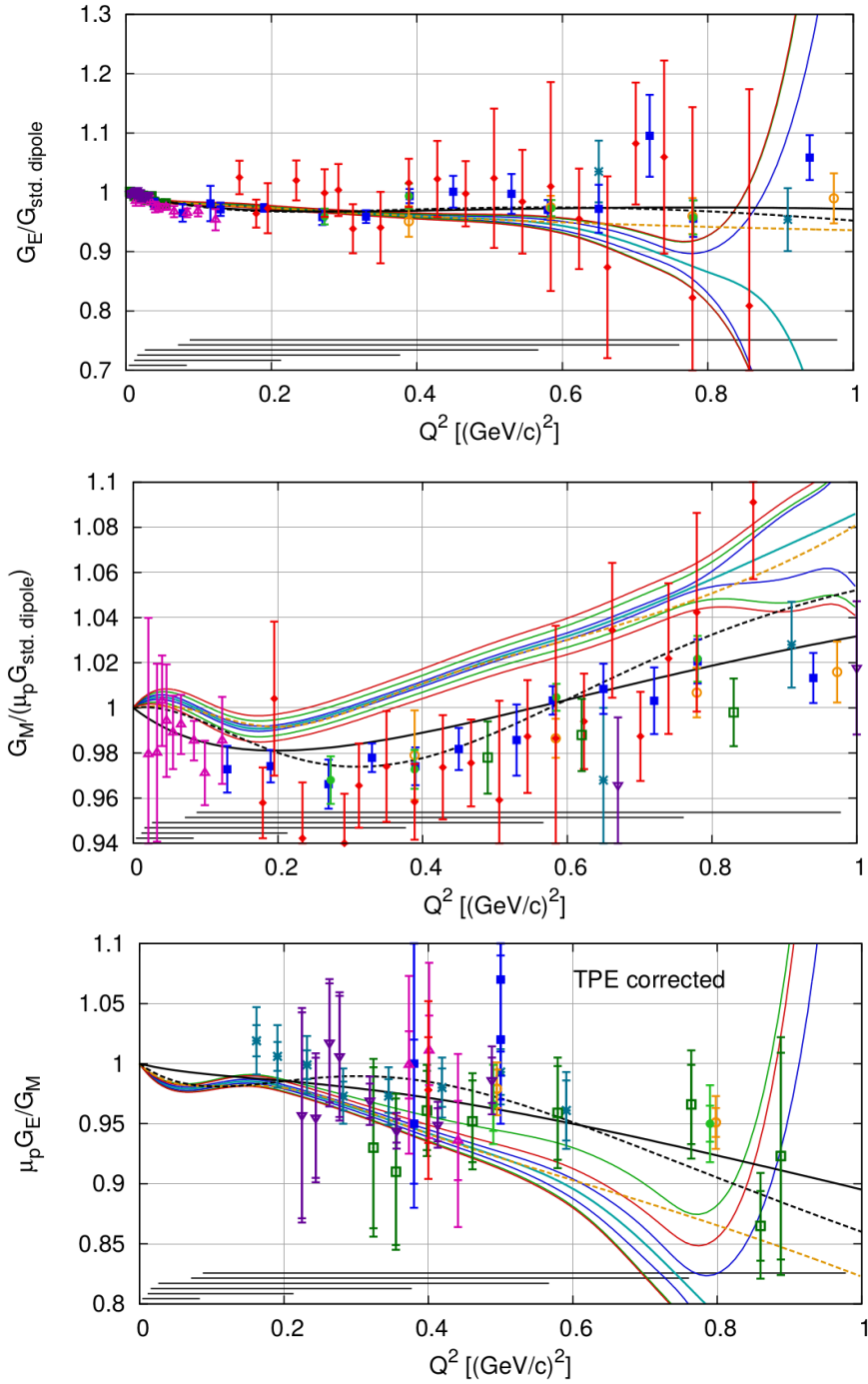


Fig. 2.7: The form factors $G_E^p(Q^2)$ (top), $G_M^p(Q^2)/\mu_p$ (middle) normalized to the standard dipole and $G_E^p(Q^2)/G_M^p(Q^2)$ (bottom) as a function of Q^2 . Yellow dashed line: fit to the data with a Friedrich-Walcher parametrization. Light blue line: Spline fit to data, area between dark blue lines: statistical 68% pointwise confidence band, between green lines: additional experimental systematic error, between red lines: additional theoretical systematic error. Black solid and dashed lines are previous fits to old data. Details on the analysis and the used data can be found in the Reference [71]. (Original figures from Reference [71].)

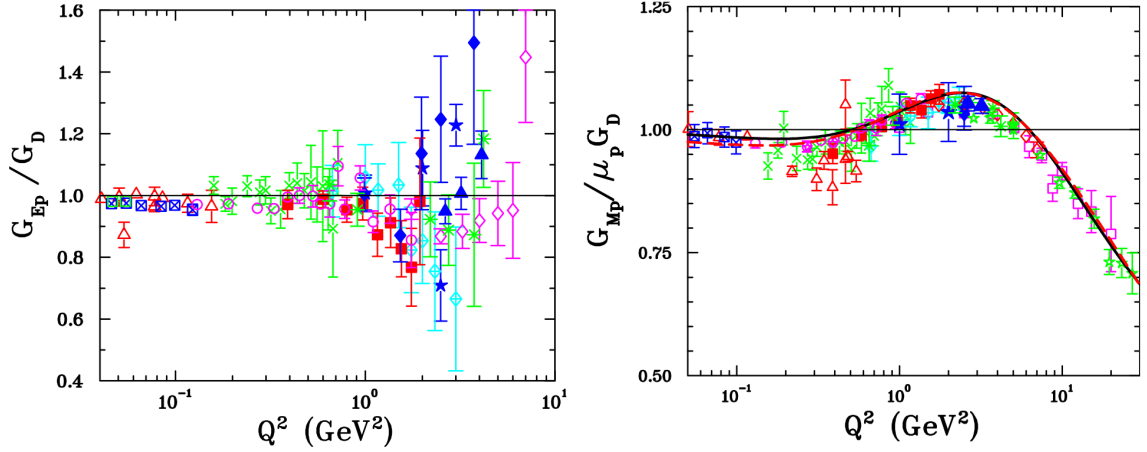


Fig. 2.8: (Left) Measurements of the electric proton FF divided by the dipole FF $G_E^p(Q^2)/G_D(Q^2)$ via Rosenbluth separation method. Results are quoted from: open triangles [57], crosses [58], open circles [59], filled diamonds [60], filled squares [61], crossed diamonds [62], crossed squares [63], open squares [64], filled stars [65] open diamonds [66], asteriks [67] and filled triangles [68]. (Right) Measurements of the magnetic proton FF divided by the dipole FF $G_M^p(Q^2)/\mu_p G_D(Q^2)$ via Rosenbluth separation method. Results are from same sources as for $G_E^p(Q^2)/G_D(Q^2)$ and additionally under the assumption $\mu_p G_E^p/Q^2 = 1$ from: open squares [69], open stars [70]. The solid (dashed) fit is from Reference [72] ([73]). (Original figures from [6]).

2.3.2 Proton form factor from polarization transfer

In the late 1990's an alternative experimental technique for the investigation of nucleon form factors in spacelike momentum transfer has been developed: the so-called polarization transfer measurement. Given a longitudinal polarized electron beam and an unpolarized proton target, this technique measures the polarization of the recoiling proton after the scattering:

$$\vec{e}^-(k_1) + p(p_1) \rightarrow e^-(k_2) + \vec{p}(p_2) \quad (2.40)$$

where \vec{e}^- and \vec{p} the polarized incident electron and the polarized proton after scattering and the polarization transfer. In contrast to the Rosenbluth separation, the polarization transfer method aims to measure the ratio between the electric and magnetic form factors $\mu_p G_E^p(Q^2)/G_M^p(Q^2)$ instead of the separated values. A possible deviation from unity would lead to the conclusion of different electric and magnetic charge distributions in the proton, conflicting to the statement in Equation 2.39. During the scattering process between the longitudinal polarized electron and the unpolarized proton, a polarization transfer occurs, which gives the method its name. After the interaction, the proton possesses a polarization

with two components with respect to the scattering plane, a longitudinal one P_1 and a transverse one P_t , which are in the Born approximation:

$$P_t = \sqrt{1 - \epsilon^2} (2h) \frac{G_M^2(Q^2)}{\sigma_R} \quad P_1 = -\sqrt{\frac{2\epsilon(1-\epsilon)}{\tau}} (2h) \frac{G_E(Q^2)G_M(Q^2)}{\sigma_R} \quad (2.41)$$

with h as the helicity of the incident electron. The ratio of the measured polarization components is related to the ratio of the electric and magnetic form factors:

$$\frac{G_E^p(Q^2)}{G_M^p(Q^2)} = -\frac{P_t}{P_1} \sqrt{\frac{\tau(1+\epsilon)}{2\epsilon}} \quad (2.42)$$

In contrast to the Rosenbluth separation method, the measured ratio of $\mu_p G_E^p(Q^2)/G_M^p(Q^2)$ has been found to deviate from unity. The decrease is almost linear with rising Q^2 and has been described by a linear fit to the experimental results [80] with:

$$\frac{\mu_p G_E^p(Q^2)}{G_M^p(Q^2)} = 1 - 0.13 \left(\frac{Q^2}{\text{GeV}^2} - 0.04 \right) \quad (2.43)$$

The results from the References [74] - [76] on the proton electromagnetic FF ratio with the polarization transfer method are shown in Figure 2.9 and compared to the results obtained with the Rosenbluth separation method (green points) from the References [77] - [79]. A significant discrepancy between the results extracted with the Rosenbluth separation and the polarization transfer method is observed. Results from the Rosenbluth separation are approximately consistent with 1, while the results from the polarization transfer method decrease almost linearly with Q^2 . One explanation for this deviation is the effect of two-photon exchange, shown as a Feynman diagram in Figure 2.6 (d) and (e). This effect is not taken into consideration for the results extracted with the Rosenbluth separation, while in the results from the polarization transfer method, the two-photon exchange contribution is canceled out due to the fraction P_t/P_1 in Equation 2.42.

2.3.3 Proton form factor from annihilation

The first results on the effective FF of the proton $|G_{\text{eff}}^p(q^2)|$ in the TL momentum transfer region have been published in 1973 by the ADONE73 experiment in Frascati, Italy [81], measured in the process $e^+e^- \rightarrow p\bar{p}$ using Equation 2.20 and 2.21. Results from the same channel and method have been published over the years by several experiments including FENICE [82], [22] and [83], the DM1 and DM2 experiments [84], [25] and [85], CLEO-c [86], BESII and BESIII [87] and [88], and recently by the CMD-3 collaboration [89]. Three experiments studied the effective FF of the proton through the time-reversed channel

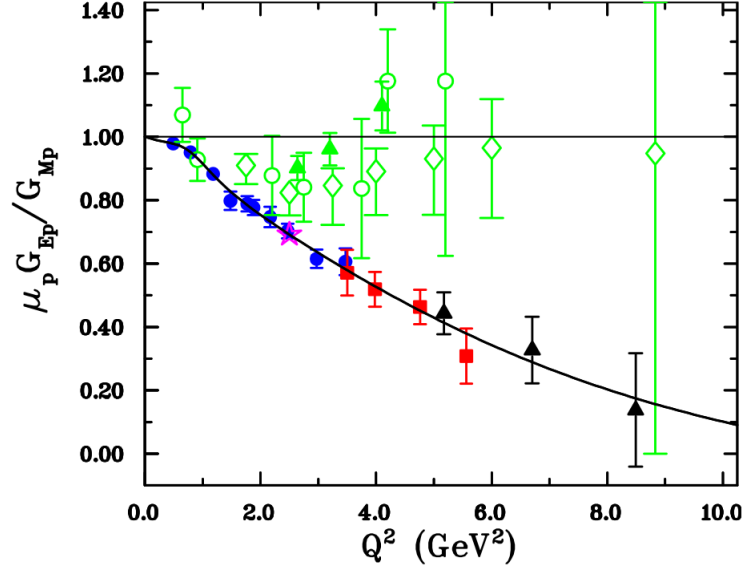


Fig. 2.9: Results on the ratio between the electric and magnetic proton form factor extracted with the polarization transfer method. The blue circles, red squares and black triangles are the results from [74] - [76], respectively. The green points are results with the Rosenbluth separation method for comparison, quoted from [77] - [79]. The black line is a fit from Kelly [72] with parameters given in [6]. (Original figure from [6]).

$p\bar{p} \rightarrow e^+e^-$, the E760 [90] and the E835 experiment [91], as well as the PS170 experiment [92]. The cross section in Born approximation for this process can be written as (neglecting the electron mass):

$$\frac{d\sigma(q^2)}{d\cos\theta_e} = \frac{\pi\alpha^2}{2q^2\beta_p} \left[\frac{1}{\tau} (1 - \cos^2\theta_e) |G_E^p(q^2)|^2 + (1 + \cos^2\theta_e) |G_M^p(q^2)|^2 \right] \quad (2.44)$$

with θ_e as the polar angle of the electron with respect to the antiproton direction in the hadronic center of mass frame, $\tau = q^2/(2m_p)^2$, and the velocity of the proton $\beta_p = \sqrt{1 - 4m_p^2/q^2}$.

The BaBar experiment studied the effective FF for the first time via the Initial-State-Radiation (ISR) method through the process $e^+e^- \rightarrow p\bar{p}\gamma_{\text{ISR}}$. Results from two different approaches have been published: for the tagged analysis (ISR photon detected) [93] and for the untagged analysis (ISR photon not detected) [94]. Recent results using the same approach has been published by the BESIII experiment in tagged [49] and untagged mode [95]. As described in the previous paragraph, the Born process of the l^+l^- annihilation is not observed independently, but always together with photons emitted by the lepton pair from the initial state in processes of the kind $l^+l^- \rightarrow N\bar{N} + x \times \gamma$ ($x \in \mathbb{N}$), shown in

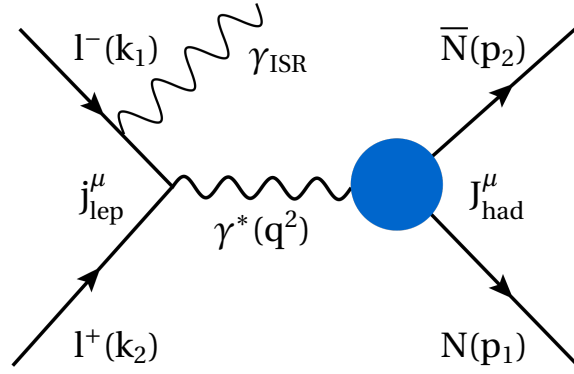


Fig. 2.10: Feynman diagram for the leading-order Initial-State-Radiation process $l^+l^- \rightarrow N\bar{N}\gamma_{\text{ISR}}$.

Figure 2.6 (f) and (g). While not always detected due to a possible low energy of the ISR photon, this process can be used as an alternative technique to the direct annihilation for the extraction of the FFs. Emission of hard photons from the initial state reduces the momentum transfer squared by the virtual photon q^2 after the lepton-antilepton annihilation, hence also the invariant mass of the nucleon-antinucleon pair in the final state. Due to the continuous energy distribution of the ISR photons, the ISR technique allows to measure nucleon FFs from their production threshold $\sqrt{s} = 2m_N$ to the CMS energy of the collected data \sqrt{s} . A Feynman diagram for this process is shown in Figure 2.10. With this approach, large luminosity data samples collected at resonances above the nucleon-antinucleon production threshold can be used to study FFs over a wide kinematic range. The cross section for an electron-positron annihilation with an ISR emission in leading-order followed by a nucleon-antinucleon production can be written as:

$$\frac{d^2\sigma_{e^+e^- \rightarrow N\bar{N}\gamma_{\text{ISR}}}(q^2)}{dq^2} = \frac{1}{s}W(s,x)\sigma_{N\bar{N}}(q^2) \quad (2.45)$$

with

$$W^{\text{LO}}(s,x) = \frac{\alpha_{\text{em}}}{\pi x} \left(\ln \frac{s}{m_e^2} \right) (2 - 2x + x^2), \quad x = \frac{2E_{\gamma_{\text{ISR}}}^*}{\sqrt{s}} = 1 - \frac{q^2}{s} \quad (2.46)$$

where the radiator function $W^{\text{LO}}(s,x)$ represents the emission probability of the photon in the initial state in the leading-order [96], m_e is the electron (positron) mass and $E_{\gamma_{\text{ISR}}}^*$ denotes the ISR photon energy in the e^+e^- CMS frame. The FF ratio $R_{\text{em}}^{\text{P}}(q^2) = |G_{\text{E}}^{\text{N}}(q^2)|/|G_{\text{M}}^{\text{N}}(q^2)|$ can be extracted in q^2 bins through an angular dependence analysis with respect to θ^* which is the angle between the nucleon (or antinucleon) momentum in the $N\bar{N}$ rest frame and the momentum of the $N\bar{N}$ system in the e^+e^- CMS frame. Similar

to the FF extraction from the direct annihilation technique described above, the disentangled FFs can be determined with an additional measurement of the luminosity and the normalization. The huge advantage of the ISR technique is the possibility to measure nucleon FFs over a wide kinematic range and especially very close to the threshold, which is not possible in the direct annihilation process due to the vanishing nucleon momentum close to the production threshold $q^2 \sim 4m_N^2$, since the final state particles are produced practically at rest and can't reach the detector. A drawback is the reduced cross section due to the radiator function $W^{LO}(s, x) \sim \alpha_{em} \sim \frac{1}{140}$.

The collected world data on the effective FF of the proton are shown in Figure 2.11 (left). In the measurement of the BaBar experiment [93], an interesting periodic oscillation behavior of the effective FF has been found, shown in Figure 2.11 (right). While no definite explanation exists until now, Reference [97] suggests "an interference effect involving re-scattering processes at moderate kinetic energies of the outgoing hadrons" implying "the presence of a large imaginary part of the TL FF".

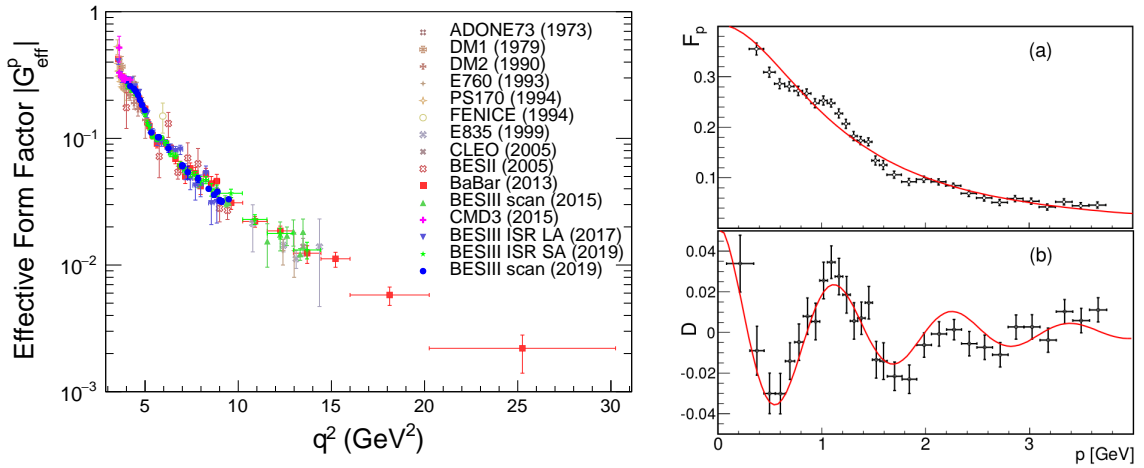


Fig. 2.11: (Left) World data on the effective FF of the proton $|G_{\text{eff}}^p|(q^2)$. Results are from the References [22], [25], [49], [81], [82], [83], [84], [85], [86], [87], [88], [90], [91], [92], [93], [95], [98], [101], and [103]. (Right) (a) Proton effective FF $|G_{\text{eff}}^p|(q^2)$ as a function of the relative final state particle momentum $|\vec{p}_p|$ from the BaBar measurement [93]. The red line is the regular background fit used by BaBar. (b) Effective FF results as in (a) after regular background fit subtraction. The red line is a fit with $F_{\text{osc}}(p) = A \cdot \exp(-Bp) \cdot \cos(Cp + D)$.

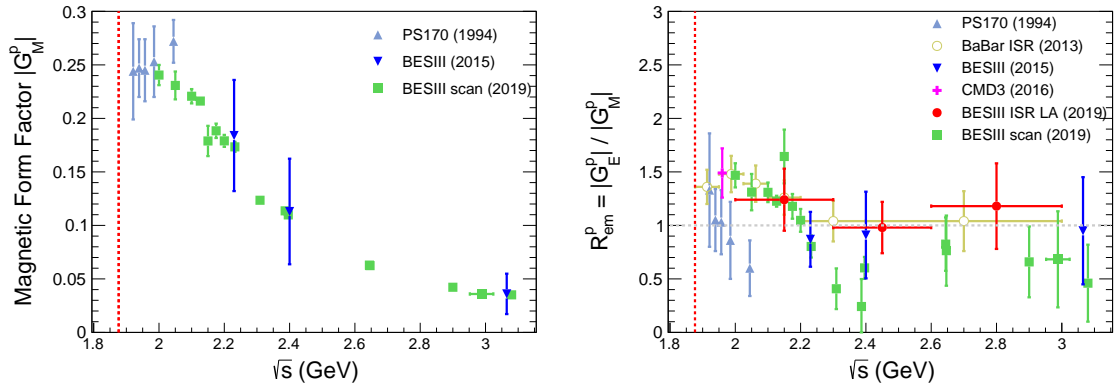


Fig. 2.12: (Left) World data on the individual magnetic FF of the proton $|G_M^p(q^2)|$. Results are from: PS170 in light blue triangles [92], BESIII scan in green squares [88] and in dark blue triangles [93]. (Right) World data on FF ratio $R_{em}^p(q^2) = |G_E^p(q^2)|/|G_M^p(q^2)|$ of the proton. Data quoted from: BESIII ISR in red full circles [95], BaBar in yellow empty circles [93], PS170 in light blue triangles [92], BESIII 2015 in dark blue triangles [88], BESIII in green squared [102] and CMD3 in pink diamonds [103]. The grey dotted-dashed line marks the value $R_{em}^p(q^2) = 1$. The red dotted-dashed line marks the production threshold.

Three experiments have published results on the magnetic FF of the proton in the TL region. The BESIII experiment used the process $e^+e^- \rightarrow \bar{p}p$ and the PS170 process measured the FF via the time-reversed $\bar{p}p \rightarrow e^+e^-$. A new measurement at BESIII [102] produced results over a large momentum transfer region $2.0 < \sqrt{s} = q < 3.08$ GeV with high precision. The results are shown in Figure 2.12 (left). The electromagnetic FF ratio $R_{em}^p(q^2) = |G_E^p(q^2)|/|G_M^p(q^2)|$ in the TL region has been measured by the BESIII [88], [102], and CMD3 [89] experiment via the process $e^+e^- \rightarrow \bar{p}p$. The BaBar experiment investigated the same process with the ISR technique, while the PS170 [92] experiment used the time-reversed channel. Results on the electromagnetic FF ratio of the proton are shown in Figure 2.12 (right).

2.3.4 Neutron form factor from electron scattering

Since no free neutron targets exist, the measurement of the neutron electric and magnetic FFs is more challenging than in the case of the proton. An additional experimental difficulty is the small magnitude of the electric FF. The first measurements on the neutron electric FF in the SL region have been performed based on the elastic electron-deuteron scattering 1971 with an experiment at DESY, Hamburg, [104]. Since the deuteron has a spin of 1, it requires three FFs, the charge, magnetic and the quadrupole FF $G_C(Q^2)$, $G_M(Q^2)$, and $G_Q(Q^2)$, respectively. The cross section formula describing this process is "Rosenbluth-like":

$$\frac{d\sigma}{d\Omega} = \left(\frac{d\sigma}{d\Omega} \right)_{\text{Mott}} \left[A(Q^2) + B(Q^2) \tan^2 \frac{\theta}{2} \right] \quad (2.47)$$

with the two structure functions $A(Q^2)$ and $B(Q^2)$ which can be separated via the Rosenbluth method. The structure functions depend on the three FFs as follows:

$$A(Q^2) = F_C^2(Q^2) + \frac{8}{9}\eta^2 F_Q^2(Q^2) + \frac{2}{3}\eta F_M^2(Q^2) \quad (2.48)$$

$$B(Q^2) = \frac{4}{3}\eta(1 + \eta)F_M^2(Q^2)$$

with $\eta = Q^2/4m_d^2$ and the deuteron mass m_d . It is not possible to extract all the three FFs from the two Equations in 2.48. Therefore also the polarization degree of freedom needs to be known, which is achieved by measuring the so called tensor polarization T_{20} :

$$T_{20} = \frac{-1}{\sqrt{2}I_0} \left[\frac{8}{3}\eta F_C F_Q + \frac{8}{9}\eta^2 F_Q^2 + \frac{1}{3}\eta(1 + 2(1 + \eta) \tan^2 \frac{\theta}{2}) F_M^2 \right] \quad (2.49)$$

with $I_0 = A(Q^2) + B(Q^2) \tan^2 \frac{\theta}{2}$. With this measurement, the decomposing of the three form factors is possible.

Several experiments measured $G_E^n(Q^2)$ by the recoil polarization method introduced above for the proton, in the quasi-elastic electron-deuteron scattering reaction $d(\vec{e}, e'\vec{n})p$, or in ${}^2\text{He}(\vec{e}, e'\vec{n})p$, the latter for example in Mainz at MAMI [105] and [106]. Hereby a polarized electron beam is used and the final state polarization of the neutron is measured. The formula used for the analysis is the same as in Equation 2.42. With this method, for the extraction of the electric form factor $G_E^n(Q^2)$, the knowledge of the magnetic form factor $G_M^n(Q^2)$ is required and usually taken from a model or parametrization, i.e. for the results in [107], a parametrization for $G_M^n(Q^2)$ from [108] has been used for the analysis.

Several experiments at MAMI in Mainz extracted the neutron electric FF by measuring the beam-target asymmetry in the ${}^3\vec{\text{He}}(\vec{e}, e'n)pp$ reaction, i.e. [109]. This is an exclusive quasi-elastic process, where electrons scatter from polarized ${}^3\text{He}$. The results from all introduced experimental methods are shown in Figure 2.13 (left).

The measurement of the neutron magnetic FFs can be divided into five groups of techniques: the cross section measurements via quasi-elastic electron-deuteron scattering [62], [110], elastic electron-deuteron cross section measurements [111], cross section measurements in the $d(e, e'p)n$ reaction i.e. [112], cross section ratio measurements in $d(e, e'n)p/d(e, e'p)n$ (mostly at MAMI in Mainz, i.e. [113] - [115], and polarization experi-

ments [116]. Quasi-elastic and elastic cross section measurements use the Rosenbluth separation method introduced in the proton FFs section above. For the quasi-elastic, both, the electron and the neutron are reconstructed in the final state and the reduced cross section can be written as follows:

$$\sigma_R = \epsilon_d(1 + \eta) \frac{\sigma(E, E', \theta_e)}{\sigma_M} = R_T + \epsilon_d R_L \quad (2.50)$$

with E and E' the initial and final state electron energy, θ_e the electron scattering angle, ϵ_d as defined in Equation 2.37 but substituting τ with η . R_T and R_L are the transverse and longitudinal response functions and proportional to $G_M^{n2}(Q^2) + G_M^{p2}(Q^2)$ and $G_E^{n2}(Q^2) + G_E^{p2}(Q^2)$, respectively, which can be separated via the Rosenbluth method for the extraction of the electric and magnetic FFs, taking the deuteron structure into account and subtracting the proton contributions. All results on the neutron magnetic FF are shown in Figure 2.13 (right).

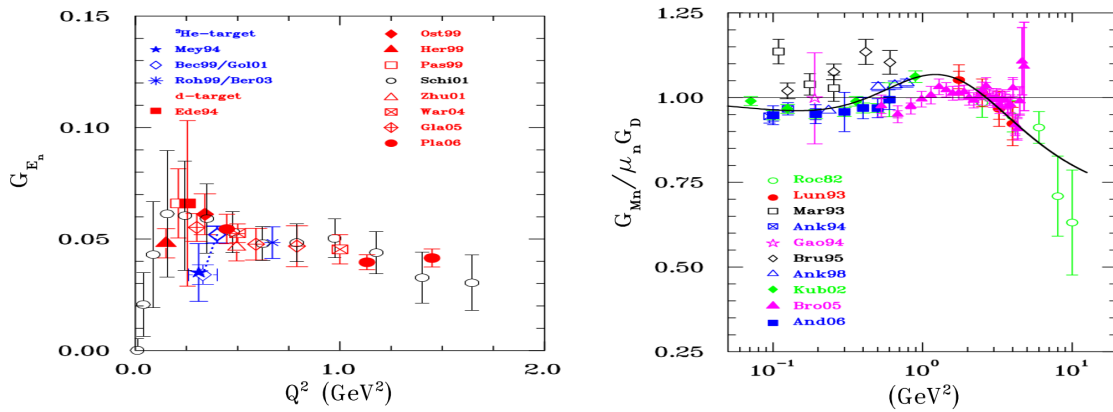


Fig. 2.13: (Left) Results on the electric neutron FF. Data from recoil polarization experiments with deuteron for red filled squares, diamonds, triangles, circles and crossed diamonds quoted from [117], [106], [105], [118], [107]. Data from beam asymmetry experiments with (a) polarized deuterium for red open squares, triangles and cross squares is quoted from [119], [120] and [121], and (b) with ³He for blue stars, blue open diamonds and blue asterisks' from [109], [122], [123] and [124]. Data from elastic eD scattering, calculated from the T_{20} tensor shown as empty white circles are from [125]. (Right) Results on the magnetic neutron FF divided by the dipole FF $G_M^n(Q^2)/\mu_n G_D(Q^2)$. Data is quoted for: green circles [126], red circles [127], black squares [128], blue crossed squares [113], black diamonds [129], blue triangles [114], green diamonds [115], pink triangles [130], blue squares [116] and pink stars [131] (Original figures from Reference [5]).

2.3.5 Neutron form factor ratio from electron scattering

As in case of the proton, the ratio of the electromagnetic FFs $\mu_n G_E^n(Q^2)/G_M^n(Q^2)$ has been measured with several experiments. The results are shown in Figure 2.14. All results come from double polarization approaches, where longitudinally polarized electrons interact with polarized deuterium [105], [106], [107], [117], [118], [119], [120], [121], [132], [133] or helium targets [109], [122], [123], [124], [134], [135], [136], [137], [138]. Either the experiments use quasi-elastic scattering of electrons and detect the recoil neutrons, or a beam-target asymmetry method is used for analysis. Since no unpolarized measurements for the neutron are available, a comparison of results as in the case of the proton for the deviation between the Rosenbluth separation and the polarization transfer technique can't be made here. Several results for the electric form factor introduced above have been calculated from ratio $\mu_n G_E^n(Q^2)/G_M^n(Q^2)$ measurements as shown in Figure 2.14.

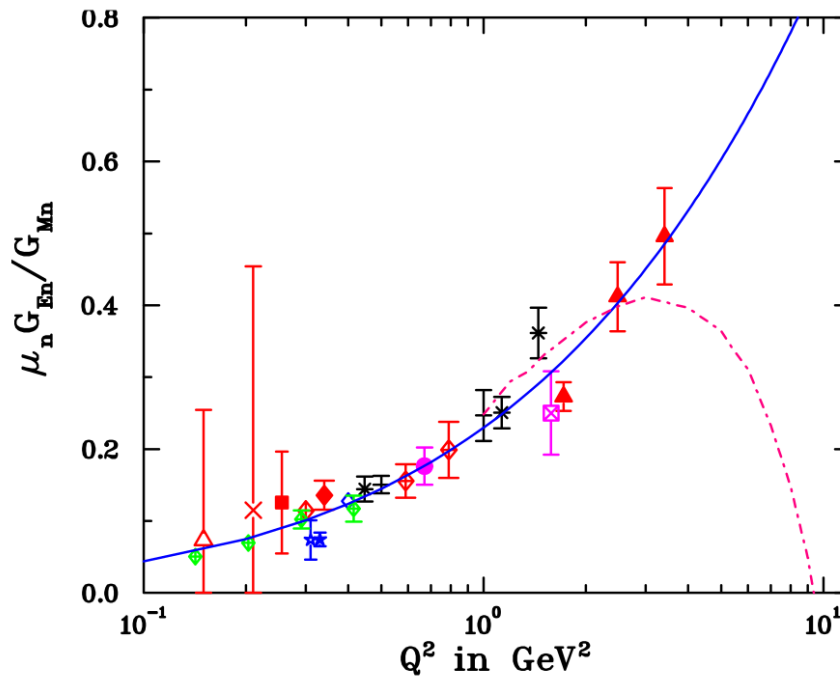


Fig. 2.14: Results on the ratio between the electric and magnetic neutron form factor measured in double polarization experiments from [105], [106], [107], [109], [117],[118], [119], [120], [121], [122], [123], [124], [132], [133], [134], [135], [136], [137], and [138]. The blue line is a fit from Kelly [72] with parameters given in [6], the dash-dotted line is a fit from a model introduced in Reference [139]. (Original figure from [6]).

2.3.6 Neutron form factor from annihilation

The effective FF of the neutron $|G_{\text{eff}}^n(q^2)|$ in the TL momentum transfer region has been investigated only by three experiments up to date. The FENICE experiment published the first results in 1994 [22], measured via the process $e^+e^- \rightarrow \bar{n}n$. Later, old data for the process $e^+e^- \rightarrow \Lambda\bar{\Lambda}$ from the DM2 experiment has been re-analyzed and results for the neutron effective FF have been extracted and published [25] under the assumption of the minimal U-spin invariance. Recently, the SND experiment [26] used the channel $e^+e^- \rightarrow \bar{n}n$ and published results on the Born cross section and effective FF close to the production threshold. All results for the effective FF of the neutron are shown in Figure 2.15. To extract the disentangled electric and magnetic FFs, as well as their ratio, an angular distribution analysis of the final state nucleons needs to be performed, as shown in Equation 2.18. No experiment so far gathered enough statistics to carry out this task. The only available results for the magnetic FF have been extracted by the FENICE experiment from the cross section similar to the effective FF under the assumption $|G_E^n| = 0$, which was favored from the study of the angular distribution of the neutron in the final state. The results are shown in Figure 2.16. No results on the electric FF of the FFs ratio of the neutron in the TL region are available.

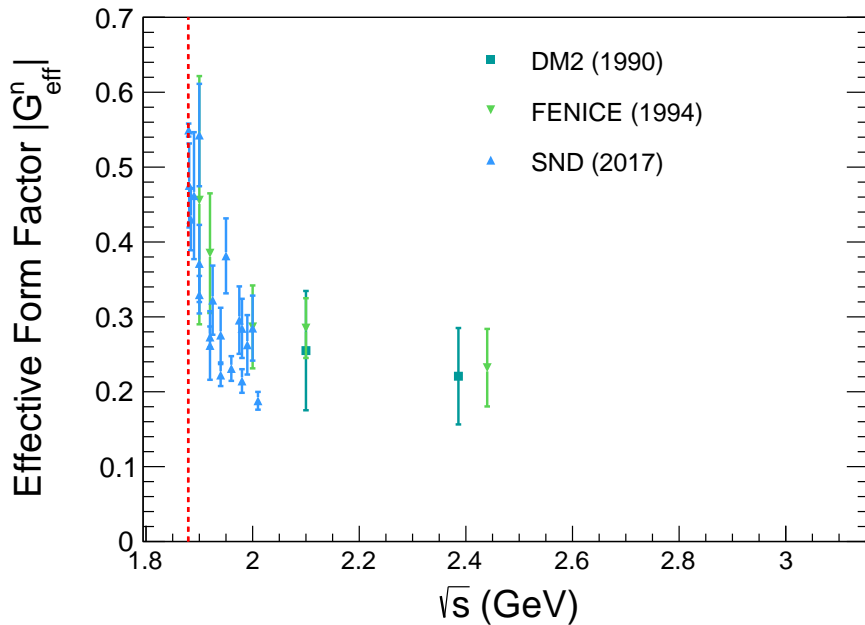


Fig. 2.15: World data on the effective FF of the neutron. Dark green squares are results from the DM2 experiment [25], light green triangles are results from the FENICE experiment [22], while blue triangles are results from the SND experiment [26]. The red line represents the production threshold for the process $e^+e^- \rightarrow \bar{n}n$.

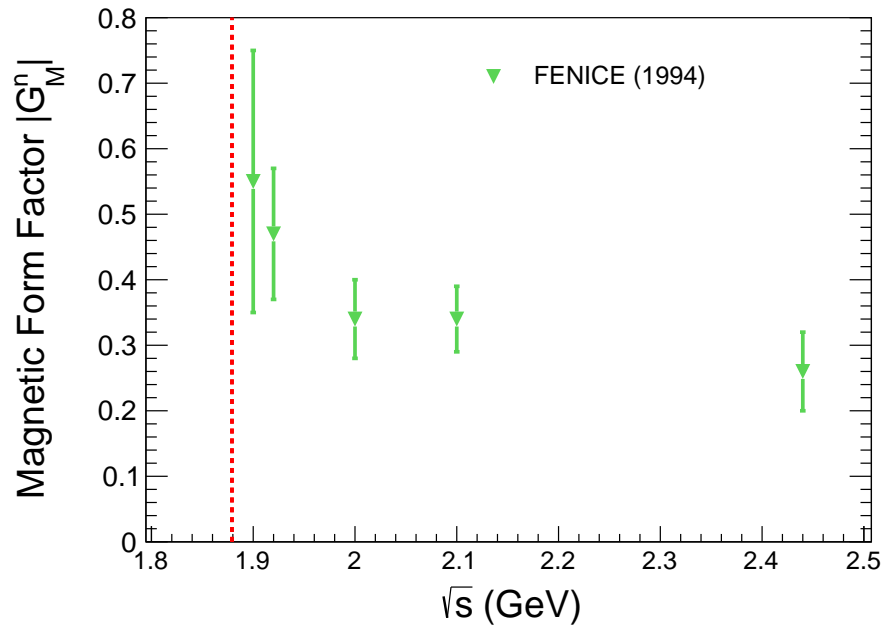


Fig. 2.16: The magnetic FF of the neutron from the FENICE experiment [22], extracted from the Born cross section under the hypothesis $|G_E^n(q^2)| = 0$. The red line represents the production threshold for the process $e^+e^- \rightarrow \bar{n}n$.

2.4 Parametrization of the electromagnetic form factor

Over the years, many attempts have been made on the theory side to understand and describe the nucleon properties and their inner dynamics. Since nucleon FFs encode the information on the strongly interacting many body-system structure, they are difficult to calculate within the QCD in the low momentum transfer region. Problems arise due to the requirement of non-perturbative methods and the involvement of approximations with limited range. The focus in this section lies on parametrizations, which are applicable to the whole momentum transfer range, the SL and the TL region.

2.4.1 Dipole behavior

One of the first attempts to parametrize the electromagnetic FFs of the nucleon has been introduced in [140], derived from a measurement of the inelastic electron-deuteron scattering. The description has been formulated before the discovery of quarks and uses a fit to data without any underlying theoretical justification. The formula takes into account the observed dipole behavior of the FF data.

$$G_E^p(Q^2) \approx \frac{G_M^p(Q^2)}{\mu_p} \approx \frac{G_M^n(Q^2)}{\mu_n} \approx \frac{G_E^n(Q^2)}{\tau\mu_n} = \frac{1}{\left(1 + \frac{Q^2}{0.71 \text{ (GeV)}^2}\right)^2}, \quad Q^2 = -q^2 \quad (2.51)$$

The parameters are $\tau = Q^2/4m_N^2$, the nucleon mass m_N , the magnetic moment of the proton and neutron μ_p and μ_n , respectively. The constant 0.71 (GeV^2) is extracted from the fit to data. Later, this parametrization has been modified in [141], to include a deviation from the pure dipole behavior, suggested from a fit to the data for the effective FF of the proton in the TL region:

$$G_M^p(q^2) = \mathcal{A} \cdot \frac{1}{\left(1 + \frac{q^2}{0.71 \text{ (GeV)}^2}\right)^2} \cdot \frac{1}{\left(1 + \frac{q^2}{m_a^2}\right)^2} \quad (2.52)$$

The parameters $\mathcal{A} = 22.5$ and $m_a^2 = 3.6 \pm 0.9 \text{ (GeV)}^2$ are extracted from the fit to the data, with the second expression describing the deviation from the dipole behavior. The discussion on the modified parametrization of the magnetic FF of the proton, shown above can be translated in a similar way to the magnetic FF of the neutron.

2.4.2 Perturbative QCD

With nucleons interacting strongly, a desirable parametrization should be based on the underlying QCD. Brodsky and Farrar have shown in [142] that the prediction by the quark counting rules valid at high momentum transfers leads to an asymptotic behavior of the nucleon electromagnetic FFs in the SL momentum transfer region. For a virtual photon with a high momentum transfer Q^2 , the nucleon appears to consist of three constituent quarks, moving collinear with the nucleon direction vector. The lowest order diagram for this process is shown Figure 2.17.

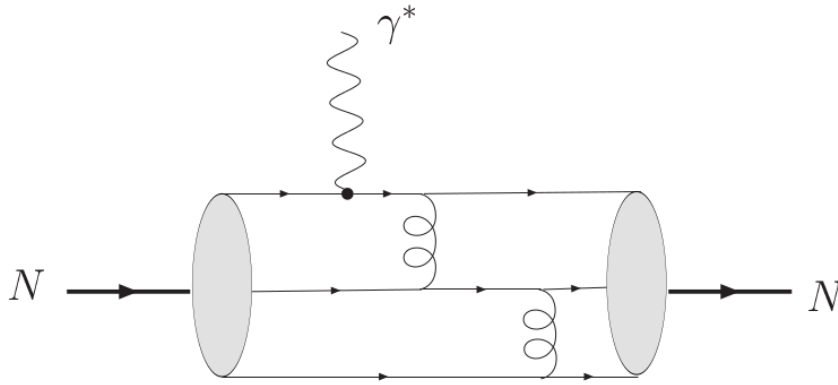


Fig. 2.17: One possible lowest order diagram in QED for the interaction between a virtual photon with high momentum and a nucleon in the pQCD framework. Original picture from [5].

The momentum of the photon is transferred equally between the three constituents through the exchange of two gluons. In total four vertices contribute to the photon-nucleon interaction, each with $\alpha_s^{1/2}$, therefore the nucleon FFs are proportional to α_s^2 , which leads to:

$$G_E(Q^2) = G_M(Q^2) \sim \frac{\alpha_s^2(Q^2)}{Q^4} \quad (2.53)$$

In the SL momentum range, α_s can be expressed in dependence of the number of quark flavors n_f and the QCD scale parameter as Λ_{QCD} (in lowest order):

$$\alpha_s(Q^2) \sim \frac{1}{\beta_0 \ln\left(\frac{Q^2}{\Lambda_{\text{QCD}}^2}\right)}, \quad \beta_0 = 11 - \frac{2}{3}n_f \quad (2.54)$$

The expressions in Equation 2.54 are formulated under the condition $Q^2 > \Lambda_{\text{QCD}}$. To translate this expression into the TL region, the following replacement is applied:

$$Q^2 \rightarrow -q^2, \quad \ln\left(\frac{Q^2}{\Lambda_{\text{QCD}}^2}\right) \rightarrow \left(\frac{q^2}{\Lambda_{\text{QCD}}^2}\right) - i\pi \quad (2.55)$$

with the condition $q^2 > \Lambda_{\text{QCD}}$. With the expressions in 2.54 and 2.55, Equation 2.53 parametrizes the TL FFs of the nucleon as following:

$$|G_E(q^2)| = |G_M(q^2)| = \frac{C}{q^4 \left[\ln\left(\frac{q^4}{\Lambda_{\text{QCD}}^2}\right) + \pi^2 \right]} \quad (2.56)$$

The parameters are determined in [143] to $C = 89.34 \text{ (GeV/c)}^2$ and $\Lambda_{\text{QCD}} = 0.3 \text{ (GeV/c)}$ from a fit to the TL data of the effective FF using the assumption $|G_{\text{eff}}(q^2)| = |G_E(q^2)| = |G_M(q^2)|$.

2.4.3 Dispersion-theoretical approach

In the dispersion-theoretical approach, FFs in the SL and TL region are related. In general, FFs in the TL region are complex function of q^2 and analytical, except for known cuts. In this framework they can be calculated only knowing their imaginary parts at these cuts. The approach can be applied to any complex function $F(z) = \mathcal{R}eF(z) + i\mathcal{I}mF(z)$, which meets the condition of analyticity, using the Cauchy integral:

$$F(z) = \frac{1}{2\pi i} \int_C dz' \frac{F(z')}{z' - z} \quad (2.57)$$

with C a closed path over the real axis and a semi-circle at infinity in the upper half-plane. If additionally $F(z)$ vanishes for $|z| \rightarrow \infty$, the dispersion relations for the real and imaginary part can be written as:

$$\begin{aligned} \mathcal{R}eF(q^2) &= \frac{1}{\pi} \mathcal{P} \int_{-\infty}^{\infty} dq'^2 \frac{\mathcal{I}mF(q'^2)}{q'^2 - q^2} \\ \mathcal{I}mF(q^2) &= -\frac{1}{\pi} \mathcal{P} \int_{-\infty}^{\infty} dq'^2 \frac{\mathcal{R}eF(q'^2)}{q'^2 - q^2} \end{aligned} \quad (2.58)$$

where \mathcal{P} is the Cauchy principal value. Following, the whole function $F(q^2)$ can be derived from only the real or imaginary part of it. In the dispersion analysis, the nucleon isoscalar and isovector FF contributions are studied separately. Based on the dispersion relation approach, a modified description for the nucleon FF parametrization is the Mainz model [144], which implements the phenomenological input from the vector meson dominance (more details in Section 2.4.8). The isoscalar and isovector components of the nucleon

FFs can be written as:

$$\begin{aligned}
 F_i^{\text{IS}}(q^2) &= \left[\sum_m \frac{a_{i,m}^{\text{IS}} L^{-1}(m_m^{\text{IS}})^2}{(m_m^{\text{IS}})^2 - q^2} \right] L(q^2) \\
 F_i^{\text{IV}}(q^2) &= \left[F_i^\rho(q^2) L(q^2) + \sum_{m \neq \rho} \frac{a_{i,m}^{\text{IV}} L^{-1}(m_m^{\text{IV}})^2}{(m_m^{\text{IV}})^2 - q^2} \right] L(q^2)
 \end{aligned}
 \tag{2.59}$$

with the function $L(q^2)$:

$$L(q^2) = \left[\ln \left(\frac{\Lambda^2 - q^2}{Q_0^2} \right) \right]^{-\gamma}
 \tag{2.60}$$

and with $i = 1, 2$, the factors $a_{i,m}^{\text{IS(IV)}}$ containing all information for the coupling of the virtual photon to the vector mesons and the transition of the vector mesons to the nucleon-antinucleon pair, m_m the meson masses, $F_i^\rho(q^2)$ describing the two-pion contribution, $L(q^2)$ controlling with Λ the transition to the pQCD inspired asymptotic behavior, γ the anomalous dimension, and $Q_0 \sim \Lambda_{\text{QCD}}$. The model describes the FF components through the 2π continuum including the $\rho(770)$, three additional vector-isovector poles $\rho'(1050)$, $\rho''(1465)$, $\rho'''(1700)$, and four vector-isoscalar meson poles $\omega(770)$, $\phi(1020)$, $S'(1650)$, and $S''(1680)$. The values for the free parameters can be found in [144] together with a detailed description of the model and the used constraints. Results for the nucleon FF parametrization in the TL momentum transfer region with this model are shown in Figure 2.18. It should be pointed out, that Figure 2.18 shows the parametrization for the magnetic FF for proton and neutron, but the experimental data shows the effective FFs.

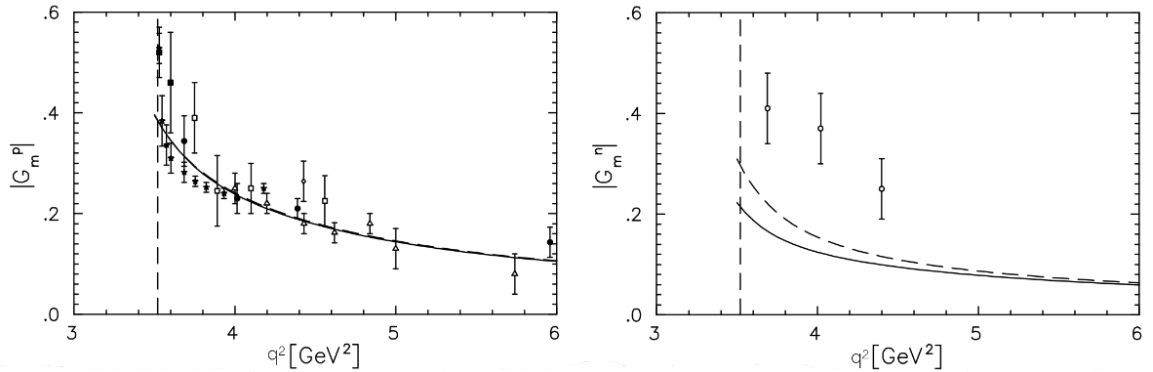


Fig. 2.18: Parametrization of the magnetic FFs of the proton and neutron in the TL region with the Mainz model [144] (experimental results are shown for the effective FFs), based on the dispersion relation approach. (Left) Results for the effective FF of the proton. (Right) Results for the effective FF of the neutron. The solid lines are the parametrization using three vector-isoscalar meson poles $\omega(770)$, and $\phi(1020)$ and $S'(1650)$. The dashed line is the same parametrization additionally including the contribution from the $S''(1680)$ pole. (Original figure from [144].)

2.4.4 Relativistic constituent quark model

In the constituent quark model (CQM), the nucleon is accounted as the ground state of a three-quark-system, confined in a potential. While the non-relativistic CQM can describe successfully the static properties of baryons like the magnetic moments [5], the calculation of the nucleon FFs with constituent masses small compared to the nucleon mass requires a relativistic treatment. To take this into account, the CQM with a linear confinement potential is extended by a quark-quark interaction carried out through the exchange of pseudo-scalar Goldstone bosons. More details on the underlying calculations for the parametrization of the nucleon FFs using the relativistic constituent quark model (rCQM) can be found in [145]. Results for the effective FFs of the proton and neutron in the TL momentum transfer region are shown in Figure 2.19.

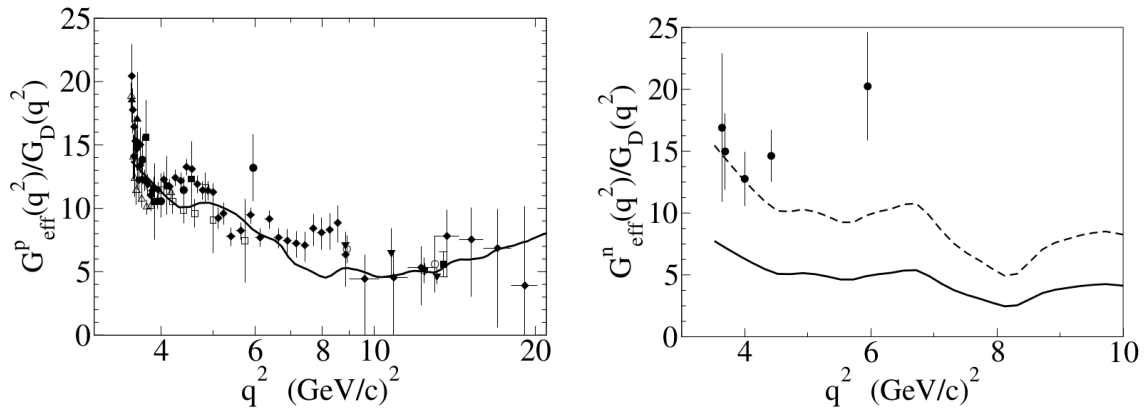


Fig. 2.19: Parametrization of the effective FFs of the proton and neutron in the TL region with the rCQM from [145]. (Left) Results for the effective FF of the proton from [101]. (Right) Results for the effective FF of the neutron from [24]. The solid lines are the parametrization with the rCQM full calculation. The dashed line is the same parametrization additionally multiplied by an arbitrary factor of 2. (Figure from [34].)

2.4.5 Lattice QCD simulation

The lattice QCD can be seen as a discrete version of the QCD. The formulation uses path integrals on a space-time lattice and bare quark masses and couplings as free parameters. The discretized lattice with the spacing a can be extrapolated in the limit $a \rightarrow 0$ to the continuum theory. Modern lattice calculations use the product of the lattice spatial box length L and the pion mass of $Lm_\pi = 4.2$ with the pion mass above $m_\pi = 149$ MeV which is larger than the physical value, equivalent to larger values for quark masses than the real measured ones. To extrapolate these results to the physical quark masses, the

chiral extrapolation needs to be applied. Details on the extrapolation can be found in the Reference [5]. The approach tunes the bare quark masses and coupling constant with respect to a , while the physical observables are left unchanged. A typical procedure starts with the choice of the coupling constant g to fix the lattice spacing and the masses for the three lightest quarks. Following, a physical quantity, for example the mass of the pion m_π and the nucleon mass in lattice units a is computed as a function of the quark masses. While the (unphysical) pion mass is used to fix the masses of the u and d quarks, the strange quark mass is fixed by the mass of the kaon or ϕ . The nucleon mass is determined by the extrapolation to the physical pion mass, with all other physical quantities following from this extrapolation. To calculate the nucleon FFs within the lattice QCD, two topological contributions need to be taken into account, which are shown in Figure 2.20 for the SL region. The left diagram shows the connected contribution, where the photon couples to one of the valence quarks. Between the quark lines, connected to the initial or final nucleon state, an arbitrary number of gluons is exchanged. If neglecting the fluctuations of these gluons into $\bar{q}q$ pairs, the calculation is denoted as quenched, in the other case as full, which includes also the sea-quark loops in the gluon lines. The right side of Figure 2.20 takes into account the $\bar{q}q$ loop coupling to the nucleon through gluon exchange. To calculate the FFs of the nucleon, the disconnected diagram (Figure 2.20 right) needs to be taken into account.

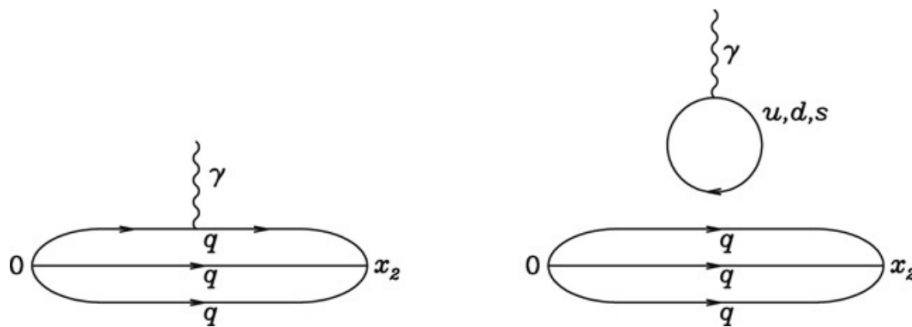


Fig. 2.20: Illustration of the two different contributions for the lattice QCD calculation of the nucleon FFs. (Left) The connected diagram, (right) the disconnected diagram is shown. (The original figure is taken from Reference [146]).

2.4.6 Chiral effective field theory

An effective field theory (EFT) is an approximation of an underlying fundamental theory with relevant degrees of freedom dependent on a specific energy scale Λ , where Λ is the boundary between the fundamental and effective regime. Since the QCD can't provide a

precise description of effects in the low momentum transfer regime, because the strong coupling constant α_s increases with a decreasing q^2 and no perturbative description can be performed, an EFT of the strong interaction in the low momentum transfer regime can be deployed to study basic symmetries and observables. The class of EFTs characterized by degrees of freedom different than the ones in the fundamental counterpart is called chiral (χ EFT).

As an example for the nucleon FF parametrization, using the χ EFT approach, results for the TL FF of the proton are discussed in the following. In Reference [147], the parametrization for the TL electromagnetic FF of the proton is developed by using four amplitudes, corresponding to the coupling between the e^+e^- and the $\bar{p}p$ systems and the coupled $^3S_1 - ^3D_1$ partial waves (details in [148]), taking into account the orbital angular momentum in the initial and final state. The total amplitude for the reaction $e^+e^- \rightarrow \bar{p}p$ can be written as a product of factors for the leptonic and hadronic vertices, reflecting if the coupling occurs in an S or D wave. The potential is derived within the χ EFT in [149] and fitted to the partial wave analysis (PWA) of $\bar{p}p$ scattering data in [150]. The results from this parametrization are shown for the effective FF of the proton $|G_{\text{eff}}^p(q^2)|$ and the FF ratio $|G_E^p(q^2)|/|G_M^p(q^2)|$ in Figure 2.21.

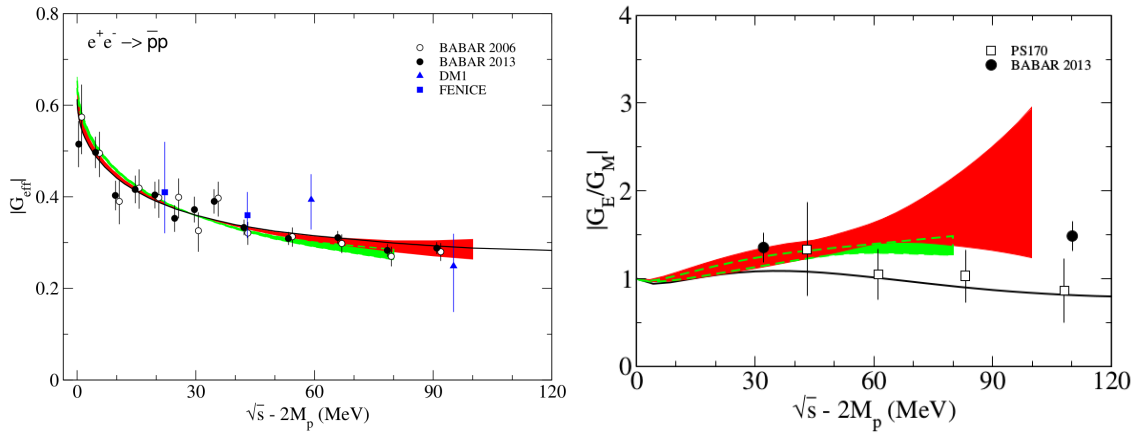


Fig. 2.21: (Left) TL effective FF of the proton with the χ EFT prediction. The green and red bands denote results from the χ EFT NLO and NNLO calculation, respectively. The solid lines are results with the Jülich model A(OBE) [151]. The experimental results are from: open circles [101], closed circles [21], triangles [84], squares [24]. (Right) TL proton form factor ratio with the χ EFT prediction. Experimental results are from [21] and [92]. (Original figure from [147]).

2.4.7 Soft collinear effective theory approach

In the soft collinear effective theory (SCET) approach, the Dirac F_1 and Pauli F_2 FFs of the nucleon are described as the sum of two contributions associated with the soft and hard rescattering sub-process, which are shown schematically in Figure 2.22 (left) and (right), respectively:

$$F_1 \simeq F_1^{(h)} + F_1^{(s)} \quad F_2 \simeq F_2^{(h)} + F_2^{(s)} \quad (2.61)$$

The hard contribution $F^{(h)}$ was studied using the QCD factorization approach [152]. The hard blob in Figure 2.22 (left) describes the hard scattering of the quarks and gluons with virtual photon energies of the order of Q^2 , which can be calculated within the perturbative QCD. The soft blob $F^{(s)}$ in Figure 2.22 (right) denotes the soft non-perturbative sub-process, which can be parametrized in terms of distribution amplitudes (DAs). The description takes into account the soft spectator scattering mechanism, where the virtual photon interacts only with one of the quarks and the other spectator quarks remain soft. This process, which was shown in [153], is assumed to dominate the nucleon FFs at low momentum transfer. This situation arises for a large range of experiments, including the analyzed BESIII data for the study of the electromagnetic TL FF of the neutron. Details on the parametrization can be found in [154]. A physical picture of the defined SCET FFs can be established by the description of the interaction between the quark-gluon hard-collinear jets and the soft background.

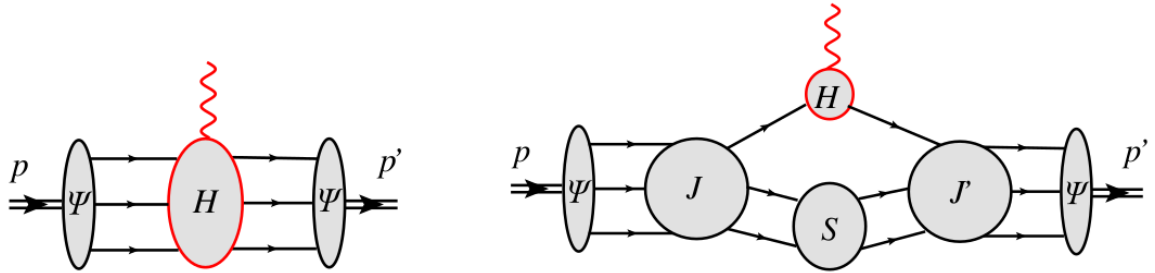


Fig. 2.22: Feynman diagrams for the virtual photon scattering of the proton. (Left) Hard sub-process, (right) soft process, as described in the text. (Original Figure from [154]).

2.4.8 Vector Meson Dominance

The Vector Meson Dominance (VMD) model describes electromagnetic interaction between a virtual photon and hadrons through mediation of vector mesons with the quantum number $J^{PC} = 1^{--}$, such as $\rho(770)$, $\omega(782)$ and $\phi(1020)$, etc., coupling directly to the virtual photon. This coupling can be seen as the hadronic contribution to photon vacuum polarization [52]. The difference of the model to the QCD is schematically shown in Figure 2.24. The VMD description of nucleon electromagnetic FFs is very successful at low energy, parameterizing them as sums of poles in q^2 represented by the vector mesons, but it shouldn't be forgotten that the VMD model is an effective description of the QCD without considering any quark and gluon dynamics.

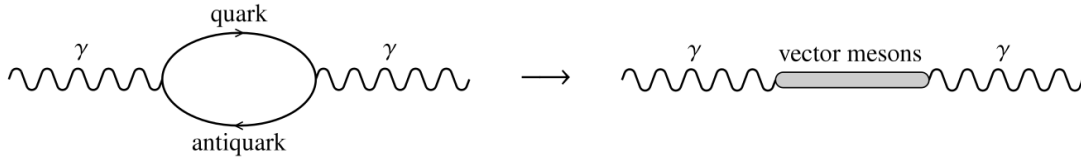


Fig. 2.23: (Left) QCD contribution to the photon vacuum polarization in terms of quark-antiquark loop. (Right) Contribution to the photon vacuum polarization through the coupling to vector mesons in the VMD model. (Original figure from [52])

The goal of VMD based models on nucleon FFs is the unified description of the electric and magnetic FFs for both, proton and neutron, over the whole momentum transfer squared range $-\infty < q^2 < \infty$. The idea, first described in the Massam-Zichichi model [155] 1966, is to decompose the neutron and proton FFs in their isospin components to distinguish the contributions from isoscalar ($I = 0$) and isovector ($I = 1$) vector mesons. The expressions for the FFs in the VMD model are:

$$F_1(q^2) = F_1^V(q^2) + F_1^S(q^2) \quad (2.62)$$

$$F_2(q^2) = F_2^V(q^2) + F_2^S(q^2)$$

Here $F_i^V(q^2)$ and $F_i^S(q^2)$ ($i = 1, 2$) stand for the isovector and isoscalar FFs, respectively. A modified VMD model has been proposed in 1972 by Iachello, Jackson and Landé [156] (IJL model) and has been further optimized by including a more precise TL complex structure [157] - [159]. This model uses a so-called intrinsic FF $g(q^2)$:

$$g(q^2) = \frac{1}{(1 - \gamma e^{i\theta} q^2)^2} \quad (2.63)$$

with dipole behavior and a complex phase for the parametrization and the propagator $D_\rho^{-1}(q^2)$ which takes into account the finite width of the ρ resonance and has a non-vanishing part in the TL region:

$$D_\rho^{-1}(q^2) = \frac{m_\rho^2 + 8\Gamma_\rho m_\pi / \pi}{m_\rho^2 - q^2 + (4m_\pi^2 - q^2)\Gamma_\rho \alpha(q^2)/m_\pi + i\Gamma_\rho 4m_\pi \beta(q^2)} \quad (2.64)$$

with

$$\alpha(q^2) = \frac{2}{\pi} \sqrt{\frac{q^2 - 4m_\pi^2}{q^2}} \ln \left[\frac{\sqrt{q^2 - 4m_\pi^2} + \sqrt{-q^2}}{2m_\pi} \right], \quad (2.65)$$

and

$$\beta(q^2) = \begin{cases} \left[\frac{\left(\frac{q^2}{4m_\pi^2} - 1 \right)^3}{\frac{q^2}{4m_\pi^2}} \right]^{1/2} & \text{for } q^2 \geq 4m_\pi^2 \\ 0 & \text{for } q^2 < 4m_\pi^2 \end{cases} \quad (2.66)$$

and with the modulus $\gamma = 0.25 \text{ (GeV/c)}^{-2}$ [157] and the complex phase θ non-vanishing for $q^2 > 0$ introduced to account for the complex FF structure in the TL region. The constants have been set to $\beta_\rho = 0.672$, $\beta_\omega = 1.102$, $\beta_\phi = 0.112$, $\alpha_\phi = -0.052$, $\Gamma_\rho = 0.112 \text{ GeV}$, $\theta = 53^\circ$ as discussed in Reference [156]. The normalization of the propagator is $D_\rho(q^2 = 0) = 1$. The IJL VMD model predicts a linearly decreasing ratio of the proton FFs $G_E^p(Q^2)/G_M^p(Q^2)$ in the SL region which is in agreement with the polarization transfer results. The expressions for the isoscalar and isovector contributions to the Dirac and Pauli FFs are:

$$\begin{aligned} F_1^V(q^2) &= \frac{1}{2} g(q^2) \left(1 - \beta_\rho + \frac{\beta_\rho}{D_\rho(q^2)} \right) \\ F_2^V(q^2) &= \frac{1}{2} g(q^2) \left(\frac{3.706}{D_\rho(q^2)} \right) \\ F_1^S(q^2) &= \frac{1}{2} g(q^2) \left((1 - \beta_\omega - \beta_\phi) - \beta_\omega \frac{m_\omega^2}{m_\omega^2 + q^2} - \beta_\phi \frac{m_\phi^2}{m_\phi^2 + q^2} \right) \\ F_2^S(q^2) &= \frac{1}{2} g(q^2) \left((-0.120 - \alpha_\phi) \frac{m_\omega^2}{m_\omega^2 + q^2} + \alpha_\phi \frac{m_\phi^2}{m_\phi^2 + q^2} \right) \end{aligned} \quad (2.67)$$

Later, this model has been extended by Gari, Krümpelmann and Lomon [160] (GKL model) to include excited vector mesons and the pQCD power-laws shown in Equation 2.34. Figure 2.24 shows data on the SL and TL nucleon FFs compared to the results from the IJL (dashed lines) and the GKL (solid lines) models. A modified VMD model is used for the Monte Carlo simulation in this work, generated with the Phokhara v9.1 [161] event generator.

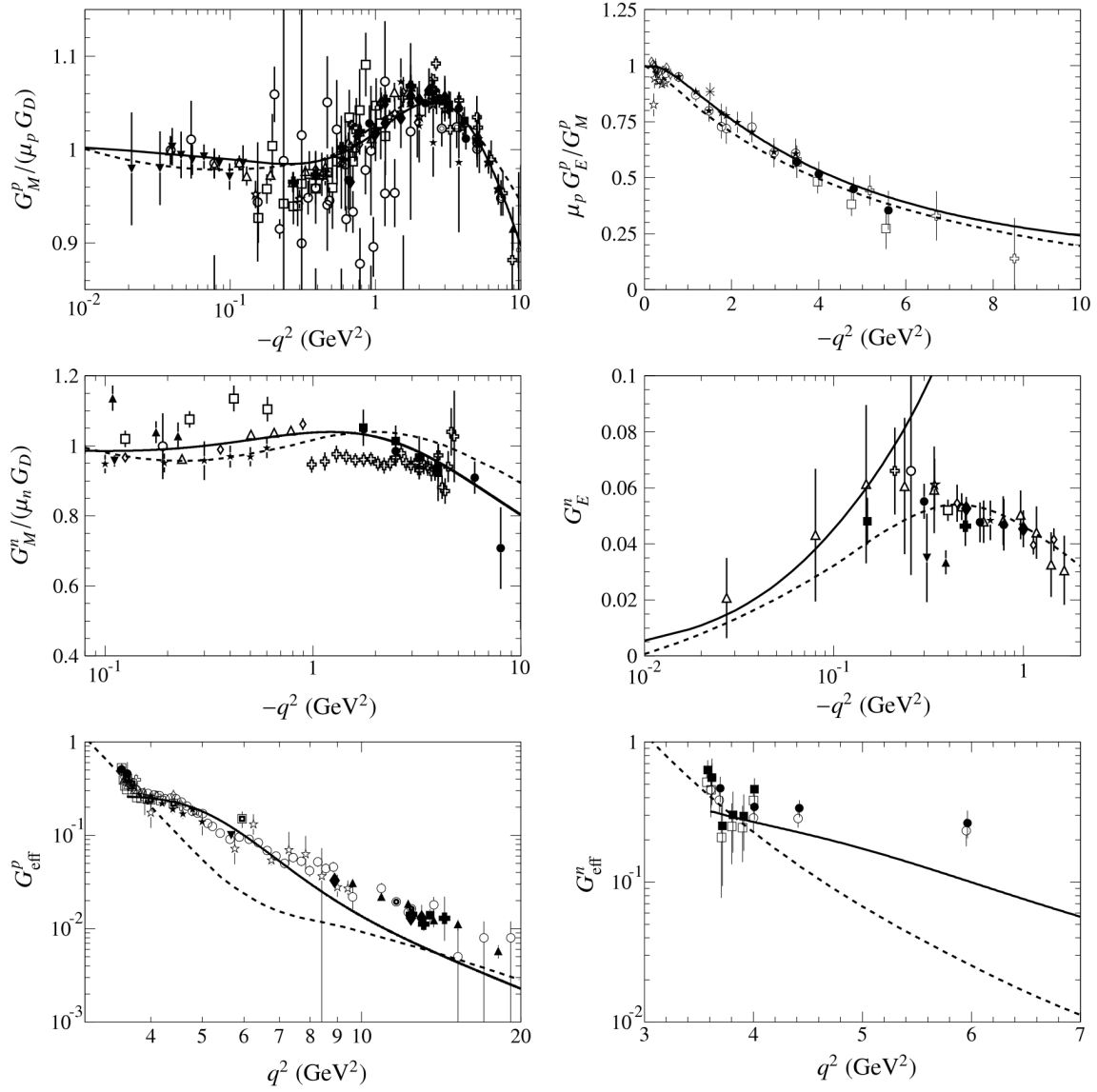


Fig. 2.24: Nucleon FFs prediction for SL and TL regions, from IJL [158] and GKL [160] model. The data on $G_M^p(Q^2)$ and $\mu_p G_E^p(Q^2)/G_M^p(Q^2)$ (only polarized experiments) are from [74] - [76] and [168] - [186]. Data on $G_M^n(Q^2)$ in SL region are from [113] - [115] and from [126] - [128]. Data on the electric neutron FF, $G_E^n(Q^2)$ in SL region are from [105] - [107], [109], [117], [119], [122], [125], and [136]. Data on the effective FF of the proton $G_{\text{eff}}^p(q^2)$ in the TL domain are from [25], [86], [87], [81], [90] - [93], [98], [99] - [100]. Data on the effective neutron FF in the TL region has been extracted from $e^+e^- \rightarrow \bar{n}n$ in [24] under two hypotheses: $|G_E^n(q^2)| = |G_M^n(q^2)|$ (empty symbols) and $G_E^n(q^2) = 0$ (solid symbols). (Original figure from Reference [52].)

Chapter 3

The BESIII Experiment

The data analysis presented in this thesis is based on experimental data collected by the BESIII experiment at the symmetric e^+e^- collider BEPCII, which is located at the Institute of High Energy Physics of the Chinese Academy of Sciences in Beijing, China. This chapter gives in Section 3.1 a brief overview of the accelerator facility BEPCII, in Section 3.2 a detailed description of the multipurpose detector BESIII, following by an introduction into the software framework as well as the collider and simulation data used in this work in Section 3.3 and 3.4, respectively. More information on the technical characteristics of the BEPCII and BESIII, as well as a complete listing of the BESIII physics program can be found in [187].

3.1 Beijing Electron Positron Collider II

The Beijing Electron Positron Collider II (BEPCII) is an upgraded version of the symmetric storage ring BEPC, which operated at the Institute of High Energy Physics (IHEP) in Beijing, China between 1989 and 2004 [188], [189]. With the upgrade, the 240 m circumference collider was modified from a single- to a symmetric double-ring design. Constructions of the BEPCII facility, which consists of an electron and positron source, a linear accelerator (linac) and a double ring collider, have been finished in 2008. The first data taking period started in 2009. Figure 3.1 shows an aerial view of the BEPCII facility.

The BEPCII operates in the center-of-mass (cms) energy range between $\sqrt{s} = 2.0 - 4.6$ GeV and has a design luminosity of $10^{33} \text{cm}^{-2} \text{s}^{-1}$ optimized for the beam energy of 1.89 GeV, which corresponds to the mass of the charmonium resonance $\psi(3770)$. The electron and



Fig. 3.1: View on the BEPCII facility center with the collider ring in the middle of the picture and the linac in the upper right part, located at the IHEP in Beijing. The BESIII detector is situated at 8 o'clock on the ring. (Original image from <http://www.ihep.ac.cn>)

positron sources provide bunches of electrons and positrons which are passed to the linac and accelerated before being stored in the double-ring. Operating in multi-bunch mode, each ring is designed to store 93 bunches with a beam current of up to 0.91 A. The bunch length for all runs except the 2015 R-Scan data collection is approximately 1.5 cm and the bunch spacing is 2.4 m, which corresponds to 8 ns. For the scan data collected in 2015, the bunch spacing was reduced to 6 ns. The two beams have a crossing angle of ± 11 mrad in the collision point, where the BESIII detector is located.

Among the design goals of the BESIII experiment are:

- Precise measurement of QCD parameters
- High accuracy studies of production and decay properties of charmonium states
- Light hadron spectroscopy
- Tests of electroweak interaction
- D-, τ -, and XYZ-physics
- Search for new physics in rare or forbidden decays

3.2 Beijing Electron Spectrometer III

The Beijing Electron Spectrometer III (BESIII) is a typical multipurpose detector, designed for the reconstruction of charged and neutral particles. A detailed description can be found in Reference [190]. A schematic cross section through the YZ-plane of the detector is shown in Figure 3.2.

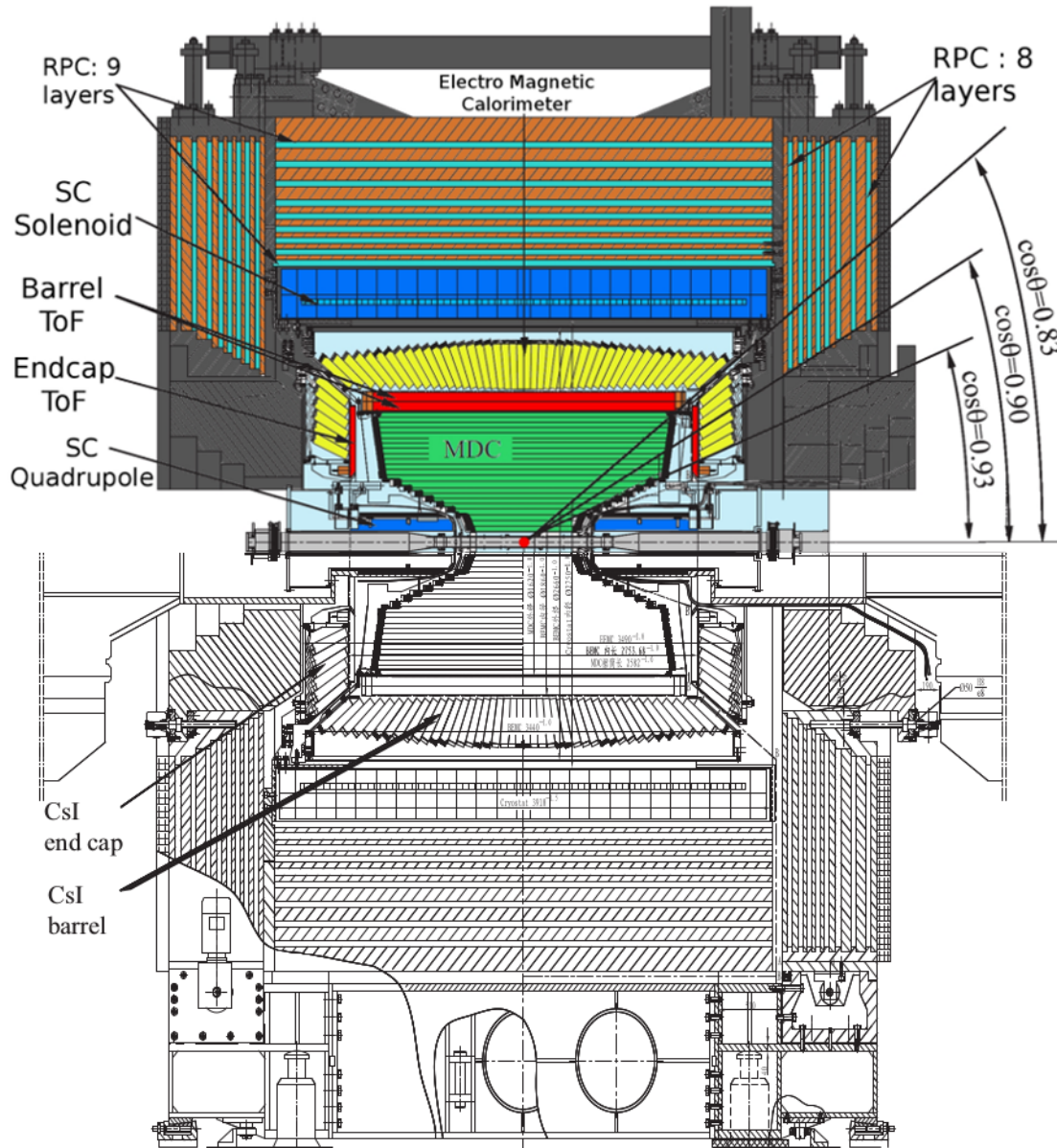


Fig. 3.2: Schematic cross section of the BESIII detector (original figure from [190]).

The detector is cylindrical shaped and built around the beryllium beam pipe where bunches of electrons and positrons collide in the interaction point (IP). The innermost part is the multilayer drift chamber (MDC), followed by the time-of-flight system (TOF) and the electromagnetic calorimeter (EMC). All of these sub-detector systems are surrounded by a superconducting solenoid magnet (SSM), which creates a homogeneous magnetic field inside the inner parts. Outside of the solenoid coil, a muon counter (MUC) system closes off the detector design. The spectrometer covers $\Delta\Omega/4\pi = 0.93$ of the solid-angle. The coverage of the polar angle θ with respect to the z-axis (which is the positron beam direction) is between 21° and 159° (shown in the right part of Figure 3.2). The main characteristics of the sub-systems are summed up in Table 3.1, while a detailed description of each follows in the next sections.

Sub-Detector	Characteristic	Performance
Coverage	Solid-angle $\Delta\Omega/4\pi$ coverage	93%
	Polar angle θ coverage	$21^\circ - 159^\circ$
MDC	Single wire $\sigma_{r\phi}$	$130 \mu\text{m}$
	σ_p/p (at 1.0 GeV/c)	0.5%
	$\sigma(dE/dx)$	6%
TOF	Barrel σ_T (single-) double-end	80 (100) ps
	Endcap σ_T single-end	110 ps
EMC	σ_E/E (at 1.0 GeV)	2.5%
	σ_{xy} (at 1.0 GeV)	0.6 cm
SSM	Solenoid magnet field	1 T
MUC	Layers in barrel/endcap	9/8
	Cut-off momentum	0.4 MeV/c

Table 3.1: Parameters and performance of the BESIII sub-systems.

3.2.1 Beam pipe and interaction region

The bunches of electrons and positrons from the BEPCII are focused by six pairs of quadrupole magnets and two beam bending magnets (OWBL). The beams collide in the interaction point (IP) under a crossing angle of 22 mrad. Beryllium, a material with low density and atomic number, has been chosen for the design of the beam pipe to minimize multiple scattering of particles produced by the e^+e^- -collisions with the beam pipe walls

before entering the detector, to withstand differential pressure, and to maintain the high vacuum of $5 \cdot 10^{-10}$ Torr inside of the beam pipe, which is necessary to reduce beam-gas related background. Good electric conductivity shields the radio frequency (RF) radiation emitted from the beam bunches. The 29.6 cm long beam pipe tube is mounted on the end plates of the inner MDC and consists of a 0.8 mm thick inner and 0.6 mm thick outer wall. An active cooling with mineral oil is realized in the 0.8 mm thick gap between the two walls to neutralize the high heat load of about 700 W generated by the beam current induced eddy currents. Figure 3.3 shows a schematic cross section of the beam pipe.

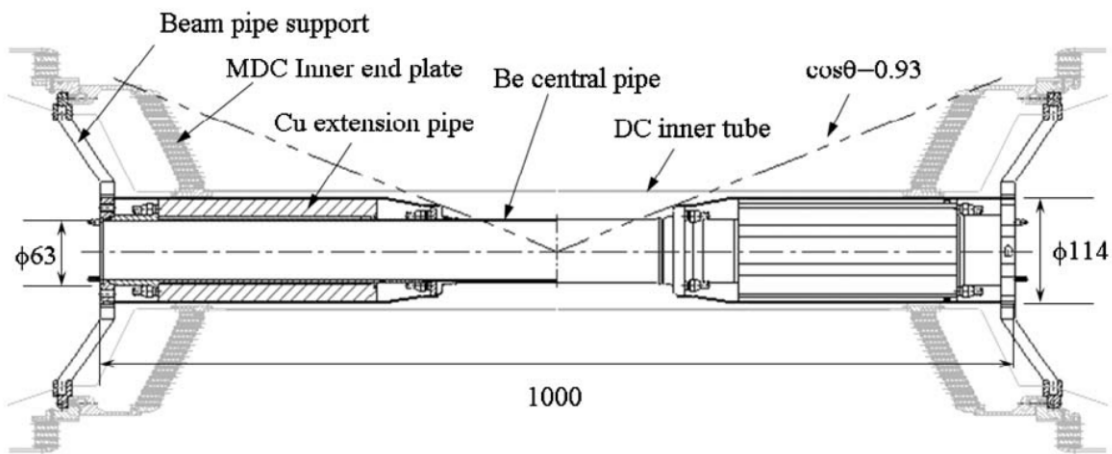


Fig. 3.3: Schematic cross-section of the beam pipe [190].

3.2.2 Momentum measurement with the tracking system

The tracking system at BESIII combines the tracking in the multilayer drift chamber (MDC), as the innermost detector part of BESIII, with the magnetic field provided by the superconducting solenoid magnet. Together the sub-systems provide a precise momentum determination of charged particles by measuring their trajectories in the magnetic field, as well as a particle identification through the measurement of their ionization energy loss dE/dx . Additionally, the MDC provides a signal for the L1 trigger for separation of physics from background events. In the following, the main functions of the MDC are listed:

- Reconstruction of charged tracks in 3D space
- Momentum measurement for charged particles
- dE/dx measurement for charged particles for particle identification
- L1 trigger signal for background rejection
- Extrapolation of charged tracks to outer sub-detectors

The MDC consists of 2 parts, the inner and the outer chamber, without any separating walls in between. A helium-based mixture of He/C₃H₈ with a ratio of 60% to 40% with a pressure of 3 mbar above atmospheric pressure is used as working gas to reduce multiple scattering effects of charged particles crossing the volume and at the same time maintaining a sufficient dE/dx resolution of better than 6% for particles perpendicular to the beam direction.

There are 43 cylindrical layers of 25 μm thick gold-plated tungsten sense wires in a stepped conical arrangement around the beam pipe, as shown in Figure 3.4, summing up to 6796 wires in total. The innermost layer of the MDC has an inner radius of 59 mm and covers a polar angle of $|\cos\theta| < 0.93$, the outermost layer has a radius of 810 mm and covers $|\cos\theta| < 0.83$, respectively. A so called drift cell is a unit of a sense wire surrounded by 8 aluminum field wires, while neighboring sense wires share the field wires between them. This arrangement guarantees a radial position resolution $\sigma_{r\phi}$ better than 130 μm. The axial position resolution of better than 4 mm is achieved through rotation of the small angle stereo layers 1-8 and 21-36 by -3.4° to 3.9° against the other layers which are arranged axially.

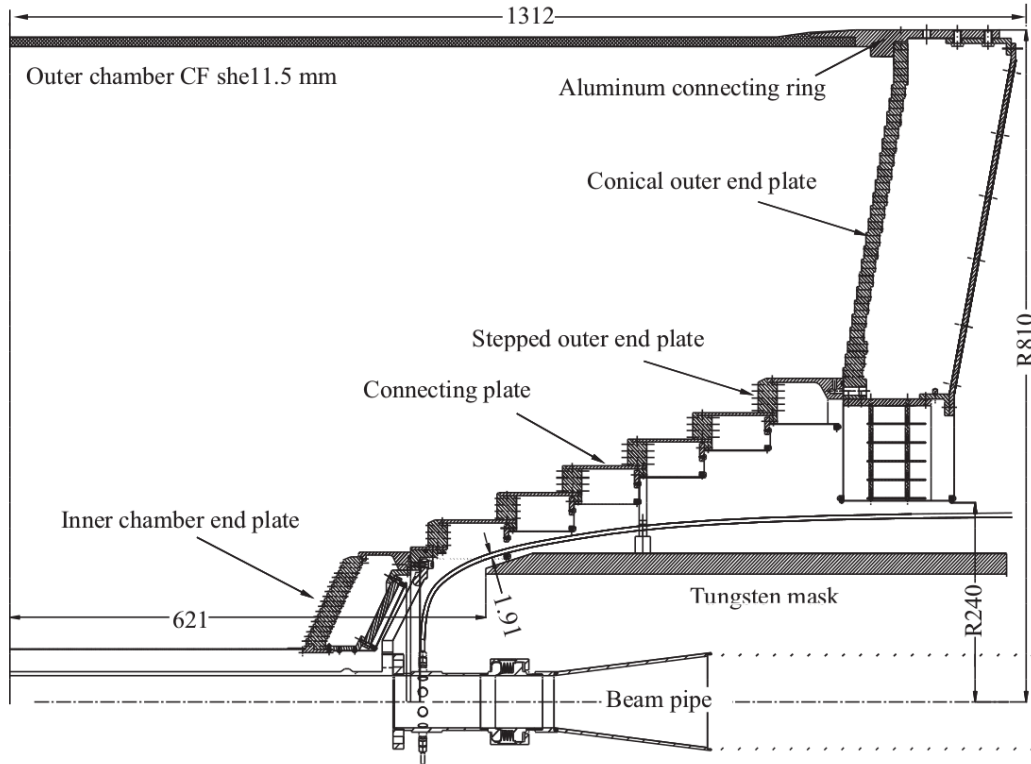


Fig. 3.4: Mechanical structure of the multilayer drift chamber [190].

The momentum measurement is possible with the help of the uniform axial magnetic field, induced by the superconducting solenoid magnet, bending the trajectories of charged particles. The momentum resolution σ_p/p is limited by the position resolution of a single wire and reaches values better than 0.5% for particles with a transverse momentum of 1 GeV/c. Scattering of the particles on the working gas or wires introduces an uncertainty in the momentum measurement. A summary with characteristics of the MDC is listed in Table 3.2.

Item	Parameter
Inner chamber radius	59 mm
Outer chamber radius	810 mm
Total length	2400 mm
Polar angle coverage of innermost layer	$ \cos\theta < 0.93$
Polar angle coverage of outermost layer	$ \cos\theta < 0.83$
Number of layers	43
Radial position $\sigma_{r\phi}$ resolution of a single wire	$< 130 \mu\text{m}$
Axial position σ_z resolution	$< 4 \text{ mm}$
Momentum resolution σ_p/p at 1 GeV/c and 90°	$< 0.5\%$
Ionization energy loss resolution $\sigma(dE/dx)$ at 90°	$< 6\%$

Table 3.2: Parameters of the Multilayer Drift Chamber (from Reference [190]).

The reconstruction of the tracks produced by charged particles is performed in a first step by a tracking algorithm. Hereby hits from single sense wires are combined to circular traces using a least-square method with a circular fit. In the next step these traces are considered as track candidates and fitted iteratively to a curved helix. In case of a successful fitting procedure additional hits in close distance around the helix are taken into account and are included into a further fit performed by a Kalman-filter method. The whole procedure has a tracking efficiency for particles with transverse momenta larger than 150 MeV/c of more than 98%, as shown from Monte Carlo simulations [191]. In a last step the charged tracks are extrapolated to the other sub-detectors for further reconstruction.

The superconducting solenoid coil (SSC) magnet at BESIII, shown as a schematic drawing in Figure 3.5 (left), generates a homogeneous 1 T field in the vicinity of the beam pipe and the MDC, TOF and EMC detectors. Charged particles are forced on a curved flight trajectory due to the Lorentz force. Measuring the curvature of their trajectories, the MDC

determines their momenta and provides a particle identification. An example for the magnetic field distribution in z-direction is shown in Figure 3.5 (right). The iron absorbers of the muon counter system, discussed in the following, provide the magnetic flux return. The flux return yoke serves also as a mechanical support structure for the inner detector parts. The length of the magnet is 3.91 m, with an inner and outer diameter of 2.75 m and 3.4 m, respectively. The coil is suspended in a cryostat, has an effective length of 3.52 m, a mean diameter of 2.97 m and is cooled to 4.2 K.

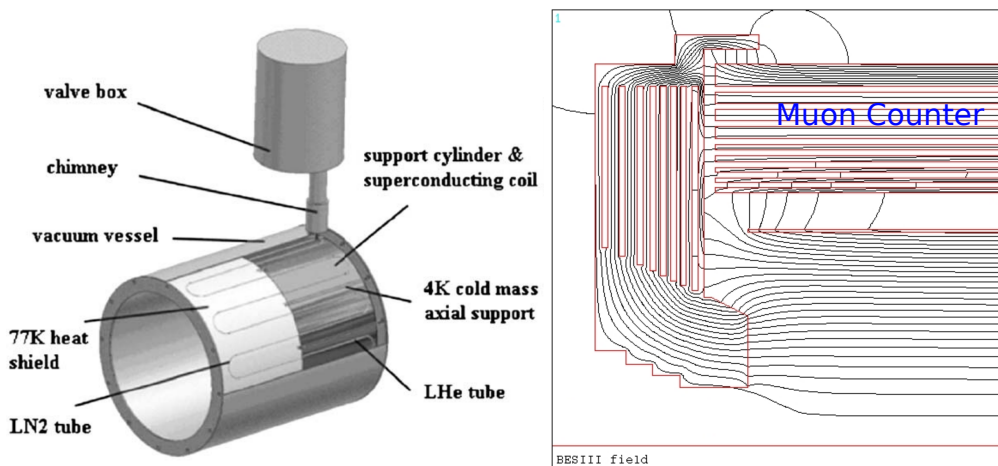


Fig. 3.5: (Left) Superconducting Solenoid. (Right) Simulation of uniformity for the magnetic field flux in the tracking volume [192].

Neutral particles, like neutrons and antineutrons in the signal process final state analyzed in this thesis, can also hit the sense wires and therefore produce signals. But without being bent in the magnetic field, only in rare cases a wrongly reconstructed charged track coming from a neutral particle from the IP is observed in the MDC. A different situation arises, if an antineutron annihilates in the EMC and produced secondary particles, mostly pions or electrons from photon conversion return to the MDC from outside. This case is discussed more detailed in Section 5.1.

3.2.3 The time-of-flight measurement

The time-of-flight (TOF) system measures the flight time of charged particles between the interaction point and the electromagnetic shower position in the TOF. It also provides a fast trigger signal as veto for cosmic rays. Combined with the dE/dx measurement from the MDC, it is the main system for particle identification at BESIII.

The TOF detector is divided into a double-layer barrel and two single-layer end cap parts which are constructed from plastic scintillators (type BC-408 [193]) with a double-end (barrel) and single-end (end caps) fine-mesh photomultiplier tubes (PMT) readout. All trapezoidal shaped scintillator bars are 50 mm thick. The barrel part with a total length of 2380 mm is placed between the MDC and the EMC. Each layer includes 88 scintillation counters and is cylindrically arranged around the beam pipe with a diameter of 810 mm for the inner and 860 mm for the outer layer, respectively. Its coverage on the polar angle range is $|\cos\theta| < 0.83$. The end caps, each consisting of 48 fan-shaped scintillator counters (type BC-404) are placed outside the MDC end plates and cover the polar angle range of $0.85 < |\cos\theta| < 0.95$, with a minimum distance of 1400 mm to the interaction point. Their inner radius is 410 mm, while the outer radius is 890 mm. The end caps layers are 480 mm long and have the width of 62 mm at the inner and 109 mm at the outer end. The PMT's are attached to the outer surface of the inner ends. Between the barrel and end cap part is a gap with cables and support structures for the MDC. A schematic cross-section through the YZ-plane of the TOF sub-detector is shown in Figure 3.6.

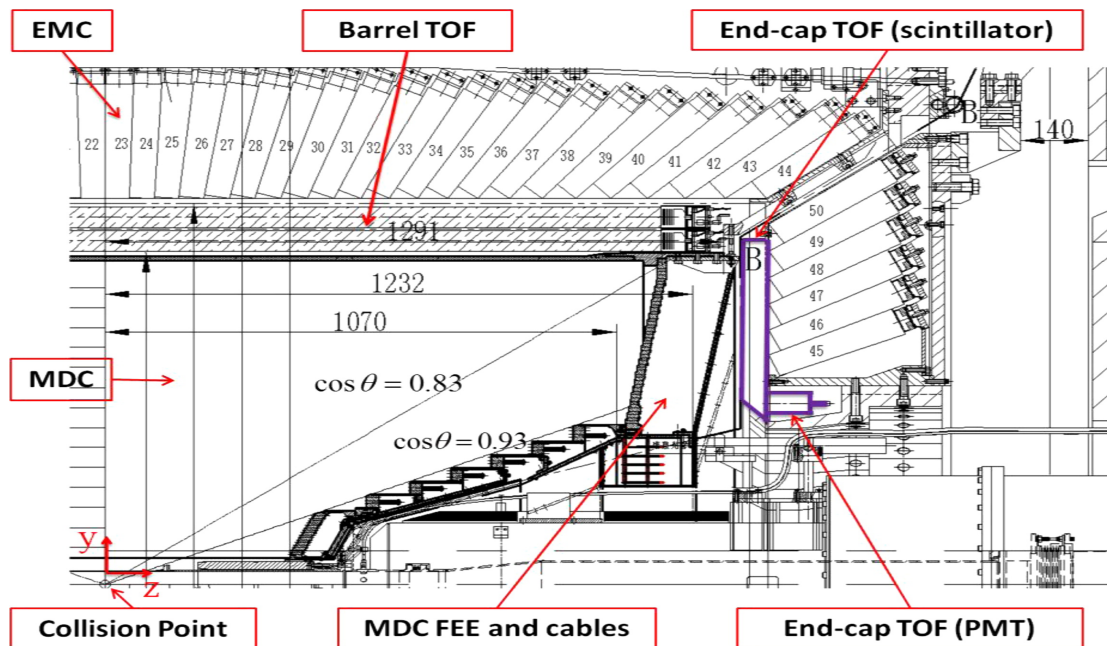


Fig. 3.6: Schematic cross section of the TOF detector [194].

The crucial characteristic for the time-of-flight measurement is the time resolution σ_T . For the double layer barrel the resolution for a muon with 1 GeV/c momentum is $\sigma_T = 80$ ps. If only one layer readout is possible, the resolution decreases to 100 ps. The single layer end caps have a resolution of 110 ps. The resolution depends mainly on the following

contributions: the scintillator counter intrinsic time resolution, the uncertainty on the determination of the interaction vertex from beam bunch length and bunch timing, the uncertainty in global timing from the RF clock system, the uncertainty in the determination of the hit position in the scintillator including light propagation, the uncertainty from the readout electronics, the uncertainty on the momentum resolution of 0.5% measured in the MDC, and the uncertainty caused by walk time due to signal amplitude fluctuations. All contributions are listed in Table 3.3.

Uncertainty source	Barrel (ps)	End cap (ps)
Intrinsic time resolution	80-90	80
Determination of the interaction vertex	35	35
Global timing from the RF clock	~20	~20
Determination of the hit position in scintillator	25	50
Readout electronics	25	25
Expected flight time (0.5% momentum resolution)	30	30
Time walk	10	10
Total resolution σ_T one layer	100-110	110
Total resolution σ_T two layers	80-90	-

Table 3.3: The contributions to the total TOF time resolution for a 1 GeV muon (more details are listed in Reference [190]).

The time resolution for other particles, like protons, pions and kaons decreases by around 20% because of strong interaction, therefore wider shower in the scintillator material leading to a larger uncertainty of the hit position determination. A simulation for the K/π separation capability of the barrel part of the TOF is shown in Figure 3.7. The thick dashed line represents the time difference between kaons and pions necessary for a 3σ K/π separation in the TOF barrel region with double layer readout, the thick solid line for single layer readout, respectively. A three standard deviation K/π separation is possible for tracks with a momentum below 700 MeV/c at $\cos\theta = 0$ central barrel region. In the outer barrel region around $\cos\theta = 0.8$ a 3σ K/π separation is possible for tracks with 1 GeV/c. The capability of the end caps is to separate kaons and pions with a momentum of 0.9 – 1 GeV/c with three standard deviations, due to the worse resolution. Table 3.4 summarizes the main parameters of the TOF system.

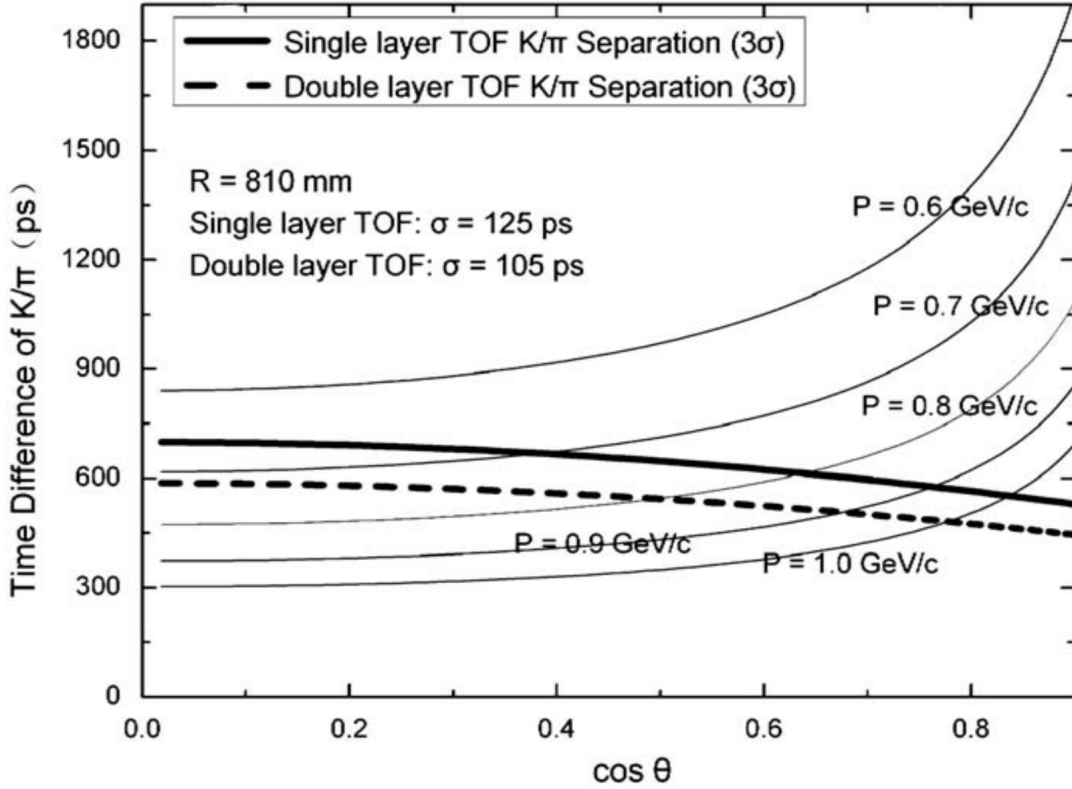


Fig. 3.7: Differential K/π separation capability of TOF [190].

Item	Parameter
Inner radius	810 mm
Outer radius	870 mm
Polar angle acceptance barrel	$ \cos\theta < 0.83$
Polar angle acceptance end caps	$0.85 < \cos\theta < 0.95$
Time resolution σ_T barrel double layer (1 GeV/c muon)	80-90 ps
Time resolution σ_T single double layer (1 GeV/c muon)	100 ps
Time resolution σ_T end caps (1 GeV/c muon)	110 ps
$3\sigma K/\pi$ separation in barrel at $\cos\theta = 0$ ($\cos\theta = 0.8$)	< 0.7 GeV/c (< 1 GeV/c)
$3\sigma K/\pi$ separation in end caps	< 0.9 -1 GeV/c

Table 3.4: Parameters of the Time-of-Flight system (from Reference [190]).

The main components of the TOF readout system are the preamplifiers mounted in PMT bases, circuits for signal time and amplitude measurement, circuits for the L1 trigger and a laser calibration system. After the pre-amplification, the PMT signals from all the 448 scintillators are read out by Time and Charge measurement modules which are contained

on the front end electronics (FEE) on HPTDC chips. Signals from 16 preamplifiers are processed by one FFE module, which has additionally two L1 trigger Fast-Control Modules (FCM) for trigger fan-out and read out control. This system builds the TOF sub-trigger (details in Section 3.2.6). A diagram of the architecture of a TOF readout electronic crate is shown in Figure 3.8

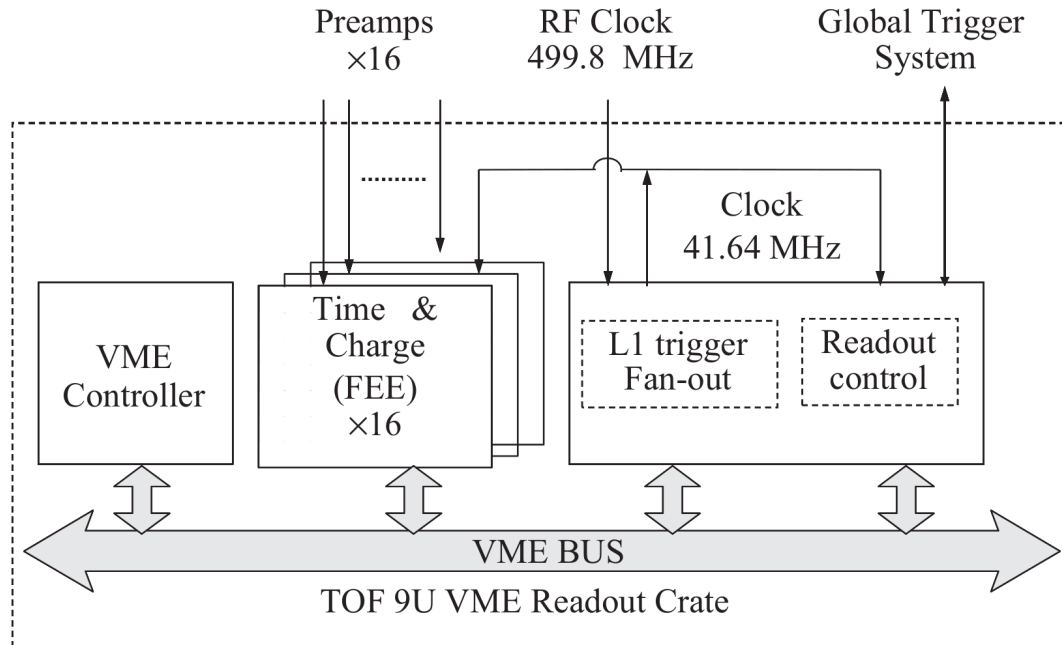


Fig. 3.8: Architecture for the TOF readout electronics [190].

The reconstruction algorithm for the TOF searches for extrapolated tracks from the MDC and matches them to TOF modules with an detected signal. After obtaining the hit position in the scintillator bar, a double-end readout from the PMT at both ends of the scintillator calculates a weighted average on the time information to extract the travel time of the particle from the interaction point. If only information from one scintillator end is available, no determination on the z-coordinate for the hit is possible with the TOF alone. In this case the hit position is determined by an extrapolation of the shower position from the electromagnetic calorimeter and sub-sequentially used for the time-of-flight measurement. Several corrections are applied on this time measurement, taking into account the effective light speed in the scintillator, the light attenuation length and others. For both, charged and neutral particles, the deposited energy in the TOF scintillators is measured. The energy deposition in the TOF is used to improve the energy resolution of electromagnetic showers in the EMC.

3.2.4 Electromagnetic calorimetry

The main purpose of the electromagnetic calorimeter (EMC) is to measure the deposition energy of charged and neutral particles passing and interacting with its material, as well as the shapes of their electromagnetic and hadronic showers. Therefore it is the most important sub-detector for this analysis. Additionally it has another sub-trigger to provide L1 trigger signals to separate physics from background events. The energy measurement is used as additional input for the particle identification algorithm (PID) in the BESIII analysis framework and can for example separate charged pions from electrons, since their deposition energy and the shape of their electromagnetic showers is very different. Neutral particles which can't be reconstructed with the standard algorithms for the MDC and TOF can be detected here. Figure 3.9 shows a schematic representation of the YZ-plane through the upper half of the EMC barrel part with its supporting structures.

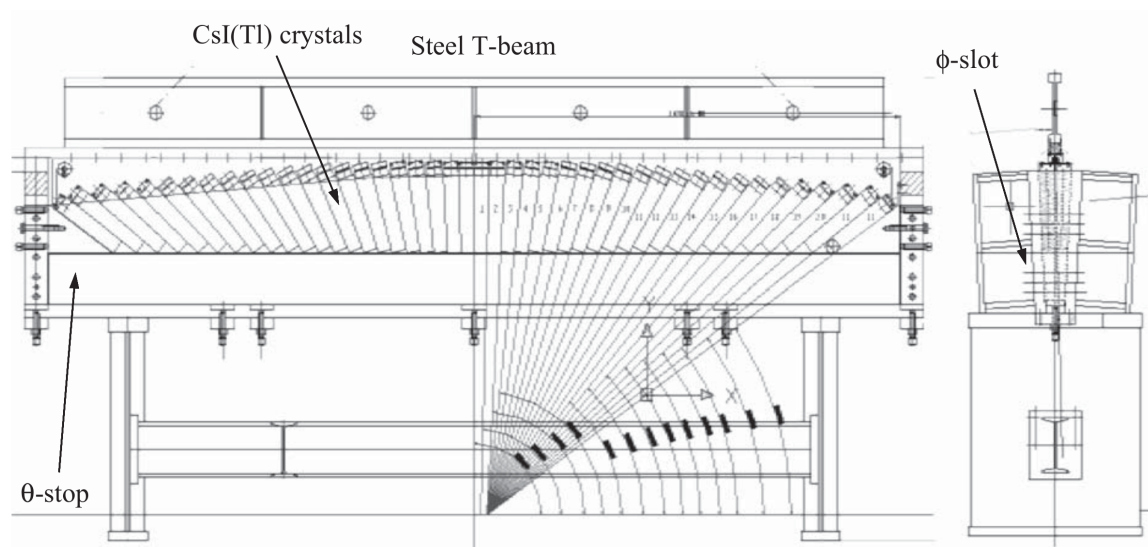


Fig. 3.9: Schematic cross-section of the EMC detector [194].

The EMC is divided into a barrel part and two end caps covering the polar region of $|\cos\theta| < 0.82$ and $0.83 < |\cos\theta| < 0.93$, respectively. The total acceptance is 93% of 4π . It consists of 6240 CsI(Tl) crystals positioned in a cylindrical arrangement of 44 rings in the barrel part and for each end cap out of six rings. Each crystal covers an angle of about 3° in polar and azimuth direction. To avoid photons coming from the interaction point escaping through gaps in between the crystals, each crystal of the barrel has a tilt of 1.5° in the ϕ -direction and between 1.5° and 3° in the θ direction, which corresponds to an offset of ± 5 cm from the IP in the beam direction. The length of each crystal with 28 cm

corresponds to 15.1 radiation lengths X_0 in CsI(Tl). The barrel crystals have a quadratic front of 52 mm length and a quadratic rear front of 64 mm. Crystals in the end caps have asymmetric forms and sizes. The inner radius of the barrel is 940 mm and a length of 2750 mm, while the end caps have an inner radius of 880 mm, an outer radius of 1100 mm and are placed in a distance of 1340 mm to the interaction point. A small gap of 50 mm between the barrel and the end caps allows space for mechanical support structures, cables and cooling pipes. The total weight of the EMC is about 25.6 tons. The main parameters of the EMC are summed up in Table 3.5.

	Item	Parameter
Geometry	Inner radius barrel	94 cm
	Barrel length	2750 mm
	Inner radius end caps	880 mm
	Outer radius end caps	1100 mm
	Polar angle acceptance barrel	$ \cos\theta < 0.82$
	Polar angle acceptance end caps	$0.83 < \cos\theta < 0.93$
	Number of CsI(Tl) crystals	6240
	Barrel crystal length	280 mm
	Barrel crystal front size	52 mm \times 52 mm
	Barrel crystal back size	64 mm \times 64 mm
Crystal properties	Radiation length X_0	1.85 cm
	Nuclear interaction length λ_I	171.5 g/cm ²
	Moliere radius	3.8 cm
	Density	4.53 g/cm ³
	Light yield (photodiode)	56000 γ 's/MeV
	Peak emission wavelength	560 nm
	Signal decay time	680 ns (64%) and 3.34 ms (36%)
	dE/dx (per mip)	5.6 MeV/cm
Performance	Energy resolution	2.5%/ \sqrt{E} (GeV) (at 1 GeV)
	Position resolution	$\sigma_{xy} < 6\text{mm}/\sqrt{E}$ (GeV) (at 1 GeV)
	Working range	20 MeV - 2.3 GeV
	Sampling cycle	50 ns

Table 3.5: Parameters of the electromagnetic calorimeter [190].

The BESIII electromagnetic calorimeter can measure energy of particles in the range between 20 MeV and 2.3 GeV. The energy resolution is $\sigma_E/E < 2.5\%$ at 1 GeV and 4 MeV at 100 MeV, while the position resolution is $\sigma_{xy} < 6$ mm. Photons and electrons deposit almost always their complete energy inside of the crystal material, taking into account 15

radiation lengths $X_0 = 1.85$ cm over the 28 cm length of the crystal material.

The EMC readout electronics with its 6240 channels measures the deposited energy in every crystal and provides a fast energy trigger. Its four main parts are the preamplifiers mounted directly on the crystals, post amplifier modules, charge digitization VME modules (Q-modules) and the test and control VME modules (Test-Control), all shown in a diagram in Figure 3.10. After the signal pulse (crystal scintillation light) is preamplified by the photodiode, it is send to the post amplifiers, which amplify and shape the signal with a $1\mu\text{s}$ shaping time. The output from the post amplifiers is send to the Q-modules in the VME crates, where the charge digitization takes place. After the charge digitization and the extraction of the energy timing information by the ADCs, digitized data is stored in compliance with the $6.4\mu\text{s}$ L1 trigger latency without data loss. The test and control module is responsible for information distribution between the fan-out module and the Q-module. It receives the charge information from the Q-modules and pass the information to the post amplifier, which forms the fast energy sum trigger signal and forwards it through the fan-out module to the L1 trigger. A block diagram of the EMC readout electronics system is shown in Figure 3.10.

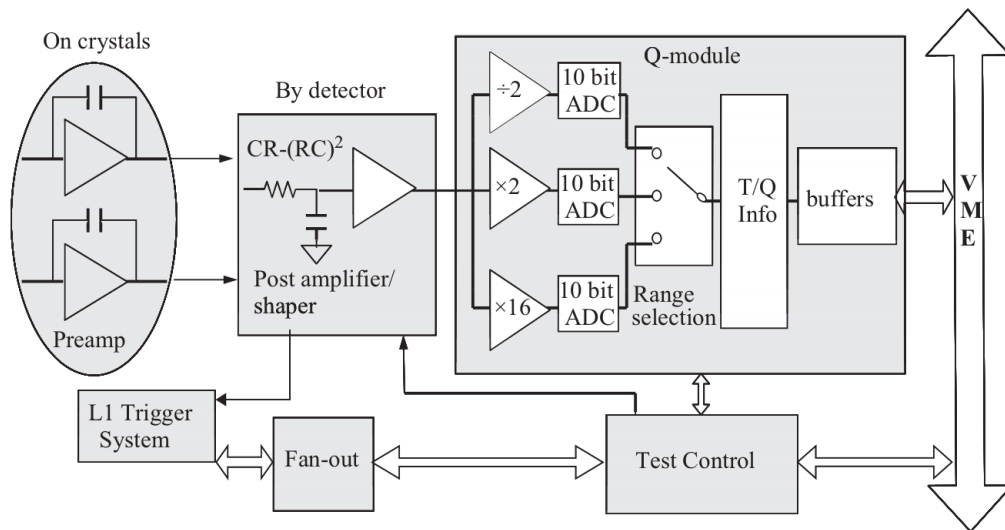


Fig. 3.10: Block diagram for the EMC readout electronics [190].

The voltage values from the crystals are proportional to the deposition energy. After preamplification and digitization by the ADC's the conversion to the deposited energy in

crystal i can be calculated with:

$$E_i = \frac{\text{ADC}_i - \text{PED}_i}{e_i \times c_i} \quad (3.1)$$

The digitized output voltage ADC is the measured value of the calorimeter. The pedestal value PED denotes the constant electronics noise, which needs to be subtracted and was measured experimentally. e_i is a conversion constant between the output voltage from the photodiode and the input charge of the preamplifier and is known from the electronics design. The energy conversion constant c_i relates the incident photon energy to the input charge of the preamplifier. It was determined as a relative value for each crystal from test beams with photons and electrons with known energies and finally obtained by calibration using real collider data such as Bhabha, radiative Bhabha and digamma processes.

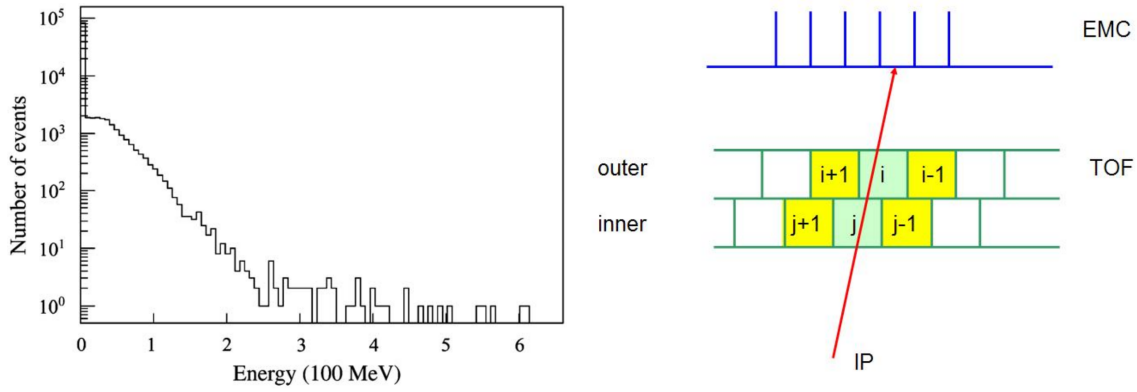


Fig. 3.11: (Left) Monte Carlo simulation of energy loss in the TOF counters for 1 GeV photons at 90° incident angle [190]. (Right) Matching of 3 sectors of both layers from TOF with a 5×5 matrix of EMC crystals for deposition energy correction. [195]

The reconstruction of electromagnetic showers in the EMC is performed in three steps. First, the voltage values from the ADCs are converted, as described above, into energy values. Second, clusters are formed around crystals with the local maximum deposited energy (seeds). Third, electromagnetic showers are reconstructed by summing the energies from clusters around the seeds, while the shower position \vec{x}_c is calculated as the energy-weighted mean of n crystals:

$$\vec{x}_c = \frac{\sum_i^n w_i \vec{x}_i}{\sum_i^n w_i} \quad (3.2)$$

Here \vec{x}_i and w_i are the position and energy of the i -th crystal. If more than one seed is found in one cluster, a splitting function divides the cluster into several showers. At last,

energy deposition in the TOF sub-detector is added to the corresponding shower. Several corrections on the deposition energy need to be applied due to the material of the beam pipe, the drift chamber and the TOF sub-detector in front of the EMC. The dominating energy loss in the EMC barrel region comes from the two 10 cm thick TOF counters bars, shown from a Monte Carlo simulation in Figure 3.11 (left). Adding the energy deposited in three neighboring sectors of the two TOF layers in front of a 5×5 matrix of EMC crystals corrects the measured deposition energy in the EMC, as shown in Figure 3.11 (right), and improves the energy resolution. A comparison between the reconstructed energy deposition of a 1 GeV photon in the EMC is shown from a MC simulation in Figure 3.12 (left). Figure 3.12 (right) shows the a simulation for the expected energy resolution for reconstructed showers.

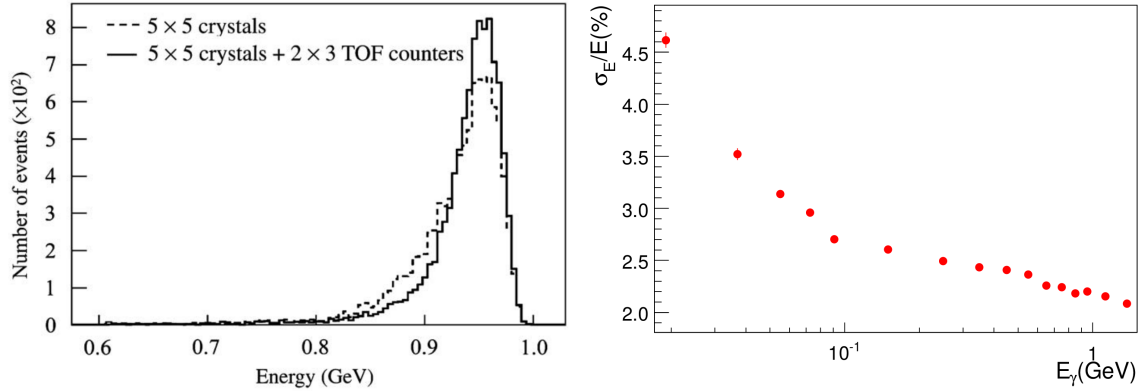


Fig. 3.12: (Left) Monte Carlo simulation for the energy deposition from a 1 GeV photon before and after correction with energy loss in the TOF. The dashed line shows the energy distribution before correction, the solid line after correction [190]. (Right) Simulation for the expected energy resolution for reconstructed showers [187].

With a nuclear interaction length of $\lambda_1^{\text{emc}} = 171.5 \text{ g/cm}^2$ [50] in CsI(Tl), the density of CsI(Tl) $\rho^{\text{emc}} = 4.53 \text{ g/cm}^3$ [50] and the crystal length $L^{\text{emc}} = 28 \text{ cm}$ the probability of interaction between neutrons or antineutrons and the EMC crystals can be approximately calculated as:

$$P = 1 - \exp(-L^{\text{emc}} \cdot \rho^{\text{emc}} / \lambda_1^{\text{emc}}) = 52\% \quad (3.3)$$

Consequently, only for approximately half of $e^+e^- \rightarrow \bar{n}n$ events, an interaction between one of the final state particles and the EMC crystals is detected, which reflects the low selection efficiency for the signal process $e^+e^- \rightarrow \bar{n}n$ in Section 8.1.

3.2.5 Muon detection system

The muon detection system/counter (MUC) at BESIII is mainly designed to detect muons and efficiently separate them from pions and other hadrons. In this analysis it is used as a veto for cosmic ray background, since it provides an unique possibility to separate between particles coming from inside and outside of the detector. It is constructed of resistive plate counters (RPCs), which are placed in between the steel plates of the magnetic flux return yoke of the SCC. Similar to the TOF and EMC, the MUC is divided into a barrel part organized in octants and consisting of nine layers of RPCs and two end caps with each eight RPC layers. The nine layers in the barrel region have a total thickness of 56 cm, arranged with the first RPC layer before the first steel plate of the magnet yoke and continuing to alternate. In the end caps, the first of eight RPC layers is placed behind the first steel plate. The inner and outer radius of the muon counter barrel part is 1.7 m and 2.62 m, respectively. In addition, the layers alternate with the readout. In the barrel the z-position is readout from odd layers, while even layers provide information for the azimuthal position. In the end caps, odd and even layers measure the x- and y-position, respectively. The total length of the MUC is 3.94 m. The barrel region covers the polar angle of $|\cos\theta| \leq 0.75$, the end caps have a coverage between $0.75 \leq |\cos\theta| \leq 0.89$. A schematic design of the MUC through the YZ-plane is shown in Figure 3.13 (left) and through the XY-plane (right), respectively.

The RPCs are constructed from two 2mm thick parallel resistive plate electrodes made of Bakelite with a 2 mm gap for working gas in between, as shown in Figure 3.14 (left). The working gas is a mixture of Ar/C₂F₄H₂/C₄H₁₀ in a ratio of 50/42/8. Passing particles produce an avalanche or a streamer signal in the gas chamber, which is read out by 4 cm wide strips placed outside the gas volume. Two PRC modules are used as a stack for a double-gap design, with the readout strip between them to raise the detection efficiency. A schematic drawing of a double-gap PRC is shown in Figure 3.14 (right). The readout strips of the RPC layers for both, ϕ and θ position, don't have a good position resolution, based on the fact, that low momentum muons multiply scatter in the EMC, the magnet coil and the steel of the magnet yoke. But the position resolution is sufficient to reconstruct muon tracks by associating them to the MDC tracks and TOF signals which provide a much better resolution. The single gas gaps have a barrel and end caps efficiency of 96% and 95%, respectively. The cut-off momentum for muon detection is 0.4 GeV/c and the tracking efficiency with the double-gap design is around 98%. The main characteristics of the MUC system are summarized in Table 3.6.

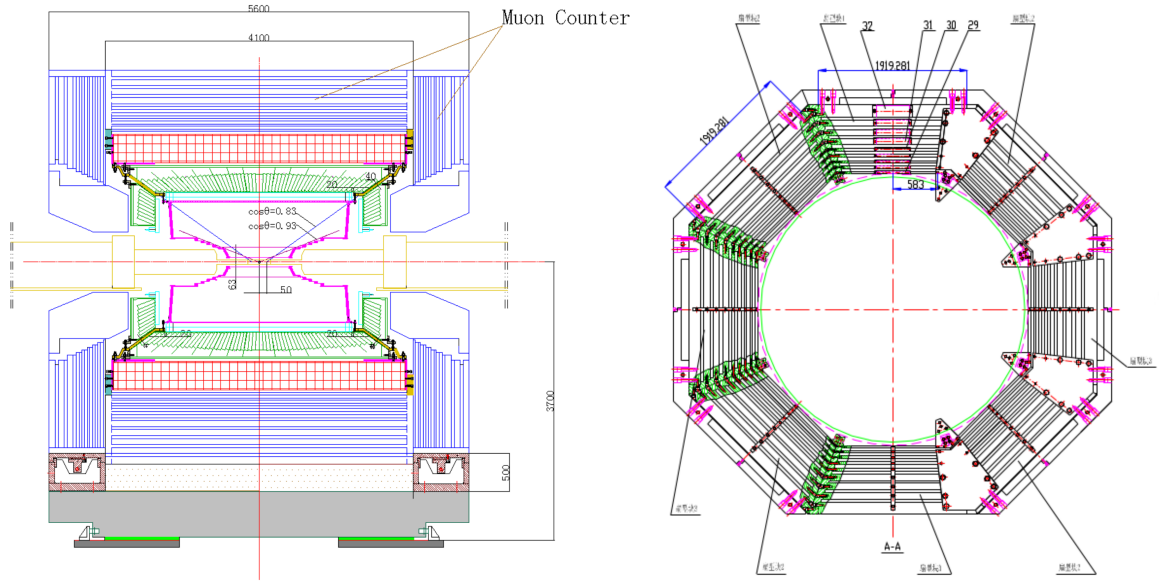


Fig. 3.13: (Left) Schematic cross-section of the MUC sub-detector. (Right) Barrel Yoke and RPC arrangement [196].

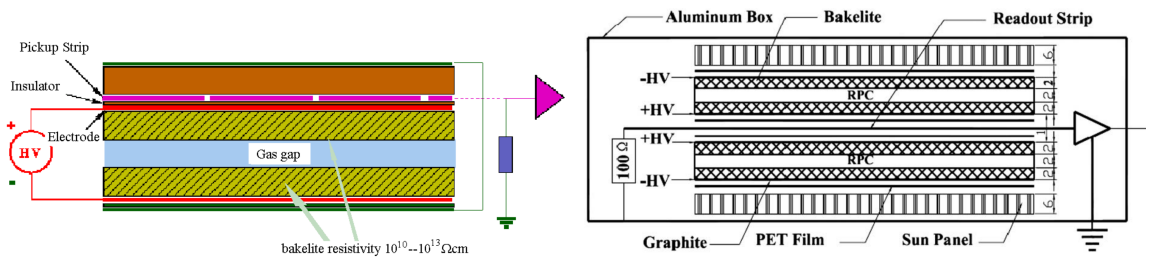


Fig. 3.14: (Left) Schematic representation of a RPC with the gas gap between resistive plates [196]. (Right) Cross-section of a RPC in double-gap design [190].

Item	Parameter
Layers in barrel/end caps	9/8
Inner/outer radius barrel	1700/2620 mm
Total thickness of steel plates in barrel	56 cm
Polar angle acceptance barrel	$ \cos\theta < 0.75$
Inner/outer radius end caps	2050/2800 mm
Total thickness of steel plates in end caps	43 cm
Polar angle acceptance end caps	$0.75 < \cos\theta < 0.89$
Average efficiency in barrel/end caps	96%/95%

Table 3.6: Properties of the Muon Counter system (from Reference [190]).

The reconstruction algorithm of the Muon Counter first searches for fired strips in both orientations (z- and azimuthal direction in barrel, x- and y-direction in end caps), then combines single hits to tracks and finally matches these tracks with extrapolated tracks from the MDC as well as with reconstructed EMC and TOF information. In case of a very low muon momentum sometimes no track can be reconstructed with hits in the muon counter. Therefore a second reconstruction attempt is performed using extrapolated MDC tracks as seed and searching for fired MUC hits in its vicinity. After the track reconstruction, several parameters like track penetration depth in the MUC, χ^2 of the MUC track reconstruction, a MUC-MDC track matching and others are used as input parameters into an Artificial Neural Network (ANN) for muon/hadron separation. For a momentum range between 0.5 GeV/c and 1.9 GeV/c for pions and muons, a selection efficiency of 90% for muons while simultaneously rejecting 96% of pions is possible [190].

Neutral hadrons like neutrons or antineutrons from the signal process' final state often penetrate the inner sub-detectors and arrive in the Muon Counter. This happens due to the missing charge and therefore no bending in the MDC, as well as the small interaction probability in the ToF and the EMC sub-detectors, as discussed in the previous sections. Assuming no interaction between a neutron (antineutron) and the material placed between the interaction point and the MUC, the interaction probability with the steel plates in the barrel region of the MUC system can be calculated with the specific hadronic interaction length $\lambda_I^{\text{muc}} = 132.1 \text{ g/cm}^2$ [50], the density of the steel $\rho^{\text{muc}} = 7.87 \text{ g/cm}^3$ [50] and the thickness of the steel plates (excluding the last 15 cm thick steel plate behind the last RPC layer) $L^{\text{muc}} = 41 \text{ cm}$ as:

$$P = 1 - \exp(-L^{\text{muc}} \cdot \rho^{\text{muc}} / \lambda_I^{\text{muc}}) = 91\% \quad (3.4)$$

From this approximation over 90% of neutrons and antineutrons will interact with the MUC and produce hits. Taking into account the interaction of these particles before they reach the Muon Counter, far less events with a signal in the MUC are expected. Additionally, no MUC based sub-trigger was implemented during the data samples collection used for this analysis (details in Section 3.2.6). Therefore events with no interaction in the EMC can't be analyzed at all and sub-sequentially all events analyzed will have a previous interaction with the MDC, TOF or EMC. Therefore the interaction probability with the MUC is reduced dramatically. The MUC signal from the signal process in this analysis is used primary for discrimination against cosmic ray background.

3.2.6 Trigger system

The BESIII trigger system is developed to separate between interesting physics events which are to be written to disc and to suppress background from cosmic rays and machine background. The second purpose of the trigger system is to reduce the event rate to a level small enough to be processed by the data acquisition system (DAQ), which is 4 kHz at maximum. A diagram to visualize the data flow and the trigger system is shown in Figure 3.15 (left).

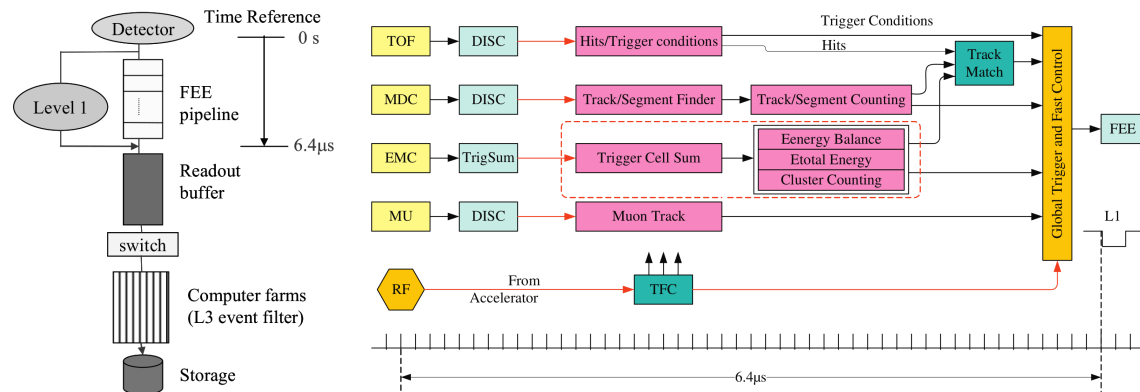


Fig. 3.15: (Left) Data flow diagram of the L1 trigger [190]. (Right) Block diagram of the trigger logic [197].

The trigger system has been realized as a two level system, a level-1 (L1) hardware trigger with a follow-up level-2 (L3) software event filter. Both parts together need to reduce Bhabha and different beam background events to a rate of 2 kHz, since the rate for interesting physics events is 2 kHz at maximum luminosity of $10^{33} \text{ cm}^{-2} \text{ s}^{-1}$ near the J/ψ region and the maximum rate to tape is around 4 kHz. Due to the high beam current, the electron and positron loss rate dominates the beam background and is estimated to be approximately 1.3×10^4 kHz. Measurements at Beijing ground level estimate the rate for cosmic ray of 1.5 kHz, which is suppressed at L1 stage mainly by the MDC and TOF sub-trigger to approximately 200 Hz. Table 3.7 shows the event rates for physics and background events in collision mode and after the L1 and L3 trigger.

Signals from the sub-detectors MDC, TOF, EMC and MUC are split in two and pipelined, one for digitization and storage and the other one for the L1 trigger. They are processed by the appropriate electronics in the VME crates to extract the basic trigger information like number of short and long tracks from the MDC, number of fired scintillators from the TOF, the number of clusters, their topology and energy deposition patterns from the EMC. The muon track information from the MUC sub-detector is also send to the L1 trigger system,

Process	Event Rate (kHz)	After L1 (kHz)	After L3 (kHz)
Physics	2	2	2
Bhabha	0.8	Pre-Scaled	Pre-Scaled
Cosmic ray	<2	~0.2	~0.1
Beam Background	>10 ⁴	<2	<1
Total	>10 ⁴	4	3

Table 3.7: Expected event rates at the J/ψ -peak (from Reference [190]).

but not used for the current trigger scheme. A track matching algorithm combines the information from the TOF, MDC and EMC sub-detectors. With this information the global trigger logic (GTL), schematically drawn in Figure 3.15 (right), decides for the event to be kept or discarded. The trigger decision latency of $6.4 \mu\text{s}$ is mainly determined by the EMC signal shaping time with its $1 \mu\text{s}$ shaping and $3 \mu\text{s}$ decay time. Since it is not possible to determine the precise bunch from which the detected event comes from, a window of 24 ns is chosen for the trigger. During this window events can come from up to 5 bunches (for the 6 ns bunch interval for the scan data set collected in 2015 [27]). Informations from sub-triggers and the global trigger are passed to the DAQ and stored for offline analysis together with the event number, the system status and possible error messages.

In this analysis, the signal process final state contains primarily only neutral particles. Therefore the most crucial sub-trigger system is from the EMC. A table with open channels for the data collection analyzed in this work is shown in Figure 3.16. Table 3.8 lists and explains the trigger conditions in the second column in Figure 3.16.

The three threshold values for the total energy deposition used during the collection of the 2015 scan data analyzed in this work are:

- $E_{\text{tot_L}} = 0.21 \text{ GeV}$
- $B_{E_{\text{tot_H}}} = 0.65 \text{ GeV}$
- $E_{\text{tot_M}} = 0.45 \text{ GeV}$

In most cases, the signal process $e^+e^- \rightarrow \bar{n}n$ contains more than one shower in the EMC (for the difference between "cluster" and "shower" please refer to Section 3.2.4), especially based on the event selection criteria discussed in Section 5.3. Therefore a signal event will be triggered usually by trigger channel 12.

			CH01 CHARGE	CH02 CHARGE	CH03	CH04 CHARGE	CH05 CHARGE	CH06 CHARGE	CH07	CH08	CH09 NEU	CH10 random	CH11	CH12 Delayed NEU	CH13	CH14	CH15	CH16
			Y	Y	N	Y	Y	Y	N	N	Y	Y	N	Y	N	N	N	N
EMC	Etot_L	09																
	NBclus.GE.1	12		Y			Y	Y							Y			
	NEclus.GE.1	13	Y															
	ECLUS_BB	3																Y
TOF	BTOF_BB	17				Y												
	NETOF.GE.2	18																
	NETOF.GE.1	19	Y															
	NBTOF.GE.2	20		Y	Y								Y					
	NBTOF.GE.1	21					Y	Y										
	NTOF.GE.1	22													Y			
MDC	LTrk_BB	42				Y							Y					
	STrk_BB	38	Y															
	NLtrk.GE.N	43																
	NLtrk.GE.2	44		Y	Y			Y										
	NLtrk.GE.1	45					Y	Y										
EMC	Nclus.GE.1	48									Y			Y				Y
	Nclus.GE.2	49																
	BEtot_H	55									Y							
	EEtot_H	56																
	Etot_M	58												Y				

Fig. 3.16: Open channels during data collection for 2015 collected data set [27], [198]. The first row denotes the trigger channel number (e.g. CH09 for channel 9), the second one stands for the physics process final state charge (if one particle in the final state carries electrical charge, the process is denoted as "CHARGE", if not, the process is denoted as "NEU" for neutral. Channel 10 is a random trigger discussed later in this sub-section), the third row marks if this channel was used during the data taking, the first column denotes the sub-detector used for trigger, the second column denotes the trigger requirements explained later in this sub-section, the third column shows an internal ID for the trigger requirement. The two red marked columns are trigger channels used for pure neutral final state processes.

Following the function and purpose of the single sub-trigger systems are explained:

- TOF signals, with a timing uncertainty of 30 ns, are the fastest to arrive at the L1 trigger. They are used to determine the event time based on charged particles hits in the MDC. This sub-system also reduces cosmic ray background through requirements on the timing information of signals in the TOF detector. Trigger conditions are based on the number of hits in the scintillator bars and on their topology.
- The MDC sub-trigger has a latency of 400 ns and separates interesting physics from background tracks associated with beam losses, synchrotron radiation and cosmic rays. A track finding algorithm combines hits from 4 so-called super-layers to track and check for a transverse momentum p_t larger than a specific threshold. If a track passes this requirement, it will be categorized as a "long" track, if it reaches the last super-layer, or as a "short" track, if it doesn't reach the last super-layer, as visualized in Figure 3.17. The trigger conditions are the number of tracks, their length and their kinematics.

Sub-trigger	Condition	Explanation
TOF	BTOF_BB	Barrel TOF back-to-back signal
	NETOF.GE2	Number of hits in the end cap TOF ≥ 2
	NETOF.GE1	Number of hits in the end cap TOF ≥ 1
	NBTOF.GE2	Number of hits in the barrel TOF ≥ 2
	NBTOF.GE1	Number of hits in the barrel TOF ≥ 1
	NTOF.GE1	Number of hits in TOF ≥ 1
MDC	LTrk_BB	Long track back-to-back
	STrk_BB	Short track back-to-back
	NLtrk.GEN	Number of long tracks $\geq N$ (N is programmable)
	NLtrk.GE2	Number of long tracks ≥ 2
	NLtrk.GE1	Number of long tracks ≥ 1
EMC	Etot_L	Total energy of all EMC exceeding the low threshold
	NBclus.GE1	Number of clusters in barrel EMC ≥ 1
	NEclus.GE1	Number of clusters in end cap EMC ≥ 1
	Eclus_BB	End cap clusters back-to-back
	Nclus.GE1	Number of clusters in all EMC ≥ 1
	Nclus.GE2	Number of clusters in all EMC ≥ 2
	BEtot_H	High threshold for total energy deposition in barrel
	EEtot_H	High threshold for total energy deposition in end caps
	Etot_M	Middle threshold for total energy deposition in EMC

Table 3.8: Trigger condition explanations for Figure 3.16 (from Reference [190]).

- The EMC sub-trigger is the only sub-system to trigger neutral events. Therefore it is the most important one in this analysis. Additionally it provides the event time for neutral events. The EMC has the largest latency of more than $1.5 \mu\text{s}$, before its signal can be used as a sub-trigger, mainly because of the long signal shaping time. The trigger conditions are based on the total energy deposition, the number of isolated energy clusters and the energy balance of different regions. For this purpose Basic Trigger Cells (BTC) are defined, which consist of sets of (4×4) crystals in the barrel region and sets of 15 crystals in the end caps, shown in Figure 3.18. These numbers of arrangement have been determined by two requirements: a trigger cell must include most of the energy from an electromagnetic shower (in the optimal case the full energy deposition is contained), but be small enough to provide precise position information. A simulation for the determination of the optimal trigger cell size is shown in Figure 3.19. To achieve a high trigger efficiency for physics events, while effectively discriminating against beam related and cosmic ray background,

the correct energy threshold needs to be set for a basic cell to pass or reject a trigger signal. From simulations a value between 80 and 100 MeV has been chosen [199], as shown in Figure 3.20 (top). Additionally, an energy threshold for the whole EMC related energy deposition is needed to ensure a high trigger efficiency for physics events and simultaneously a high rejection efficiency for background events. A simulation at $\sqrt{s} = 3.097$ GeV shows the corresponding choice for this energy threshold in Figure 3.20 (bottom). With these energy thresholds it is possible to achieve a high trigger efficiency for minimum ionization particles while discriminating effectively against beam related and cosmic background.

- No MUC sub-trigger was available during the data collection used for this analysis.

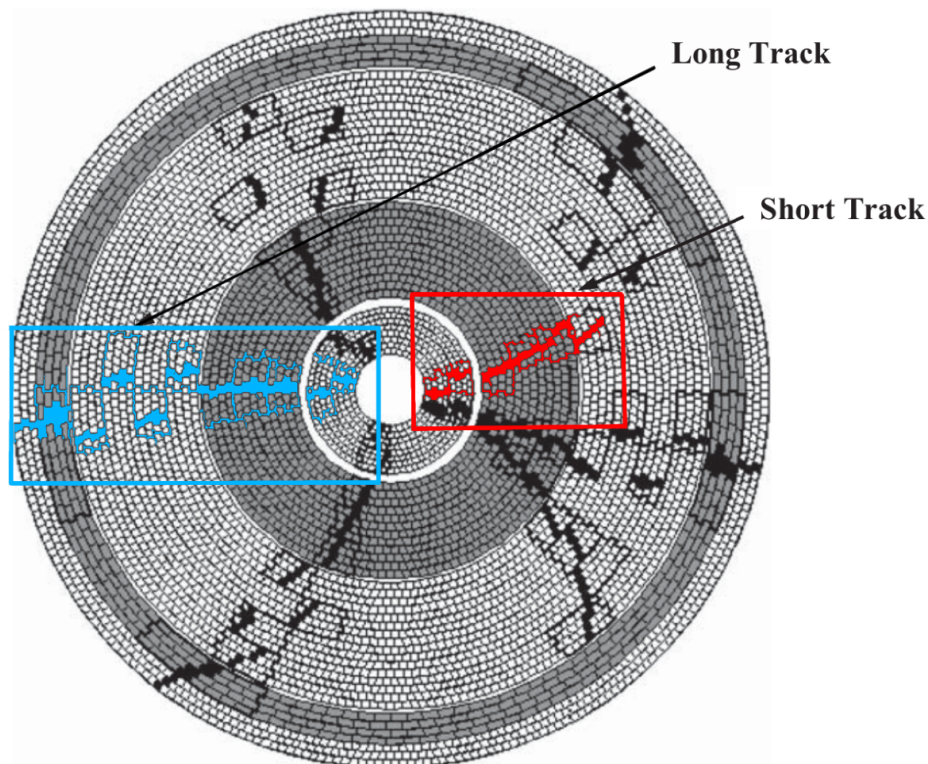


Fig. 3.17: Visualization of the short and long tracks in the MDC as defined in the text above (original figure from Reference [190]). The MDC is shown as a cut through the XY plane. The blue marked reconstructed track reaches the last super-layer, shown as the outermost white region containing three single layers, is denoted as a long track. The red marked track doesn't reach the last super-layer and is therefore denoted as a short track.

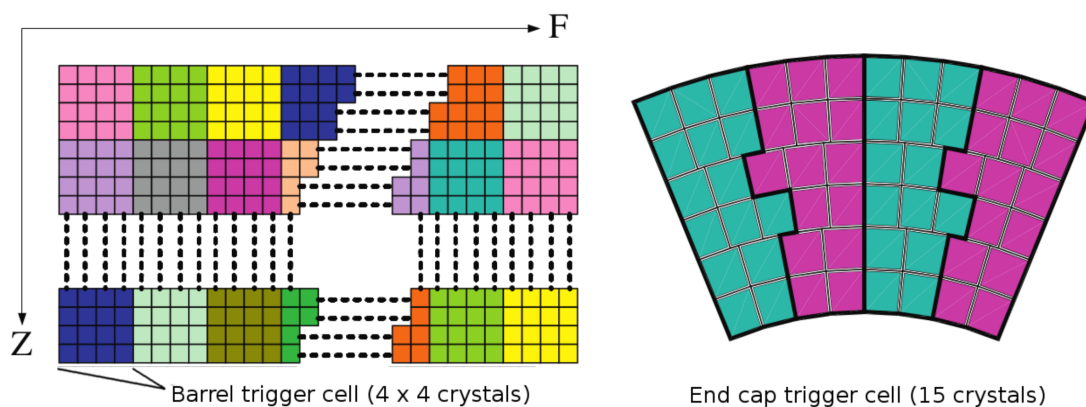


Fig. 3.18: EMC trigger cell arrangement (left) in the EMC barrel region and (right) end caps (original figure from Reference [199]).

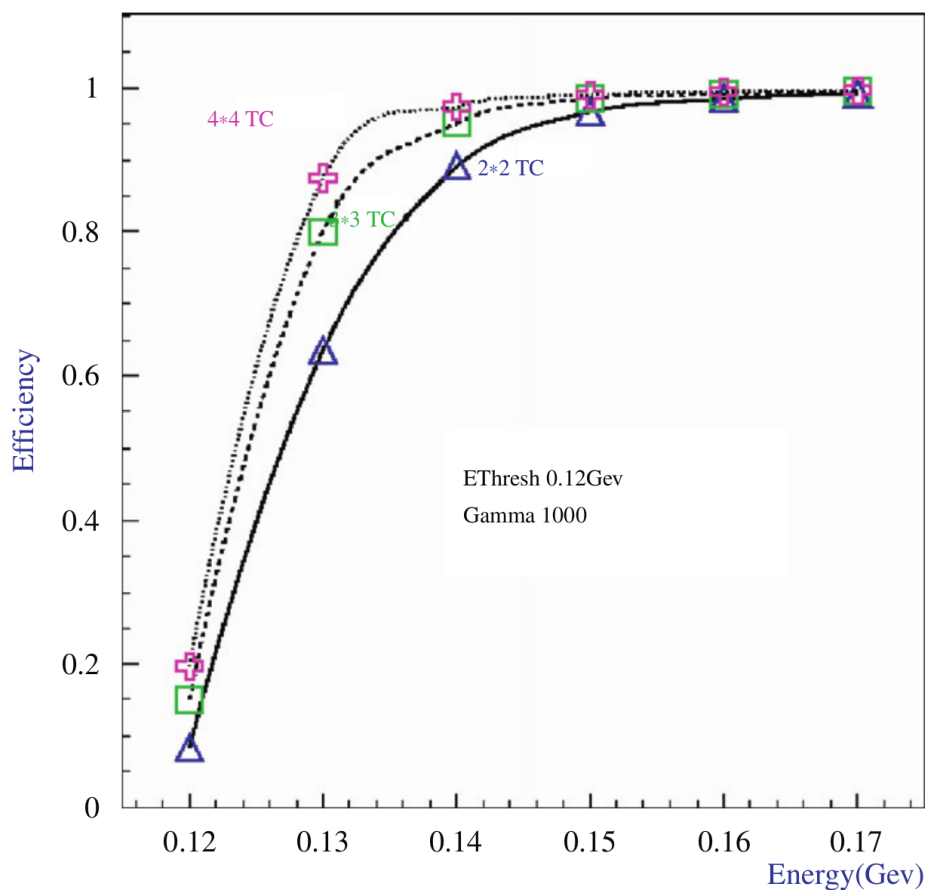


Fig. 3.19: Efficiency of crystal trigger with respect to the energy deposition in an array of 2×2 to 4×4 trigger cells. (original figure from Reference [199]).

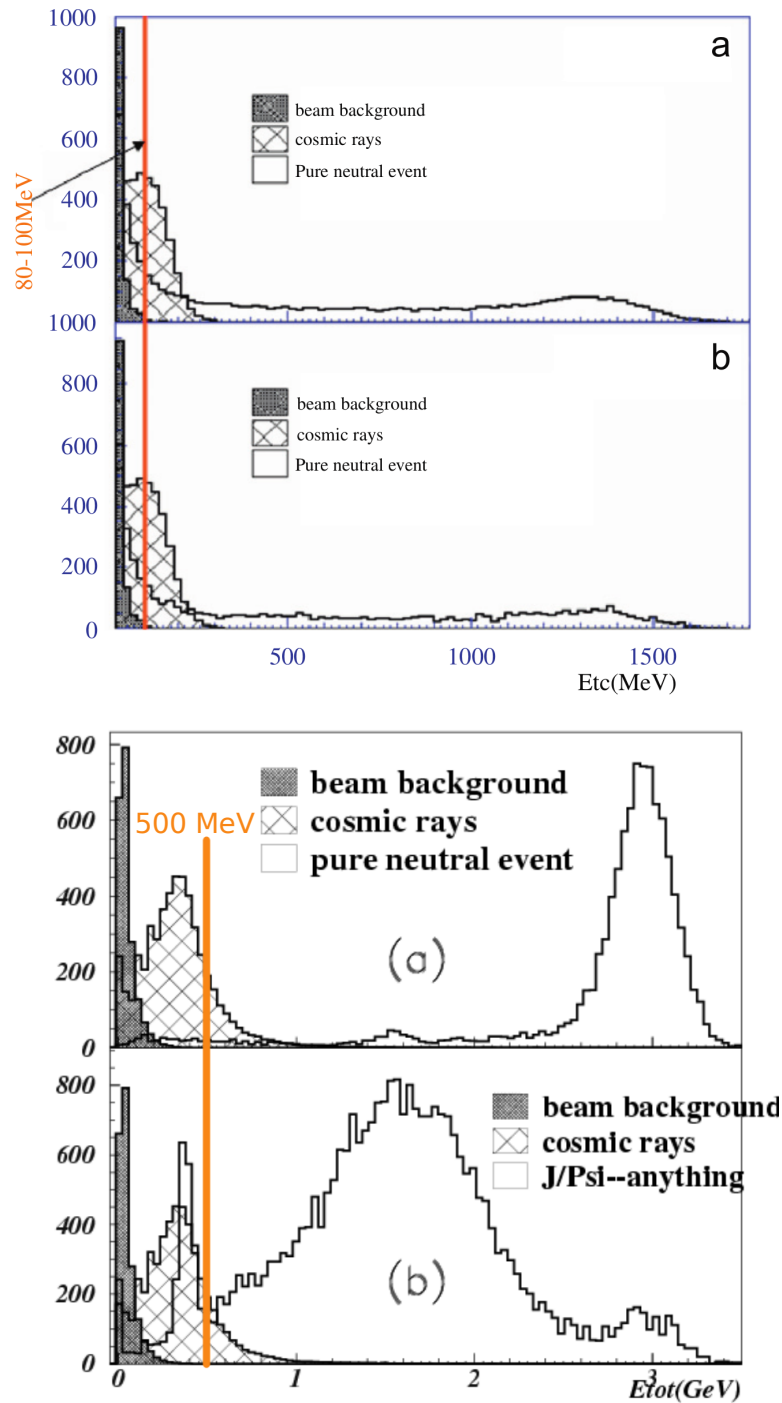


Fig. 3.20: (Top) Simulation at J/ψ center-of-mass energy of energy deposition for beam related background, cosmic ray background and pure neutral final state events in a trigger cell for the EMC barrel (a) and end cap (b). Energy deposition from cosmic rays peaks between 80-100 MeV, while beam related background events have mostly an energy deposition below 100 MeV. (Bottom) Simulation at J/ψ center-of-mass energy of energy deposition for beam related background, cosmic ray background and collision events in the whole EMC. (a) Pure neutral final state events. (b) Inclusive J/ψ to anything events. (original figures from Reference [199]).

3.3 Software framework

This section contains a basic description of the software framework for data analysis at BESIII. Additionally, further parts are dedicated to the Geant4 simulation platform, CERN's ROOT framework for data analysis and the package RooFit included in CERN's ROOT. The latter is used for various fitting procedures within this analysis.

3.3.1 BESIII Offline Software System

The BESIII Offline System (BOSS) is a framework developed for the BESIII experiment. It consists of a simulation part for the interaction of physical processes with the detector material, the calibration of collected data, and the reconstruction of events. Various analysis tools for the end user are implemented. It includes libraries for the detector sub-systems, generators for Monte Carlo simulation, algorithms for particle reconstruction and tools for physics analysis. Additionally, BOSS includes algorithms for very specific needs, like a pileup algorithm for mixing random trigger data with simulation of signal events for a proper implementation of the background. Other tools to mention are the magnetic field service, which provides a precise value of the magnetic field at any point of the detector, the particle property service to provide various particle properties and a navigation service to trace reconstructed tracks back to the Monte Carlo simulated particles. An overview of the architecture of the BOSS framework is shown in Figure 3.21 (left).

The included libraries are written in C++. Some of them are based on the GAUDI framework [200]. The compilation is performed with CMT [201], which maintains different version of packages and provides executables. BOSS is constantly expanded and optimized by scientists working at BESIII. At the time of the creation of this thesis it is running on Scientific Linux Cern SLC5 and SLC6.

The simulation part of BOSS models the detector impact of the particles with the help of Geant4 (see section 3.3.2). Information on the detector geometry and its materials is stored in Geometry Design Markup Language (GDML) [202]. Simulations of readout electronics, electronic noise, dead channels, as well as the trigger system are handled by the digitization code. Many Monte Carlo generators are included in BOSS which can simulate various physics process. Simulations contain the kinematic information of the generated particles which are stored after digitization as so-called *raw* data. The data flow during simulation process in BOSS is shown in Figure 3.21 (right).

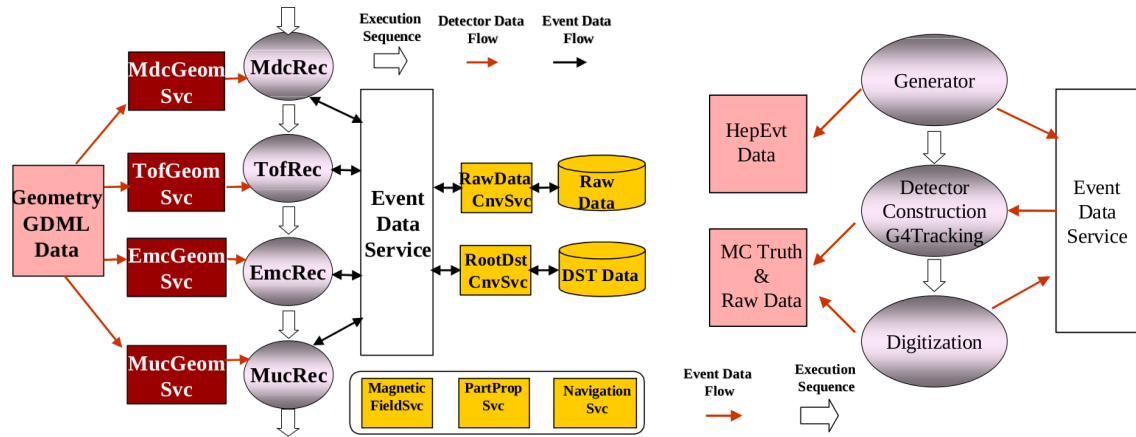


Fig. 3.21: (Left) The overall BESIII software framework architecture [203]. (Right) The BESIII event data flow in simulation [203].

The calibration part consists of the calibration framework and calibration algorithms. Calibration constants for each sub-detector are stored in ROOT format (see Section 3.3.3) and provided to both, simulation and reconstruction algorithms if needed. For example, during the reconstruction of electromagnetic showers in the EMC, the conversion between voltage from the crystals to energy values is needed, which is provided through specific calibration constants (e.g. e_i and c_i in Section 3.2.4). The calibration framework searches the correct set of calibration constants from the database and returns it to the algorithm which required them. A GUI client provides the possibility to manage the administration of the calibration database remotely. The structure of the calibration service in BOSS is shown in Figure 3.22 (left).

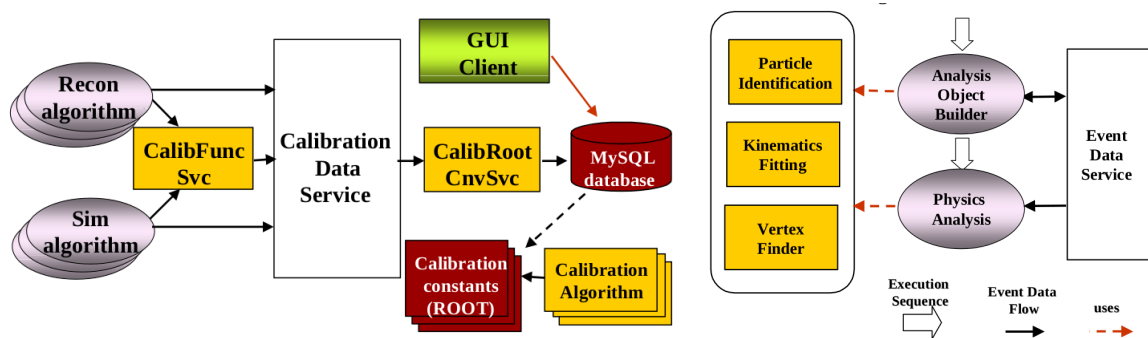


Fig. 3.22: (Left) The structure of the BESIII calibration software [203]. (Right) The structure of the analysis software in BOSS [203].

The event reconstruction is the main task of the offline software. The reconstruction part of BOSS includes a chain of reconstruction algorithms including dE/dx and tracking

algorithms for the MDC, time-of-flight reconstruction in the TOF, clustering and shower reconstruction in the EMC as well as muon track finder in the MUC. The reconstruction procedures for the different sub-detectors are described in Sections 3.2.2 to 3.2.5.

In the analysis part of BOSS, the reconstructed event information is available for various additional tools for analysis, including particle identification (PID), kinematics fitting and a vertex finder. The PID at BESIII combines information about particle momentum and dE/dx from the MDC, the time-of-flight from the TOF, energy deposition from the EMC and track information from the MUC to calculate a probability for the particle ID. Different methods for kinematics fitting are available to effectively improve the resolution for energy and momentum measurements for charged and neutral particles. The vertex finder tool helps to find both primary and also secondary vertices inside the MDC volume.

BOSS mainly supports three types of data: RAW data, reconstructed data and Data-Summary-Tape (DST) data. While reconstructed and DST data are in ROOT format for easy handling by the analyst, the RAW data is often found in so called hit-maps and other detector specific formats. In this analysis some event selection criteria aren't implemented in ready-to-use algorithms. A big part of this work was the challenge to implement methods for the simultaneous usage of RAW data and reconstructed data, for example for the time-of-flight reconstruction for neutral particles (see Appendix B) and the impact of neutral particles in the muon counter. The BOSS version used with the scan data collected in 2015 (see Table 3.10) for the reconstruction of the signal process $e^+e^- \rightarrow \bar{n}n$ is 6.6.5.p01, while some selection efficiency corrections are studied from 2009 and 2011 J/ψ data (see Table 3.9) under the BOSS version 6.6.4.p01 and 6.6.4.p03.

3.3.2 Detector response simulation with the Geant4

The Geant4 [204], [205] (**Geometry and tracking**) software platform is developed at CERN for the simulation of detector response caused by particle interaction with material. Geant4 is based on the object oriented C++ programming language and can store any geometrical shape information with the GDML [202] (Geometry Design Markup Language) framework. A variety of materials used in detectors can be simulated by Monte Carlo techniques concerning their response to interaction with different particles. Geant4 is used by many modern experiments in the topic of particle physics like BESIII, ATLAS, BaBar BELLE or PANDA to name some. Geant4 is extensively used in the simulation part of the BESIII Offline Software (see Section 3.3.1).

3.3.3 CERN ROOT for statistical treatment and visualization of data

The ROOT [206] software framework, a standard tool collection for data analysis used in particle physics, is developed by CERN. It is used for both, data processing and analysis as well as for the visualization of results. It is extensively used throughout this thesis. Published in a first version in 1994, it provides a constantly increasing variety of libraries, classes and methods for data analysis and is available on most operating systems like Linux, Windows, Mac OS and others. Originally designed to handle the extreme amount of data from the LHC experiments, today ROOT is used not only in physics experiments, but more and more often in industry and IT for big data, data mining, visualization of results, multivariate analysis and other applications. For this analysis, the ROOT version 6.10/06 has been used.

3.3.4 Fitting and toy Monte Carlo studies with RooFit

RooFit [207] is a set of libraries, providing pre-defined methods for the modeling of expected distributions and also including tools for different fit application. It enables to simulate "Toy Monte Carlo" samples and to visualize the analysis. Originally developed by scientists of the BaBar experiment, today it is used widely by the particle physics community for data analysis. A main aspect of the RooFit core design is the function to model probability density functions (PDF's) of experimentally measured distributions. The latter are described in terms of parameters, taking into account the statistical nature of such experimental data. The RooFit framework is mainly used for the signal extraction in Chapter 7 and the angular analysis in Section 9.2 via dedicated fit methods, as discussed in detail in the corresponding sections.

Another application of the RooFit framework within this thesis is the study of the angular distribution in Section 9.2 via the Toy Monte Carlo method. After determining the results from the angular analysis of the collider data, a massive MC study is performed to verify the extracted values and their errors. This approach has the advantage, that the experimental measurement can be simulated and repeated many times and therefore a distribution of the resulting parameters can be studied through the whole statistical phase-space.

3.4 The data set of the BESIII experiment

BESIII is operating in the so called τ -charm center-of-mass (c.m.) region, since it covers the energy range of various charmonium resonances and the threshold for τ leptons pair production. With the main goals of the BESIII experiment being charmonium spectroscopy, D -meson physics, τ physics, XYZ physics and search for new physics beyond the Standard Model, next to the study of form factors and the measurement of the hadronic ratio, it is natural that the BESIII detector collected large amount of data over this region. The center-of-mass energy of BESIII is adjusted between 2.0 GeV and 4.6 GeV, to cover the previously named topics. These studies are possible since the BESIII experiment collected some of the world's largest data sets for the resonances at these cms energies, here quoting for example the $J/\psi(3097)$ data set [208]. Figure 3.23 shows a selection of data collected by BESIII in comparison with other experiments.

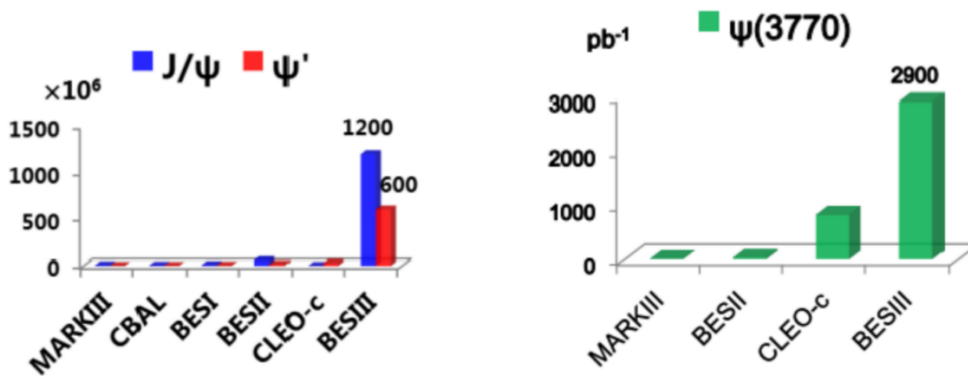


Fig. 3.23: Comparison of data sets collected by BESIII and other experiments for the charmonium resonances $J/\psi(3097)$, $\psi(3686)$ and $\psi(3770)$, showing that BESIII has the world largest data sets at these energies. In the left histogram numbers of events are shown.

The data sets at BESIII are generally categorized in two classes. One group, characterized by large luminosity samples with fixed center-of-mass energies at resonances, is listed in Table 3.9. These data have been collected mainly for the study of charmonium resonances and the XYZ states, where the BESIII contributions include new discoveries, for example the $X_c(3900)$ [209], as well as improvements on exciting results, for example a new measurement of the Muon Anomaly $(g-2)_\mu$ [210].

\sqrt{s} (GeV)	\mathcal{L}_{int} (pb ⁻¹)	Year	Sample
3.097	1.3×10 ⁹ events [211]	2009 + 2012	J/ψ(3097)
3.686	0.5×10 ⁹ events [212], [213]	2009 + 2012	ψ(3686)
3.773	2916.94 [214]	2010 + 2011	ψ(3770)
4.009	481.96 [215]	2011	ψ(4040)
4.180	3000 [215]	2016	ψ(4180)
4.230	1047.34 [215]	2013	Y(4260)
4.260	825.67 [215]	2013	Y(4260)
4.360	539.84 [215]	2013	Y(4360)
4.420	1028.89 [215]	2014	Y(4420)
4.600	566.93 [215]	2014	Y(4600)

Table 3.9: Large luminosity data sets collected at resonances.

The other category is characterized as sets of scan data over a large energy range with low luminosities per data point and is summarized in Table 3.10. These data are dedicated for physics on the hadronic R measurement ($\sigma_{e^+e^- \rightarrow \text{hadrons}}/\sigma_{e^+e^- \rightarrow \mu^+\mu^-}$), τ physics, baryon form factor measurements and measurements of line-shapes for various resonances.

\sqrt{s} range (GeV)	Scan points	\mathcal{L}_{int} (pb ⁻¹)	Year	Sample
2.232 - 3.671	12	156.94 [216]	2011	R-scan τ mass
3.800 - 4.600	104	800 [217]	2014	R-scan line-shape
2.000 - 3.080	23	759.59 [27], [198]	2015	Energy scan

Table 3.10: Scan data sets collected at discrete center-of-mass energies \sqrt{s} .

The accurate measurement of the integrated luminosity is crucial for physics analysis. The BESIII experiment has a rough "online" luminosity measurement in real time during the data taking, mainly performed by using the EMC endcaps and used for data quality monitoring. After the data taking is finalized, an accurate luminosity determination is performed by studying well understood QED processes like Bhabha, dimuon and digamma final states, including background subtraction and corrections on trigger and detector efficiencies. In these studies the accuracy on the luminosity measurements reaches 1%.

In this work the signal process $e^+e^- \rightarrow \bar{n}n$ is analyzed by using the energy scan data set between 2.0 and 3.08 GeV, which is summed up in Table 3.11. Efficiency corrections are studied from the J/ψ data sets at 3.097 GeV [214] as listed in Table 3.9.

\sqrt{s} (GeV)	Run Number	Data Taking Period	\mathcal{L}_{int} (pb^{-1}) [27]
2.0000	41729 - 41909	15.04.18 - 15.04.27	$10.074 \pm 0.005 \pm 0.067$
2.0500	41911 - 41958	15.04.27 - 15.04.29	$3.344 \pm 0.003 \pm 0.027$
2.1000	41588 - 41727	15.04.11 - 15.04.17	$12.167 \pm 0.006 \pm 0.085$
2.1266	42004 - 43253	15.05.01 - 15.06.18	$108.49 \pm 0.02 \pm 0.94$ [198]
2.1500	41533 - 41570	15.04.09 - 15.04.11	$2.841 \pm 0.003 \pm 0.024$
2.1750	41416 - 41532	15.04.03 - 15.04.09	$10.625 \pm 0.006 \pm 0.091$
2.2000	40989 - 41121	15.03.12 - 15.03.19	$13.699 \pm 0.007 \pm 0.092$
2.2324	41122 - 41239	15.03.20 - 15.03.25	$11.856 \pm 0.007 \pm 0.087$
2.3094	41240 - 41411	15.03.26 - 15.04.02	$21.089 \pm 0.009 \pm 0.143$
2.3864	40806 - 40951	15.03.02 - 15.03.07	$22.549 \pm 0.010 \pm 0.176$
2.3960	40459 - 40769	15.02.14 - 15.02.28	$66.869 \pm 0.017 \pm 0.475$
2.5000	40771 - 40776	15.02.28 - 15.02.28	$1.098 \pm 0.002 \pm 0.009$
2.6444	40128 - 40296	15.01.31 - 15.02.07	$33.722 \pm 0.013 \pm 0.216$
2.6464	40300 - 40435	15.02.07 - 15.02.12	$34.003 \pm 0.013 \pm 0.282$
2.7000	40436 - 40439	15.02.13 - 15.02.13	$1.034 \pm 0.002 \pm 0.007$
2.8000	40440 - 40443	15.02.13 - 15.02.13	$1.008 \pm 0.002 \pm 0.031$
2.9000	39775 - 40069	15.01.16 - 15.01.29	$105.253 \pm 0.025 \pm 0.905$
2.9500	39619 - 39650	15.01.11 - 15.01.12	$15.942 \pm 0.010 \pm 0.143$
2.9810	39651 - 39679	15.01.12 - 15.01.13	$16.071 \pm 0.010 \pm 0.095$
3.0000	39680 - 39710	15.01.13 - 15.01.14	$15.881 \pm 0.010 \pm 0.110$
3.0200	39711 - 39738	15.01.14 - 15.01.15	$17.290 \pm 0.011 \pm 0.123$
3.0800	39355 - 39618	14.12.31 - 15.01.10	$126.185 \pm 0.029 \pm 0.921$
Sep. Beam 2.2324	41959 - 41999	15.04.30 - 15.04.30	non-collision mode
Sep. Beam 2.6444	40777 - 40804	15.02.28 - 15.03.02	non-collision mode

Table 3.11: Data sets used for the $e^+e^- \rightarrow \bar{n}n$ analysis in this work. The data was collected in 2015. The first error of the luminosity is statistical, the second one is the systematic uncertainty. Data sets marked in orange are not used for data analysis due to their small integrated luminosity. The last two lines list so-called "separated beam data" which is collected under the condition, that the e^+ and e^- beams are in non-collision setting. These data will be used for the study of beam related and cosmic ray background.

Chapter 4

The Monte Carlo Simulation

Several Monte Carlo (MC) simulations for signal and background processes have been produced for this analysis. In this chapter, all event generators used in this work are introduced and their characteristics are discussed. The signal MC simulation is described in detail in Section 4.2, the simulation of various background processes is discussed in Section 4.3, the simulation of processes, which are used for efficiency studies is listed in Section 4.4. All simulations produced for this analysis are summed up in the Appendix A.1. Monte Carlo simulations for the signal process $e^+e^- \rightarrow \bar{n}n$ and background processes are used for the optimization of the signal event selection criteria and the estimation of physics background contamination. They are also used for an estimation of the signal event selection efficiency, including QED corrections for Initial-State-Radiation events and vacuum polarization. The simulation software BOOST [218] (BESIII Object Oriented Simulation Tool) is based on a GEANT4 package [204], [205] and includes the following components: event generators; the description of geometry and materials of the BESIII detector; particle tracking and detector response including the digitization models [187], [190]; a database with the detector conditions and running performance.

After the simulation by an event generator, the BOOST package manages the digitization, taking into account the detector response and run-specific characteristics by using the correct run numbers and calibration tables from the corresponding data collection. These specifications include for example the number of bunches per trigger window and a pile-up algorithm responsible for mixing randomly triggered physics events to the signal. After this step, the so called RAW data is produced, including the signal response in the different sub-detectors. The reconstruction algorithm combines this information to tracks in the

MDC, hits in the TOF, showers in the EMC and hits in the MUC. Finally the algorithm produces reconstructed data, denoted as DST, ready for data analysis. The full chain for the simulation process is shown in Figure 4.1.

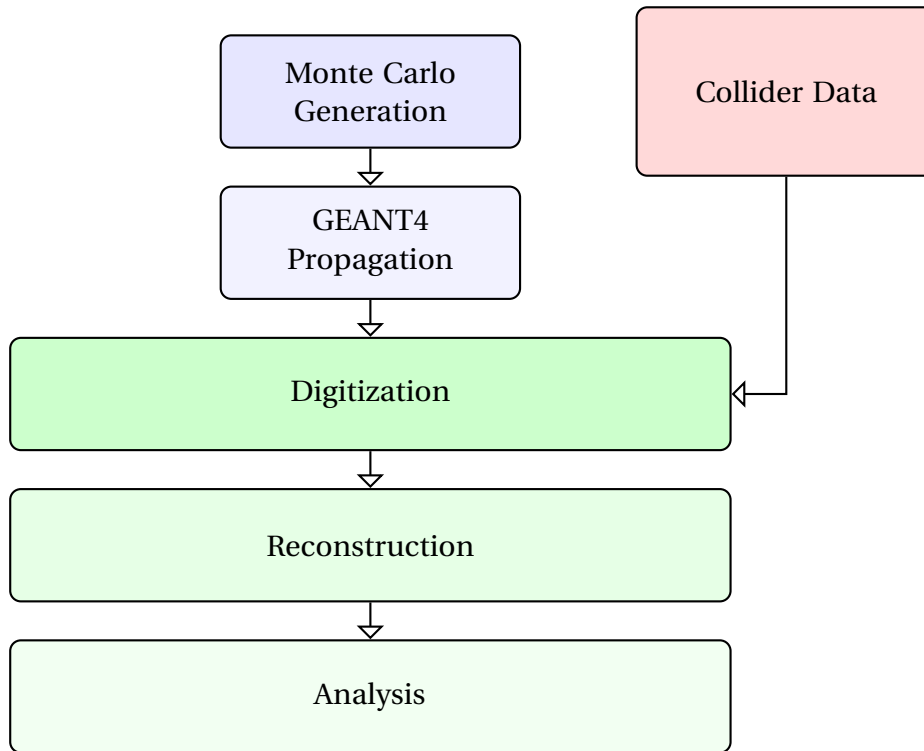


Fig. 4.1: Diagram of the standard simulation process chain in BOOST. As a comparison, the collider data processing chain is included.

4.1 Monte Carlo event generators for the physics simulation

Monte Carlo event generators are widely used in high energy physics and can be divided into two classes: one class is used for the simulation of the detector design and its optimization as well as particle interaction with the detector material. The second class is used in physics analysis and produces simulations of one (or several) physics event, which can be produced in a collider. Here, a short introduction for the second class is given.

The purpose of Monte Carlo event generators is to simulate the desired event as realistic as possible. However, the experimental situation is usually too complicated to solve the underlying set of equations analytically or numerically. Taking into account that the

physics processes generated from particle collisions are subject to probabilities, described through matrix elements, Monte Carlo event generators are based on probability density functions (PDFs) which can be modeled, using random numbers and statistical sampling techniques. Therefore there is no need to write down and solve the complicated equations for the desired process. The PDFs can be provided through data driven methods, be theory driven, or from a combination of both by fitting the experimental data with the theoretical prediction. Most physical processes can be divided into individual problems, neglecting the effects of correlation between them. With this factorization method, the single sub-processes can be calculated separately. Figure 4.2 shows a phenomenological visualization of the different sub-processes calculated separately with an MC event generator.

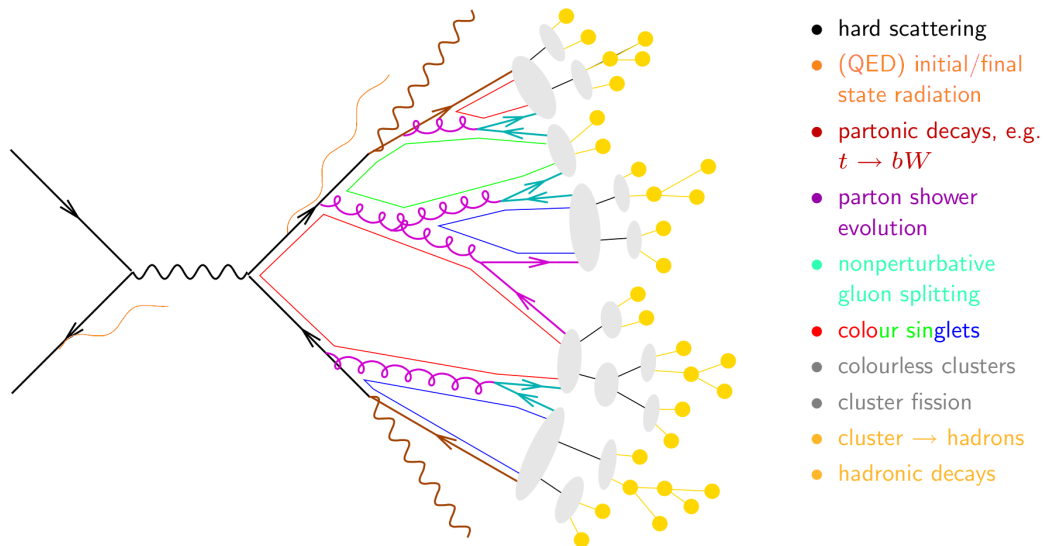


Fig. 4.2: Phenomenological visualization of the different phases for the simulation of an event with a Monte Carlo event generator. Image adapted from D. Zeppenfeld (PITP 05 lectures).

Based on the discussion in [219], the general steps for an event simulation with a MC event generator for the timelike momentum transfer region including hadron production can be divided into:

- The so-called hard process, where the initial particles are generated with their initial momenta in the hard collision. Often the leading order matrix element is used for this reaction. In the example shown in Figure 4.2, the hard process is visualized by the four black arrows with the virtual photon line in between on the left side of the plot. Modern MC event generators can include the treatment of Initial- and Final-State-Radiation, represented by the pink wave-lines, by calculating the hard process in higher orders. In principle, this calculation is exact up to the considered order.

- The parton shower phase describes the QCD evolution, where the colored quarks and gluons evolve from the hard scale (fixed by the momentum transfer from the initial state) to the so-called infrared cut-off. This process includes the QCD Bremsstrahlung, where quarks radiate gluons, which branch again to quark-anti-quark pairs. This phase is calculated within the resummed perturbation theory.
- In the hadronization phase, the evolved partons are formed into hadrons, taking into account the confinement. Since perturbative methods are failing for the long-distance physics of this effect, phenomenological models are used for the modeling of this phase. In Figure 4.2 this sub-step is indicated through the gray blobs on the right side of the plot.
- In the last step possible decays of unstable hadrons (often heavy resonances) into stable particles are modeled. This secondary particle decay is modeled with the help of effective theories and with experimentally measured branching ratios.

Given a set of input parameters for a specific physics event, the Monte Carlo event generator calculates the listed sub-phases and provides the end-user with the four-momenta of the final state particles produced in the interaction, which can be subsequently fed into the detector description simulation for further analysis, as shown in Figure 4.1.

4.2 The signal Monte Carlo simulation

For the simulation of the signal channel $e^+e^- \rightarrow \bar{n}n$ two different generators are used, Phokhara v9.1 [161] for the main analysis, and ConExc [220] included in the BesEvtGen-00-03-18 [221] simulation package as a cross check. With Phokhara, signal events can be generated up to the Next-to-Next-to-Leading Order (NNLO) in the QED, including higher order processes with up to two Initial State Radiation photons emitted before the e^+e^- interaction. ConExc can only generate signal events up to the Next-to-Leading Order (NLO). Both generators are capable of simulation of the Vacuum Polarization (VP), with ConExc using the implementation by Fred Jegerlehner [222], while in Phokhara the choice between the implementation by Fred Jegerlehner or Thomas Teubner [223] is possible. Since the final state $e^+e^- \rightarrow \bar{n}n$ is electrically neutral, no QED Final-State-Radiation (FSR) effects occur. In the next section, details for the signal MC simulation are listed.

4.2.2 The initial form factor parametrization

The main signal simulation in this analysis is performed with Phokhara v9.1. As an input for the cross section and FFs of the neutron, the VMD model shown in Section 2.4.5 is used, taking into account nucleon electromagnetic FFs in both the SL and TL region. For the meson and nucleon masses and widths, values from the PDG [50] are taken. Other model parameters are extracted from experimental results. A global fit to available world data for the effective FF of the nucleon in the SL and TL region, as well as to the ratio of the nucleon FF's in the SL region (and to the ratio in the TL region in case of the proton) has been performed to extract the remaining parameters. Details on this parametrization can be found in [224]. The simulated Born cross section, the electric and magnetic FFs and their ratio, implemented in Phokhara v9.1, are shown in Figure 4.3 and 4.4.

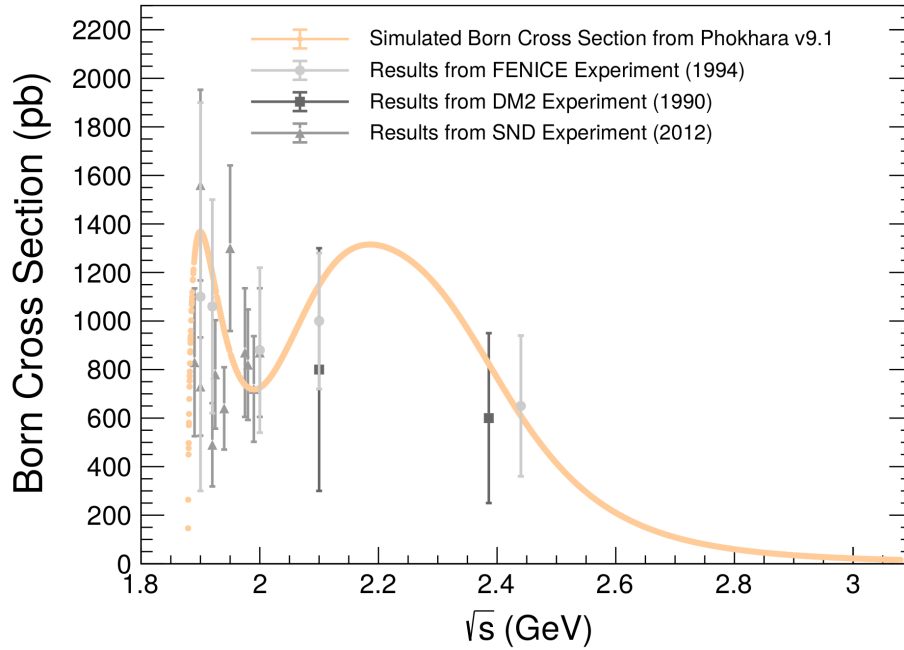


Fig. 4.3: Original Born cross section of the process $e^+e^- \rightarrow \bar{n}n$ simulated with Phokhara v9.1 using settings as shown in Table 4.1. The orange dots are the Born cross section output from Phokhara. Light gray dots are results from the FENICE experiment, dark gray squares are results from the DM2 experiment, while gray triangles represent recent results from the SND experiment. The parametrization is explained in the text.

Phokhara v9.1 has many options for end-users. Table 4.1 shows an input card with the used settings for the signal MC generation (settings for other processes are neglected).

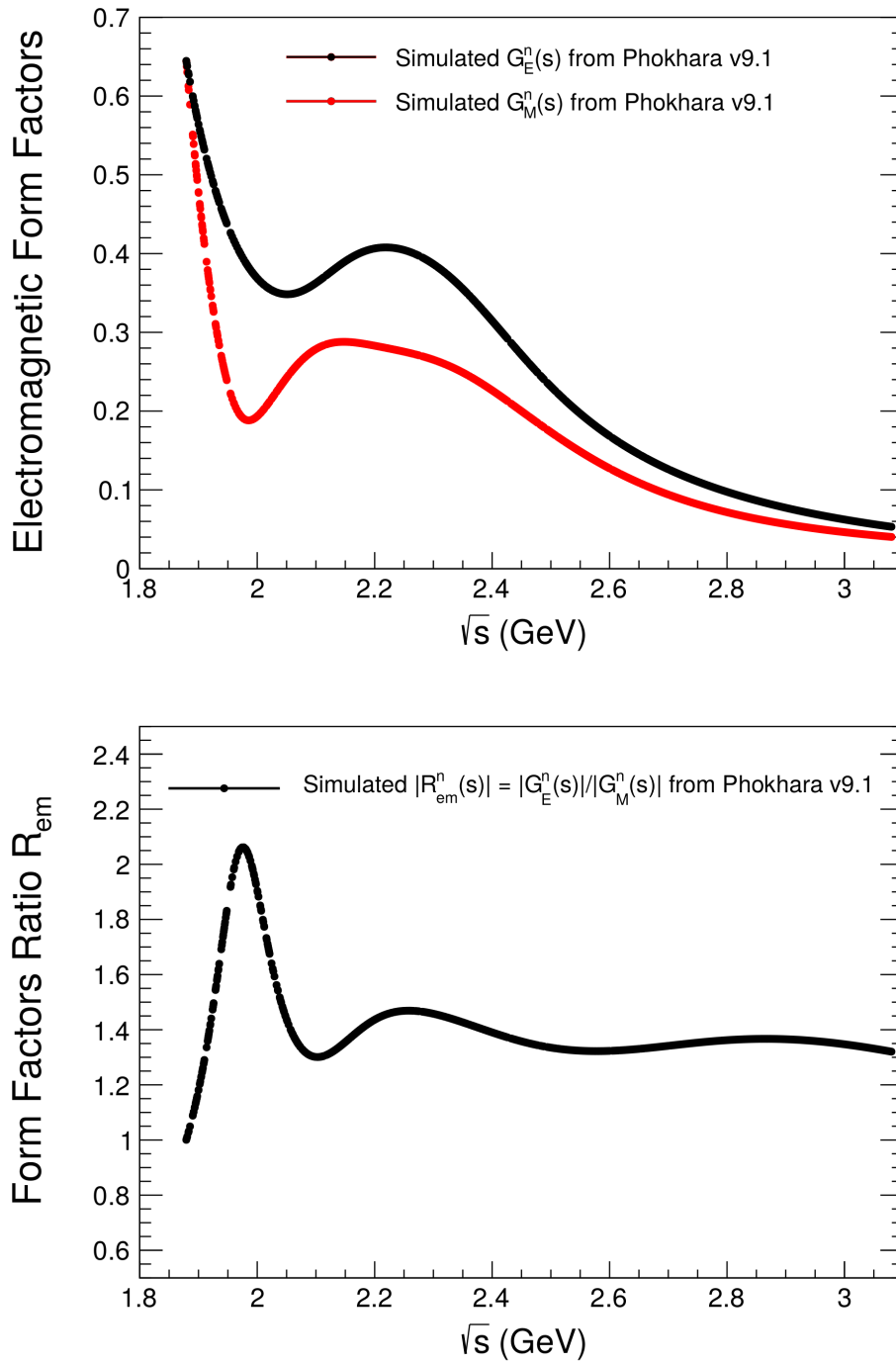


Fig. 4.4: (Top) Simulation for the electromagnetic FFs of the neutron. The red and black dots represent the electric $|G_E^n(s)|$ and magnetic $|G_M^n(s)|$ FF, respectively. (Bottom) Simulation for the electromagnetic FFs ratio $|R_{em}^n(s)| = |G_E^n(s)|/|G_M^n(s)|$. The Simulation was performed using Phokhara v9.1 and the settings are as shown in Table 4.1. The parametrization is explained in the text.

Setting	Value	Explanation
Phokhara.ScanMode	1	Born process generation
Phokhara.NLO	1	NNLO corrections implemented
Phokhara.SoftPhotonCutoff	0.1 MeV	Cutoff value for radiative photons
Phokhara.Channel	5	$e^+e^- \rightarrow \bar{n}n$ final state
Phokhara.VacuumPolarization	2	Vacuum polarization from [223]
Phokhara.Ecm	\sqrt{s}	Center-of-mass energy for sample
Phokhara.ProtonFormfactor	2	Form factors parametrization (see text)
Phokhara.MinPhotonEnergy	0.05 GeV	Minimum ISR photon energy (NLO)
Phokhara.MinPhotonAngle	0.0°	Minimum ISR photon angle
Phokhara.MaxPhotonAngle	180.0°	Maximum ISR photon angle
Phokhara.MinHadronsAngle	0.0°	Minimum hadrons angle
Phokhara.MaxHadronsAngle	180.0°	Maximum hadrons angle

Table 4.1: Input card for Phokhara v9.1 signal MC generation of the process $e^+e^- \rightarrow \bar{n}n(\gamma_{\text{ISR}}\gamma_{\text{ISR}})$.

The original parametrization for the Born cross section for $e^+e^- \rightarrow \bar{n}n$ in the ConExc generator uses a fit to the FENICE results from [23], shown in Figure 4.5. Therefore, the Born cross section is only defined up to $\sqrt{s} \sim 2.44$ GeV. To generate signal simulation samples for the analyzed collider data range of $\sqrt{s} = [2.0 - 3.08]$ GeV, the original Phokhara parametrization is passed as input to ConExc. Details on the tuning method are discussed in the next paragraph. The simulation process of the ConExc generator is similar to Phokhara. An input card, shown in Table 4.2, includes the most crucial information for the simulation. The ConExc generator uses as input the Born cross section and a parameter for the angular distribution of events to be simulated. Since the angular shape of the signal process $e^+e^- \rightarrow \bar{n}n$ is not known, an isotropic distribution is assumed. For radiative events, a phase-space (PHSP) model is used.

Setting	Explanation
Particle vpho \sqrt{s}	Definition of virtual photon decay at \sqrt{s}
Decay vpho	Start of Born process decay chain
1.0 ConExc 1;	Fraction of decay / model name / process
Enddecay	End of decay chain
Decay vhdr	Start of radiative process decay chain
1.0 n0 anti-n0 PHSP;	Fraction of decay / final state / angular model
Enddecay	End of decay chain
End	End of Simulation

Table 4.2: Input card for ConExc signal MC generation of the process $e^+e^- \rightarrow \bar{n}n(\gamma_{\text{ISR}})$.

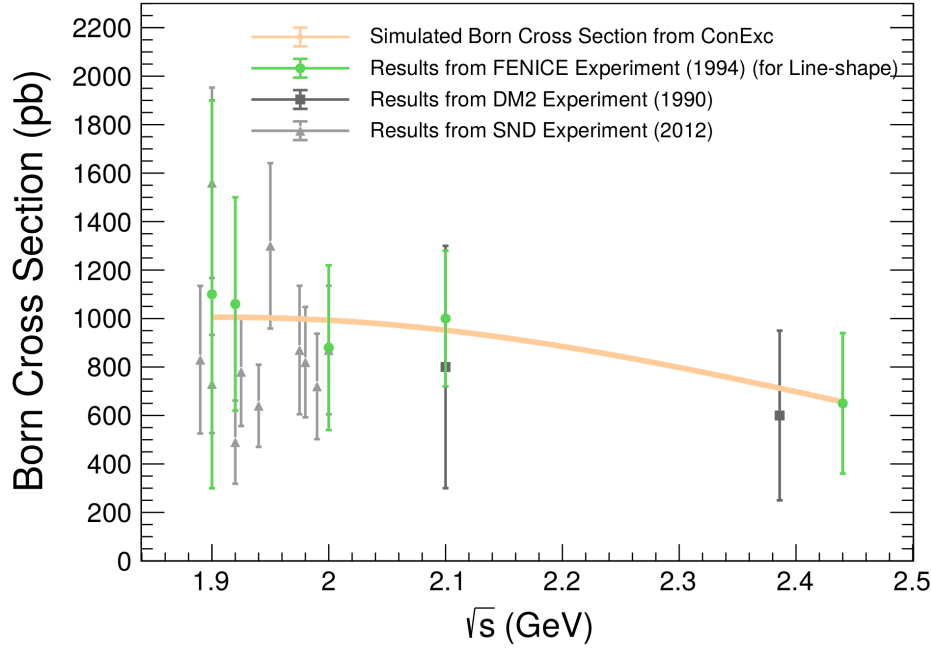


Fig. 4.5: Original Born cross section of the process $e^+e^- \rightarrow \bar{n}n$ simulated with ConExc using settings as shown in Table 4.2. The green dots represent results from the FENICE experiment, which are used for the FF parametrization. The orange line is the Born cross section output from ConExc. Dark gray dots are results from the DM2 experiment, while light gray dots represent recent results from the SND experiment, both not used for ConExc parametrization.

4.2.3 The iterative optimization of the form factor model

Since the implemented Born cross section, as well as the electromagnetic form factors are either based on proton results or only on very scarce neutron results, the signal MC prediction by both generators (Phokhara and ConExc) is inaccurate. This leads to inaccurate signal efficiencies and wrong angular distributions, affecting the results in this analysis. To remedy this issue, an iterative approach for the signal MC simulation optimization is chosen. The full data analysis is performed and the extracted results are used as input for the next MC simulation iteration. In particular, the combined results from the three categories (details in Section 5.2 and 11) are used. The whole data analysis procedure is repeated to obtain new results by using the modified MC simulation. This process is repeated until the signal MC simulation selection efficiency (Section 8.1) multiplied with the radiative correction factor (Section 8.7) is stable. The results presented in this thesis are from the final MC tuning iteration, if not denoted differently.

The Phokhara generator uses a parametrization for $G_E^n(s)$ and $G_M^n(s)$ as input for the calculation of the Born cross section. Since the values for the electric and magnetic FFs $G_E^n(s)$ and $G_M^n(s)$ are not known precisely at all \sqrt{s} , the assumption for $|R_{em}^n(s)| = 1$ is used, leading to $|G_E^n(s)| = |G_M^n(s)| = |G_{eff}^n(s)|$. Due to this reason, the effective FF results, obtained in Chapter 11 are taken for the parametrization of both, $G_E^n(s)$ and $G_M^n(s)$. The following function $f_{tune}(s)$ is fitted to the combined results from the three categories σ_{Born}^n (from Table 9.3), as well to the results from the SND experiment [26]. The results from the FENICE experiment are systematically larger compared to the results from this analysis and therefore neglected.

$$f_{tune}(s) = \left(\sqrt{1 - \frac{4m_n^2}{s}} \frac{p1}{\sqrt{s}^{p2}} + C(\cos\phi, \sin\phi) \frac{p3}{s - m_{BW}^2 + C(0,1)\sqrt{s}\sigma_{BW}} \right)^2 \quad (4.1)$$

For the parametrization of $G_{eff}^n(s)$, the function $f_{tune}(s)$ is modified as following:

$$f_{tune}^{eff}(s) = \sqrt{\frac{f_{tune}(s)}{\frac{4\pi\alpha^2\beta}{3s} \left(1 + \frac{2m_n^2}{s}\right)}} \quad (4.2)$$

The function $f_{tune}(s)$ takes into account that at the production threshold at $\sqrt{s} \sim 1.878$ GeV the theory predicts the cross section and the effective FF to be zero. The parameters m_{BW} and σ_{BW} are the mass and width of a modified Breit-Wigner function, the functions $C(\cos\phi, \sin\phi)$ and $C(0, 1)$ are complex. Together with the parameters $p1$, $p2$ and $p3$, they are free to be determined by the fit optimization.

The input parameters of the ConExc generator are the Born cross section and the factor α_{ang} which takes into account the angular distribution of the hadronic final state. The same parametrization, obtained from the fit in Equation 4.1, is used for the MC simulation tuning. The fit parameters from the last two MC tuning iterations are shown in Table 4.3. The fits to the results are shown in Figure 4.6.

Tuning	p1	p2	p3	ϕ (rad)	m_{BW} (GeV ²)	σ_{BW} (GeV)	χ^2 / ndf
2. last	$7.598 \cdot 10^7$	20.296	7.672	1.639	2.421	0.355	56.6/6
final	$-2.503 \cdot 10^7$	18.627	8.309	0.970	2.372	0.310	31.0/6

Table 4.3: Fit parameter for the last two signal MC tuning iterations, obtained from the fit of the function in Equation 4.1 to the data described in this section.

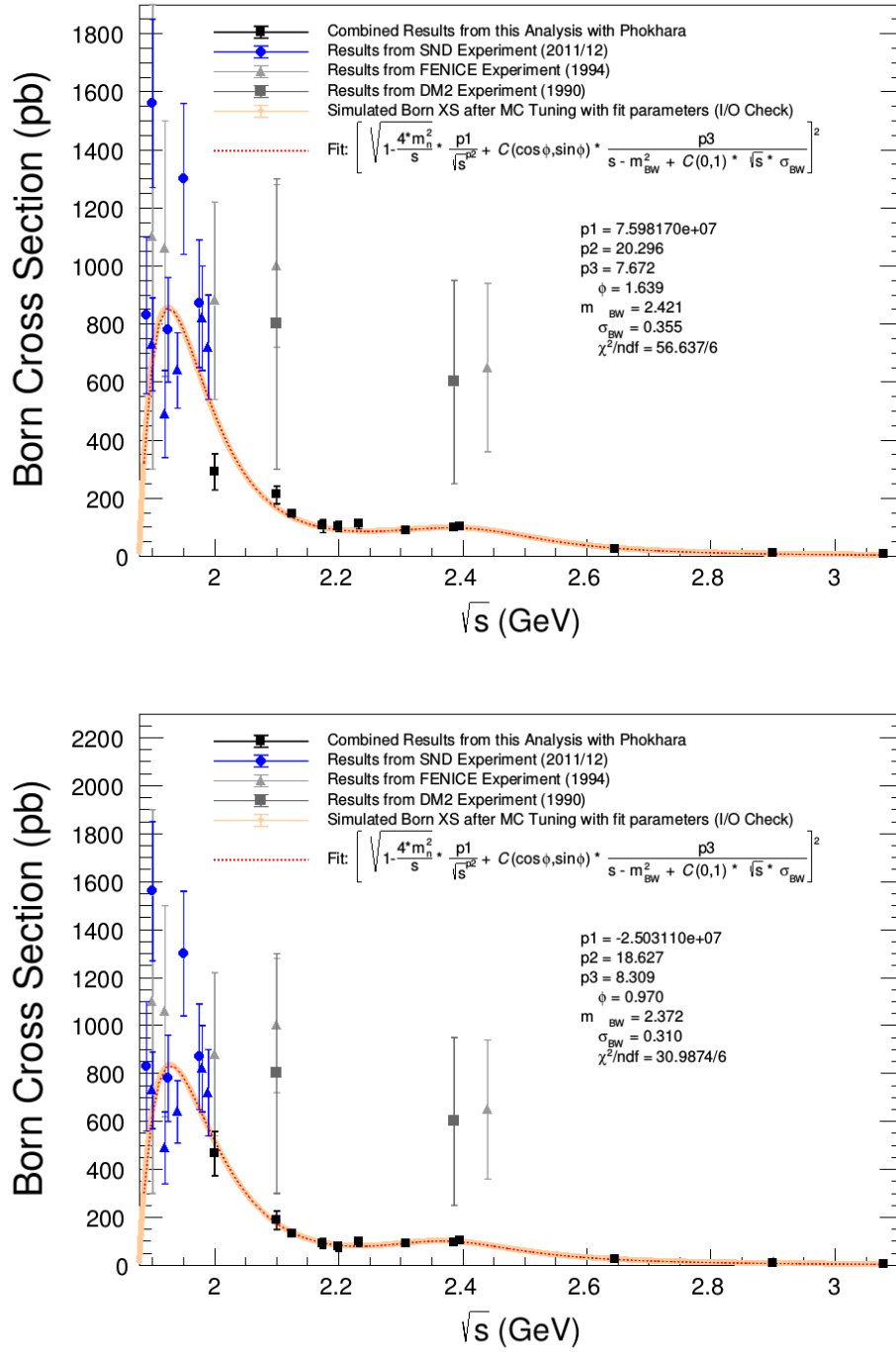


Fig. 4.6: (Top) Second last iteration, (bottom) final iteration. Black dots are results from this analysis used for tuning in the corresponding figure (in the top figure the results are extracted with the 3rd last MC tuning iteration, in the bottom one, with the 2nd last). Blue dots are results from the SND experiment quoted from [26], the orange line is the Phokhara v9.1 parametrization for the Born cross section, the red-dashed line is the fit function described in 4.1 with the fit parameters shown below. For comparison, results from the FENICE (light gray triangles) and DM2 (dark gray squares) experiments are shown, which are not used for MC tuning.

4.3 The simulation of the dominant physics background

Various physics background channels have been considered for the estimation of background contamination in this analysis. For the simulation of the QED background channels $e^+e^- \rightarrow e^+e^- + m \times \gamma_{\text{ISR}}$, $\gamma\gamma + m \times \gamma_{\text{ISR}}$ and $\mu^+\mu^- + m \times \gamma_{\text{ISR}}$ ($m = 0, 1$) the Monte Carlo event generator Babayaga v3.5 [225] is used, which provides a high precision for the simulation of QED processes below $\sqrt{s} = 12$ GeV. The process $e^+e^- \rightarrow \gamma\gamma(\gamma_{\text{ISR}})$ is a pure neutral final state and contributes significantly to the pre-selected events, as shown in Section 5.3. Thus, this background is generated at every analyzed \sqrt{s} . In contrast, the leptonic Bhabha $e^+e^- \rightarrow e^+e^-(\gamma_{\text{ISR}})$ and di-muon $e^+e^- \rightarrow \mu^+\mu^-(\gamma_{\text{ISR}})$ processes have two charged particles in the final state, and therefore shouldn't pass the pre-selection criterion S_1 requiring no charged tracks from Interaction Point (details in Section 5.3). Considering the large cross section, especially for the Bhabha process, huge MC simulation samples would be needed to generate the same luminosity for this process, as present in the collider data. These channels have been generated only at $\sqrt{s} = 2.3960$ GeV for the study of suppression power from the selection criteria for these background processes. The outcome verified the expectation for these channels to be rejected effectively with the pre-selection as shown in Section 5.4. Therefore they are considered under control and not simulated for other center-of-mass energies.

Multi-hadronic background samples with events of the type $e^+e^- \rightarrow \bar{q}q + m \times \gamma_{\text{ISR}} \rightarrow \text{hadrons} + m \times \gamma_{\text{ISR}}$, ($q = u, d, s$, $m = 0, 1$) are generated according to the luminosity in the collider data at each analyzed \sqrt{s} . The $\bar{q}q$ pair represents different two- and multi-hadronic final states. The generated samples include events up to the next-to-leading order with contributions from the Initial-State-Radiation. The simulation of vacuum polarization is considered by using the implementation by Fred Jegerlehner [222]. The angular distribution for experimentally measured final states is generated by using results extracted with the Partial Wave Analysis (PWA) and in phase space for not yet measured processes, respectively. The simulation is based on the ConExc [220] and the LundArLw [226] models implemented within the BesEvtGen package [221], a dedicated collection of event generators for the physics accessible at the BESIII experiment. It is worth mentioning, that the signal process $e^+e^- \rightarrow \bar{n}n$ is included by default in this simulation. For the data analysis, this process is manually excluded and studied with the exclusively produced samples, which are discussed in Section 4.2.

Details for all simulated background samples are listed in the Appendix A.1.

4.4 The simulation for the efficiency correction

A precisely calculated reconstruction efficiency is crucial for the calculation of the results for the Born cross section and the FFs of the neutron. As discussed in Section 4.2, the Monte Carlo simulation for the signal process is imperfect. In this analysis, the MC reconstructed efficiency is corrected with a data-driven method. The detailed efficiency correction study can be found in Section 8.2 - 8.4.

To study the efficiency of the signal selection criteria $S_1 - S_7$ and S_9 (details for the signal selection are shown in Section 5.3) from data, clean samples for the neutron and antineutron are required. Therefore two channels are chosen, where the two signal final state particles can be easily identified: for the study of the criteria for the antineutron selection, the channel $e^+e^- \rightarrow J/\psi \rightarrow p\bar{n}\pi^-$ is chosen, for the corresponding study of the neutron related selection criteria, the charge conjugated channel $e^+e^- \rightarrow J/\psi \rightarrow \bar{p}n\pi^+$ is employed. Both channels have two charged particles in the final state, therefore the selection of the antineutron/neutron EMC shower benefits from the possibility of a kinematic fit to the missing momentum. To compare the differences between collider data and simulation for the quoted cut criteria, Monte Carlo simulation samples for $e^+e^- \rightarrow J/\psi \rightarrow p\bar{n}\pi^-$, $e^+e^- \rightarrow J/\psi \rightarrow \bar{p}n\pi^+$ are produced at $\sqrt{s} = 3.097$ GeV with the KKMC + LundArLw models of the BesEvtGen generator in the available phase space. To control the background contamination after the selection of the $p\bar{n}\pi^-$ and $\bar{p}n\pi^+$ final states, an inclusive sample for J/ψ decaying into multi-hadronic final states ($\bar{q}q$) is produced in phase-space with the same models. The event generator KKMC [227] is used to simulate processes of the kind $e^+e^- \rightarrow \bar{f}f + m \times \gamma_{\text{ISR}}$ with the final state fermion pair $f = \mu, \tau, \nu, u, d, s, c, b$. Initial- and Final-State Radiation are calculated up to the second order ($m = 0, 1, 2, \dots, \infty$), while electroweak corrections are implemented to the first order. The kinematics are generated in phase space. Possible decays of unstable hadrons in the final state are simulated using the LundArLw model implemented in BesEvtGen.

For the data-driven correction of the selection criterion S_8 in Section 8.3, the process $e^+e^- \rightarrow \bar{p}p$ is used. The simulation for $e^+e^- \rightarrow \bar{p}p$ is produced with the ConExc generator similar to the signal simulation in Section 4.1 at all analyzed \sqrt{s} .

A table with details for the produced MC simulation, as discussed in this section, can be found in the Appendix A.1.

Chapter 5

The Event Selection for the Signal Process $e^+e^- \rightarrow \bar{n}n$

In this chapter the event selection for the signal process $e^+e^- \rightarrow \bar{n}n$ is discussed in detail. Since the signal process' final state only contains neutral particles, the most important sub-detector for the signal reconstruction is the electromagnetic calorimeter. The signal process can also be reconstructed with the help of the time-of-flight detector. Most of the physics background can be suppressed by applying selection criteria on the electromagnetic and hadronic showers produced by the signal final state particles. Other main background sources are either beam related, or cosmic rays. The latter can be effectively rejected by criteria applied on observables from the muon counter sub-detector. The response of the signal process in each sub-detector is discussed in Section 5.1. The strategy for the event selection and classification is presented in Section 5.2 and discussed in detail in Section 5.3. A summary is given in Section 5.4.

5.1 The detector response of the signal events

A typical detector response of the signal process $e^+e^- \rightarrow \bar{n}n$ is discussed for each sub-detector in this Section. Figure 5.1 shows such a response in the XY view of the BESIII detector system. All relevant parts of the detector from the inner- to the outermost one are discussed with respect to the signal interaction. The small circle in the middle of Figure 5.1 is the beam pipe, surrounded by the brown area, which represents the inner drift chamber of the MDC. The inner blue circle stands for the MDC, the yellow circle shows the TOF

system followed by the EMC shown as the outer blue circle, and finally enclosed by the MUC, represented by the pink octagon.

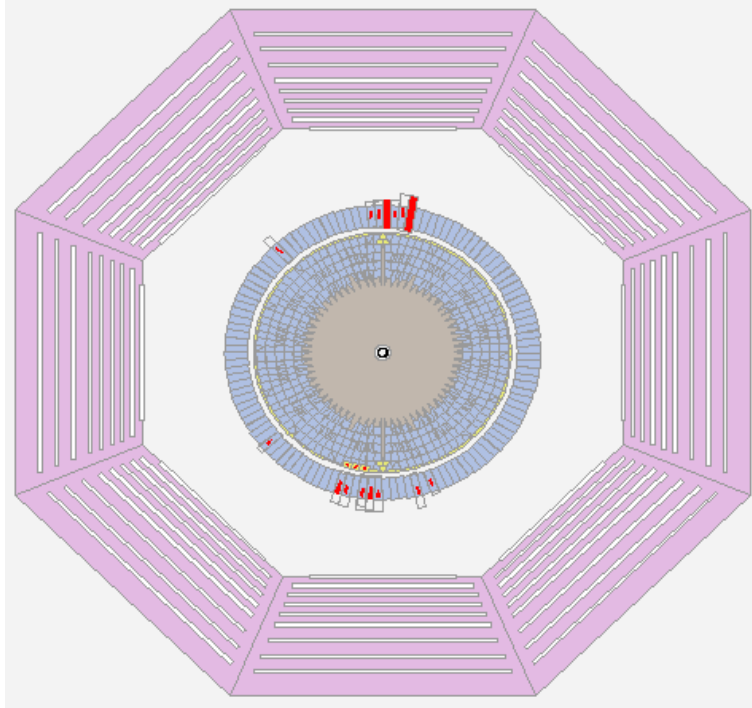


Fig. 5.1: Detector response for a signal event at $\sqrt{s} = 2.3960$ GeV shown in XY view of the BESIII detector. The brown filled circle around the center point is the MDC, where no signal is observed for this event. The following blue round structure represents the EMC endcaps, here without any response. The two yellow circles are the double layer TOF system, a weak response is visible at the direction 6 o'clock. Following is the EMC barrel region, shown as a circle of blue crystals. Here the two signal particles are clearly visible as red marked detector response in the CaI(Tl) crystals of the EMC at opposite sides of the detector. The most outer structure is the MUC, shown in pink without any signal for this event.

In the **Multilayer Drift Chamber**, charged tracks are reconstructed. The signal process' final state contains two neutral hadrons, the neutron and the antineutron, which cross the MDC usually without producing any response, therefore no charged tracks with the origin in the Interaction Point (IP) region are detected. Charged tracks outside the interaction region can occur from the signal process. Neutrons and antineutrons can produce charged mesons and protons as a result of the strong interaction in the EMC. Further, produced neutral pions can be followed by pair production and a subsequent charged track. If the charged particles are produced with a direction vector showing to the MDC, charged tracks can be detected. Additionally after the antineutron loses its kinetic energy through elastic and inelastic scattering in the crystal material, it can annihilate in the EMC and produce secondary charged particles entering the MDC. This process introduces charged tracks

outside of the interaction region. All these effects are discussed below, in the paragraph for the EMC.

The **Time-of-Flight** system of the BESIII detector is constructed for the detection of charged particles and their flight time measurement. For the analysis of the signal process $e^+e^- \rightarrow \bar{n}n$, a method has been developed to measure the flight time of neutral particles (details can be found in the Appendix C), which is used for signal selection of category A and B events (details on the signal classification are discussed in Section 5.2, the analyses under category A and B are shown in the Appendix B). The probability for interaction of signal particles with the two layers of the TOF system, here as an example with a momentum of 0.6 GeV/c which is equivalent to the particle momentum in the signal event at a center-of-mass energy of ~ 2.23 GeV, can be calculated according to the following formula:

$$P_{\bar{n}(n)}^{\text{tof}}(0.6 \text{ GeV}/c) = \sigma_{p\bar{n}(n)} \times (\rho_H + 6\rho_C) \times L_{\text{tof}} \quad (5.1)$$

$L_{\text{tof}} = 10$ (cm) is the total perpendicular width of the two layer scintillator TOF system [228]. $\sigma_{p\bar{n}}(0.6 \text{ GeV}/c) = 1.5 \cdot 10^2$ mb and $\sigma_{pn}(0.6 \text{ GeV}/c) = 0.4 \cdot 10^2$ mb are the cross section for the interaction of a proton with an antineutron and neutron, respectively [50]. $\rho_H = 5.23 \cdot 10^{22}/\text{cm}^3$ and $\rho_C = 4.74 \cdot 10^{22}/\text{cm}^3$ are the numbers of hydrogen and carbon atoms per cm^3 [193] (TOF scintillator material description from [228]). The probability of interaction is therefore 13.5% for the neutron and 50.5% for the antineutron. Nevertheless, for the main selection strategy in this thesis, introduced in detail in Section 5.3, the TOF based detection of the signal process is not considered, but used within the two complementary signal event selections introduced in the Appendix B (see also Section 5.2).

The **ElectroMagnetic Calorimeter** is the most crucial sub-detector for the event selection presented in this thesis. Therefore the interaction of neutrons and antineutrons with the EMC is discussed in detail in the following (based on the discourse in [229]).

Neutrons and antineutrons produce hadronic showers, which consist of several components: the electromagnetic and hadronic energy deposition and the invisible energy deposition. Due to the lack of electrical charge, neutrons and antineutrons do not undergo Coulomb interaction, neither with atomic electrons, nor with the nucleus in matter. Instead, they penetrate the material until a possible strong interaction with the nucleus occurs. Because of the short range of the strong force and the small size of the nucleon compared to an atom, neutrons and antineutrons have to pass very closely to the nucleus (1 nucleon size of $\sim 10^{-15}$ m) to be able to interact. Therefore they have a low interaction

probability. Additionally, the interaction of neutrons with the nucleus is strongly energy dependent, due to different processes in different energy ranges. To distinguish between the difference in their behavior, neutrons are roughly classified into "high-energy" (kinetic energy of the neutron $E_n \geq 1$ GeV), "fast" (100 keV $< E_n < 10$ MeV) and "slow" neutrons ($E_n < 1$ eV), all theoretically possible to contribute to the data which is analyzed in this thesis.

Hadrons statistically interact on average one time strongly with a nucleus after passing a distance called hadronic interaction length λ_I . For a simplistic calculation of the material specific hadronic interaction length, sometimes referred to as mean free path, the cross section for a collision between two neutrons or protons is approximated to:

$$\sigma_{\text{collision}} \approx 4 \times 10^{-26} \text{ cm}^2 \quad (5.2)$$

For a nucleus with an atomic number A and a diameter $A^{1/3}$ times the neutron diameter, the cross section is $A^{2/3}$ times $\sigma_{\text{collision}}$. This leads to an interaction cross section σ_{int} between a neutron and a nucleus of:

$$\sigma_{\text{int}} \approx 4 \times 10^{-26} A^{2/3} \text{ cm}^2 \quad (5.3)$$

With the Avogadro number $N_A = 6.022 \times 10^{23}$, the material density ρ , and the number of scattering centers per volume $N = \rho \times N_A / A$, the hadronic interaction length is:

$$\lambda_I = \frac{1}{N \times \sigma_{\text{int}}} \approx \frac{A^{1/3}}{\rho} \times \frac{1}{N_A \times 4 \times 10^{-26}} \approx \frac{A^{1/3}}{\rho} \times 35 \text{ g/cm}^2 \quad (5.4)$$

This approximation is valid for materials with a proton number $Z \geq 15$ and $\sqrt{s} \approx 1 - 100$ GeV, which is true for the characteristics of the BESIII experiment. For lower energies, quantum mechanical effects significantly alter this approximation. High-energy neutrons typically interact with the nucleus by breaking it up, which leads to a production and scattering of unstable fragments, returning over several steps to a stable condition through the emission of photons. This leads to hadronic and electromagnetic showers in the EMC. Additionally to a breaking-up of the nucleus, a collision with only one proton or neutron of the nucleus is possible, leading to an excited nucleus and secondary hadron production, typically consisting mostly of charged and neutral pions. The probability of the production of other hadrons is suppressed with the increasing hadron mass. The secondary hadrons can undergo further strong interactions with other nuclei leading to more hadronic showers in the EMC, if the energy of the initial neutron is high enough.

Neutral pions decay almost instantly ($\tau = (8.4 \pm 0.6) \cdot 10^{-17}$ s) into photon pairs, which produce electromagnetic showers. The excited nucleus becomes stable within a short time through the emission of photons, leading to additional electromagnetic showers in the EMC. A further possible process is the so-called "spallation", where a neutron can strike out another neutron or proton from the nucleus, leading to secondary electromagnetic and hadronic showers. The sum of these effects leads to an electromagnetic and hadronic shower avalanche.

Fast neutrons and antineutrons are characterized by a set of four effects, listed as follows:

- Elastic scattering: neutrons or antineutrons scatter elastically on nuclei, losing a part of the kinetic energy.
- Inelastic scattering: neutrons and antineutrons collide with a nucleus and excite it during the interaction process. The de-excitation leads to the emission of photons or other radiation, producing electromagnetic and hadronic showers in the EMC. The neutron can undergo further strong interaction with other nuclei.
- The neutron capture of a nucleus: This process leads to the emission of a charged particle or a follow-up fission, producing electromagnetic or hadronic showers. This effect doesn't occur for antineutrons.
- The radiative neutron capture: here, the absorption of the neutron leads to an excitation of the nucleus, followed by a photon emission, which leads to electromagnetic showers.

The highest probability for a reaction of slow neutrons is the elastic scattering and neutron capture, described above. In addition to all of these processes, a possible annihilation of antineutrons with a neutron from the EMC material after losing most of their kinetic energy can arise, leading to a cascade of hadrons. Photons emitted from excited nuclei or secondary particles can interact with the EMC through the photoelectric effect, Compton scattering, or electron-positron pair production, possibly leading to electromagnetic showers. Charged secondary particles undergo ionization, which can lead to further electromagnetic showers and/or charged tracks leading to a response in the MDC.

A non-negligible part of the energy of neutrons and antineutrons isn't detected in the EMC. This "invisible" part consists of the energy needed to break open the atoms of the crystal material. Some energy is undetected since it's carried away by core fragments with extremely long reach. Further undetected energy comes from charged pions decaying

into muons and neutrinos which pass the calorimeter material almost without interaction. Finally, the largest part of the undetected energy of a neutron or antineutron is due to the small hadronic interaction probability for hadrons with the BESIII EMC material, which can be calculated with the help of the material specific hadronic interaction length $\lambda_I = 175.5 \text{ g/cm}^2$, the density $\rho = 4.53 \text{ g/cm}^3$ and the perpendicular length of the CsI(Tl) crystals $L = 28 \text{ cm}$:

$$P_{n(\bar{n})}(\text{EMC}) = 1 - e^{-L \times \rho / \lambda_I} \sim 50\% \quad (5.5)$$

In the following is an example with possible effects from neutron and antineutron interaction with the EMC material. The fraction between the different effects is energy dependent and subject to strong fluctuations.

- Elastic scattering: $n(\bar{n}) + \text{nucleus} \rightarrow n(\bar{n}) + \text{nucleus}$
- Inelastic scattering: $n(\bar{n}) + \text{nucleus} \rightarrow \pi^+ + \pi^- + \pi^0 + \dots + \text{nucleus}^*$
 - $\text{nucleus}^* \rightarrow \text{nucleus} + n/p/\alpha/\pi/\text{nuclear fission}$
 - $\pi^0 \rightarrow \gamma + \gamma$
 - $\gamma + \text{nucleus} \rightarrow e^+ + e^- + \text{nucleus}$
- Neutron absorption and capture
- Radiative neutron capture with photon emission
- Spallation, leading to a secondary nucleon struck out of the nucleus.

To illustrate the different processes within a hadronic shower, an exemplary hadronic shower development occurring from a neutron is shown in Figure 5.2.

The shower development stops, when the secondary particles lose enough kinetic energy through further inelastic collisions and fall below the pion production threshold. The cascade of interactions includes many different particle types, which are subject to different processes in the EMC. The most relevant are listed below:

- π^0 's decay almost instantly to a γ pair, each of them possibly interacts through either the photoelectric absorption process, Compton scattering, or electron-positron pair production and can therefore initiate electromagnetic showers.
- Charged mesons, mostly π^+ 's and π^- 's can undergo secondary interactions leading to a cascade. Another possibility is a decay and following production of muons and neutrinos, which usually escape the EMC without any interaction.

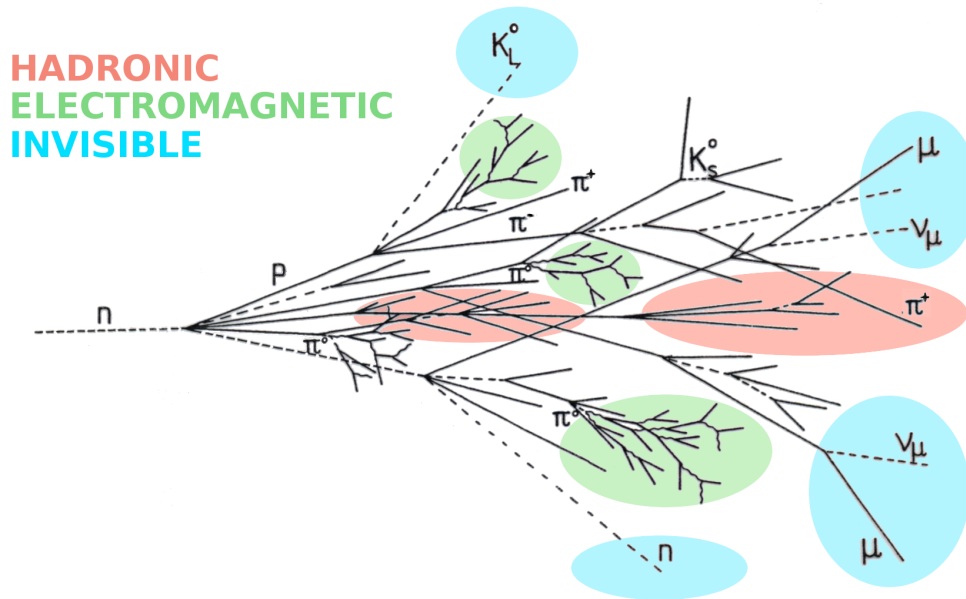


Fig. 5.2: Example for the development of a hadronic shower in the EMC. Red, green and blue regions denote hadronic, electromagnetic and invisible components of the shower, respectively. Based on figure in Reference [230].

- Nucleons arising from a nuclear break-up. Protons produced in this way are losing their energy through ionization and possibly strongly interact with other nucleons in the EMC material leading to a cascade. Produced neutrons can strongly interact similar to protons or leave the detector material without interaction.
- Photons from nuclear excitation produce electromagnetic showers.

These processes of hadron interaction with the crystals in the EMC lead to a shower development, much more complicated than a pure electromagnetic one. Following is a short summary of the detector response characteristics to expect from the signal process in this analysis:

- With the material specific hadronic interaction length and the crystal size of the BE-SIII detector, only a fraction of all neutrons or antineutrons will produce a response in the electromagnetic calorimeter, which was initially not build for the purpose of hadron detection.
- If an interaction happens, the showers are expected to be deeper and wider than e.m. showers from photons and electrons. On average more than one shower is expected to be detected, since the BESIII calorimeter doesn't possess the capability for hadronic shower reconstruction and therefore will assume a set of e.m. showers.

- The energy deposition from neutrons and antineutrons measured with the EMC is not representative for their initial kinetic energy. Antineutrons deposit on average more energy due to the annihilation. The position of the detected shower, associated with the neutron or antineutron, differs from the true position of the particle due to scattering effects and/or earlier interaction with the TOF detector material.

The probability of interaction for neutrons and antineutrons inside of the EMC is 50%, as shown in Equation 5.5. Therefore only half of neutrons or antineutrons interact with the EMC at all, and those producing a detector response do not necessarily deposit all of their energy. Since no full energy deposition is available, no kinematic fit can be performed for the signal selection. Instead the introduced selection strategy in Section 5.3 takes into account the shape of the hadronic showers and the unique kinematic behavior of the signal process two-body final state in the EMC.

The **Muon Counter** is the outermost layer of the sub-detector arrangement. Initially built for muon detection, in this analysis it is used for background subtraction. Because of the pure neutral final state of the signal process, a high background contamination from beam related processes and cosmic rays is observed, usually rejected by means of the MDC sub-trigger. Especially the latter can be effectively suppressed with the MUC by requiring the events not to have a detector response in the outer layers, which is equivalent with particles either passing from inside the detector through the whole MUC material, or coming from outside of the detector, which is typical for cosmic rays. The interaction probability of the signal process $e^+e^- \rightarrow \bar{n}n$ with the MUC can be calculated according the Equation 5.5 to be $P_{n(\bar{n})}(\text{MUC}) = 96.4\%$ when using the material specific hadronic interaction length $\lambda_1 = 132.1 \text{ g/cm}^2$, the density $\rho = 7.87 \text{ g/cm}^3$, and the thickness of steel plates of the flux return yoke of the SC in MUC barrel region of $L = 56 \text{ cm}$ inserted between the resistive plates. It should be pointed out, that this high interaction probability doesn't take into account, that many neutrons and/or antineutrons already interacted with the detector, before reaching the MUC. Since a large fraction of signal events interacts in the TOF and EMC, before reaching the MUC, in most cases no response from the final state particles of the signal process can be observed in the Muon Counter. If a response is observed, than mostly in the first few layers, as shown in Figure 5.7, which confirms the expectation.

The **Trigger System** of BESIII has several channels for triggering various physical events. For the specific case of a pure neutral final state, only two open trigger channels were implemented at the time when the scan data analyzed in this work has been collected

in 2014/15. Both channels use the interaction of particles in the EMC. Channel number 9 is triggered if at least one cluster in the barrel region with an energy deposition of 650 MeV is detected. Channel number 12 is triggered if at least two clusters with a total energy deposition of 450 MeV in the whole EMC are detected. The exact definition of "cluster" and "shower" and their difference can be found in Section 3.2.6. In the presented selection a minimum energy deposition of 540 MeV is required to ensure a high trigger efficiency.

5.2 Concept of the data analysis

The selection of the signal channel $e^+e^- \rightarrow \bar{n}n$ in this analysis is performed under three different categories using a sequential approach according to a valid time-of-flight signal of antineutron and neutron, respectively. The first category, denoted as A, analyzes only events with a valid response from the TOF for both final state particles. Category B events must have a response in the TOF associated with the antineutron, while the neutron isn't allowed to have a TOF response. Finally, in category C only events without a TOF response associated with the final state particles are analyzed. The approach is described as following:

- (i) Only events with zero charged tracks from the Interaction Point are selected.
- (ii) The most energetic shower in the EMC in $|\cos\theta| < 0.8$ is selected as the \bar{n} candidate, to reject background in the large $|\cos\theta|$ range.
- (iii) Events with TOF hits in ± 3 TOF counters around the \bar{n} EMC position ($\Delta\Phi^1 = |\Phi_{\text{TOF1}} - \Phi_{\bar{n}}^{\text{EMC}}| < 3 \text{ TOFcounters} \approx 25^\circ$) are passed to the categories A and B, all others events are analyzed under the selection of category C.
- (iv) Events with TOF hits in ± 3 TOF counters around the opposite direction of the \bar{n} candidate ($\Delta\Phi^2 = |\Phi_{\text{TOF2}} - \Phi_{\bar{n}}^{\text{recoil}}| < 3 \text{ TOFcounters} \approx 25^\circ$) are analyzed under the selection of category A, without this requirement under the criteria for category B.

This sequential approach prevents a "double-counting" of events and ensures a maximum signal events yield over the full center-of-mass energy range as will be discussed in Chapter 11. A visualization of this analysis strategy flow is shown in Figure 5.3. In this thesis, the signal events are analyzed under the category C classification. The analysis of category A and B events has been performed by Jifeng Hu and Xiaorong Zhou, respectively, and are summarized in the Appendix B.

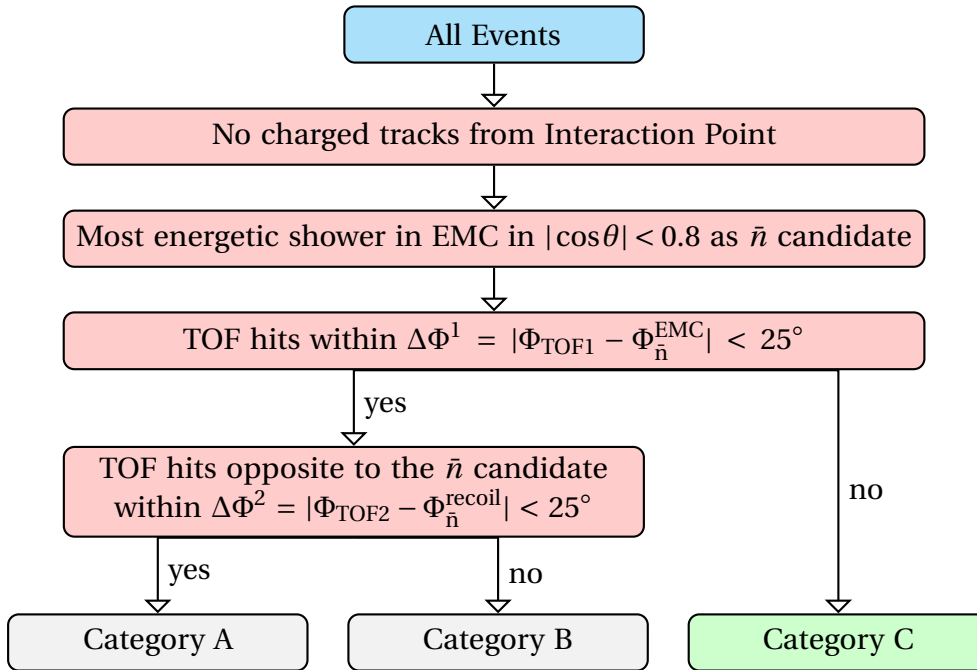


Fig. 5.3: Analysis strategy flow. In this thesis the analysis of signal events classified as category C is presented in detail. Explanations for this graphic are given in the text above.

After the classification of the signal events, as discussed above, the data analysis is performed in the following order:

- The selection of the signal process under the category C classification is described starting from Section 5.3.
- The background contamination after selection is discussed in Chapter 6.
- The signal events are extracted via a fit to the opening angle between the antineutron and neutron shower in the EMC. Details for this method are listed in Chapter 7.
- A discussion of the reconstruction efficiency, as well as several efficiency corrections can be found in Chapter 8.
- In Chapter 9 the results for the Born cross section and the form factors of the neutron are presented for the category C signal events.
- Chapter 10 is dedicated to the estimation of the systematic uncertainties.
- The results from all three categories A, B, and C are combined using an error weighting method to improve the statistics and cross-check the results from the single categories. The final set of results is given in Chapter 11.

5.3 The signal selection with the category C approach

5.3.1 Pre-selection

Before selecting the signal final state's particles, a number of event level selection criteria is applied to reject events containing charged tracks as well as signal process events with a TOF signal as described in Section 5.2, since the latter are analyzed under different strategies and summarized in the Appendix B. This selection strategy is based mainly on observables from the electromagnetic calorimeter for both the antineutron and the neutron selection. It is applied sequentially as the third step after the selection strategies A and B, introduced in Section 5.2. Therefore the signal events with TOF information for any of the final state particles are rejected to avoid double counting. If not quoted differently, all figures show selection criteria distributions at $\sqrt{s} = 2.3960$ GeV, with all previous conditions applied. The selection criteria are applied in the following order:

1. **S₁**: Only events without a signal in the main drift chamber (MDC) are selected. Instead of the definition used in general in BESIII analyses (maximum distance to IP in xy plane $R_{xy} < 1$ cm, in z direction $R_z < 10$ cm, $\cos\theta < 0.93$), a charged track is defined here as a response in the MDC without any quality criteria applied to take into account all charged tracks, such as those coming from the IP, as well as from secondary particles. The number of charged tracks N_{charged} contained in the selected event must be therefore:

$$N_{\text{charged}} = 0$$

2. **S₂**: The event must contain at least two good EMC showers (EMS) with a deposition energy $E > 25(50)$ MeV in the barrel (endcap) region of the EMC. Further requirements on the energy deposition of the EMC showers are applied during the signal final state's particle selection later on. No EMC timing requirement on the selected showers is made in this analysis:

$$N_{\text{shower}} \geq 2 \quad \&\& \quad E_{\text{shower}} > 0.025 (0.05) \text{ GeV}$$

3. **S₃**: The most energetic shower is required to be located in the region of the polar angle θ with respect to the positron beam direction (z-axis) with $|\cos(\theta)| < 0.75$ and is not allowed to have an associated TOF response. With the requirement on the position in the EMC barrel region, beam related background is suppressed. Figure 5.4 shows the $\cos\theta$ distribution of the most energetic shower:

$$|\cos(\theta)_{\bar{n}}| < 0.75 \quad \&\& \quad t_{\bar{n}} \text{ invalid}$$

5.3.2 The selection of the antineutron

After the preliminary selection from Section 5.3.1 is applied, the most energetic shower in an event is identified as the antineutron \bar{n} . The following selection criteria are applied in this order:

1. **S₄**: To reject machine background and to ensure a high trigger efficiency (as illustrated in Sections 3.2.6 and 5.1), the deposition energy of the most energetic shower $E_{\bar{n}}$ is required to be larger than 0.5 GeV and smaller than 2.0 GeV. Figure 5.4 shows the deposition energy for signal MC simulation, collider data in collision and in non-collision mode, as well as background MC simulations.

$$0.5 \text{ GeV} < E_{\bar{n}} < 2.0 \text{ GeV}$$

2. **S₅**: The second moment of the antineutron shower $2M_{\bar{n}}$ is required to be larger than 20, where the second moment is defined as:

$$2M_{\bar{n}} = \frac{\sum_i E_i r_i^2}{E_{\bar{n}}} > 20$$

where E_i is the deposition energy in the i -th crystal and r_i the distance between the center of the i -th crystal and the center of gravity of the shower. With this requirement the most contributing physics background process $e^+e^- \rightarrow \gamma\gamma$ is strongly suppressed, because electromagnetic showers have a smaller width, as discussed in Section 5.1. Figure 5.5 shows the distribution of the second moment for signal MC simulation, collider data in collision and in non-collision mode and background MC simulations.

3. **S₆**: To further reduce the $e^+e^- \rightarrow \gamma\gamma$ background as well as the beam related background, a cut on the number of hits from all EMC showers inside of a 50° cone around the \bar{n} shower is performed. The variable $N_{\text{hits}}^{50\text{cone}}$ is defined as a cone around the vector between the IP and the \bar{n} position in the EMC with an opening angle of 50° . The value for this selection criteria is set to be:

$$35 < N_{\text{hits}}^{50\text{cone}} < 100$$

Figure 5.5 shows the distribution of $N_{\text{hits}}^{50\text{cone}}$ for signal, data and backgrounds.

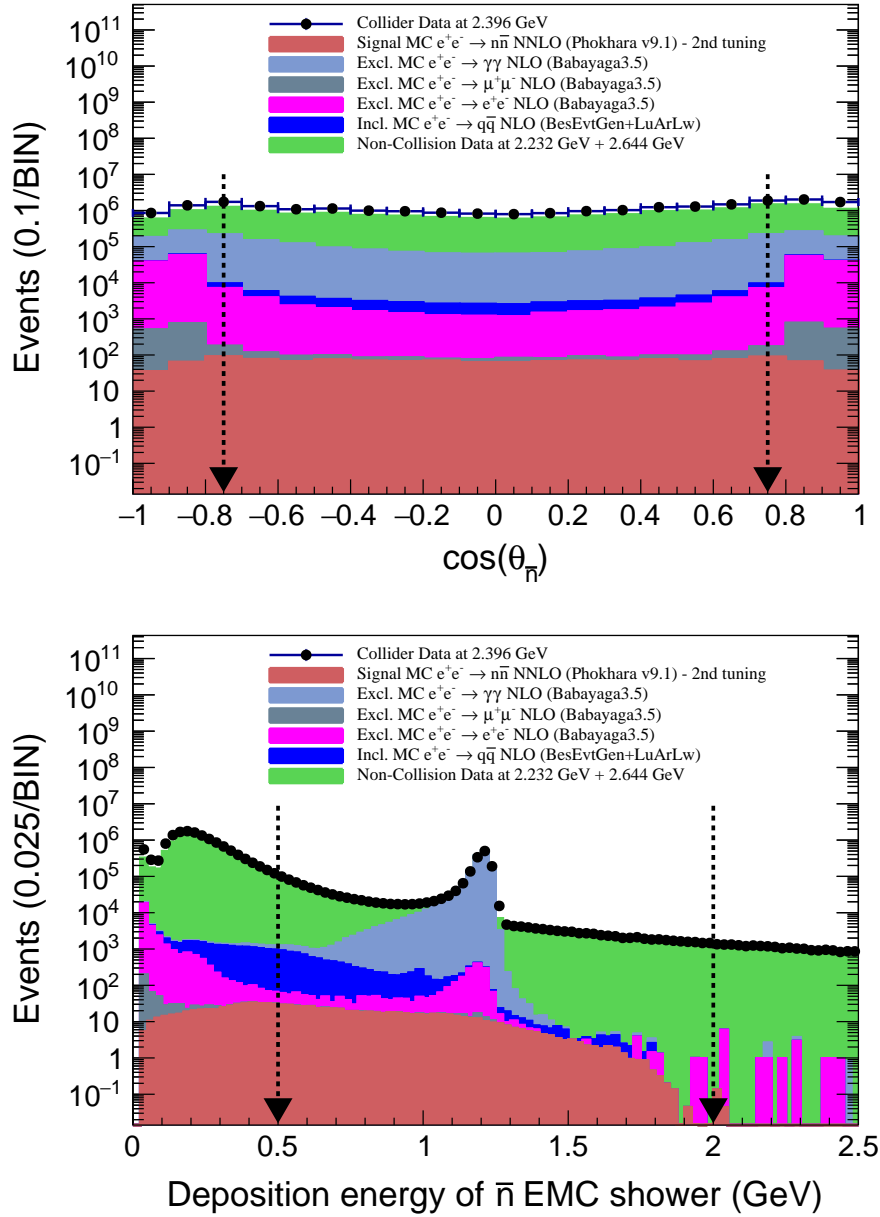


Fig. 5.4: Top: Angular distribution of the \bar{n} shower in the EMC. Bottom: Energy deposition of the \bar{n} shower in the EMC. Black dots with error bars represent the distribution from the collider data, the histogram in red is the signal MC simulation generated with Phokhara v9.1, the light blue histogram is the $e^+e^- \rightarrow \gamma\gamma$ (NLO) background MC, the pink histogram is the $e^+e^- \rightarrow e^+e^-$ (NLO) background MC, the grey histogram is the $e^+e^- \rightarrow \mu^+\mu^-$ (NLO) background MC, all generated with Babayaga 3.5 in NLO. The dark blue histogram represents the hadronic background (signal events excluded) MC, the green histogram is the distribution from beam background using combined non-collision data samples at $\sqrt{s} = 2.2324$ and 2.6444 GeV. All background except the beam related one is scaled to the luminosity in data, while the latter is scaled by the data taking time according to Table 6.3. Black arrows indicate the cut criteria.

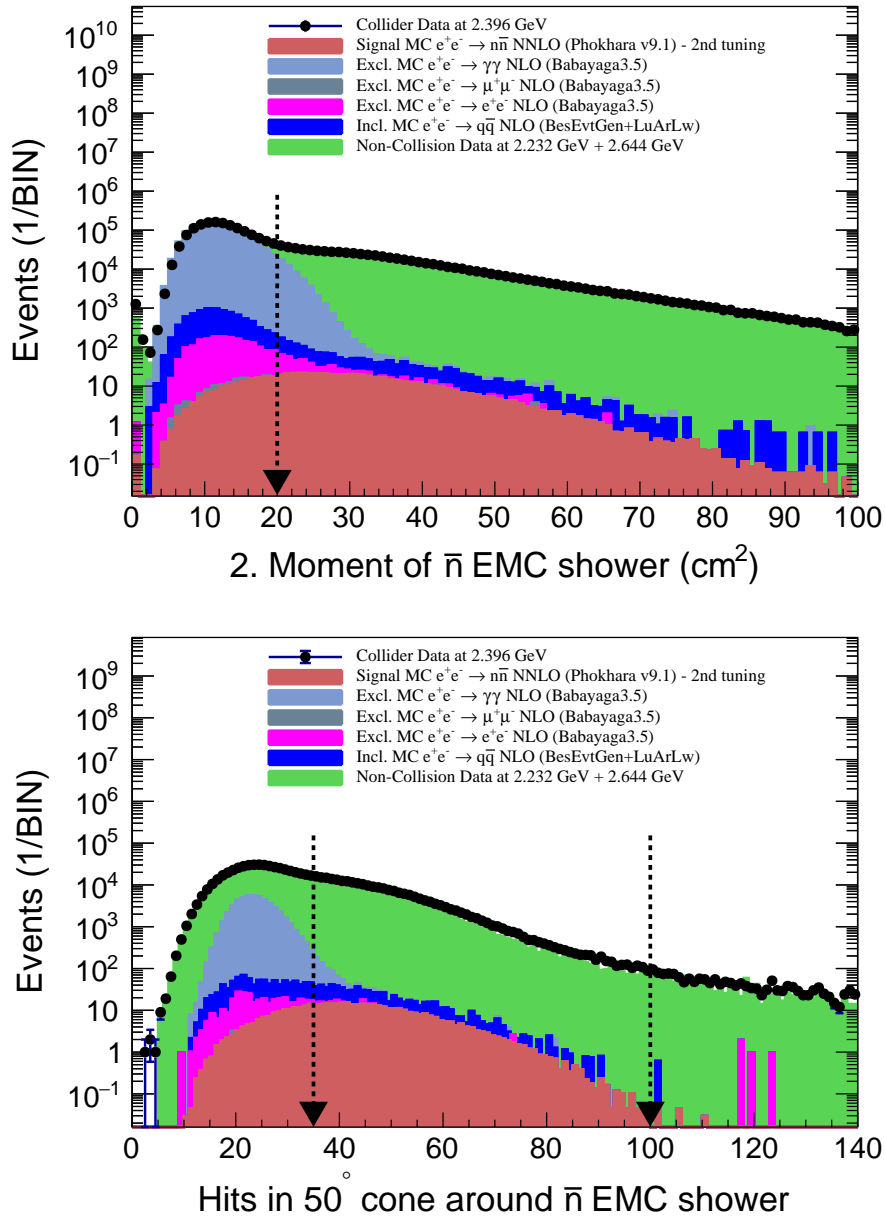


Fig. 5.5: Top: Second moment distribution of the \bar{n} shower in the EMC. Bottom: The number of hits of all EMC showers in 50° around and including the \bar{n} shower in EMC. Black dots with error bars represent the distribution from the collider data, the histogram in red is the signal MC simulation generated with Phokhara v9.1, the light blue histogram is the $e^+e^- \rightarrow \gamma\gamma$ (NLO) background MC, the pink histogram is the $e^+e^- \rightarrow e^+e^-$ (NLO) background MC, the grey histogram is the $e^+e^- \rightarrow \mu^+\mu^-$ (NLO) background MC, all generated with Babayaga 3.5 in NLO. The dark blue histogram represents the hadronic background (signal events excluded) MC, the green histogram is the distribution from beam background using combined samples at $\sqrt{s} = 2.2324$ and 2.6444 GeV. All background except the beam related one is scaled to the luminosity in data, while the latter is scaled by the data taking time according to Table 6.3. Black arrows indicate the cut criteria.

5.3.3 The selection of the neutron

After the antineutron selection, the neutron is selected in the following way. First, the most energetic shower outside of a 90° cone of the antineutron shower is identified as the neutron candidate. The 90° cone is defined in the same way as the cone for the antineutron observable $N_{\text{hits}}^{50\text{cone}}$ (see Section 5.3.2). To suppress beam related and $e^+e^- \rightarrow \gamma\gamma$ background, a condition on the deposition energy of the neutron E_n is applied:

1. **S₇**: To reject low energetic machine background, the deposition energy E_n of the most energetic shower outside of a 90° -cone around the \bar{n} shower is required to be larger than 0.06 GeV. Due to the small kinetic energy of the neutron below the center of mass energy of $\sqrt{s} = 2.3$ GeV, the lower threshold is set to 0.04 GeV for the corresponding data sets. For the whole energy region, the neutron upper energy threshold is required to be 0.6 GeV to suppress $e^+e^- \rightarrow \gamma\gamma$ and various two- and multihadronic background processes, as shown in Figure 5.6:

$$0.04 \text{ (0.06) GeV} < E_n < 0.6 \text{ GeV}$$

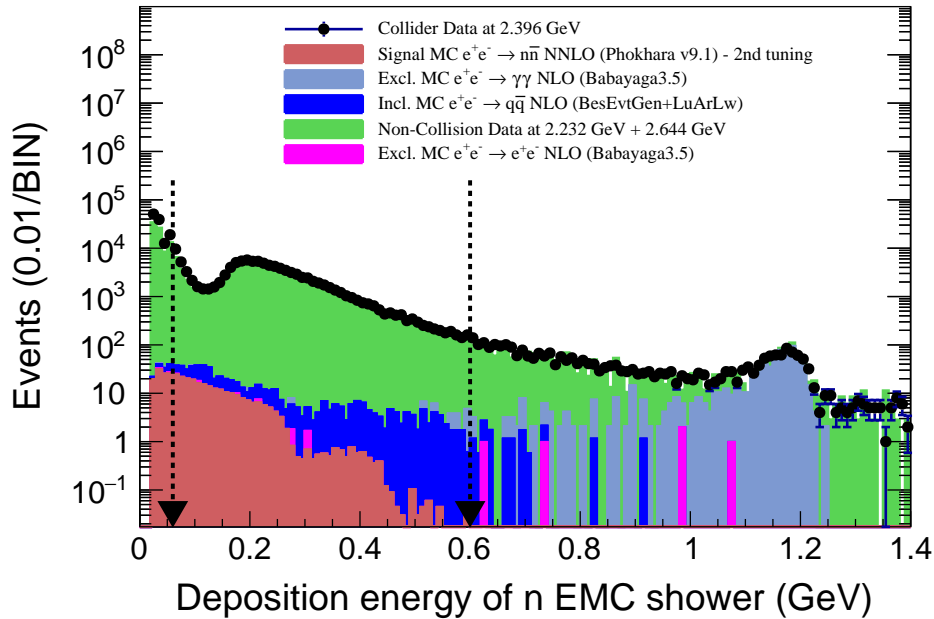


Fig. 5.6: Energy deposition of the n shower in EMC. Black dots with error bars represent the distribution from collider data, the histogram in red the signal MC simulation generated with Phokhara v9.1, the light blue histogram is the $e^+e^- \rightarrow \gamma\gamma$ (NLO) background generated with Babayaga 3.5 in NLO. The dark blue histogram represents the hadronic background (signal events excluded), the green histogram is the distribution from beam background using combined samples at 2.2324 and 2.6444 GeV. All background except the beam related one is scaled to the luminosity in data, and by the data taking time according to Table 6.3, respectively. Black arrows indicate the cut criteria.

5.3.4 Additional selection criteria for background rejection

In Section 5.3.2 and 5.3.3 the signal final state particles n and \bar{n} have been selected. Further selection criteria are required to reject multihadronic and beam related background:

1. **S₈**: To reject multihadronic background processes, the observable E_{extra} is introduced, which is defined as:

$$E_{\text{extra}} = E_{\text{total}} - E_{\bar{n}}^{50\text{cone}} - E_n^{20\text{cone}} < 0.15 \text{ GeV}$$

where E_{total} is the total deposition energy of an event in the EMC, $E_{\bar{n}}^{50\text{cone}}$ the deposition energy of all EMC showers inside a 50° cone around the vector between the IP and the \bar{n} position in the EMC and $E_n^{20\text{cone}}$ the deposition energy of all EMC showers inside a 20° cone around the vector between the IP and the n position in the EMC. The cut value on this variable is determined to be 0.15 GeV, which is illustrated in Figure 5.7. An extensive study for this criterion was performed by Samer Ahmed.

2. **S₉**: To further reduce beam related and cosmic background, a cut on the last layer with hits in the MUC is applied. The value for this selection criterion is determined to be:

$$l_{\text{MUC}} < 6$$

Figure 5.7 shows the distribution of l_{MUC} for signal MC simulation, collider data and various background processes simulation.

3. **S₁₀**: The last selection criterion is a cut on the opening angle between the center of gravity of the reconstructed position of the \bar{n} and n shower in the EMC $\langle \angle_{\bar{n}}^n \rangle$. Considering the two-body event kinematics of the signal process $e^+e^- \rightarrow \bar{n}n$, a large opening angle for the leading order of the signal process is expected, while multi-body event final states and beam related noise will be suppressed effectively. This criterion rejects a large fraction of above mentioned background, while only a few signal events are lost. Most of these rejected signal events are reconstructed under a misidentification of either the antineutron or the neutron shower, which has the positive effect that the signal reconstruction becomes cleaner. The cut value on the opening angle $\langle \angle_{\bar{n}}^n \rangle$ is set to:

$$\langle \angle_{\bar{n}}^n \rangle > 150^\circ$$

Figure 5.8 (top) shows the opening angle for MC simulations and collider data, Figure 5.8 (bottom) shows the opening angle after all selection criteria.

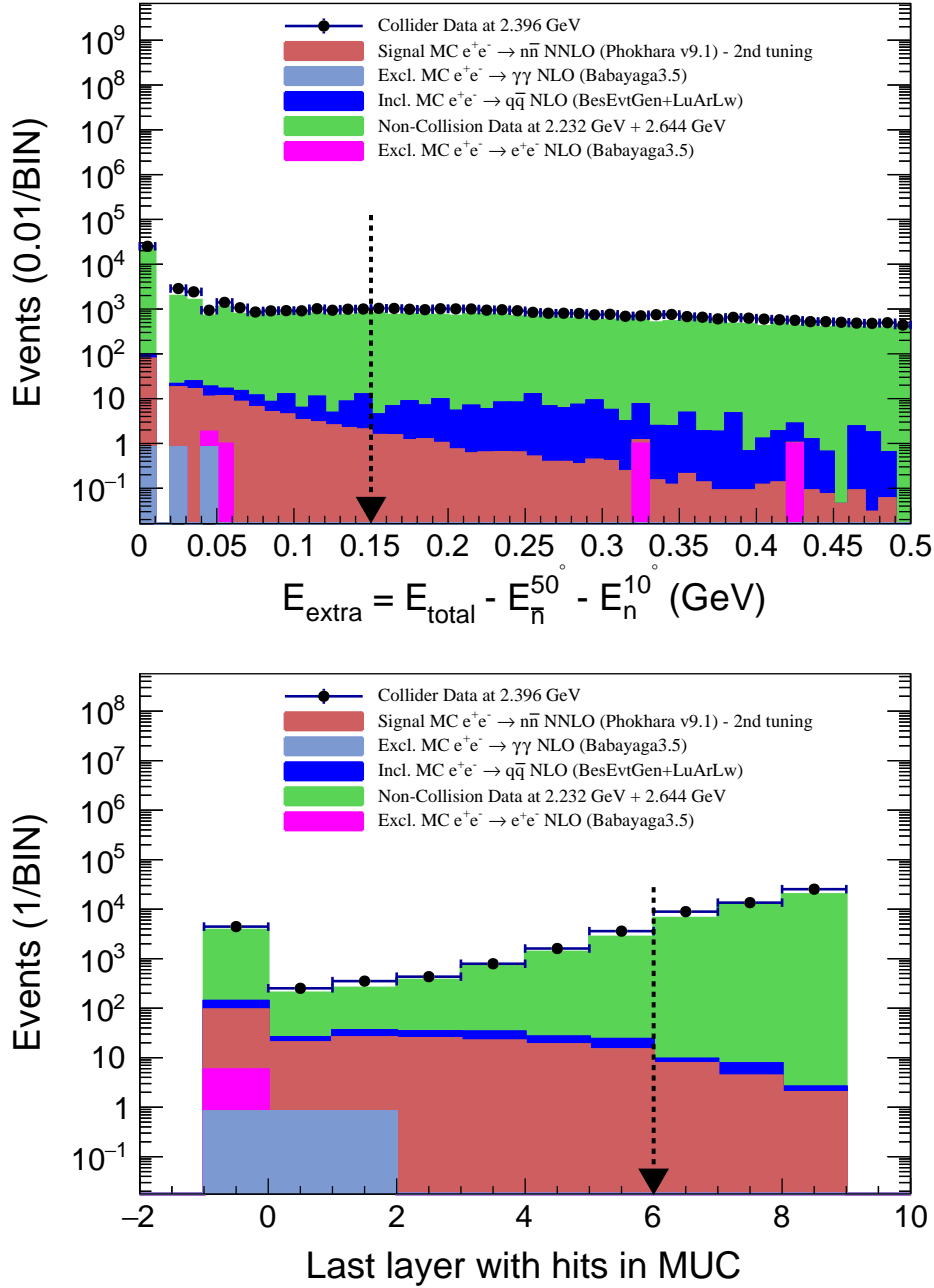


Fig. 5.7: Top: Energy deposition outside of the 50° -cone around the \bar{n} shower and of the 20° -cone around the n shower in EMC. Bottom: Last layer with hits in the MUC. Black dots with error bars represent the distribution from collider data, the histogram in red the signal MC simulation generated with Phokhara v9.1, the light blue histogram is the $e^+e^- \rightarrow \gamma\gamma$ (NLO) background generated with Babayaga 3.5 in NLO. The dark blue histogram represents the hadronic background (signal events excluded), the green histogram is the distribution from beam background using combined samples at 2.2324 and 2.6444 GeV. All background except the beam related one is scaled to the luminosity in data, and by the data taking time according to Table 6.3, respectively. Black arrows indicate the cut criteria.

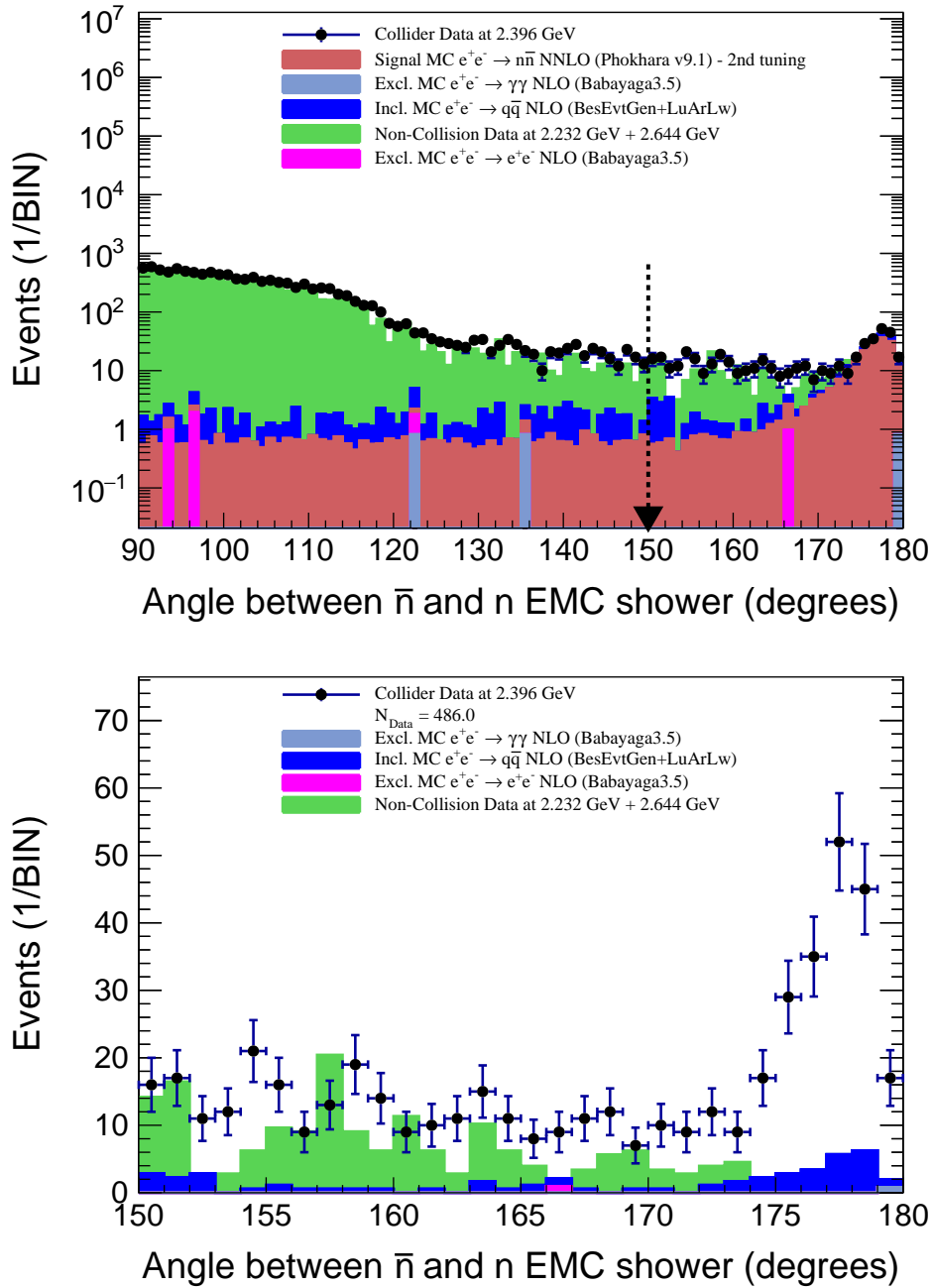


Fig. 5.8: Top: Opening angle between the \bar{n} and n . Bottom: Opening angle between the \bar{n} and n after all selection criteria. The region of collider data not described by background distribution is the expected signal process. Black dots with error bars represent the distribution from collider data, the histogram in red the signal MC simulation generated with Phokhara v9.1, the light blue histogram is the $e^+e^- \rightarrow \gamma\gamma$ (NLO) background generated with Babayaga 3.5 in NLO. The dark blue histogram represents the hadronic background (signal events excluded), the green histogram is the distribution from beam background using combined samples at 2.2324 and 2.6444 GeV. All background except the beam related one is scaled to the luminosity in data, and by the data taking time according to Table 6.3, respectively. Black arrows indicate the cut criteria.

5.4 The summary of all selection criteria

Table 5.1 summarizes the selection criteria from Section 5.3.1 to 5.3.4 and the individual cut values. The developed algorithm performs the signal process selection exactly in the shown order.

Selection	Notation	Expression	Criterion	Unit
Preliminary selection	S_1	N_{charged}	$= 0$	#
	S_2	N_{shower}	≥ 2	#
		E_{shower}	$> 0.025 (0.05)$	GeV
	S_3	$ \cos\theta_{\bar{n}} $ $t_{\bar{n}}$	< 0.75 invalid	# ns
Antineutron selection	S_4	$E_{\bar{n}}$	$[0.5, 2]$	GeV
	S_5	$2M_{\bar{n}}$	> 20	cm^2
	S_6	$N_{\text{hits}}^{50\text{cone}}$	$> 35 \ \&\& \ < 100$	#
Neutron selection	S_7	E_n	$[0.04 (0.06), 0.6]$	GeV
Background rejection	S_8	E_{extra}	< 0.15	GeV
	S_9	l_{MUC}	< 6	#
	S_{10}	$\langle n_{\bar{n}} \rangle$	> 150	degree

Table 5.1: Summary of the selection criteria $S_1 - S_{10}$ from Section 5.3.1 to 5.3.4 for the signal process $e^+e^- \rightarrow \bar{n}n$. The selection is performed in the presented order.

After the signal process selection as discussed in this chapter, the collider data set is still contaminated with background, which is mainly beam related and multi-hadronic, as can be seen in Figure 5.8 (bottom). This remaining background is discussed in the next chapter. Since it is not possible to effectively suppress the background contribution with cuts on the accessible observables, a different approach is chosen, as will be discussed in Chapter 7.

Chapter 6

The Evaluation of the Background Contamination

The statistics for collider data, signal MC simulation and the remaining background from non-collision data and simulation after the applied signal selection is discussed as follows. In Section 6.1 all background processes contributing to the selected events at all \sqrt{s} are listed. Section 6.2 discusses their individual contributions.

6.1 Remaining background in the selected events

Table 6.1 summarizes the cut flow with the change of the event numbers after each selection criterion exemplarily at $\sqrt{s} = 2.3960$ GeV. The scale factor \mathcal{F} is calculated according to the luminosity of the collider data at the corresponding \sqrt{s} , while the scale factor $\mathcal{F}_{\text{beam}}$ for the non-collision data is calculated according to the data taking time (DTT) and discussed in Section 6.2.1. After all selection criteria ($S_1 - S_{10}$) are applied, only a small number of physics background events remains in the selected data at large values of the opening angle $170^\circ < \langle \bar{\alpha}_n \rangle < 180^\circ$ as shown in Figure 5.8 (bottom). The most contributing physics background processes over the whole opening angle range are two- or multi-hadronic, while QED processes $e^+e^- \rightarrow \gamma\gamma$, $e^+e^- \rightarrow e^+e^-$ and $e^+e^- \rightarrow \mu^+\mu^-$ are negligible. The overall largest background contribution is beam- and cosmic ray-related and populates mainly the lower region in the opening angle distribution $\langle \bar{\alpha}_n \rangle < 170^\circ$. The distributions of the opening angle between the neutron and antineutron at all \sqrt{s} are shown in Figure 6.2. The misidentification rate for the neutron shower is studied with the signal MC simulation. An event is considered badly reconstructed or misidentified, if the matching angle between

Notation	Data	Signal MC	$\gamma\gamma$ MC	$\bar{q}q$ MC	Sep. Beam	e^+e^- MC	$\mu^+\mu^-$ MC
Total	6.078×10^8	500K	10M	5M	1.332×10^8	88.65M	1.5M
Category C	36815904	131841	2922933	2617590	7741212	1949972	33506
S ₁	24441687	91583	2888981	54465	5465335	233662	4045
S ₃	16406691	71173	1738347	41353	3848510	32874	533
S ₄	2161595	42912	1732904	14146	228183	1988	30
S ₅	734212	33294	63314	1754	193664	251	2
S ₆	238059	23087	367	641	62001	16	0
S ₇	111393	16251	3	524	31831	7	0
S ₈	59246	15239	3	186	17127	5	0
S ₉	11473	14289	3	176	3222	1	0
S ₁₀	486	11997	1	76	52	1	0
\mathcal{F}	-	0.015	0.817	0.569	2.838	0.935	0.700
Selected	486	180	1	43	148	1	0

Table 6.1: Summary of events passing the selection criteria $S_1 - S_{10}$ from Section 5.3.1 to 5.3.4 for the signal MC simulation $e^+e^- \rightarrow \bar{n}n$, collider data in collision and non-collision mode and various background MC simulations at $\sqrt{s} = 2.3960$ GeV. The signal process is excluded in the $\bar{q}q$ sample. The scale factor \mathcal{F} is calculated according to the luminosity of data for MC simulation, and data taking time for beam related background, respectively.

the truth position of the generated particle and the reconstructed shower position $\angle_{\text{shower}}^{\text{truth}}$ is between $10^\circ - 90^\circ$ or larger than 90° , respectively. Figure 6.1 shows these contributions at $\sqrt{s} = 2.3960$ GeV. The former contributing is 5.8%, the latter one is 0.5%.

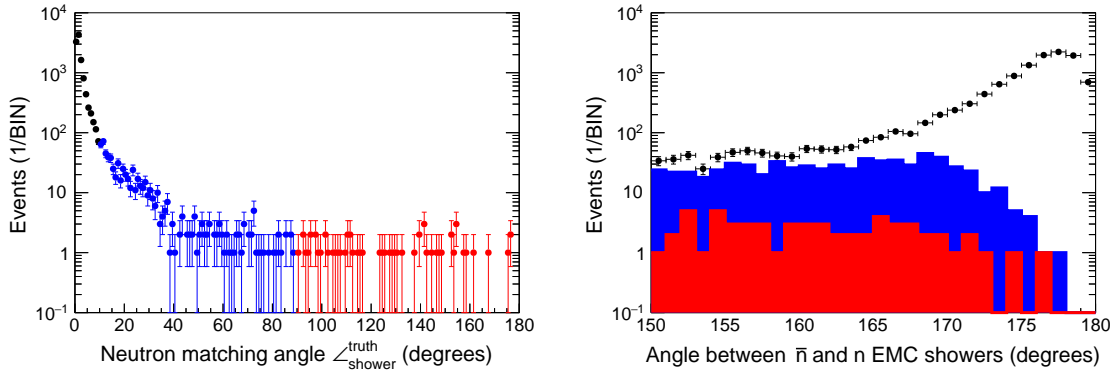


Fig. 6.1: Signal MC simulation with Phokhara v9.1. (Left) The matching angle between the generated and reconstructed neutron shower $\angle_{\text{shower}}^{\text{truth}}$ after all applied selection criteria ($S_1 - S_{10}$) at $\sqrt{s} = 2.3960$ GeV. Black dots are good reconstructed events. Events with $10^\circ < \angle_{\text{shower}}^{\text{truth}} < 90^\circ$ are denoted as badly reconstructed (blue), events with $\angle_{\text{shower}}^{\text{truth}} > 90^\circ$ are denoted as misidentified (red). (Right) The corresponding events in the opening angle between neutron and antineutron $\langle \bar{n} \rangle_n$ representation.

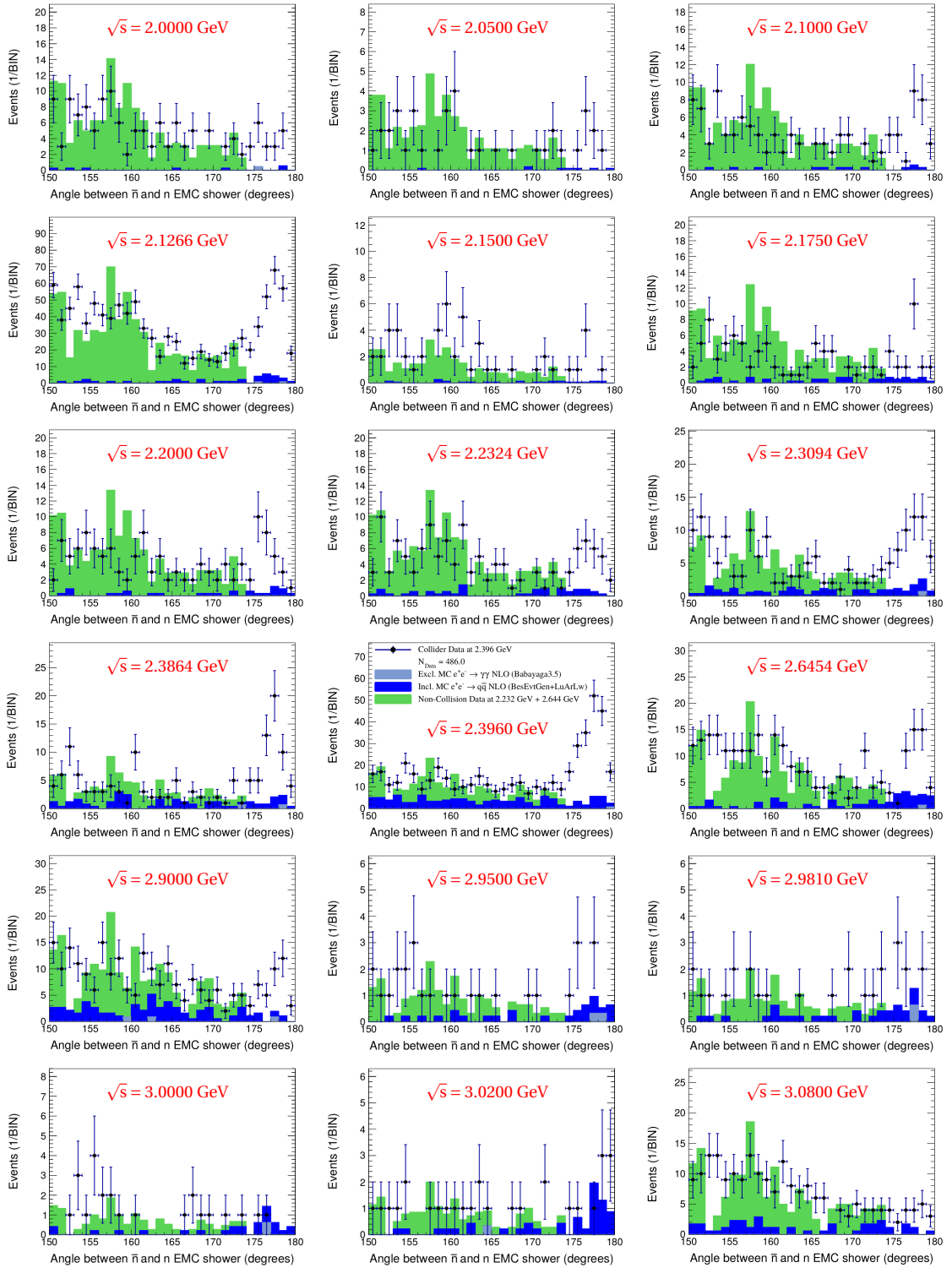


Fig. 6.2: Opening angle between the $\bar{\nu}$ and ν EMC shower after applied selection criteria at all analyzed \sqrt{s} . Black dots are the collider data, the green histogram the data in non-collision mode, the blue histogram is the hadronic ($e^+e^- \rightarrow \bar{q}q \rightarrow \text{hadrons}$) background, the light blue histogram represents the digamma background. The region in collider data at large angles which is not described by the background distribution is the expected signal process. Signal events are excluded from the $e^+e^- \rightarrow \bar{q}q \rightarrow \text{hadrons}$ simulation.

While the badly reconstructed events will be treated in Section 7.1, the number of misidentified events is negligible and will be included into the systematic uncertainty in Chapter 10. The numbers of the survived events for collider data and simulation at all \sqrt{s} are listed in Table 6.2.

\sqrt{s} (GeV)	Data	Tot. MC + Sep. Beam	Signal MC	$\gamma\gamma$ MC	$\bar{q}q$ MC	Sep. Beam
2.0000	138	149	16	1	2	130
2.0500	37	54	8	0	1	45
2.1000	116	144	29	0	4	111
2.1266	1019	915	240	2	38	635
2.1500	52	38	6	0	2	30
2.1750	95	139	20	0	11	108
2.2000	128	155	25	0	9	121
2.2324	129	152	22	0	12	118
2.3094	169	158	42	1	24	91
2.3864	141	151	56	1	34	60
2.3960	486	357	165	1	43	148
2.6454	258	255	69	1	34	151
2.9000	240	246	41	3	60	142
2.9500	27	28	5	1	5	17
2.9810	26	27	5	1	6	15
3.0000	24	25	5	1	5	14
3.0200	28	29	5	1	8	15
3.0800	205	188	28	0	31	129

Table 6.2: Summary of events passing the selection criteria $S_1 - S_{10}$ from Section 5.3.1 to 5.3.4 for signal MC simulation, collider data in collision and non-collision mode and various background MC simulations at all \sqrt{s} . The signal process is excluded in the $\bar{q}q$ sample. All simulations and the non-collision background are scaled according to the luminosity of data, and data taking time, respectively.

The number of selected events in collider data and the sum of signal MC simulation and remaining background events are shown in the second and third row of Table 6.2, respectively. For several analyzed center-of-mass energies, these numbers are not consistent. Following reasons can lead to this inconsistency. The non-collision data (denoted as Sep. Beam) is only available at the two center-of-mass energies $\sqrt{s} = 2.2324$ GeV and $\sqrt{s} = 2.6444$ GeV. Even if the included contributions are approximately stable over the analyzed energy range (see discussion in Section 6.2.1), the scaled number of events passing all selection criteria can be imprecise. Additionally, the number of signal MC simulation events after event selection is only an approximation, since dependent on the

input model for the form factors, which are to be measured in this work. The final signal extraction is performed via fit to data in the next chapter.

6.2 Evaluation of the background contamination

As discussed in the previous section, the QED background is effectively suppressed after the signal selection shown in Section 5.3. For the majority of all center-of-mass energies, the remaining dominant background is beam related and from cosmic rays. With rising \sqrt{s} the fraction between the hadronic and non-collision background contribution changes in favor of the latter. The non-collision background is discussed in the next section, followed by the discussion of the hadronic contribution.

6.2.1 The beam related and the cosmic ray background

The beam related and the cosmic ray background is studied from two sets of non-collision data, collected at $\sqrt{s} = 2.2324$ and 2.6444 GeV. The discussion is based on the study from Reference [231]. The contributions to the non-collision background are listed below:

- Synchrotron radiation (SR): the intensity of the SR rises with higher \sqrt{s} of the particles in the BEPCII collider, but is low energetic and strongly suppressed after the signal selection criteria from Section 5.3 are applied. Simulations in [231] show on average a negligible amount of fired crystals in the EMC coming from SR. during each trigger window of 24 ns.
- Beam-gas inelastic Bremsstrahlung: the beam-gas induced background is nearly proportional to the total beam current, which is approximately stable for all collected sets of data with different \sqrt{s} . A simulation of the beam-gas induced particles in the BESIII detector at the center-of-mass energy $\sqrt{s} = 3.773$ GeV is shown in Figure 6.3.
- Beam-gas elastic Coulomb scattering: the same arguments, as discussed above for the inelastic Bremsstrahlung apply. Simulations in [231] show on average 51 fired EMC crystals coming from the inelastic Bremsstrahlung and elastic Coulomb scattering during each trigger window.
- Touschek effect: it describes the scattering between the particles in the same bunch. The Touschek effect is proportional to the square of the number of particles in a bunch and the number of bunches and therefore also stable for the data sets at all center-of-mass energies \sqrt{s} .

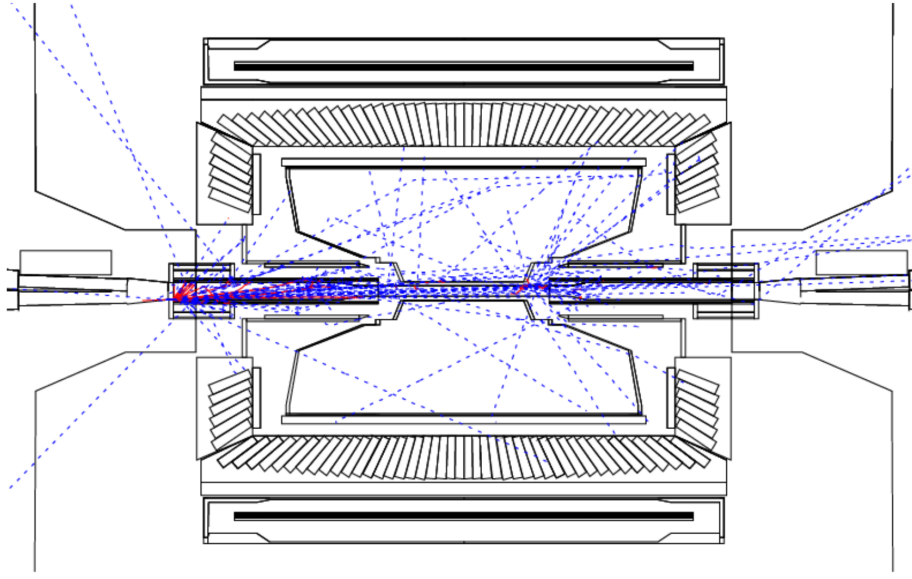


Fig. 6.3: Simulation of beam-gas induced particles in the BESIII detector including inelastic Bremsstrahlung and Coulomb scattering at $\sqrt{s} = 3.773$ GeV (original figure from [231]).

- The cosmic radiation is considered stable over time. The cosmic rays flux in Beijing is around $170\text{m}^{-2}\text{s}^{-1}$ leading to $N_{\text{cosmic}} = 1500/\text{s}$ inside the BESIII detector [231].

As discussed above, the beam related and cosmic background is approximately stable for all data sets used in this analysis. Therefore it is legit to use the two non-collision samples for the study of these effects at all \sqrt{s} . All the background contributions mentioned above are usually effectively suppressed by the BESIII L1 and L3 hard- and software trigger (as discussed in Section 3.2.6), which are based on the MDC and TOF sub-detector, as well as a vertex cut in the MDC. The signal process in this analysis has a pure neutral final state and therefore doesn't trigger these sub-trigger systems, therefore a large contribution from the mentioned background effects is observed. A precise simulation of the above discussed effects is not possible. Therefore a data-driven approximation is chosen. The non-collision samples at $\sqrt{s} = 2.2324$ and 2.6444 GeV are used for the background study. For comparison with collision data, the amount of selected events from these samples needs to be scaled to the luminosity of the corresponding collider data set. Two possibilities exist to achieve this goal. The most precise scaling can be achieved by using the vacuum pressure conditions $P_{\text{run(sep)}}$ in the collision region and the integrated beam currents $I_{\text{run(sep)}}$ during collision (run) and non-collision (sep) mode, multiplied by the number of events in the non-collision sample N_{sep} . The number of the beam related background events N_{beam} can be then calculated with the following equation:

$$N_{\text{beam}} = N_{\text{sep}} \times \left(\int_{\text{run}} P_{\text{run}} \times I_{\text{run}} dt \right) / \left(\int_{\text{sep}} P_{\text{sep}} \times I_{\text{sep}} dt \right) \quad (6.1)$$

Unfortunately, the pressure values in the interaction region for each run aren't available for analysis. An alternative method uses the hypothesis of an approximately stable rate of each of the above discussed effects over the whole center-of-mass range \sqrt{s} . The scale factor $\mathcal{F}_{\text{beam}}$ is calculated according to the data taking time $\text{DTT}_m^{\sqrt{s}}$ ($m = \text{beam, data}$) via:

$$\mathcal{F}_{\text{beam}}^{\sqrt{s}} = \frac{\text{DTT}_{\text{data}}^{\sqrt{s}}}{\left(\text{DTT}_{\text{beam}}^{2.2324} + \text{DTT}_{\text{beam}}^{2.6444} \right)} \quad (6.2)$$

The results for the corresponding scale factor $\mathcal{F}_{\text{beam}}$ at all \sqrt{s} are shown in Table 6.3:

\sqrt{s} (GeV)	Run Number	Data Taking Time (h:m:s)	Scale Factor $\mathcal{F}_{\text{beam}}$
2.0000	41729-41909	123:01:09	1.57
2.0500	41911-41958	42:25:51	0.54
2.1000	41588-41727	104:54:20	1.39
2.1266	42004-43253	599:03:17	7.65
2.1500	41533-41570	28:23:23	0.36
2.1750	41416-41532	102:12:30	1.30
2.2000	40989-41121	113:49:35	1.45
2.2324	41122-41239	111:27:27	1.42
2.3094	41240-41411	137:27:51	1.75
2.3864	40806-40951	89:43:45	1.44
2.3960	40459-40769	222:28:34	2.84
2.6444	40128-40296	115:24:39	1.47
2.6464	40300-40435	112:05:06	1.43
2.9000	39775-40069	214:01:57	2.73
2.9500	39619-39650	25:35:22	0.33
2.9810	39651-39679	22:25:15	0.29
3.0000	39680-39710	20:53:33	0.27
3.0200	39711-39738	22:22:02	0.29
3.0800	39355-39618	194:48:13	2.49
2.2324 separated beam	41959-41999	38:43:45	-
2.6444 separated beam	40777-40804	39:40:04	-

Table 6.3: Summary of the time used for the collider data collection. The scale factor $\mathcal{F}_{\text{beam}}$ for the non-collision background is calculated according to the DTT of a specific data sample and a combined sample of separated beam data at $\sqrt{s} = 2.2324 + 2.6444$ GeV.

6.2.2 The hadronic background

The hadronic background is studied individually for each analyzed center-of-mass energy \sqrt{s} with the inclusive $e^+e^- \rightarrow \bar{q}q \rightarrow \text{hadrons}$ MC simulation samples. The characterization "inclusive" means that all kinematically possible hadronic final states are generated according to either the experimentally measured cross section, or under a simplified phase-space calculation (LundAreaLaw model) for yet unmeasured final states. The originally included signal process $e^+e^- \rightarrow \bar{n}n$ is manually excluded from the inclusive MC simulation.

Anticipating the fit method for the extraction of signal events in the next chapter, the hadronic background needs to be studied for its distribution in the opening angle $\langle \angle_{\bar{n}n}^{\bar{n}n} \rangle$ observable. A peaking hadronic background in the opening angle region populated by the signal process events can bias the extracted number of signal events and therefore must be taken into account. The focus of this study lies on the determination of the correct normalization for the inclusive hadronic background at each analyzed center-of-mass energy.

Background events from the $e^+e^- \rightarrow \bar{q}q \rightarrow \text{hadrons}$ MC simulation which pass all the signal event selection criteria ($S_1 - S_{10}$ in Section 5.3.1 to 5.3.4) are sorted by the event topology (final states), not considering possibly different intermediate states. No significant contribution from this background source is observed in the signal region ($\langle \angle_{\bar{n}n}^{\bar{n}n} \rangle > 170^\circ$) for center-of-mass energies lower than $\sqrt{s} < 2.3$ GeV. For center-of-mass energies above $\sqrt{s} > 2.3$ GeV, a small, but visible peaking behavior is observed in the signal region $\langle \angle_{\bar{n}n}^{\bar{n}n} \rangle > 170^\circ$, as shown in Figure 6.2. The largest hadronic background contribution is coming mostly from neutral final state two-hadron events due to event kinematics very similar to the one of the signal process $e^+e^- \rightarrow \bar{n}n$. Dependent on the center-of-mass energy, the dominant hadronic background processes are $e^+e^- \rightarrow \bar{K}^0 K^0 (\pi^0)$ and $e^+e^- \rightarrow \bar{n}n \pi^0 (\pi^0)$. The trend to more contributing channels is observed for rising \sqrt{s} , possible due to a larger available phase-space. Channels with only one contributing event are neglected in this background study, since the number of events is considered to be equal zero within the statistical error and therefore negligible. The hadronic background topology at different \sqrt{s} is shown in Table 6.4. Here, $n\text{Evt}$ denotes the number of the selected hadronic background events from a specific process. After scaling the sum of $n\text{Evt}$ in each \sqrt{s} sample with \mathcal{F} to the individual luminosity of the collider data, the amount of the survived background events $N_{\text{had}}^{\text{bkg}}$ is used as the corresponding normalization parameter for the hadronic background in the opening angle fit approach, which is discussed in the next chapter.

\sqrt{s} (GeV)	Final states	nEvt	$N_{\text{had}}^{\text{bkg}}$	\sqrt{s} (GeV)	Final states	nEvt	$N_{\text{had}}^{\text{bkg}}$
2.0000	$K^0\bar{K}^0$	3	1	2.3960	$K^0\bar{K}^0$	43	39
	$\pi^0\pi^0K^0$	2			$\bar{n}n\pi^0$	9	
2.0500	$K^0\bar{K}^0$	7	1		$K^0\bar{K}^0\pi^0$	6	
	$K^0\bar{K}^0$	5	3		$\bar{n}n\pi^0\pi^0$	6	
2.1000	$\bar{n}n\pi^0$	4	3	$\pi^-\bar{n}\pi^0p$	5		
	$K^0\bar{K}^0$	19		2.6454	$K^0\bar{K}^0$	56	
2.1266	$\bar{n}n\pi^0$	8	32		$\bar{n}n\pi^0$	10	
	$\pi^-\pi^0K^0K^+$	2	$\pi^-\bar{n}\pi^0p$		5		
	$K^0\bar{K}^0$	14	2	$K^0\bar{K}^0\pi^0$	5		
2.1500	$\bar{n}n\pi^0$	8	2	$\bar{n}n\pi^0\pi^0$	5		
	$K^0\bar{K}^0$	23		2.9000	$\bar{n}n\pi^0$	33	
2.1750	$\bar{n}n\pi^0$	13	11		$\bar{n}nK^0\pi^0$	19	
	$\pi^-\bar{p}\bar{n}$	3	$\bar{n}n\pi^0\pi^0$		13		
	$\pi^0\pi^0$	2	$K^0\bar{K}^0(\pi^0)$		13		
2.2000	$K^0\bar{K}^0$	14	12	$\bar{n}n\pi^+\pi^-(\pi^0)$	10		
	$\bar{n}n\pi^0$	11		$\pi^-\bar{p}\bar{n}K^0$	6		
2.2324	$\bar{n}n\pi^0$	20	16	2.9500	$K^0\bar{K}^0$	15	4
	$K^0\bar{K}^0$	15			$K^0\bar{K}^0\pi^0$	1	
	$K^0\bar{K}^0\pi^0$	2		2.9810	$K^0\bar{K}^0$	19	4
	$\pi^-\bar{p}\bar{n}$	2			$K^0\bar{K}^0\pi^0$	3	
2.3094	$\bar{n}n\pi^0$	54	23	3.0000	$K^0\bar{K}^0$	19	4
	$K^0\bar{K}^0$	47			$K^0\bar{K}^0$	28	
	$\pi^-\bar{p}\bar{n}$	9		3.0200	$K^0\bar{K}^0\pi^0$	3	7
	$\pi^-\bar{p}\bar{n}\pi^0$	8			$\bar{n}n\pi^0$	3	
$K^0\bar{K}^0\pi^0$	2	3.0800	$\bar{n}n\pi^0$	15	27		
2.3864	$\bar{n}n\pi^0$		31	$K^0\bar{K}^0$		9	
	$K^0\bar{K}^0$		23	$\bar{n}nK^0\pi^0$		8	
$\bar{n}n\pi^0\pi^0$	7		32	$\bar{n}n\pi^0\pi^0$		5	
$\pi^-\bar{p}\bar{n}\pi^0$	3	3	$\bar{n}n\pi^+\pi^-\pi^0$	4			
$K^0\bar{K}^0\pi^0$	2		$\bar{n}n\pi^+\pi^-$	4			
				$\pi^-\bar{p}\bar{n}K^0$	3		

Table 6.4: Topological study of the hadronic background from the inclusive MC simulation after the signal selection ($S_1 - S_{10}$). The signal process is excluded. The number of events is scaled according to the luminosity in data and channels with only 1 event are neglected.

Chapter 7

The Extraction of the Signal Events

The statistics after the signal selection are shown in Table 6.2. Physics-, beam related-, and cosmic ray background still significantly contribute to the selected data. The remaining background after the applied signal selection can't be further reduced by means of selection criteria. To extract the number of events for the signal process $e^+e^- \rightarrow \bar{n}n$, a fit to the opening angle between the antineutron and neutron showers in the EMC $\langle \theta_{\bar{n}n} \rangle$ is performed. The modeling of the signal component is discussed in Section 7.1, for the background component in Section 7.2, respectively. The composite model fit is shown in Section 7.3, while at the end of this chapter in Section 7.4 a summary of the extracted number for the signal events at all center-of-mass energies is given.

7.1 The modeling of the signal component

To model the signal component of the total fit, firstly attention needs to be paid to signal events with misidentified neutron EMC showers. Figure 7.1 shows the distribution of the opening angle between the EMC showers selected as neutron and antineutron. At the two lowest \sqrt{s} data sets, a significant amount of misidentified neutron showers is observed, while for higher energies, this effect becomes negligible. Nevertheless, to eliminate this effect, the shape for the signal fit component is extracted from an optimized signal MC simulation sample after matching the neutron shower in the EMC with its truth position under the restriction of maximum 10° deviation. This modification will be also taken into account, when calculating the signal MC simulation selection efficiency. In the following, the signal shape of the opening angle is modeled by a Crystal Ball function shown in Equation 7.1. In a first step, the parameters for the signal shape are obtained at different

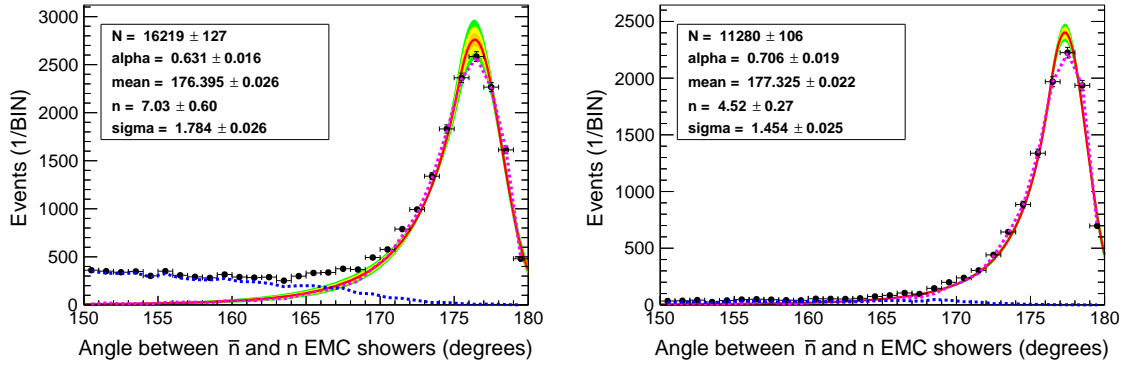


Fig. 7.1: Fit results for the parameters of the signal shape component for the composite model fit in Section 7.3. Phokhara v9.1 is used for signal MC simulation. The Crystal Ball function from Equation 7.1 is used for the fit. Results are shown for $\sqrt{s} = 2.0000$ and 2.3960 GeV. Black points with errors are representing the opening angle after the selection in Section 5.3. The blue dashed line shows events with a misidentified EMC shower for the neutron, while the magenta dashed line shows events with the MC truth matching described in the text. The red line is the fit result with the Crystal Ball function. The orange, yellow, and green band represents the 1, 2, and 3 sigma interval of the fit, respectively.

\sqrt{s} from the signal MC. The results for $\sqrt{s} = 2.0000$ and 2.3960 GeV are shown in Figure 7.1, for all other energies in the Appendix A. The fit parameters are shown in the plots.

$$\text{Fit}_{\text{CB}}(s, \alpha, n, \text{mean}, \sigma, N_{\text{sig}}) = N_{\text{sig}} \cdot \begin{cases} \exp\left(-\frac{(\sqrt{s}-\text{mean})^2}{2\sigma^2}\right), & \text{for } \frac{\sqrt{s}-\text{mean}}{\sigma} > -\alpha \\ A \cdot \left(B - \frac{\sqrt{s}-\text{mean}}{\sigma}\right)^{-n}, & \text{for } \frac{\sqrt{s}-\text{mean}}{\sigma} \leq -\alpha \end{cases} \quad (7.1)$$

$$N = \frac{1}{\sigma(C+D)} \quad A = \left(\frac{n}{|\alpha|}\right)^n \cdot \exp\left(-\frac{|\alpha|^2}{2}\right) \quad B = \frac{n}{|\alpha|} - |\alpha|$$

$$C = \frac{n}{|\alpha|} \cdot \frac{1}{n-1} \cdot \exp\left(-\frac{|\alpha|^2}{2}\right) \quad D = \sqrt{\frac{\pi}{2}} \cdot \left(1 + \text{Erf}\left(\frac{|\alpha|}{\sqrt{2}}\right)\right)$$

Here, mean represents the mean value of the Gaussian part of the function with respect to \sqrt{s} , σ is the HMF $W/2$, n and α are taking into account the radiative tail, while N_{sig} is the normalization and stands for the number of events under the fit. The signal parameters are obtained from the Crystal Ball fit and used as initial values in the signal component of the composite model fit to the collider data distributions in Section 7.3.

7.2 The modeling of the background component

The selected events in collider data contain beam related and hadronic background. While the hadronic background includes several two- and multi-hadronic channels, as shown in the topological discussion in Section 6.2.2, and will be modeled in Section 7.2.2, the next section shows the modeling of the beam related and cosmic ray component.

7.2.1 The beam related and the cosmic ray component

The background in the separated beam samples contains several effects, as described in Section 6.2.1. Since it is not possible to simulate all of these effects precisely for all data sets, a fit is used to describe the opening angle distribution in the separated beam samples at $\sqrt{s} = 2.2324$ and 2.6444 GeV and extract the parameters for this background component. A Chebychev polynomial function of the 3rd order is chosen as the model for the shape:

$$Fit_{\text{beam}}(s, N_i, p1, p2, p3) = N_{\text{beam}} \cdot [1 + p1 \cdot \sqrt{s} + p2 \cdot (2 \cdot s - 1) + p3 \cdot (4s^{3/2} - 3 \cdot \sqrt{s})] \quad (7.2)$$

To determine the parameters for the beam related background component of the composite model fit in Section 7.3, the Chebychev polynomial fit Fit_{beam} is applied simultaneously to the separated beam samples at $\sqrt{s} = 2.2324$ and 2.6444 and to the corresponding collider data, with the signal region $\langle \bar{n} \rangle > 170^\circ$ excluded for the two latter samples. In the composite model fit, the normalization N_{beam} represents the number of beam related events. The four relevant data sets are shown in Figure 7.2.

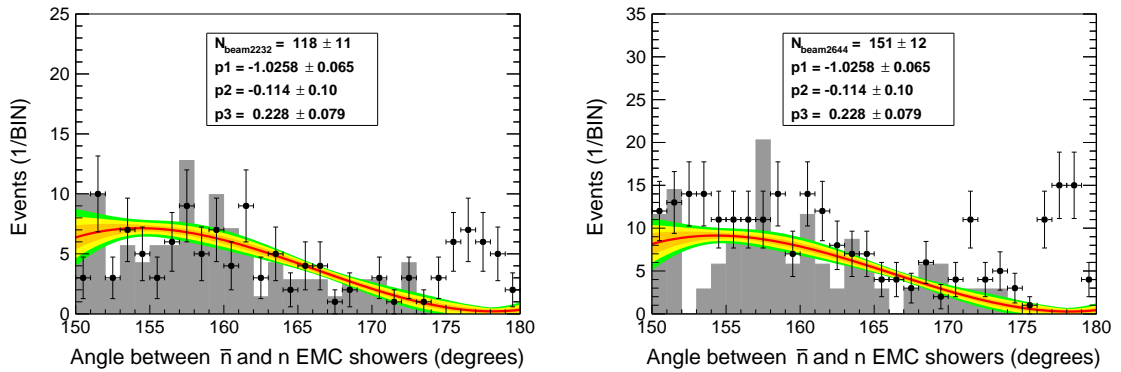


Fig. 7.2: The opening angle for data in collision and non-collision mode. The beam related background and collider data at $\sqrt{s} = 2.2324$ and 2.6444 GeV are shown, in the left and right plot, respectively. Black points with errors are collider data, while the gray histograms are produced from separated beam samples, all after the selection in Section 5.3. The red line is the fit result with the Chebychev polynomial function. The orange, yellow, and green band represents the 1, 2, and 3 sigma interval of the fit, respectively.

The parameters p_1 , p_2 , and p_3 are shared, while N_{beam} is the normalization in each sub-set. The Chebychev polynomial fit to the two collision data sets at $\sqrt{s} = 2.2324$ and 2.6444 GeV is considered as legit, since the hadronic contribution is flat and negligible in the fitting range ($\langle \bar{n} \rangle < 170^\circ$), as shown in Figure 6.2, therefore the shared parameters p_1 , p_2 , and p_3 are not biased. In the next step the hypothesis from Section 6.2.1, that the beam related background is approximately constant over the whole analyzed energy range, is studied. Therefore the collider data at $\sqrt{s} = 2.1266$ and 2.3960 GeV are shown together with a combined non-collision data sample for beam related background. As seen from Figure 7.3, the combined sample of beam related background can describe the background shape in data, as well as the normalization via the data taking time. The hadronic background contribution is considered flat and small and is not shown in the figure.

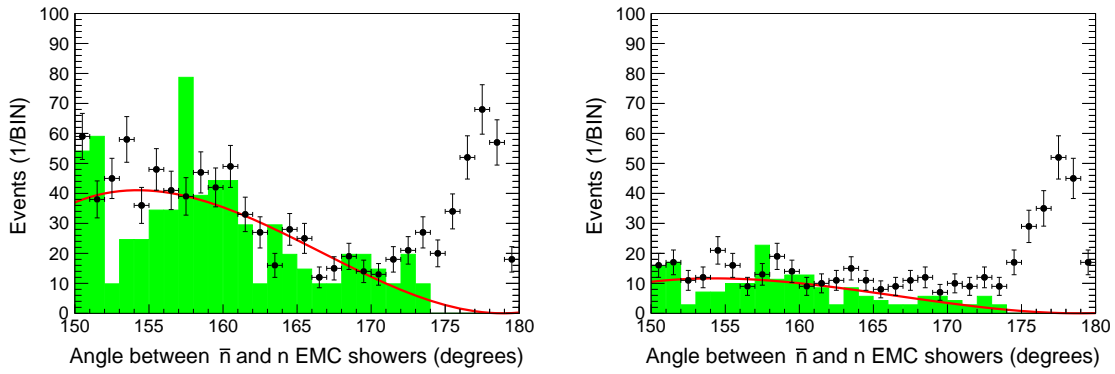


Fig. 7.3: Beam related and cosmic background (green histogram) from the combined separated beam samples at $\sqrt{s} = 2.2324$ and 2.6444 GeV together with collider data (black dots with errors) at (left) $\sqrt{s} = 2.1266$ GeV and (right) 2.3960 GeV. The beam related background is scaled according to Table 6.3. The red line is the 3rd order Chebychev polynomial with input parameters from the fit, as discussed above. The hadronic background is not shown.

In the composite model fit in Section 7.3, the beam related background component is fitted to all collider data sets, sharing the parameters p_1 , p_2 , and p_3 within their errors, while the normalization is individual.

7.2.2 The hadronic background component

The hadronic background have been studied in Section 6.2.2. Results from the topology study, shown in Table 6.4, indicate that with varying \sqrt{s} , the number and kind of contributing hadronic background channels changes and also the shape variates. Especially at higher \sqrt{s} , several two-hadronic channels can show a slight peaking behavior in the signal region above $\langle \bar{n} \rangle > 170^\circ$. Due to this reason, it is not purposeful to fit this

background component with an analytic function, even if the hadronic contribution to the total background is tiny compared to the beam related one for most \sqrt{s} . Instead a different approach is chosen. A Kernel Density Estimator (KDE) method implemented in the RooFit package [207] is used to model an energy individual shape for the hadronic background at each \sqrt{s} . This Probability-Density-Function (PDF) is a non-parametric representation of the survived events after the event selection from the hadronic MC simulation sample. With this method, each event in an specific $e^+e^- \rightarrow \bar{q}q \rightarrow \text{hadrons}$ MC simulation sample is described by a Gaussian function. The total shape of the hadronic background is modeled as an unbinned superposition of these Gaussians, sharing an equal surface, but varying in width, dependant on the event density in the corresponding histogram bin. For the composite model fit in Section 7.3, the following options for the shape estimation are used: The parameter ρ defines the "smoothness" of the Gaussian superposition and is left in the neutral option $\rho = 1$. The option for minimizing edge effects is chosen to "mirror" (*MirrorLeft*) the distribution to the lower opening angle range below 150° to take into account, that the distribution doesn't vanish below this value. At the upper range of the opening angle, no mirroring is allowed, since no events above 180° can populate the distribution. The normalization is fixed to the number of hadronic events $N_{\text{had}}^{\text{bkg}}$, which has been extracted in the topology study and summed up in Table 7.1. The computed PDF's for all analyzed \sqrt{s} are shown in Figure 7.4.

\sqrt{s} (GeV)	nEvt	\mathcal{F}_{had}	$N_{\text{had}}^{\text{bkg}}$	\sqrt{s}	nEvt	\mathcal{F}_{had}	$N_{\text{had}}^{\text{bkg}}$
2.0000	5	0.277	1	2.3864	66	0.483	32
2.0500	7	0.089	1	2.3960	69	0.569	39
2.1000	9	0.315	3	2.6454	81	0.462	37
2.1266	29	1.106	32	2.9000	94	0.592	56
2.1500	20	0.071	2	2.9500	17	0.214	4
2.1750	41	0.262	11	2.9810	21	0.210	4
2.2000	25	0.333	12	3.0000	19	0.203	4
2.2324	39	0.282	16	3.0200	34	0.217	7
2.3094	120	0.191	23	3.0800	48	0.567	27

Table 7.1: Hadronic background events extracted from the topology study in Section 6.2.2 at different \sqrt{s} . The value for nEvt denotes the amount of hadronic events passing the event selection, excluding channels with only 1 event. $N_{\text{had}}^{\text{bkg}}$ is additionally scaled with \mathcal{F}_{had} to the luminosity of the collider data, as shown in Table A.3. The values for the topological study are quoted from Table 6.4.

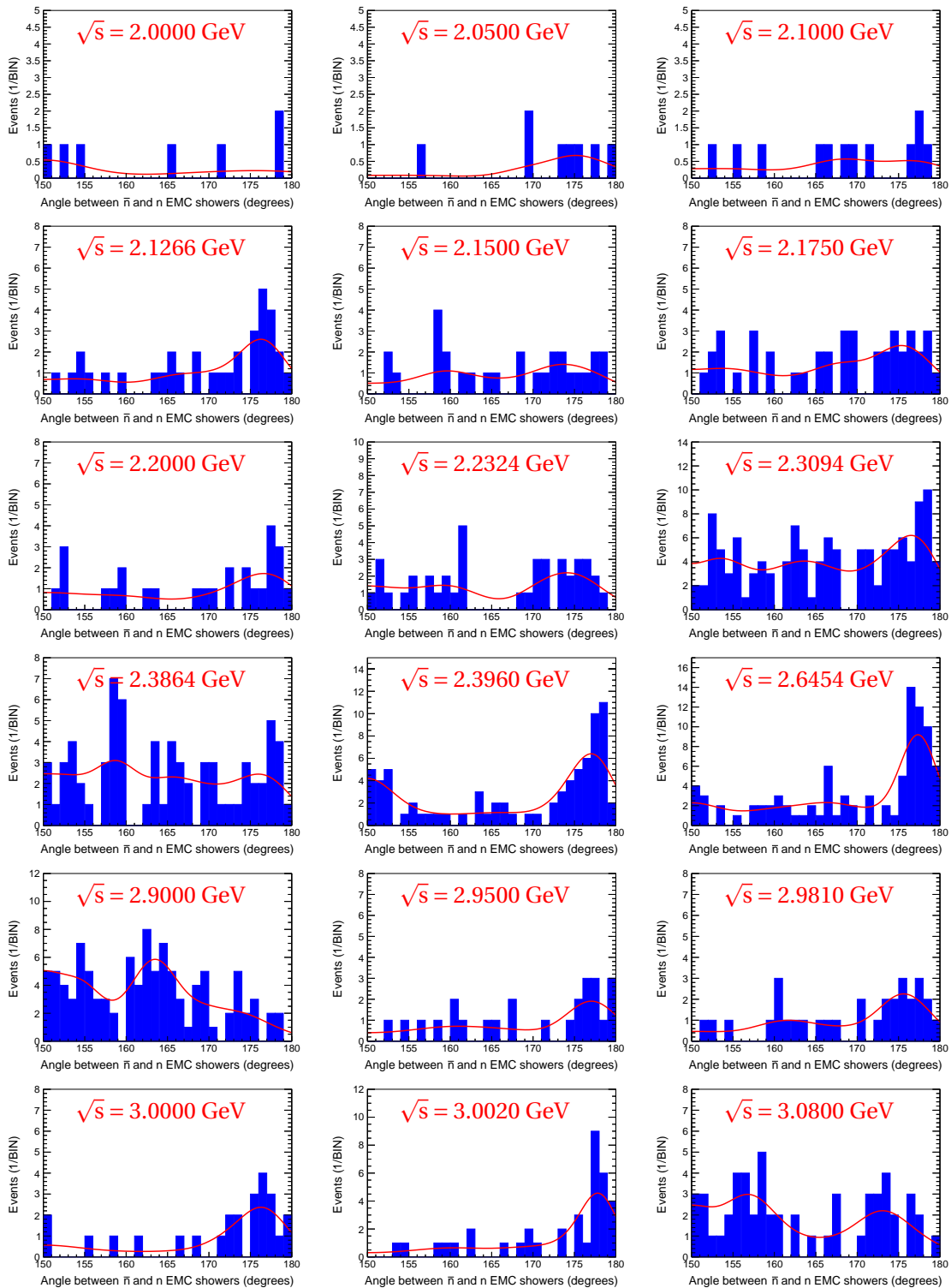


Fig. 7.4: Probability density functions for the hadronic background component of the composite model fit in Section 7.3 at different \sqrt{s} . The PDF's have been computed with inclusive hadronic MC simulation using the Kernel Density Estimator method. In this figure, the normalization according the collider data is not applied.

7.3 The fit of the combined model to the BESIII data set

After the modeling of the individual components for the signal process and the various background contributions in the collider data, the total fit model is constructed as follows:

$$\mathcal{F}it_{total}(s) = N_{sig} \cdot PDF_{sig} + N_{beam} \cdot PDF_{beam} + N_{had}^{bkg} \cdot PDF_{had} \quad (7.3)$$

The parameters N_{sig} , N_{beam} , and N_{had}^{bkg} are the number of signal, beam related, and hadronic background, respectively. The parameters for the number of signal and beam related events are set floating, while the number of hadronic background is fixed to the values extracted from the topological study, as shown in Table 7.1, within the limits of the corresponding statistical errors. The probability density functions (PDF's) PDF_{sig} , PDF_{beam} , and PDF_{had} are discussed in Sections 7.1, 7.2.1, and 7.2.2, respectively. They represent the shapes of the signal and background events with respect to the opening angle $\angle_{\bar{n}n}^{\bar{n}}$ between the \bar{n} and n shower in the EMC. The signal shape parameters mean, σ , n , and α are fixed within their individual errors to the corresponding data set at a specific \sqrt{s} . The parameters $p1$, $p2$, and $p3$ for the shape of the beam related background are fixed within their errors to the values, extracted in Section 7.2.1, and shared between the collider data at all \sqrt{s} and the two separated beam sets. The PDF's for the hadronic background contribution are non-parametric and fixed to the corresponding data sets.

For each data set at a specific \sqrt{s} an individual total PDF $\mathcal{F}it_{total}(s)$ is constructed, taking into account the specific normalization for the hadronic background from the topology study. Each model is applied to the corresponding collider data at one \sqrt{s} and a set of Negative Logarithmic Likelihood (NLL) values is calculated. The composite model fit algorithm optimizes a global NLL value, taking into account the local NLL's at each \sqrt{s} . Therefore, the solution is optimal globally, while it may be not optimal at a specific \sqrt{s} . This approach has the advantage of an increased fit stability, taking into account the poor statistics in collider data at several \sqrt{s} .

For the fit optimization, the RooFit package [207] is used. After minimizing the negative log-Likelihood with MIDGARD by means of a modified version of the Davidson-Fletcher-Powell method [232], the HESSE algorithm calculates a full second-derivatives matrix of the model parameter space to improve the uncertainty calculation. A following MINOS error analysis is performed for a further optimization of the parameter errors estimation.

\sqrt{s} (GeV)	Parameter							Normalization			
	mean	σ	n	α	p1	p2	p3	KDE	N_{sig}	N_{beam}	$N_{\text{had}}^{\text{bkg}}$
2.0000	176.4	1.8	7.0	0.6	-1.026	-0.114	0.228	fixed	free	free	1 ± 1
2.0500	176.6	1.8	5.5	0.7	shared	shared	shared	fixed	free	free	1 ± 1
2.1000	176.8	1.8	3.6	0.8	shared	shared	shared	fixed	free	free	3 ± 2
2.1266	177.1	1.5	5.0	0.6	shared	shared	shared	fixed	free	free	32 ± 6
2.1500	176.8	1.7	3.3	0.8	shared	shared	shared	fixed	free	free	2 ± 1
2.1750	176.9	1.8	2.5	0.9	shared	shared	shared	fixed	free	free	11 ± 3
2.2000	176.9	1.7	2.8	0.9	shared	shared	shared	fixed	free	free	12 ± 3
2.2324	177.0	1.7	2.4	0.9	shared	shared	shared	fixed	free	free	16 ± 4
2.3094	177.0	1.7	2.9	1.0	shared	shared	shared	fixed	free	free	23 ± 5
2.3864	177.1	1.7	3.7	0.9	shared	shared	shared	fixed	free	free	32 ± 6
2.3960	177.3	1.5	4.5	0.7	shared	shared	shared	fixed	free	free	39 ± 6
2.6454	177.2	1.8	1.9	0.9	shared	shared	shared	fixed	free	free	37 ± 6
2.9000	177.3	1.7	1.0	1.1	shared	shared	shared	fixed	free	free	56 ± 7
2.9500	177.3	1.7	1.1	1.1	shared	shared	shared	fixed	free	free	4 ± 2
2.9810	177.5	1.4	1.3	0.9	shared	shared	shared	fixed	free	free	4 ± 2
3.0000	177.5	1.4	1.3	0.9	shared	shared	shared	fixed	free	free	4 ± 2
3.0200	177.5	1.4	1.3	0.9	shared	shared	shared	fixed	free	free	7 ± 3
3.0800	177.3	1.7	1.0	1.2	shared	shared	shared	fixed	free	free	27 ± 5

Table 7.2: Configuration for the composite model fit. The parameters shown are used as initial values. The shown signal PDF parameter are extracted in Section 7.1 and used as initial values for the fit. As the parameter limit, the largest deviation within the parameter sets is used. The parameters for the beam related background, as studied in Section 7.2.1, are fixed within their errors to the collider data. The shape for the hadronic background is fixed, its normalizations are fixed to the values from the topology study in Table 6.4 within their statistical uncertainty.

Applying the discussed procedure to the collider data for all analyzed \sqrt{s} samples, the number of signal process events $e^+e^- \rightarrow \bar{n}n$ is extracted at all energies. The configuration of the composite model fit is shown in Table 7.2, the result at $\sqrt{s} = 2.3960$ GeV is shown in Figure 7.5 and discussed in detail in the following. Results for all other center-of-mass energy data sets are shown in Appendix A. In the top left panel of Figure 7.5 the composite model fit is described by the blue line, with the red, green, pink dashed lines being the signal, beam related, and hadronic background component, respectively. Events from collider data are shown as black dots with errors, their number is denoted N_{data} . The yields from the signal events, the beam related and the hadronic background events extracted with the fit are denoted as N_{fit} , N_{beam} , and $N_{\text{had}}^{\text{bkg}}$, respectively. Since the fit optimization is performed by minimizing the negative logarithmic Likelihood (NLL) value, the shown

reduced χ^2/ndof is calculated as a cross check and not used for fit optimization. From a first visual examination, the composite model describes the collider data very well. The value of $\chi^2/\text{ndof} = 0.8$ confirms this observation. For a better judgment on the goodness of a NLL fit, the so-called Pull distribution can be surveyed. Shown in Figure 7.5 bottom left, it is calculated via $\text{Pull} = N_{\text{data}} - N_{\text{fit}}/\Delta_{\text{data}}|_{\text{bin}}$ and describes the deviation of the fit value at a specific bin from the corresponding value in the collider data. As shown, at $\sqrt{s} = 2.3960$ GeV the Pull distribution fluctuates within the 1 sigma interval around zero.

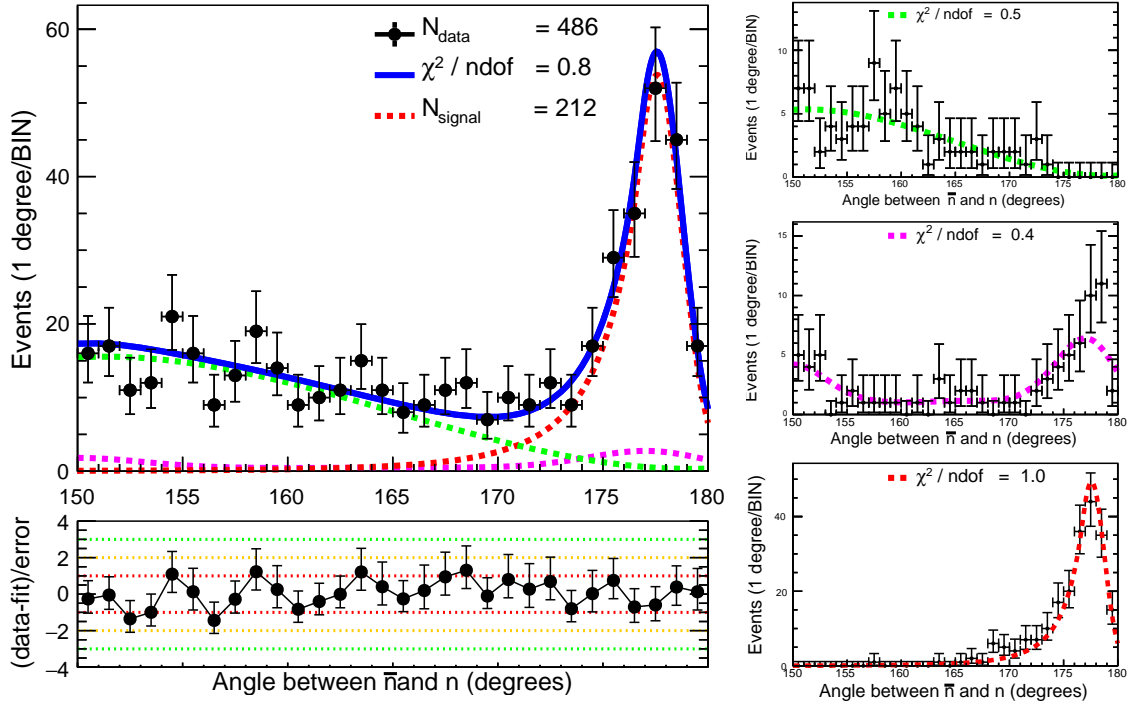


Fig. 7.5: Results from the composite fit model from Equation 7.3 applied to collider data at $\sqrt{s} = 2.3960$ GeV. (Top) The black points are collider data, the red dashed line is the signal process component for the signal yield extraction. The green dashed line is the beam related background component, the pink dashed line is the hadronic background component. The fit is performed by minimizing the global negative log-likelihood of the composite model, the shown χ^2 is calculated only for a judgment of the goodness of fit. The value of N_{data} is the number of selected data after the signal selection in Section 5.3. The value of N_{fit} is the number of extracted signal events. (Bottom) Pull distribution = $(\text{data} - \text{fit-value}) / \Delta_{\text{data}}$. The red, orange, and green dashed lines indicate the 1, 2, and 3 σ interval. (Left) From top to bottom: fits of the individual components: beam-related and cosmic ray background, inclusive hadron MC simulation background, signal MC simulation. The single component fits are unscaled and shown only for visualization purpose.

For the angular analysis in Section 9.3 the differential signal yield per bin of the $\cos\theta$ distribution of the antineutron EMC shower is needed. The same composite model fit method is applied for each bin of the angular distribution, using the individual fit parameters obtained from the total fit at the corresponding \sqrt{s} . The angular analysis is performed for the individual data set at $\sqrt{s} = 2.1266$ GeV, as well as for combined data at $\sqrt{s} = [2.3864 - 2.3960]$, $[2.0000 - 2.1000]$, $[2.1500 - 2.3094]$ and $[2.6454 - 2.9500]$. Results from the composite model fit to the collider data in each bin of $|\cos\theta_{\bar{n}}| < 0.7$ are shown at $\sqrt{s} = 2.3960$ in Figure 7.6, for other energies in the Appendix A.

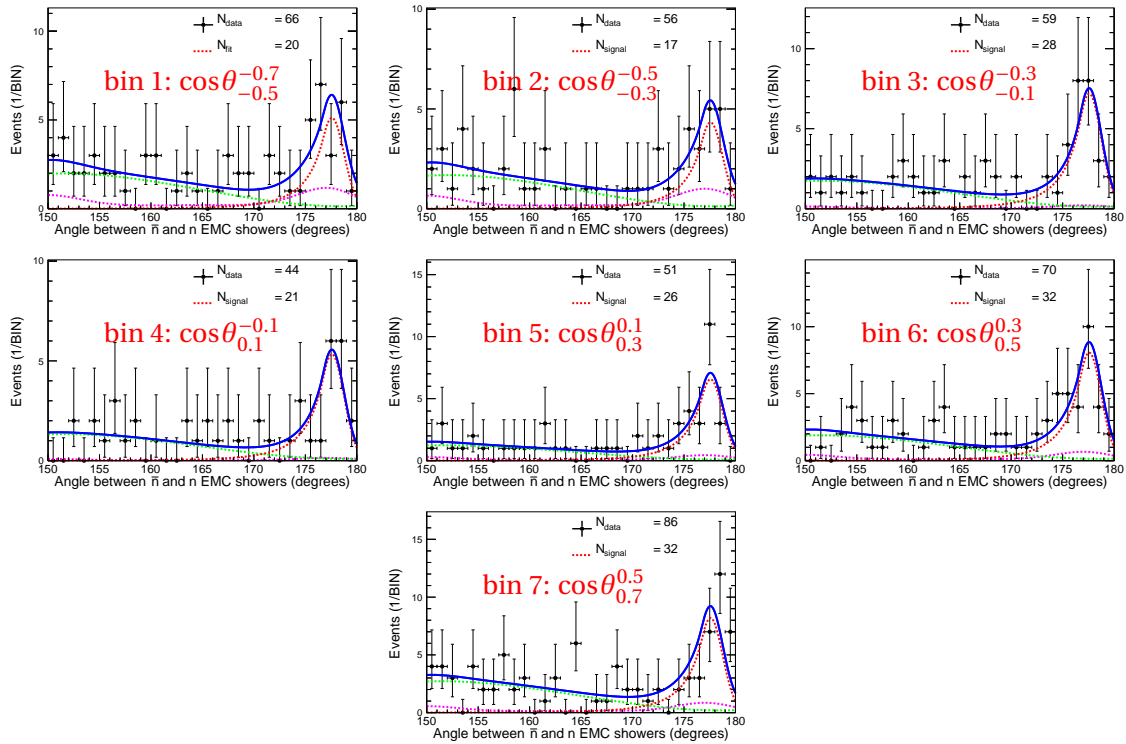


Fig. 7.6: Composite model fit from Equation 7.3 applied to collider data at different $\cos\theta_{\bar{n}}$ bins at $\sqrt{s} = 2.3960$ GeV with the model parameters extracted from the global composite model fit. From left to right, from top to bottom, the $\cos\theta_{\bar{n}}$ bins are shown starting from $-0.7 < \cos\theta_{\bar{n}} < -0.5$ in 0.2 steps. The black points are collider data, the red dashed line is the signal process component for the signal yield extraction. The green dashed line is the beam related background component, the pink dashed line is the hadronic background component. The fit is performed by minimizing the global negative log-likelihood of the composite model, the shown χ^2 is calculated only for a judgment of the goodness of fit. The value of N_{data} is the number of selected data after the signal selection in Section 5.3. The value of N_{fit} is the number of extracted signal events.

The differential signal yield is shown for the data set at $\sqrt{s} = 2.3960$ GeV in Figure 7.6 and summarized for all data sets in Table 7.3. Due to the low statistics, the fit stability isn't optimal for the data sets with small luminosities. Furthermore, the signal yield shows fluctuation dependent on the initial fit parameters. To obtain a stable angular distribution for the extraction of the magnetic form factor and the form factor ratio in Chapter 9, a second approach based on massive MC simulation is used to extract the differential signal yield, as explained step-by-step in the following:

- The opening angle distribution for each \sqrt{s} and bin from collider data is used to generate one hundred thousand (100k) corresponding MC distributions, taking into account the statistical fluctuations in the bins and using the same (total) amount of events as in the original distribution.
- The composite model fit to the opening angle from Equation 7.3 is applied to each of these MC distributions and the signal yield is extracted.
- The resulting distribution of the signal yield amount from the 100k simulations per bin and data set is subject to a Gaussian fit. The mean and sigma value from the Gaussian fit is denoted as the signal yield value and the corresponding statistical error, respectively. In cases, where the signal yield doesn't follow a Gaussian distribution due to a low statistics in the original data distribution, the mean and standard deviation values of the histogram are taken as the signal yield value and the corresponding error, respectively.

The distributions for the extraction of the signal yield per bin with the MC based approach are shown at $\sqrt{s} = 2.3960$ GeV together with the Gaussian fit for the extraction of the mean and sigma value in Figure 7.7. The mean value is used as the signal yield, the corresponding sigma value is used as the statistical uncertainty. The values for all bins and \sqrt{s} are listed in Table 7.3. The results in Figure 7.7 correspond to the signal yield extraction via standard fit in Figure 7.6. By comparing the signal yield from the approach 1 (Table 7.3) it can be seen that the signal yield obtained with the two approaches is very good in agreement while the statistical error is reduced and the stability of the results increased with the second approach. Plots for the differential signal yield obtained with both methods at all center-of-mass energies \sqrt{s} are shown in the Appendix A.

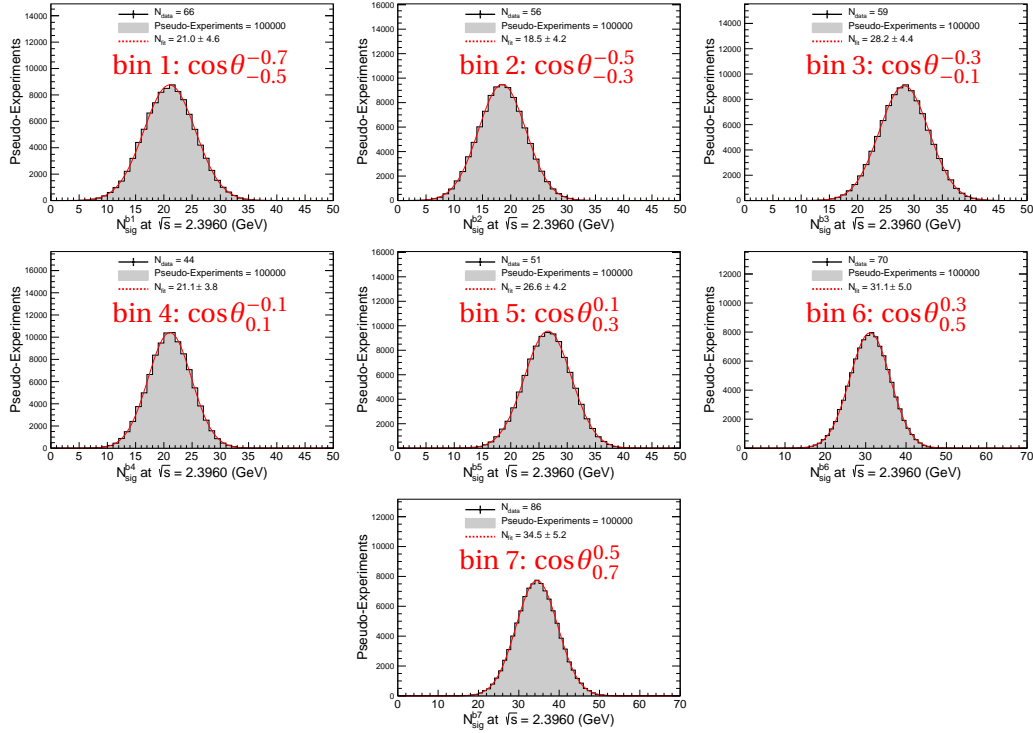


Fig. 7.7: The differential signal yield extraction based on a massive MC simulation approach at $\sqrt{s} = 2.3960$ GeV. The gray histogram is the signal yield distribution from the MC based pseudo-data. The red line is the Gaussian fit for the extraction of the mean and sigma parameters.

7.4 The summary of the extracted signal from collider data

Table 7.3 shows the signal yield extracted with the composite model fit from Section 7.3 for all energies. Additionally, the differential signal yield per $0.2 \cos \theta_{\bar{n}}$ of the analyzed angular distribution of the antineutron EMC shower is shown, which is used for the angular analysis in Section 9.2. Possible differences between the total amount of extracted signal events and the sum of the events per bin arise from statistical fluctuations in collider data. Table 7.4 shows the extracted signal yield with the massive MC simulation approach, as described in Section 7.3. By comparing the differential results shown in the two following tables, one finds them very well in agreement.

\sqrt{s}	$N_{\text{fit}}^{\text{tot}}$	$N_{\text{fit}}^{\text{bin1}}$	$N_{\text{fit}}^{\text{bin2}}$	$N_{\text{fit}}^{\text{bin3}}$	$N_{\text{fit}}^{\text{bin4}}$	$N_{\text{fit}}^{\text{bin5}}$	$N_{\text{fit}}^{\text{bin6}}$	$N_{\text{fit}}^{\text{bin7}}$
2.0000	26 ± 5	3.9 ± 2.2	1.4 ± 1.5	0 ± 0.5	0.8 ± 1.1	1.4 ± 1.6	5.0 ± 2.7	6.3 ± 3.1
2.0500	10 ± 3	2.1 ± 1.7	1.0 ± 1.0	0 ± 0.5	3.2 ± 1.8	0 ± 0.8	0.4 ± 1.0	2.2 ± 1.8
2.1000	31 ± 6	3.2 ± 2.0	5.1 ± 2.4	6.2 ± 2.6	7.9 ± 3.0	2.4 ± 3.2	4.3 ± 2.6	0 ± 2.0
2.1266	277 ± 16	29.7 ± 6.5	32.7 ± 6.7	34.6 ± 6.7	24.5 ± 5.6	31.4 ± 7.9	43.7 ± 7.4	27.7 ± 6.8
2.1500	7 ± 3	0.9 ± 1.0	0 ± 0.5	3.0 ± 1.7	2.0 ± 1.4	0.8 ± 1.1	0 ± 0.5	0 ± 0.6
2.1750	20 ± 5	3.1 ± 2.1	3.2 ± 2.0	1.0 ± 1.1	4.9 ± 3.4	2.1 ± 1.6	5.1 ± 2.7	2.1 ± 1.9
2.2000	35 ± 6	3.5 ± 2.5	5.3 ± 2.9	6.6 ± 2.9	0.7 ± 1.6	1.5 ± 2.7	10.5 ± 3.6	3.9 ± 2.4
2.2324	27 ± 5	1.8 ± 1.6	3.9 ± 2.4	3.1 ± 2.0	4.3 ± 2.4	0.8 ± 1.0	6.8 ± 3.7	3.4 ± 2.3
2.3094	52 ± 7	12.4 ± 3.8	7.8 ± 3.2	0.6 ± 1.5	3.1 ± 1.9	7.7 ± 3.0	12.7 ± 3.9	1.7 ± 1.8
2.3864	57 ± 7	10.5 ± 3.5	4.5 ± 2.4	11.6 ± 4.5	6.3 ± 3.9	4.3 ± 2.3	6.4 ± 2.8	8.6 ± 3.2
2.3960	212 ± 14	20.0 ± 5.6	17.0 ± 6.2	28.3 ± 5.8	21.0 ± 5.0	25.8 ± 9.9	31.8 ± 6.5	32.2 ± 6.6
2.6454	44 ± 8	5.2 ± 3.4	5.9 ± 3.0	12.2 ± 4.2	0.9 ± 1.0	1.7 ± 2.0	10.5 ± 3.9	4.2 ± 2.9
2.9000	48 ± 8	5.2 ± 3.1	7.8 ± 3.1	4.6 ± 3.1	3.0 ± 2.4	3.3 ± 2.4	4.3 ± 2.8	8.5 ± 4.1
2.9500	7 ± 3	0 ± 0.5	0 ± 0.6	0 ± 0.6	3.4 ± 2.0	1.5 ± 1.7	3.2 ± 1.7	0 ± 0.6

Table 7.3: Summary of extracted signal events $N_{\text{fit}}^{\text{tot}}$ from collider data at different \sqrt{s} , using the composite model fit method (approach 1), described in this section. The values with the index bin(i) are extracted with the composite model fit to the opening angle $\langle \theta_n^{\hat{n}} \rangle$ with respect to the angular distribution bins i , as described in the text. The difference between the total number of signal events $N_{\text{fit}}^{\text{tot}}$ and the sum of the differential signal yield $N_{\text{fit}}^{\text{bin}(i)}$ at a specific \sqrt{s} is due to statistical fluctuations in collider data.

\sqrt{s}	$N_{\text{mc}}^{\text{bin1}}$	$N_{\text{mc}}^{\text{bin2}}$	$N_{\text{mc}}^{\text{bin3}}$	$N_{\text{mc}}^{\text{bin4}}$	$N_{\text{mc}}^{\text{bin5}}$	$N_{\text{mc}}^{\text{bin6}}$	$N_{\text{mc}}^{\text{bin7}}$
2.0000	3.9 ± 2.2	1.6 ± 1.5	0 ± 0	0.9 ± 1.1	1.6 ± 1.6	5.1 ± 2.7	7.2 ± 3.1
2.0500	2.2 ± 1.8	1.1 ± 1.0	0 ± 0	3.2 ± 1.8	0 ± 0	0.1 ± 0.1	2.5 ± 1.8
2.1000	3.4 ± 2.0	5.2 ± 2.4	6.3 ± 2.6	7.9 ± 3.0	2.5 ± 3.1	4.5 ± 2.6	0 ± 0.1
2.1266	31.3 ± 6.5	33.4 ± 6.7	35.7 ± 6.7	25.5 ± 5.6	32.2 ± 6.2	45.0 ± 7.4	30.3 ± 6.8
2.1500	1.0 ± 1.0	0 ± 0.1	3.0 ± 1.7	2.1 ± 1.4	0.9 ± 1.1	0 ± 0.1	0 ± 0.1
2.1750	3.4 ± 2.1	3.2 ± 1.7	1.1 ± 1.1	4.9 ± 3.4	2.2 ± 1.6	5.2 ± 2.7	2.4 ± 2.2
2.2000	3.8 ± 2.5	5.4 ± 2.9	6.6 ± 2.9	0.9 ± 1.7	2.3 ± 1.6	10.7 ± 3.6	4.1 ± 2.4
2.2324	1.9 ± 1.6	4.1 ± 2.4	3.4 ± 2.0	4.3 ± 2.4	0.9 ± 1.0	7.0 ± 3.8	3.9 ± 2.3
2.3094	12.7 ± 3.8	7.9 ± 3.2	0.8 ± 1.5	3.2 ± 1.9	7.8 ± 3.0	13.0 ± 4.0	2.2 ± 1.8
2.3864	10.5 ± 3.5	4.5 ± 2.4	11.6 ± 4.5	6.3 ± 3.7	4.3 ± 2.3	6.4 ± 2.8	8.6 ± 3.2
2.3960	20.6 ± 5.6	17.4 ± 5.3	28.9 ± 5.8	21.5 ± 5.0	26.2 ± 10.0	32.5 ± 6.5	33.6 ± 6.6
2.6454	5.9 ± 3.4	6.2 ± 3.4	12.7 ± 4.2	1.2 ± 1.3	2.0 ± 2.0	10.9 ± 3.9	4.8 ± 2.9
2.9000	5.0 ± 3.6	8.0 ± 3.1	5.0 ± 3.3	3.2 ± 2.4	3.5 ± 2.4	4.9 ± 2.8	8.9 ± 4.2
2.9500	0 ± 0.1	0 ± 0.1	0 ± 0.1	3.4 ± 2.0	1.5 ± 1.7	3.2 ± 1.7	0 ± 0.1

Table 7.4: Summary of the extracted signal events for the angular analysis using the massive MC simulation based approach (approach 2), as described in the text. The notation is the same as in Table 7.3.

Chapter 8

The Reconstruction Efficiency

In this chapter the determination of the signal reconstruction efficiency is discussed. The signal reconstruction efficiency is crucial for the analysis, since it needs to be applied as a correction to the extracted number of signal events for the determination of the absolute Born cross section in Section 9.1. An equivalent correction is also required for the angular distribution of the antineutron to determine the disentangled form factors, as discussed in Section 9.3. Results for the reconstruction efficiency are evaluated with two different signal MC simulations for comparison, using the generators Phokhara and ConExc are shown in Section 8.1. Furthermore, several corrections for the signal reconstruction efficiency are introduced in the following sections. Corrections for the efficiency difference between collider data and signal MC simulation are discussed in Section 8.2 - 8.4. The reconstruction efficiency loss due to the BESIII trigger system is discussed in Section 8.5. Differences between data and simulation due to the model dependency of the angular shape for the final state particles are discussed in Section 8.6. Corrections from higher orders of the signal process, as well as the contribution of the vacuum polarization are implemented in the correction factor $(1 + \delta)$ and discussed in Section 8.7, followed by a summary of all corrections in Section 8.8.

8.1 Reconstruction efficiency from signal MC simulation

The reconstruction efficiency derived from the signal MC simulation ϵ^{MC} , from now denoted as "signal efficiency", is calculated using:

$$\epsilon^{\text{MC}} = \frac{N^{\text{rec}}}{N^{\text{gen}}} \quad (8.1)$$

with N^{rec} and N^{gen} the number of reconstructed and generated signal events, respectively. The corresponding error $\Delta\epsilon^{\text{MC}}$ is calculated with $\Delta N^{\text{rec}} = \sqrt{N^{\text{rec}}}$ and $\Delta N^{\text{gen}} = \sqrt{N^{\text{gen}}}$ using:

$$\Delta\epsilon^{\text{MC}} = \sqrt{\left(\frac{\Delta N^{\text{rec}}}{N^{\text{gen}}}\right)^2 + \left(\frac{\Delta N^{\text{gen}} \cdot N^{\text{rec}}}{(N^{\text{gen}})^2}\right)^2} \quad (8.2)$$

For the angular analysis in Section 9.2, the differential signal efficiency $\frac{d\epsilon^{\text{MC}}}{d\cos\theta}$ with respect to cosine of the polar angle $\cos\theta_{\bar{n}}$ is required, which is calculated in a similar way for each bin i of the angular distribution $\cos\theta$ using:

$$\left(\frac{d\epsilon^{\text{MC}}}{d\cos\theta}\right)_i = \frac{N_i^{\text{rec}}}{N_i^{\text{gen}}}, \quad \left(\Delta\frac{d\epsilon^{\text{MC}}}{d\cos\theta}\right)_i = \sqrt{\left(\frac{\Delta N_i^{\text{rec}}}{N_i^{\text{gen}}}\right)^2 + \left(\frac{\Delta N_i^{\text{gen}} \cdot N_i^{\text{rec}}}{(N_i^{\text{gen}})^2}\right)^2} \quad (8.3)$$

An example for the differential signal efficiency distribution at $\sqrt{s} = 2.12655$ GeV and $\sqrt{s} = 2.3960$ GeV is shown in Figure 8.9, distributions at all other \sqrt{s} are shown in Figure A.22. The signal efficiency depends on the input cross section for the MC simulation, especially on the radiative processes including one or two photons from the initial state. In this analysis the signal MC simulation is iteratively optimized with the previously obtained results for the Born cross section (see Section 4.2.2). The signal efficiency shown in Table 8.1 is calculated with the MC simulation samples from the generators Phokhara v9.1 used for analysis and ConExc in BesEvtGen 00-03-18 as cross-check using the final version of the form factor parametrization.

ϵ^{MC}					
\sqrt{s} (GeV)	Phokhara	ConExc	\sqrt{s} (GeV)	Phokhara	ConExc
2.0000	0.0031 ± 0.0001	0.0034 ± 0.0001	2.3864	0.0225 ± 0.0002	0.0232 ± 0.0002
2.0500	0.0074 ± 0.0001	0.0075 ± 0.0001	2.3960	0.0226 ± 0.0002	0.0236 ± 0.0002
2.1000	0.0115 ± 0.0002	0.0115 ± 0.0002	2.6454	0.0264 ± 0.0002	0.0274 ± 0.0002
2.1266	0.0130 ± 0.0002	0.0134 ± 0.0002	2.9000	0.0225 ± 0.0002	0.0228 ± 0.0002
2.1500	0.0149 ± 0.0002	0.0151 ± 0.0002	2.9500	0.0221 ± 0.0002	0.0225 ± 0.0002
2.1750	0.0154 ± 0.0002	0.0159 ± 0.0002	2.9810	0.0207 ± 0.0002	0.0216 ± 0.0002
2.2000	0.0168 ± 0.0002	0.0174 ± 0.0002	3.0000	0.0209 ± 0.0002	0.0211 ± 0.0002
2.2324	0.0180 ± 0.0002	0.0193 ± 0.0002	3.0200	0.0203 ± 0.0002	0.0206 ± 0.0003
2.3094	0.0188 ± 0.0002	0.0193 ± 0.0003	3.0800	0.0195 ± 0.0002	0.0190 ± 0.0002

Table 8.1: Summary of the signal reconstruction efficiencies at different \sqrt{s} derived with the signal MC simulation based on 500000 generated events using Phokhara v9.1 and ConExc.

8.2 Efficiency correction C_{dm}

For the accurate determination of the cross section and the form factors, a precise knowledge of the selection efficiency is crucial. As described in Section 4.2, the simulation of hadronic showers in the material of the EMC is imperfect, therefore differences in the distributions of the signal selection variables between simulation and collider data occur, as shown in Figure 8.4. This leads to an imprecise selection efficiency, which needs to be corrected according to real data, therefore a data-driven method is developed.

This section discusses the correction of the signal channel selection requirements $S_1 - S_7$, including the pre-selection and the selection of the signal final state particles. For the determination of the signal efficiency correction factor C_{dm} , samples of neutrons and antineutrons with high purity are required to study the differences between real data and MC simulation. The BESIII experiment collected large data samples at $\sqrt{s} = 3.097$ [208], the center of mass energy of the J/ψ resonance, containing over 1.3 billions J/ψ events. In this analysis, the two control channels $J/\psi \rightarrow p\bar{n}\pi^-$ and $J/\psi \rightarrow \bar{p}n\pi^+$ are used to select highly pure neutron and antineutron samples.

8.2.1 The selection of $J/\psi \rightarrow p\bar{n}\pi^-$ and $J/\psi \rightarrow \bar{p}n\pi^+$ control channels

The event selection for the control channels $J/\psi \rightarrow p\bar{n}\pi^-$ and $J/\psi \rightarrow \bar{p}n\pi^+$ is loosely based on the approach discussed in [211]. The selection criteria are listed as follows:

- (1) Two charged tracks, one for p (\bar{p}) and π^- (π^+), are selected under the requirement of a well defined production vertex. The closest approach from the beam interaction point to the reconstructed track must not exceed $R_{xy} < 1$ cm and $R_z < 10$ cm, with R_{xy} and R_z being the distances of the vertex in xy - and z - direction to the IP, respectively. Both tracks must not exceed $|\cos\theta| < 0.93$ in the polar angle plane.
- (2) The BESIII Particle Identification System (PID) is used to identify exactly one (anti-) proton and negatively (positively) charged pion from the previously selected two charged tracks. The total charge in the event is required to be zero. The PID system uses for particles identification the energy loss from passage of charged particles through matter dE/dx measured in the MDC, the time-of-flight measured in the first and second layer of the TOF system, as well as the TOF based energy measurement. With this configuration, the demanded particles are discriminated against pions, kaons and protons. The probability of the demanded particle (i.e. a proton) is

required to be larger than the probability for a pion and kaon. Its absolute probability must be larger than 0.001.

- (3) To improve the momentum resolution, a fit on the common vertex is performed and required to be valid, taking into account the helix of both charged tracks.
- (4) An one-constraint kinematic fit is performed, using as input the hypothesis of a J/ψ particle in rest with a small momentum correction due to the crossing angle between the electron and positron beam, the two charged tracks identified (anti-)proton and negatively (positively) charged pion and neutron mass as the missing mass as the constraint. The fit is required to be valid with a reduced $\chi^2 < 5$. The χ^2 distributions for the channels $J/\psi \rightarrow p\bar{n}\pi^-$ and $J/\psi \rightarrow \bar{p}n\pi^+$ are shown in Figure 8.1.
- (5) The recoil mass $m_{p\pi}^{\text{recoil}}$ of the $p\pi^-$ ($\bar{p}\pi^+$) system is required to be within ± 30 MeV around the nominal mass of the \bar{n} (n). The distributions for both control channels are shown in Figure 8.2.

After these selection criteria are applied to the collider data and the MC simulation for the control samples, a background study with the inclusive MC simulation is performed to identify possible background contaminations. The hadronic background fraction in the selected samples for the processes $J/\psi \rightarrow p\bar{n}\pi^-$ and $J/\psi \rightarrow \bar{p}n\pi^+$ is measured to 0.43% and 0.17%, respectively. A further cross-check is performed to verify a background free (or poor) selection of the control samples by calculating the branching fractions and comparing them to the known PDG values. Therefore the data distributions of the recoil mass $m_{p\pi}^{\text{recoil}}$ for both control samples are fitted with a Gaussian function. The event yield

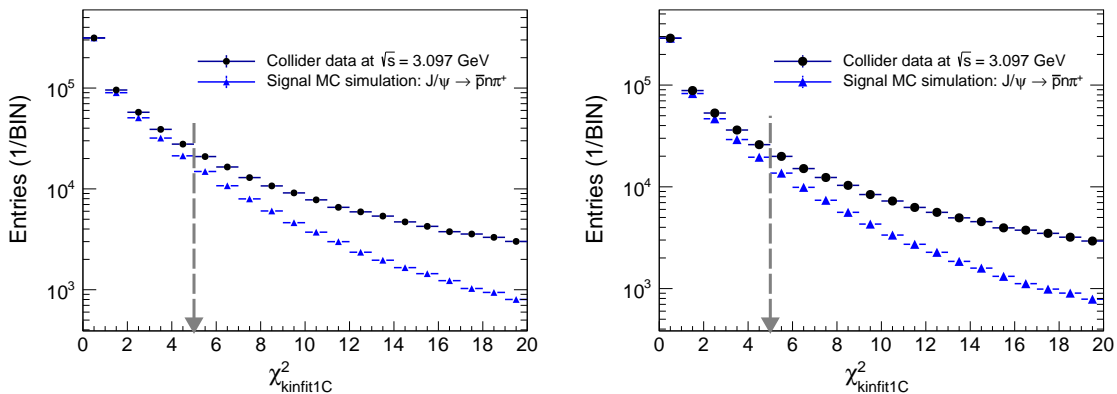


Fig. 8.1: χ^2 from the 1C kinematic fit: (top) to $J/\psi \rightarrow p\bar{n}\pi^-$ data and MC simulation (bottom) to $J/\psi \rightarrow p\bar{n}\pi^-$ data and MC simulation. Black dots are collider data, blue dots are MC simulation, both at $\sqrt{s} = 3.097$ GeV.

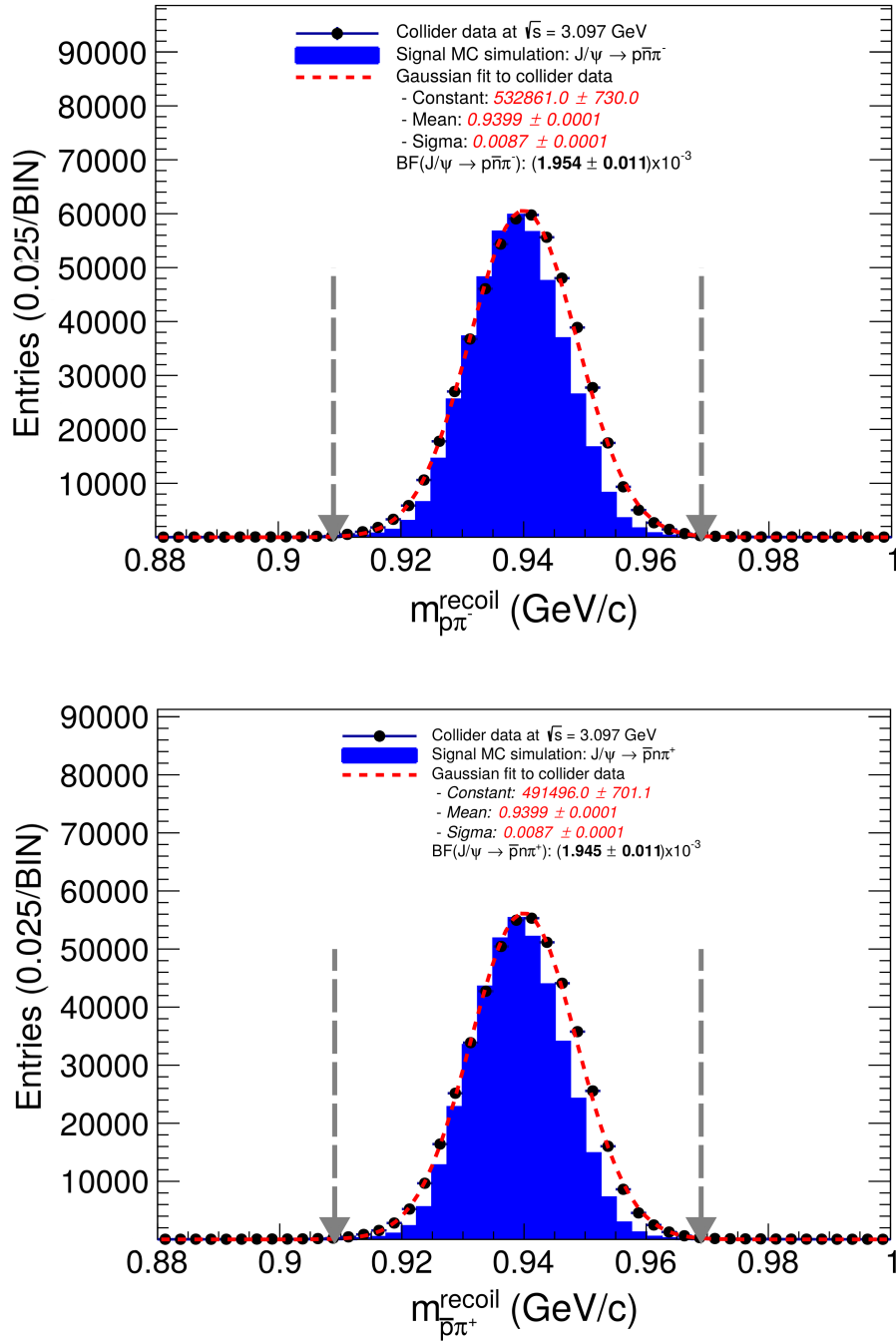


Fig. 8.2: The recoil mass $m_{p\pi}^{\text{recoil}}$ of the $p\pi^-$ ($\bar{p}\pi^+$) system: (Top) from $J/\psi \rightarrow p\bar{n}\pi^-$ data and MC simulation and (bottom) from $J/\psi \rightarrow p\bar{n}\pi^+$ data and MC simulation. Black dots are collider data, blue histograms are MC simulation, both at $\sqrt{s} = 3.097$ GeV. The red dashed line is a Gaussian fit to the collider data, the red fit parameters are extracted from the fit results. The values for the branching fractions shown in the plots are calculated according to Equation 8.4. The grey dashed arrows indicate the requirement (5).

is used to calculate the branching ratios $\text{BR}(J/\psi \rightarrow p\bar{n}\pi^-)$ and $\text{BR}(J/\psi \rightarrow \bar{p}n\pi^+)$ according to Equation 8.4:

$$\text{BR}_{J/\psi \rightarrow p\bar{n}\pi^- (\bar{p}n\pi^+)} = \frac{N_{J/\psi \rightarrow p\bar{n}\pi^- (\bar{p}n\pi^+)}^{\text{fit}}}{N_{J/\psi} \cdot \epsilon_{J/\psi \rightarrow p\bar{n}\pi^- (\bar{p}n\pi^+)}^{\text{MC}}} \quad (8.4)$$

with $N_{J/\psi \rightarrow p\bar{n}\pi^-}^{\text{fit}} = 532861 \pm 730$ ($N_{\bar{p}n\pi^+}^{\text{fit}} = 491496 \pm 701$) the event numbers obtained from the fits on data, $N_{J/\psi} = 1.311 \pm 0.007 \times 10^9$ the number of J/ψ events in the analyzed collider data and $\epsilon_{J/\psi \rightarrow p\bar{n}\pi^-}^{\text{MC}} = 0.2081 \pm 0.0002$ ($\epsilon_{\bar{p}n\pi^+}^{\text{MC}} = 0.1928 \pm 0.0002$) the signal efficiencies for each control channel obtained from $J/\psi \rightarrow p\bar{n}\pi^-$ and $J/\psi \rightarrow \bar{p}n\pi^+$ MC simulations. The results for the branching fractions are calculated to (errors are only statistical):

$$\text{BR}_{J/\psi \rightarrow p\bar{n}\pi^-} = (1.954 \pm 0.011) \times 10^{-3} \quad \text{BR}_{J/\psi \rightarrow \bar{p}n\pi^+} = (1.945 \pm 0.011) \times 10^{-3} \quad (8.5)$$

Compared to the value for $\text{BR}_{J/\psi \rightarrow p\bar{n}\pi^-} = (2.12 \pm 0.09) \times 10^{-3}$ from the PDG [50], the result obtained in this analysis is within 1σ , which shows that the background level is negligible and the selected samples can be used as pure neutron and antineutron samples to correct the signal efficiency in $e^+e^- \rightarrow \bar{n}n$ signal MC simulation. No official results for $\text{BR}_{J/\psi \rightarrow \bar{p}n\pi^+}$ are available up to date (September 2019), therefore it is assumed that as a charged conjugated channel to $J/\psi \rightarrow p\bar{n}\pi^-$, the branching fraction $\text{BR}_{J/\psi \rightarrow \bar{p}n\pi^+}$ is comparable.

8.2.2 The selection of \bar{n} and n showers from $J/\psi \rightarrow p\bar{n}\pi^-$ and $J/\psi \rightarrow \bar{p}n\pi^+$

After the applied selection criteria (1) - (5) in Section 8.2.1, further criteria are needed to select the $\bar{n}(n)$ EMC showers from the control samples $J/\psi \rightarrow p\bar{n}\pi^-$ and $J/\psi \rightarrow \bar{p}n\pi^+$ under same conditions as in $e^+e^- \rightarrow \bar{n}n$ and to calculate the selection efficiency for both signal final state particles from data and MC simulation. Criteria with the index a are applied to the $J/\psi \rightarrow p\bar{n}\pi^-$ channel:

- (6_a) Most energetic shower in EMC in a 50° cone around the recoil momentum direction of the $p\pi^-$ system taken as \bar{n} candidate. This requirement is equivalent to the choice of the most energetic EMC shower as \bar{n} candidate in signal channel selection (see Section 5.3.1).
- (7_a) Angle between $p\pi^-$ recoil momentum direction and most energetic EMC shower is limited to $< 15^\circ$. This criterion ensures the choice of correct EMC shower as the \bar{n} candidate and is studied from signal MC simulation for $e^+e^- \rightarrow \bar{n}n$ in Figure 8.3.
- (8_a) No associated TOF signal $t_0 < 0$, to exclude a classification into category A or B (details are discussed in Section 5.2). Further, the polar angle range of the \bar{n} is

restricted to $|\cos\theta_{\bar{n}}| < 0.75$. These requirements are equivalent to the signal channel selection criterion S_3 .

- (9_a) Selection criteria for signal channel $e^+e^- \rightarrow \bar{n}n$ S_1 and $S_4 - S_6$ (details can be found in Section 5.3). The event level criterion S_2 (minimum of two EMC showers in the event) is neglected, since with this approach either the neutron, or the antineutron selection efficiency corrections are studied, but not both at the same time.

To study the signal efficiency differences coming from requirements applied on the neutron, the following criteria with the index b are applied to the $J/\psi \rightarrow \bar{p}n\pi^+$ channel for both, collider data and MC simulation at $\sqrt{s} = 3.097$ GeV:

- (6_b) Most energetic shower in EMC in a 50° cone around the recoil momentum direction of the $\bar{p}\pi^+$ system taken as n candidate.
- (7_b) Angle between $\bar{p}\pi^+$ recoil direction and most energetic EMC shower $< 10^\circ$. The choice for the cut value is studied from MC simulation, as shown in Figure 8.3.
- (8_b) Selection criteria S_7 for signal channel $e^+e^- \rightarrow \bar{n}n$ (as discussed in Section 5.3.3).

The criterion on the angle between the $p\pi^-$ ($\bar{p}\pi^+$) recoil direction and EMC shower is studied by comparing the particle's true position on generator level (before reconstruction) and the EMC shower position after reconstruction using $e^+e^- \rightarrow \bar{n}n$ signal MC. The maximum deviation between the generated and reconstructed shower position in the EMC is taken as the cut value to be 15° (10°) for the \bar{n} (n) shower as shown in Figure 8.3. A comparison of the selection variables between collider data and the MC simulation is shown in Figure 8.4. The particle momentum is adjusted to the one in the signal MC.

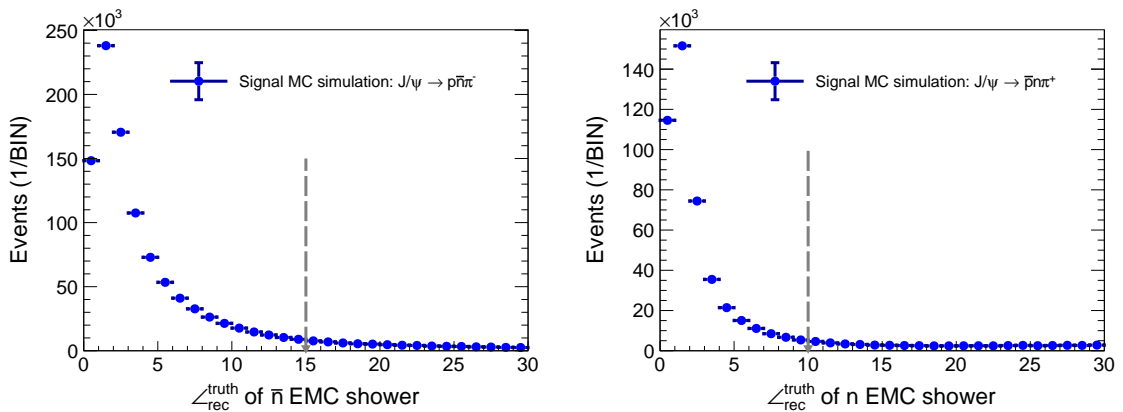


Fig. 8.3: The angle between the generated position and the reconstructed EMC shower position of (left) \bar{n} and (right) n. Both samples are $e^+e^- \rightarrow \bar{n}n$ signal MC simulations at $\sqrt{s} = 2.396$ GeV after the full selection $S_1 - S_{10}$ applied. Gray arrows indicate the selection requirements 7_a and 7_b .

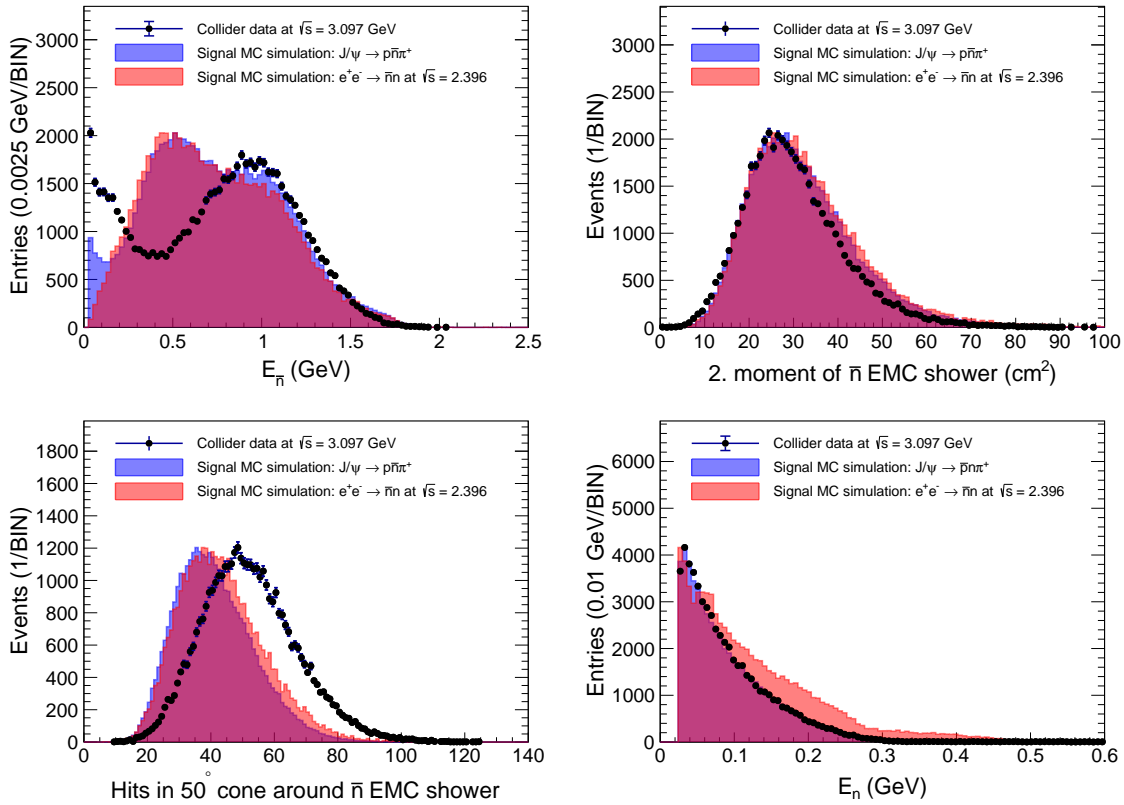


Fig. 8.4: Comparison of the selection variables for $e^+e^- \rightarrow \bar{n}n$ between collider data (back dots) and $J/\psi \rightarrow \bar{p}n\pi^+$ ($J/\psi \rightarrow \bar{p}n\pi^+$) MC simulation (blue histograms) at $\sqrt{s} = 3.0970$ GeV, with the $p\pi^-$ ($\bar{p}\pi^+$) recoil momentum range restricted to the momentum of \bar{n} (n) in $e^+e^- \rightarrow \bar{n}n$ at $\sqrt{s} = 2.3960$ GeV. The red histograms are from signal channel MC simulations $e^+e^- \rightarrow \bar{n}n$ at $\sqrt{s} = 2.3960$ GeV. (Top left) Deposited energy of \bar{n} shower in EMC, (top right) second moment of \bar{n} shower in EMC, (bottom left) number of hits in a 50° cone around the \bar{n} shower in EMC, (bottom right) deposited energy of n shower in EMC.

Visible differences between the signal and control channel MC simulation in the distributions shown in Figure 8.4 vanish with the ultimate selection applied to $e^+e^- \rightarrow \bar{n}n$ ($S_1 - S_{10}$) and are negligible. This confirms our expectation, since an EMC shower coming from a specific particle should have the same detector response independently of the physical process, as long as the momentum of the particle is the same. The final precision of the correction factor C_{dm} depends on the statistics of the control channels $J/\psi \rightarrow \bar{p}n\pi^-$ and $J/\psi \rightarrow \bar{p}n\pi^+$ and the choice of binning (neglecting the statistics in the MC simulations for this control channels). The binning with respect to the angular distribution $\cos\theta_{\bar{n}}$ is fixed to the choice of the binning for the angular analysis of 0.2 by means of $\cos\theta_{\bar{n}}$. The step size of the binning with respect to the recoil momentum $|\vec{p}|$ of $p\pi^-$ ($\bar{p}\pi^+$) is chosen to be 0.1 GeV/c. Figure 8.5 shows the momentum distributions of \bar{n} and n in the control

samples, after applying the final selection criteria (1) to (8_a) for $J/\psi \rightarrow p\bar{n}\pi^-$ and (1) to (7_b) for $J/\psi \rightarrow \bar{p}n\pi^+$, respectively.

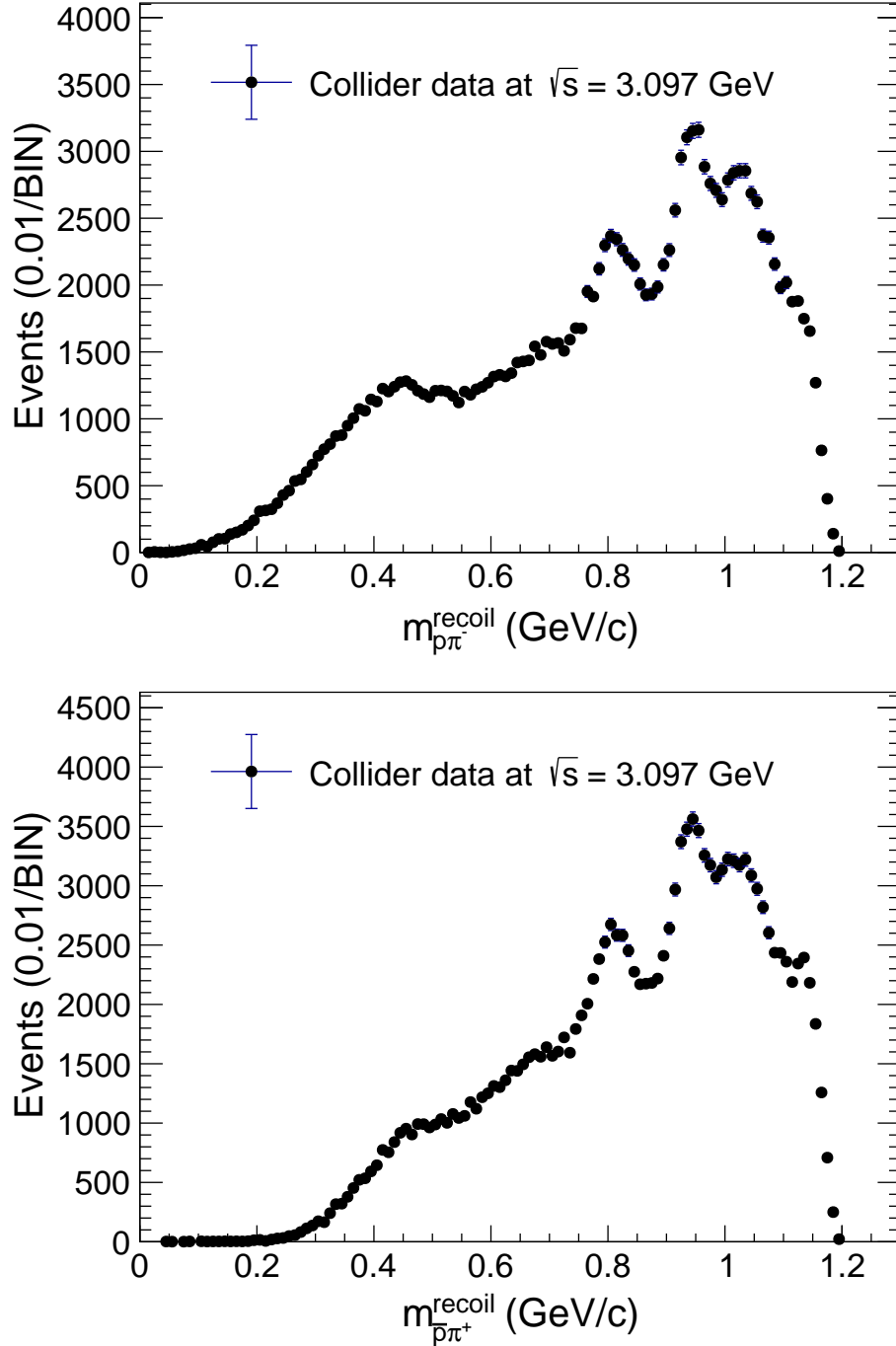


Fig. 8.5: The recoil momenta of (top) $p\pi^-$ and (bottom) $\bar{p}\pi^+$ from collider data after the selection of the process $J/\psi \rightarrow p\bar{n}\pi^-$ ($\bar{p}n\pi^+$) at $\sqrt{s} = 3.097$ GeV and the application of the selection criteria (1) to (8_a) and (1) to (7_b), respectively.

8.2.3 The calculation of C_{dm}

The efficiency difference between data and MC simulation can now be studied by applying the same conditions to the real data and MC simulations control samples as to the signal channel $e^+e^- \rightarrow \bar{n}n$ ($S_0 - S_6$ without S_1 to the $J/\psi \rightarrow p\bar{n}\pi^-$ channel, S_0 and S_7 to the $J/\psi \rightarrow \bar{p}n\pi^+$ channel). The cut efficiencies are defined as following:

$$\epsilon_{\bar{n}} = \frac{N_{\bar{n}}^{9a}}{N_{\bar{n}}^5} \quad \epsilon_n = \frac{N_n^{8b}}{N_n^5} \quad (8.6)$$

with quadratical errors similar to Equation 8.2. Here, the nominator is the number of events passing the selection criteria (1) – (9_a) for the \bar{n} control channel and (1) – (8_b) for the n control channel, respectively. The denominator is the number of events after the criteria (1) – (5) for both channels. The difference between collider data and MC simulation in the selection efficiency can be expressed as their ratio. The cut efficiencies, as well as their differences between collider data and MC simulations are shown with respect to the $p\pi^-$ ($\bar{p}\pi^+$) recoil momentum $|\vec{p}_{p\pi^-}^{\text{recoil}}|$, which corresponds to the particle's momenta $|\vec{p}_{\bar{n}(n)}|$ in the signal channel $e^+e^- \rightarrow \bar{n}n$.

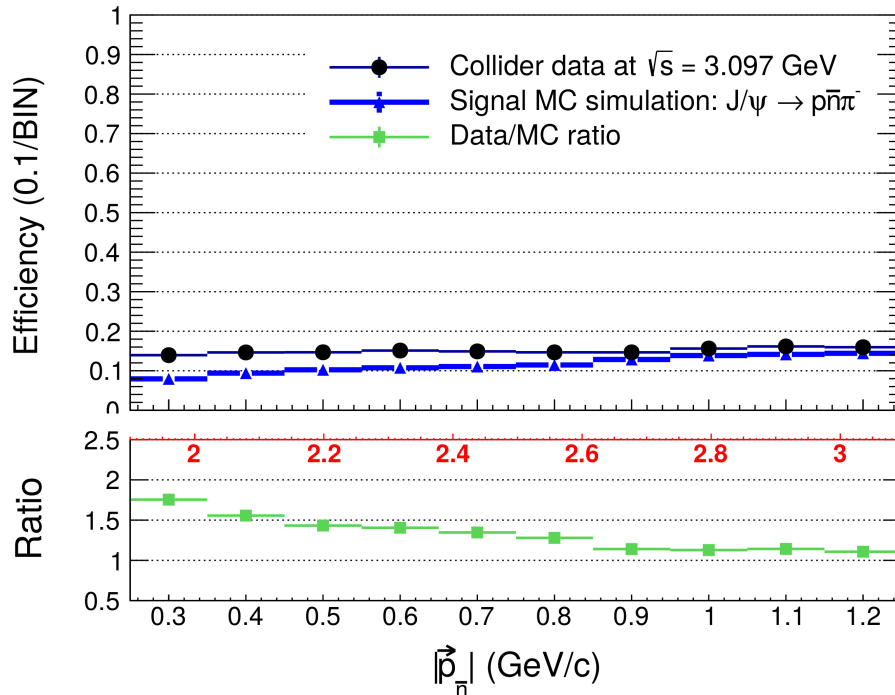


Fig. 8.6: Efficiency of the \bar{n} selection according to Section 5.3.2 from collider data (black dots) and MC simulation for $J/\psi \rightarrow p\bar{n}\pi^-$ (blue dots), both at $\sqrt{s} = 3.097$ GeV, as well as their ratio (green dots) with respect to the recoil momentum of the $p\pi^-$ system. The red scale represents the corresponding \sqrt{s} in the signal channel $e^+e^- \rightarrow \bar{n}n$.

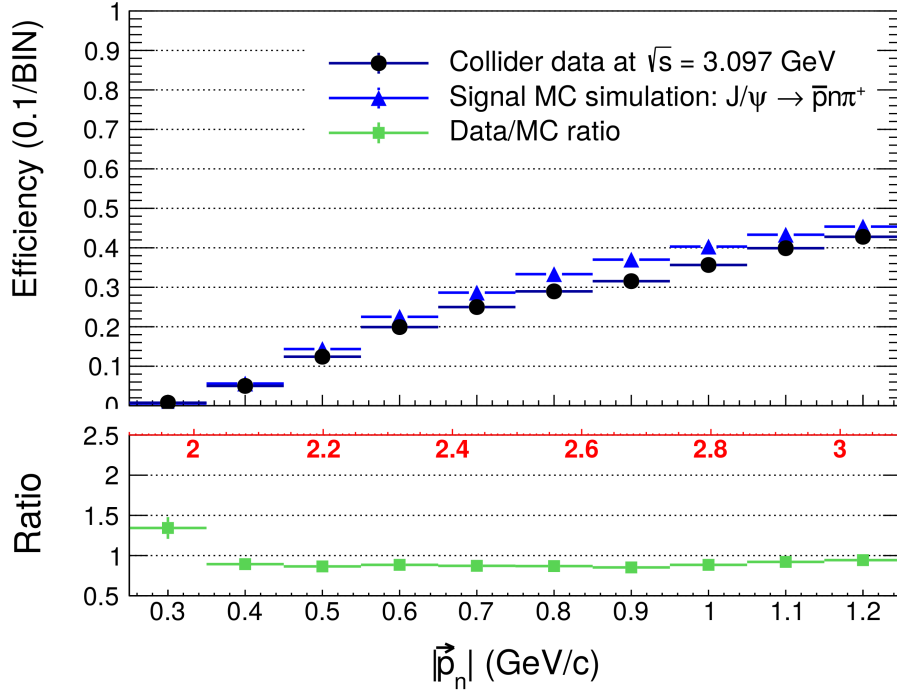


Fig. 8.7: Efficiency of the n selection according to Section 5.3.3 from collider data (black dots) and MC simulation for $J/\psi \rightarrow \bar{p}n\pi^+$ (blue dots), both at $\sqrt{s} = 3.097$ GeV, as well as their ratio (green dots) with respect to the recoil momentum of the $\bar{p}\pi^+$ system. The red scale represents the corresponding \sqrt{s} in the signal channel $e^+e^- \rightarrow \bar{n}n$.

The particle momentum is calculated via:

$$|\vec{p}_{p\pi^-(\bar{p}\pi^+)}^{\text{recoil}}| \equiv |\vec{p}_{\bar{n}(n)}| = \sqrt{\left(\frac{\sqrt{s}}{2}\right)^2 - m_{\bar{n}(n)}^2} \quad (8.7)$$

Results for the cut efficiencies and their ratios are shown in Figure 8.6 and 8.7. For a precise determination of the absolute correction factor for the differences between data and MC simulation according to the signal channel selection criteria $S_1 - S_7$, the correction factor C_{dm} is determined with respect to the signal particle's absolute momentum $|\vec{p}| = p$ (according to Equation 8.7) and their polar distribution in the $\cos\theta_{\bar{n}}$ range. In the following small deviations from a 2-particle back-to-back kinematics coming from ISR contributions and the boost from the crossing angle between the e^+ and e^- beams are neglected. The total correction C_{dm} combines the single correction for the \bar{n} and n selection criteria:

$$C_{dm} = \sum_{p, \cos\theta} \frac{\epsilon_{\bar{n}}^{\text{data}}(p, \cos\theta) \cdot \epsilon_n^{\text{data}}(p, -\cos\theta)}{\epsilon_{\bar{n}}^{\text{MC}}(p, \cos\theta) \cdot \epsilon_n^{\text{MC}}(p, -\cos\theta)} w(p, \cos\theta) = \mathcal{M}(p, \cos\theta) \cdot w(p, \cos\theta)$$

$$C_{\text{dm}}^{\text{abs}} = \sum_{j,k} \mathcal{M}_{j,k} \cdot w_{j,k} \quad \text{and} \quad \Delta C_{\text{dm}}^{\text{abs}} = \sqrt{\sum_{j,k} (\Delta \mathcal{M}_{j,k})^2 \cdot w_{j,k}^2} \quad (8.8)$$

where $\epsilon_{\bar{n}}$ and ϵ_n are the double differential efficiencies of \bar{n} and n obtained from the control samples $J/\psi \rightarrow p\bar{n}\pi^-$ ($J/\psi \rightarrow \bar{p}n\pi^+$) from data and MC simulation, respectively. The normalized frequency $w(p, \cos\theta)$ (i.e. normalized event distribution in the p - $\cos\theta_{\bar{n}}$ -space) from signal MC simulation is retrieved after all selection criteria applied and used to weight the double differential correction matrix $\mathcal{M}_{p,\cos\theta}$. To account for the back-to-back behavior of the signal process, a negative sign of $\cos\theta_{\bar{n}}$ for the n efficiencies is added. The absolute value $C_{\text{dm}}^{\text{abs}}$ is needed for the extraction of the Born cross section and is calculated as the sum of all entries of the product from the correction matrix $\mathcal{M}_{p,\cos\theta}$ and $w_{p,\cos\theta}$. $\Delta \mathcal{M}_{j,k}$ as the individual error in the corresponding bin j,k from the correction matrix $\mathcal{M}_{p,\cos\theta}$. Results for the single components used for the calculation of C_{dm} at $\sqrt{s} = 2.3960$ GeV are shown in Figure 8.8. Results at other \sqrt{s} are presented in the Appendix A.3. Numerical results for $C_{\text{dm}}^{\text{abs}}$ from the main signal MC simulation with Phokhara v9.1, as well as for comparison from the signal MC simulation with ConExc are shown in Table 8.2.

\sqrt{s} (GeV)	C_{dm}				Phokhara	ConExc
	Phokhara	ConExc	\sqrt{s} (GeV)	Phokhara		
2.0000	1.377 ± 0.035	1.375 ± 0.034	2.3864	1.169 ± 0.011	1.167 ± 0.011	
2.0500	1.267 ± 0.021	1.267 ± 0.021	2.3960	1.168 ± 0.011	1.167 ± 0.011	
2.1000	1.251 ± 0.017	1.254 ± 0.017	2.6454	1.006 ± 0.009	1.006 ± 0.009	
2.1266	1.247 ± 0.016	1.247 ± 0.014	2.9000	1.033 ± 0.010	1.032 ± 0.010	
2.1500	1.237 ± 0.014	1.235 ± 0.014	2.9500	1.049 ± 0.010	1.046 ± 0.010	
2.1750	1.235 ± 0.014	1.234 ± 0.014	2.9810	1.050 ± 0.010	1.048 ± 0.010	
2.2000	1.232 ± 0.013	1.231 ± 0.013	3.0000	1.059 ± 0.010	1.056 ± 0.010	
2.2324	1.228 ± 0.013	1.216 ± 0.013	3.0200	1.061 ± 0.011	1.057 ± 0.010	
2.3094	1.227 ± 0.013	1.227 ± 0.013	3.0800	1.062 ± 0.011	1.059 ± 0.008	

Table 8.2: Summary of the efficiency corrections due to differences between data and MC simulation for selection variables $S_1 - S_7$ at different \sqrt{s} for signal MC simulation based on 500000 generated events using Phokhara v9.1, as well as ConExc in BesEvtGen-00-03-18 as a cross check.

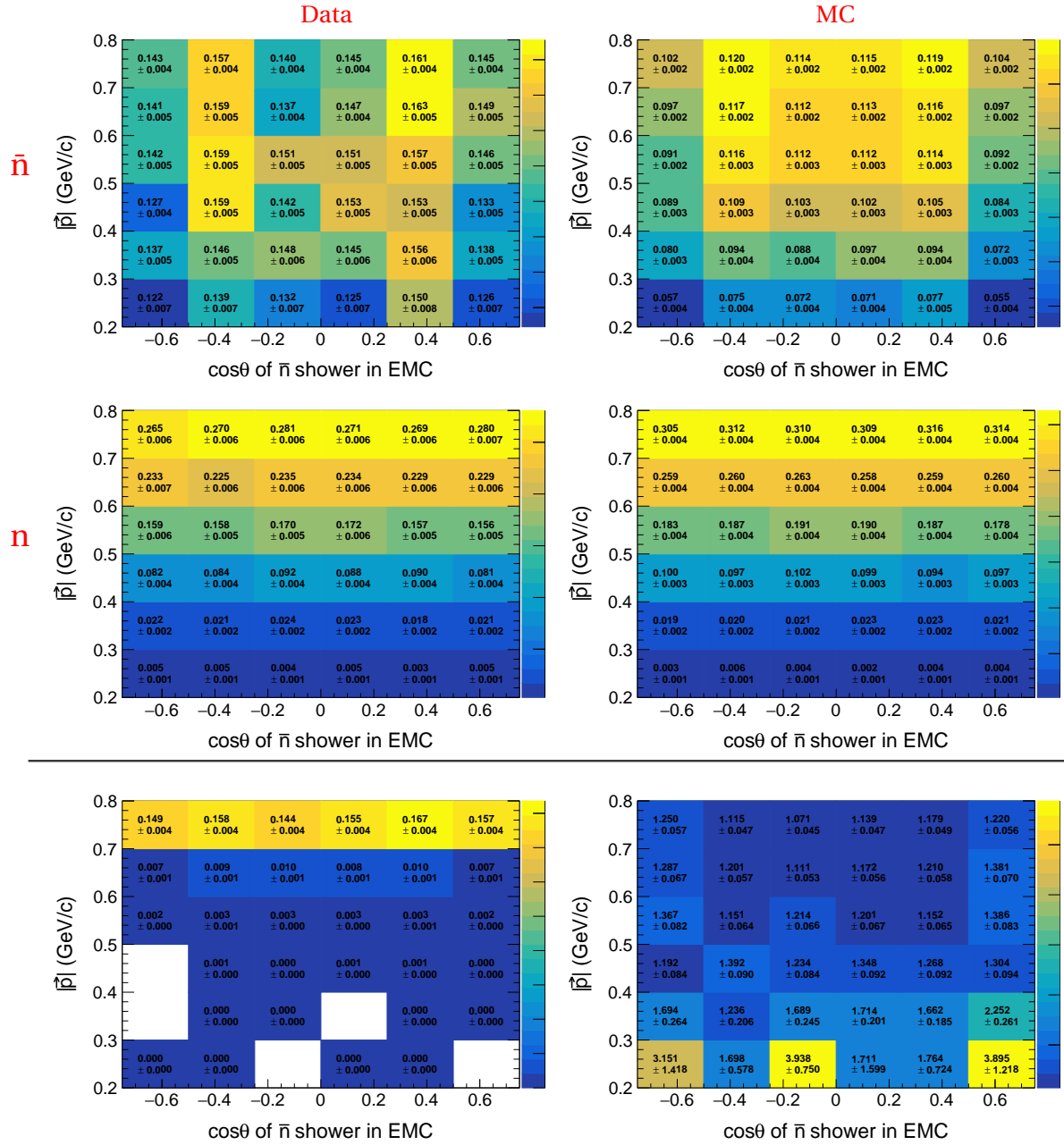


Fig. 8.8: 2-dimensional distributions used for the calculation of C_{dm} at $\sqrt{s} = 2.3960$ GeV. (Upper left) Selection efficiency $\epsilon_{\bar{n}}^{\text{data}}(p, \cos\theta)$, (upper right) selection efficiency $\epsilon_{\bar{n}}^{\text{MC}}(p, \cos\theta)$, (middle left) selection efficiency $\epsilon_n^{\text{data}}(p, \cos\theta)$, (middle right) selection efficiency $\epsilon_n^{\text{MC}}(p, \cos\theta)$. For the former four plots, collider data and MC simulation for $J/\psi \rightarrow p\bar{n}\pi^-$ ($J/\psi \rightarrow \bar{p}n\pi^+$) are used. The momentum range $|\vec{p}|$ is chosen to represent the final state particles momenta at $\sqrt{s} = 2.3960$ GeV. (Lower left) Normalized frequency distribution $w_{p, \cos\theta}$ of signal MC simulation (Phokhara v9.1) for $e^+e^- \rightarrow \bar{n}n$ after all selection criteria $S_1 - S_{10}$ listed in Section 5.3 applied. (Lower right) Correction matrix $\mathcal{M}_{\vec{p}, \cos\theta}$ of efficiencies from data over MC. The value for $C_{\text{dm}}^{\text{abs}}(2.3960 \text{ GeV}) = 1.168 \pm 0.011$ shown in Table 8.2 is calculated by multiplying the lower 2D histograms and summing up over all bins.

A differential correction factor with respect to the polar angle range $\frac{dC_{dm}}{d\cos\theta}$, similar to the differential signal efficiency in Equation 8.3, is needed for the angular analysis in Section 9.2. Therefore, a similar approach is used as in Equation 8.2.3, summing over only the absolute momentum p bins and evaluating the correction for each $\cos\theta_{\bar{n}}$ bin. As an example, the differential corrections $\frac{dC_{dm}}{d\cos\theta}$ at $\sqrt{s} = 2.1266$ GeV and $\sqrt{s} = 2.3960$ GeV are shown together with the differential signal efficiencies $\frac{d\epsilon^{MC}}{d\cos\theta}$ at the same \sqrt{s} in Figure 8.9.

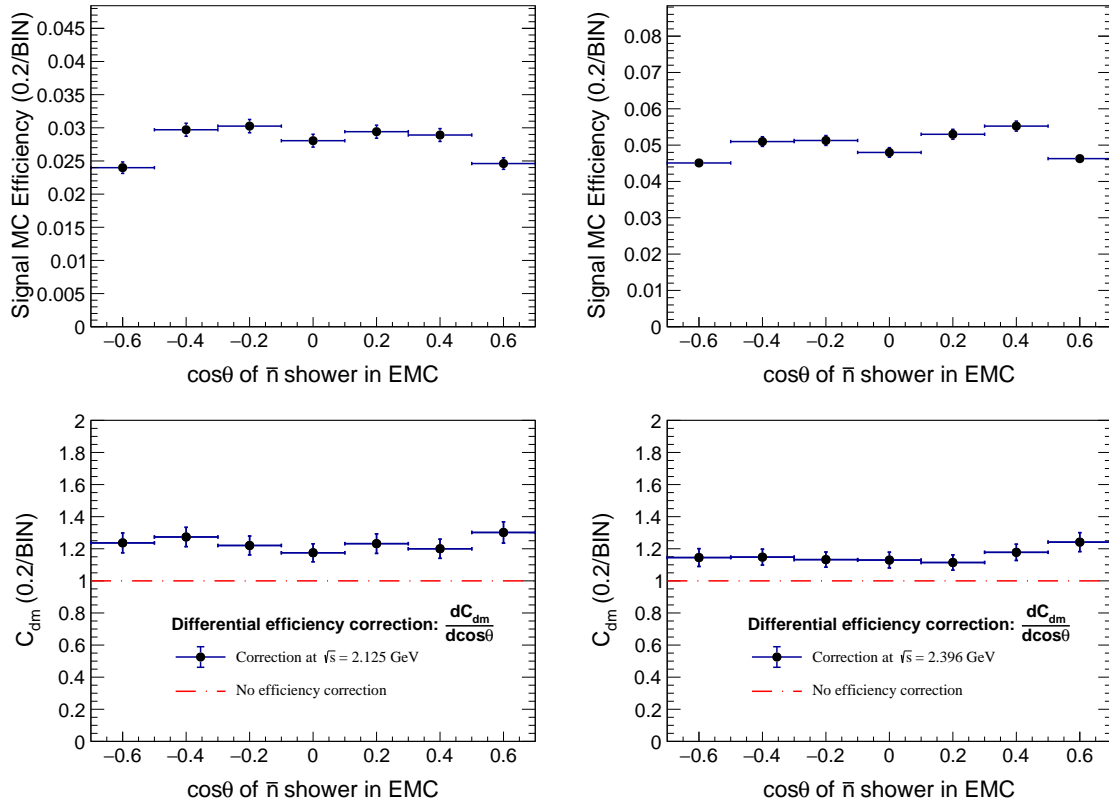


Fig. 8.9: (Top) Differential signal efficiencies $\frac{d\epsilon^{MC}}{d\cos\theta}$ from signal MC simulation with Phokhara 9.1. (Bottom) Differential corrections due to efficiency differences between data and MC simulation $\frac{dC_{dm}}{d\cos\theta}$ with weighting $w_{p,\cos\theta}$ from signal MC simulation with Phokhara v9.1. (Left) at $\sqrt{s} = 2.1266$ GeV, (right) at $\sqrt{s} = 2.3960$ GeV. The red dotted-dashed lines in the lower plots indicate a differential correction of 1 (equal to no correction) as a comparison.

Differential signal efficiencies $\frac{d\epsilon^{MC}}{d\cos\theta}$ and corrections due to efficiency differences between data and MC $\frac{dC_{dm}}{d\cos\theta}$ for other \sqrt{s} are shown in the appendix in Figures A.24 and A.22. Distributions derived from the cross check signal MC simulation with ConExc are shown in the appendix in Figure A.23 and A.25, respectively.

8.3 Efficiency correction due to the selection criterion S_8

The selection criterion S_8 (E_{extra}) in Section 5.3 must be studied for efficiency differences between signal MC simulation and data, similar to the criteria discussed in the previous section. In contrast to the criteria $S_1 - S_7$, the efficiency correction C_{ee} for the selection criterion E_{extra} cannot be studied from the control samples introduced in Section 8.2. The additional deposited energy in the event is not correlated with the \bar{n} and n final state particles in $e^+e^- \rightarrow \bar{n}n$ and is considered as an event level criterion. The approach, chosen to determine this efficiency correction, uses the hypothesis that events such as $e^+e^- \rightarrow \bar{p}p$ behave in a similar way in the EMC, as the analyzed signal channel $e^+e^- \rightarrow \bar{n}n$. This is legit, since both, protons and neutrons and their anti-particles, are hadrons with almost the same mass and undergo a similar hadronic interaction in the EMC. The approach chosen in this analysis is divided into three steps: first, the stability of the selection requirement of E_{extra} is studied systematically with respect to the Born cross section in Section 8.3.1. In a second step, the efficiency correction C_{ee}^{data} is calculated by using the results from the analysis of the process $e^+e^- \rightarrow \bar{p}p$ in the collider data and the signal MC simulation for $e^+e^- \rightarrow \bar{n}n$ in Section 8.3.2. The discussed study until this point has been mainly performed by Samer Ahmed (PhD thesis in preparation). In the final step, a fit to the extracted correction values $C_{ee}^{\text{data}}(s)$ at different \sqrt{s} is applied and the final correction $C_{ee}^{\text{fit}}(s)$ is derived at all \sqrt{s} from the fit parameters (as discussed in Section 8.3.3). The last step is required, since the data-driven method for the extraction of $C_{ee}^{\text{data}}(s)$ suffers from low statistics at the majority of all analyzed \sqrt{s} after the $e^+e^- \rightarrow \bar{p}p$ selection. Therefore, the extracted values for this correction factor become very large and the method is not suitable for a precise determination of the Born cross section for the signal.

8.3.1 Stability plateau for the cut determination

The first step to determine the efficiency correction due to the cut value for the selection criterion E_{extra} is a study of stability of the Born cross section, derived under the variation of the cut value for the E_{extra} criterion. The Born cross section is calculated under a systematical variation of the cut value on this criterion. All selection criteria introduced in Section 5.3 are fixed, while the value of the cut on E_{extra} is varied from $E_{\text{extra}} = 0 - 0.2$ GeV. The variation is performed in 0.01 GeV steps as a function of E_{extra} cut value. Figure 8.10 shows the extracted Born cross section values as a function of E_{extra} . A stable plateau is identified between $E_{\text{extra}} = \{0.1, 0.2\}$ GeV. The final value is chosen to be $E_{\text{extra}} < 0.15$ GeV. This value has been introduced already in the discussion of the selection criteria in Section 5.3.

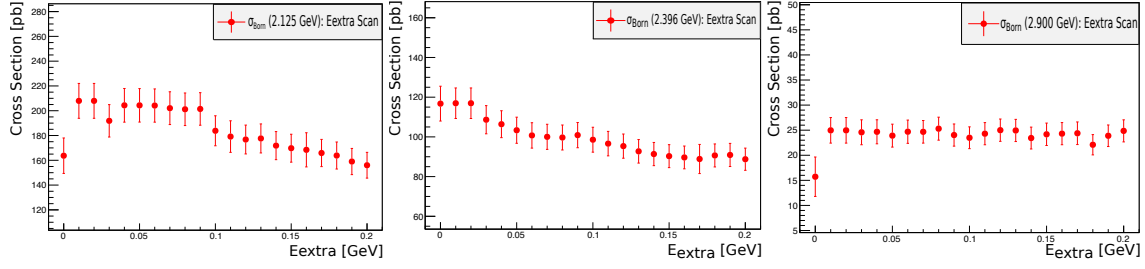


Fig. 8.10: Born cross section for $e^+e^- \rightarrow \bar{n}n$ under variation of the cut value for the selection criterion E_{extra} . The variation is performed in 0.01 GeV steps. An approximately stable plateau (within uncertainties), independent from \sqrt{s} , is identified between 0.1 – 0.2 GeV. The final cut value is set to $E_{\text{extra}} < 0.15$ GeV. (Left) at $\sqrt{s} = 2.1266$ GeV, (middle) at $\sqrt{s} = 2.3960$ GeV, (right) at $\sqrt{s} = 2.9000$ GeV. The figures have been provided by Samer Ahmed (PhD thesis in preparation).

8.3.2 The extraction of C_{ee}^{data} from the collider data using $e^+e^- \rightarrow \bar{p}p$

To study the cut efficiency difference of the E_{extra} signal selection criterion between $e^+e^- \rightarrow \bar{p}p$ data and $e^+e^- \rightarrow \bar{n}n$ signal MC simulation for the signal efficiency correction C_{ee} , the analysis method developed in [102] is used. The process $e^+e^- \rightarrow \bar{p}p$ is selected from the same data set, as analyzed for the signal process study of $e^+e^- \rightarrow \bar{n}n$. The only difference to the $e^+e^- \rightarrow \bar{p}p$ signal selection in [102] is a replacement of the $E_p/|\vec{p}|$ criterion by the requirement of $|\cos\theta_p| < 0.8$. This excludes any EMC based criteria and therefore possible biases on the determination of E_{extra} . The signal selection variable E_{extra} is selected in the $e^+e^- \rightarrow \bar{p}p$ final state in the same way as shown in Section 5.3.4 for the signal selection and compared to the distribution from $e^+e^- \rightarrow \bar{n}n$. The correction factor C_{ee} is defined as the cut efficiency $\epsilon_{ee}^{\bar{p}p}(\text{data})$ from the selected $e^+e^- \rightarrow \bar{p}p$ collider data divided by the cut efficiency $\epsilon_{ee}^{\bar{n}n}(\text{MC})$ obtained from the $e^+e^- \rightarrow \bar{n}n$ signal MC simulation:

$$C_{ee}^{\text{data}} = \frac{\epsilon_{ee}^{\bar{p}p}(\text{data})}{\epsilon_{ee}^{\bar{n}n}(\text{MC})} \quad \Delta C_{ee}^{\text{data}} = \sqrt{\left(\frac{\Delta\epsilon_{ee}^{\bar{p}p}(\text{data})}{\epsilon_{ee}^{\bar{n}n}(\text{MC})}\right)^2 + \left(\frac{\epsilon_{ee}^{\bar{p}p}(\text{data}) \cdot \Delta\epsilon_{ee}^{\bar{n}n}(\text{MC})}{(\epsilon_{ee}^{\bar{n}n}(\text{MC}))^2}\right)^2} \quad (8.9)$$

$$\epsilon_{ee} = \frac{N_{\text{after cut}}}{N_{\text{before cut}}} \quad \Delta\epsilon_{ee} = \sqrt{\left(\frac{\Delta N_{\text{after cut}}}{N_{\text{before cut}}}\right)^2 + \left(\frac{N_{\text{after cut}} \cdot \Delta N_{\text{before cut}}}{N_{\text{before cut}}^2}\right)^2}$$

A comparison of the E_{extra} distribution between selected $e^+e^- \rightarrow \bar{p}p$ events in data and in $e^+e^- \rightarrow \bar{n}n$ signal MC simulation at $\sqrt{s} = 2.3960$ GeV is shown in Figure 8.11. The values for C_{ee}^{data} , derived as described above, are listed in Table 8.3.

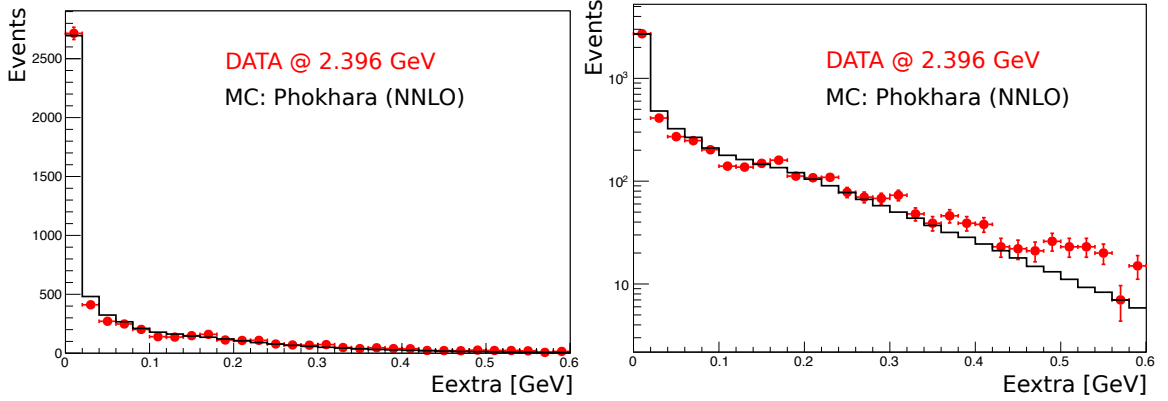


Fig. 8.11: Comparison of the E_{extra} distribution at $\sqrt{s} = 2.396$ GeV between $e^+e^- \rightarrow \bar{p}p$ data and $e^+e^- \rightarrow \bar{n}n$ signal MC simulation. (Left) linear scale, (right) logarithmic scale. The normalization of the signal MC simulation is chosen to be the same as in $e^+e^- \rightarrow \bar{p}p$ data. Red dots represent the $e^+e^- \rightarrow \bar{p}p$ data, while the black histogram is the $e^+e^- \rightarrow \bar{n}n$ signal MC simulation. The figures have been provided by Samer Ahmed.

\sqrt{s} (GeV)	Phokhara	ConExc	$\mathcal{C}_{ee}^{\text{data}}$ \sqrt{s} (GeV)	Phokhara	ConExc
2.0000	0.738 ± 0.024	0.740 ± 0.022	2.3864	0.883 ± 0.063	0.883 ± 0.063
2.0500	0.792 ± 0.039	0.796 ± 0.039	2.3960	0.883 ± 0.036	0.881 ± 0.036
2.1000	0.768 ± 0.022	0.766 ± 0.022	2.6454	0.904 ± 0.070	0.898 ± 0.070
2.1266	0.799 ± 0.011	0.796 ± 0.011	2.9000	0.873 ± 0.093	0.869 ± 0.092
2.1500	not extracted		2.9500	0.876 ± 0.262	0.873 ± 0.261
2.1750	0.857 ± 0.033	0.850 ± 0.033	2.9810	not extracted	
2.2000	0.881 ± 0.034	0.875 ± 0.034	3.0000	0.890 ± 0.309	0.887 ± 0.308
2.2324	0.916 ± 0.043	0.919 ± 0.063	3.0200	0.981 ± 0.303	0.982 ± 0.303
2.3094	0.902 ± 0.052	0.906 ± 0.053	3.0800	0.945 ± 0.113	0.940 ± 0.112

Table 8.3: Summary of the efficiency corrections $\mathcal{C}_{ee}^{\text{data}}$ derived by the data-driven method at different \sqrt{s} using Phokhara v9.1 and ConExc as a cross check.

The results for the $\mathcal{C}_{ee}^{\text{data}}$ correction shown in Table 8.3 fluctuate strongly because of the low statistics after the $e^+e^- \rightarrow \bar{p}p$ selection, introducing additionally a larger uncertainty. To provide more precise correction values, a fit to the correction is performed in the next section.

8.3.2 The fit to the $\mathcal{C}_{ee}^{\text{data}}$ values for the extraction of \mathcal{C}_{ee}

The error on this correction is strongly correlated with the statistics of the selected $e^+e^- \rightarrow \bar{p}p$ events from data. Since the corresponding number of events in data is small at several

\sqrt{s} , the error on this correction grows very large. A modified approach is chosen for the calculation of the values and their errors, as described in the following. Under the hypothesis that this correction is based on a systematical difference between the data and MC simulation, it is considered to follow a smooth and differentiable function. Taking this argument into account, the values listed in Table 8.3 are fitted by the arbitrary function:

$$f_{C_{ee}}(s) = p_1 + p_2 \times \text{Erf}\left[\frac{(\sqrt{s} - p_3)}{p_4}\right] + \sqrt{s} \times p_5 \quad (8.10)$$

The fit is shown in Figure 8.12. The final values with errors for C_{ee} are taken from the fit at the corresponding \sqrt{s} . The correction factor C_{ee} at all \sqrt{s} is listed in Table 8.4.

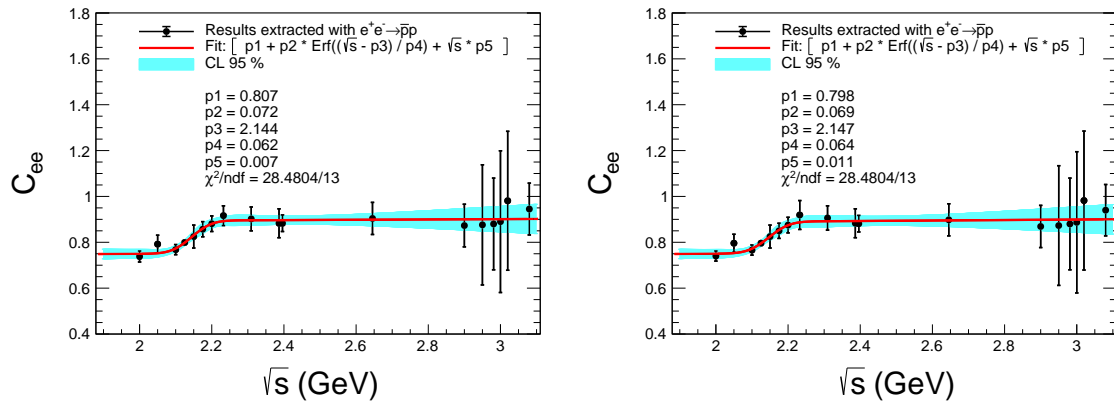


Fig. 8.12: Fit of the function from Equation 8.10 to the results of C_{ee}^{data} extracted from the $e^+e^- \rightarrow \bar{p}p$ collider data and $e^+e^- \rightarrow \bar{n}n$ signal MC simulation (black dots with errors). (Left) with Phokhara v9.1, (right) with ConExc. The red line is the fit using the parameters as shown in the figures. The light blue band is the error from fit at 95% confidence level.

\sqrt{s} (GeV)	C_{ee}		\sqrt{s} (GeV)	C_{ee}	
	Phokhara	ConExc		Phokhara	ConExc
2.0000	0.750 ± 0.019	0.750 ± 0.018	2.3864	0.897 ± 0.019	0.893 ± 0.021
2.0500	0.752 ± 0.016	0.753 ± 0.015	2.3960	0.897 ± 0.018	0.893 ± 0.021
2.1000	0.773 ± 0.011	0.772 ± 0.011	2.6454	0.898 ± 0.027	0.895 ± 0.027
2.1266	0.798 ± 0.009	0.795 ± 0.009	2.9000	0.900 ± 0.046	0.898 ± 0.047
2.1500	0.830 ± 0.014	0.825 ± 0.014	2.9500	0.901 ± 0.051	0.899 ± 0.052
2.1750	0.860 ± 0.019	0.854 ± 0.020	2.9810	0.901 ± 0.053	0.899 ± 0.054
2.2000	0.881 ± 0.019	0.874 ± 0.019	3.0000	0.901 ± 0.055	0.899 ± 0.056
2.2324	0.892 ± 0.019	0.887 ± 0.021	3.0200	0.901 ± 0.057	0.899 ± 0.058
2.3094	0.896 ± 0.021	0.892 ± 0.024	3.0800	0.902 ± 0.062	0.900 ± 0.063

Table 8.4: Summary of the efficiency corrections C_{ee} derived from the fit at different \sqrt{s} for signal MC simulation using Phokhara v9.1 and ConExc in as a cross check.

8.4 Efficiency correction due to the selection criterion S_9

The efficiency correction C_{muc} required due to the selection criterion S_9 (l_{muc}) is studied with a similar method as presented in Section 8.2 for the correction C_{dm} . Because of the event level characteristic of this cut (the largest layer with hits in the moun system can have a signal due to the interaction of the \bar{n} or n with the MUC), correlations between the impact of both final state particles need to be taken into account. Unfortunately, it is not possible to extract this correlation from the two individual samples \bar{n} or n from $J/\psi \rightarrow p\bar{n}\pi^-$ ($J/\psi \rightarrow \bar{p}n\pi^+$). This issue is negligible due to the fact, that the individual corrections from $J/\psi \rightarrow p\bar{n}\pi^-$ ($J/\psi \rightarrow \bar{p}n\pi^+$) are small and therefore negligible, as shown in the following study. Also the very loose cut requirement on the signal process $e^+e^- \rightarrow \bar{n}n$ of $l_{\text{muc}} < 6$ guarantees that no underestimated systematic uncertainty due to this requirement is introduced. The total correction C_{muc} is evaluated as the product of the individual corrections $C_{\text{muc}, \bar{n}}$ and $C_{\text{muc}, n}$. To derive the individual distributions, the cut efficiencies are calculated as follows:

$$\epsilon_{\bar{n}(n)}^{\text{MC}} = \frac{N_{\bar{n}(n), \text{ after cut}}^{\text{MC}}}{N_{\bar{n}(n), \text{ before cut}}^{\text{MC}}} \quad \text{and} \quad \epsilon_{\bar{n}(n)}^{\text{data}} = \frac{N_{\bar{n}(n), \text{ after cut}}^{\text{data}}}{N_{\bar{n}(n), \text{ before cut}}^{\text{data}}} \quad (8.11)$$

with $N_{\bar{n}(n), \text{ before cut}}^{\text{data(MC)}}$ the number of events before applying the cut S_9 in Section 5.3.4 and $N_{\bar{n}(n), \text{ after cut}}^{\text{data(MC)}}$ the number of events after applying this cut. The efficiency corrections $C_{\text{muc}, \bar{n}}^{\text{abs}}$ and $C_{\text{muc}, n}^{\text{abs}}$ for the Born cross section calculation are defined as fractions of $\epsilon_{\bar{n}(n)}^{\text{Data}}$ over $\epsilon_{\bar{n}(n)}^{\text{MC}}$. The final correction factor C_{muc} is calculated as:

$$C_{\text{muc}} = C_{\text{muc}, \bar{n}}^{\text{abs}} \cdot C_{\text{muc}, n}^{\text{abs}} = \frac{\epsilon_{\bar{n}}^{\text{data}} \cdot \epsilon_n^{\text{data}}}{\epsilon_{\bar{n}}^{\text{MC}} \cdot \epsilon_n^{\text{MC}}} \quad (8.12)$$

The correction factor C_{muc} is determined at all \sqrt{s} and listed in Table 8.5. The correction is calculated by using the main signal MC simulation generator Phokhara v9.1 and by using the signal MC simulation generator ConExc as a cross check. This signal selection efficiency correction is very small and therefore negligible and consequently not applied neither in the calculation of the Born cross section nor in the angular analysis in Section 9.3. Instead, it is included as a systematic uncertainty on the signal selection in Chapter 10.

\sqrt{s} (GeV)	C_{muc}		\sqrt{s} (GeV)	C_{muc}	
	Phokhara	ConExc		Phokhara	ConExc
2.0000	1.004 ± 0.026	1.004 ± 0.024	2.3864	1.008 ± 0.010	1.008 ± 0.009
2.0500	1.003 ± 0.017	1.003 ± 0.016	2.3960	1.008 ± 0.009	1.007 ± 0.009
2.1000	1.003 ± 0.013	1.003 ± 0.013	2.6454	1.007 ± 0.009	1.007 ± 0.009
2.1266	1.004 ± 0.012	1.004 ± 0.012	2.9000	1.000 ± 0.009	1.000 ± 0.009
2.1500	1.006 ± 0.012	1.006 ± 0.012	2.9500	0.998 ± 0.010	0.998 ± 0.010
2.1750	1.007 ± 0.011	1.007 ± 0.011	2.9810	0.998 ± 0.010	0.998 ± 0.010
2.2000	1.007 ± 0.011	1.007 ± 0.011	3.0000	1.011 ± 0.010	1.011 ± 0.010
2.2324	1.006 ± 0.011	1.006 ± 0.010	3.0200	1.011 ± 0.010	1.011 ± 0.010
2.3094	1.006 ± 0.010	1.006 ± 0.010	3.0800	1.012 ± 0.010	1.012 ± 0.007

Table 8.5: Summary of the efficiency corrections due to differences between data and MC simulation for the selection variable S_9 at different \sqrt{s} for signal MC simulation based on 500000 generated events using Phokhara v9.1, as well as ConExc in BesEvtGen-00-03-18 as a cross check.

The differential correction factor $\frac{dC_{\text{muc}}}{d\cos\theta}$ at $\sqrt{s} = 2.1266$ and $\sqrt{s} = 2.3960$ GeV is shown in Figure 8.13. The differential corrections at all other \sqrt{s} , as well as the cross-check derived with ConExc signal MC simulation, are shown in the appendix in Figure A.26 and A.27, respectively.

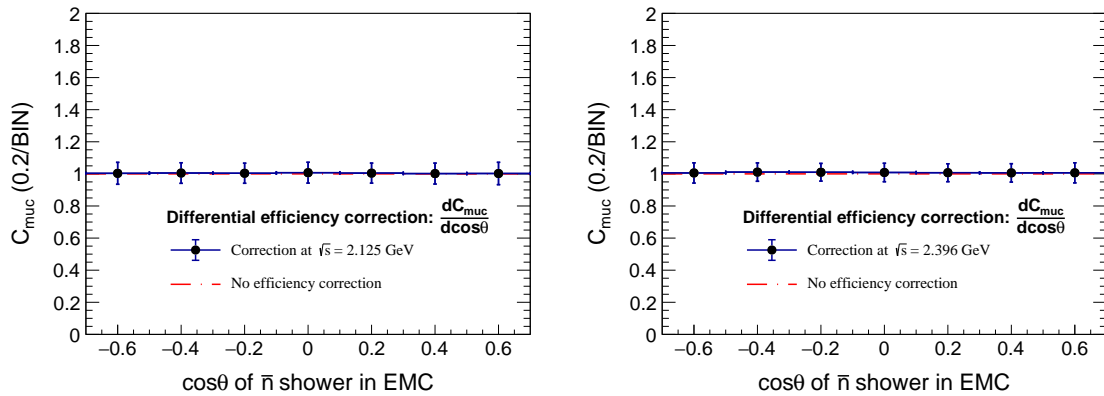


Fig. 8.13: The differential correction factor $\frac{dC_{\text{muc}}}{d\cos\theta}$ from signal MC simulation with Phokhara v9.1 at $\sqrt{s} = 2.1266$ and $\sqrt{s} = 2.3960$ GeV. The red dotted-dashed lines indicate a differential correction of 1 (equal to no correction) as a comparison.

8.5 The efficiency correction C_{trg} due to the BESIII trigger

The correction factor C_{trg} takes the signal efficiency loss due to the imperfect BESIII trigger system into account. Since the signal process $e^+e^- \rightarrow \bar{n}n$ contains only neutral final state particles, only the trigger channels 9 and 12 are used, as shown in Figure 8.14. The efficiency of the EMC sub-trigger on the signal process is studied carefully in the following.

			CH01 CHARGE	CH02 CHARGE	CH03	CH04 CHARGE	CH05 CHARGE	CH06 CHARGE	CH07	CH08	CH09 NEU	CH10 random	CH11	CH12 Delayed NEU	CH13	CH14	CH15	CH16
EMC	Etot_L	09	Y	Y	N	Y	Y	Y	N	N	Y	Y	N	Y	N	N	N	N
	NBclus.GE.1	12		Y				Y							Y			
	NEclus.GE.1	13	Y															
	ECLUS_BB	3																Y
TOF	BTOF_BB	17				Y										Y		
	NETOF.GE.2	18																
	NETOF.GE.1	19	Y															
	NBTOF.GE.2	20		Y	Y								Y					
	NBTOF.GE.1	21					Y	Y										
	NTOF.GE.1	22													Y			
MDC	LTrk_BB	42				Y							Y					
	STrk_BB	38	Y															
	NLTrk.GE.N	43																
	NLTrk.GE.2	44		Y	Y			Y										
	NLTrk.GE.1	45					Y											
EMC	NClus.GE.1	48									Y							Y
	NClus.GE.2	49												Y				
	BEtot_H	55									Y							
	EEtot_H	56																
	Etot_M	58												Y				

Fig. 8.14: Open trigger channels (marked with "Y" in the third row) at the time of the data collection for the scan data sets quoted from [27] and [198]. The signal process $e^+e^- \rightarrow \bar{n}n$, as a pure neutral final state, can only be triggered by channel 9 or 12, marked in red.

Table 8.14 shows that only the energy deposition (BEtot_h in channel 9 and Etot_M in channel 12) of the signal process is relevant for the trigger efficiency. The requirement for the amount of clusters is always fulfilled because of the signal selection criterion S_2 , since the number of clusters in the EMC is always larger than the number of showers, as explained in Chapter 3. The trigger efficiency is determined in three steps:

1. First, the trigger response function, based on the energy deposition in the EMC, is studied with a data-driven method in Section 8.5.1.
2. In Section 8.5.2, the signal MC simulation is modified to take into account the imperfect description of the hadronic showers in the EMC.
3. In the last step, the trigger efficiency correction factor is determined as an absolute value for the determination of the Born cross section, as well as with respect to the angular distribution of the signal final state in the EMC, later to be applied as a correction for the angular analysis. The results are presented in Section 8.5.3.

8.5.1 The energy deposition related trigger response function

In this study, the trigger response function $f(E_{\text{total}}^i)$ based on the analysis in [233] is used:

$$f(E_{\text{total}}^i) = 0.5 + 0.5 \cdot \text{Erf}\left(\frac{E_{\text{total}} - a}{b}\right) \quad (8.13)$$

whith $\text{Erf}(x)$ as an error function, E_{total} the total energy deposition in a single event and a and b free parameters. To obtain these parameters from data, three control samples are studied, the final state $e^+e^- \rightarrow \bar{p}p$, $J/\psi \rightarrow \bar{p}p$ and the final states array $e^+e^- \rightarrow$ hadronic inclusive as a cross check. The event selection for the $\bar{p}p$ final state is listed as following:

- Two valid charged tracks are reconstructed in the MDC. To fulfill the validation criterion, the charged tracks are required to be within the MDC angular coverage of $|\cos\theta| < 0.93$, within maximum 1 cm in the plane perpendicular to the beam and within maximum ± 10 cm in the beam axis direction with respect to the interaction point (IP).
- The BESIII Particle Identification (PID) with the combined information from the dE/dx and TOF measurement calculates the probability of the track under the pion, kaon or proton hypothesis. The highest probability is assigned to each of the two tracks. Events must have a proton and an antiproton particle hypothesis assigned to the two tracks.
- To suppress Bhabha background events, a the polar angle of each track is limited to $|\cos\theta| < 0.8$.
- To suppress multi-hadronic events, the requirement $\theta_{\bar{p}p}^{\text{cm}} > 179^\circ$ is applied on the opening angle between the two tracks in the center-of-mass system.
- A condition on the momentum of both final state particles is applied, covering five times the momentum resolution $|p_{\text{mea}} - p_{\text{exp}}| < 5\sigma_{\bar{p},p}$, with p_{mea} and p_{exp} the measured and expected momentum of proton and antiproton, respectively, both in the center-of-mass system. $\sigma_{\bar{p}p}$ is the corresponding resolution.

With this selection, the final state $e^+e^- (J/\psi) \rightarrow \bar{p}p$ is free of background. Figure 8.15 shows the survived signal events with respect to the momentum of the proton at $\sqrt{s} = 2.1266, 2.3960, 2.6444, \text{ and } 3.0970$ GeV.

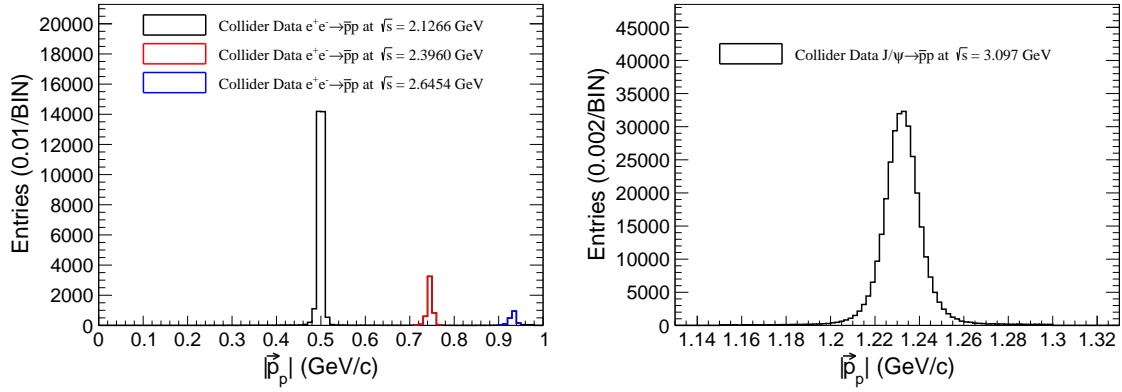


Fig. 8.15: Survived events from the process $e^+e^- \rightarrow \bar{p}p$ after the above introduced selection with respect to the proton momentum $p_p = |\vec{p}|_p$ (left) at three energies of the scan data $\sqrt{s} = 2.1266, 2.3960, 2.6444$ GeV and (right) from the J/ψ data set collected in 2012.

To study the trigger efficiency dependence on the total energy deposition in the EMC, including all showers (with and without the EMC shower quality requirements introduced in Section 5.3.1), the following requirements are applied:

$$\epsilon_{\text{trg}(9)} = \frac{N_{\text{trigger}[3]=\text{valid} \ \&\& \ \#\text{showers} \geq 2 \ \&\& \ \text{trigger}[9]=\text{valid}}}{N_{\text{trigger}[3]=\text{valid} \ \&\& \ \#\text{showers} \geq 2}}$$

$$\epsilon_{\text{trg}(12)} = \frac{N_{\text{trigger}[3]=\text{valid} \ \&\& \ \#\text{B_showers} \geq 1 \ \&\& \ \text{trigger}[12]=\text{valid}}}{N_{\text{trigger}[3]=\text{valid} \ \&\& \ \#\text{B_showers} \geq 1}}$$

$$\epsilon_{\text{trg}(9 \text{ and } 12)} = \frac{N_{(\text{trigger}[3]=\text{valid} \ \&\& \ \#\text{showers} \geq 2) \ \&\& \ (\text{trigger}[9]=\text{valid} \ || \ \text{trigger}[12]=\text{valid})}}{N_{\text{trigger}[3]=\text{valid} \ \&\& \ \#\text{showers} \geq 2}} \quad (8.14)$$

The condition on the trigger channel 3 to be valid $\text{trigger}[3] = \text{valid}$ is required to avoid biases for events, only triggered either by channel 9 or 12. Figure 8.16 shows the dependency of the trigger efficiency on the total energy deposition in the EMC for the processes $e^+e^- \rightarrow \bar{p}p$ and $J/\psi \rightarrow \bar{p}p$, therefore the EMC subtrigger efficiency is necessary to be studied for the $e^+e^- \rightarrow \bar{n}n$ signal process. Differences between the two studied samples are observed. While the knee-point in the $J/\psi \rightarrow \bar{p}p$ process is consistent to the results in the publication [234], it is at higher energies in the scan data set. The efficiency curves below 0.4 GeV are neglected (chosen conservatively lower as the signal process energy requirement), since they are not necessary for the signal process due to the $E_{\bar{n}} > 0.5$ GeV requirement.

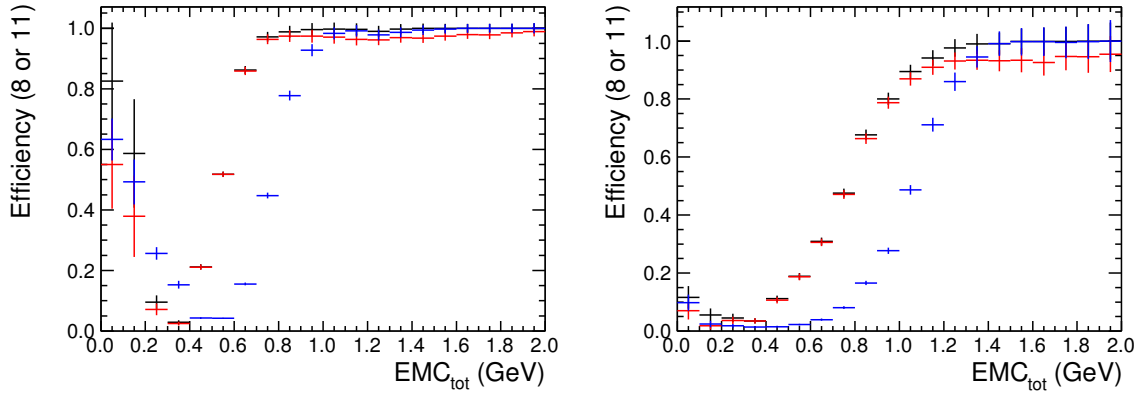


Fig. 8.16: Trigger efficiency with respect to the total energy deposition in the EMC from the control samples (left) $e^+e^- \rightarrow \bar{p}p$ in the scan data set collected in 2015 and (right) from $J/\psi \rightarrow \bar{p}p$ in data collected in 2012 at $\sqrt{s} = 3.0970$ GeV. The total energy deposition in the EMC EMC_{tot} includes good and bad showers (with and without quality criteria). Black dots show the trigger efficiency with both channels 9 and 12 $\epsilon_{trg}(9$ and 12), blue dots with $\epsilon_{trg}(9)$ and red dots with channel $\epsilon_{trg}(12)$. The plots are provided by Xiaorong Zhou.

The selection criteria for the cross check final states array $e^+e^- \rightarrow \bar{q}q \rightarrow \text{hadrons}$ are listed below:

- The number of valid charged tracks in the MDC is required to be larger than 2. The validation criteria are: the charged tracks are required to be within the MDC angular coverage of $|\cos\theta| < 0.93$, within maximum 1 cm in the plane perpendicular to the beam and within maximum ± 10 cm in the beam axis direction with respect to the interaction point (IP).
- The Particle Identification is applied to each track with the requirement of at least one proton, pion or kaon to be identified in each event, using the combined information from the dE/dx and TOF measurement calculates the probability of the track under the pion, kaon or proton hypothesis.
- the trigger channel 5 is pre-required to avoid biases in events triggered either by channel 9 or 12.

The hadronic inclusive final states are studied from the collider data collected at $\sqrt{s} = 3.0970$ GeV in 2009 and 2012, as well as for scan data sets, collected in 2012 and 2014/15 (latter is the data set used for the analysis of the signal final state $e^+e^- \rightarrow \bar{n}n$). The results are shown in Figure 8.17.

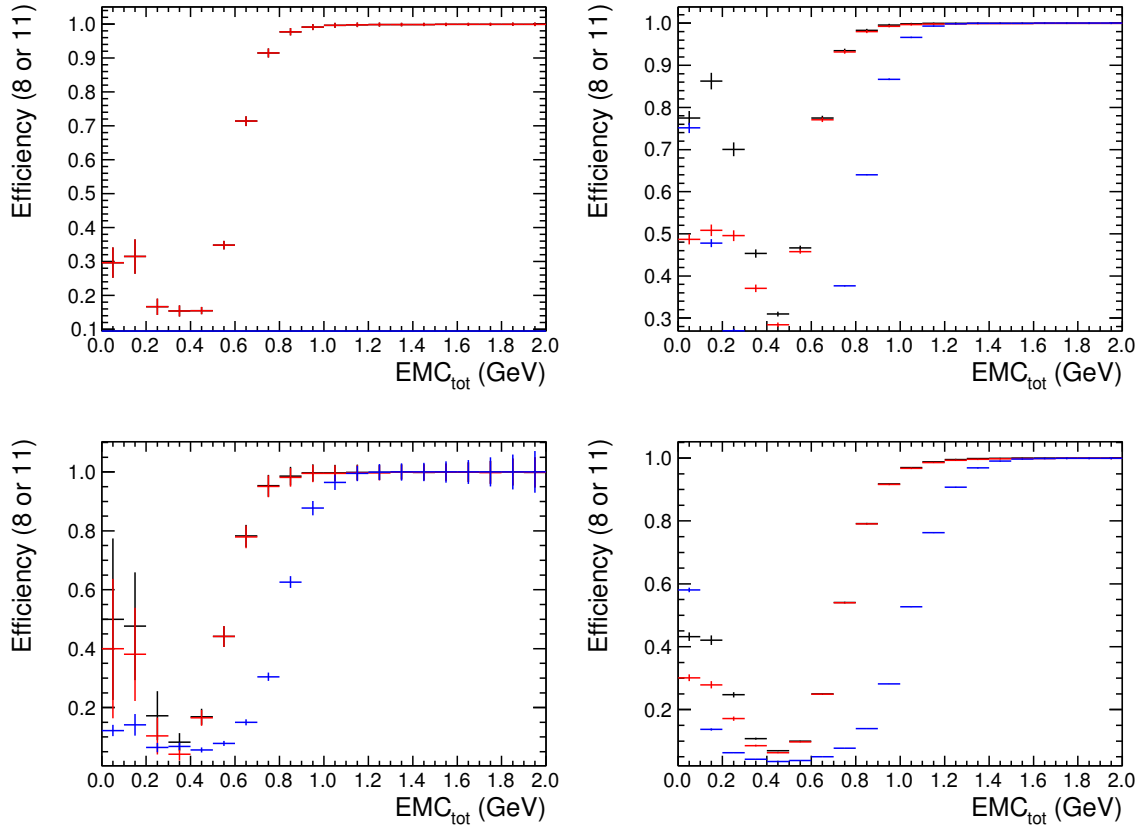


Fig. 8.17: Trigger efficiency with respect to the total energy deposition in the EMC from the final state array $e^+e^- \rightarrow \text{hadrons}$ from the control samples (upper left) collider data at $\sqrt{s} = 3.0970$ GeV collected in 2009, (upper right) collected in 2012, (lower left) scan data set collected in 2012 and (lower right) scan data set collected in 2015 (used for main analysis of $e^+e^- \rightarrow \bar{n}n$). The total energy deposition EMC_{tot} includes good and bad showers (with and without quality criteria). Black dots show the trigger efficiency with both channels 9 and 12 $\epsilon_{\text{trg}}(9 \text{ and } 12)$, blue dots with $\epsilon_{\text{trg}}(9)$ and red dots with channel $\epsilon_{\text{trg}}(12)$. For the signal final state $e^+e^- \rightarrow \bar{n}n$, the black results are important, since it can be triggered by channel 9, as well as channel 12. Here, a difference on the knee-point is observed. Data collected before 2015 show a knee-point around 0.8 GeV, while results from the scan data collected in 2015 show a knee-point around 1.0 GeV. This difference can be caused by a hardware trigger tuning between the different data collection runs, as well as by a modification of the software-based trigger requirements. The missing contribution of $\epsilon_{\text{trg}}(9)$ in the upper left plot is caused by the non-existing trigger channel 9 in the year of collection (2009). The plots are provided by Xiaorong Zhou.

Since the BESIII trigger is applied online during data taking on raw data before reconstruction, the conditions used are slightly different than after data reconstruction. To study possible biases, the trigger efficiency curve is derived from the R-scan data set and the $e^+e^- \rightarrow \bar{p}p$ selection for reconstructed data (as described above), as well as from raw

data. For the latter, the condition of at least two EMC showers is replaced by at least two EMC clusters. Figure 8.18 (left) shows, that the curves are in agreement in the important energy region above 0.4 GeV. Furthermore, the EMC based selection variables introduced in Section 5.3 are correlated with the total energy deposition in the EMC. Therefore the trigger efficiency needs to be studied under conditions as close as possible to the signal channel final state $e^+e^- \rightarrow \bar{n}n$ selection. Figure 8.18 (right) shows no strong change in the trigger efficiency under varying conditions.

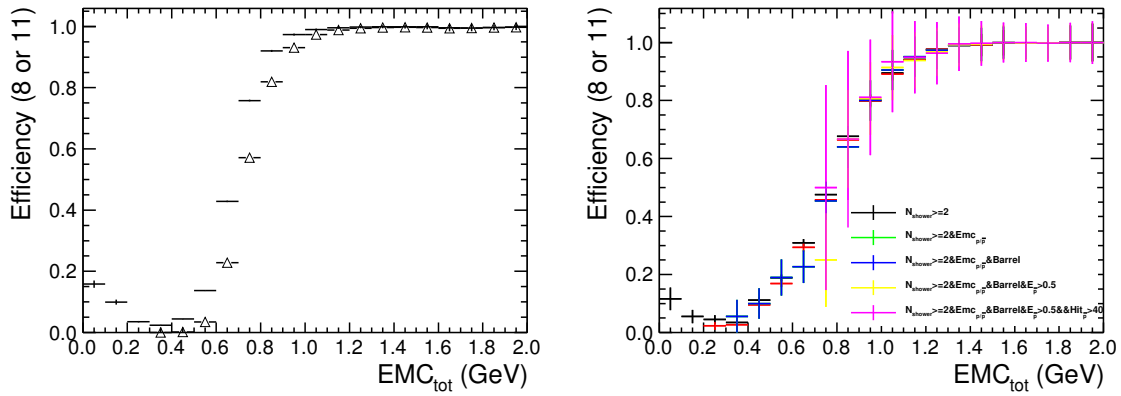


Fig. 8.18: Comparison of the trigger efficiency $\epsilon_{\text{trg}}(9 \text{ and } 12)$ (left) between RAW (triangles) and DST (dots) data and (right) under different selection requirements. The collider data used are from the scan data set collected in 2015. The plots are provided by Xiaorong Zhou.

To calculate the trigger efficiency for the signal process $e^+e^- \rightarrow \bar{n}n$, the results for the combined trigger efficiency $\epsilon_{\text{trg}}(9 \text{ and } 12)$ are used, since both trigger channels can contribute to the final efficiency. For the parametrization of the trigger efficiency for $e^+e^- \rightarrow \bar{n}n$, Function 8.13 is fitted to the control samples $e^+e^- \rightarrow \bar{p}p$ in Figure 8.16 (left) and to $e^+e^- \rightarrow \bar{q}q \rightarrow \text{hadrons}$ in Figure 8.17 (lower right) in the range above 0.4 GeV. The results are shown in Figure 8.19. The parameters a and b for the trigger response function 8.13 are derived to:

$$a = 0.758 \pm 0.005, \quad b = 0.334 \pm 0.009 \quad \text{for } e^+e^- \rightarrow \bar{p}p \quad (8.15)$$

$$a = 0.7390 \pm 0.0005, \quad b = 0.2100 \pm 0.0009 \quad \text{for } e^+e^- \rightarrow \text{hadronis} \quad (8.16)$$

For the final trigger efficiency correction C_{trg} , the parameters obtained with $e^+e^- \rightarrow \bar{p}p$ are used. As the systematic uncertainty on the trigger efficiency correction in Chapter 10, the parameters obtained with $e^+e^- \rightarrow \bar{q}q \rightarrow \text{hadrons}$ will be used.

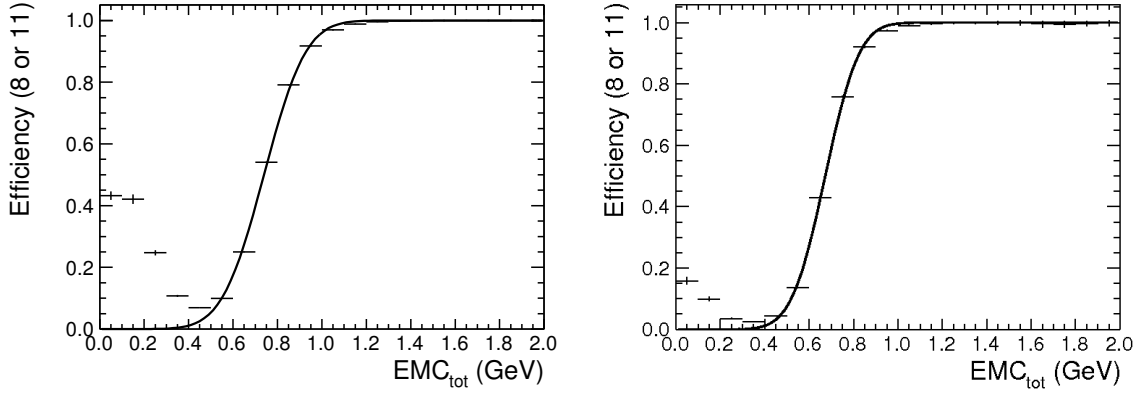


Fig. 8.19: Fit of the EMC-based trigger efficiency ϵ_{trg} (9 and 12) with the Function 8.13 to the collider data set collected in 2015 (left) for the $e^+e^- \rightarrow \bar{p}p$ control sample and (right) for the $e^+e^- \rightarrow \bar{q}q \rightarrow \text{hadrons}$ control sample. The plots are provided by Xiaorong Zhou.

8.5.2 Modification of the signal MC simulation $e^+e^- \rightarrow \bar{n}n$

As described in detail in Section 8.2 and shown in Figure 8.4 (upper left) and (lower right), the simulation of the energy deposition from hadronic showers in the EMC is imperfect. Calculating the trigger efficiency correction C_{trg} from signal MC simulation for $e^+e^- \rightarrow \bar{n}n$ would therefore introduce an error. In this analysis a data driven approach is used. The energy deposition from the \bar{n} and n EMC shower in the signal MC simulation is replaced by equivalent observables from data, derived with the control samples $J/\psi \rightarrow p\bar{n}\pi^-$ ($\bar{p}n\pi^+$) as introduced in Section 8.2. In each signal MC simulation event passing the final signal selection, the variables $E_{\bar{n}}^{50\text{cone}}$ and $E_n^{50\text{cone}}$, which denote the sums of energy deposition in 50° around the \bar{n} and n EMC showers are replaced by the sums of energy deposition of all showers in the EMC around the recoil momenta $|\vec{p}_{p\pi^-}^{\text{recoil}}|$ in the data control samples. The event from the data control samples with the closest particle momentum to the one in the MC simulation is used for the replacement of the observables discussed above. Additionally, it must fulfill the following requirement to make sure, that the particle momentum in data is similar to the one to be replaced in the signal MC simulation:

$$\left| |\vec{p}_{\bar{n}}| - |\vec{p}_{p\pi^-}^{\text{recoil}}| \right| < 0.1 \text{ GeV}, \quad \left| |\vec{p}_n| - |\vec{p}_{\bar{p}\pi^+}^{\text{recoil}}| \right| < 0.1 \text{ GeV} \quad (8.17)$$

Each event from the control samples is used only once for the replacement. The statistical uncertainty is limited by the statistics in the control samples $J/\psi \rightarrow p\bar{n}\pi^-$ ($\bar{p}n\pi^+$). Figure 8.20 shows the total energy deposition in the EMC from original MC simulation and after the replacement at $\sqrt{s} = 2.1266$ and $\sqrt{s} = 2.3960$ GeV.

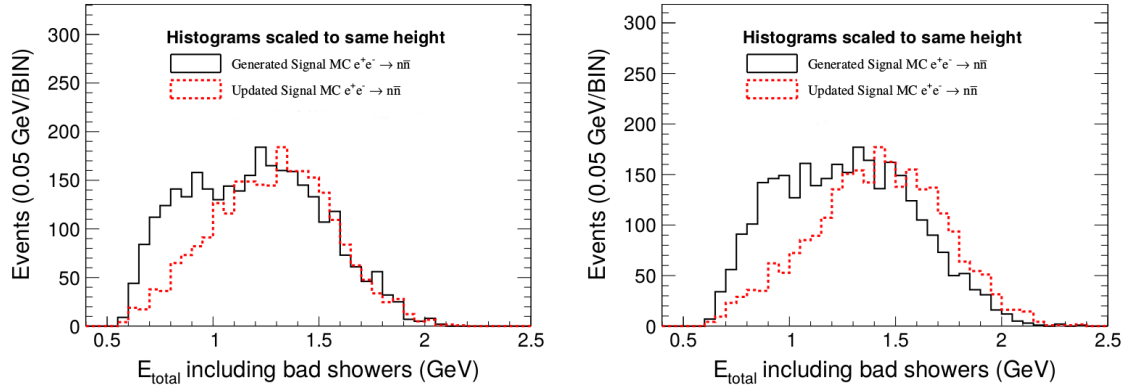


Fig. 8.20: (Top) Total energy deposition in the EMC from MC simulation with Phokhara v9.1 (black histogram) and the replaced distribution (red histogram) from the control channels as discussed above. (Left) At $\sqrt{s} = 2.1266$ GeV, (right) at $\sqrt{s} = 2.3960$ GeV.

After the replacement, the trigger efficiency based on the total energy deposition in the EMC isn't sensitive to the MC simulation, but follows the characteristics in data.

8.5.3 The calculation of C_{trg} for the signal channel $e^+e^- \rightarrow \bar{n}n$

the trigger efficiency correction C_{trg} is derived by using the total energy deposition in the EMC from modified signal MC simulation (as discussed in Section 8.5.2) for the trigger response function from Equation 8.13 with the parameters from the Reference 8.15. Figure 8.21 shows the distributions from Figure 8.20 with the calculated C_{trg} efficiency correction factors. Results for all other \sqrt{s} in the appendix in Figure A.28.

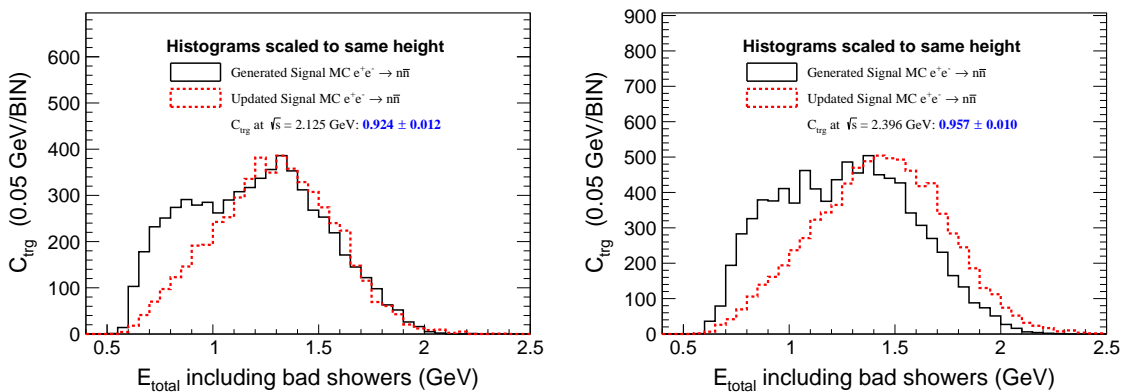


Fig. 8.21: Total energy deposition in the EMC from MC simulation with Phokhara v9.1 (black histogram) and the replaced distribution (red histogram) from the control channels as discussed above. (Left) At $\sqrt{s} = 2.1266$, (right) at $\sqrt{s} = 2.3960$ GeV.

The angular trigger efficiency correction $\frac{dC_{\text{trg}}}{d\cos\theta}$, shown in Figure 8.22 for $\sqrt{s} = 2.1266$ and 2.3960 GeV (other \sqrt{s} are shown in Figure A.29), is not significantly dependent on the angular position $\cos\theta$ of the \bar{n} EMC shower, therefore negligible and applied only as an absolute correction in the angular analysis discussed in Section 9.2. Table 8.6 lists results for C_{trg} at all analyzed \sqrt{s} derived using the main MC generator Phokhara v9.1. As cross check, results derived with the generator ConExc are presented for comparison.

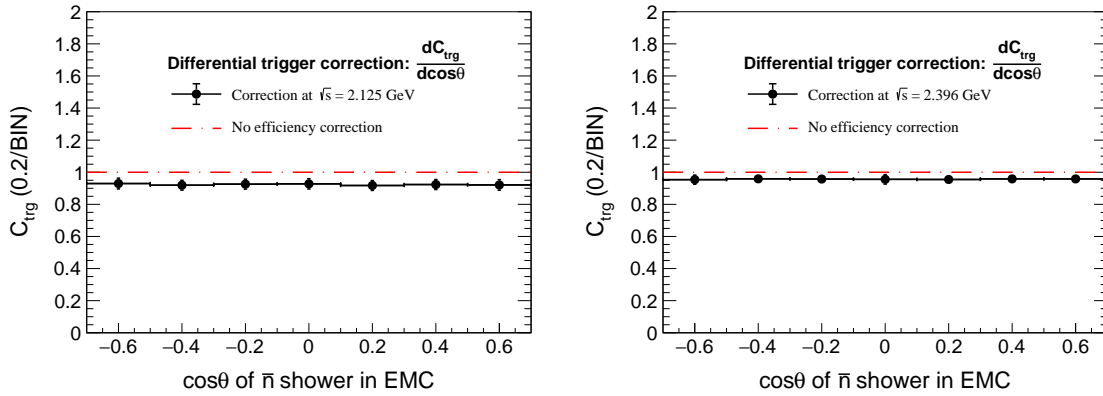


Fig. 8.22: Differential correction factor $\frac{dC_{\text{trg}}}{d\cos\theta}$ from signal MC simulation with Phokhara v9.1 at $\sqrt{s} = 2.1266$ GeV (left) and 2.3960 GeV (right). The red dotted-dashed lines indicate a differential correction of 1 (equal to no correction).

\sqrt{s} (GeV)	C_{trg}				
	Phokhara	ConExc	\sqrt{s} (GeV)	Phokhara	ConExc
2.0000	0.893 ± 0.028	0.888 ± 0.028	2.3864	0.958 ± 0.010	0.959 ± 0.010
2.0500	0.916 ± 0.015	0.911 ± 0.015	2.3960	0.957 ± 0.010	0.958 ± 0.010
2.1000	0.918 ± 0.012	0.921 ± 0.012	2.6454	0.972 ± 0.010	0.971 ± 0.009
2.1266	0.924 ± 0.012	0.925 ± 0.012	2.9000	0.974 ± 0.010	0.976 ± 0.010
2.1500	0.929 ± 0.012	0.929 ± 0.012	2.9500	0.980 ± 0.010	0.980 ± 0.010
2.1750	0.918 ± 0.012	0.918 ± 0.012	2.9810	0.978 ± 0.010	0.977 ± 0.010
2.2000	0.924 ± 0.012	0.923 ± 0.012	3.0000	0.978 ± 0.012	0.977 ± 0.012
2.2324	0.928 ± 0.012	0.929 ± 0.012	3.0200	0.979 ± 0.014	0.978 ± 0.014
2.3094	0.951 ± 0.011	0.950 ± 0.011	3.0800	0.978 ± 0.027	0.979 ± 0.027

Table 8.6: Summary of efficiency corrections due to BESIII trigger system C_{trg} at different \sqrt{s} for signal MC simulation based on 500000 generated events using Phokhara v9.1, as well as ConExc in BesEvtGen-00-03-18 as a cross check.

8.6 Efficiency correction C_{mod} due to the form factor model

The signal MC simulation selection efficiency strongly depends on the form factor model. Figure 8.23 shows the angular distribution of the \bar{n} for category C events at $\sqrt{s} = 2.3960$ GeV with the nominal form factor parametrization under $G_E^n(s) = G_M^n(s)$, as well as for two extreme cases generated under $G_E^n(s) = 0$ and $G_M^n(s) = 0$ for comparison.

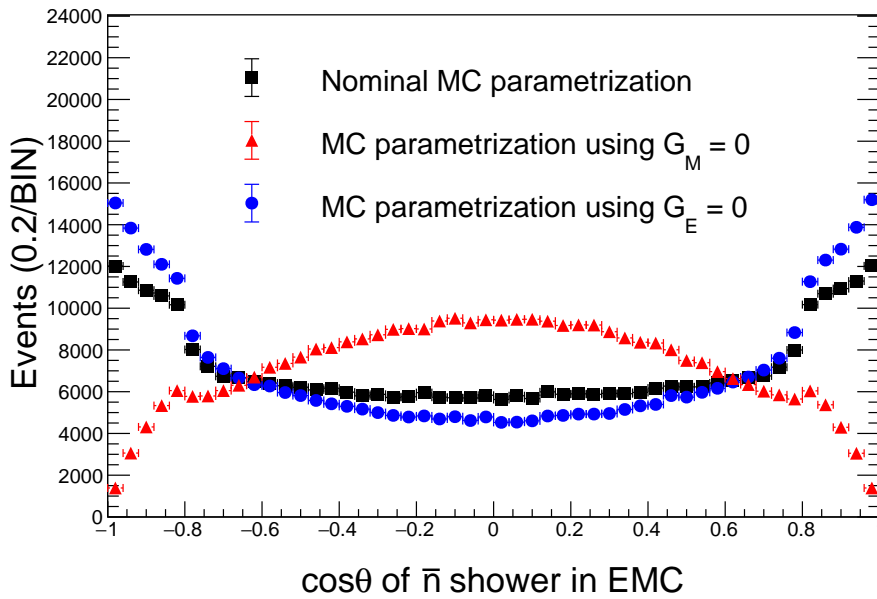


Fig. 8.23: Angular distribution of the antineutron at $\sqrt{s} = 2.3960$ GeV for the nominal form factor parametrization using $G_E^n(s) = G_M^n(s)$ in black and the two extreme parametrization cases with $G_E^n(s) = 0$ (red) and $G_M^n(s) = 0$ (blue). The events are shown at generator level for the category C classification, after rejecting all events with category A and B characteristics. The simulation is based on 500000 generated events using Phokhara v9.1.

Taking into account the determination method for the selection efficiency, described in Section 8.1 and the selection criterion S_3 on the polar range, different event numbers in the region $0.75 < |\cos\theta_{\bar{n}}| < 1.0$ directly propagate to a change of the selection efficiency under the variation of the form factor model. Without anticipating the results from the angular analysis of the signal channel final state in Section 9.2, it will become clear, that a precise determination of the polar distribution shape at all \sqrt{s} is not possible due to the low statistics for the majority of the data samples. Instead, no correction C_{mod} due to the polar distribution shape is performed in this analysis, but is taken into account as a systematic uncertainty δ_{mod} in Section 10.1.4.

8.7 The radiative correction factor $(1 + \delta)$

The observable for the extraction of the timelike form factors of the neutron is the Born cross section. The Born cross section differs from the observed cross section by the so called radiative correction factor $(1 + \delta)$, as shown in Equation 2.26. The radiative correction factor includes higher order QED corrections and the vacuum polarization, as discussed in Section 2.2.2. In the up to date available MC generators for the signal process $e^+e^- \rightarrow \bar{n}n$, corrections due to radiative events such as $e^+e^- \rightarrow \bar{n}n(m \times \gamma_{\text{ISR}})$ ($m = 1, 2$) are implemented up to the NLO ($m = 1$) in ConExc and up to the NNLO ($m = 2$) in Phokhara v9.1. The correction due to the vacuum polarization is implemented in both generators. Figure 8.24 shows the Feynman diagrams for the implemented corrections.

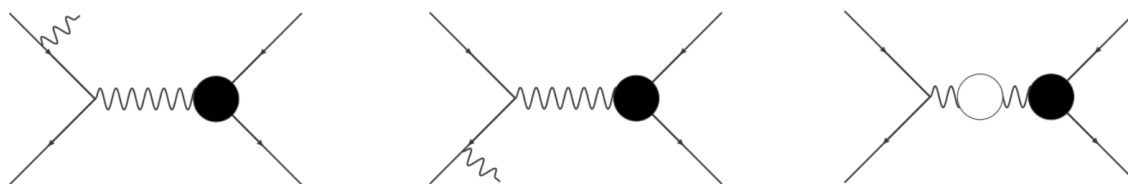


Fig. 8.24: Feynman diagrams for the QED corrections to $e^+e^- \rightarrow \bar{n}n$. (Left and middle) Initial State Radiation, (right) vacuum polarization. (Original figures from [49]).

These corrections are based on non-trivial theoretical calculations. They affect the normalization of the Born cross section, as well as the polar shape of the final state particles in the signal process and are gathered directly from the signal MC generator output. In both generators, the radiative corrections depend on the input parametrization for the Born cross section. The aspect is important to emphasize that the values quoted in this analysis are extracted with the final signal MC simulation form factor parametrization. Both signal MC generators provide the absolute radiative correction $(1 + \delta)$ for the simulation of signal MC samples at all \sqrt{s} . In case of the differential Born cross section, the signal MC generator Phokhara v9.1 provides a method to extract the shape of the differential correction $\frac{d(1+\delta)}{d\cos\theta}$. Therefore a signal MC simulation sample is generated in Born ($m = 0$) and Next-to-Leading Order ($m = 0, 1, 2$) and the ratio of the generated NNLO to the Born cross section is extracted. The ConExc generator does not provide this option for the Born cross section simulation, hence the ratio of events without radiative photons ($m = 0$) over the total number of generated events ($m = 0, 1$) is calculated to get an approximation for the differential angular correction. In both cases, the differential distribution is scaled with the corresponding absolute $(1 + \delta)$ factor. The results for the absolute $(1 + \delta)$ correction and the differential angular correction $\frac{d(1+\delta)}{d\cos\theta}$ at $\sqrt{s} = 2.1266$ and 2.3960 GeV are shown in

Table 8.7 and Figure 8.25, respectively. Differential radiative corrections at all energies are shown for Phokhara v9.1 signal MC simulation in Figure A.30 and for ConExc signal MC simulation in Figure A.31 as a cross-check.

\sqrt{s} (GeV)	$(1 + \delta)$		\sqrt{s} (GeV)	$(1 + \delta)$	
	Phokhara	ConExc		Phokhara	ConExc
2.0000	0.985 ± 0.004	0.982 ± 0.001	2.3864	1.111 ± 0.006	1.107 ± 0.001
2.0500	1.080 ± 0.005	1.076 ± 0.001	2.3960	1.115 ± 0.006	1.111 ± 0.001
2.1000	1.184 ± 0.005	1.183 ± 0.001	2.6454	1.568 ± 0.009	1.551 ± 0.001
2.1266	1.241 ± 0.006	1.235 ± 0.001	2.9000	2.182 ± 0.014	2.162 ± 0.001
2.1500	1.281 ± 0.006	1.278 ± 0.001	2.9500	2.320 ± 0.015	2.287 ± 0.001
2.1750	1.309 ± 0.007	1.305 ± 0.001	2.9810	2.393 ± 0.015	2.364 ± 0.001
2.2000	1.311 ± 0.007	1.308 ± 0.001	3.0000	2.446 ± 0.016	2.410 ± 0.001
2.2324	1.276 ± 0.007	1.276 ± 0.001	3.0200	2.492 ± 0.016	2.458 ± 0.001
2.3094	1.147 ± 0.006	1.144 ± 0.001	3.0800	2.647 ± 0.017	2.605 ± 0.001

Table 8.7: Summary of efficiency corrections due to radiative correction factor $(1 + \delta)$ at different \sqrt{s} for signal MC simulation based on 500000 generated events using Phokhara v9.1, as well as ConExc in BesEvtGen-00-03-18 as a cross check.

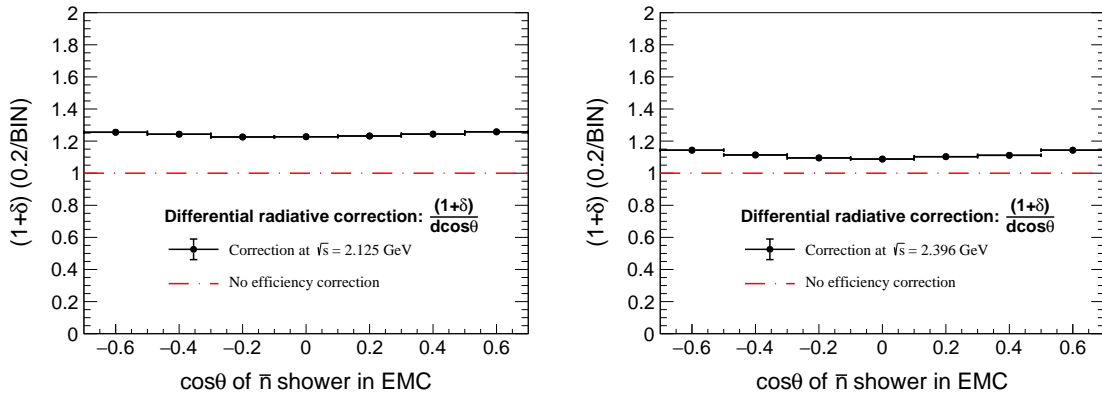


Fig. 8.25: Differential radiative correction $\frac{d(1+\delta)}{d\cos\theta}$ from signal MC simulation with Phokhara v9.1 at $\sqrt{s} = 2.1266$ and 2.3960 GeV. The red dotted-dashed lines indicate a differential correction of 1 (equal to no correction).

8.8 Summary of the signal efficiency and its corrections

Table 8.8 shows the signal efficiency and all efficiency corrections calculated using the Phokhara v9.1. The values are quoted from the Tables 8.1, 8.2, 8.4, 8.5, 8.6, and 8.7. Values gathered with the ConExc event generator are listed in the appendix in Table A.5.

\sqrt{s} (GeV)	ϵ^{MC} (%)	C_{dm}	C_{ee}	C_{muc}	C_{trg}	$(1 + \delta)$
2.0000	0.31 ± 0.01	1.377 ± 0.035	0.750 ± 0.019	1.004 ± 0.026	0.893 ± 0.028	0.985 ± 0.004
2.0500	0.74 ± 0.01	1.267 ± 0.021	0.752 ± 0.016	1.003 ± 0.017	0.916 ± 0.015	1.080 ± 0.005
2.1000	1.15 ± 0.02	1.251 ± 0.017	0.773 ± 0.011	1.003 ± 0.013	0.918 ± 0.012	1.184 ± 0.005
2.1266	1.30 ± 0.02	1.247 ± 0.016	0.798 ± 0.009	1.004 ± 0.012	0.924 ± 0.012	1.241 ± 0.006
2.1500	1.49 ± 0.02	1.237 ± 0.014	0.830 ± 0.014	1.006 ± 0.012	0.929 ± 0.012	1.281 ± 0.006
2.1750	1.54 ± 0.02	1.235 ± 0.014	0.860 ± 0.019	1.007 ± 0.011	0.918 ± 0.012	1.309 ± 0.007
2.2000	1.68 ± 0.02	1.232 ± 0.013	0.881 ± 0.019	1.007 ± 0.011	0.924 ± 0.012	1.311 ± 0.007
2.2324	1.80 ± 0.02	1.228 ± 0.013	0.892 ± 0.019	1.006 ± 0.011	0.928 ± 0.012	1.276 ± 0.007
2.3094	1.88 ± 0.02	1.227 ± 0.013	0.896 ± 0.021	1.006 ± 0.010	0.951 ± 0.011	1.147 ± 0.006
2.3864	2.25 ± 0.02	1.169 ± 0.011	0.897 ± 0.019	1.008 ± 0.010	0.958 ± 0.010	1.111 ± 0.006
2.3960	2.26 ± 0.02	1.168 ± 0.011	0.891 ± 0.018	1.008 ± 0.009	0.957 ± 0.010	1.115 ± 0.006
2.6454	2.64 ± 0.02	1.006 ± 0.009	0.898 ± 0.027	1.007 ± 0.009	0.972 ± 0.010	1.568 ± 0.009
2.9000	2.25 ± 0.02	1.033 ± 0.010	0.900 ± 0.046	1.000 ± 0.009	0.974 ± 0.010	2.181 ± 0.014
2.9500	2.21 ± 0.02	1.049 ± 0.010	0.901 ± 0.051	0.998 ± 0.010	0.980 ± 0.010	2.320 ± 0.015
2.9810	2.07 ± 0.02	1.050 ± 0.010	0.901 ± 0.053	0.998 ± 0.010	0.978 ± 0.010	2.393 ± 0.015
3.0000	2.09 ± 0.02	1.059 ± 0.010	0.901 ± 0.055	1.011 ± 0.010	0.978 ± 0.012	2.446 ± 0.016
3.0200	2.03 ± 0.02	1.061 ± 0.011	0.901 ± 0.057	1.011 ± 0.010	0.979 ± 0.014	2.492 ± 0.016
3.0800	1.95 ± 0.02	1.062 ± 0.011	0.902 ± 0.062	1.012 ± 0.010	0.978 ± 0.027	2.647 ± 0.017

Table 8.8: Summary of signal MC reconstruction efficiency and its corrections from Tables 8.1, 8.2, 8.4, 8.5, 8.6, and 8.7 based on 500000 signal events generated with Phokhara v9.1. The Born cross section input model from the final iteration of the form factor parametrization is used.

Along with the luminosity quoted from Table 3.11 and the number of signal events extracted from data, as discussed in Chapter 7, the listed values in Table 8.8 are used to calculate the Born cross section and the corresponding effective form factor in Section 9.1. The differential reconstruction efficiency and its corrections are applied to the differential signal yield from collider data for the determination of the magnetic form factor and the form factor ratio in Section 9.2.

Chapter 9

The Extraction of the Results

The results from this work are shown in this chapter, including: the Born cross section $\sigma_{\text{Born}}^{\text{ind}}(s)$ and effective form factor $|G_{\text{eff}}^{\text{ind}}(s)|$ for the signal process $e^+e^- \rightarrow \bar{n}n$ in Section 9.1; the magnetic form factor $G_{\text{M}}^{\text{ind}}(s)$ and the electromagnetic form factor ratio of the neutron $R_{\text{em}}^{\text{ind}} = |G_{\text{E}}^{\text{n}}(s)|/|G_{\text{M}}^{\text{n}}(s)|$ in Section 9.3. The final results from this analysis combine three individually analyzed sub-data sets, as discussed in Section 5.2, with only one of them subject of this thesis. The combined results for the Born cross section $\sigma_{\text{Born}}(s)$ and effective form factor $|G_{\text{eff}}(s)|$ are determined in Section 9.2. The final results for $G_{\text{M}}^{\text{n}}(s)$ and $R_{\text{em}}^{\text{n}} = |G_{\text{E}}^{\text{n}}(s)|/|G_{\text{M}}^{\text{n}}(s)|$ are extracted in Section 9.4 via a simultaneous fit to the three individual angular distributions of the antineutron (from the three signal selection classification categories). A discussion is postponed to Chapter 11, where the final results are shown including the systematic uncertainty.

9.1 The individual results for $\sigma_{\text{Born}}^{\text{ind}}(s)$ and $|G_{\text{eff}}^{\text{ind}}(s)|$

The Born cross section $\sigma_{\text{Born}}(s)$ for the signal process $e^+e^- \rightarrow \bar{n}n$ is given by the following equation, where the left side is the theoretical and the right side the experimentally accessible representation.

$$\sigma_{\text{Born}}(s) = \frac{4\pi\alpha^2\beta C}{3s} \cdot \left[|G_{\text{M}}^{\text{n}}(s)|^2 + \frac{2m_{\text{n}}^2}{s} |G_{\text{E}}^{\text{n}}(s)|^2 \right] = \frac{N_{\text{sig}}}{\mathcal{L} \cdot \epsilon^{\text{MC}} \cdot C_{\text{cor}} \cdot (1 + \delta)} \quad (9.1)$$

Here, N_{sig} is the number of signal events in data, extracted in Chapter 7; the luminosity \mathcal{L} is quoted from Table 3.11; the signal MC efficiency ϵ^{MC} and its combined correction C_{cor} representing the product of C_{dm} , C_{ee} , C_{trg} , as well as the radiative correction $(1 + \delta)$ are

discussed in Chapter 8. These values are calculated using Phokhara v9.1 for all factors dependent on the signal MC simulation and summarized in Table 9.1. With the Coulomb correction $C = 1$ for neutral final states, as discussed in Section 2.2, and assuming the identity of the electric and magnetic form factors $|G_E^n(s)| = |G_M^n(s)| = |G_{\text{eff}}^n(s)|$, the Born cross section can be rewritten to:

$$\sigma_{\text{Born}}(s) = \frac{4\pi\alpha^2\beta}{3s} \left(1 + \frac{2m_n^2}{s}\right) |G_{\text{eff}}^n(s)|^2 \quad (9.2)$$

The effective form factor $|G_{\text{eff}}^n(s)|$ is be calculated as:

$$|G_{\text{eff}}^n(s)| = \sqrt{\frac{\sigma_{\text{Born}}(s)}{\frac{4\pi\alpha^2\beta}{3s} \cdot \left(1 + \frac{2m_n^2}{s}\right)}} \quad (9.3)$$

The individual results for $\sigma_{\text{Born}}^{\text{ind}}$ and $|G_{\text{eff}}^{\text{ind}}(s)|$ from $e^+e^- \rightarrow \bar{n}n$ are summarized in Table 9.2. The errors are solely on a statistical basis. The individual Born cross section and effective form factor at all analyzed \sqrt{s} are shown in Figure 9.1 and 9.2, respectively.

\sqrt{s} (GeV)	N_{sig}	\mathcal{L} (pb $^{-1}$)	ϵ^{MC} (%)	C_{dm}	C_{ee}	C_{trg}	$(1 + \delta)$
2.0000	26 ± 5	10.074 ± 0.005	0.31 ± 0.01	1.377 ± 0.035	0.750 ± 0.019	0.893 ± 0.028	0.985 ± 0.004
2.0500	10 ± 3	3.344 ± 0.003	0.74 ± 0.01	1.267 ± 0.021	0.752 ± 0.016	0.916 ± 0.015	1.080 ± 0.005
2.1000	31 ± 6	12.167 ± 0.006	1.15 ± 0.02	1.251 ± 0.017	0.773 ± 0.011	0.918 ± 0.012	1.184 ± 0.005
2.1266	277 ± 16	108.49 ± 0.02	1.30 ± 0.02	1.247 ± 0.016	0.798 ± 0.009	0.924 ± 0.012	1.241 ± 0.006
2.1500	7 ± 3	2.841 ± 0.003	1.49 ± 0.02	1.237 ± 0.014	0.830 ± 0.014	0.929 ± 0.012	1.281 ± 0.006
2.1750	20 ± 5	10.625 ± 0.006	1.54 ± 0.02	1.235 ± 0.014	0.860 ± 0.019	0.918 ± 0.012	1.309 ± 0.007
2.2000	35 ± 6	13.699 ± 0.007	1.68 ± 0.02	1.232 ± 0.013	0.881 ± 0.019	0.924 ± 0.012	1.311 ± 0.007
2.2324	27 ± 5	11.856 ± 0.007	1.80 ± 0.02	1.228 ± 0.013	0.892 ± 0.019	0.928 ± 0.012	1.276 ± 0.007
2.3094	52 ± 7	21.089 ± 0.009	1.88 ± 0.02	1.227 ± 0.013	0.896 ± 0.021	0.951 ± 0.011	1.147 ± 0.006
2.3864	57 ± 7	22.549 ± 0.010	2.25 ± 0.02	1.169 ± 0.011	0.897 ± 0.019	0.958 ± 0.010	1.111 ± 0.006
2.3960	212 ± 14	66.869 ± 0.017	2.26 ± 0.02	1.168 ± 0.011	0.891 ± 0.018	0.957 ± 0.010	1.115 ± 0.006
2.6454	44 ± 8	67.725 ± 0.013	2.64 ± 0.02	1.006 ± 0.009	0.898 ± 0.027	0.972 ± 0.010	1.568 ± 0.009
2.9000	48 ± 8	105.253 ± 0.025	2.25 ± 0.02	1.033 ± 0.010	0.900 ± 0.046	0.974 ± 0.010	2.182 ± 0.014
2.9500	7 ± 3	15.942 ± 0.010	2.21 ± 0.02	1.049 ± 0.010	0.901 ± 0.051	0.980 ± 0.010	2.320 ± 0.015
2.9810	8 ± 3	16.071 ± 0.010	2.07 ± 0.02	1.050 ± 0.010	0.901 ± 0.053	0.978 ± 0.010	2.393 ± 0.015
3.0000	0 ± 3	15.881 ± 0.010	2.09 ± 0.02	1.059 ± 0.010	0.901 ± 0.055	0.978 ± 0.012	2.446 ± 0.016
3.0200	3 ± 3	17.290 ± 0.011	2.03 ± 0.02	1.061 ± 0.011	0.901 ± 0.057	0.979 ± 0.014	2.492 ± 0.016
3.0800	21 ± 6	126.185 ± 0.029	1.95 ± 0.02	1.062 ± 0.011	0.902 ± 0.062	0.978 ± 0.027	2.647 ± 0.017

Table 9.1: Summary of all values for the calculation of the $e^+e^- \rightarrow \bar{n}n$ Born cross section and the effective form factor of the neutron. Values are taken from Table 7.3, 3.11, 8.1, 8.2, 8.4, 8.6, and 8.7. All values related to the signal MC simulation are gathered from the generator Phokhara v9.1 and the final iteration for the form factor parametrization used in the signal MC simulation, as described in Section 4.2.1.

Due to the low statistics in the collider data, no signal could be extracted for the data set at the center-of-mass energy of $\sqrt{s} = 3.0000$ GeV. Instead, an upper limit is calculated by using the non-vanishing statistical uncertainty for the signal yield at $\sqrt{s} = 3.0000$ GeV. The upper limit is determined at the confidence level of 95%.

\sqrt{s} (GeV)	$\sigma_{\text{Born}}^{\text{ind}}(s)$ (pb)	$ G_{\text{eff}}^{\text{ind}}(s) $ ($\times 10^2$)
2.0000	912.67 ± 194.90	29.18 ± 3.12
2.0500	424.26 ± 144.16	19.02 ± 3.23
2.1000	212.61 ± 39.60	13.14 ± 1.22
2.1266	172.09 ± 11.63	11.74 ± 0.40
2.1500	144.11 ± 57.71	10.69 ± 2.14
2.1750	94.22 ± 29.57	8.62 ± 1.35
2.2000	116.48 ± 23.62	9.56 ± 0.97
2.2324	99.87 ± 23.10	8.85 ± 1.02
2.3094	110.17 ± 18.24	9.35 ± 0.77
2.3864	100.84 ± 15.22	9.05 ± 0.68
2.3960	125.77 ± 10.67	10.12 ± 0.43
2.6454	18.21 ± 3.80	4.08 ± 0.43
2.9000	10.26 ± 2.08	3.28 ± 0.33
2.9500	8.62 ± 4.44	3.05 ± 0.79
2.9810	10.27 ± 5.49	3.36 ± 0.90
3.0000	< 3.96 (CL95%)	< 2.10 (CL95%)
3.0200	4.16 ± 3.90	2.16 ± 1.28
3.0800	3.44 ± 1.12	2.00 ± 0.33

Table 9.2: Individual results for the Born cross section and effective form factor of the neutron, calculated with values from Table 9.1 from category C classified signal events (this work). The results at $\sqrt{s} = 3.0000$ GeV is an upper limit at CL95%, since the number of signal events in data extracted at this center-of-mass energy is zero. The shown uncertainties are statistical.

The results shown in Table 9.2 and in the Figures 9.1 and 9.2 represent the analysis for the signal selection classification category developed by the author. For an improved statistical uncertainty, the final results are calculated by combining this set of results with the results from the two other signal selection classification categories (summarized in the Appendix B) via an error-weighted approach, shown in the following section. The discussion of the results is postponed to Chapter 11, where the final results from this analysis are shown including their systematical uncertainty.

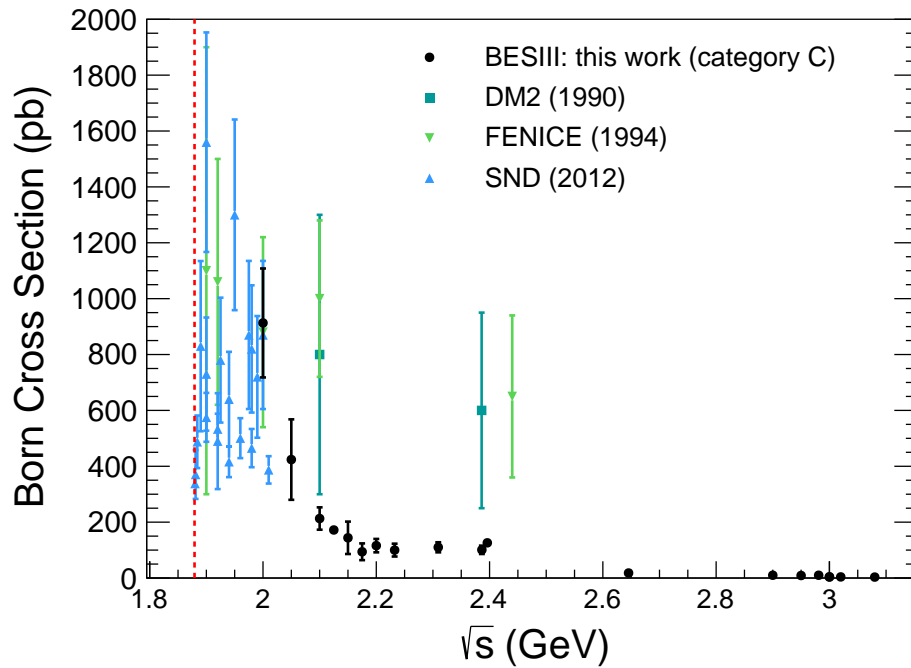


Fig. 9.1: Individual results for the Born cross section of the process $e^+e^- \rightarrow \bar{n}n$ from category C classified signal events (this work). Black dots indicate the results from this analysis, as shown in Table 9.2, with statistical uncertainties only. Emerald squares show results from the DM2 experiment, green downward triangles are results from the Fenice experiment, blue upward triangles are results from the SND experiment. The red dashed line shows the production threshold for the signal process. The shown uncertainties are statistical.

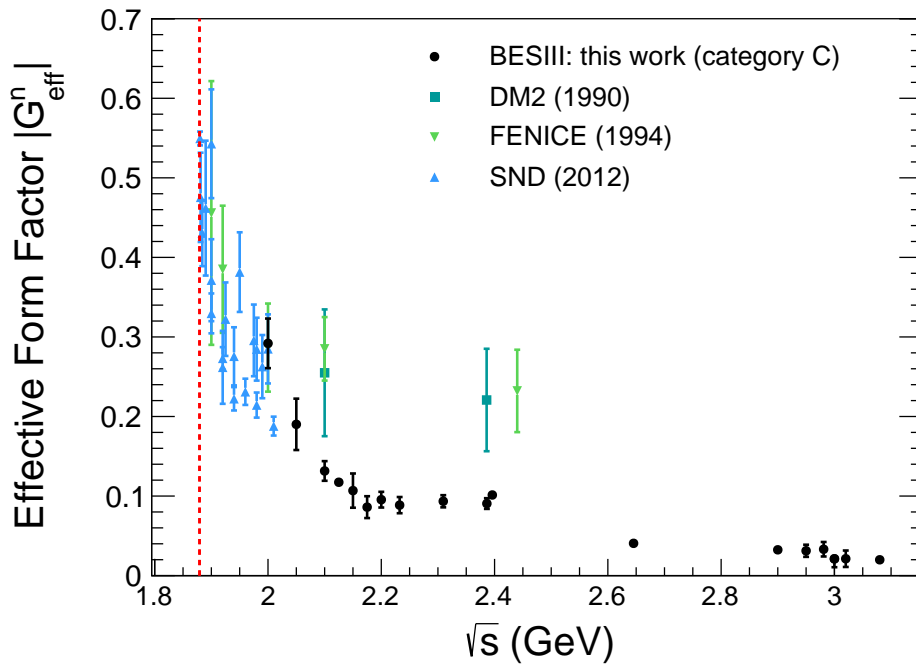


Fig. 9.2: Effective form factor of the neutron. Data and notation are identical to Figure 9.1.

9.2 The combined results for $\sigma_{\text{Born}}^n(s)$ and $|G_{\text{eff}}^n(s)|$

The values for the Born cross section for the process $e^+e^- \rightarrow \bar{n}n$ from three event selection classification categories $\sigma_{\text{Born}}^A(s)$, $\sigma_{\text{Born}}^B(s)$, and $\sigma_{\text{Born}}^C(s)$ are compared with each other in Table 9.3 and in the Figure 9.3. Since the two external sets of results (denoted as A and B) are determined by using the signal MC simulation with the ConExc generator included in the BesEvtGen-00-03-18 framework, the results from this work (denoted as C) are calculated accordingly for consistency, in comparison with the individual results shown in the previous section, which are calculated with the event generator Phokhara v9.1. Both sets of results, obtained with the Phokhara v9.1 and the ConExc Monte Carlo event generator are consistent within their uncertainties.

It is observed that the results from the three event selection classification categories are consistent with each other within one standard deviation at all center-of-mass energies. As discussed in Section 5.2, the three signal selection classification categories do not share any selected event between each other, but are statistically independent. Therefore an error-weighted combination of the three sets of results for the improvement of the statistical uncertainty is possible without introducing any correlations. For the error-weighted combination approach the following formula is used:

$$\sigma_{\text{Born}}^n = w_A \sigma_A + w_B \sigma_B + w_C \sigma_C, \quad \Delta \sigma_{\text{Born}}^n = \sqrt{\frac{1}{\sum W_j}} \quad (9.4)$$

with

$$w_i = \frac{W_i}{\sum W_j}, \quad W_j = \frac{1}{\Delta \sigma_j^2}, \quad (i, j = A, B, C).$$

where σ_i and $\Delta \sigma_i$ are the cross-section and its error calculated in the category A, B, and C, respectively. Values for the combined cross section $\sigma_{\text{Born}}^n(s)$ and the combined effective form factor $|G_{\text{eff}}^n(s)|$ are listed in Table 9.3.

A direct consequence of the error-weighted approach is the greatly improved statistical uncertainty, visible through the comparison of the category-individual results $\sigma_{\text{Born}}^i(s)$ ($i, j = A, B, C$) with the final values after combination $\sigma_{\text{Born}}^n(s)$. Additionally, the distribution of the result after the error-weighted combination shows a smaller fluctuation between neighboring values with respect to the center-of-mass energy.

\sqrt{s} (GeV)	$\sigma_{\text{Born}}^{\text{A}}$ (s)(pb)	$\sigma_{\text{Born}}^{\text{B}}$ (s)(pb)	$\sigma_{\text{Born}}^{\text{C}}$ (s)(pb)	$\sigma_{\text{Born}}^{\text{n}}$ (s)(pb)	$ G_{\text{eff}}^{\text{n}}(\text{s}) (\times 10^2)$
2.0000	320.1 ± 61.0	570.4 ± 159.8	836.7 ± 178.5	599.8 ± 54.3	20.7 ± 1.3
2.0500	321.9 ± 103.1	120.4 ± 112.5	422.5 ± 143.6	307.2 ± 67.2	16.0 ± 1.9
2.1000	170.2 ± 39.9	258.4 ± 46.9	212.7 ± 39.6	220.6 ± 24.1	13.1 ± 0.8
2.1266	132.0 ± 11.4	142.9 ± 10.4	167.8 ± 11.3	154.1 ± 6.4	11.0 ± 0.2
2.1500	89.0 ± 65.2	256.0 ± 78.2	142.7 ± 57.1	153.1 ± 37.6	11.7 ± 1.4
2.1750	90.8 ± 34.1	110.4 ± 25.0	91.9 ± 28.8	96.2 ± 16.5	8.9 ± 0.7
2.2000	52.1 ± 22.8	92.0 ± 18.4	112.5 ± 22.8	90.2 ± 12.1	8.5 ± 0.6
2.2324	72.5 ± 28.3	93.4 ± 20.2	95.2 ± 22.0	87.0 ± 13.2	8.4 ± 0.6
2.3094	91.8 ± 23.5	81.3 ± 13.6	107.3 ± 17.8	97.6 ± 9.8	8.6 ± 0.5
2.3864	74.9 ± 19.3	84.4 ± 11.8	92.8 ± 14.8	87.0 ± 8.3	8.5 ± 0.4
2.3960	95.0 ± 11.7	88.9 ± 7.0	120.5 ± 10.2	107.0 ± 5.2	9.0 ± 0.2
2.6454	36.3 ± 8.8	22.5 ± 3.1	17.7 ± 3.7	25.1 ± 2.3	4.6 ± 0.2
2.9000	16.7 ± 4.5	6.8 ± 1.3	10.2 ± 2.1	11.7 ± 1.1	3.0 ± 0.2
2.9500	0.0 ± 8.2	7.5 ± 3.8	8.6 ± 4.4	7.0 ± 2.7	2.8 ± 0.5
2.9810	14.3 ± 11.8	7.4 ± 3.8	9.9 ± 5.3	11.1 ± 3.0	3.1 ± 0.5
3.0000	8.3 ± 7.7	8.7 ± 3.8	0.0 ± 4.0	5.9 ± 2.7	2.9 ± 0.5
3.0200	16.7 ± 11.7	10.4 ± 3.9	4.2 ± 3.9	9.3 ± 3.0	3.3 ± 0.5
3.0800	7.1 ± 2.5	3.7 ± 0.9	1.8 ± 0.6	5.2 ± 0.5	1.8 ± 0.2

Table 9.3: Comparison of the category-individual results for the Born cross section and effective form factor of the neutron and their error-weighted σ_{Born} combination according to the Equation 9.4. The results from this work are denoted as category C. The results for all categories have been calculated using the ConExc Monte Carlo generator included in the BesEvtGen-00-03-18 framework. The shown uncertainties are statistical.

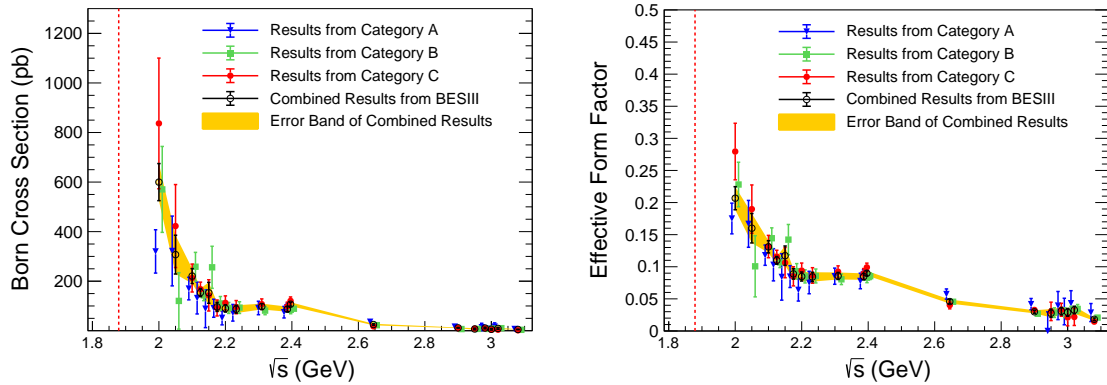


Fig. 9.3: Comparison of the results for (left) the Born cross section and (right) the effective form factor for the process $e^+e^- \rightarrow \bar{n}n$ from the three signal selection classification categories. Results shown in blue, green and red are extracted with the signal selection classification category A, B, and C, respectively, all with statistical uncertainty only. The black open circles are the combined results using the formula from Equation 9.4. The yellow band represents the statistical uncertainty of the combined results.

9.3 Extraction of individual results for $G_M^{\text{ind}}(s)$ and $R_{\text{em}}^{\text{ind}}(s)$

The main goal of this thesis is the extraction of the magnetic form factor of the neutron $G_M^n(s)$ and the electromagnetic form factor ratio $R_{\text{em}}^n(s) = |G_E^n(s)|/|G_M^n(s)|$. The differential Born cross section with respect to the antineutron EMC shower position, introduced in Equation 2.18, is expressed in terms of $G_E^n(s)$ and $G_M^n(s)$:

$$\frac{d\sigma_{\text{Born}}(s)}{d\cos\theta_{\bar{n}}^{\text{CM}}} = \frac{\pi\alpha^2\beta C}{2s} \left[|G_M^n(s)|^2 (1 + \cos^2\theta_{\bar{n}}^{\text{CM}}) + \frac{1}{\tau} |G_E^n(s)|^2 (1 - \cos^2\theta_{\bar{n}}^{\text{CM}}) \right] \quad (9.5)$$

As discussed before, for pure neutral final states like the signal channel $e^+e^- \rightarrow \bar{n}n$, the Coulomb factor C is equal 1, τ is equal to $\frac{s}{4m_n^2}$, $\beta = \sqrt{1 - \frac{1}{\tau}}$ is the velocity of the antineutron, while $\theta_{\bar{n}}^{\text{CM}}$ is the polar angle of the energy weighted \bar{n} EMC shower position (the reconstructed position of the antineutron in the EMC) with respect to the horizontal position of the positron beam, denoted as the z -axis, in the center-of-mass (CM) frame. The polar angle distribution of the antineutron in the analyzed range of $|\cos\theta_{\bar{n}}| < 0.7$ is divided into 7 bins with a bin width of 0.2. The value of the function in Equation 9.5 is subject to fluctuations within the large bin width. Therefore, the fit function is modified to the integral-over-the-bin-width form, instead of taking into account the bin center value. In theory, Equation 9.5 is only valid in the center-of-mass (CM) frame. Considering the small crossing angle between the electron and positron beam of 22 mrad (discussed in the collider description in Section 3.1), a small boost for the \bar{n} EMC shower into the CM frame is required to satisfy the theoretical condition. In this analysis the situation is different due to unique properties of the BESIII detector. Since the purpose of the BESIII EMC is to detect electromagnetic showers, the reconstruction of hadronic showers is imperfect, as discussed in Section 5.1. The same argument is applied to the reconstruction of the hadronic shower energy deposition due to the hadronic interaction length of less than one. These characteristics introduce a significant position uncertainty due to a boost of the final state particles into the CM system. Therefore the boost is neglected. Instead, the effect of the position uncertainty due to the missing boost is studied by smearing the fit function value for each bin of the $\cos\theta_{\bar{n}}$ distribution with the position resolution extracted from the signal MC simulation. The resolution is determined with a Voigtian fit to the angle between the reconstructed particle position in the EMC and the simulated position from the event generator, as shown in Figure 9.4. The resolution $\mathcal{R}(s)$ is taken into account

within the following expression:

$$\frac{d\sigma_{\text{Born}}(s)}{d\cos\theta_{\bar{n}}} = \frac{\pi\alpha^2\beta}{2s} |G_M^n(s)|^2 \left[(1 + \cos^2\theta_{\bar{n}}) + (R_{\text{em}}^n(s))^2 \frac{1}{\tau} \sin^2\theta_{\bar{n}} \right] \otimes \mathcal{R}(s) \quad (9.6)$$

with

$$(R_{\text{EM}}^n(s))^2 = |G_E^n(s)|^2 / |G_M^n(s)|^2 \quad \theta_{\bar{n}} : \text{polar angle in Laboratory frame}$$

The expression $\otimes \mathcal{R}(s)$ represents the convolution with the resolution of the \bar{n} EMC shower position at a specific \sqrt{s} . The experimentally accessible differential Born cross section can be expressed in terms of the differential signal yield via:

$$\frac{d\sigma_{\text{Born}}(s)}{d\cos\theta_{\bar{n}}} = \frac{\frac{dN_{\text{sig}}}{d\cos\theta_{\bar{n}}}}{\mathcal{L} \frac{de^{\text{MC}}}{d\cos\theta_{\bar{n}}} \frac{dC_{\text{cor}}}{d\cos\theta_{\bar{n}}} \frac{d(1+\delta)}{d\cos\theta_{\bar{n}}}} \quad (9.7)$$

with $\frac{dC_{\text{cor}}}{d\cos\theta_{\bar{n}}}$ as the product of the differential correction $\frac{dC_{\text{dm}}}{d\cos\theta_{\bar{n}}}$ and the absolute corrections C_{ee} , and C_{trg} . By comparing Equation 9.6 and 9.7, the fit function for the angular analysis is derived as shown at the right side of Equation 9.8:

$$\frac{\frac{dN_{\text{sig}}}{d\cos\theta_{\bar{n}}}}{\mathcal{L} \frac{de^{\text{MC}}}{d\cos\theta_{\bar{n}}} \frac{dC_{\text{cor}}}{d\cos\theta_{\bar{n}}} \frac{d(1+\delta)}{d\cos\theta_{\bar{n}}}} = A(s) \left[(1 + \cos^2\theta_{\bar{n}}) + (R_{\text{EM}}^n(s))^2 \frac{1}{\tau} \sin^2\theta_{\bar{n}} \right] \otimes \mathcal{R}(s) \quad (9.8)$$

with the overall normalization:

$$A(s) = \frac{\pi\alpha^2\beta\hbar c |G_M^n(s)|^2}{2s}$$

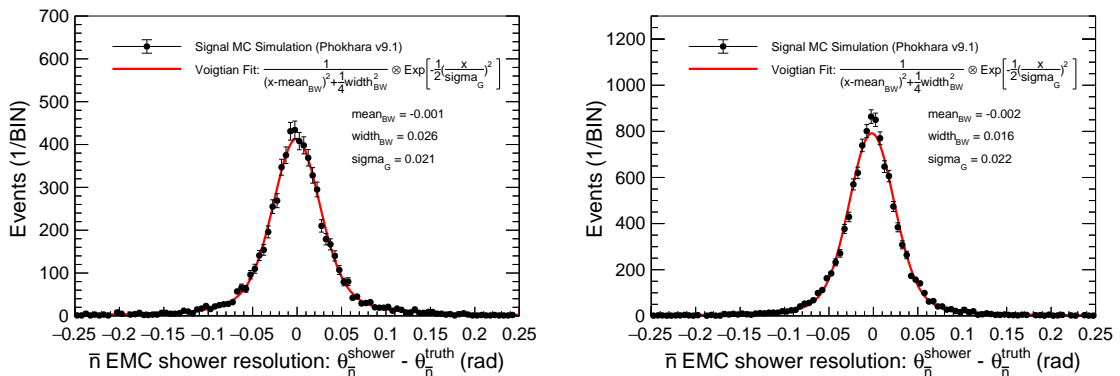


Fig. 9.4: The resolution of the \bar{n} EMC shower position reconstruction. (Left) At $\sqrt{s} = 2.1266$ GeV, (right) at $\sqrt{s} = 2.3960$ GeV. As a fit function for the resolution extraction, the Voigtian distribution is used, which is a Breit-Wigner-Distribution convoluted with a Gaussian.

Here, $R_{\text{em}}^{\text{n}}(s)$ and the normalization $A(s)$ are free parameters of the function to be determined by the fit. \hbar is the reduced Planck constant, c is the speed of light, their quadratic product is $(\hbar \cdot c)^2 = 0.389379338 \times 10^6 \text{ GeV}^2 \cdot \text{nb}$.

The raw angular distribution of the antineutron has been extracted in Chapter 7 with two complementary methods, the simple fit to the opening angle between the neutron and antineutron (listed in Table 7.3) and the massive Monte Carlo simulation based study, as summarized in Table 7.4. Several corrections need to be applied to the raw angular distribution, as discussed in Chapter 8. The following corrections are extracted using the Phokhara v9.1 event generator. As a cross-check, the same corrections are determined with the ConExc event generator, as shown in the Appendix A:

- The differential signal event reconstruction efficiency $\frac{d\epsilon^{\text{MC}}}{d\cos\theta_{\bar{n}}}$.
- The efficiency corrections for differences between collider data and signal Monte Carlo simulation $\frac{dC_{\text{dm}}}{d\cos\theta_{\bar{n}}}$, $\frac{dC_{\text{ee}}}{d\cos\theta_{\bar{n}}}$, and $\frac{dC_{\text{muc}}}{d\cos\theta_{\bar{n}}}$.
- The trigger efficiency correction $\frac{dC_{\text{trg}}}{d\cos\theta_{\bar{n}}}$.
- The radiative correction factor $\frac{d(1+\delta)}{d\cos\theta_{\bar{n}}}$.

All used corrections are shown for the data set at $\sqrt{s} = 2.3960 \text{ GeV}$ in Figure 9.5.

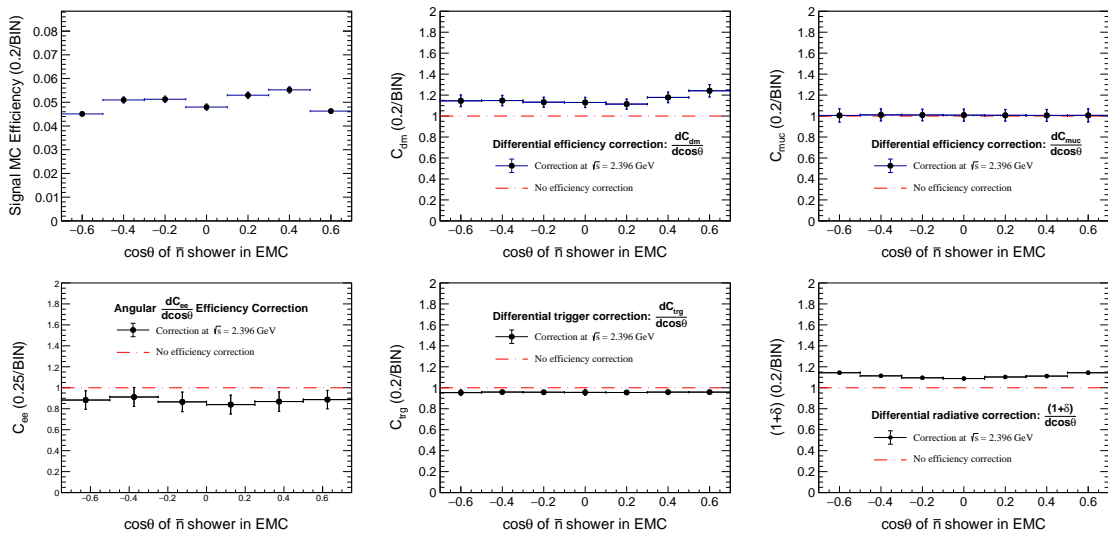


Fig. 9.5: Differential selection efficiency (top left), efficiency correction $\frac{dC_{\text{dm}}}{d\cos\theta_{\bar{n}}}$ (top middle), $\frac{dC_{\text{ee}}}{d\cos\theta_{\bar{n}}}$ (top right), $\frac{dC_{\text{muc}}}{d\cos\theta_{\bar{n}}}$ (bottom left), $\frac{dC_{\text{trg}}}{d\cos\theta_{\bar{n}}}$ (bottom middle), and the radiative correction factor $\frac{d(1+\delta)}{d\cos\theta_{\bar{n}}}$ (bottom right) at $\sqrt{s} = 2.3960 \text{ GeV}$. The red dashed lines indicate no correction.

As can be seen from Figure 9.5, the angular corrections $\frac{dC_{ee}}{d\cos\theta_{\bar{n}}}$, $\frac{dC_{trg}}{d\cos\theta_{\bar{n}}}$, and $\frac{dC_{muc}}{d\cos\theta_{\bar{n}}}$ are flat within their individual bin uncertainties. Therefore the two former corrections are used as an absolute correction to the normalization of the angular distribution, while the latter is included in the systematic uncertainty, since negligible due to its size.

To obtain the magnetic form factor and the form factor ratio, the right side of Equation 9.8 is used as the fit function to the corrected angular distribution. The fit is optimized by minimizing the $\chi^2 = \sum_i \frac{N_i^{\text{ang}} - N_i^{\text{cor}}}{\Delta N_i}$, with N_i^{ang} the fit value, N_i^{cor} the corrected signal yield in bin i and ΔN_i the error in the corresponding bin i . Figure 9.6 shows the difference between the fit results with the simple fit from Equation 9.5, the integral-over-the-bin-width form of the fit, and the fit function from Equation 9.8 with the position resolution taken into account. The comparison is shown for the combined data set at $\sqrt{s} = (2.3864 - 2.3960) = 2.3936$ GeV. No obvious difference can be seen between the fit results under different conditions. The resolution effects are negligible. For the final results, a fit with the right side of the Equation 9.8 is used while neglecting the convolution with the position resolution.

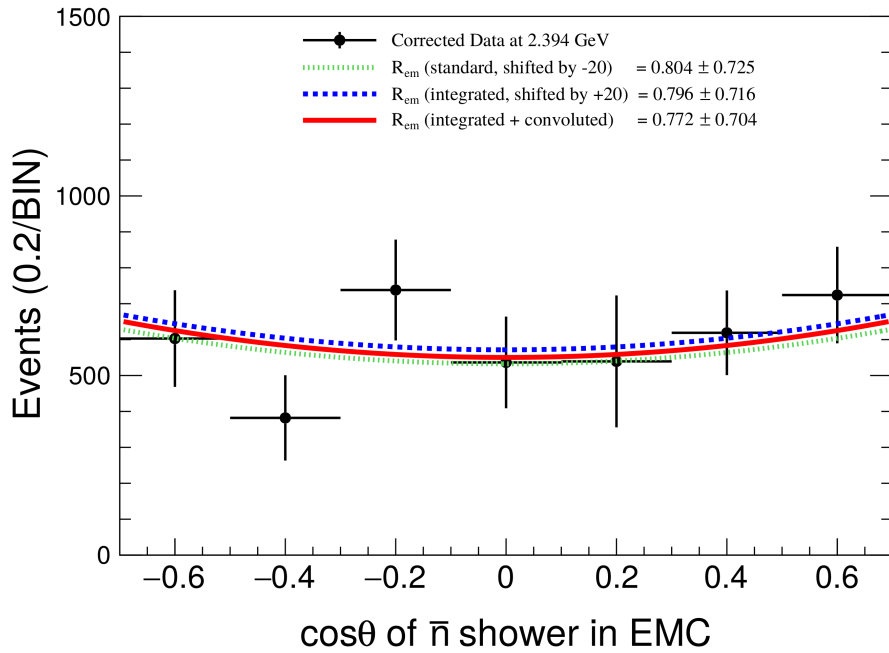


Fig. 9.6: Differential signal yield in data at $\sqrt{s} = 2.3936$ GeV corrected with the differential reconstruction efficiency $\frac{d\epsilon^{\text{MC}}}{d\cos\theta_{\bar{n}}}$, the differential corrections $\frac{dC_{dm}}{d\cos\theta_{\bar{n}}}$, $\frac{d(1+\delta)}{d\cos\theta_{\bar{n}}}$, and the absolute corrections C_{ee} , C_{trg} . The green dashed curve (shifted by -20) is the fit from Equation 9.5, the blue dashed curve (shifted by +20) uses the integral-over-bin-width form, the red curve is the fit from Equation 9.8 additionally taking into account the position resolution.

The data sets used for the angular analysis are the corrected collider data at $\sqrt{s} = 2.1266$ GeV and four luminosity weighted combinations at $\sqrt{s} = (2.0000 - 2.1000) = 2.0516$ GeV, at $\sqrt{s} = (2.1500 - 2.3094) = 2.2380$ GeV, at $\sqrt{s} = (2.3864 - 2.3960) = 2.3936$ GeV, and at $\sqrt{s} = (2.6444 - 2.9500) = 2.8130$ GeV. Figure 9.7 shows the angular fit results with the function from Equation 9.8 after minimization of the χ^2 .

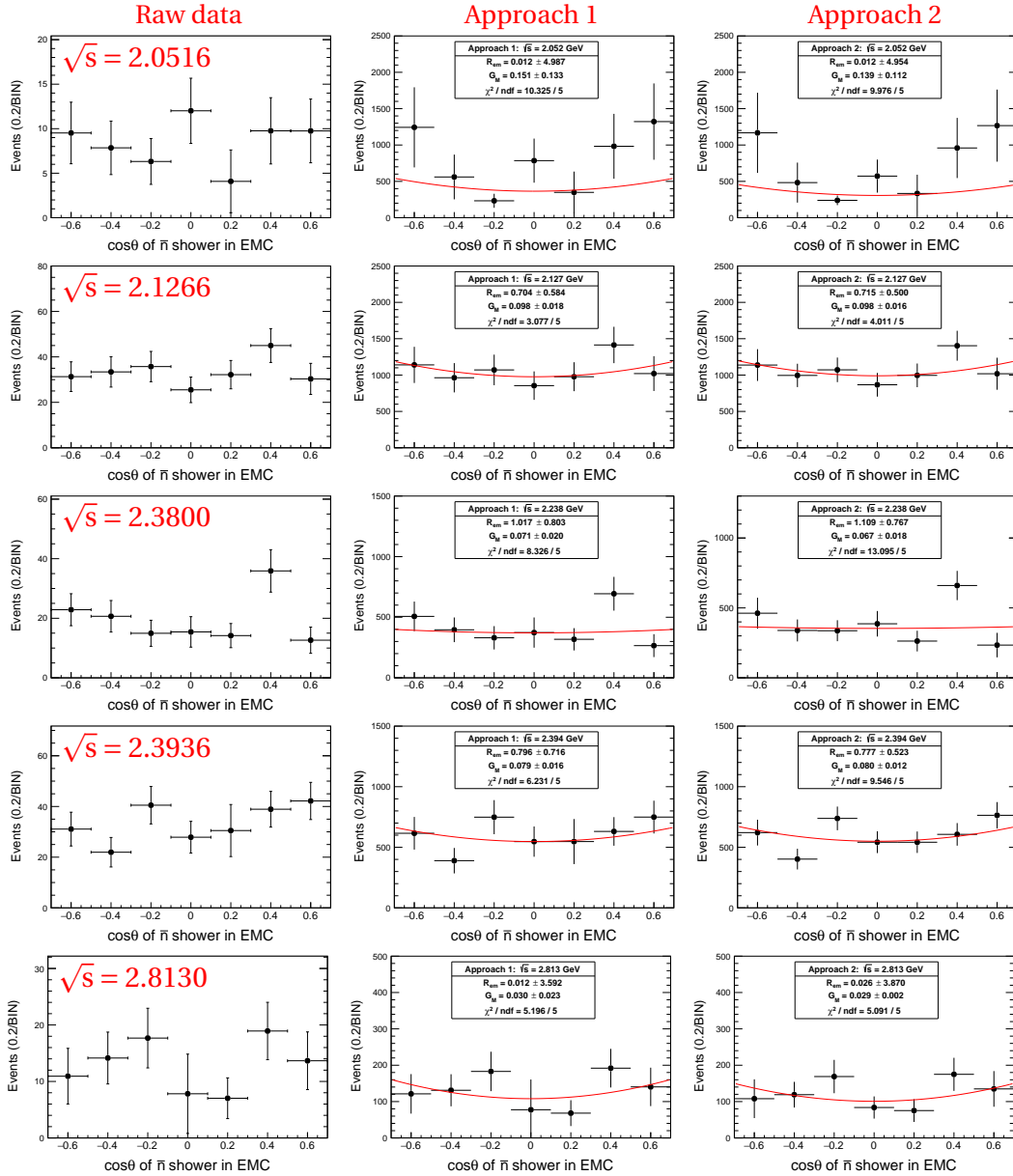


Fig. 9.7: (Left) The raw signal yield from collider data extracted with approach 1 in Section 7.3. The histograms for the combined data sets are added here before correction for a better visualization. (Middle) Angular analysis using the corrected signal yield extracted with approach 1. (Right) Angular analysis using the corrected signal yield extracted with approach 2. The red line is the fit function from Equation 9.8.

The results for $G_M^{\text{ind}}(s)$ and $R_{\text{em}}^{\text{ind}}(s) = |G_E^{\text{n}}(s)|/|G_M^{\text{n}}(s)|$ are summarized in Table 9.4 and shown in the Figures 9.8 and 9.9. Two sets of results are compared, using the right side of the Equation 9.8 to fit the corrected differential signal yield obtained with the simple fit to the opening angle (approach 1) and the massive MC simulation study for the signal yield extraction (approach 2), respectively, as described in Section 7.3. While the results at $\sqrt{s} = 2.1266$ GeV, $\sqrt{s} = 2.2380$ GeV, and $\sqrt{s} = 2.3936$ GeV are considered as stable, the results at the other two \sqrt{s} are subject to strong fluctuations due to the poor statistics in the extracted signal events from data. The two sets of results are consistent within their uncertainties. The discussion of the results is postponed to Chapter 11, where the combined results from the three signal selection classification categories are discussed under an increased statistics and including the systematic uncertainty.

\sqrt{s} (GeV)	Signal Yield from Standard Fit			Signal Yield from MC Study		
	$R_{\text{em}}^{\text{ind}}(s)$	$ G_M^{\text{ind}}(s) (\times 10^2)$	χ^2/ndf	$R_{\text{em}}^{\text{ind}}(s)$	$ G_M^{\text{ind}}(s) (\times 10^2)$	χ^2/ndf
2.0000	} 0.012 ± 4.987	15.12 ± 13.31	10.3/5	0.012 ± 4.954	13.86 ± 11.23	10.0/5
2.0500						
2.1000						
2.1266	0.704 ± 0.584	9.81 ± 1.84	3.1/5	0.715 ± 0.500	9.83 ± 1.62	4.0/5
2.1500	} 1.017 ± 0.803	7.11 ± 1.95	8.3/5	1.109 ± 0.767	6.68 ± 1.83	13.1/5
2.1750						
2.2000						
2.2324						
2.3094	} 0.796 ± 0.716	7.90 ± 1.55	6.2/5	0.777 ± 0.523	7.97 ± 1.17	9.5/5
2.3864						
2.3960						
2.6454	} 0.012 ± 3.592	3.05 ± 0.23	5.2/5	0.026 ± 3.870	2.95 ± 0.22	5.1/5
2.9000						
2.9500						
2.9810	} not extracted					
3.0000						
3.0200						
3.0800						

Table 9.4: Individual results for $|G_M^{\text{ind}}(s)|$ and $R_{\text{em}}^{\text{ind}}(s) = |G_E^{\text{n}}(s)|/|G_M^{\text{n}}(s)|$ for the category C classified signal events, extracted with the angular analysis. The left set of results uses the signal yield extracted with approach 1 from Table 7.3, while the rights set uses the signal yield extracted with approach 2 from Table 7.4. The shown uncertainties are statistical only.

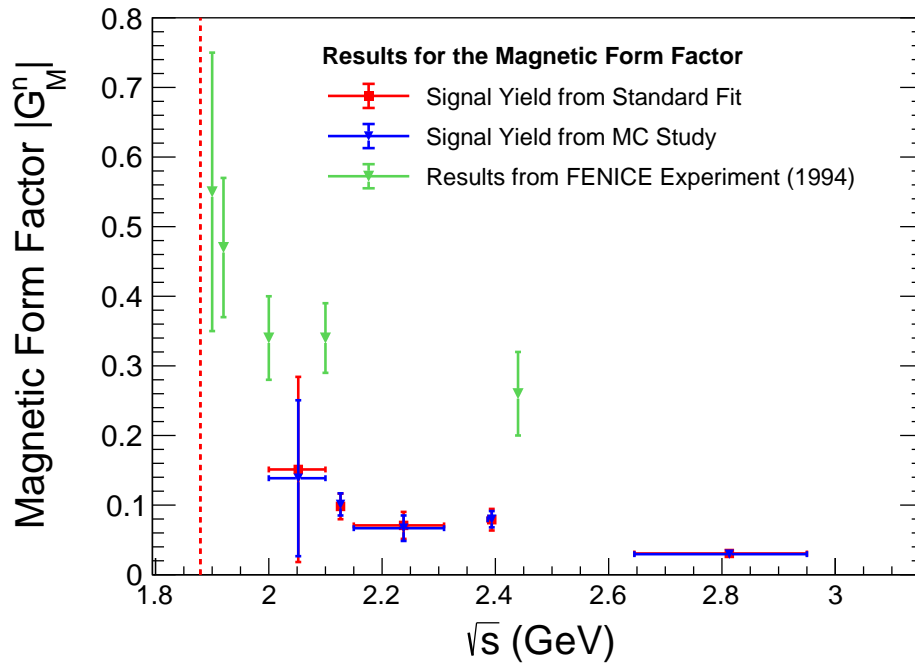


Fig. 9.8: Individual results for the magnetic form factor of the neutron $|G_M^{\text{ind}}(s)|$ from category C classified signal events. Red squared are the results with approach 1, blue triangles are results with the approach 2, as shown in Table 9.4. Green downward triangles are results from the FENICE experiment extracted from the Born cross section under the hypothesis $G_E^n = 0$. The red dashed line shows the production threshold for the signal process. The errors of the results from this analysis are statistical.

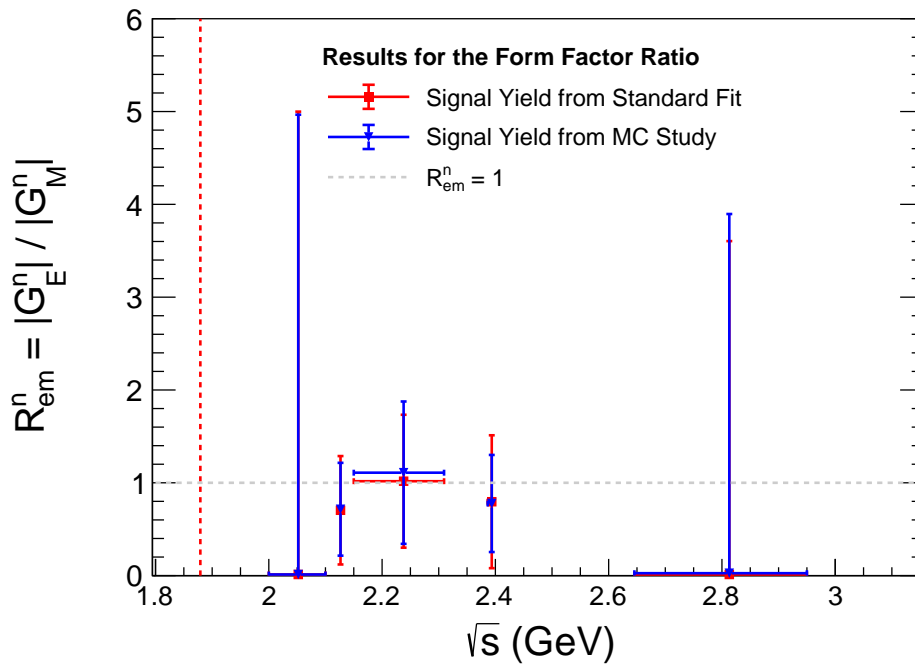


Fig. 9.9: The form factor ratio of the neutron. The data and notation is the same as in Figure 9.8.

9.4 Extraction of the combined results for $G_M^n(s)$ and $R_{em}^n(s)$

The individual results for the magnetic form factor and the form factor ratio of the neutron have been extracted for the category C classified signal events (this work) in the previous section. To improve the precision and the stability of the results from the angular analysis, the magnetic form factor $G_M^n(s)$ and the form factor ratio $R_{em}^n(s)$ are extracted simultaneously from the three signal selection classification categories in the following. As in the case of the combined results for the Born cross section and the effective form factor of the neutron in Section 9.2, the two external sets of angular distributions (denoted as A and B) are determined by using the signal MC simulation with the ConExc generator included in the BesEvtGen-00-03-18 framework. Therefore the angular distributions from this work (denoted as C) are calculated with the efficiency corrections extracted with the ConExc signal MC simulation for consistency (and using the MC based signal yield extraction), in comparison with the individual results shown in the previous section, which are calculated with the event generator Phokhara v9.1.

Three different approaches for the extraction of the final results are studied. All three of them have the fit function to the angular distributions in common, using the integral-over-the-bin-width form of the right side of Equation 9.8. The three different approaches are discussed below.

- Approach 1: The three corrected angular distributions of the antineutron per data set are subject to a simultaneous angular analysis. The fit function is applied simultaneously to each sub-set, while the global χ^2 is minimized. The results are shown in Figure 9.10.
- Approach 2: The three corrected angular distributions of the antineutron per data set are added, using the error weighting method in Equation 9.4 for the calculation of the combined content and uncertainty in each bin. The fit function from Equation 9.8 is applied to the resulting distribution at each analyzed \sqrt{s} . The results from the approach 2 are shown in Figure 9.11.
- Approach 3: This approach uses an extensive Monte Carlo simulation to extract the results. The details of the MC based analysis are discussed in the following. The results are shown in the Figures 9.13 and 9.14.

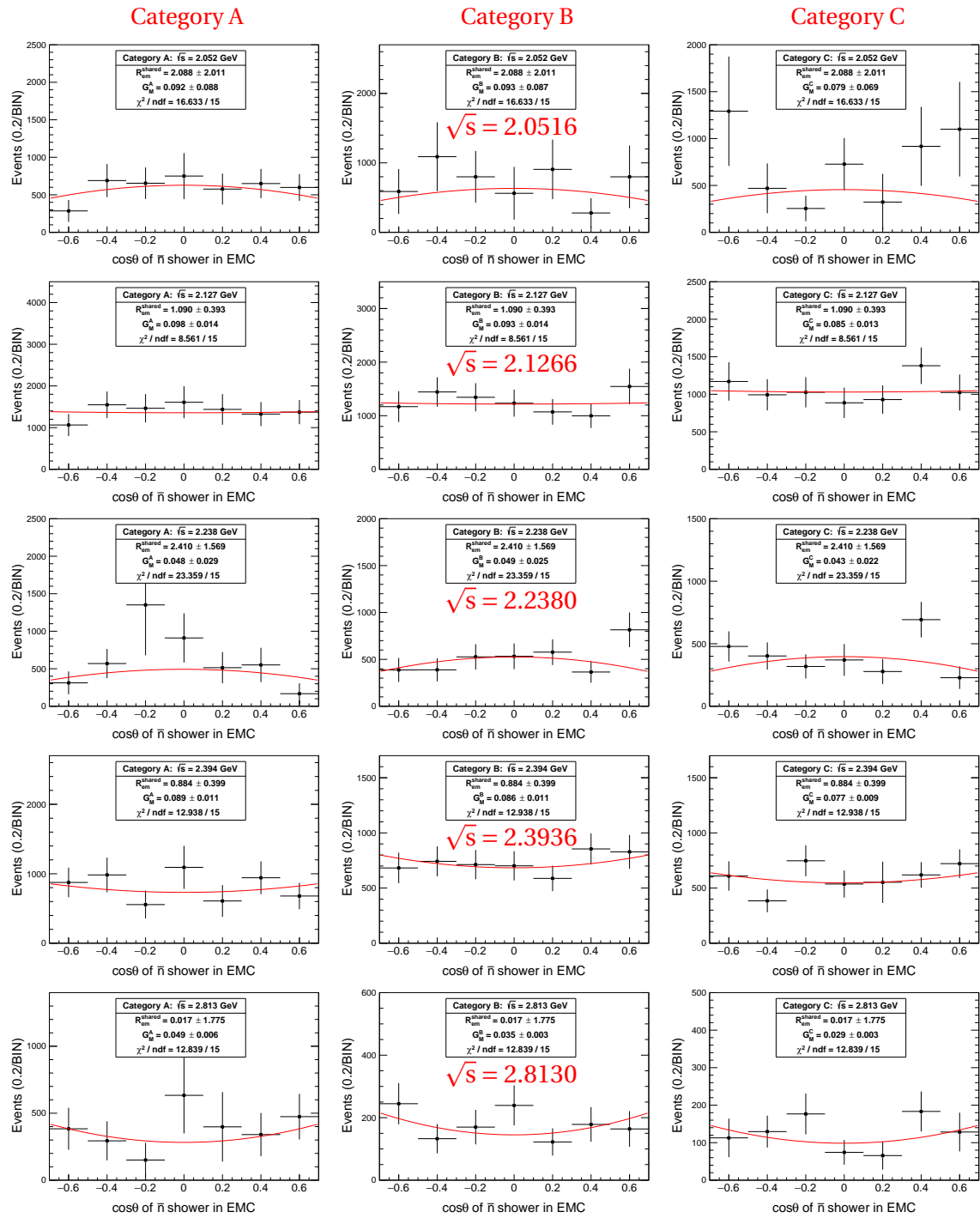


Fig. 9.10: Simultaneous angular analysis with approach 1: fit to the corrected angular distributions from the three categories for the five data sets at $\sqrt{s} = 2.0516$ GeV (top column), at 2.1266 GeV (2nd column), at 2.2380 GeV (3rd column), 2.3936 (4rd column), and 2.8130 GeV (column row). The left, middle and right row shows results from category A, B, and C, respectively. Black dots represent the corrected data yields, the red lines show the fit results with the right side of Equation 9.8 and the shared fit parameter for the ratio R_{em}^{simu} .

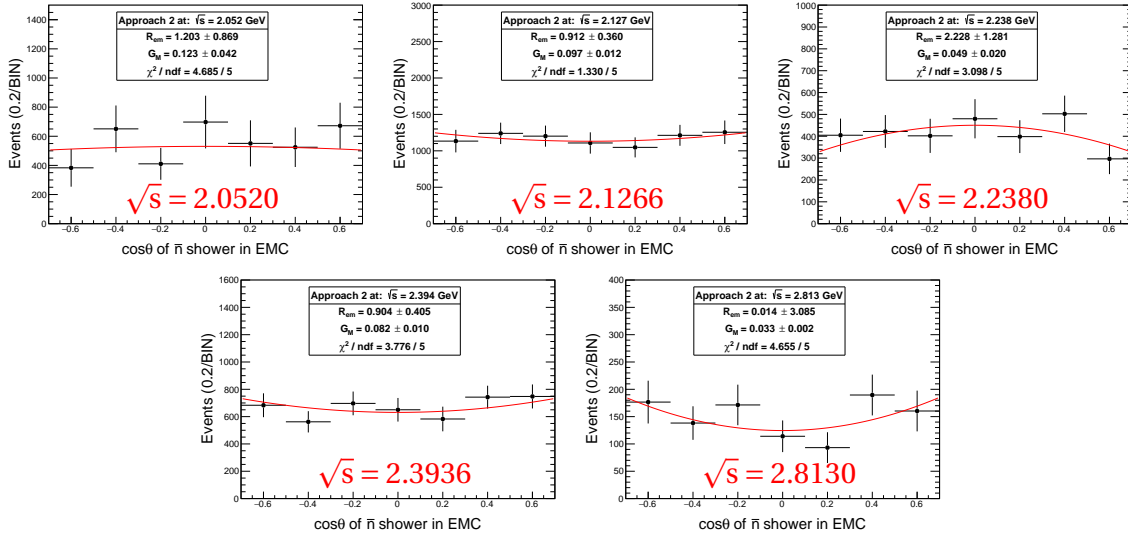


Fig. 9.11: Simultaneous angular analysis with approach 2: the corrected angular distributions from the three categories for the five data sets at $\sqrt{s} = 2.0516$ GeV (top left), at 2.1266 GeV (top middle), at 2.2380 GeV (top right), 2.3936 (bottom left), and 2.8130 GeV (bottom right) are added by using the error-weighted method from Equation 9.4. Black dots represent the combined and corrected signal yields from data, the red lines show the fit results with the right side of Equation 9.8 and the shared fit parameter for the ratio R_{em}^{add} .

The Monte Carlo simulation based analysis for the extraction of the magnetic form factor and form factor ratio of the neutron is considered due to the following reasons: even with the simultaneous approach for the angular analysis, several bins in the combined data sets still suffer from a very low number of selected events. For example, the data set at $\sqrt{s} = (2.6444 - 2.9500)$ GeV only contains approximately 43, 98, and 52 reconstructed signal events over the whole analyzed $\cos\theta_{\bar{n}}$ range from the signal classification categories A, B, and C, respectively, distributed over 7 bins. The standard fit routine (i.e. approach 1) is using the CERN ROOT's TMinuit algorithm, which takes into account symmetric Gaussian statistical bin uncertainties for the fit results optimization. As a general approximation, this approach can only be used for bin values above 30 events, which is not the case for the discussed example. If bin values contain less than 30 events, the uncertainty should be asymmetric and the whole error calculation is not following anymore a straight forward textbook approach for the statistical uncertainty treatment. The error treatment of approach 1 and 2 is performed under the assumption of Gaussian errors, which is not true for all bins in every analyzed data set, as discussed above. Following this discussion, the statistical uncertainty must be treated in a different way, since the used fit routine doesn't provide an adequate approximation for data sets with a low statistics per bin.

The MC based analysis is performed with the goal to extract the results for the magnetic form factor and form factor ratio of the neutron with a more precise treatment of the statistical uncertainty as it is possible with the approaches 1 and 2, as discussed above. Following, the details for the MC based analysis are discussed at the example of the combined data set at $\sqrt{s} = 2.8130$. In the first step, the value of the form factor ratio R_{em}^{mcbda} (mcbda = MC based data analysis) is determined:

- The distributions from the three signal selection classification categories A, B, and C, as shown in Figure 9.10 (bottom), are used as seeds to generate 100k random MC distributions per category, taking into account the statistical fluctuation in each bin and the corresponding total statistics for the reconstructed events (43, 98, and 52 in category A, B, and C, respectively). An example for a set of random distribution is shown in Figure 9.12.
- Each set of three MC distribution (for the three categories) is fitted simultaneously by the nominal fit routine from Equation 9.8. The resulting distribution of the results for the form factor ratio, extracted from the 100k simulations, is shown in Figure 9.13 (left).
- In an optimal case, the distribution of the results for the form factor ratio is expected to follow a Gaussian function, with the parameter for the mean value representing the true form factor ratio and the sigma parameter representing the statistical uncertainty. As can be seen in Figure 9.13 (left), the distribution is not Gaussian-like. The reasons for this observation are the above discussed low statistics in the collider data, which is used as seed for the random angular distribution generation, as well as the specific boundaries of fit function, i.e. the lower limit for the ratio parameter

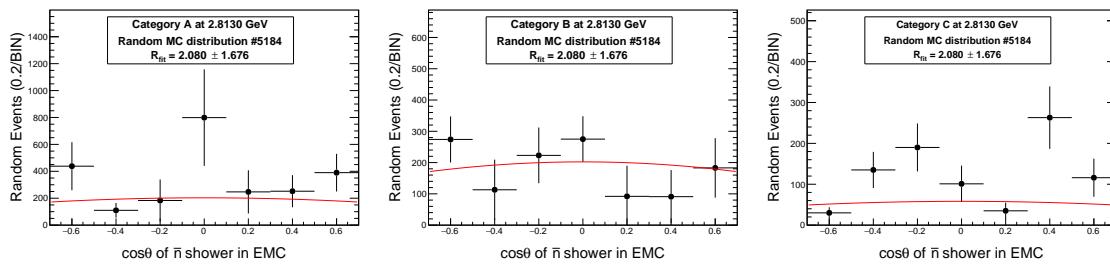


Fig. 9.12: Random MC angular distributions based on the corrected angular distributions of the antineutron from the three signal selection classification categories A, B, and C (Figure 9.10 bottom) at $\sqrt{s} = 2.8130$ GeV. The distributions are generated within the statistical fluctuation of the original distributions from data under the corresponding total statistics (43, 98, and 52 reconstructed events in category A, B, and C, respectively). The red lines show the simultaneous fit with the shared parameter for the ratio R_{em}^{simu} .

of 0. This leads to the observed non-Gaussian-like behavior of the resulting ratio distribution and to the fact, that a standard approach for the extraction of the mean value for the ratio and the Gaussian width as the statistical uncertainty is not applicable in this case. Instead, a fit with a convoluted Gaussian and Landau functions is used to extract the most probable value (MPV) as the results for the form factor ratio R_{em}^{mcbda} . The MVP is defined as the value which is extracted with the highest probability and is not equal to the mean or median for the discussed case due to the highly skewed distribution. Additionally, the results from the 100k simulations for the magnetic form factor $G_M^{i,mcbda}(s)$ is extracted for the three categories (one distribution per category). For each fit result (one resulting value for R_{em}^{mcbda} and one value for $G_M^{i,mcbda}(s)$ per category), the correlations between the determined parameters is obtained. For each distribution, the MPV and it's corresponding error is extracted. An example of the $G_M^{i,mcbda}(s)$ distributions for the data set at $\sqrt{s} = 2.3936$ is shown in Figure 9.15. The asymmetry of the uncertainty is negligible, therefore the larger value is used conservatively as the statistical uncertainty.

In the second step, the statistical uncertainty ΔR_{em}^{mcbda} is extracted for the result obtained in the first step. In the following approach a set of varying input values for the FF ratio R_{in} with the corresponding statistics of the reconstructed signal events in data is used to

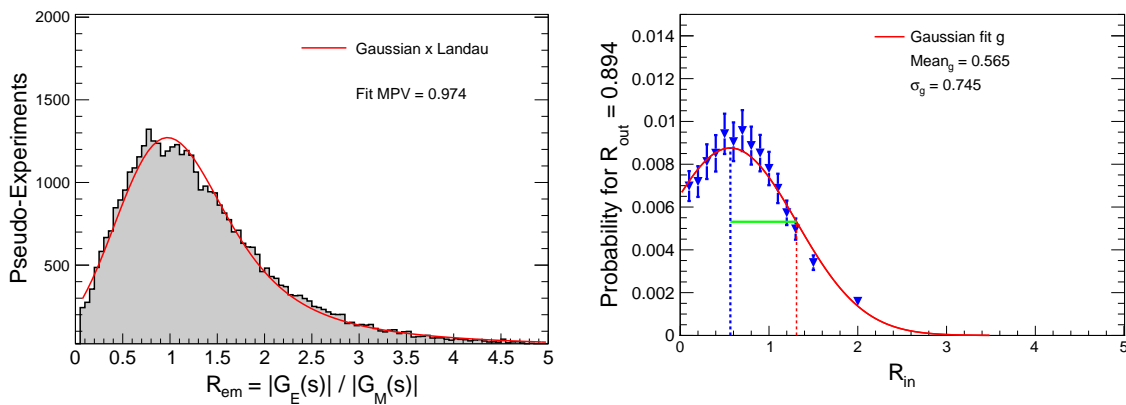


Fig. 9.13: (Left) Extraction of the most probable value for the ratio R_{em}^{mcbda} from the distribution of 100k MC simulation results based on the distributions for the combined data set at $\sqrt{s} = 2.8130$ (as shown in Figure 9.10 bottom) and the individual statistics for the reconstructed events per category. The fit function is a convolution of a Gaussian and a Landau function, shown as a red line. (Right) Extraction of the statistical uncertainty ΔR_{em}^{mcbda} for the FF's ratio $R_{em}^{mcbda} = 0.974$ from a set of MC simulations, based on the individual statistics for the reconstructed events per category and varying input values R_{in} . The fit function is a Gaussian shown as a red line. The standard deviation of the Gaussian fit is taken as the statistical uncertainty of the form factor ratio $R_{em}^{mcbda} = 0.974$.

simulate the spread of the previously obtained result for R_{em}^{mcbda} . The standard deviation of the spread is considered as the statistical uncertainty:

- First, a set of Monte Carlo simulations for angular distributions is produced with varying input values for the ratio R_{in} (i.e. $R_{in} = [0.1 - 2.0]$). This approach is similar to the determination of the results for R_{em}^{mcbda} discussed above. All the characteristics of the simulation stay the same (100k simulations per R_{in} value, three distributions per simulation), except that instead of using the corrected collider data angular distributions of the antineutron from the three categories as seeds for the MC simulation, an arbitrary value for R_{in} is used together with the correct statistics from the collider data for each of the three angular distributions (i.e. 43, 98, and 52 reconstructed events in category A, B, and C, respectively, at $\sqrt{s} = 2.813$ GeV).
- Each set of three distribution is fitted as described in the approach 1 and the most probable value for the FF ratio is extracted. A distribution with the resulting MPV's for the FF is obtained for each R_{in} . The following quantity is calculated with the results for each R_{in} : the number of entries in the bin which represents the previously obtained value for R_{em}^{mcbda} divided by the number of MC simulation (=100000). This quantity can be considered as a conditional pseudo-probability distribution $W(R_{em}^{mcbda}, R_{in}) = \text{entries in bin}(R_{em}^{mcbda}) / \text{total entries}$. This quantity is also dependent on the bin width, but since the bin width is constant for all simulations, this dependence is canceled out. For each R_{in} , a result for $W(R_{em}^{mcbda}, R_{in})$ is obtained. The distribution of $W(R_{em}^{mcbda} = 0.974, R_{in} = [0.1 - 2.0])$ at $\sqrt{s} = 2.813$ GeV is shown in Figure 9.13 (right).
- The distribution of $W(R_{em}^{mcbda}, R_{in})$ is subject to a fit with a Gaussian function. Since only the standard deviation (FWHM) of the distribution is required for further analysis, a normalization to unity, as it would be required for a true probability distribution, is not necessary, due to the fact that the normalization does not change the FWHM value. To provide reasonable and consistent errors for the discussed fit routine, a relative uncertainty of $\Delta W(R_{em}^{mcbda}, R_{in}) = 10\%$ is considered for each extracted pseudo-probability value $W(R_{em}^{mcbda}, R_{in})$. The fit with a Gaussian function is performed and the statistical uncertainty ΔR_{em}^{mcbda} is derived from the Gaussian fit parameter for the standard deviation (shown as the green line in Figure 9.13 right).

The results for R_{em}^{mcbda} and the corresponding statistical uncertainty ΔR_{em}^{mcbda} from this approach at other \sqrt{s} are shown in Figure 9.14.

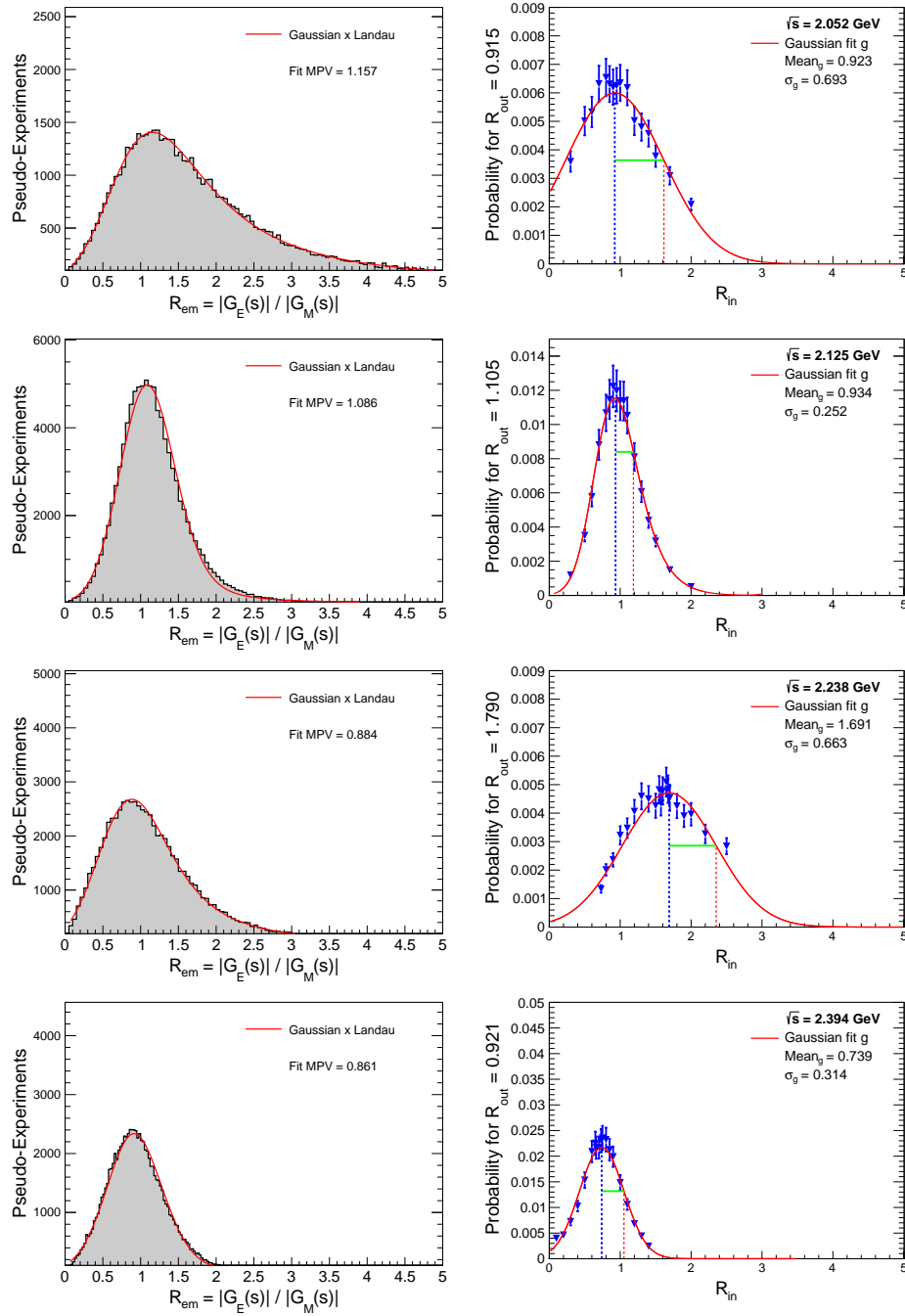


Fig. 9.14: (Left) Determination of the most probable value for the ratio. The grey histograms show the distributions of the ratio from the 100k MC simulations. The red line shows the fit results using a Landau function convoluted with a Gaussian. The most probable value is listed in the figures and denoted as R_{em}^{mcbda} . (Right) MC simulation based data analysis of the corresponding statistical uncertainty ΔR_{em}^{mcbda} . The blue triangles with errors show results for the conditional probability $W(R_{em}^{mcbda}, R_{in})$ from the second step of the strategy with varying R_{in} . The red line is a Gaussian function for the determination of the standard deviation of the $W(R_{em}^{mcbda}, R_{in})$ distribution, which is considered as the statistical uncertainty ΔR_{em}^{mcbda} for the FF ratio R_{em}^{mcbda} .

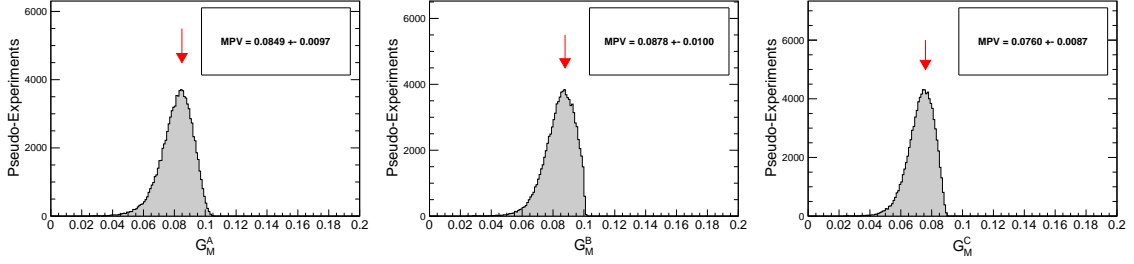


Fig. 9.15: The distributions of the results for the category-individual magnetic form factor $|G_M^{i,mcbda}(s)|$ extracted from 100k simulations at $\sqrt{s} = 2.3936$ GeV. The asymmetry of the uncertainty is negligible, therefore the larger value is used conservatively as the statistical uncertainty.

Approach 1 and 3 have the calculation of the average magnetic form factor in common. Before the combination of the results, a possible correlation between the free parameters from the simultaneous fit are identified. The extracted results for the category-individual magnetic form factors $|G_M^i(s)|$ ($i = A, B, C$) correlate with each other and with the parameter for the form factor ratio $R_{em}^{shared}(s)$. These correlations need to be taken into account for the statistical uncertainty of the individual magnetic form factor results via:

$$\Delta G_M^i = J V_{R,A_i} J^T \quad (9.9)$$

with the Jacobian matrix J and its transpose J^T :

$$J = \begin{pmatrix} \frac{\partial G_M^A}{\partial R_{em}} & \frac{\partial G_M^A}{\partial A_1} & \frac{\partial G_M^A}{\partial A_2} & \frac{\partial G_M^A}{\partial A_3} \\ \frac{\partial G_M^B}{\partial R_{em}} & \frac{\partial G_M^B}{\partial A_1} & \frac{\partial G_M^B}{\partial A_2} & \frac{\partial G_M^B}{\partial A_3} \\ \frac{\partial G_M^C}{\partial R_{em}} & \frac{\partial G_M^C}{\partial A_1} & \frac{\partial G_M^C}{\partial A_2} & \frac{\partial G_M^C}{\partial A_3} \end{pmatrix} = \begin{pmatrix} -\frac{G_M^A \tau R_{em}}{1 + \tau R_{em}^2} & \frac{G_M^A}{2A_1} & 0 & 0 \\ -\frac{G_M^B \tau R_{em}}{1 + \tau R_{em}^2} & 0 & \frac{G_M^B}{2A_2} & 0 \\ -\frac{G_M^C \tau R_{em}}{1 + \tau R_{em}^2} & 0 & 0 & \frac{G_M^C}{2A_3} \end{pmatrix}$$

and the covariance matrix:

$$V_{R,A_i} = \begin{pmatrix} \Delta R_{em}^2 & \text{cov}(R_{em}, A_1) & \text{cov}(R_{em}, A_2) & \text{cov}(R_{em}, A_3) \\ \text{cov}(R_{em}, A_1) & \Delta A_1^2 & \text{cov}(A_1, A_2) & \text{cov}(A_1, A_3) \\ \text{cov}(R_{em}, A_2) & \text{cov}(A_1, A_2) & \Delta A_2^2 & \text{cov}(A_2, A_3) \\ \text{cov}(R_{em}, A_3) & \text{cov}(A_1, A_3) & \text{cov}(A_2, A_3) & \Delta A_3^2 \end{pmatrix}$$

The parameters A_i and ΔA_i ($i = 1, 2, 3$) are the normalization factors and the corresponding statistical errors from the three individual angular distributions (one per category), which are simultaneously fitted using the Equation 9.8. The average value $|G_M^{av}(s)|$ and its uncertainty is determined similar to the combined results for the Born cross section, using

the formula for the error-weighted combination from Equation 9.4. The results for the magnetic form factor and the form factor ratio, simultaneously extracted from the three signal selection classification categories, are shown for the three discussed approaches in Table 9.5.

\sqrt{s} (GeV)	Approach 1: Results from the simultaneous fit				
	$G_M^A (\times 10^2)$	$G_M^B (\times 10^2)$	$G_M^C (\times 10^2)$	$G_M^{\text{av, simu}} (\times 10^2)$	$R_{\text{em}}^{\text{simu}}$
2.0000 - 2.1000	9.2 ± 6.2	9.2 ± 6.5	7.9 ± 5.9	8.7 ± 3.6	2.088 ± 2.011
2.1266	9.8 ± 1.4	9.3 ± 1.4	8.5 ± 1.3	9.2 ± 0.8	1.090 ± 0.393
2.1500 - 2.3094	4.8 ± 2.2	4.9 ± 2.4	4.3 ± 2.1	4.6 ± 1.3	2.410 ± 1.569
2.3864 - 2.3960	8.9 ± 1.1	8.6 ± 1.1	7.7 ± 0.9	8.3 ± 0.6	0.884 ± 0.399
2.6454 - 2.9500	4.7 ± 0.4	3.5 ± 0.2	2.9 ± 0.2	3.4 ± 0.1	0.017 ± 1.219
\sqrt{s} (GeV)	Approach 2: Results from the addition of the categories				
	-		$G_M^{\text{add}} (\times 10^2)$	$R_{\text{em}}^{\text{add}}$	
2.0000 - 2.1000	-		12.3 ± 4.2	1.203 ± 0.869	
2.1266	-		9.7 ± 1.2	0.912 ± 0.360	
2.1500 - 2.3094	-		4.9 ± 2.0	2.228 ± 1.281	
2.3864 - 2.3960	-		8.2 ± 1.0	0.904 ± 0.405	
2.6454 - 2.9500	-		3.3 ± 0.2	0.014 ± 3.085	
\sqrt{s} (GeV)	Approach 3: Results from the MC simulation based data analysis				
	$G_M^{\text{A,MPV}} (\times 10^2)$	$G_M^{\text{B,MPV}} (\times 10^2)$	$G_M^{\text{C,MPV}} (\times 10^2)$	$G_M^{\text{av, mcbda}} (\times 10^2)$	$R_{\text{em}}^{\text{mcbda}}$
2.0000 - 2.1000	12.7 ± 4.0	15.7 ± 4.0	10.7 ± 3.4	12.5 ± 2.3	1.157 ± 0.693
2.1266	9.6 ± 1.1	9.5 ± 1.1	8.2 ± 0.9	9.0 ± 0.6	1.086 ± 0.252
2.1500 - 2.3094	7.4 ± 2.0	9.4 ± 2.5	7.5 ± 2.0	7.9 ± 1.2	0.884 ± 0.663
2.3864 - 2.3960	8.5 ± 1.0	8.8 ± 1.0	7.6 ± 0.9	8.2 ± 0.5	0.861 ± 0.314
2.6454 - 2.9500	3.6 ± 0.8	3.3 ± 0.8	2.3 ± 0.5	2.8 ± 0.4	0.974 ± 0.745

Table 9.5: Results for the category-individual magnetic form factors G_M^i , their average G_M^{av} , and form factor ratio $R_{\text{em}} = |G_E|/|G_M|$ at $\sqrt{s} = 2.1266$ and the combined data samples obtained with the three approaches discussed in this section. The errors are statistical.

Figure 9.16 shows a comparison between the results from the three used approached for the average magnetic form factor and the form factor ratio of the neutron.

From Table 9.5 and Figure 9.16 can be seen, that the results from the three approaches are consistent within their statistical uncertainties. The results from the different approaches for two large luminosity data sets at $\sqrt{s} = 2.1266$ GeV and at $\sqrt{s} (2.3864 - 2.3960) = 2.3936$ GeV with the largest statistics per bin are very well in agreement. The results at $\sqrt{s} = (2.0000 - 2.1000) = 2.0520$ GeV for the approach 2 and 3 show similar values, while the MC simulation based data analysis approach has a significantly smaller uncertainty. The results for the data set at $\sqrt{s} = (2.1500 - 2.3094) = 2.2380$ GeV from the approach 1 and 2 show similar values, but are in agreement with the results from approach 3 within the uncertainties. The results for the data set at $\sqrt{s} = (2.644 - 2.9500) = 2.8130$ GeV show the advantage of the approach 3. The results for the form factor ratio obtained with the first 2 approaches show very small values with an unphysical uncertainty including negative values, while approach 3 provides more precise results with a value and uncertainty within the expectations. We consider the approach 3 (using a massive MC simulation for the extraction of the results) as the most precise one. For the final results from this work and their discussion in Chapter 11, the values from approach 3 are used.

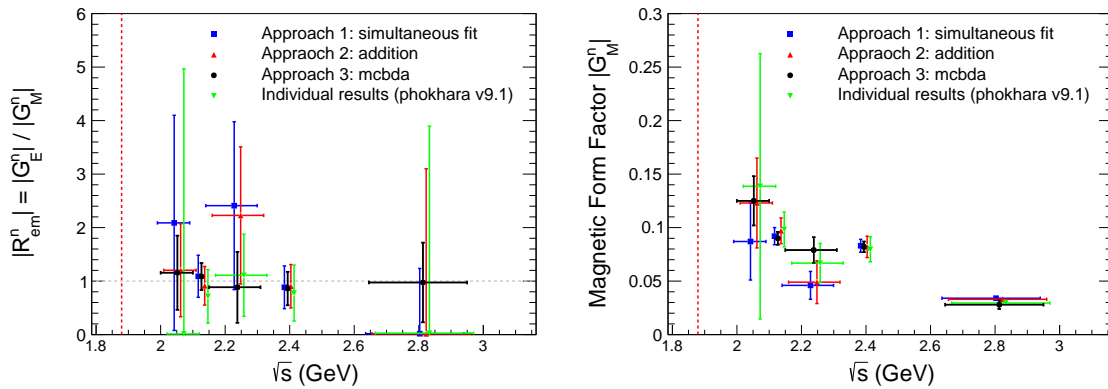


Fig. 9.16: The results for the form factor ratio (left) and the magnetic form factor of the neutron (right) with the three approaches discussed in this section. The blue, red, and black data are from approach 1, 2, and 3, respectively. The uncertainties are statistical only. The results for the approach 1 and 2 are shifted by $\sqrt{s} - 0.01$ and $+ 0.01$ for a better visualization. The green data (shifted by $\sqrt{s} + 0.02$) show the individual results from Table 9.4 (approach 2).

Chapter 10

Systematic Uncertainties

In this chapter the systematic uncertainties of the results in this analysis are estimated. Sources for systematic uncertainties are discussed for the results on the Born cross section and effective form factor in Section 10.1, for the results of the form factor ratio in Section 10.2, and for the results of the magnetic form factor in Section 10.3. The systematic uncertainty on the combined results is discussed in Section 10.4.

10.1 Systematic uncertainty of the Born cross section

The systematic uncertainty of the Born cross section and effective form factor includes sources from the luminosity measurement, the signal selection, the signal yield extraction via the composite model and fit range, the simulation model dependence of the angular distribution, the trigger efficiency correction and the signal MC generator dependant radiative events contribution. The individual contributions are assumed to be independent. The total systematic uncertainty on the Born cross section $\delta_{\text{sys}}^\sigma$ at each \sqrt{s} is calculated to:

$$\delta_{\text{sys}}^\sigma(s) = \sqrt{\delta_{\text{L}}^2(s) + \delta_{\text{sel}}^2(s) + \delta_{\text{fit}}^2(s) + \delta_{\text{model}}^2(s) + \delta_{\text{trg}}^2(s) + \delta_{\text{rad}}^2(s)} \quad (10.1)$$

with the individual contributions discussed in the following.

10.1.1 the luminosity measurement

The uncertainty δ_{L} due to the luminosity measurement for the analyzed data sets is quoted from [27], where it was determined individually for each \sqrt{s} , never exceeding 1%. The uncertainty at $\sqrt{s} = 2.1266$ GeV is quoted from [198]. This uncertainty is added in

quadrature to the other systematic uncertainties, as shown in Equation 10.1, for the main results of this analysis (results for the category C classified selection strategy in Chapter 9), while treated independently and considered only once, when the results from the three selection categories A, B, and C are combined in Section 11. This approach prevents an underestimation of this source due to the combination of the systematic sources from three categories. The values for δ_L at all \sqrt{s} are shown in Table 10.2.

10.1.2 The signal selection

Due to potential differences between collider data and signal MC simulation, systematic shifts in the efficiency δ_{sel} can occur, when applying selection criteria. This kind of uncertainties shift the nominal results systematically into one direction and differ from statistical fluctuation uncertainties, which cancel out in the high statistical limit. Several approaches exist to study this kind of effects. One method uses the variation of selection requirements and comparing of the results to the nominal one. Another approach is the usage of a different, well understood selection strategy, uncorrelated to the main analysis. Here a different strategy is used. The differences between collider data and signal MC simulation have been carefully studied via data-driven methods in Chapter 8 and corrected accordingly. Therefore the possible systematical shift is taken into account within the efficiency correction in Chapter 8. One standard error of the efficiency correction factor for each selection criterion is used to obtain the systematic uncertainty δ_{sel} . The error of the correction factor C_{dm} includes the selection criteria $S_1 - S_7$, the errors ΔC_{ee} and ΔC_{muc} estimate the systematic uncertainties for the criteria S_8 and S_9 , respectively. The selection criterion S_{10} on the opening angle range $\langle \alpha_n^{\bar{n}} \rangle > 150^\circ$ is included into the systematic uncertainty of the fitting procedure in the next paragraph. The three systematic uncertainties are added in quadrature to calculate the systematics of the signal selection δ_{sel} . All contributions to δ_{sel} and its calculated value at each \sqrt{s} are shown in Table A.6 in the Appendix A.4.1.

10.1.3 The signal yield extraction

The systematic uncertainty of the signal yields extraction δ_{fit} includes the fitting range δ_{range} , the neutron misidentification δ_{miss} and the fit model for signal δ_{sig} and background δ_{bg} . All contributions to the systematical uncertainty from the signal yield extraction are propagated using:

$$\delta_{\text{fit}} = \sqrt{(\delta_{\text{miss}})^2 + (\delta_{\text{range}})^2 + (\delta_{\text{sig}})^2 + (\delta_{\text{bg}})^2} \quad (10.2)$$

The contribution δ_{miss} denotes the systematic uncertainty from misidentified neutrons. For the calculation of the signal MC selection efficiency, an additional cut on the angle between the EMC shower position after reconstruction and the generated truth position of the neutron is performed with a value of $\angle_{\text{shower}}^{\text{truth}} < 10^\circ$, as discussed in Section 8.1. EMC showers identified as the neutron with a deviation of $10^\circ < \angle_{\text{shower}}^{\text{truth}} < 90^\circ$ are consistently not considered during the fit procedure for the signal yield extraction. In contrast, neutron EMC showers with values larger than $\angle_{\text{shower}}^{\text{truth}} > 90^\circ$ are considered as misidentified. Figure 10.1 (top) shows the good, bad reconstructed, and misidentified EMC showers of the neutron for $\sqrt{s} = 2.0000, 2.3960, \text{ and } 3.0800$ GeV. The bottom part of the same figure shows the opening angle distribution at the same \sqrt{s} with the three contributions to the neutron EMC showers. The relative difference between the selection efficiency including the misidentified neutron EMC showers to the nominal selection efficiency is taken as the systematic uncertainty due to the neutron misidentification δ_{miss} . Plots for the misidentification of the neutron at other \sqrt{s} together with the calculated values for this systematic uncertainty are shown in the Appendix A.4.2.

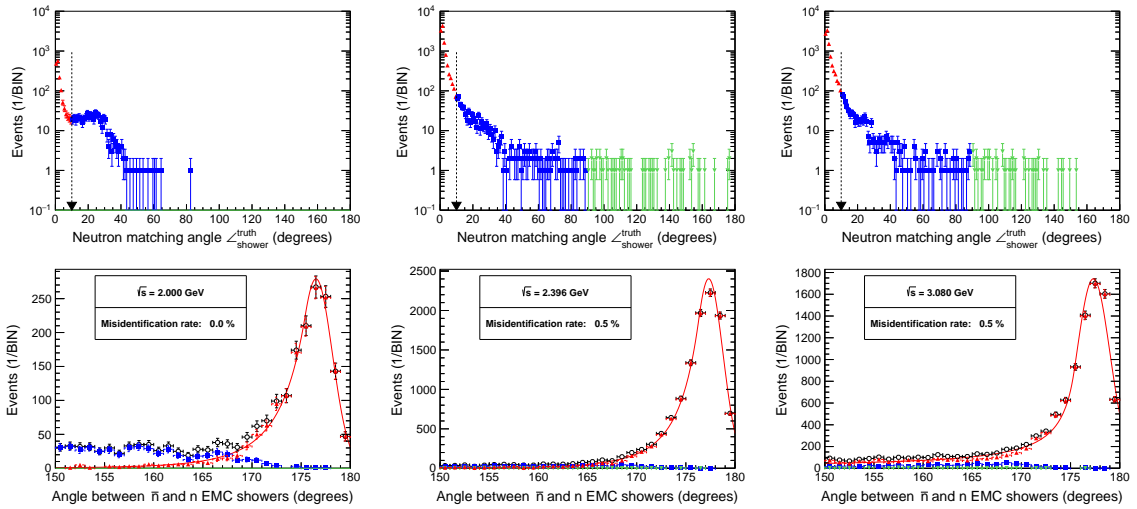


Fig. 10.1: (Top) Polar angle between the reconstructed neutron EMC shower position and the generated position $\angle_{\text{shower}}^{\text{truth}}$ at $\sqrt{s} = 2.0000, 2.3960, \text{ and } 3.0800$ GeV. Red entries show events with correctly identified neutron showers, badly reconstructed neutrons with $10^\circ < \angle_{\text{shower}}^{\text{truth}} < 90^\circ$ are shown in blue, while misidentified neutron showers are shown in green. The black arrow denotes the additional criterion applied for the signal MC simulation. (Bottom) The signal shape model for signal yield extraction at the corresponding c.m. energies. The fit model is shown as the red line taking into account only correctly identified neutron EMC showers shown as red triangles.

The contribution δ_{range} takes into account the fitting range of the opening angle for the signal yield extraction. The fit range is varied from 150° to 155° . The difference of the Born cross section to the nominal results is taken as the systematic uncertainty. Plots with the opening angle fit under the reduced range together with the calculated values for this systematic uncertainty are shown in the appendix A.4.2.

The contributions δ_{sig} and δ_{bg} take into account the systematic uncertainty due to the signal and background shape model. To study these uncertainty, the model for the signal component is changed from the nominal Crystal-Ball function to the signal MC shape. The model for the beam-related background is changed from the Chebychev 3rd order polynomial to the non-parametric shape derived with the KDE (Kernel-Density-Estimator) method, as for the hadronic background estimation in section 7.2.2. Both contributions are studied separately. The Born cross section is derived under the modified conditions and the difference to the nominal values for the Born cross section is taken as the systematic uncertainty contribution. Plots with the opening angle fits using the alternative shapes together with the method specific options and the calculated values for both systematic uncertainties are shown in the Appendix A.4.2.

10.1.4 The model dependence of the angular distribution $\cos\theta_{\bar{n}}$

The form factor model directly affects the extracted results in this analysis due to an impact on the signal MC simulation selection efficiency and the corresponding efficiency corrections. Due to limited statistics in most of the data samples and therefore no possibility to analyze the final state particles angular shape distributions, the uncertainty on the form factor model δ_{model} is calculated by using signal MC simulation with the input values for the form factor ratio shown in Table 10.1.

\sqrt{s} (GeV)	$R_{\text{em}}^{\text{min}}$ (s)	$R_{\text{em}}^{\text{nominal}}$ (s)	$R_{\text{em}}^{\text{max}}$ (s)
2.0000 - 2.1000	0.15	1.00	3.40
2.1266	1.00	1.00	2.05
2.1500 - 2.3094	0.65	1.00	1.70
2.3864 - 2.3960	0.55	1.00	1.40
2.6444 - 2.9500	0	1.00	1.70
2.9810 - 3.0800	0	1.00	3.40

Table 10.1: Form factor ratio input values for signal MC produced for the evaluation of δ_{model} . The values are chosen to include the combined results with their uncertainties.

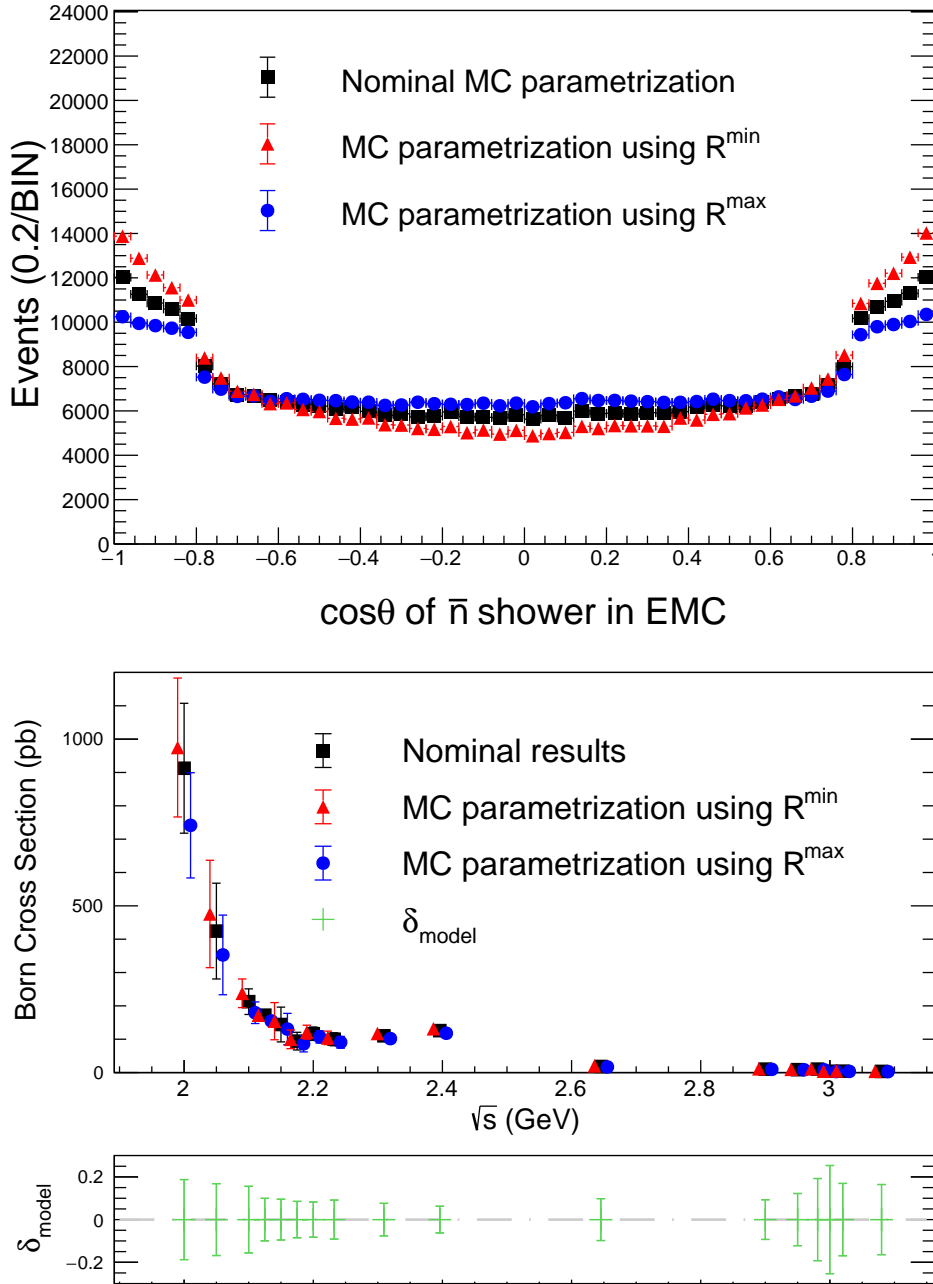


Fig. 10.2: (Top) The angular distribution of the antineutron for category C classified signal events from MC truth at $\sqrt{s} = 2.3960$ GeV with the standard parametrization and with the two extreme cases under the parametrization $R_{\text{em}}^{\min} = 0.55$ and $R_{\text{em}}^{\max} = 1.4$. (Bottom) Extracted Born cross section under the standard parametrization and the two extreme limits using R_{em}^{\max} (shifted by +10 MeV) and R_{em}^{\min} (shifted by -10 MeV). The lower pad shows the systematic uncertainty on the Born cross section from the model dependence δ_{model} . The event generator Phokhara v9.1 is used.

The values for the form factor ratio in Table 10.1, used as input to the event generator for the study of δ_{model} , are anticipated from the combined results for the ratio in Chapter 11. The angular distribution with the standard parametrization is shown for $\sqrt{s} = 2.3960$ GeV together with the two extreme cases under the parametrization $R_{\text{em}}^{\text{min}} = 0.55$ and $R_{\text{em}}^{\text{max}} = 1.40$ in Figure 10.2 (top). The signal selection efficiency and the affected corrections $(1 + \delta)$ and C_{dm} are calculated as shown in Section 8 and propagated through the full data analysis. The largest deviation between the standard results and the results extracted with the extreme limits on the Born cross section is taken as the systematic uncertainty. The results at all \sqrt{s} are shown in Figure 10.2 (bottom). All parameters for the calculation of this systematic uncertainty are listed in the Appendix A.4.3.

10.1.5 The trigger efficiency

The systematic uncertainty of the trigger efficiency correction is discussed and tested in detail in Section 8.5. As a consequence, the same method is applied while using the parametrization of the trigger response function acquired from the inclusive hadronic selection as shown in Equation 8.16. The difference between these, and the nominal

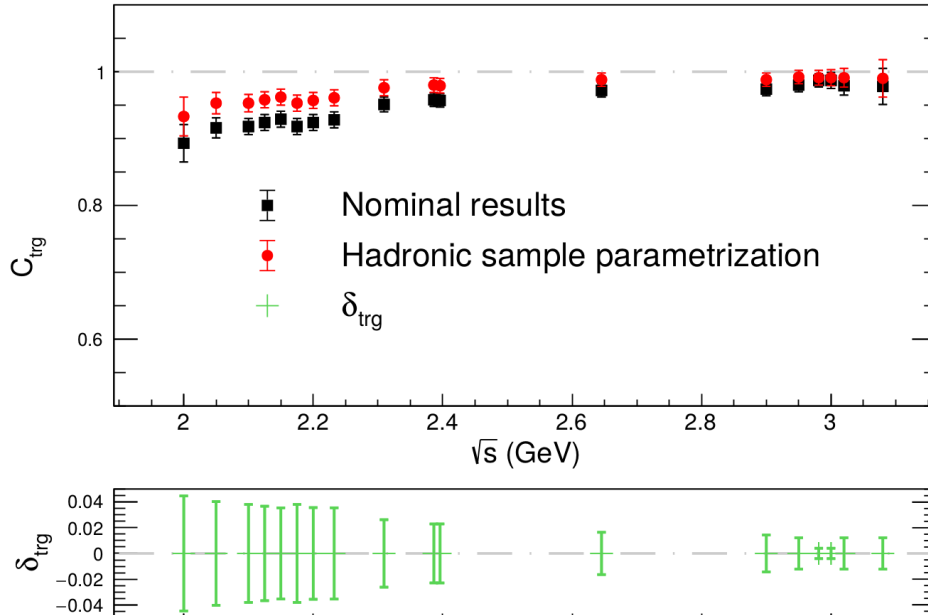


Fig. 10.3: Trigger efficiency with the nominal (black dots) and the hadronic parametrization (red dots). The lower pad shows the relative difference (relative difference = half bar length) between the two parametrizations which is taken as the systematic uncertainty δ_{trg} . The shown values are from Table A.13.

results from Table 8.6 are taken as the systematic uncertainty δ_{trg} . The results obtained with the inclusive hadronic data samples and the values for the uncertainty δ_{trg} at all \sqrt{s} are shown in the Appendix A.4.4 and in Figure 10.3.

10.1.6 The radiative correction

The systematic uncertainty occurring from radiative events of the form $e^+e^- \rightarrow \bar{n}n + m \times \gamma_{\text{ISR}}$ ($m = 1, 2$) is estimated by comparing the product of the signal MC simulation selection efficiency and the radiative correction factor $\epsilon^{\text{MC}} \times (1 + \delta)$ between the final and second last signal MC form factor parametrization. The products of the signal MC selection efficiency and the radiative correction factor $\epsilon^{\text{MC}} \times (1 + \delta)$ for the final and second last parametrization together with their relative difference denoted as the systematic uncertainty δ_{rad} are shown in Figure 10.4. The values for the calculation of the corresponding uncertainty are shown in the Appendix A.4.5 and are calculated with higher precision than shown. The drop around $\sqrt{s} = 2.3$ GeV is due to the selection criterion requirement change from $S_6 = 0.04$ GeV below $\sqrt{s} = 2.3$ to $S_6 = 0.06$ GeV above $\sqrt{s} = 2.3$, and the corresponding change in the signal selection efficiency. The vacuum polarization included in the radiative correction factor $(1 + \delta)$ is for both signal MC version the same and therefore not subject to systematical shifts.

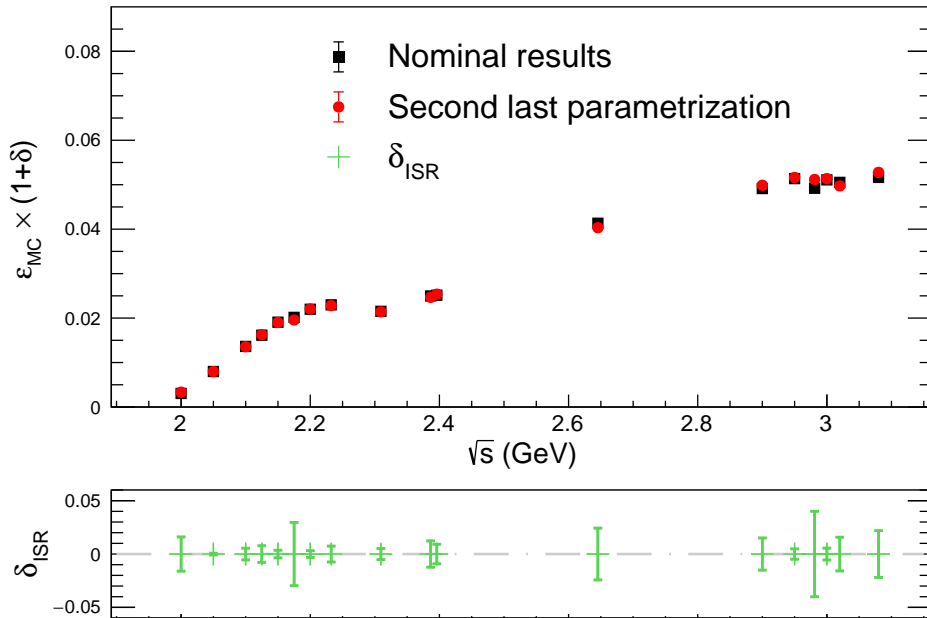


Fig. 10.4: The products of the signal MC selection efficiency and the radiative correction factor $\epsilon^{\text{MC}} \times (1 + \delta)$ for the final (black dots) and second last (red dots) parametrization. The lower pad shows their relative difference denoted as the systematic uncertainty δ_{rad} . The values in this plots are taken from Table A.14.

10.1.7 Summary of the systematic uncertainties on σ_{Born} and $|G_{\text{eff}}|$

All systematic uncertainties discussed in Section 10.1, together with the total values δ_{sys} for the Born cross section σ_{Born} and the effective form factor $|G_{\text{eff}}|$ at all center-of-mass energies \sqrt{s} are listed in Table 10.2. The total value of δ_{sys} is calculated according to Equation 10.1. For most results below $\sqrt{s} = 2.9500$ GeV, the systematic error is smaller than the corresponding statistical uncertainty, when compared to the results in Table 9.2. For results extracted from data samples at $\sqrt{s} = 2.9500$ GeV and above, the systematic uncertainty exceeds the statistical one. This behavior is observed due to the low statistics and therefore strong fluctuation of the fit for the signal yield extraction, as shown from the individual contributions to δ_{fit} at the corresponding \sqrt{s} in Table A.11.

\sqrt{s} (GeV)	δ_{L} (%)	δ_{sel} (%)	δ_{fit} (%)	δ_{model} (%)	δ_{trg} (%)	δ_{rad} (%)	$\delta_{\text{sys}}^{\sigma}$ (%)	$\delta_{\text{sys}}^{\text{eff}}$ (%)
2.0000	0.67	4.77	11.83	18.76	4.48	1.60	23.19	11.60
2.0500	0.81	3.11	10.25	16.84	4.04	0.08	20.38	10.19
2.1000	0.70	2.39	9.52	15.61	3.81	0.55	18.85	9.42
2.1266	0.87	2.18	11.06	10.00	3.68	0.77	15.52	7.76
2.1500	0.84	2.33	15.47	9.55	3.55	0.36	18.69	9.35
2.1750	0.86	2.65	11.85	8.25	3.81	2.97	15.63	7.81
2.2000	0.67	2.48	11.42	8.25	3.57	0.31	14.76	7.38
2.2324	0.73	2.54	12.00	9.15	3.56	0.75	15.75	7.87
2.3094	0.68	2.69	6.43	7.62	2.63	0.52	10.69	5.35
2.3864	0.78	2.37	5.49	6.26	2.30	1.23	9.08	4.54
2.3960	0.68	2.35	7.16	6.26	2.30	0.92	10.13	5.07
2.6454	0.74	2.93	16.80	9.81	1.65	2.43	19.01	9.95
2.9000	0.86	4.83	11.89	9.30	1.44	1.50	16.01	8.01
2.9500	0.90	5.24	77.89	12.23	1.22	0.48	79.01	39.51
2.9810	0.59	5.51	21.59	19.25	1.33	4.01	29.75	14.87
3.0000	0.69	5.67	57.10	25.35	1.33	0.56	62.75	31.38
3.0200	0.71	5.84	27.84	16.95	1.23	1.58	33.19	16.59
3.0800	0.73	6.36	18.98	16.44	1.23	2.19	26.03	13.02

Table 10.2: Summary of systematic uncertainties on the Born cross section $\delta_{\text{sys}}^{\sigma}$ and the effective form factor $\delta_{\text{sys}}^{\text{eff}}$ at different \sqrt{s} for signal MC simulation generated with Phokhara 9.1 using the cross section line-shape input from the final signal MC form factor parametrization. Values are taken from Tables 3.11, A.6, A.11, A.12, A.13, and A.14.

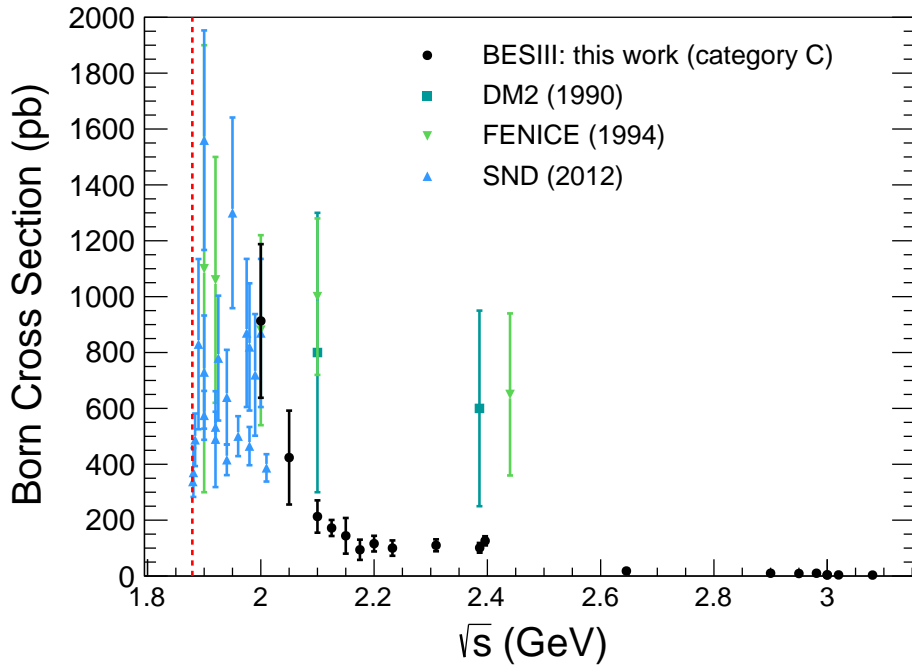


Fig. 10.5: Results for the Born cross section of the process $e^+e^- \rightarrow \bar{n}n$ from category C classified signal events. Black dots are the results from this analysis, as shown in Table 9.1 including the systematic uncertainties from Table 10.2. Emerald squares are results from the DM2 experiment, green triangles are results from the FENICE experiment, blue triangles are results from the SND experiment. The red dashed line shows the production threshold for the signal process.

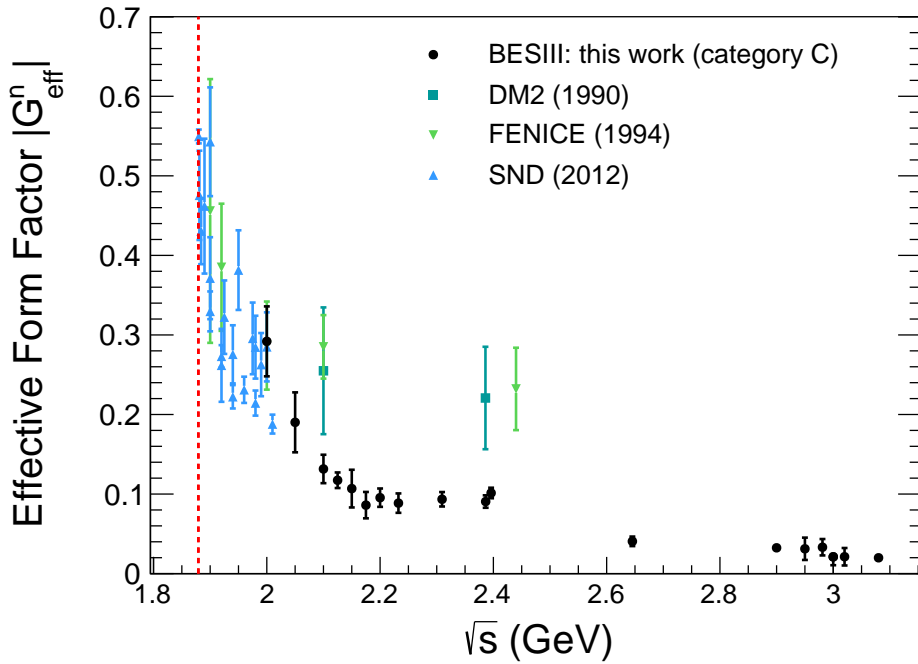


Fig. 10.6: Effective form factor of the neutron. The data and notation is the same as in Figure 9.1.

10.2 Systematic uncertainty on the form factor ratio

The form factor ratio is extracted as discussed in detail in Section 9.2. From the Function 9.6 can be seen, that the value of form factor ratio only depends on the curvature of the differential corrected signal yield distribution. Therefore, only sources which influence the polar angular shape of the antineutron EMC shower distribution and characteristics of the angular fit procedure are considered for the systematic uncertainty of the form factor ratio. As sources for the systematic uncertainty, the differential signal selection δ_{dsel} , the differential signal yield extraction δ_{dfit} , the bin width of the angular distribution δ_{bin} , the fit range for the angular fit $\delta_{\text{dfitrange}}$, and the form factor parametrization of the signal MC simulation δ_{drad} are considered. The total systematic uncertainty for the form factor ratio extraction is calculated by adding the individual contributions in quadrature.

10.2.1 The differential signal selection

The systematic uncertainty on the ratio induced by the signal selection δ_{dsel} is evaluated in a similar way to the corresponding uncertainty on the Born cross section in Section 10.1.2. As the systematic uncertainty introduced by the signal selection δ_{dsel} , the standard errors of the differential efficiency corrections $\frac{dC_{\text{dm}}}{d\cos\theta_{\bar{n}}}$ including the selection criteria $S_1 - S_7$, as well as $\frac{dC_{\text{ee}}}{d\cos\theta_{\bar{n}}}$ and $\frac{dC_{\text{mic}}}{d\cos\theta_{\bar{n}}}$, which take into account the selection criteria S_8 and S_9 , are considered. The other corrections are flat and therefore don't change the shape of the angular distribution, as shown in Figure 9.5. Instead of a quadratic addition of the three contributions, the impact of these errors on the extraction of the form factor ratio is investigated. The systematic uncertainty due to the signal selection on the individual results for the form factor ratio $R_{\text{em}}^{\text{ind}}(s)$ and the magnetic form factor $G_{\text{M}}^{\text{ind}}(s)$ is investigated with a massive MC simulation approach as following:

1. The reconstructed angular distribution for the position of the antineutron shower in the EMC D_{nominal} , with the reconstructed signal events as listed in Table 7.4, corrected according to Table 8.8 is used for the simulation. The distribution at $\sqrt{s} = 2.3936$ GeV is shown in Figure 10.7 (left).
2. The distribution D_{nominal} is used to produce 100000 MC distributions D_{random}^i ($i = 1 - 100k$). The value of reconstructed events $N_{\text{random}}^{i,j}$ in each bin $j = (1 - 7)$ of D_{random}^i is fluctuating around the corresponding $N_{\text{nominal}}^{i,j}$ within the uncertainty from the nominal distribution D_{nominal} . The relative uncertainty $\Delta N_{\text{random}}^{i,j} / N_{\text{random}}^{i,j}$ is set to be equal to the nominal relative uncertainty $\Delta N_{\text{nominal}}^{i,j} / N_{\text{nominal}}^{i,j}$.

3. Each D_{random}^i is subject to a fit with the function from Equation 9.8 (not taking the position resolution into account) and the results for R_{random}^i and $G_{M, \text{random}}^i$ are extracted, as shown in Figure 10.7 (right).
4. The distribution of R_{random}^i is subject to a fit with a Landau function convoluted with a Gaussian. The most probable value MPV is taken as the results for $R^{\text{std}}(s)$. The magnetic FF $G_M^{\text{std}}(s)$ is extracted from the normalization distribution as the corresponding value to $R^{\text{std}}(s)$. An example is shown in Figure 10.8 (top). The results for $R^{\text{std}}(s)$ can show a deviation to the nominal results in Table 9.4 (right). The deviation occurs due to the different methods used for the extraction of the results. For the samples at $\sqrt{s} = 2.0516$ and 2.8130 GeV, the statistics in the nominal distribution D_{nominal} is very low. Therefore the distribution of the resulting $R^{\text{std}}(s)$ does not follow a shape which can be fitted by the Landau function convoluted with a Gaussian. Instead the values for the mean and the standard deviation is taken directly from the histogram D_{random}^i . While the results in Table 9.4 are extracted by a single fit to the reconstructed and corrected angular distribution of the antineutron, this study uses a massive MC simulation approach to obtain the statistically most probable values for the results.
5. In the next step, two modified distributions D_- and D_+ which are based on D_{nominal} are used as input to produce two extreme sets of MC distributions $D_{-, \text{random}}^i$ ($i = 1 - 100\text{k}$) and $D_{+, \text{random}}^i$ ($i = 1 - 100\text{k}$). The approach is visualized in Figure 10.8 (bottom). For each of the two cases, the bin-specific total systematic uncertainty from the selection $\delta N_{ij}^{\text{sel}}$ is used to alter D_{nominal} and change the shape of the ratio

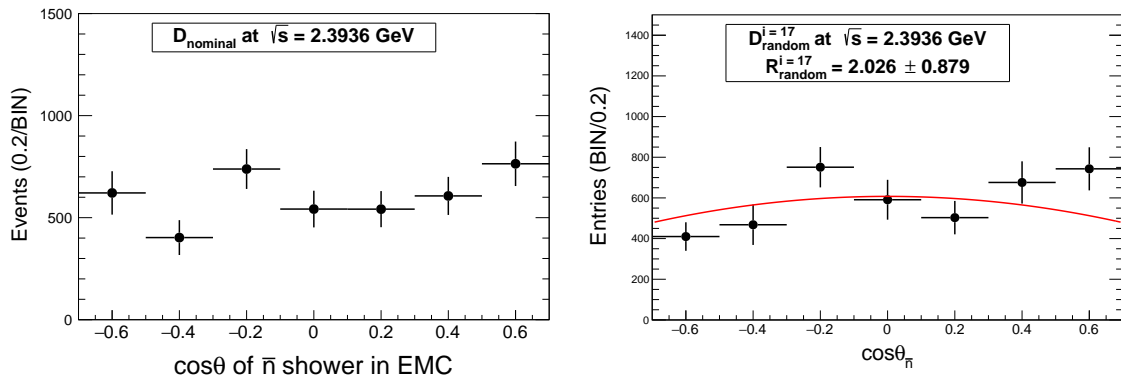


Fig. 10.7: (Left) The distribution of the reconstructed and corrected signal events from collider data D_{nominal} at $\sqrt{s} = 2.3936$ GeV. (Right) A corresponding randomly generated angular distribution D_{random}^i . The red line shows the fit with the function from Equation 9.8 for the extraction of R_{random}^i and $G_{M, \text{random}}^i$.

as extreme as possible compared to the nominal shape of D_{nominal} . The bin-specific total systematic uncertainty from the selection $\delta N_{ij}^{\text{sel}}$ as determined as following:

$$\delta N_{ij}^{\text{sel}} = \sqrt{(\Delta C_{\text{dm}}^{ij})^2 + (\Delta C_{\text{ee}}^{ij})^2 \times (C_{\text{muc}}^{ij})^2} \quad (j = 1 - 7) \quad (10.3)$$

In the case of D_- , $\delta N_{ij}^{\text{sel}}$ is subtracted from N_{random}^{ij} for $j = 1, 2, 6, 7$ and added for $j = 3, 4$, and 5. In the case of D_+ the bins j for subtraction and addition are exchanged. The steps 1 - 4 from above are repeated and a result is obtained for $R^+(s)$ and $G_M^+(s)$ as well as for $R^-(s)$ and $G_M^-(s)$ as shown in Figure 10.9. This way, the shape of D_{nominal} is changed as much as possible under the two extreme cases, and the possible deviation on the results for the ratio and the magnetic form factor coming from the signal selection are obtained. The systematical uncertainty on the form factor ratio

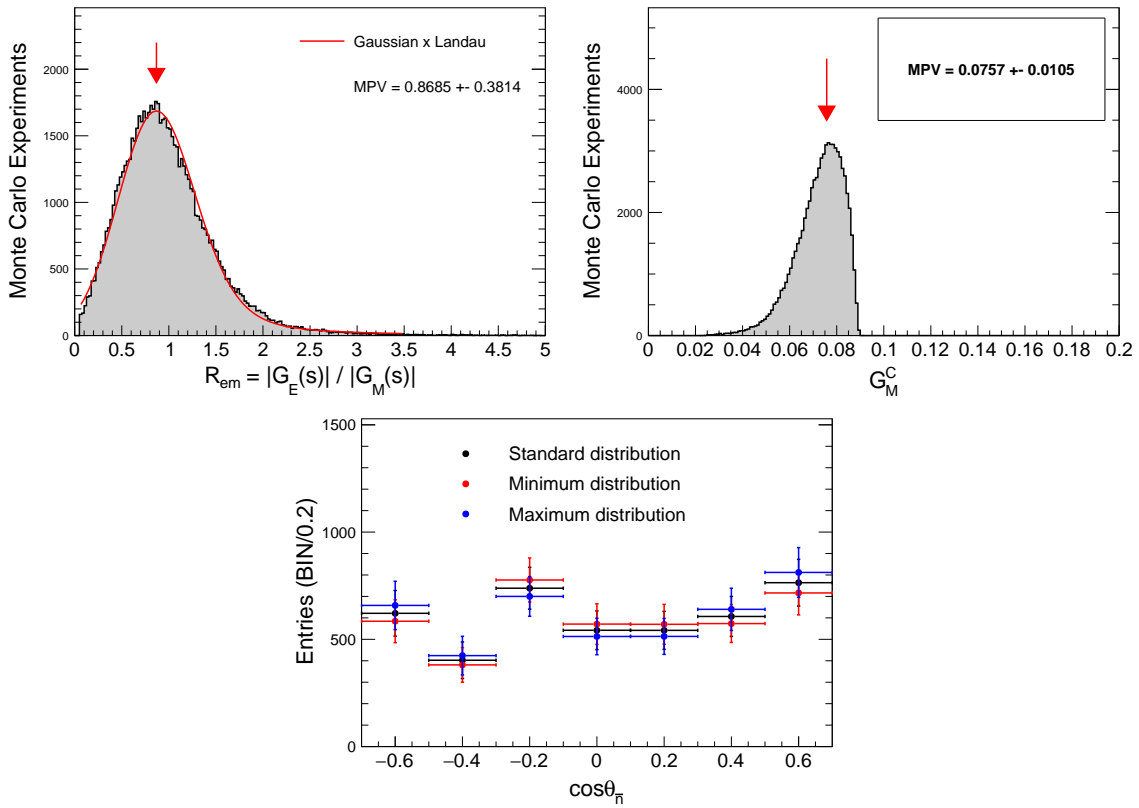


Fig. 10.8: (Top left) The distribution for R_{random}^i and (top right) the distribution for $G_{M, \text{random}}^i$ at $\sqrt{s} = 2.3936$ GeV. The red line is the fit with a Landau function convoluted with a Gaussian for the extraction of the MPVs as $R^{\text{std}}(s)$ and the corresponding magnetic FF $G_M^{\text{std}}(s)$. (Bottom) The nominal angular distribution D_{nominal} with D_- and D_+ , respectively.

$R_{em}^n(s)$ and the magnetic form factor $G_M(s)$ results from Table 9.4 is determined via:

$$\delta_{d\text{sel}}^R(s) = \pm \left| R^{\text{std}}(s) - R^\pm(s) \right| / R^{\text{std}}(s) \quad (10.4)$$

\sqrt{s} (GeV)	R_{em}^{std}	R_{em}^-	R_{em}^+	$\delta_{d\text{sel}}^R$ (%)	$G_M^{\text{std}} (\times 10^2)$	$G_M^- (\times 10^2)$	$G_M^+ (\times 10^2)$	$\delta_{d\text{sel}}^{G_M}$ (%)
2.0516	$1.042 \pm 0.742 (\times 10^3)$	$1.020 \pm 0.723 (\times 10^3)$	$1.105 \pm 0.831 (\times 10^3)$	6.0 2.1	13.92 ± 0.02	15.47 ± 0.01	12.35 ± 0.02	11.1 11.3
2.1266	0.947 ± 0.413	1.193 ± 0.417	0.737 ± 0.391	26.0 22.2	8.66 ± 1.56	7.87 ± 1.45	9.33 ± 1.47	7.7 9.1
2.2380	0.910 ± 0.265	0.771 ± 0.241	1.082 ± 0.244	18.9 15.3	7.14 ± 0.77	7.40 ± 0.68	6.76 ± 0.69	3.6 5.3
2.3936	0.869 ± 0.381	1.197 ± 0.413	0.648 ± 0.353	37.7 25.4	7.57 ± 1.05	6.83 ± 1.10	8.09 ± 0.90	9.8 6.9
2.8130	$1.563 \pm 3.011 (\times 10^2)$	$1.652 \pm 3.045 (\times 10^2)$	$1.417 \pm 2.847 (\times 10^2)$	5.69 9.3	2.92 ± 0.04	2.93 ± 0.04	2.86 ± 0.04	0.3 2.1

Table 10.3: Results from the MC simulation for the determination of $\delta_{d\text{sel}}^R$ and $\delta_{d\text{sel}}^{G_M}$. The values for R_{em}^{std} are within their errors in agreement with the nominal results for R_{em}^{ind} from Table 9.4 (right). The uncertainty $\delta_{d\text{sel}}^R$ is shown with respect to the \sqrt{s} in Figure 10.10.

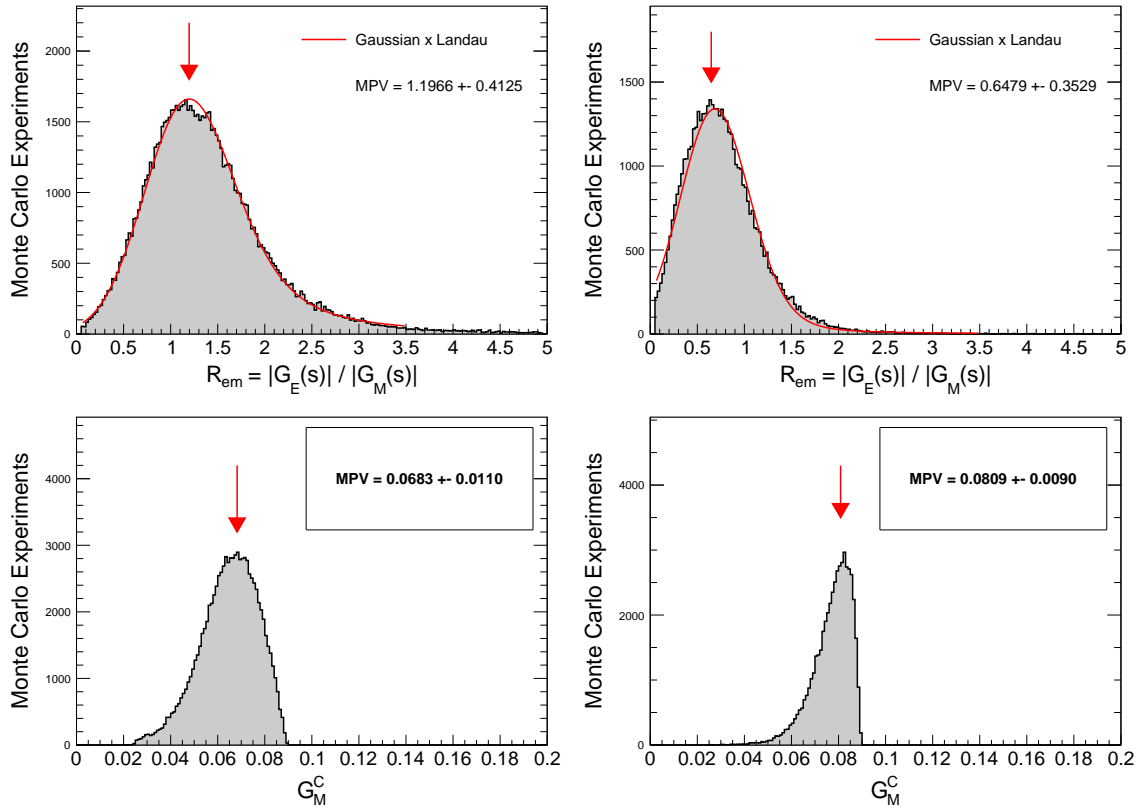


Fig. 10.9: The distribution of the results for (left) $R_{em}^- (s)$ and $G_M^-(s)$ as well as for (right) $R_{em}^+ (s)$ and $G_M^+(s)$ obtained from the 100k MC simulations of D_- and D_+ at $\sqrt{s} = 2.3936$ GeV. The red line is the fit with a Landau function convoluted with a Gaussian for the extraction of $R_{em}^- (s)$ and $R_{em}^+ (s)$, respectively, and the corresponding magnetic FFs.

Plots for the study of the systematic uncertainties on the individual results for the magnetic form factor and the form factor ratio due to the signal selection at other center-of-mass energies are shown in the appendix in Figure A.37 and Figure A.38. Plots with the results for the systematic uncertainty on the individual results for the magnetic form factor and the form factor ratio due to the signal selection are shown in Figure 10.10. The results for $\delta_{\text{dysel}}^{\text{R}}(s)$ and $\delta_{\text{dysel}}^{\text{G}_M}(s)$ at all \sqrt{s} are shown in Table 10.3 with all values used for their calculation.

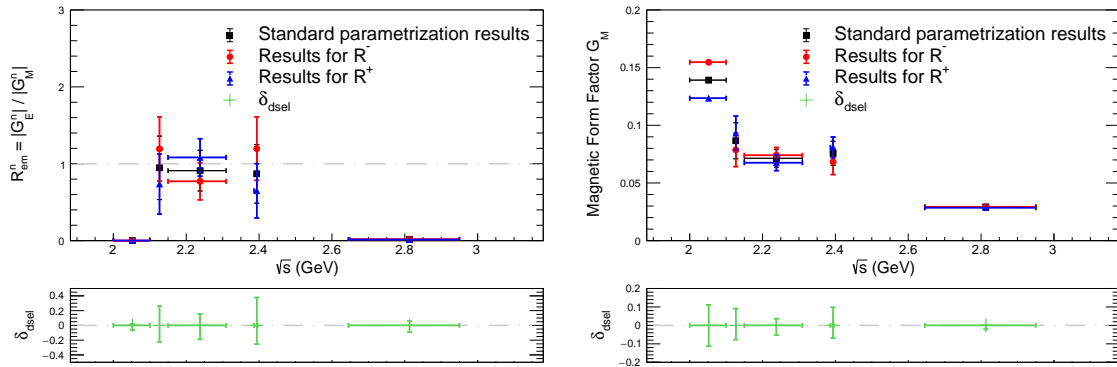


Fig. 10.10: (Left) (Top panel) The results for the form factor ratio. Back squares show the nominal results, red and blue dots show the results with the two extreme cases. (Lower panel) The asymmetric systematic uncertainty δ_{dysel} on the FF ratio. (Right) The corresponding plots for the magnetic form factor.

10.2.2 The differential signal yield extraction

The systematic uncertainty from the signal yield extraction δ_{dfit} for the form factor ratio is investigated in a similar way as described in Section 10.1.3 for the corresponding systematic uncertainty on the Born cross section. The same four contributions are considered and the total uncertainty is calculated according Equation 10.5 as the quadratic sum of the contributions:

$$\delta_{\text{dfit}} = \sqrt{(\delta_{\text{dmiss}})^2 + (\delta_{\text{drange}})^2 + (\delta_{\text{dsig}})^2 + (\delta_{\text{dbg}})^2} \quad (10.5)$$

The variation of each contribution is performed as discussed in detail in Section 10.1.3. The range is varied from 150° to 155° . The signal shape is changed from the Crystall-Ball parametrization to the non-parametric signal MC simulation shape. The beam-related background shape is changed from the Chebychev polynomial to the non-parametric shape derived with the KDE (Kernel Density Estimator) method. No variation is performed for the hadronic background, since the nominal shape is non-parametric and the fraction

of this background is negligible. The relative difference to the nominal results is taken as the individual systematic uncertainty contribution. The only exception is the contribution δ_{dmiss} , since no statement for the differential misidentification rate of the neutron is possible from the signal MC simulation due to the up-to-date unmeasured angular distribution. Instead, a luminosity weighted value for δ_{dmiss} is calculated according the Tables 3.11 and A.7 as following:

$$\delta_{\text{dmiss}} = \left(\sum_i \delta_{\text{miss}}^i \times \mathcal{L}^i \right) / \left(\sum_i \mathcal{L}^i \right) \quad (10.6)$$

The contributions δ_{miss}^i and \mathcal{L}^i denote the systematic uncertainty from the neutron misidentification and the luminosity at the corresponding \sqrt{s} . The results for the individual contributions are shown in the Appendix A.4.7 to A.4.10.

10.2.3 The bin width of the angular distribution

To investigate the bin width of the angular distribution as a possible systematic uncertainty source, a MC based study is performed. As a testing ground, the results for the form factor ratio $R_{\text{em}}^n(s) = 0.796$ at $\sqrt{s} = 2.3960$ GeV, as derived in Section 9.3 with approach 1, is chosen.

An angular distribution is generated ten thousand times using as input the quoted results for the ratio for three sets of pseudo-distributions with different bin widths in the angular range of $|\cos\theta_{\bar{n}}| < 0.7$, and setting the number of the bins to 5, the nominal 7, 9, and 14 bins. To ensure, that the results aren't biased by the statistics in a single bin, the number of events is set to one million for each MC distribution. In the next step, a fit is performed with the formula in Equation 9.6 to each of the distributions for each set of bin widths, and $R_{\text{em}}^n(s)$ is extracted. In the last step, the distributions for the extracted ratio values are fitted by a Gaussian function. The mean and sigma values denote the mean ratio value with the corresponding uncertainty for each case of the binning. Except of the different amount of bins and therefore consequently different bin widths between the four sets, all parameters are fixed to be the same. Figure 10.11 shows the results from this study for each set of distributions with different bin width. With a variation of the number of bins/bin widths, no systematical shift is introduced for the extraction of the form factor ratio. Therefore the bin width is no source for a systematic uncertainty and δ_{bin} won't be considered in this analysis.

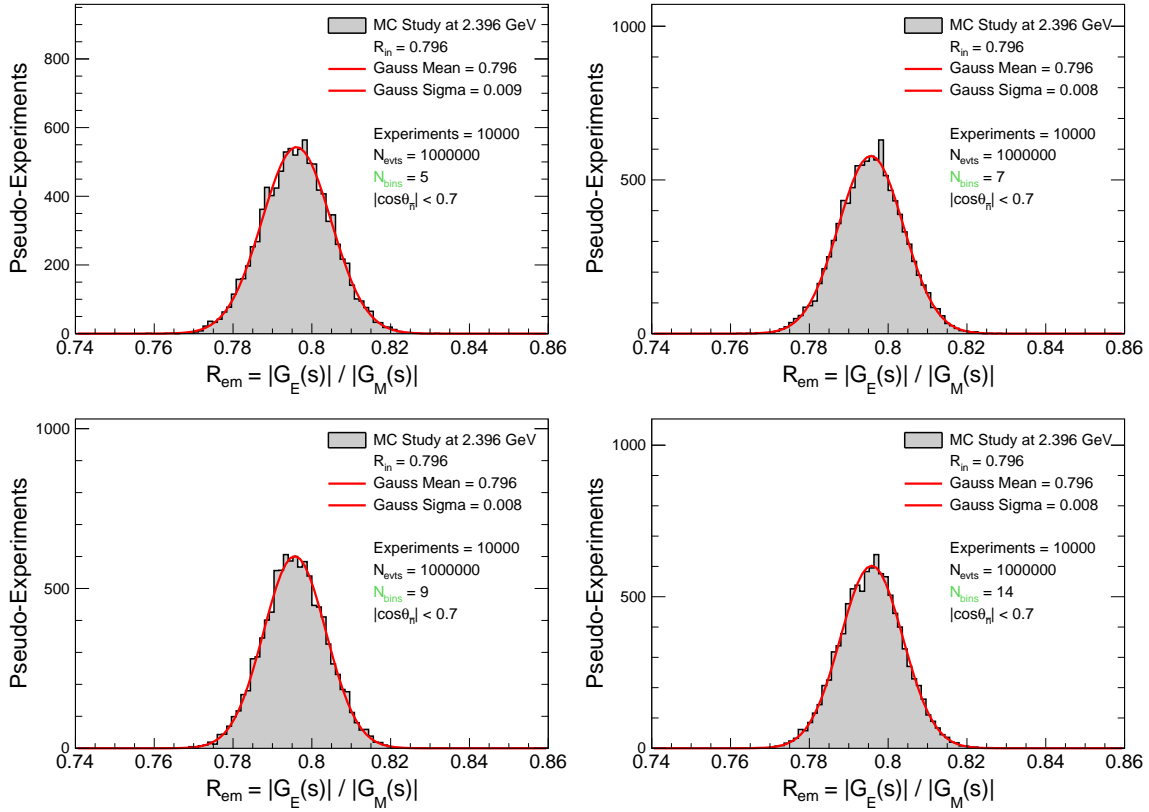


Fig. 10.11: MC study for the investigation of a possible systematic uncertainty of the form factor ratio due to the bin width δ_{bin} in the angular distribution. Each of the four sets contains ten thousand angular distributions and is generated with the input ratio of $R_{em}^n(s) = 0.796$ at $\sqrt{s} = 2.3960$ GeV with one million events, in the range of $|\cos\theta_{\bar{n}}| < 0.7$ and 5, the nominal 7, 9, and 10 bins. The grey histogram is the distribution for the ratio results after a fit with the function from Equation 9.6. The red line is the Gaussian fit for the extraction of the mean value. The four sets of results show the same mean value, leading to the conclusion, that the bin width is not a systematic uncertainty source for the ratio extraction.

10.2.4 The range of the angular fit

The fit range of the angular fit function from Equation 9.6 is investigated for the introduction of a systematic uncertainty on the form factor ratio extraction. A similar MC study, as shown in the previous paragraph, is employed. Instead of a variation of the bin width, the fit range is varied in this study. Four sets of distributions are generated with the fit range of $|\cos\theta_{\bar{n}}| < 0.6$, the nominal $|\cos\theta_{\bar{n}}| < 0.7$, $|\cos\theta_{\bar{n}}| < 0.8$, and $|\cos\theta_{\bar{n}}| < 1.0$, while the bin width is left constant with a value 0.2 and the bin number is fixed accordingly. The results are shown in Figure 10.12. As an outcome from this study, no systematical shift is introduced by the fit range. The only observed effect is a decreasing statistical uncertainty

with an increased fit range, showing itself in the changing sigma values from the Gaussian fit. As a consequence, the fit range $\delta_{\text{dffitrange}}$ is not considered as a systematic source.

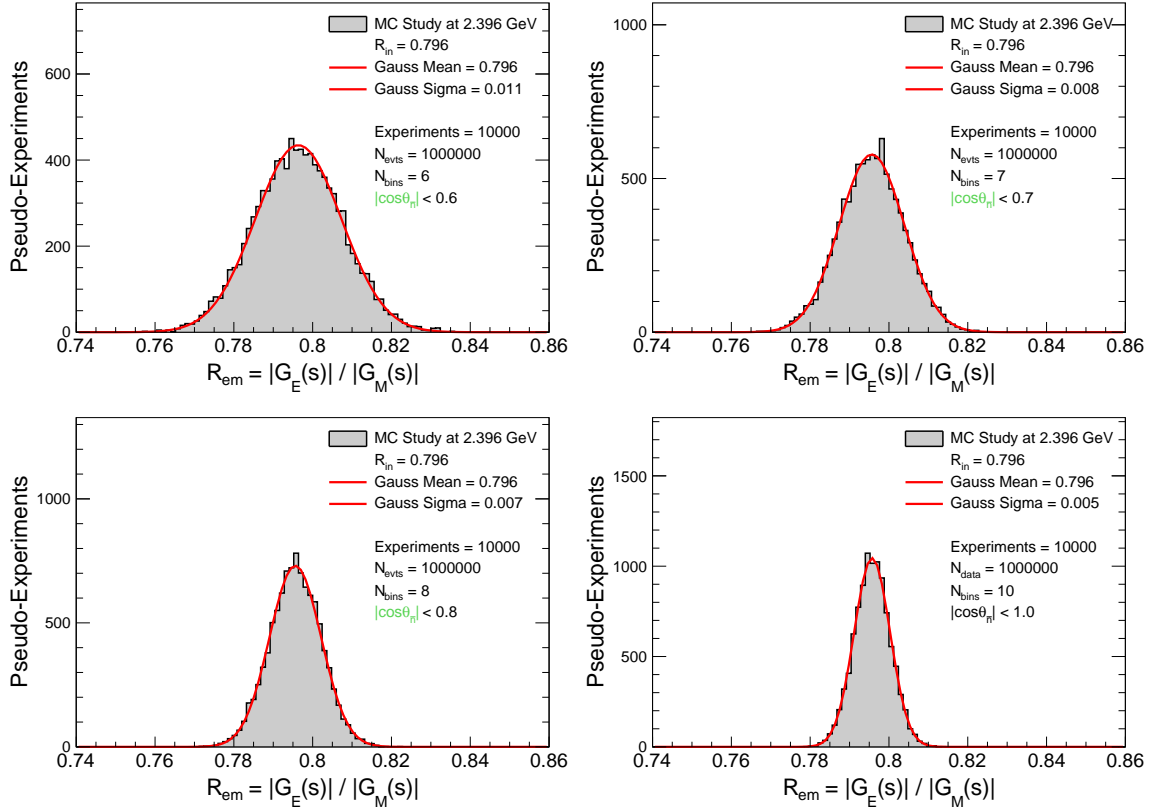


Fig. 10.12: MC study for the investigation of a possible systematic uncertainty of the form factor ratio due to the fit range for the fit of the angular distribution. Each of the four sets contains ten thousand angular distributions and is generated with the input ratio of $R_{\text{em}}^n(s) = 0.796$ at $\sqrt{s} = 2.3960$ GeV with one million events, in the range of $|\cos\theta_{\bar{n}}| < 0.6$, the nominal $|\cos\theta_{\bar{n}}| < 0.7$, $|\cos\theta_{\bar{n}}| < 0.8$, and $|\cos\theta_{\bar{n}}| < 1.0$ and the corresponding number of bins, while the bin width is fixed to 0.2. The grey histogram is the distribution for the ratio results after a fit with the function from Equation 9.6. The red line is the Gaussian fit for the extraction of the mean and sigma value. The four sets of results show the same mean value, leading to the conclusion, that the fit range $\delta_{\text{dffitrange}}$ is not a systematic uncertainty source for the ratio extraction.

10.2.5 The signal MC form factor parametrization

To study the systematic uncertainty δ_{drad} , taking into account the radiative events of the kind $e^+e^- \rightarrow \bar{n}n + m \times \gamma_{\text{ISR}}$ ($m = 1, 2$), a similar estimation is performed as in the case of the corresponding systematic uncertainty of the Born cross section in Section 10.1.7. The effect on the form factor ratio extraction is investigated by calculating the results with the differential signal MC simulation efficiency $\frac{d\epsilon^{\text{MC}}}{d\cos\theta_{\bar{n}}}$, the corresponding efficiency

corrections, and the radiative correction factor $\frac{d(1+\delta)}{d\cos\theta_{\bar{n}}}$ from the second last signal MC simulation form factor parametrization. The relative difference to the nominal results is taken as the systematic uncertainty δ_{drad} . Figure 10.13 shows the difference between the nominal results and the results on the form factor ratio obtained with the parameters discussed above.

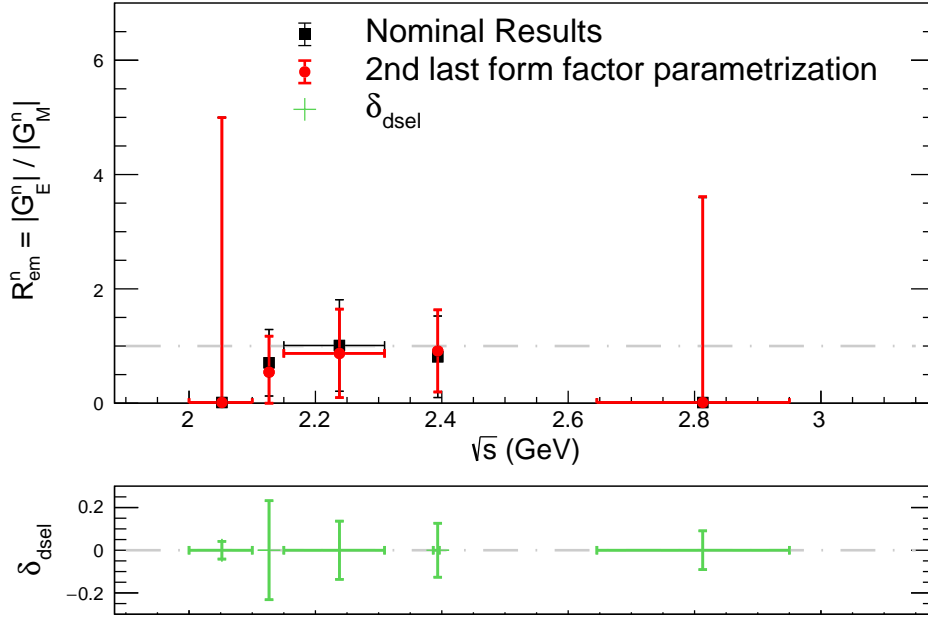


Fig. 10.13: The investigation of the systematic uncertainty from the signal MC simulation model for the ISR event contribution. Results on the form factor extraction with the final parametrization are shown in the top plot as black squares. Results obtained with the second last form factor parametrization are shown as red dots. The lower plot shows the relative difference between the two sets of results, denoted as the systematic uncertainty from the iterative MC form factor parametrization optimization. The values presented in this figure are shown in the Appendix A.4.12.

10.2.6 Summary of the systematic uncertainties on $R_{\text{em}}^{\text{ind}}(s)$

Table 10.4 summarizes the systematic uncertainties for the individual results for the form factor ratio $R_{\text{em}}^{\text{ind}}(s)$. As discussed in the Sections 10.2.3 and 10.2.4, the binning of the angular distribution and the fitting range of the angular fit for the magnetic form factor and magnetic form factor extraction are not subject of a systematic shift and therefore not considered in the total systematic uncertainty $\delta_{\text{sys}}^{\text{R}}$.

\sqrt{s} (GeV)	δ_{dtsel} (%)	δ_{dfit} (%)	δ_{bin} (%)	$\delta_{\text{dfitrangle}}$ (%)	δ_{drad} (%)	$\delta_{\text{sys}}^{\text{R}}$ (%)
2.0516	± 6.0 ± 2.1	± 2.1			+4.2	± 29.9 ± 7.6
2.1266	± 26.0 ± 22.2	± 24.0		Not a systematic uncertainty	-23.2	± 40.1 ± 35.4
2.2380	± 28.9 ± 15.3	± 29.3			-13.6	± 35.8 ± 34.9
2.3936	± 37.7 ± 25.4	± 16.7			+12.7	± 30.4 ± 43.1
2.8130	± 5.7 ± 9.3	± 14.1			+9.1	± 16.9 ± 17.7

Table 10.4: Summary of systematic uncertainties on the individual results for the form factor ratio $\delta_{\text{sys}}^{\text{R}}$ at different \sqrt{s} . Values are taken from Tables 10.3, A.19, and A.4.12.

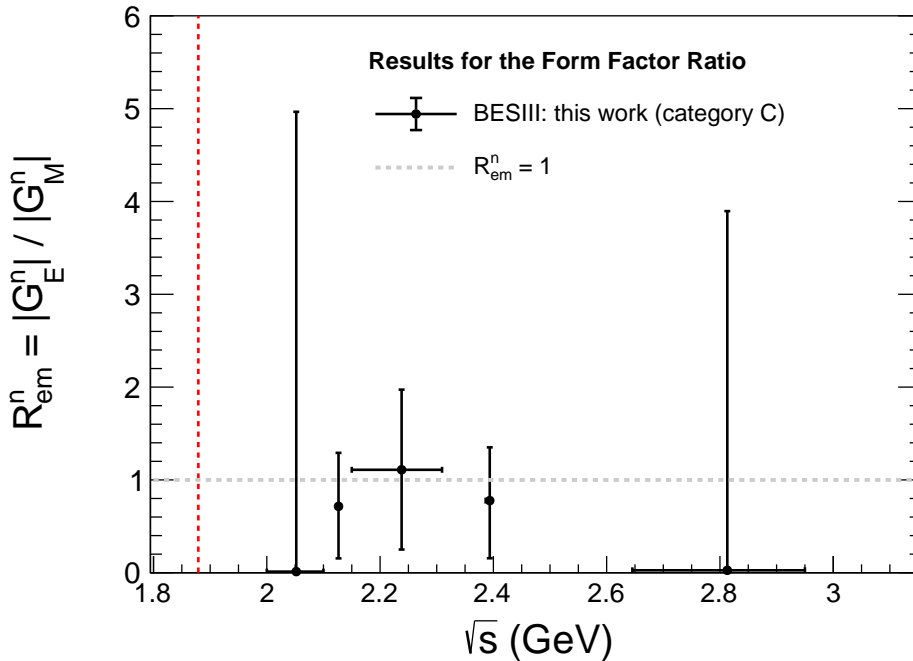


Fig. 10.14: Results for the form factor ratio of the neutron $R_{\text{em}}^{\text{ind}}$ obtained with category C classified signal events including the systematic uncertainty. The black dots are the results obtained with the MC approach, as listed in Table 9.4 (right). The red dashed line shows the production threshold for the signal process $e^+e^- \rightarrow \bar{n}n$. The shown uncertainty is combined from the statistical and the systematical one.

10.3 Systematic uncertainty of the magnetic form factor

The systematic uncertainty $\delta_{\text{sys}}^{\text{GM}}$ on the individual results of the magnetic form factor $G_{\text{M}}^{\text{ind}}(s)$ takes into account the individual uncertainties derived with the differential approach for the angular distribution, as discussed for the form factor ratio in Section 10.2, as well as the remaining absolute uncertainties, discussed for the Born cross section in Section 10.1. The following contributions are considered: the differentially investigated uncertainties from the signal selection δ_{dysel} , from the differential signal yield extraction δ_{dfit} , and from the form factor parametrization of the signal MC simulation δ_{drad} . Additionally, the uncertainties investigated w.r.t the overall normalization from the luminosity measurement δ_{L} , from the form factor model dependency of the angular distribution δ_{model} , and from the trigger efficiency correction δ_{trg} are considered, using the luminosity weighted average for the combined \sqrt{s} :

$$\delta_{\text{dx}} = \frac{\sum_i \delta_x^i \times \mathcal{L}^i}{\sum_i \mathcal{L}^i} \quad (x = \text{L}, \text{model}, \text{trg}) \quad (10.7)$$

In Equation 10.7, i stands for the \sqrt{s} used for the corresponding combined data set and δ_{dx} denotes the luminosity weighted systematic uncertainty. The total uncertainty for the magnetic form factor $\delta_{\text{sys}}^{\text{GM}}$ is calculated as the quadratic addition of the individual contributions:

$$\delta_{\text{sys}}^{\text{GM}} = \sqrt{(\delta_{\text{dysel}})^2 + (\delta_{\text{dfit}})^2 + (\delta_{\text{drad}})^2 + (\delta_{\text{dL}})^2 + (\delta_{\text{dmodel}})^2 + (\delta_{\text{dtrg}})^2} \quad (10.8)$$

All systematic uncertainties of the magnetic form factor are summarized in Table 10.5. The results for the magnetic form factor, taking into account the systematic uncertainty, are presented in Figure 10.15.

\sqrt{s} (GeV)	δ_{dysel} (%)	δ_{dfit} (%)	δ_{drad} (%)	δ_{dL} (%)	δ_{dmodel} (%)	δ_{dtrg} (%)	$\delta_{\text{sys}}^{\text{GM}}$ (%)
2.0516	$\pm \begin{smallmatrix} 11.1 \\ 11.3 \end{smallmatrix}$	± 4.8	+ 3.0	± 0.7	± 17.0	± 4.1	$\pm \begin{smallmatrix} 21.5 \\ 21.4 \end{smallmatrix}$
2.1266	$\pm \begin{smallmatrix} 7.7 \\ 9.1 \end{smallmatrix}$	± 6.4	+ 4.9	± 0.9	± 10.0	± 3.7	$\pm \begin{smallmatrix} 15.5 \\ 15.2 \end{smallmatrix}$
2.2380	$\pm \begin{smallmatrix} 3.6 \\ 5.3 \end{smallmatrix}$	± 7.6	+ 4.4	± 0.7	± 8.3	± 3.3	$\pm \begin{smallmatrix} 13.1 \\ 12.8 \end{smallmatrix}$
2.3936	$\pm \begin{smallmatrix} 9.8 \\ 6.9 \end{smallmatrix}$	± 2.7	- 4.3	± 0.7	± 6.3	± 2.3	$\pm \begin{smallmatrix} 12.2 \\ 10.9 \end{smallmatrix}$
2.8130	$\pm \begin{smallmatrix} 0.3 \\ 2.1 \end{smallmatrix}$	± 5.5	+ 0.4	± 0.8	± 9.7	± 1.5	$\pm \begin{smallmatrix} 11.3 \\ 11.5 \end{smallmatrix}$

Table 10.5: Summary of systematic uncertainties on the magnetic form factor $\delta_{\text{sys}}^{\text{GM}}$ at different \sqrt{s} . Values are taken from Tables 10.3, A.19, A.4.12, A.21, A.22, and A.23.

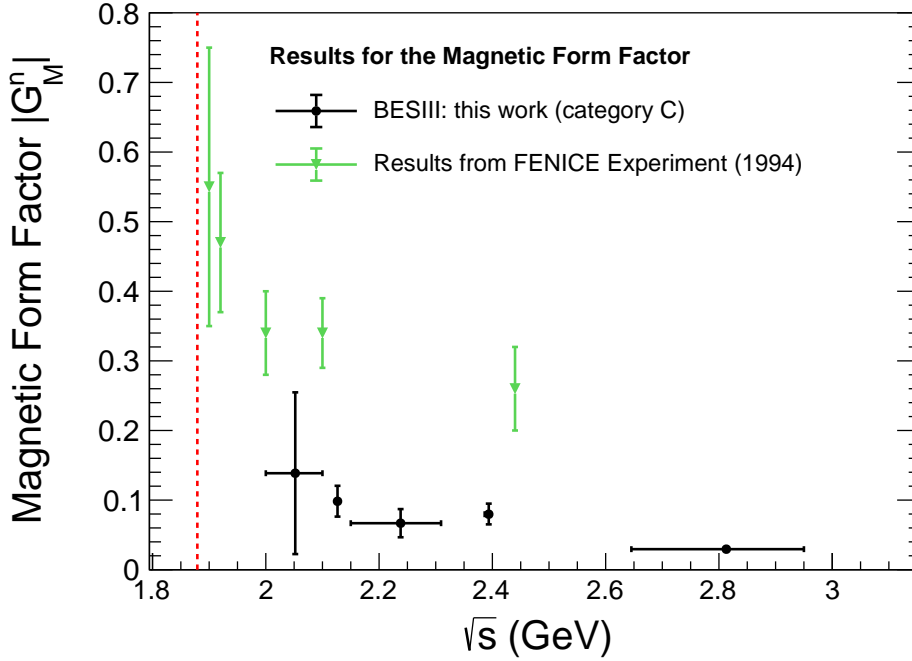


Fig. 10.15: Results for the magnetic form factor of the neutron $G_M^{\text{ind}}(s)$ from category C classified signal events. The black dots are the results obtained with the MC approach, as listed in Table 9.4 (right). The green downward triangles are results from the FENICE experiment under the assumption of $|G_E(s)| = 0$. The red dashed line shows the production threshold for the signal process $e^+e^- \rightarrow \bar{n}n$. The shown uncertainty is combined from the statistical and the systematical one.

10.4 Combined systematic uncertainties on R_{em} and G_M

In the previous sections the systematic uncertainties for the individual results of the magnetic form factor and form factor ratio from Section 9.3 have been introduced. For the systematic uncertainty of the combined results for R_{em} and G_M , correlations between the individual categories need to be taken into account. The category-individual systematic uncertainties on R_{em}^i and G_M^i with $(i = A, B, C)$ are shown in the Tables 10.4, 10.5, and in the Appendix B for the two external categories, respectively. As discussed in Section 9.4, the values for R_{em}^{mcbda} and $G_M^{\text{av,mcbda}}$, extracted with the approach 3, are used as the final results from this work. The systematic uncertainties on R_{em}^{mcbda} and $G_M^{\text{av,mcbda}}$ are studied with a massive MC simulation in a similar way, as discussed for the systematic uncertainty on the individual result due to the signal selection in Section 10.2.1. The general approach stays the same, while the following changes are introduced:

- The simulation for the nominal results is performed for the three distributions from the three signal selection classification categories using the corrected angular

distributions from collider data D_{nominal}^A , D_{nominal}^B , and D_{nominal}^C , as shown in Figure 9.10. 100000 sets of three MC distributions D_{random}^{ki} ($i = 1 - 100k$), ($k = A, B, C$) are produced.

- Each set is subject to a simultaneous fit, similar to the fit in approach 1 from Section 9.4, and the results for $R_{\text{shared},\text{random}}^{\text{std},i}$ with the corresponding values for $G_{M,\text{random}}^{\text{std},k,i}$ are extracted. The nominal value for the form factor ratio $R_{\text{shared}}^{\text{std}}(s)$ is extracted from a fit with a Landau function convoluted with a Gaussian to the resulting $R_{\text{shared},\text{random}}^{\text{std},i}$ distribution, in a similar way as shown in Section 10.2.1. The error-weighted average value of the MPVs from the three corresponding normalization distributions are taken as the $G_M^{\text{av,std}}(s)$. An example for the nominal shared form factor ratio result with this approach at $\sqrt{s} = 2.3936$ GeV is shown in Figure 10.16 (bottom left).
- In the next step, the two extreme cases, similar to the discussion in Section 10.2.1 are analyzed. Additionally to the usage of the angular distributions from three categories instead of one, as discussed above for the nominal results of $R_{\text{shared}}^{\text{std}}(s)$ and $G_M^{\text{av,std}}(s)$, the distributions for the extreme cases are produced slightly different when compared to the discussion in Section 10.2.1. The reason is the following: The

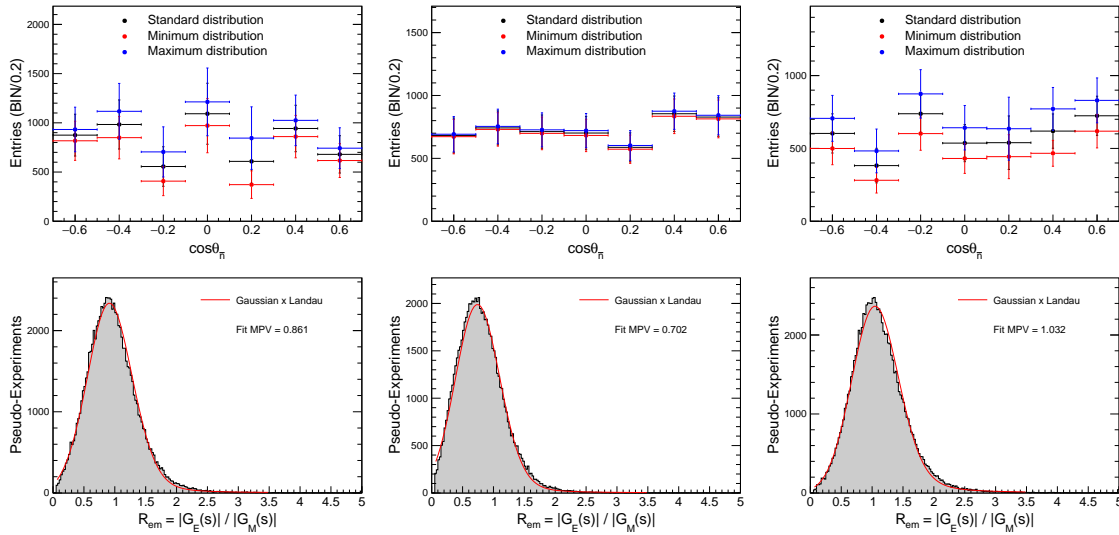


Fig. 10.16: (Top) Nominal (black), minimal (red), and maximal (blue) angular distributions obtained by the three categories as discussed above at $\sqrt{s} = (2.3864 - 2.3960)$ GeV. Category A, B, and C are shown from left to right). (Bottom) The distribution for the ratio from the 100k MC simulations, using systematical variations of the category-individual angular distributions shown in black in the top panel of this figure. The most probable value MPVs R_{std} , R^- and R^+ are extracted from a fit with a convolution between a Landau function with a Gaussian to the ratio distribution.

angular distributions from the three categories for a specific data set often show an opposite curvature (for example if comparing the three distributions at $\sqrt{s} = 2.0516$ GeV in Figure 9.10). To avoid a compensation between the three categories when altering the shape of the nominal distributions by adding and subtracting the individual systematic bin uncertainty, a pure addition and subtraction, respectively, is used for the two extreme cases. Another modification is the inclusion of the corresponding systematic uncertainty from the signal yield extraction to the category- and bin-individual error for the addition and subtraction. A visualization of this modified approach for the two extreme cases is shown in Figure 10.16 (top). The difference between the results from the two extreme cases to the results for $R_{shared}^{std}(s)$ and $G_M^{av, std}(s)$ from the nominal distributions is taken as the combined systematic uncertainty δ_{var}^R and $\delta_{var}^{G_M}$ due to the signal selection and signal yield extraction. An example for the distributions for the nominal results and the two extreme cases at $\sqrt{s} = 2.3936$ GeV is shown for the FF ratio in Figure 10.16 (bottom) and for the magnetic form factor in Figure 10.17.

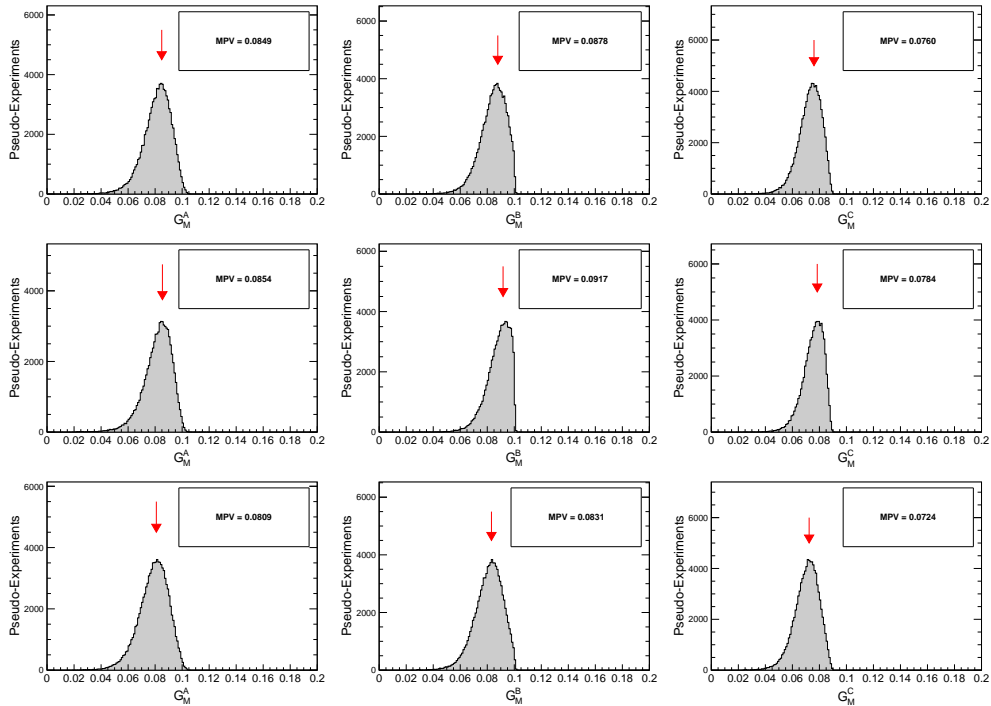


Fig. 10.17: Distributions for the magnetic FF from the 100k simulations for the data set at $\sqrt{s} = 2.3936$ GeV (from left to right for category A, B, and C), using systematical variations of the category-individual angular distributions shown in black in the top panel of Figure 10.16. The middle and bottom row show the equivalent distributions from the minimal/maximal systematic variation of the category-individual nominal angular distributions. The red arrows indicate the most probable value (MPV).

The total systematic uncertainty on the magnetic form factor is calculated via:

$$\delta^{\text{sys}} G_M^{\text{av,mcbda}} = \sqrt{(\delta_{\text{dL}})^2 + (\delta_{\text{dtrg}}^{\text{av}})^2 + (\delta_{\text{var}})^2} \quad (10.9)$$

The value for δ_{dL} is the luminosity weighted average over \sqrt{s} from the individual systematic uncertainties on the luminosity from Table 3.11. The systematic uncertainty from the trigger efficiency is the error-weighted average from the individual uncertainties δ_{dtrg}^i ($i = A, B, C$) combined similarly to Equation 9.4. The final systematic uncertainties for the combined results on the ratio and the magnetic form factor are shown in Table 10.6.

\sqrt{s} (GeV)	δ_{dL} (%)	$\delta_{\text{dtrg}}^{\text{av}}$ (%)	δ_{var} (%)	$\delta^{\text{sys}} G_M^{\text{av,mcbda}}$ (%)	$\delta^{\text{sys}} R_{\text{em}}^{\text{mcbda}}$ (%)
2.0516	± 0.70	± 4.42	$\pm \begin{smallmatrix} 0.11 \\ 1.07 \end{smallmatrix}$	$\pm \begin{smallmatrix} 4.41 \\ 4.57 \end{smallmatrix}$	$\pm \begin{smallmatrix} 0.26 \\ 8.04 \end{smallmatrix}$
2.1266	± 0.87	± 4.58	$\pm \begin{smallmatrix} 15.93 \\ 6.17 \end{smallmatrix}$	$\pm \begin{smallmatrix} 4.89 \\ 7.68 \end{smallmatrix}$	$\pm \begin{smallmatrix} 15.93 \\ 6.17 \end{smallmatrix}$
2.2380	± 0.73	± 4.04	$\pm \begin{smallmatrix} 4.20 \\ 4.68 \end{smallmatrix}$	$\pm \begin{smallmatrix} 5.93 \\ 6.19 \end{smallmatrix}$	$\pm \begin{smallmatrix} 91.74 \\ 23.53 \end{smallmatrix}$
2.3936	± 0.71	± 3.33	$\pm \begin{smallmatrix} 2.67 \\ 4.87 \end{smallmatrix}$	$\pm \begin{smallmatrix} 4.37 \\ 5.95 \end{smallmatrix}$	$\pm \begin{smallmatrix} 19.74 \\ 18.47 \end{smallmatrix}$
2.8130	± 0.82	± 2.33	$\pm \begin{smallmatrix} 0.11 \\ 1.07 \end{smallmatrix}$	$\pm \begin{smallmatrix} 2.47 \\ 3.89 \end{smallmatrix}$	$\pm \begin{smallmatrix} 3.70 \\ 4.00 \end{smallmatrix}$

Table 10.6: Summary of systematic uncertainties on the form factor ratio $\delta^{\text{sys}} R_{\text{em}}^{\text{mcbda}}$ and on the magnetic FF $\delta^{\text{sys}} G_M^{\text{av,mcbda}}$ results using the combined analysis shown as approach 3 in Table 9.5 at all analyzed \sqrt{s} .

The results for the magnetic form factor and the form factor ratio obtained with the approach 3 in Section 9.4 are shown in Figure 10.18, including the systematical uncertainty as determined in this section.

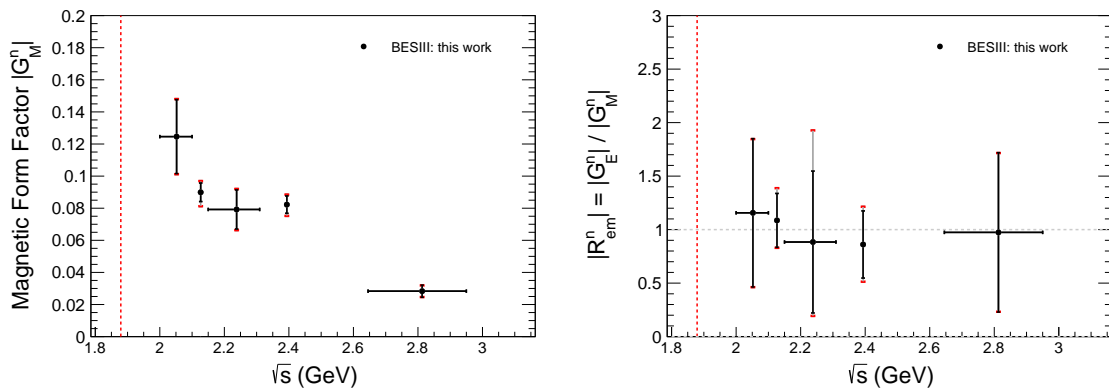


Fig. 10.18: Results including the systematic uncertainty for (left) the energy weighted average magnetic form factor $G_M^{\text{av,mcbda}}$ obtained with the approach 3 at different energies (\sqrt{s}); and (right) for the form factor ratio $R_{\text{em}}^{\text{mcbda}}$ as listed in Table 9.5. The black error bars indicate the statistical uncertainty while the grey error bars with red endings include the statistical and systematic uncertainty.

Chapter 11

The Discussion of the Final Results

The individual results for the signal selection classification category C (contribution by the author) for the Born cross section $\sigma_{\text{Born}}(s)$ and effective form factor $|G_{\text{eff}}^n(s)|$ are extracted in Section 9.1 and for the magnetic form factor $G_M^n(s)$ and the electromagnetic form factor ratio of the neutron $R_{\text{em}}^n = |G_E^n(s)|/|G_M^n(s)|$ in Section 9.3. The combined results including the two external signal selection classification categories A and B, performed by Xiaorong Zhou and Jifeng Hu and not subject of this thesis, are extracted in Section 9.2 and 9.4 respectively. The discussion is based on the combined results, listed in Table 11.1. The final results for the Born cross section and effective form factor are discussed in Section 11.1 and 11.2, respectively. The discussion of the results for the magnetic form factor and the form factor ratio are covered by the Section 11.3 and 11.4, respectively. A comparison between the results in the SL and TL region is made in Section 11.5. In the last section in this chapter the asymptotic behavior between the SL and TL results is studied.

11.1 The Born cross section results

The combined results, listed in Table 11.1, are compared to existing measurements in the following. The Born cross section for the signal process $e^+e^- \rightarrow \bar{n}n$ is shown together with previous measurements in Figure 11.1. The results for the Born cross section from this analysis are in agreement with the previous measurements from the FENICE experiment and the SND experiment at 2.0 GeV. The results from the DM2 and the FENICE experiments are systematically larger at higher \sqrt{s} , while still in agreement within two sigma with the results from this work. While the results from the old measurements decrease only slowly with a rising \sqrt{s} , the decrease with respect to the center-of-mass energy for

\sqrt{s} (GeV)	\mathcal{L}_{int} (pb $^{-1}$)	$\sigma_{\text{Born}}^{\text{av}}$ (pb)	$ G^{\text{av}} $ ($\times 10^2$)	G_M^{av} ($\times 10^2$)	$R_{\text{em}} = \left \frac{G_E}{G_M} \right $
2.0000	10.074	$599.8 \pm 54.3 \pm 44.6$	$20.7 \pm 1.3 \pm 1.0$	$12.46 \pm 2.30 \pm_{0.57}^{0.55}$	$1.157 \pm 0.693 \pm_{0.093}^{0.003}$
2.0500	3.343	$307.2 \pm 67.2 \pm 16.9$	$16.0 \pm 1.9 \pm 0.7$		
2.1000	12.167	$220.6 \pm 24.1 \pm 16.8$	$13.1 \pm 0.8 \pm 0.5$	$8.99 \pm 0.58 \pm_{0.69}^{0.44}$	$1.086 \pm 0.252 \pm_{0.067}^{0.173}$
2.1250	108.490	$154.1 \pm 6.4 \pm 14.8$	$11.0 \pm 0.2 \pm 0.5$		
2.1500	2.841	$153.1 \pm 37.6 \pm 18.4$	$11.7 \pm 1.4 \pm 0.6$	$7.92 \pm 1.22 \pm_{0.49}^{0.47}$	$0.884 \pm 0.663 \pm_{0.208}^{0.811}$
2.1750	10.625	$96.2 \pm 16.5 \pm 7.5$	$8.9 \pm 0.7 \pm 0.3$		
2.2000	13.699	$90.2 \pm 12.1 \pm 8.5$	$8.5 \pm 0.6 \pm 0.4$		
2.2324	11.856	$87.0 \pm 13.2 \pm 8.4$	$8.4 \pm 0.6 \pm 0.4$	$8.23 \pm 0.54 \pm_{0.49}^{0.36}$	$0.861 \pm 0.314 \pm_{0.159}^{0.170}$
2.3094	21.089	$97.6 \pm 9.8 \pm 6.4$	$8.6 \pm 0.5 \pm 0.3$		
2.3864	22.549	$87.0 \pm 8.3 \pm 6.0$	$8.5 \pm 0.4 \pm 0.3$	$2.83 \pm 0.38 \pm_{0.11}^{0.07}$	$0.974 \pm 0.745 \pm_{0.036}^{0.036}$
2.3960	66.869	$107.0 \pm 5.2 \pm 5.8$	$9.0 \pm 0.2 \pm 0.3$		
2.644(+2)	67.714	$25.1 \pm 2.3 \pm 2.0$	$4.6 \pm 0.2 \pm 0.2$	not extracted	
2.9000	105.253	$11.7 \pm 1.1 \pm 0.8$	$3.0 \pm 0.2 \pm 0.1$		
2.9500	15.942	$7.0 \pm 2.7 \pm 0.6$	$2.8 \pm 0.5 \pm 0.2$		
2.9810	16.071	$11.1 \pm 3.0 \pm 0.9$	$3.1 \pm 0.5 \pm 0.2$		
3.0000	15.881	$5.9 \pm 2.7 \pm 1.1$	$2.9 \pm 0.5 \pm 0.2$		
3.0200	17.290	$9.3 \pm 3.0 \pm 1.0$	$3.3 \pm 0.5 \pm 0.2$		
3.0800	126.185	$5.2 \pm 0.5 \pm 0.4$	$1.8 \pm 0.2 \pm 0.1$		

Table 11.1: Summary of the final results from this work. The results for the combined Born cross sections $\sigma_{\text{Born}}^{\text{av}}$ and effective form factors $|G^{\text{av}}|$ are quoted from Table 9.3. The results for the form factor ratio R_{em} and the magnetic form factor are quoted from Table 9.5 (approach 3). The first value for the uncertainty denotes the statistical one, the latter denotes the systematic uncertainty.

the BESIII results obtained in this work is much stronger. In general, our results are much more precise than any previous measurement and extend the knowledge of the Born cross section for $e^+e^- \rightarrow \bar{n}n$ up to $\sqrt{s} = 3.08$ GeV. The Born cross section for the signal process $e^+e^- \rightarrow \bar{n}n$ is compared to two selected sets of results for the process $e^+e^- \rightarrow \bar{p}p$ in Figure 11.2. Both sets of the results for the proton are measured at the BESIII experiment. The measurement from Reference [102] uses the same data set for analysis, as used for analysis in this work. This results are suited very good for comparison, since possible systematic shifts present within the BESIII data and/or framework cancel out due to the analysis of the same data set. The results for the Born cross section obtained with this analysis are considerably smaller than the corresponding values for the proton in the range $\sqrt{s} = 2.0 - 2.3$ GeV. The extracted values above $\sqrt{s} = 2.3$ GeV are better in agreement with the results for the proton channel, showing a difference of maximum one to two standard deviations. A interesting feature of this comparison is the trend of the results. While decreasing much stronger with rising \sqrt{s} than the results from the proton channel until $\sqrt{s} = 2.3$ GeV, the shape is in a good agreement above this value.

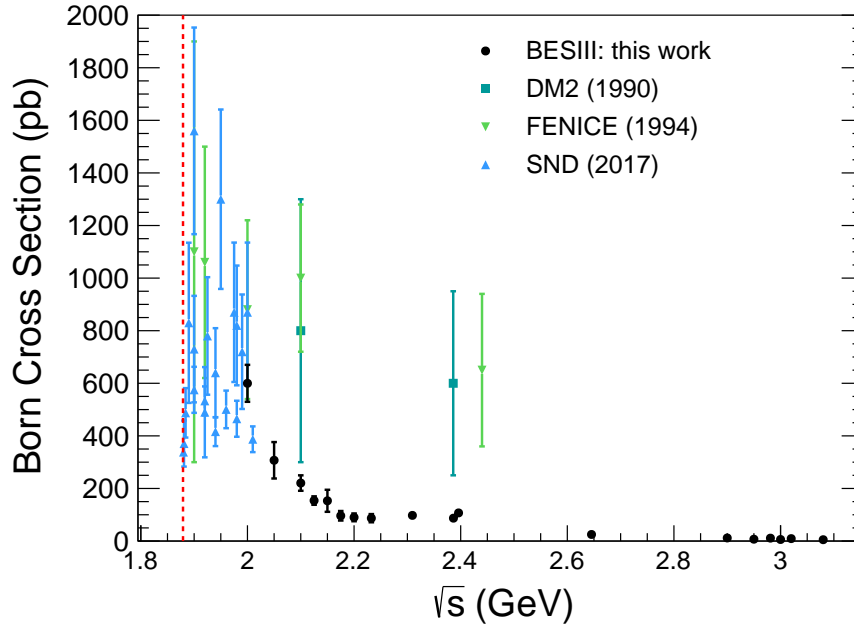


Fig. 11.1: Comparison between the combined results for the Born cross section obtained with this analysis and existing measurements. Dark green squares are results from the DM2 experiment [25], light green triangles are results from the FENICE experiment [22], while blue triangles are results from the SND experiment [26]. The red dashed line denotes the signal process production threshold.

The ratio of the Born cross sections for the process $e^+e^- \rightarrow \bar{n}n$ over $e^+e^- \rightarrow \bar{p}p$ at the same center-of-mass energies is shown in Figure 11.3. The Born cross section for the proton channel includes the Sommerfeld-Gamov factor for the Coulomb interaction $C(y) = y/(1 - e^{-y})$, with $y = 2m_p \alpha_{em} \pi / (q\beta)$. For the following comparison, the Born cross section of the proton channel is divided by the Sommerfeld-Gamov factor to exclude this effect. Several models, based on different descriptions of the nucleon, provide predictions for this ratio. While the model from Reference [162] predicts values for the cross section ratio of $1/4$ (taking into account the charge contributions of the leading valence quarks of the neutron and proton, predicting a value for the discussed ratio of $(\sigma_{\text{Born}}^{e^+e^- \rightarrow \bar{n}n}) / (\sigma_{\text{Born}}^{e^+e^- \rightarrow \bar{p}p}) \sim (q_d/q_u)^2 = 0.25$), other models from [163], [164], [165], [166] predict a ratio of < 1 , the latter consistent with our results. Our results disagree with predictions of values $\gg 1$, for example from a soliton model in Reference [167]. This analysis shed new light into the puzzle arisen with the unexpected results from the FENICE experiment. While the results from the FENICE experiment support a ratio larger than one, with the Born cross section for $e^+e^- \rightarrow \bar{n}n$ nearly twice as large as for the proton channel $e^+e^- \rightarrow \bar{p}p$, which is not the case for our results.

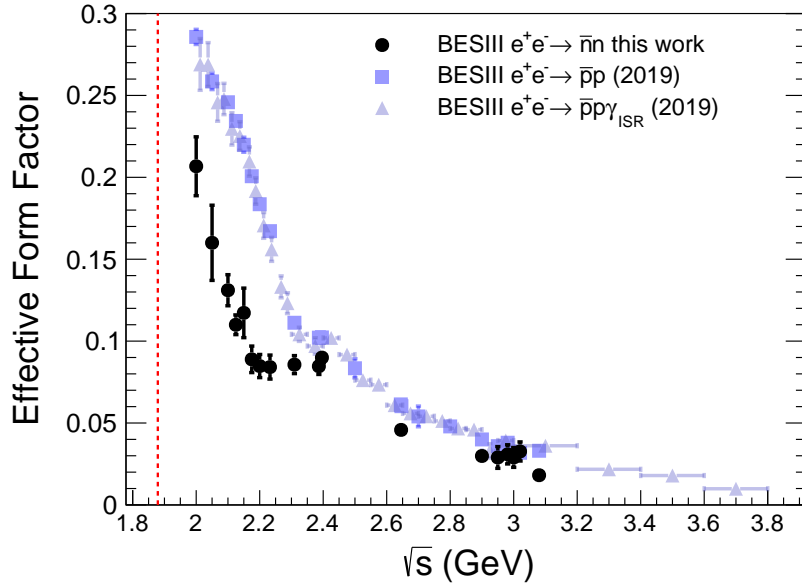


Fig. 11.2: Comparison for the Born cross section for the process $e^+e^- \rightarrow \bar{n}n$ obtained with this analysis to the Born Cross section for the process $e^+e^- \rightarrow \bar{p}p$. The results for the proton shown as triangles are quoted from the untagged ISR analysis [235], results shown as squares are from the Reference [102].

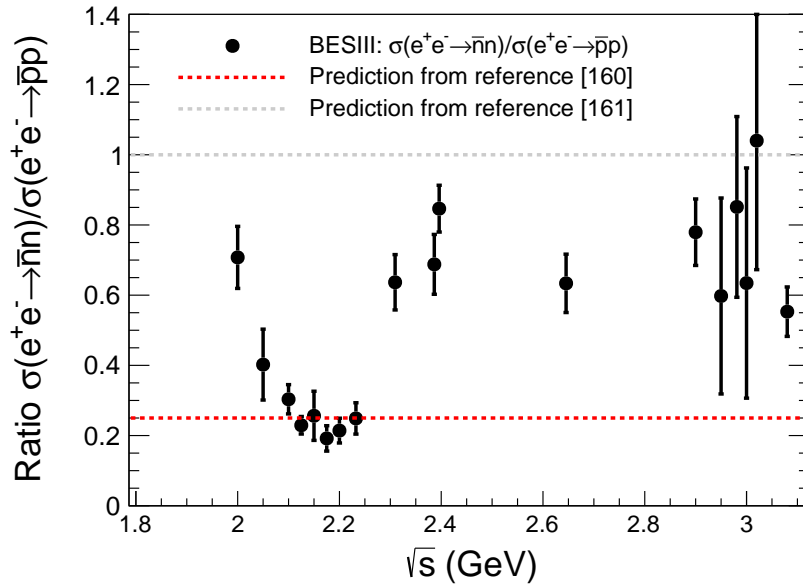


Fig. 11.3: The Ratio of the Born cross sections for the process $e^+e^- \rightarrow \bar{n}n$ from this analysis over $e^+e^- \rightarrow \bar{p}p$ from [102]. The red dashed line is the prediction from Reference [162]. The gray dashed line is the prediction from the model in [163]. Our results agree better with the prediction from Reference [163].

11.2 The effective form factor results

Figure 11.4 shows a comparison of the baryon form factors $|G_{\text{eff}}^B(s)|$, including the results for the signal channel analyzed in this work from Table 11.1, the reactions $e^+e^- \rightarrow \bar{p}p$, $e^+e^- \rightarrow \bar{\Lambda}\Lambda$, $e^+e^- \rightarrow \bar{\Sigma}^0\Sigma$, and the corresponding radiative processes. For a better representation, the baryon form factors are shown with respect to the individual baryon-pair-mass M_{BB} reduced center-of-mass energy \sqrt{s} . This work adds results for the effective form factor of the neutron over a large momentum transfer region to the database. The results for the neutron are better in agreement with results for the baryons Λ , Σ^0 from the production threshold \sqrt{s}^{thr} to $\sim \sqrt{s}^{\text{thr}} + 0.3$ GeV. For higher momentum transfer values, the results for the neutron are better in agreement with the proton channel. The situation at the threshold shows large effective form factor values for the Λ and the neutron channel contradicting the expectation of a vanishing cross section at the threshold for neutral baryons.

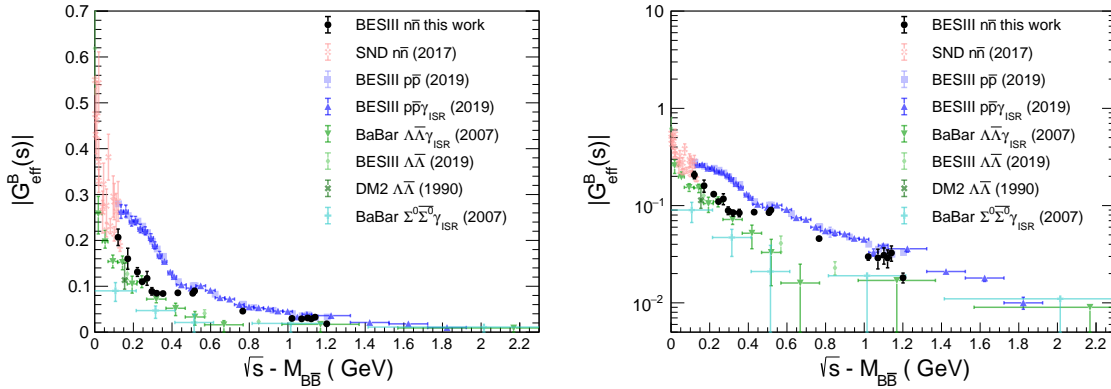


Fig. 11.4: Comparison of the results from this work with the effective form factors of different baryons. Results from this analysis are shown as black dots. The notation of the other results is shown in the plots. (Left) linear (right) logarithmic.

The results from the BaBar experiment [21] show an interesting oscillation behavior of the effective form factor after subtraction of the modified dipole parametrization from Equation 2.52, as discussed in detail in the Reference [97]. A similar approach is used here for comparison. Figure 11.5 (left) shows the fit with the modified dipole parametrization to the effective form factor results from the BaBar experiment [93] (top panel) and the resulting oscillating behavior (bottom panel). The parameters for the modified dipole parametrization of the effective form factor of the proton $\mathcal{A}(p) = 7.7 \text{ GeV}^{-4}$ and $m_\alpha^2(p) = 14.8 \text{ GeV}^2$ are determined in Reference [97]. The parameters for the neutron channel are extracted in

the same reference from the FENICE results for the effective form factor of the neutron to $\mathcal{A} = 22.5(n) \text{ GeV}^{-4}$ and $m_\alpha(n) = 3.6 \text{ GeV}$. Since the used parametrization is based on old measurements with poor precision which deviate from the results in this thesis, the normalization parameter $\mathcal{A}(n)$ from the Equation 2.52 is determined from a new fit to the results in this work to be $\mathcal{A}(n)^{\text{new}} = 4.87 \pm 0.09 \text{ GeV}^{-4}$, while the pole parameter is fixed to the proton results $m_\alpha^2(n) = 14.8 \text{ GeV}^2$. The obtained function is used with the approach discussed above for the study of a possible oscillation of the effective FF of the neutron, as shown in Figure 11.5 (right). For the origin of this oscillation within the effective form factor of the proton, several possibilities are discussed, i.e. interference effects from final state rescattering [236], or a resonant structure as discussed in [237]. The results for the effective form factor of the neutron obtained from this work with the new determined parameters and the investigation of the oscillation behavior with the modified parametrization are shown in Figure 11.6.

The oscillating behavior of the effective form factor of the neutron after subtraction of the modified dipole function is observed in the results from this work, as shown in Figure 11.6. An individual fit to the neutron results and a simultaneous fit to the oscillating data from the proton (from the BaBar experiment) and the neutron (from this work) is performed

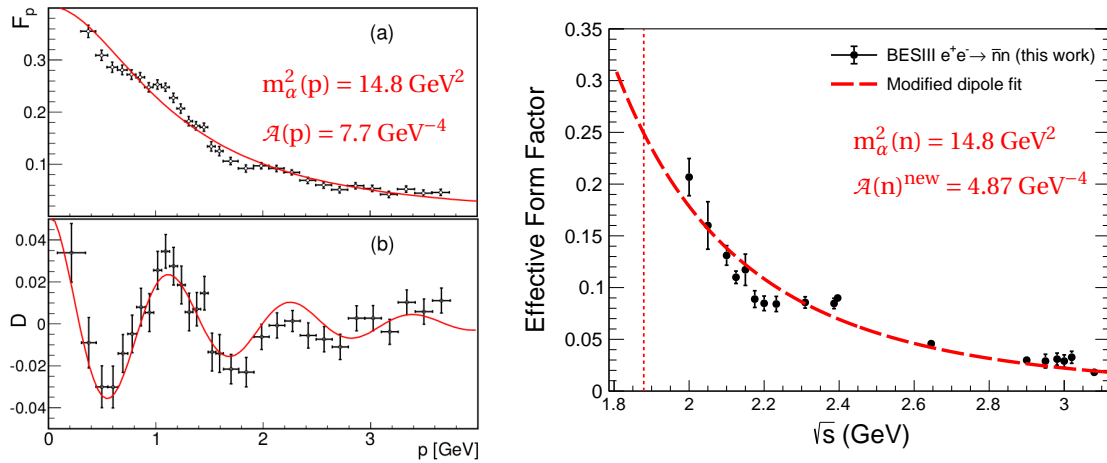


Fig. 11.5: (Left) (a) Proton effective FF $|G_{\text{eff}}^p(q^2)|$ as a function of the relative final state particle momentum $|\vec{p}|$ from the BaBar measurement [93]. The red line is the modified dipole parametrization with the function from Equation 2.52. (b) Effective FF results as in (a) after regular background fit subtraction. The red line is a fit with the function from Equation 11.1. (Right) The effective form factor for the process $e^+e^- \rightarrow \bar{n}n$ from this analysis and a fit with the function from Equation 11.1 with a fixed value for $m_\alpha^2(n) = 14.8 \text{ GeV}^2$.

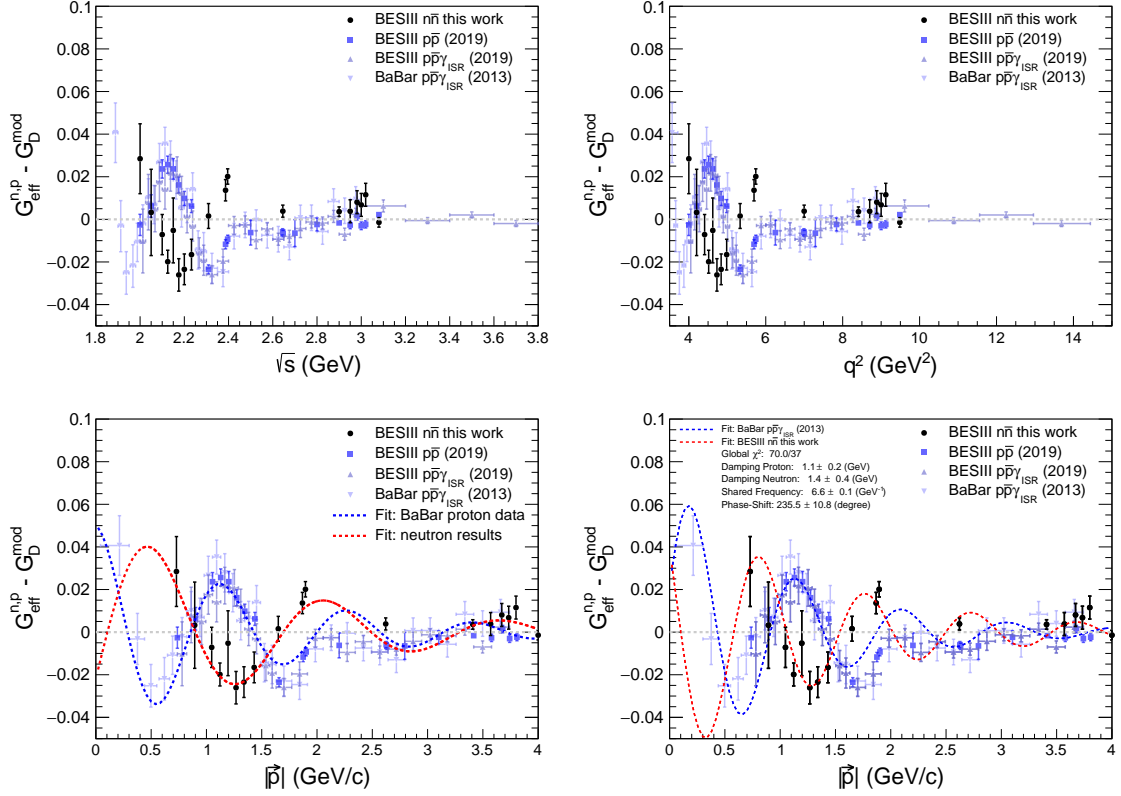


Fig. 11.6: The effective form factor from of the neutron measured in this analysis after subtraction of the function from Equation 2.52 with the parameter $\mathcal{A}(n)^{\text{new}} = 4.87 \text{ GeV}^{-4}$. The results from this thesis, shown as black dots, are compared with the results for the proton from [235] and [102], shown as blue squares and red triangles, respectively. (Top left) oscillating effective form factor w.r.t the center-of mass-energy \sqrt{s} ; (top right) oscillating effective form factor w.r.t q^2 ; (bottom) oscillating effective form factor w.r.t to the relative momentum of the final state particles. The red dashed curve is a fit to the oscillation of the EFF of the neutron with Equation 11.1. The blue dashed curve is a fit to the oscillation of the EFF of the proton with Equation 11.1. In the bottom left plot the fit parameters are determined from the individual data sets. In the bottom right plot, the oscillation parameter $C_{p,n}$ is shared, while all other parameters are individual.

with the function from Reference [236]:

$$F_{\text{osc}}(p, n) = A_{p,n} \exp(-B_{p,n}|p|) \cos(C_{p,n}|p| + D_{p,n}) \quad (11.1)$$

The fit to the individual results for the neutron is shown in Figure 11.6 (bottom left). The parameters of the function from Equation 11.1 are determined by the fit to the neutron results to be $A_n = 5.3 \pm 1.6 (\times 10^{-2})$, $B_n^{-1} = 1.6 \pm 0.7 \text{ GeV}$, $|C_n| = 3.9 \pm 0.1 \text{ GeV}^{-1}$ and $D_n = -4.3 \pm 0.3 \text{ (rad)}$ with a $\chi^2/\text{ndof} = 2.5$. The parameters for the proton data are de-

terminated in Reference [236] with a fit to the BaBar results to be $A_p = 5.0 \pm 1.0 (\times 10^{-2})$, $B_p^{-1} = 1.4 \pm 0.4 \text{ GeV}$, $|C_p| = 5.5 \pm 0.2 \text{ GeV}^{-1}$ and $D_p = 0.03 \pm 0.3 \text{ (rad)}$ with a $\chi^2/\text{ndof} = 1.1$. The results for the simultaneous fit are shown in Figure 11.6 (bottom right). The parameters for the normalizations $A_{p,n} = 7.0 \pm 3.7 (6.3 \pm 3.3) (\times 10^{-2})$, for the oscillation damping $B_{p,n}^{-1} = 1.1 \pm 0.2 (1.4 \pm 0.4) \text{ GeV}$, and the phase $D_{p,n} = -1.3 \pm 0.1 (-5.4 \pm 0.2) \text{ (rad)}$ are optimized for the individual data sets, while the oscillation parameter $|C_{p,n}| = 6.6 \pm 0.1 \text{ GeV}^{-1}$ is shared. The reduced χ^2/ndof is equal to 1.9. The oscillation of the neutron results shows a phase shift of $\Delta D_{p,n} = (235.5 \pm 10.8)^\circ$ when compared to the proton results. The results from this work clearly show an analogous behavior for the neutron, when compared to the proton results. Future studies of this effect with the goal to explain the origin for the oscillating behavior of the effective form factors of the nucleon in the TL domain are highly anticipated. This analysis provides the first data from the neutron channel.

11.3 The magnetic form factor results

The results for the magnetic form factor of the neutron from this work as listed in Table 11.1 are shown in Figure 11.7. No dedicated results for the magnetic form factor, except of the ones obtained in this work, are available up to date. The results from the FENICE experiment are obtained from the effective form factor under the hypothesis of $G_E^n(s) = 0$.

The results in this work are extracted for the first time from the angular distribution of the final state particles. Since there is no comparison possible due to the lack of existing results, the results for the magnetic FF of the neutron $G_M^n(q^2)$ from this work are compared to different FF parametrizations in Figure 11.7. The models compared with the results from this work are:

- The modified dipole parametrization, introduced in Equation 2.52.
- The pQCD inspired parametrization as follows:

$$|G_E(q^2)| = |G_M(q^2)| = \frac{C}{q^4 \left[\ln \left(\frac{q^4}{\Lambda_{\text{QCD}}^2} \right) + \pi^2 \right]} \quad (11.2)$$

The parameters are determined in [143] to $C = 89.34 (\text{GeV}/c)^2$ and $\Lambda_{\text{QCD}} = 0.3 (\text{GeV}/c)$ from a fit to the TL data of the effective FF using the assumption $|G_{\text{eff}}(q^2)| = |G_E(q^2)| = |G_M(q^2)|$.

- The dispersion-theoretical approach denoted as the "Mainz model", based on the Vector-Meson Dominance (VMD), using isoskalar and isovector components of the nucleon form factors to decompose the neutron and proton FFs in their isospin components to distinguish the contributions from isoscalar ($I = 0$) and isovector ($I = 1$) vector mesons. The expressions for the FFs in the VMD model are:

$$\begin{aligned} F_1(q^2) &= F_1^V(q^2) + F_1^S(q^2) \\ F_2(q^2) &= F_2^V(q^2) + F_2^S(q^2) \end{aligned} \quad (11.3)$$

Here $F_i^V(q^2)$ and $F_i^S(q^2)$ ($i = 1, 2$) stand for the isovector and isoscalar FFs, respectively. With this approach the Mainz model describes the electric and magnetic Sachs form factors as:

$$\begin{aligned} F_i^{IS}(q^2) &= \left[\sum_m \frac{a_{i,m}^{IS} L^{-1}(m_m^{IS})^2}{(m_m^{IS})^2 - q^2} \right] L(q^2) \\ F_i^{IV}(q^2) &= \left[F_i^\rho(q^2) L(q^2) + \sum_{m \neq \rho} \frac{a_{i,m}^{IV} L^{-1}(m_m^{IV})^2}{(m_m^{IV})^2 - q^2} \right] L(q^2) \end{aligned} \quad (11.4)$$

with the function $L(q^2)$:

$$L(q^2) = \left[\ln \left(\frac{\Lambda^2 - q^2}{Q_0^2} \right) \right]^{-\gamma} \quad (11.5)$$

and with $i = 1, 2$, the factors $a_{i,m}^{IS(IV)}$ containing all information for the coupling of the virtual photon to the vector mesons and the transition of the vector mesons to the nucleon-antinucleon pair, m_m the meson masses, $F_i^\rho(q^2)$ describing the two-pion contribution, $L(q^2)$ controlling with Λ the transition to the pQCD inspired asymptotic behavior, γ the anomalous dimension, and $Q_0 \sim \Lambda_{\text{QCD}}$. The model describes the FF components through the 2π continuum including the $\rho(770)$, three additional vector-isovector poles $\rho'(1050)$, $\rho''(1465)$, $\rho'''(1700)$, and four vector-isoscalar meson poles $\omega(770)$, $\phi(1020)$, $S'(1650)$, and $S''(1680)$. The values for the free parameters can be found in [144] together with a detailed description of the model and the used constraints.

- The modified VMD parametrization by Iachello, Jackson and Landé [224] (IJL model). It has been further optimized by including a more precise TL complex structure. This model uses a so-called intrinsic FF $g(q^2)$:

$$g(q^2) = \frac{1}{(1 - \gamma e^{i\theta} q^2)^2} \quad (11.6)$$

with dipole behavior and a complex phase for the parametrization and the propagator $D_\rho^{-1}(q^2)$ which takes into account the finite width of the ρ resonance and has a non-vanishing part in the TL region:

$$D_\rho^{-1}(q^2) = \frac{m_\rho^2 + 8\Gamma_\rho m_\pi / \pi}{m_\rho^2 - q^2 + (4m_\pi^2 - q^2)\Gamma_\rho \alpha(q^2)/m_\pi + i\Gamma_\rho 4m_\pi \beta(q^2)} \quad (11.7)$$

with

$$\alpha(q^2) = \frac{2}{\pi} \sqrt{\frac{q^2 - 4m_\pi^2}{q^2}} \ln \left[\frac{\sqrt{q^2 - 4m_\pi^2} + \sqrt{-q^2}}{2m_\pi} \right], \quad (11.8)$$

and

$$\beta(q^2) = \begin{cases} \left[\frac{\left(\frac{q^2}{4m_\pi^2} - 1 \right)^3}{\frac{q^2}{4m_\pi^2}} \right]^{1/2} & \text{for } q^2 \geq 4m_\pi^2 \\ 0 & \text{for } q^2 < 4m_\pi^2 \end{cases} \quad (11.9)$$

with the modulus $\gamma = 0.25 \text{ (GeV/c)}^{-2}$ and the complex phase θ non-vanishing for $q^2 > 0$ introduced to account for the complex FF structure in the TL region. The constants have been set to $\beta_\rho = 0.672$, $\beta_\omega = 1.102$, $\beta_\phi = 0.112$, $\alpha_\phi = -0.052$, $\Gamma_\rho = 0.112 \text{ GeV}$, $\theta = 53^\circ$ in the Reference [224]. The normalization of the propagator is $D_\rho(q^2 = 0) = 1$. The IJL VMD model predicts a linearly decreasing ratio on the proton FFs $G_E^p(Q^2)/G_M^p(Q^2)$ in the SL region which is in agreement with the polarization transfer results. The expressions for the isoscalar and isovector contributions to the Dirac and Pauli FFs are:

$$\begin{aligned} F_1^V(q^2) &= \frac{1}{2}g(q^2) \left(1 - \beta_\rho + \frac{\beta_\rho}{D_\rho(q^2)} \right) \\ F_2^V(q^2) &= \frac{1}{2}g(q^2) \left(\frac{3.706}{D_\rho(q^2)} \right) \\ F_1^S(q^2) &= \frac{1}{2}g(q^2) \left((1 - \beta_\omega - \beta_\phi) - \beta_\omega \frac{m_\omega^2}{m_\omega^2 + q^2} - \beta_\phi \frac{m_\phi^2}{m_\phi^2 + q^2} \right) \\ F_2^S(q^2) &= \frac{1}{2}g(q^2) \left((-0.120 - \alpha_\phi) \frac{m_\omega^2}{m_\omega^2 + q^2} + \alpha_\phi \frac{m_\phi^2}{m_\phi^2 + q^2} \right) \end{aligned} \quad (11.10)$$

The results for the magnetic form factor of the neutron from this work are compared to the different model predictions, as discussed above, in Figure 11.7.

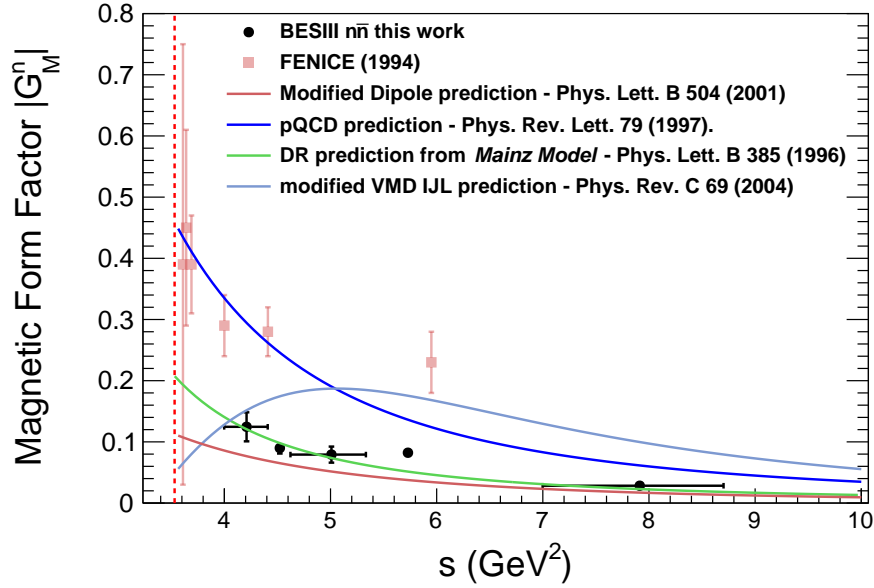


Fig. 11.7: Comparison of the results for the magnetic form factor from this work with the modified dipole parametrization (bordeaux line) with the parametrization based on the effective form factor results from this work, the pQCD inspired model (dark blue line), and VMD ILJ model (light blue line). The black dots are the results from this work. The light red squares are the results from the FENICE experiment under the hypothesis $G_E^n(q^2) = 0$.

The results obtained in this work are well in agreement with the prediction from the Mainz parametrization based on the dispersion relation approach from Reference [144]. The comparison of the magnetic form factor results from this work with the model predictions based on the modified dipole parametrization as discussed in Section 2.4.1, the pQCD inspired parametrization shown in Section 2.4.2, and the VMD IJL parametrization discussed in Section 2.4.8 is shown in Figure 11.7. Our results are not well in agreement with the three model parametrizations. The main reason is that the parametrizations have been optimized to the only available magnetic form factor results from the FENICE experiment, which are systematically larger than the results obtained in this work. The modified dipole parametrization was already discussed above. The results from this thesis are not well in agreement with the pQCD inspired prediction from Reference [143], shown as a dark blue line in Figure 11.7. The prediction with the VMD IJL parametrization from Reference [157] is also based on the results from FENICE (and the world data for the nucleon form factor in the SL and TL domain). Therefore, the normalization is overestimated in the model prediction, compared to the results obtained in this thesis.

11.4 The form factor ratio results

For the comparison of the electromagnetic form factor ratio of the neutron with other baryons we use again the representation with respect to a reduced center-of-mass energy, taking into account the individual baryon-pair-masses. The results for the ratio R_{em} for the neutron shown in Figure 11.8 are in agreement with $R_{\text{em}} = 1$ over the whole momentum range. While the baryonic form factor ratio R_{em} is by definition equal to 1 at the baryon pair production threshold, it not necessarily needs to follow this value for momentum transfers above the threshold. While having large uncertainties in our measurement, these results are the first available, therefore no comparison can be made to existing experiments. Instead, one can compare our results with the proton and the Λ channel. Concerning the proton, the best accuracy is reached for the results for the process $e^+e^- \rightarrow \bar{p}p$ [102]. This analysis uses the same data set as used for the study in this work. A comparison with this set of results shows, that our results for the neutron channel are in agreement with the results for the proton and the Λ channel within the uncertainty.

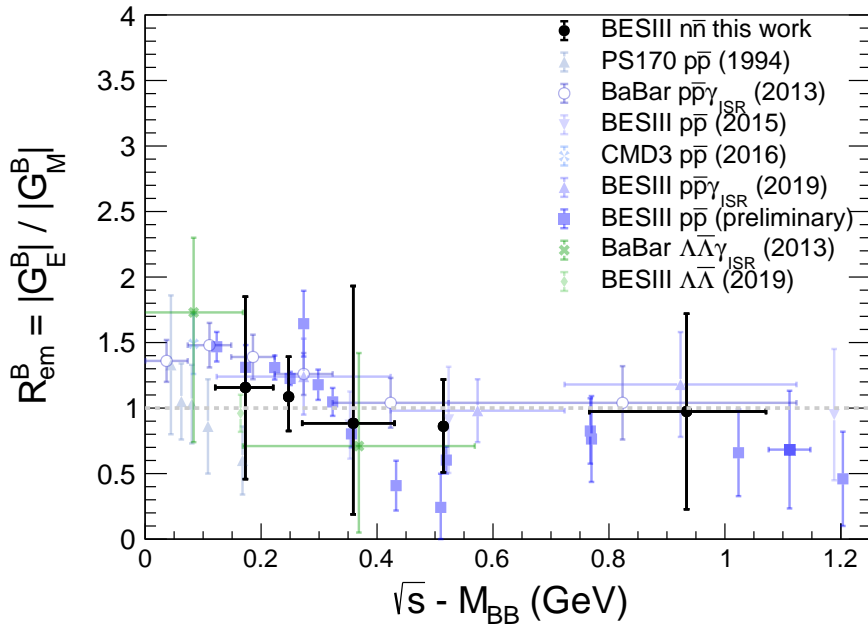


Fig. 11.8: Comparison of the electromagnetic FF ratio R_{em} of the neutron from this work with the available results for the proton and the Λ channel.

11.5 Comparison with the results in the space-like region

In this section, the results for the disentangled electromagnetic form factors of the neutron in the TL momentum transfer domain are compared to the results in the SL momentum transfer region. Figure 11.9 shows the comparison for the magnetic form factor $|G_M^n|$ (top), the FF ratio $|R_{em}^n| = |G_E^n|/|G_M^n|$ (bottom) and for the results for $|G_E^n|$ (middle). The momentum transfer region below the production threshold for the neutron-antineutron pair final state between $0 < q^2 < (2m_n)^2$ is called the "unphysical region". To access the time-like form factors in the unphysical region, the reaction $\bar{N}N \rightarrow l^+l^-\pi^0$ can be studied, where $N(\bar{N})$ is a nucleon (antinucleon) and $l^- (l^+)$ is a lepton (antilepton). For the proton, the measurement of the reaction $\bar{p}p \rightarrow e^+e^-\pi^0 (\rightarrow \mu^+\mu^-\pi^0)$ will be possible at the future PANDA experiment [238]. Since there are no existing free neutron (or antineutron) targets, there is no known access to a reaction of the kind $\bar{n}n \rightarrow l^+l^-\pi^0$.

The magnetic form factor $G_M^n(Q^2)$ in the SL region has been found to follow a dipole-like parametrization:

$$G_M/G_D \sim 1 \quad G_D = \frac{1}{\left(1 + \frac{Q^2}{0.71 \text{ (GeV)}^2}\right)^2}, \quad Q^2 = -q^2, \quad \mu_n = -1.91 \times \mu_N \quad (11.11)$$

The right side of Figure 11.9 (top) shows that the results for $G_M^n(Q^2)/\mu_n G_D(Q^2)$ in the SL region are well in agreement with unity. Results from this analysis in the TL region are shown on the left side of the same plot. The first observation to mention is that the TL results are around 2 – 3 times larger than the data set in the SL region (enhancement factor $f_{TL} \sim 2 - 3$). It can be seen, that the TL results from this work are approximately in agreement with unity multiplied with the additional enhancement factor f_{TL} within the uncertainties: $\sim 1 \times f_{TL}$.

The electric FF of the neutron in the TL region has been calculated from the two extracted parameters from the angular analysis in Table 11.1. A similar decrease of the TL results for $q^2 \rightarrow \infty$ is observed as of the SL results for $-q^2 \rightarrow -\infty$. Further, as in the case of the magnetic FF, the results for the electric FF in the TL region are $f_{TL} \sim 2 - 3$ times larger than in the SL momentum transfer domain.

The FF ratio is shown in Figure 11.9 (bottom). As already discussed above, the results from this analysis for the electromagnetic FF ratio in agreement with 1 (in this representation the TL ratio results are multiplied with μ_n and therefore agree with $R_{em}^n(TL) \sim 1 \times \mu_n$).

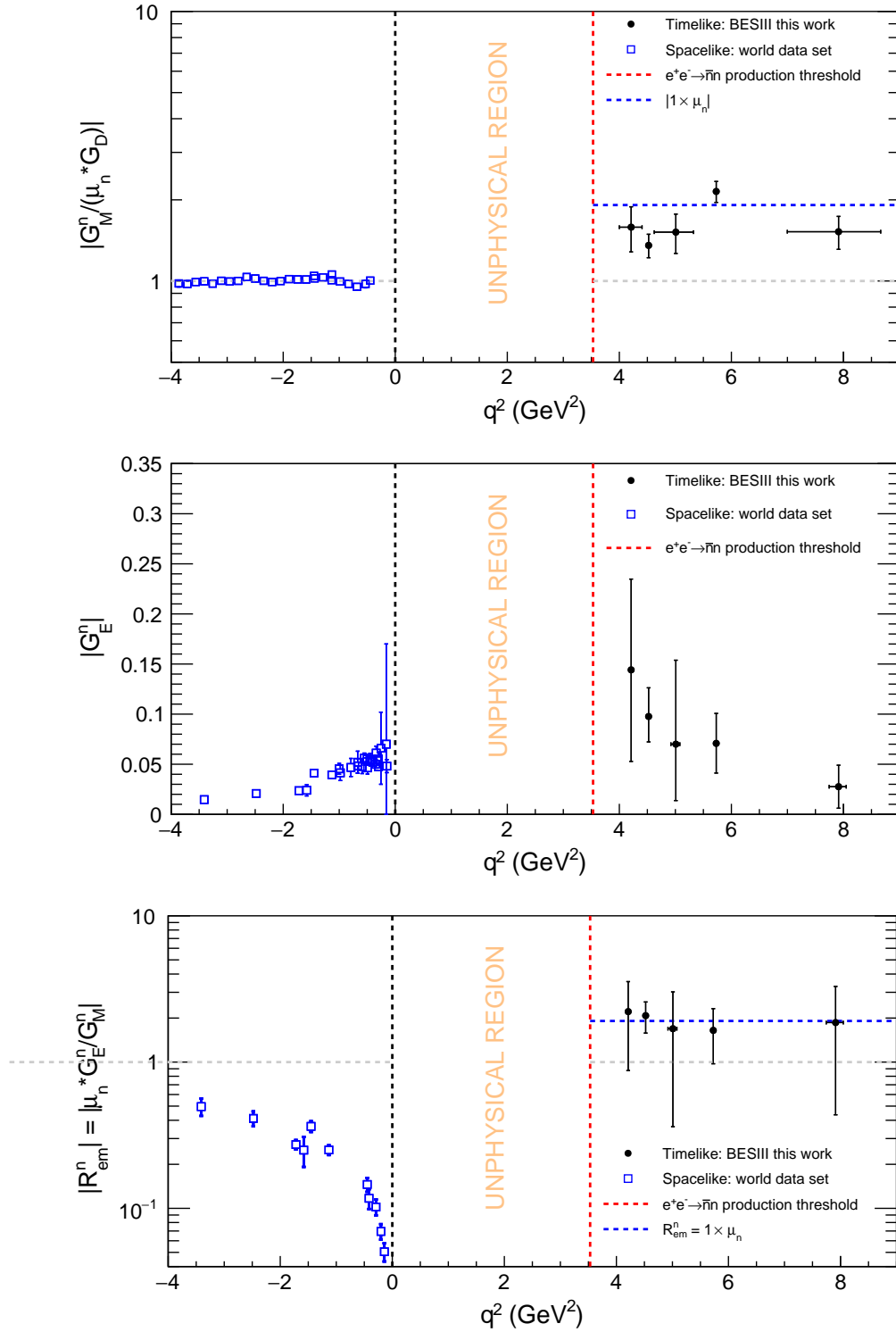


Fig. 11.9: (Top) Comparison of the experimental results between the SL and TL momentum transfer domain. (Top) Magnetic FF $G_M^n(q^2)$, (middle) electric FF $G_E^n(q^2)$, and (bottom) FF ratio $|R_{em}^n| = |\mu_n G_M^n(q^2)/G_E^n(q^2)|$. Black dots are the results for the TL region from this work, Table 11.1. Blue open squares are the world data sets on the corresponding quantity in the SL region [239].

11.6 Asymptotic behavior between in the SL and TL region

With the comparison between our results for the effective form factor $G_{\text{eff}}^n(q^2)$ and the magnetic form factor $G_M^n(q^2)$ (Table 11.1) in the TL momentum transfer region and the world data set for the magnetic form factor $G_M^n(Q^2)$ in the SL region [239], a test for a pQCD prediction can be made. While this study is theoretically based on the magnetic form factor, the inclusion of the effective form factor results in the TL region is justified by the measured values for the form factor ratio of $R_{\text{em}}^n(q^2) \sim 1$, as listed in Table 11.1, leading to the identity $R_{\text{em}}^n(q^2) \sim 1 \rightarrow G_E^n(q^2) \sim G_M^n(q^2) \sim G_{\text{eff}}^n(q^2)$. The pQCD predicts that for a "high" momentum transfer region the asymptotic behavior for the magnetic form factor should lead to equal absolute values in the SL and TL region (here the "high momentum transfer" region is not defined from theory). Figure 11.10 shows a first attempt to determine the center-of-mass energy for the parity of the absolute magnetic (effective) form factor values between the SL and TL momentum transfer region. As discussed above, the magnetic FF in the TL region is approximately equal to the dipole form factor in the discussed momentum range $G_M(Q^2) = G_D(Q^2)$. In a initial approximation, a linear function is used to describe the intersection of the TL and SL values for both the proton and the neutron data, in the representation $G_M(Q^2, q^2)$ vs. momentum transfer squared. The result for the magnetic form factor at $q^2 \sim 8 \text{ GeV}^2$ is excluded from the fit. The asymptotic behavior is determined via:

$$p_1^{\text{TL}} + p_2^{\text{TL}} \times |q^2| = q_1^{\text{SL}} + q_2^{\text{SL}} \times |Q^2| \quad (11.12)$$

with p_1 , p_2 , and q_1 , q_2 the parameters of the linear fit of the TL and SL magnetic form factor data, respectively. The form factors satisfy the condition $G_M^n(q^2) = G_M^n(Q^2)$ at $28.7 \pm 13.9 \text{ GeV}^2$ for the neutron. Using the same approach and the available data from [239] for the proton, the comparison shows a value of $17.6 \pm 1.3 \text{ GeV}^2$. The parity between the magnetic (and effective) form factor results in the SL and TL region is reached for both nucleons around $\sim 18 \text{ GeV}^2$ within the uncertainties. Further measurements in the TL region, preferably at high q^2 , could reduce the uncertainty from a linear regression and provide a first test for the above mentioned pQCD prediction for the asymptotic behavior of the form factors. Furthermore, a determination of the parity should use a modified fit function, taking into account the oscillation of the results in the TL momentum transfer region, as has been discussed in the text above.

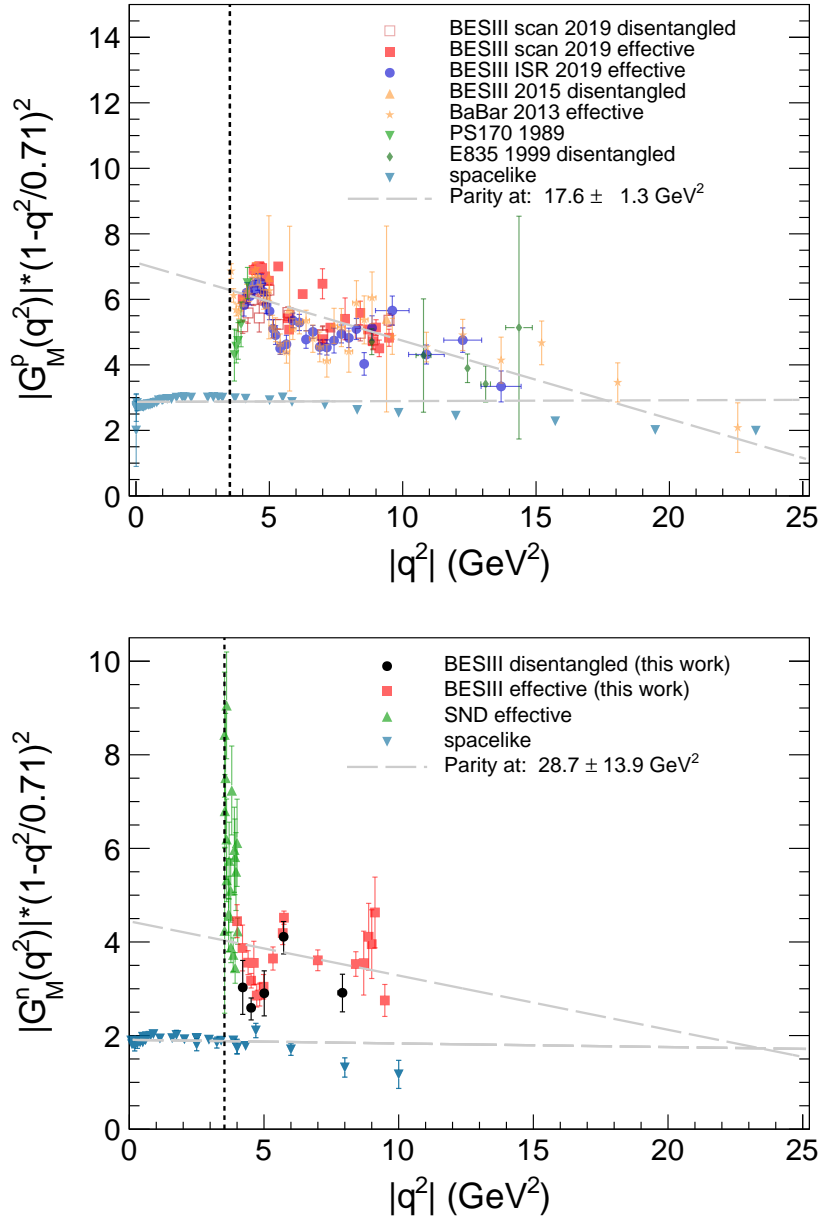


Fig. 11.10: Comparison of the experimental results for the magnetic form factor in the SL and TL momentum transfer domain, scaled with the simple dipole expression. (Top) Experimental results for the proton. The TL data is from the PS170, BESIII (mini-scan 2015), E835 (scan 1989), BESIII (ISR 2019) BaBar (ISR 2013), and BESIII (scan 2019). The results in the SL region are the world data set. (Bottom) Experimental results for the neutron. The TL results from this work are shown as black dots for the disentangled FF and as red squares for the effective FF. The disentangled result at $q^2 \sim 8 \text{ GeV}^2$ is excluded from the fit. Effective FF results from the SND experiment are shown as green triangles. The blue squares are the SL world data.

Chapter 12

Conclusion

The first measurement of the timelike electromagnetic form factor of the neutron, using a data set collected with the BESIII detector at the BEPCII collider in Beijing with an integrated luminosity of 651 pb^{-1} between 2.00 and 3.08 GeV is performed in this work. Three different signal event classification strategies based on the detection method of the signal final state particles are developed. The event classification is orthogonal - signal events are not double counted. The categories A and B are developed by Xiaorong Zhou and Jifeng Hu and not subject of this thesis. The results for the Born cross section from the three categories are in good agreement with each other. The results are combined with an error weighted method for a higher statistical precision.

The Born cross section of the signal process $e^+e^- \rightarrow \bar{n}n$ has been measured at 18 center-of-mass energies. The best statistical precision is reached for the 108.490 pb^{-1} of data at $\sqrt{s} = 2.1266 \text{ GeV}$ with a relative uncertainty of 4.1%, and for the 66.896 pb^{-1} of data at $\sqrt{s} = 2.3960 \text{ GeV}$ with a relative uncertainty of 4.8%. Results at most of the other center-of-mass energies show a relative precision between 9-20%, while the five data sets with small luminosities don't exceed relative uncertainties of 50%, as listed in Table 11.1. The systematic uncertainty takes into account the following contributions: the uncertainty from the luminosity measurement; the systematic uncertainty contributions from all applied cut criteria in the signal process selection; the extraction of the number of signal events via fit to the opening angle between the two neutron and antineutron; the uncertainty from the Monte Carlo simulation input model for the form factors; the uncertainty from the trigger efficiency correction; the uncertainty from the correction for the radiative events and vacuum polarization. Over all analyzed energies, the dominant contributions to the

total systematic uncertainty come from the fit for the signal yield extraction and from the MC simulation input model for the form factors. Except for the high luminosity data at $\sqrt{s} = 2.1266$, the statistical uncertainty is the dominant one.

The results for the Born cross section obtained in this work are compared to existing measurements. A direct comparison with the FENICE and DM2 results can be made at the center-of-mass energies $\sqrt{s} = 2.0, 2.1$, and around 2.4 GeV. Our new results disagree with the FENICE and DM2 measurements, showing systematically lower values for the Born cross section. A comparison with the results obtained by the SND experiment can only be made at $\sqrt{s} = 2.0$, where our results are in agreement with the SND measurement. The statistical and the total precision of the final results introduced in this thesis significantly exceeds all previous measurements of the Born cross section.

To study the puzzle arisen from the unexpected FENICE measurement, showing a larger Born cross section for the neutron channel $e^+e^- \rightarrow \bar{n}n$ than for the proton channel $e^+e^- \rightarrow \bar{p}p$, a comparison between the results from this work and the corresponding proton analysis at the same center-of-mass energies from arxiv is made. Compared to the results for the proton, the Born cross section declines stronger in the range $\sqrt{s} = 2.00 - 2.20$ GeV, but becomes similar above approximately $\sqrt{s} = 2.30$ GeV. The Born cross section ratio $\sigma_{e^+e^- \rightarrow \bar{n}n}^{\text{Born}} / \sigma_{e^+e^- \rightarrow \bar{p}p}^{\text{Born}}$ is extracted for both nucleons. The surprising result from the FENICE experiment, showing a ratio larger than one is not observed from this measurement. Two different predictions are compared to the experimental results for the cross section ratio, both of them not able to describe the experimental data in a satisfying manner.

The results for the effective form factor of the neutron $G_{\text{eff}}^n(s)$ has been investigated for an oscillating behavior, as have been previously observed in the results for the effective form factor of the proton in the same center-of-mass range, as discussed in [97]. A modified dipole parametrization is used for the oscillation study, taking into account the normalization of our results. An oscillating behavior has been found (Figure 11.6). Moreover, using these results and the original BaBar results for the proton from Reference [21], a simultaneous fit successfully has been performed to the nucleon FF oscillation with a shared frequency parameter, showing a good agreement between the experimental results and the model. The phase shift between the results from this work compared to the corresponding results for the proton from the BaBar experiment is determined to $(235.5 \pm 10.8)^\circ$.

By combining several data sets, the resulting luminosity of the five combined data sets is high enough to analyze the angular distribution for the extraction of the electromagnetic form factors of the neutron. For the first time it was possible to extract the disentangled electric and magnetic form factor of the neutron in the timelike region. The magnetic form factor of the neutron is measured at the center-of-mass energies $\sqrt{s} = 2.0000 - 2.1000$, 2.1266 , $2.1500 - 2.3094$, $2.3864 - 2.3960$, and at $2.6444 - 2.9000$ GeV with the best statistical precision of $\sim 6.5\%$ at $\sqrt{s} = 2.1266$ and $\sqrt{s} = 2.3864 - 2.3960$ GeV, as listed in Table 11.1. The systematic uncertainty of the magnetic form factor takes into account the same contributions as the Born cross section, analyzed with respect to the angular distribution. The largest systematic uncertainty contribution arises from the Monte Carlo simulation form factor input model. The statistical uncertainty is dominant at all energies. The FENICE collaboration has published at four values of \sqrt{s} the only results for the magnetic form factor, where they have assumed $G_E^n(s) = 0$. Our analysis is free of any assumption. As in the case of the Born cross section, our measurement shows systematically lower values for the magnetic form factor $G_M^n(s)$ than the FENICE results. A comparison between the experimental results for $G_M^n(s)$ with the parametrization from the Mainz model from Reference [144], which is based on the dispersion relation approach, shows a good agreement. The prediction with the modified dipole parametrization from Reference [140] shows an agreement with a slightly underestimation compared to our results. The predictions from the VMD based parametrization from Reference [159] and the pQCD inspired parametrization from Reference [143] are overestimating our results. The latter three parametrizations have been not optimized to the results from this work. Adjusting the parametrization to the new data obtained with this analysis, will improve the agreement.

The results for the electromagnetic form factor ratio of the neutron is measured with the best statistical precision of 23% and 36% at $\sqrt{s} = 2.1266$ and $\sqrt{s} = 2.3860 - 2.3960$ GeV, respectively. The statistical precision for the other results is between 60 – 76%. The systematic uncertainty takes into account contributions from the differential signal selection and signal extraction, as well as from the iterative optimization of the form factor model within the Monte Carlo simulation, with the largest contribution in the order of $< 30\%$ for most of the samples coming from the differential selection and the fit for the differential signal yield. The statistical uncertainty is dominant at all analyzed center-of-mass energies, except for the upper limit of the systematical uncertainty on the result at $\sqrt{s} = 2.2380$ GeV. The results support the hypothesis of $G_E^n(s)/G_M^n(s) = 1$, contradicting the hypothesis of $G_E^n(s) = 0$ used in the FENICE experiment.

The results for the magnetic form factor of the neutron obtained in this work provides us with the possibility to test the prediction from the pQCD that the results from the SL and TL domain must be in agreement for large momentum transfers. A simple linear regression to the sets of results in both domains shows an agreement around $|q^2|(\text{n}) \sim 28.7 \pm 13.9 \text{ GeV}^2$, compared to $|q^2|(\text{p}) \sim 17.6 \pm 1.3 \text{ GeV}^2$ in case of the proton. Because of the oscillating structure in the effective form factor data and the large uncertainty of the disentangled magnetic form factor results, a final conclusion for the parity of the SL and TL results of the neutron is not drawn within this work.

The results obtained in this work significantly improve the precision of the experimentally measured Born cross section and consequently the effective form factor of the neutron and show an oscillating structure, similar to the one observed for the effective form factor of the proton. Moreover, the measurement of the magnetic form factor and the form factor ratio of the neutron in the timelike region provides for the first time insight into this field of the nucleon structure and dynamics.

Additional Details for the Analysis Performed by the Author

In Appendix A additional details for the analysis performed by the author of this thesis are summarized. Additional information on the generated MC simulation samples are listed starting from Section A.1. In Section A.2 plots with details for the signal yield extraction for the Born cross section measurement and the differential signal yield extraction for the angular analysis are shown. The differential reconstruction efficiency and its corrections at all \sqrt{s} are listed in Section A.3. A detailed summary of the systematic uncertainties on the Born cross section and the results from the angular analysis, as discussed in Section 10, are shown in Section A.4.

A1 Details for the Monte Carlo simulation

The number of produced events for the signal and background simulation is chosen to be approximately the same or larger than the luminosity of the data sample at the corresponding center-of-mass energy. Table A.1 lists all MC simulation samples for the signal process $e^+e^- \rightarrow \bar{n}n(\gamma_{\text{ISR}})$, the Tables A.2 and A.3 and Figures A.1 and A.2 show the generated simulations for the background estimation, while Table A.4 sums up the background simulation samples generated for the efficiency studies.

\sqrt{s} (GeV)	\mathcal{L}_{int} (pb ⁻¹)	$\sigma_{\bar{n}n}^{\text{NNLO}}$ (pb)	N_{exp}	N_{gen}	Scale-Factor \mathcal{S}
2.0000	10.074 ± 0.005 ± 0.067	511.8 ± 1.6	5155	500K	0.010
2.0500	3.344 ± 0.003 ± 0.027	327.5 ± 1.2	1095	500K	0.002
2.1000	12.167 ± 0.006 ± 0.085	207.8 ± 0.8	2528	500K	0.005
2.1266	108.49 ± 0.02 ± 0.94	170.1 ± 0.7	18454	500K	0.037
2.1500	2.841 ± 0.003 ± 0.024	142.0 ± 0.6	403	500K	0.001
2.1750	10.625 ± 0.006 ± 0.091	122.8 ± 0.5	1304	500K	0.003
2.2000	13.699 ± 0.007 ± 0.092	110.3 ± 0.5	1511	500K	0.003
2.2324	11.856 ± 0.007 ± 0.087	101.9 ± 0.5	1208	500K	0.002
2.3094	21.089 ± 0.009 ± 0.143	106.7 ± 0.5	2250	500K	0.005
2.3864	22.549 ± 0.010 ± 0.176	111.3 ± 0.5	2510	500K	0.005
2.3960	66.869 ± 0.017 ± 0.475	109.6 ± 0.5	7329	500K	0.015
2.6454	67.725 ± 0.013 ± 0.282	39.1 ± 0.2	2648	500K	0.005
2.9000	105.253 ± 0.025 ± 0.905	17.2 ± 0.1	1810	500K	0.004
2.9500	15.942 ± 0.010 ± 0.143	15.3 ± 0.1	244	500K	0.001
2.9810	16.071 ± 0.010 ± 0.095	14.2 ± 0.1	228	500K	0.001
3.0000	15.881 ± 0.010 ± 0.110	13.6 ± 0.1	216	500K	0.001
3.0200	17.290 ± 0.011 ± 0.123	13.0 ± 0.1	225	500K	0.001
3.0800	126.185 ± 0.029 ± 0.921	11.5 ± 0.1	1451	500K	0.003

Table A.1: Signal MC simulation for the process $e^+e^- \rightarrow \bar{n}n(\gamma_{\text{ISR}})$ generated with Phokhara v9.1 for signal optimization and efficiency determination. The integrated luminosity of the collider data \mathcal{L}_{int} is quoted from Table 3.11, the cross section for this process is not known and to be determined in this analysis. Here, $\sigma_{\bar{n}n}^{\text{NNLO}}$ is taken from generator after final MC tuning in Next-to-Next-to-Leading Order. The number of expected events is calculated with $N_{\text{exp}} = \mathcal{L}_{\text{int}} \times \sigma_{\bar{n}n}^{\text{NNLO}}$, N_{gen} is the number of generated events and \mathcal{S} is the scale-factor according to the luminosity of data. Additionally a set of samples have been generated with ConExc for cross check.

\sqrt{s} (GeV)	\mathcal{L}_{int} (pb $^{-1}$)	$\sigma_{\gamma\gamma}^{\text{NLO}}$ (pb)	N_{exp}	N_{gen}	Scale-Factor \mathcal{S}
2.0000	$10.074 \pm 0.005 \pm 0.067$	87910	885605	2M	0.443
2.0500	$3.344 \pm 0.003 \pm 0.027$	83300	278555	2M	0.139
2.1000	$12.167 \pm 0.006 \pm 0.085$	79520	967520	2M	0.484
2.1266	$108.49 \pm 0.02 \pm 0.94$	77780	8438352	10M	0.844
2.1500	$2.841 \pm 0.003 \pm 0.024$	75810	215376	2M	0.108
2.1750	$10.625 \pm 0.006 \pm 0.091$	74190	788269	2M	0.394
2.2000	$13.699 \pm 0.007 \pm 0.092$	72500	993178	2M	0.497
2.2324	$11.856 \pm 0.007 \pm 0.087$	70380	834425	2M	0.417
2.3094	$21.089 \pm 0.009 \pm 0.143$	65730	1386180	2M	0.693
2.3864	$22.549 \pm 0.010 \pm 0.176$	61630	1389695	2M	0.695
2.3960	$66.869 \pm 0.017 \pm 0.475$	61110	4086365	5M	0.817
2.6454	$67.725 \pm 0.013 \pm 0.282$	50200	3399795	5M	0.680
2.9000	$105.253 \pm 0.025 \pm 0.905$	41820	4401680	5M	0.880
2.9500	$15.942 \pm 0.010 \pm 0.143$	40010	637839	2M	0.319
2.9810	$16.071 \pm 0.010 \pm 0.095$	39510	634965	2M	0.317
3.0000	$15.881 \pm 0.010 \pm 0.110$	38970	618883	2M	0.309
3.0200	$17.290 \pm 0.011 \pm 0.123$	38540	666357	2M	0.333
3.0800	$126.185 \pm 0.029 \pm 0.921$	37030	4672631	5M	0.935

Table A.2: Background MC simulation for the process $e^+e^- \rightarrow \gamma\gamma(\gamma_{\text{ISR}})$ generated with Babayaga 3.5. The integrated luminosity of the collider data \mathcal{L}_{int} is quoted from Table 3.11, the observed cross section in Next-to-Leading Order $\sigma_{\gamma\gamma}^{\text{NLO}}$ is taken from the generator, the number of expected events is calculated with $N_{\text{exp}} = \mathcal{L}_{\text{int}} \times \sigma_{\gamma\gamma}^{\text{NLO}}$, N_{gen} is the number of generated events and \mathcal{S} is the scale-factor according to the luminosity of data.

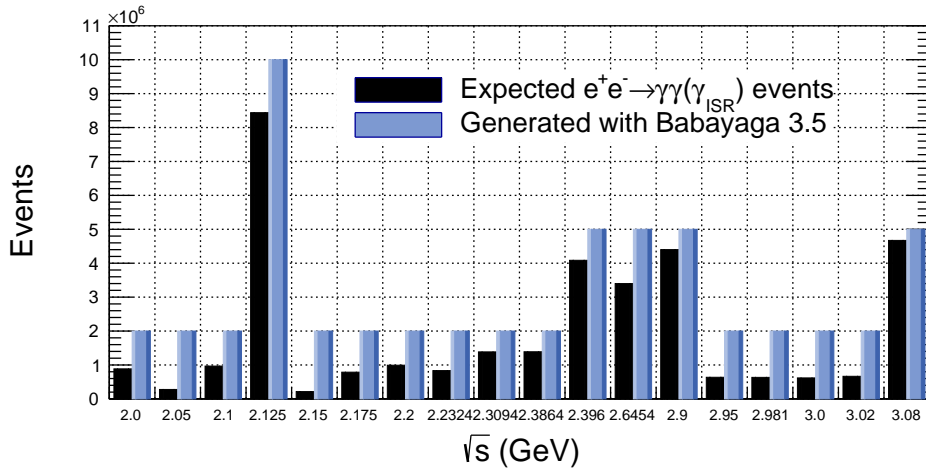


Fig. A.1: Expected and generated $e^+e^- \rightarrow \gamma\gamma(\gamma_{\text{ISR}})$ events. Details are listed in Table A.2.

\sqrt{s} (GeV)	\mathcal{L}_{int} (pb $^{-1}$)	$\sigma_{\bar{q}q}^{\text{NLO}}$ (pb)	N_{exp}	N_{gen}	Scale-Factor \mathcal{S}
2.0000	10.074 \pm 0.005 \pm 0.067	55013	554201	2M	0.277
2.0500	3.344 \pm 0.003 \pm 0.027	53326	178322	2M	0.089
2.1000	12.167 \pm 0.006 \pm 0.085	51742	629545	2M	0.315
2.1266	108.49 \pm 0.02 \pm 0.94	50971	5529844	5M	1.106
2.1500	2.841 \pm 0.003 \pm 0.024	50174	142544	2M	0.071
2.1750	10.625 \pm 0.006 \pm 0.091	49405	524928	2M	0.262
2.2000	13.699 \pm 0.007 \pm 0.092	48601	665785	2M	0.333
2.2324	11.856 \pm 0.007 \pm 0.087	47615	564523	2M	0.282
2.3094	21.089 \pm 0.009 \pm 0.143	45227	953792	5M	0.191
2.3864	22.549 \pm 0.010 \pm 0.176	42866	966585	2M	0.483
2.3960	66.869 \pm 0.017 \pm 0.475	42558	2845811	5M	0.569
2.6454	67.725 \pm 0.013 \pm 0.282	34095	2309084	5M	0.462
2.9000	105.253 \pm 0.025 \pm 0.905	28102	2957820	5M	0.592
2.9500	15.942 \pm 0.010 \pm 0.143	26838	427851	2M	0.214
2.9810	16.071 \pm 0.010 \pm 0.095	26074	419035	2M	0.210
3.0000	15.881 \pm 0.010 \pm 0.110	25612	406744	2M	0.203
3.0200	17.290 \pm 0.011 \pm 0.123	25144	434740	2M	0.217
3.0800	126.185 \pm 0.029 \pm 0.921	22483	2837017	5M	0.567

Table A.3: Background MC simulation for the process $e^+e^- \rightarrow \bar{q}q(\gamma_{\text{ISR}}) \rightarrow \text{hadrons}(\gamma_{\text{ISR}})$ generated with BesEvtGen. The integrated luminosity of the collider data \mathcal{L}_{int} is quoted from Table 3.11, the observed cross section in Next-to-Leading Order $\sigma_{\bar{q}q}^{\text{NLO}}$ is taken from the generator, the number of expected events is calculated with $N_{\text{exp}} = \mathcal{L}_{\text{int}} \times \sigma_{\bar{q}q}^{\text{NLO}}$, N_{gen} is the number of generated events and \mathcal{S} is the scale-factor according to the luminosity.

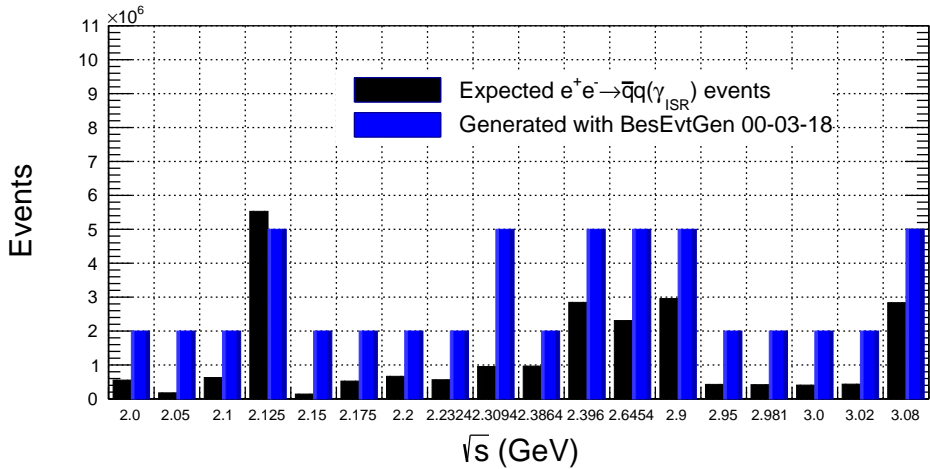


Fig. A.2: Expected and generated events with hadronic final states. Details are listed in Table A.3.

Table A.4 summarizes the MC simulation for the QED background estimation from the processes $e^+e^- \rightarrow e^+e^-(\gamma_{\text{ISR}})$ and $e^+e^- \rightarrow \mu^+\mu^-(\gamma_{\text{ISR}})$ after the signal selection. Further MC simulation samples have been produced for the study of the signal reconstruction efficiency and its corrections. The BhaBha simulation has a predicted cross section of 1282.5 nb at $\sqrt{s} = 2.3960$ GeV, therefore approximately 86 millions events are expected and the scale-factor is 0.953. The di-muon process has a cross section of 15.7 nb, leading to approximately 1.05 millions events and a scaling factor of 0.700. Both cross sections have been taken from the Babayaga 3.5 generator. With ca. 1.3 billions of J/ψ events in the collider data at $\sqrt{s} = 3.0969$ GeV, as shown in Table 3.9 and a branching fraction of $2.12 \pm 0.09 \times 10^{-3}$ [50] into the $p\bar{n}\pi^-$ final state, approximately 2.756 millions events in collider data are expected. The scale-factor is 0.551. For the charged conjugated process $J/\psi \rightarrow \bar{p}n\pi^-$ a similar branching fraction and thus, expected number of events in data and scale-factor are assumed. The simulation for $e^+e^- \rightarrow \bar{p}p(\gamma_{\text{ISR}})$ for all center-of-mass energies analyzed in this thesis is only used to study the cut efficiency of a selection criterion in Section 8.3 and the trigger efficiency correction in Section 8.5, therefore no exact cross-sections and scale-factors are required.

Purpose	Sample	\sqrt{s} (GeV)	Generator	N_{gen}
Background estimation	$e^+e^- \rightarrow e^+e^-(\gamma_{\text{ISR}})$	2.3960	Babayaga 3.5	90M
Background estimation	$e^+e^- \rightarrow \mu^+\mu^-(\gamma_{\text{ISR}})$	2.3960	Babayaga 3.5	1.5M
Efficiency studies	$J/\psi \rightarrow p\bar{n}\pi^-(\gamma_{\text{ISR}})$	3.0969	BesEvtGen	5M
Efficiency studies	$J/\psi \rightarrow n\bar{p}\pi^+(\gamma_{\text{ISR}})$	3.0969	BesEvtGen	5M
Efficiency studies	$e^+e^- \rightarrow \bar{p}p(\gamma_{\text{ISR}})$	Table 3.11	ConExc	500K

Table A.4: Summary of different MC simulations used in this analysis for the estimation of the background contamination in collider data after the signal selection and for efficiency studies.

Additional plots for the signal extraction

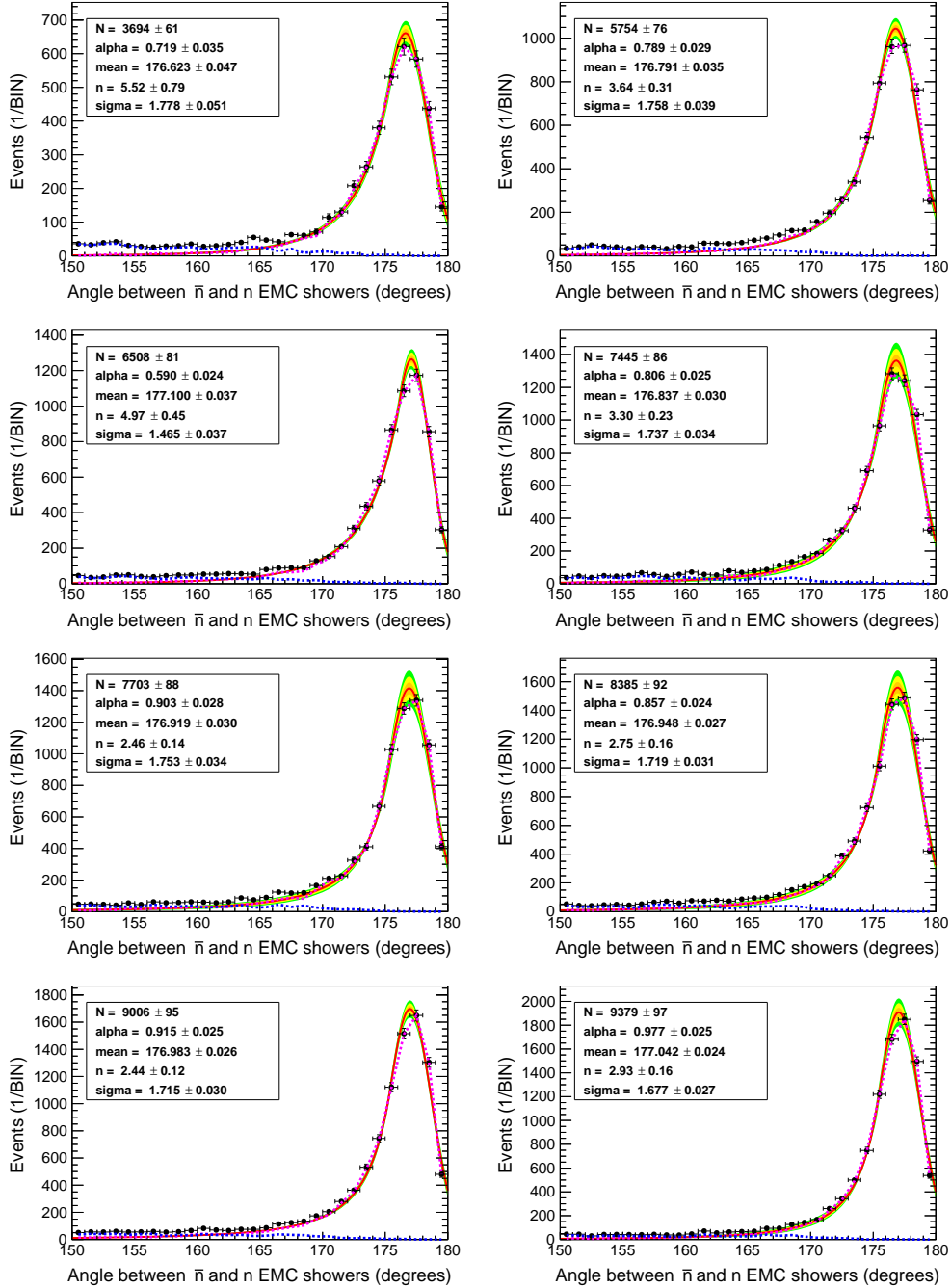


Fig. A.3: Fit to the opening angle between the $\bar{\nu}$ and ν of the signal MC simulation for the extraction of the signal shape parameters for the composite fit in Section 7.3. Phokhara v9.1 is used as the signal MC simulation. The Crystal Ball function from Equation 7.1 is used for the fit. Results are shown at the $\sqrt{s} = 2.0500, 2.1000, 2.1266, 2.1500, 2.1750, 2.2000, 2.2324,$ and 2.3094 GeV. The notation and color representation are the same as in Figure 7.1.

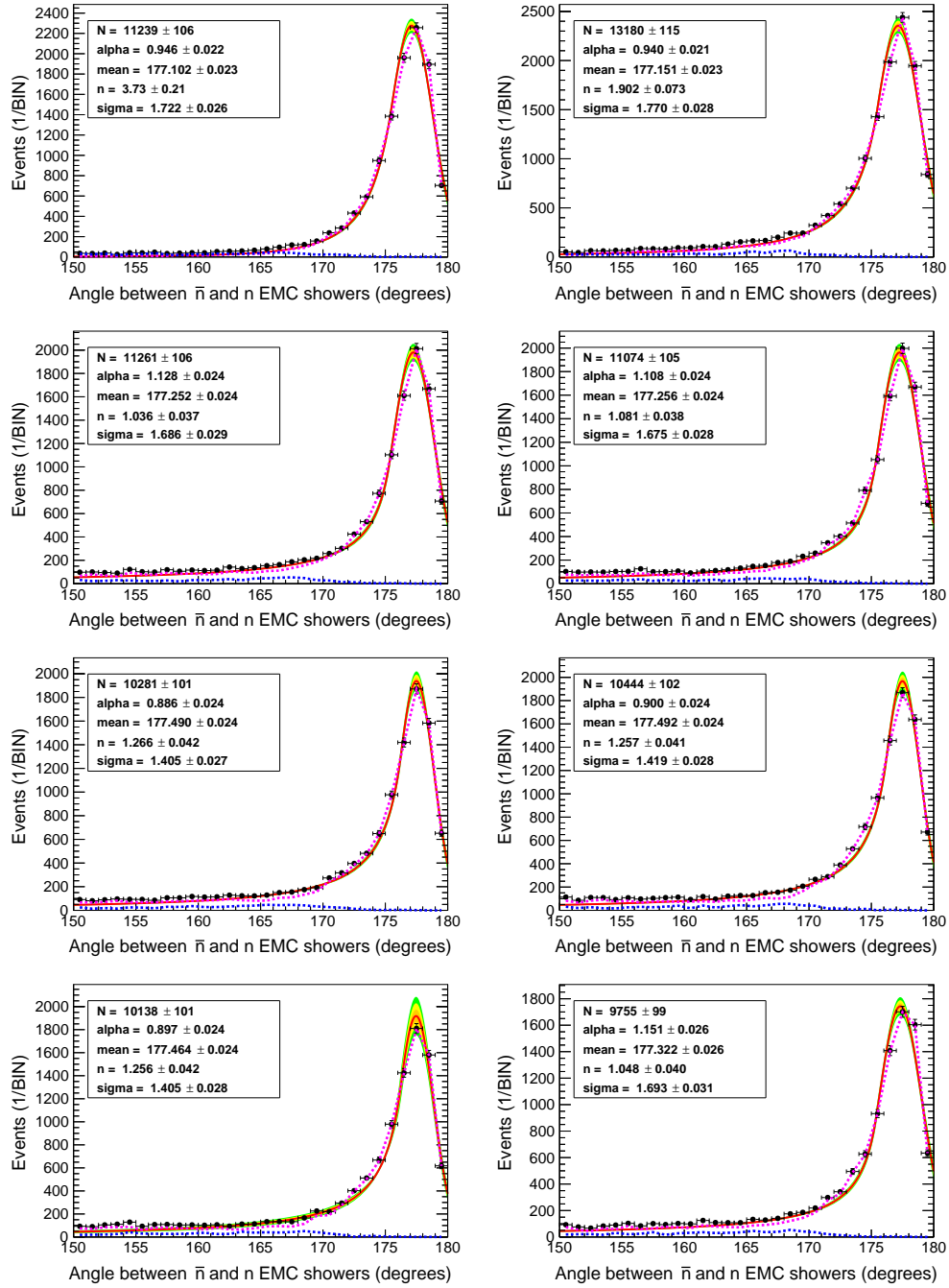


Fig. A.4: Fit to the opening angle between the \bar{n} and n of the signal MC simulation for the extraction of the signal shape parameters for the composite fit in Section 7.3. Phokhara v9.1 is used as the signal MC simulation. The Crystal Ball function from Equation 7.1 is used for the fit. Results are shown at the $\sqrt{s} = 2.3864, 2.6454, 2.9000, 2.9500, 2.9810, 3.0000, 3.0200,$ and 3.0800 GeV. The notation and color representation are the same as in Figure 7.1.

Plots of the composite fit model to the collider data at all \sqrt{s}

Figures A.5, A.6, and A.7 show the signal yield extraction, according to the fit function from Equation 7.3 in Chapter 7, from the collider data at all \sqrt{s} . The black dots show the collider data after the signal selection, as discussed in Section 5. The red dashed line is the signal process component of the composite fit for the signal yield extraction as discussed in Section 7.1. The green dashed line is the beam related and cosmic ray background component, the pink dashed line is the hadronic background component, both as discussed in Section 7.2. The fit is performed by minimizing the global negative log-likelihood of the composite model, the shown χ^2 is calculated only for an additional judgment of the goodness of fit. N_{data} is the number of selected events from collider data after the signal selection in Section 5.3. N_{fit} is the number of the extracted signal events with the composite fit model from Section 7.3. Additionally, the figures show the Pull distribution at the corresponding \sqrt{s} . The Pull distribution is defined as $\text{Pull}_i = (N_i^{\text{data}} - N_i^{\text{fit}}) / \Delta N_i^{\text{data}}$. The red, orange, and green dashed lines in the plots for the Pull distributions indicate the 1, 2, and 3 σ interval.

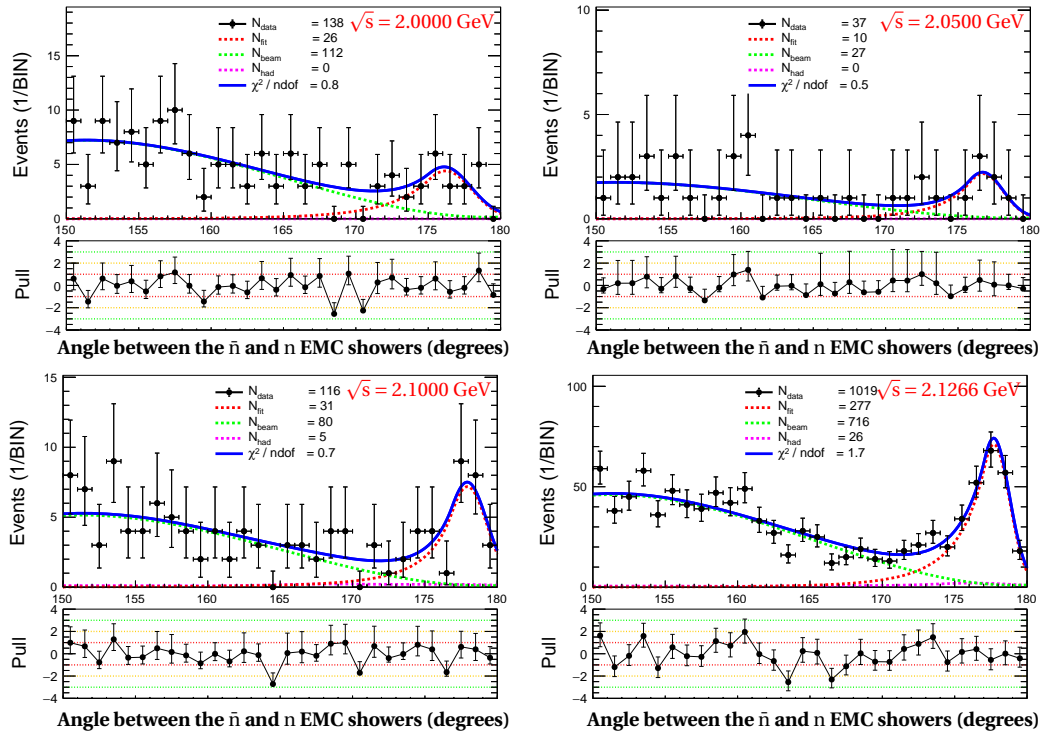


Fig. A.5: Signal yield extraction with the composite fit model from the Equation 7.3 applied to the collider data at $\sqrt{s} = 2.0000, 2.0500, 2.1000,$ and 2.1266 GeV. (Top panel) Composite fit model applied to the collider data. (Bottom panel) Corresponding Pull distribution.

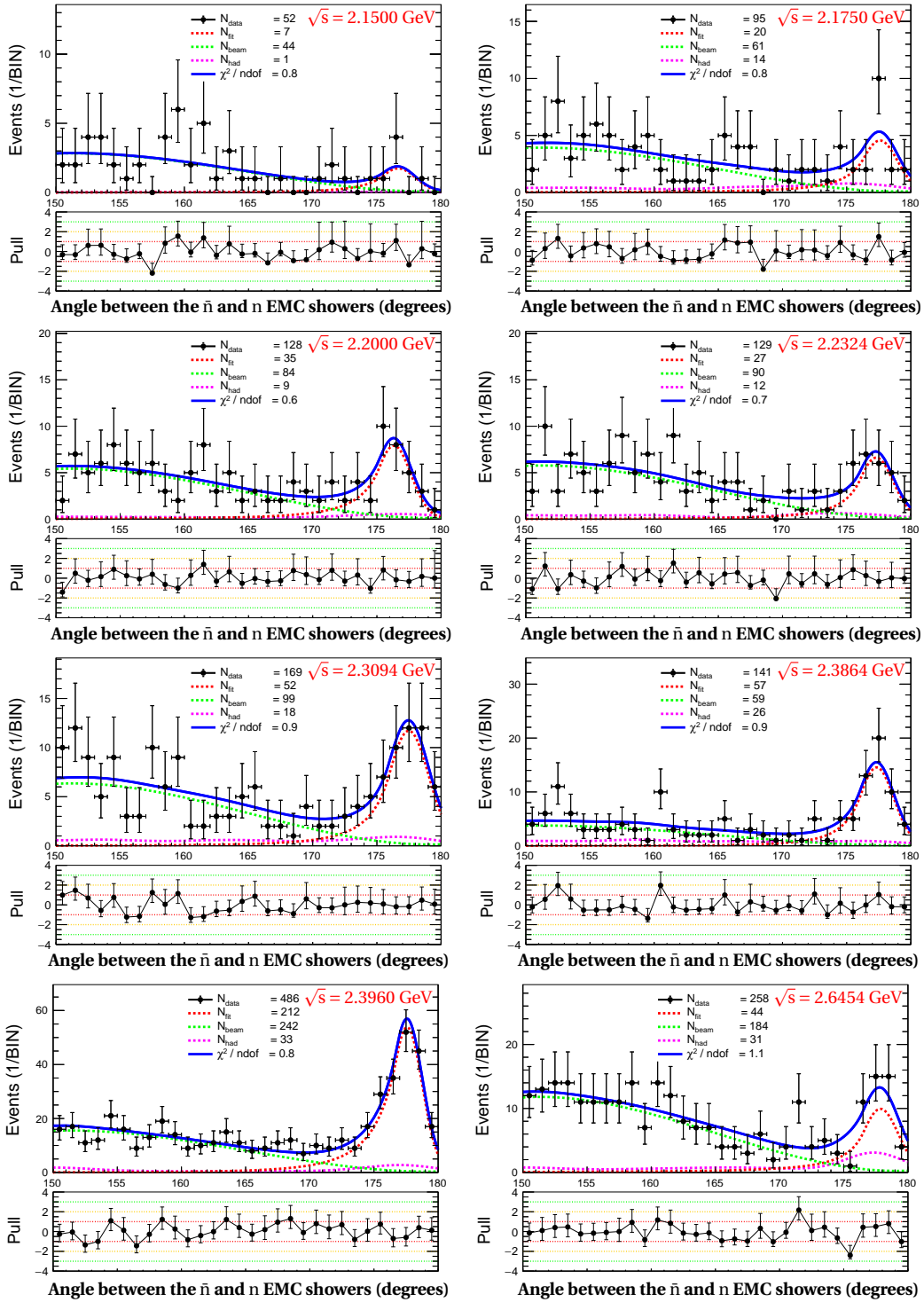


Fig. A.6: Signal yield extraction with the composite fit model from the Equation 7.3 applied to the collider data at $\sqrt{s} = 2.1500, 2.1750, 2.2000, 2.2324, 2.3094, 2.3864, 2.3960,$ and 2.6454 GeV. (Top panel) Composite fit model applied to the collider data. (Bottom panel) Corresponding Pull distribution.

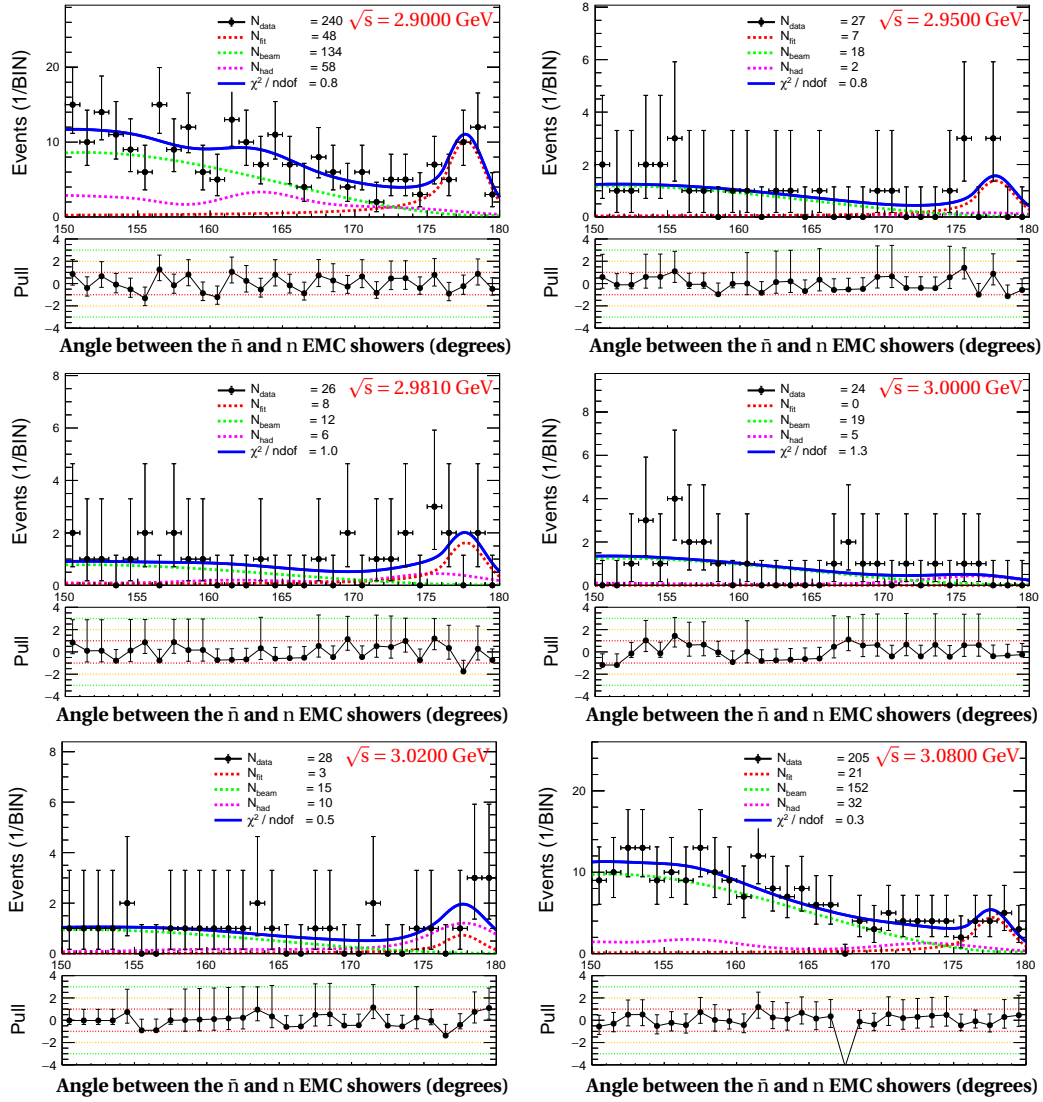


Fig. A.7: Signal yield extraction with the composite fit model from the Equation 7.3 applied to the collider data at $\sqrt{s} = 2.9000, 2.9500, 2.9810, 3.0000, 3.0200,$ and 3.0800 GeV. (Top panel) Composite fit model applied to the collider data. (Bottom panel) Corresponding Pull distribution.

Plots of the composite fit model to the collider data at all \sqrt{s}

Figures A.8 to A.21 show the composite fit model from Equation 7.3 applied to the opening angle distribution from the collider data. The distributions from the collider data are after the signal selection (as discussed in Chapter 5), for different $\cos\theta_{\bar{n}}$ bins at all analyzed \sqrt{s} . The analyzed $\cos\theta_{\bar{n}}$ range between -0.7 and 0.7 is divided into 7 bins with a bin width of 0.2. The signal yield is extracted for each bin individually.

The initial parameters for the composite fit are taken from the optimized composite fit to the integrated signal events in the collider data for the Born cross section calculation. The black dots are the collider data after the signal selection. The red dashed line is the signal model for the signal yield extraction, as discussed in Section 7.1. The green dashed line is the beam related and cosmic ray background component, the pink dashed line is the hadronic background component, both as discussed in Section 7.2. The fit is performed by minimizing the global negative log-likelihood of the composite model, the shown χ^2 is calculated only for an additional judgment of the goodness of fit. N_{data} is the number of selected events from collider data after the signal selection in Section 5.3. N_{fit} is the number of the extracted signal events with the composite fit model from Section 7.3.

Additionally, plots for the corresponding signal yield extraction with the massive MC simulation approach is shown. The gray histograms are the signal yield distributions from the MC simulation, based on the corresponding distributions from the collider data. The red line is the Gaussian fit for the extraction of the mean and sigma parameters, which are used as the extracted signal yields with the MC approach and the corresponding statistical uncertainties. For bins with a very low statistics, the MC approach show non-Gaussian resulting distribution for the signal yield. In the case of a non-converging Gaussian fit, the mean value and the corresponding uncertainty is extracted directly from the histogram.

The extracted signal events in each bin of the analyzed $\cos\theta_{\bar{n}}$ distribution are summarized in Table 7.3 for the approach with the composite fit model applied to the collider data. The summary of the extracted signal events with the massive MC simulation approach is shown in Table 7.4.

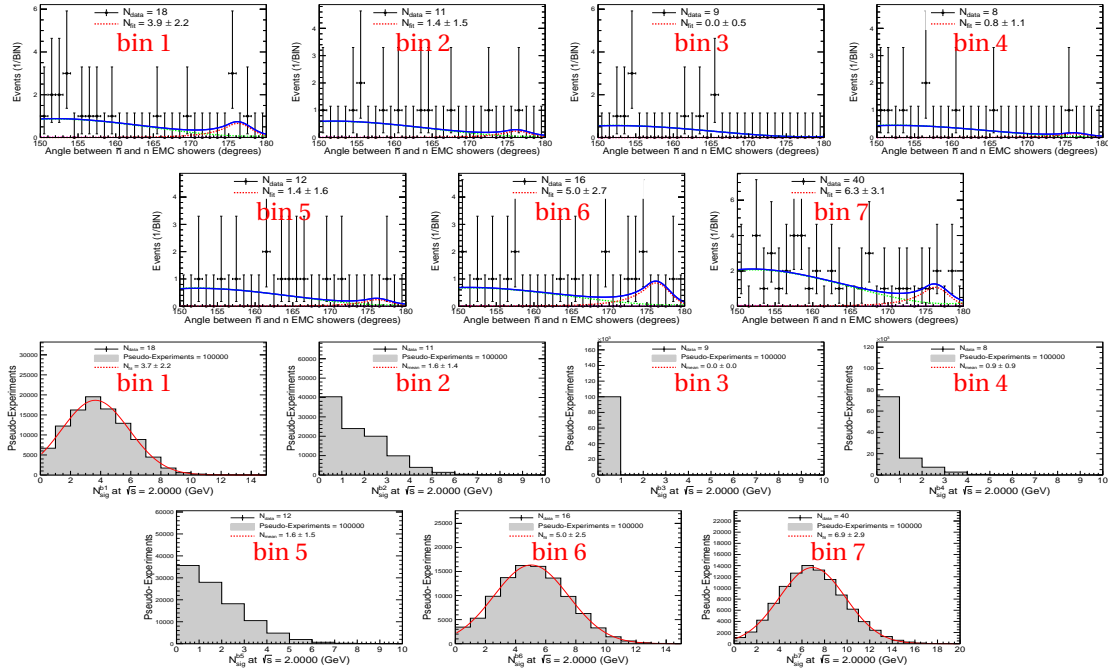


Fig. A.8: Differential signal yield at $\sqrt{s} = 2.0000$ GeV, (top) extracted with the composite fit model and (bottom) with the massive MC simulation. The notation is explained above.

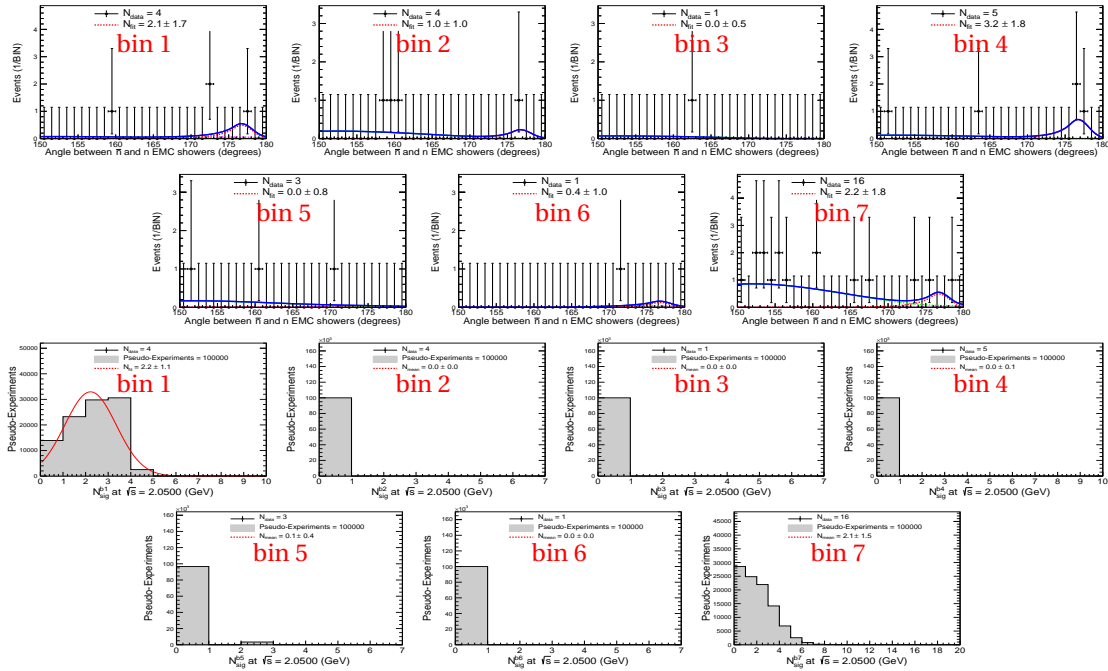


Fig. A.9: Differential signal yield at $\sqrt{s} = 2.0500$ GeV, (top) extracted with the composite fit model and (bottom) with the massive MC simulation. The notation is explained above.

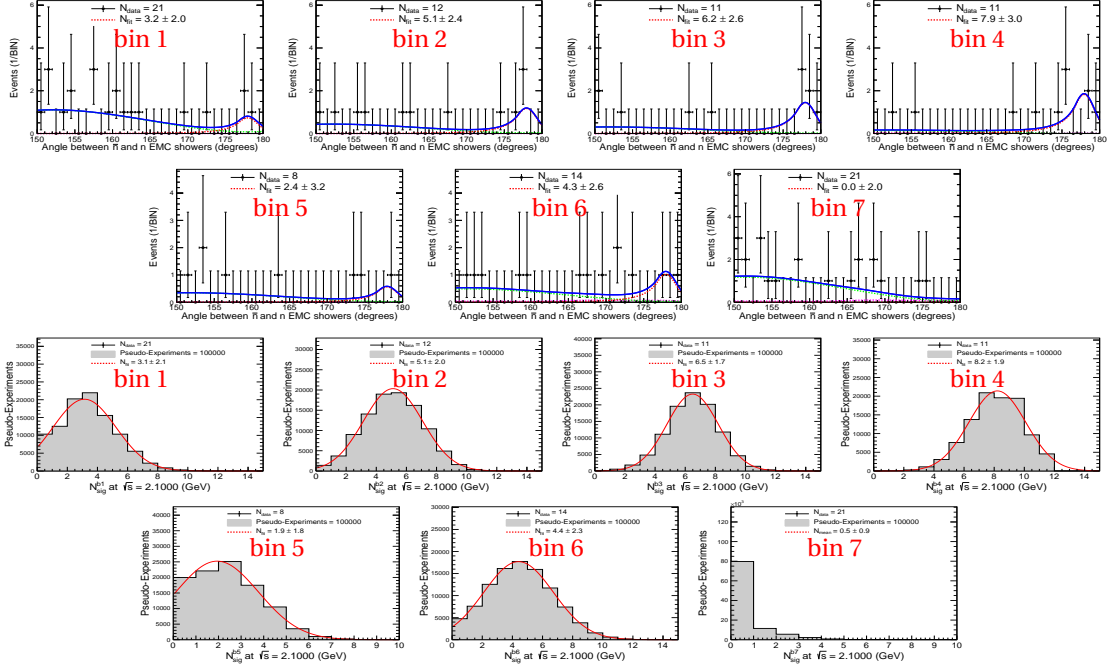


Fig. A.10: Differential signal yield at $\sqrt{s} = 2.1000$ GeV, (top) extracted with the composite fit model and (bottom) with the massive MC simulation. The notation is explained above.

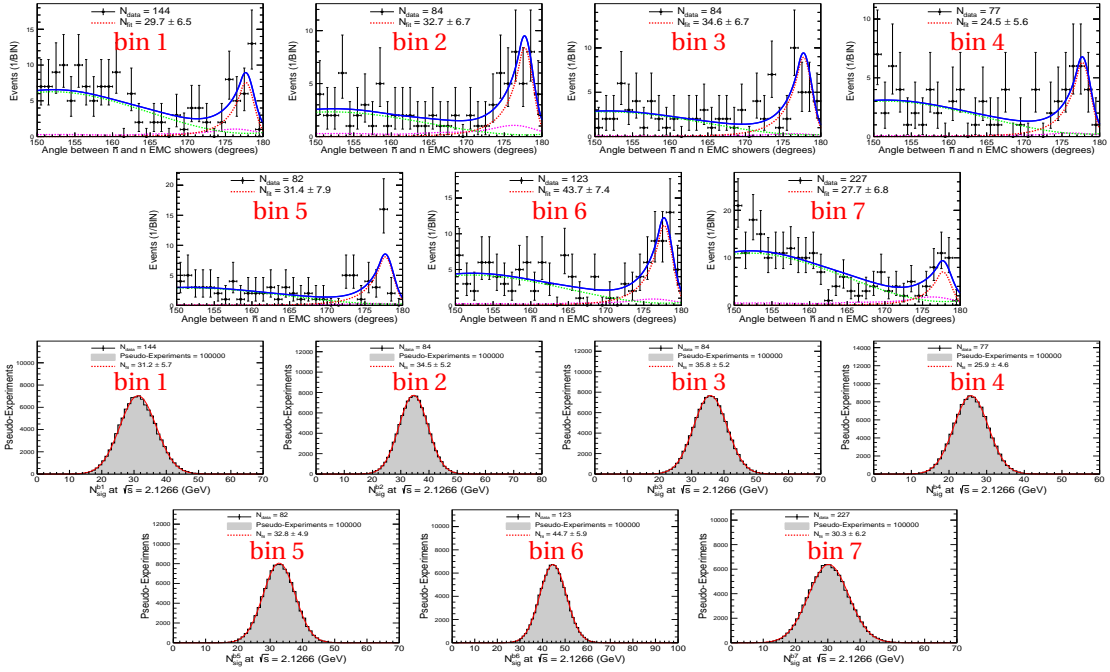


Fig. A.11: Differential signal yield at $\sqrt{s} = 2.1266$ GeV, (top) extracted with the composite fit model and (bottom) with the massive MC simulation. The notation is explained above.

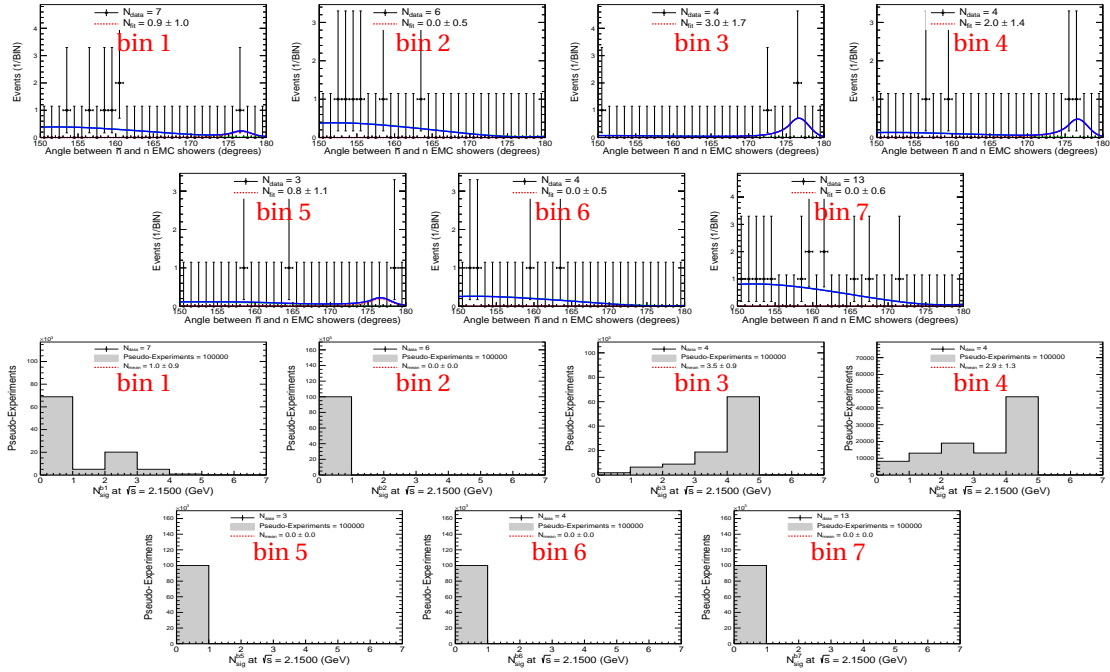


Fig. A.12: Differential signal yield at $\sqrt{s} = 2.1500$ GeV, (top) extracted with the composite fit model and (bottom) with the massive MC simulation. The notation is explained above.

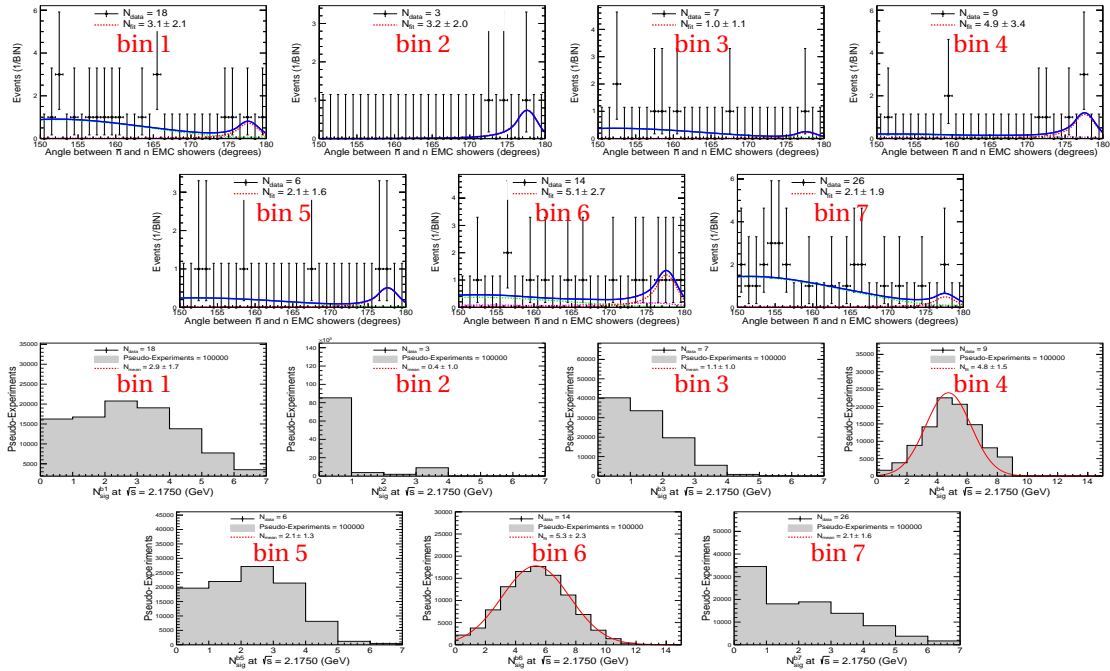


Fig. A.13: Differential signal yield at $\sqrt{s} = 2.1750$ GeV, (top) extracted with the composite fit model and (bottom) with the massive MC simulation. The notation is explained above.

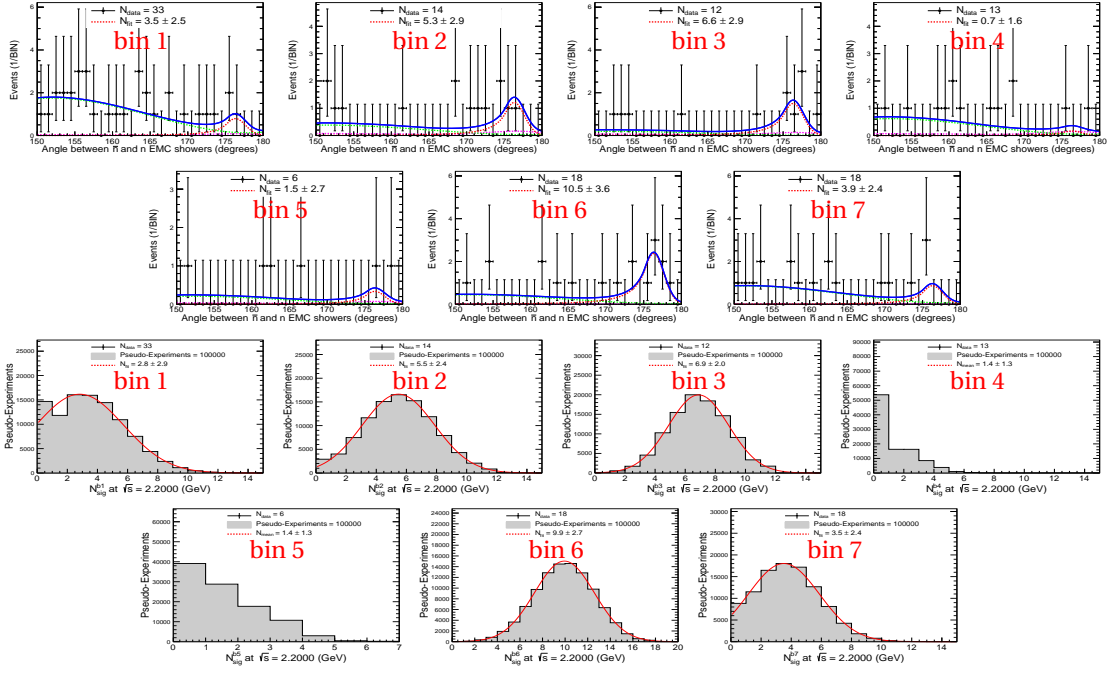


Fig. A.14: Differential signal yield at $\sqrt{s} = 2.2000$ GeV, (top) extracted with the composite fit model and (bottom) with the massive MC simulation. The notation is explained above.

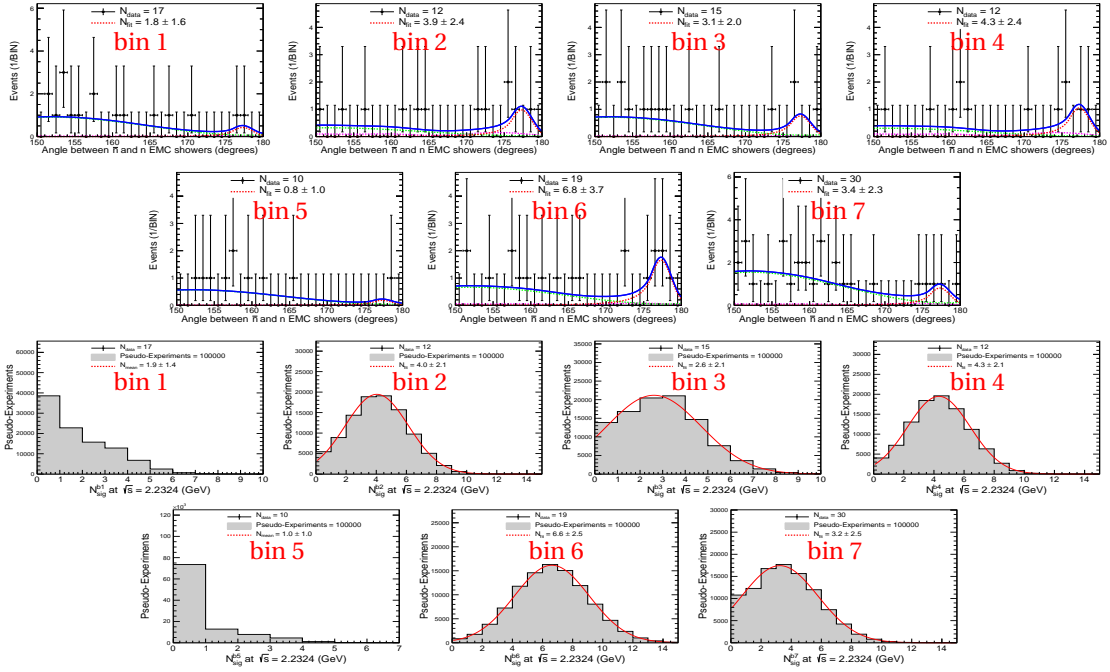


Fig. A.15: Differential signal yield at $\sqrt{s} = 2.2324$ GeV, (top) extracted with the composite fit model and (bottom) with the massive MC simulation. The notation is explained above.

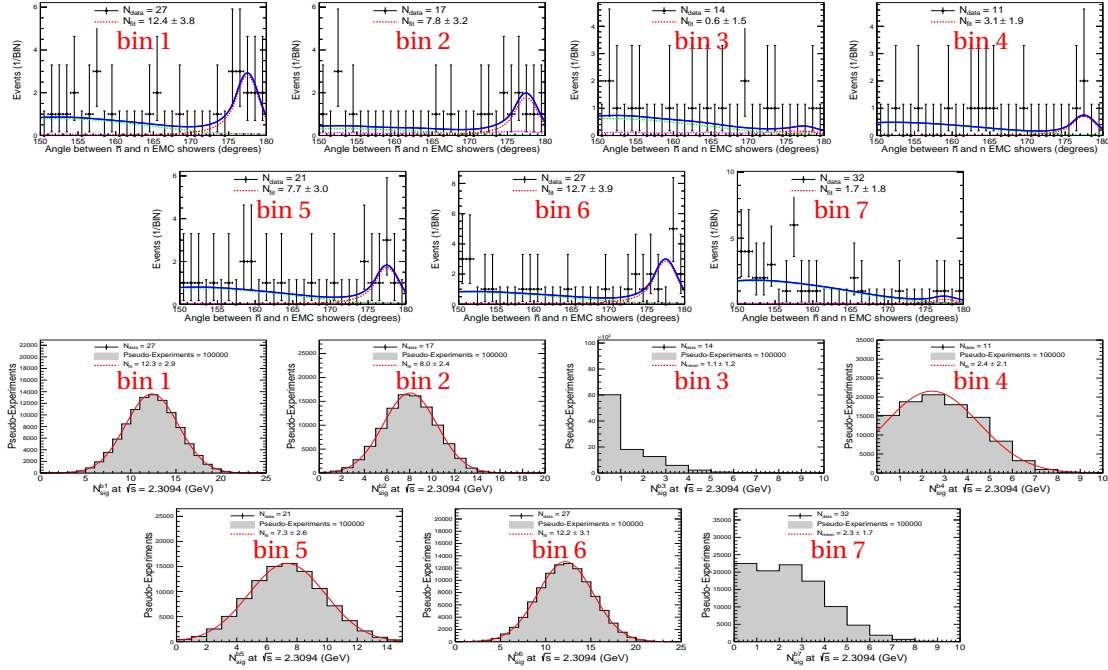


Fig. A.16: Differential signal yield at $\sqrt{s} = 2.3094$ GeV, (top) extracted with the composite fit model and (bottom) with the massive MC simulation. The notation is explained above.

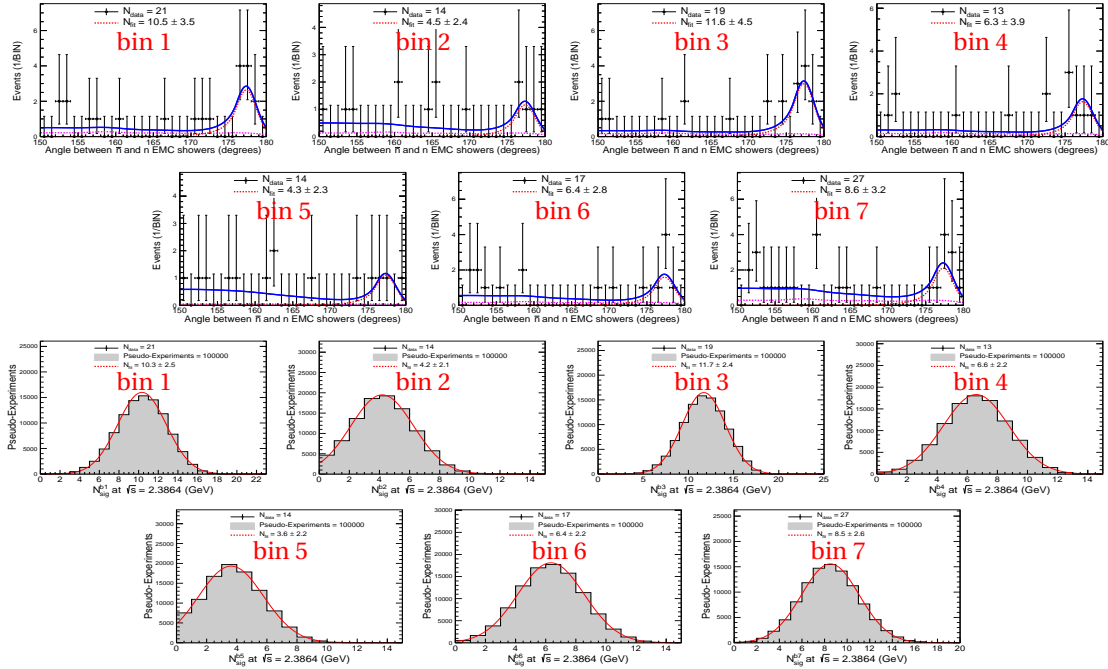


Fig. A.17: Differential signal yield at $\sqrt{s} = 2.3864$ GeV, (top) extracted with the composite fit model and (bottom) with the massive MC simulation. The notation is explained above.

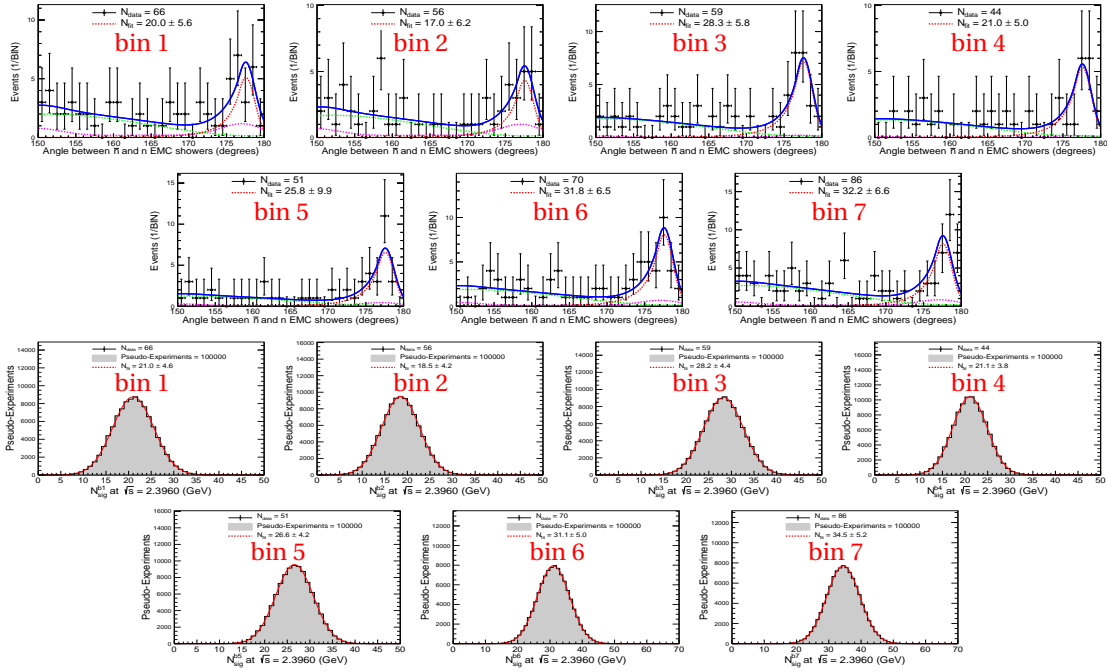


Fig. A.18: Differential signal yield at $\sqrt{s} = 2.3960$ GeV, (top) extracted with the composite fit model and (bottom) with the massive MC simulation. The notation is explained above.

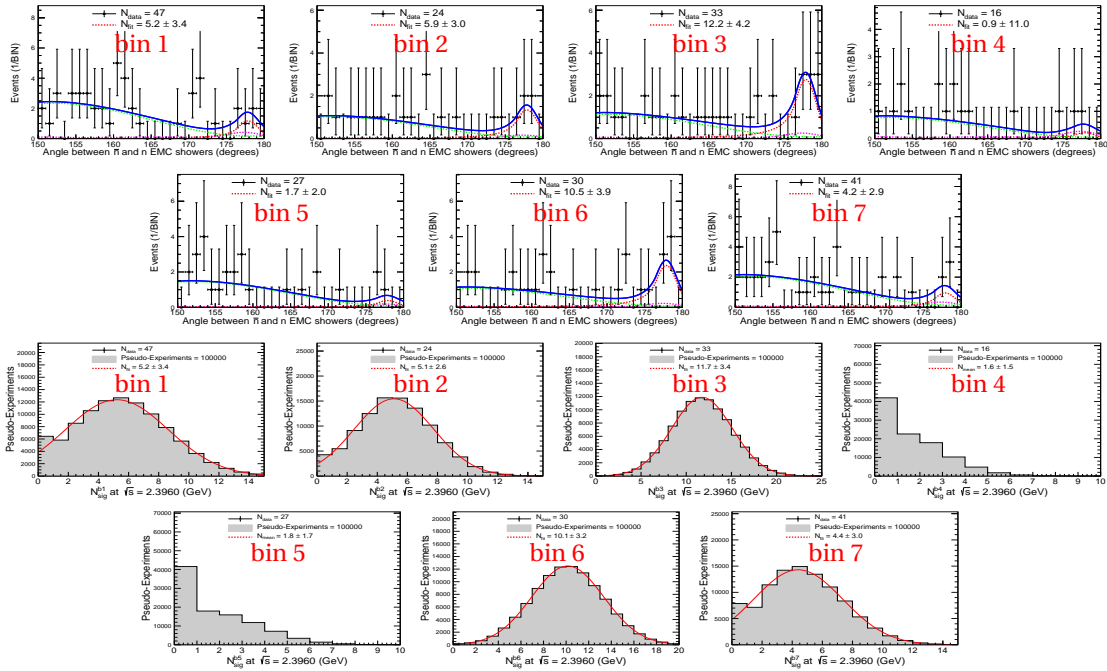


Fig. A.19: Differential signal yield at $\sqrt{s} = 2.6454$ GeV, (top) extracted with the composite fit model and (bottom) with the massive MC simulation. The notation is explained above.

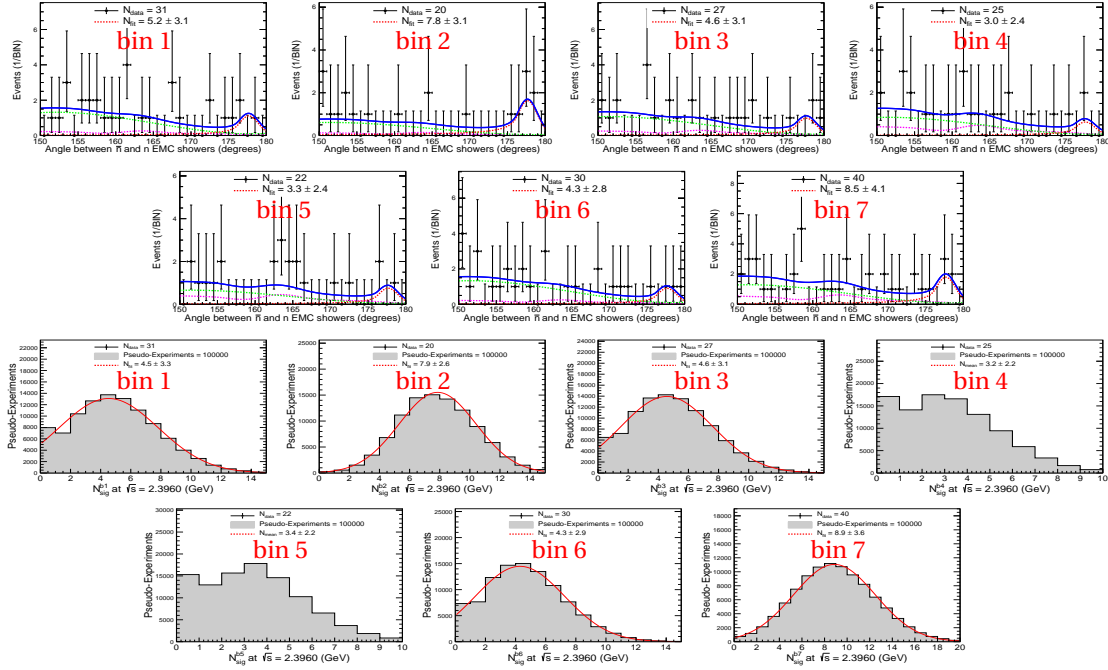


Fig. A.20: Differential signal yield at $\sqrt{s} = 2.9000$ GeV, (top) extracted with the composite fit model and (bottom) with the massive MC simulation. The notation is explained above.

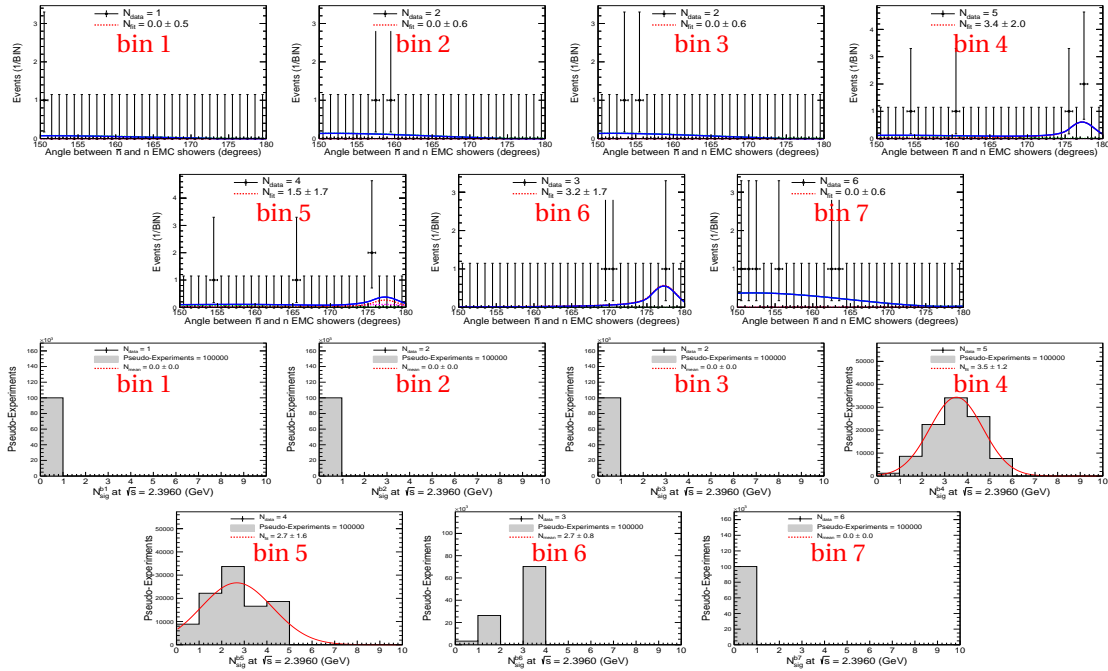


Fig. A.21: Differential signal yield at $\sqrt{s} = 2.9500$ GeV, (top) extracted with the composite fit model and (bottom) with the massive MC simulation. The notation is explained above.

Differential signal efficiency and its corrections

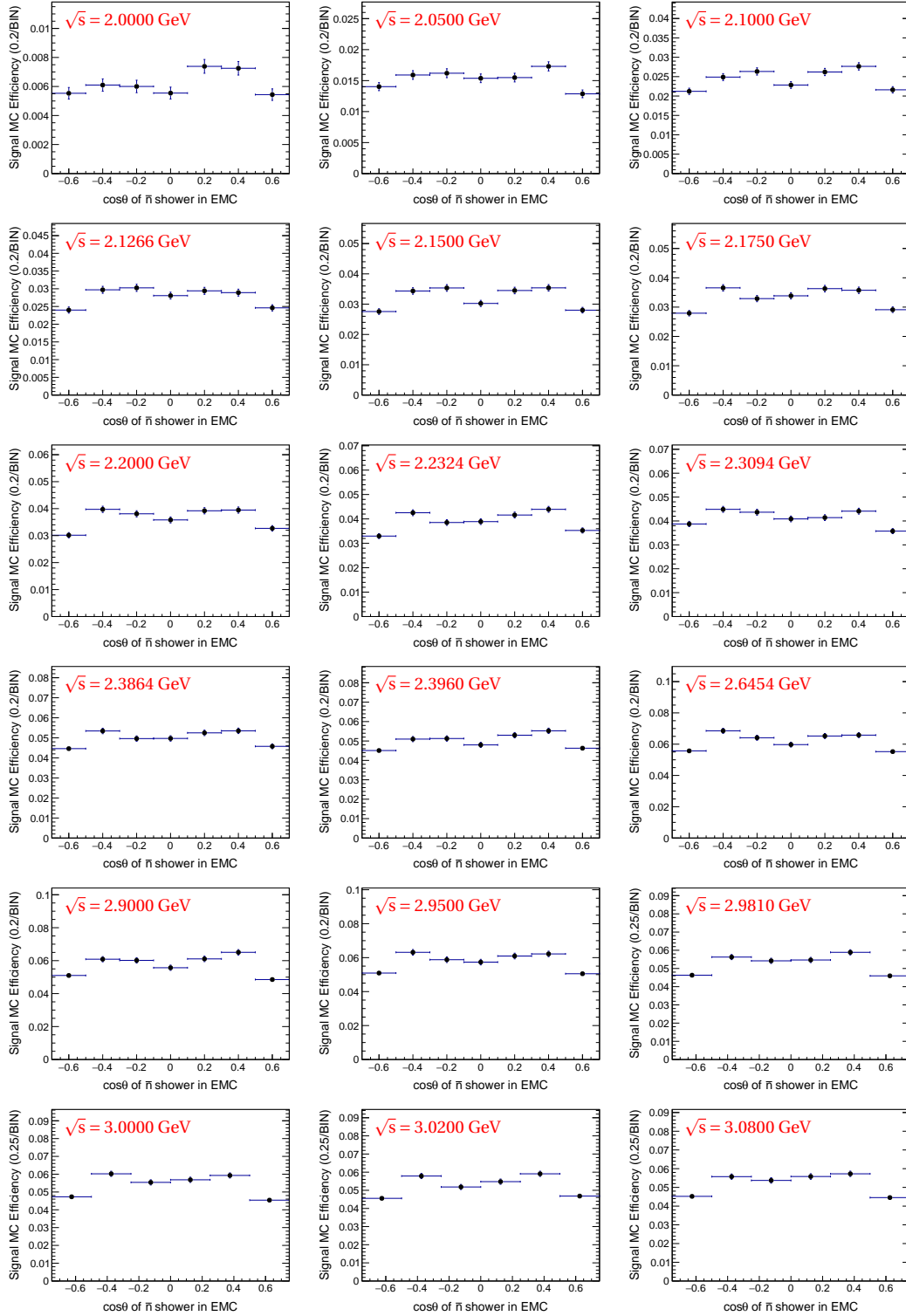


Fig. A.22: Differential signal efficiency $\frac{d\epsilon^{\text{MC}}}{d\cos\theta}$ from the signal MC simulation with Phokhara v9.1 at all analyzed center-of-mass energies \sqrt{s} according to Table 3.11.

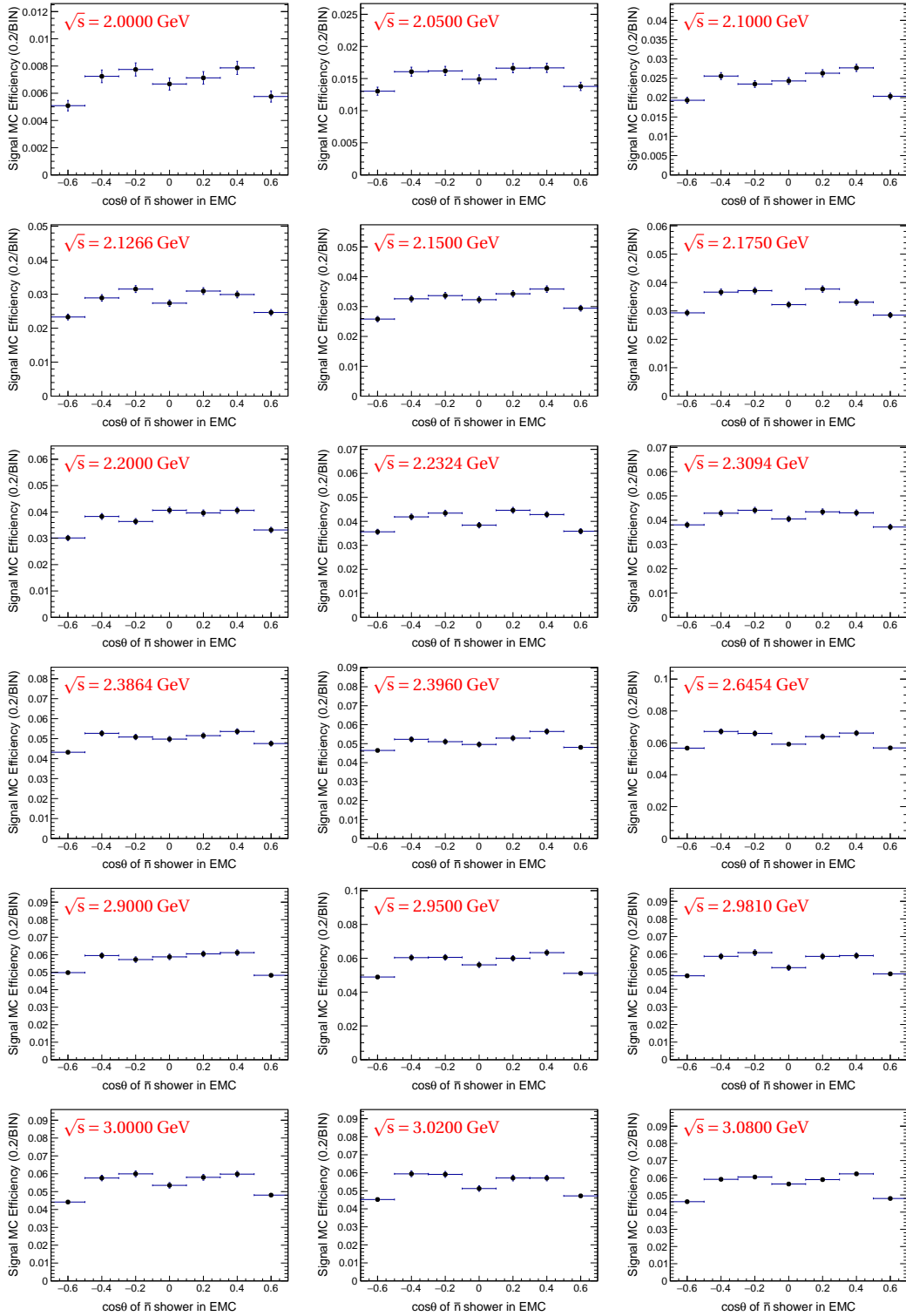


Fig. A.23: Differential signal efficiency $\frac{d\epsilon^{\text{MC}}}{d\cos\theta}$ from the signal MC simulation with ConExc at all analyzed center-of-mass energies \sqrt{s} according to Table 3.11.

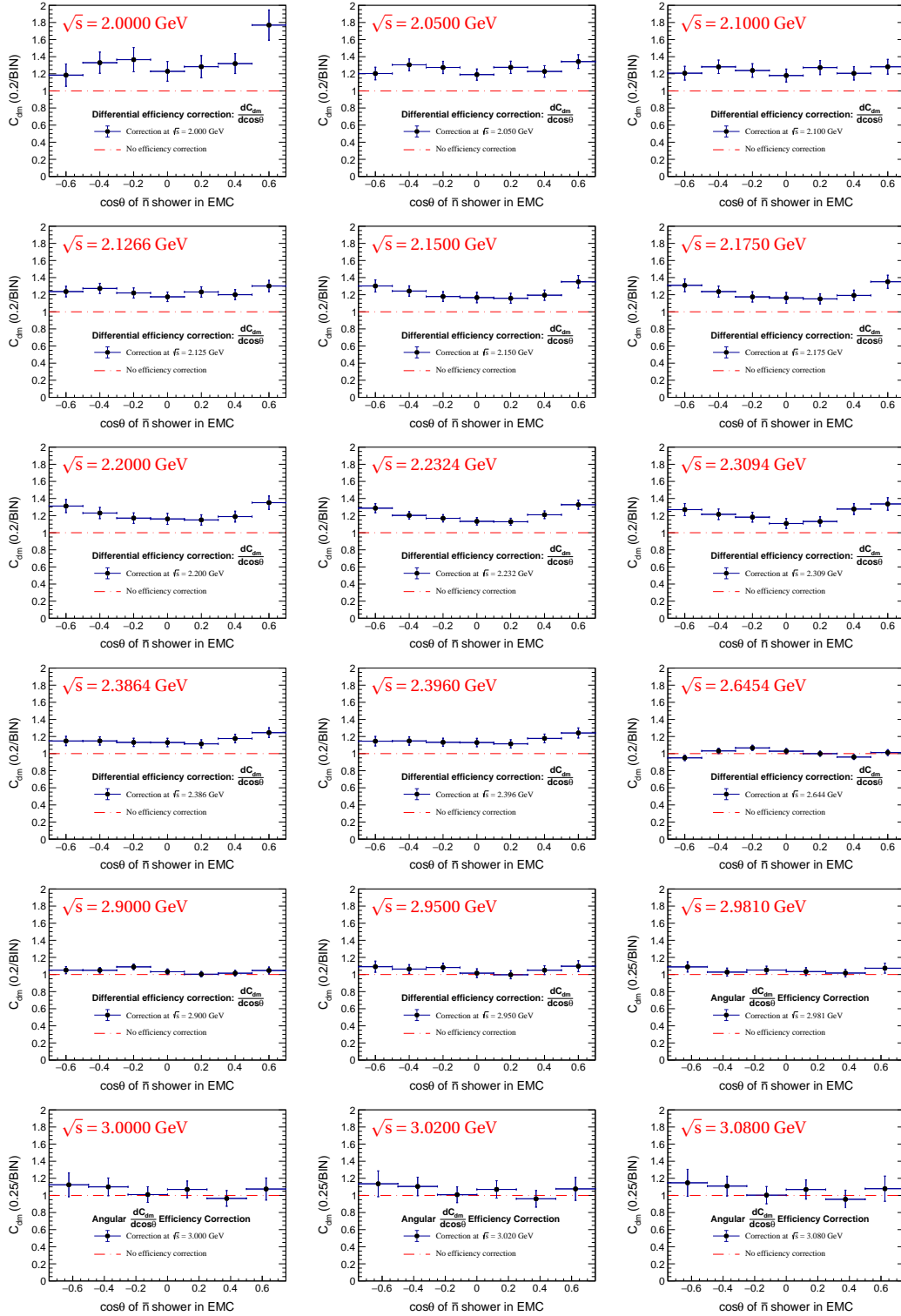


Fig. A.24: Differential correction factor $\frac{d\mathcal{E}_{dm}}{d\cos\theta}$ determined from the signal MC simulation with Phokhara v9.1 at all analyzed center-of-mass energies \sqrt{s} according to Table 3.11. The red dotted-dashed lines indicate a differential correction of 1 (equal to no correction).

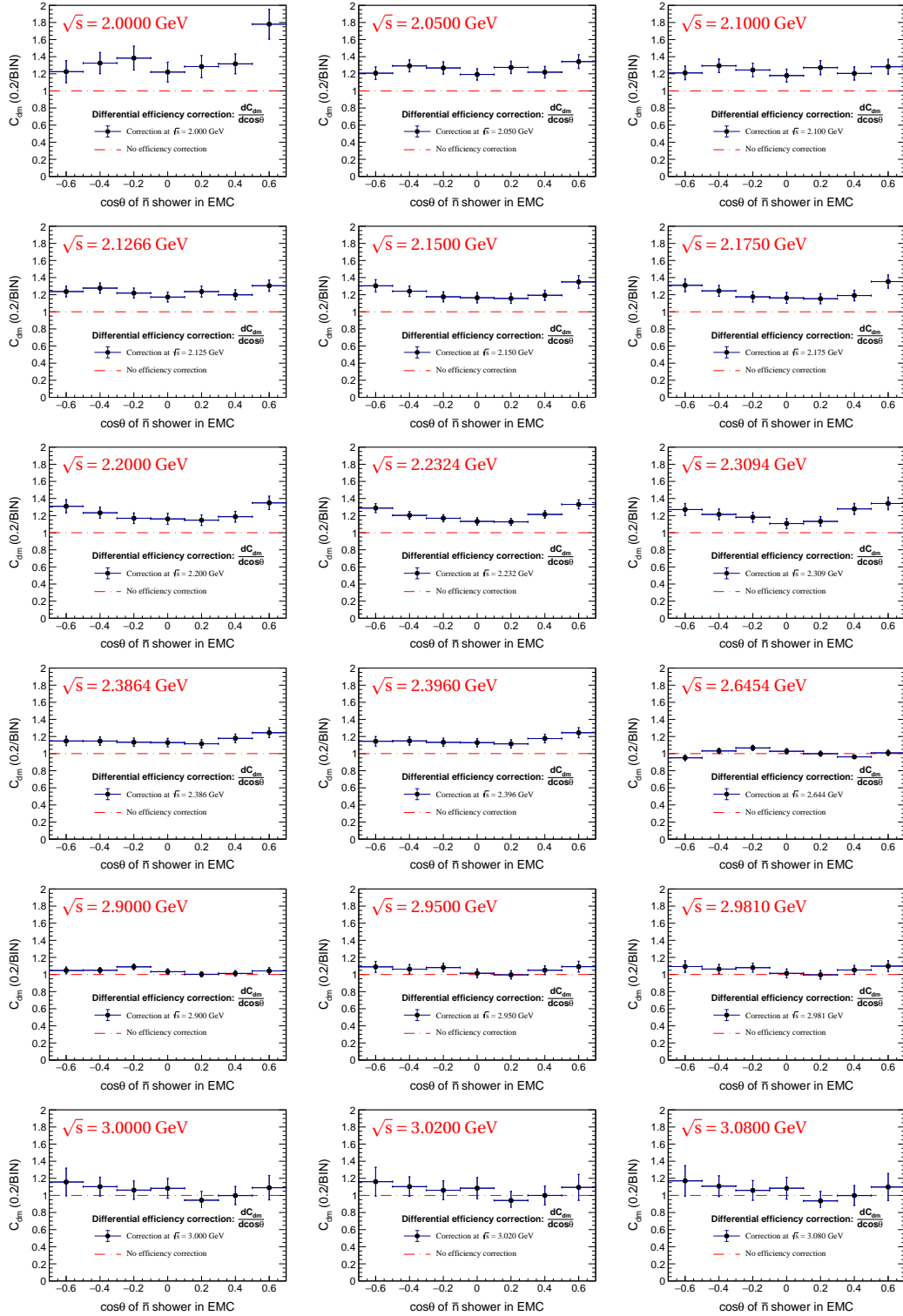


Fig. A.25: Differential correction factor $\frac{dC_{dm}}{d\cos\theta}$ determined from the signal MC simulation with ConExc at all analyzed center-of-mass energies \sqrt{s} according to Table 3.11. The red dotted-dashed lines indicate a differential correction of 1 (equal to no correction).

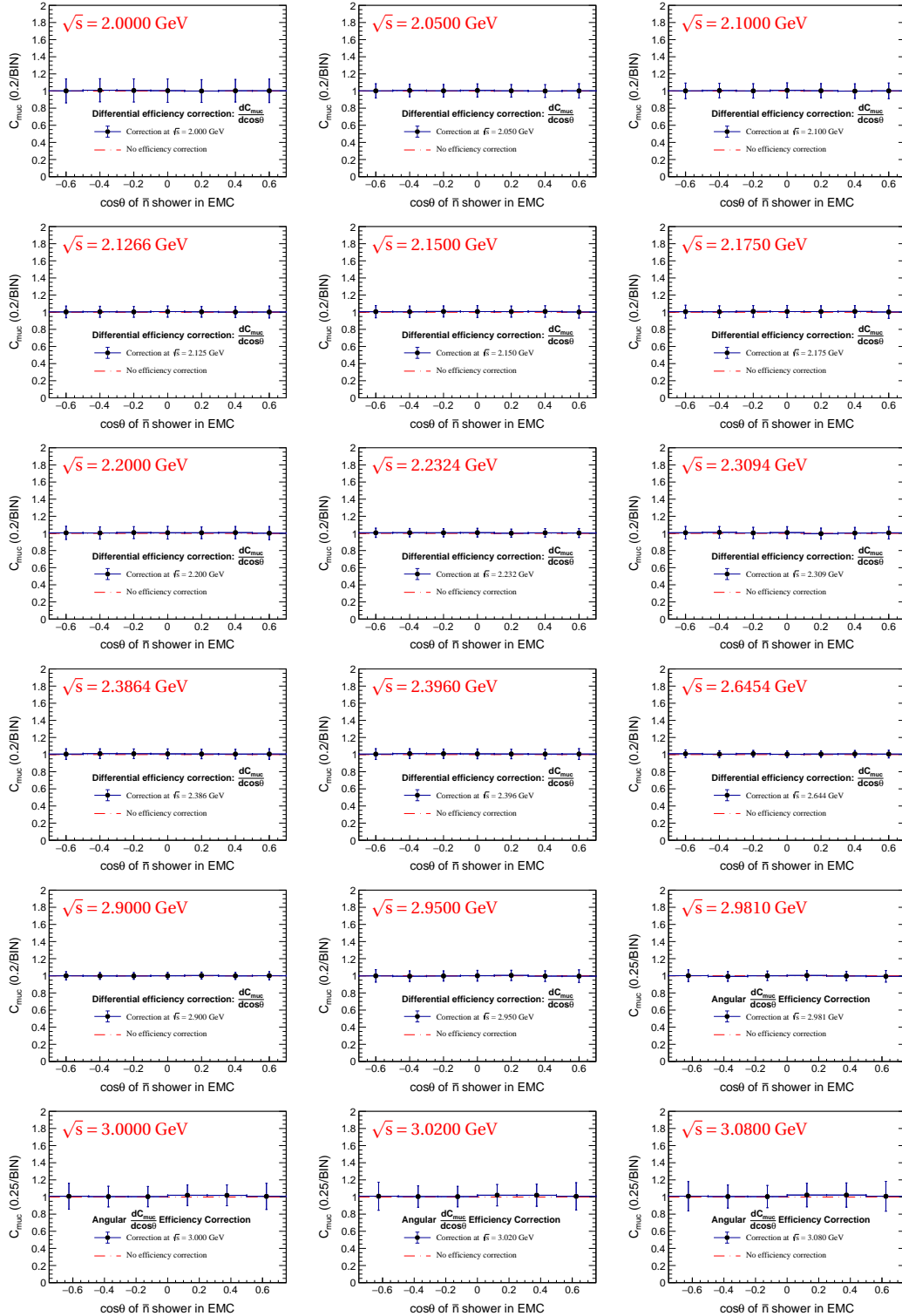


Fig. A.26: Differential correction factor $\frac{dC_{muc}}{d\cos\theta}$ determined from the signal MC simulation with Phokhara v9.1 at all analyzed center-of-mass energies \sqrt{s} according to Table 3.11. The red dotted-dashed lines indicate a differential correction of 1 (equal to no correction).

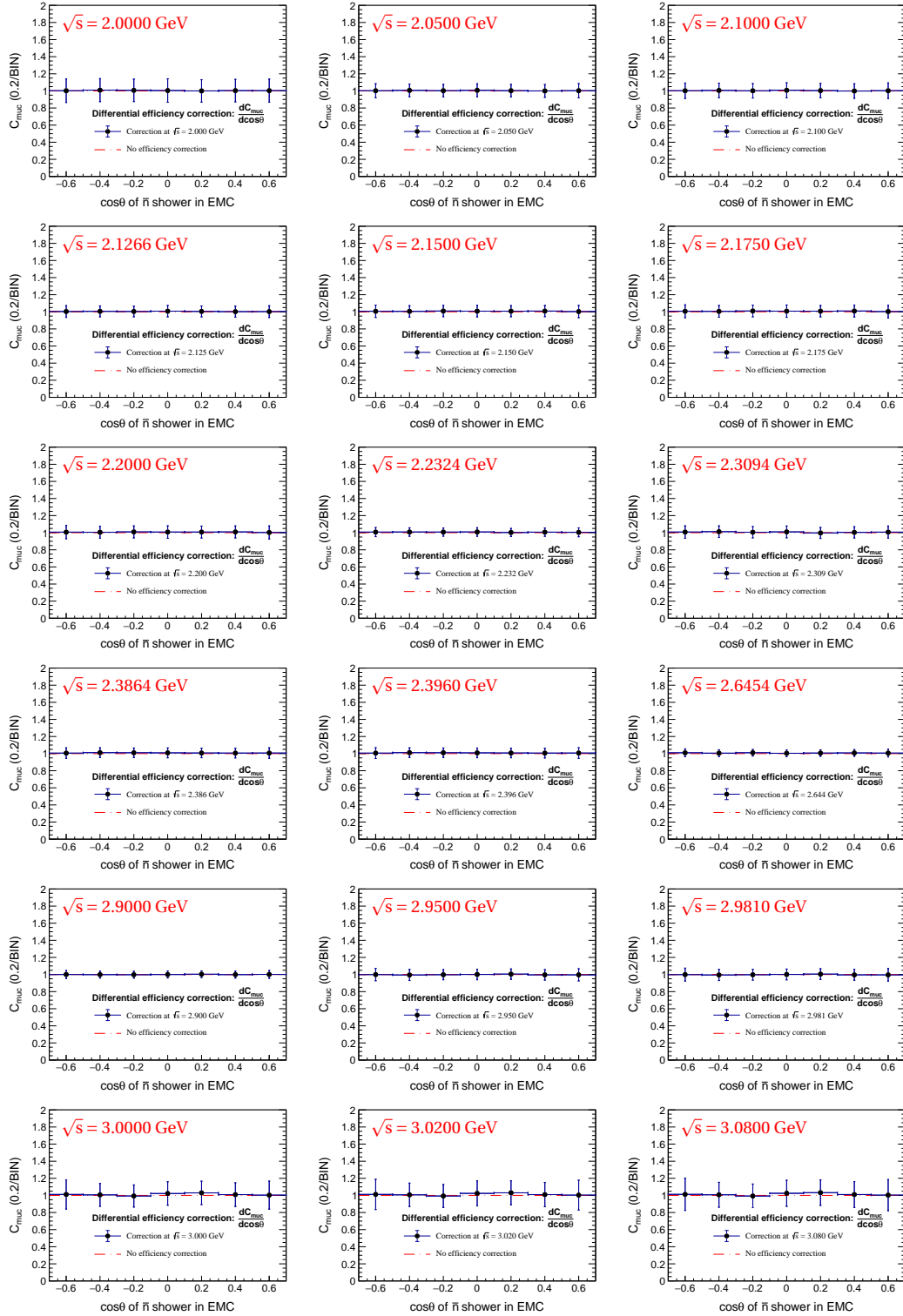


Fig. A.27: Differential correction factor $\frac{dC_{\text{muc}}}{d\cos\theta}$ determined from the signal MC simulation with ConExc at all analyzed center-of-mass energies \sqrt{s} according to Table 3.11. The red dotted-dashed lines indicate a differential correction of 1 (equal to no correction).

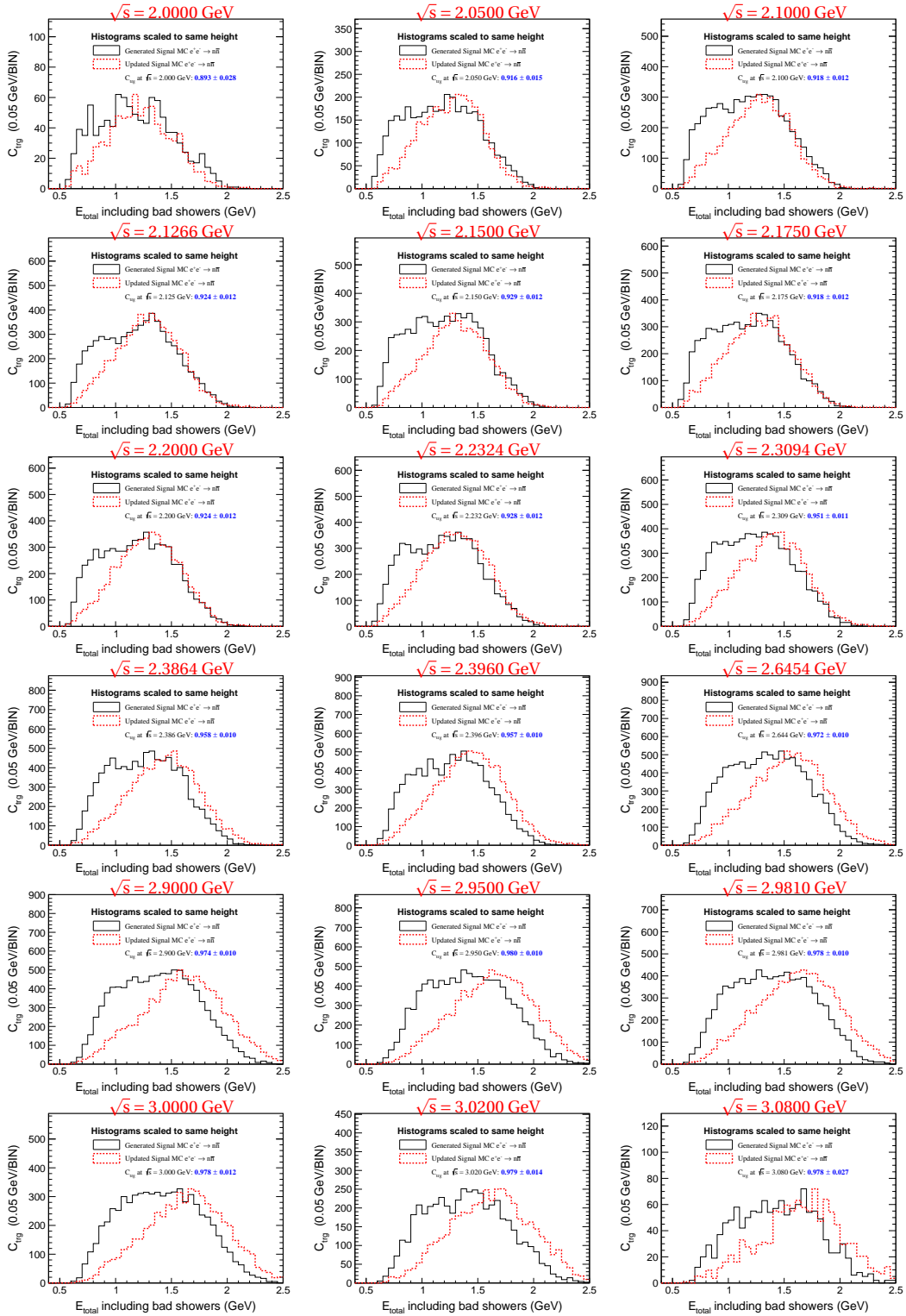


Fig. A.28: Total energy deposition in the EMC from MC simulation with Phokhara v9.1 and the replaced distribution as discussed in Section 8.5 at all analyzed \sqrt{s} according to Table 3.11. The black histograms are the original deposited energies, while the red histograms are the replaced energy distributions. The value for the trigger correction C_{trig} is listed in the plots.

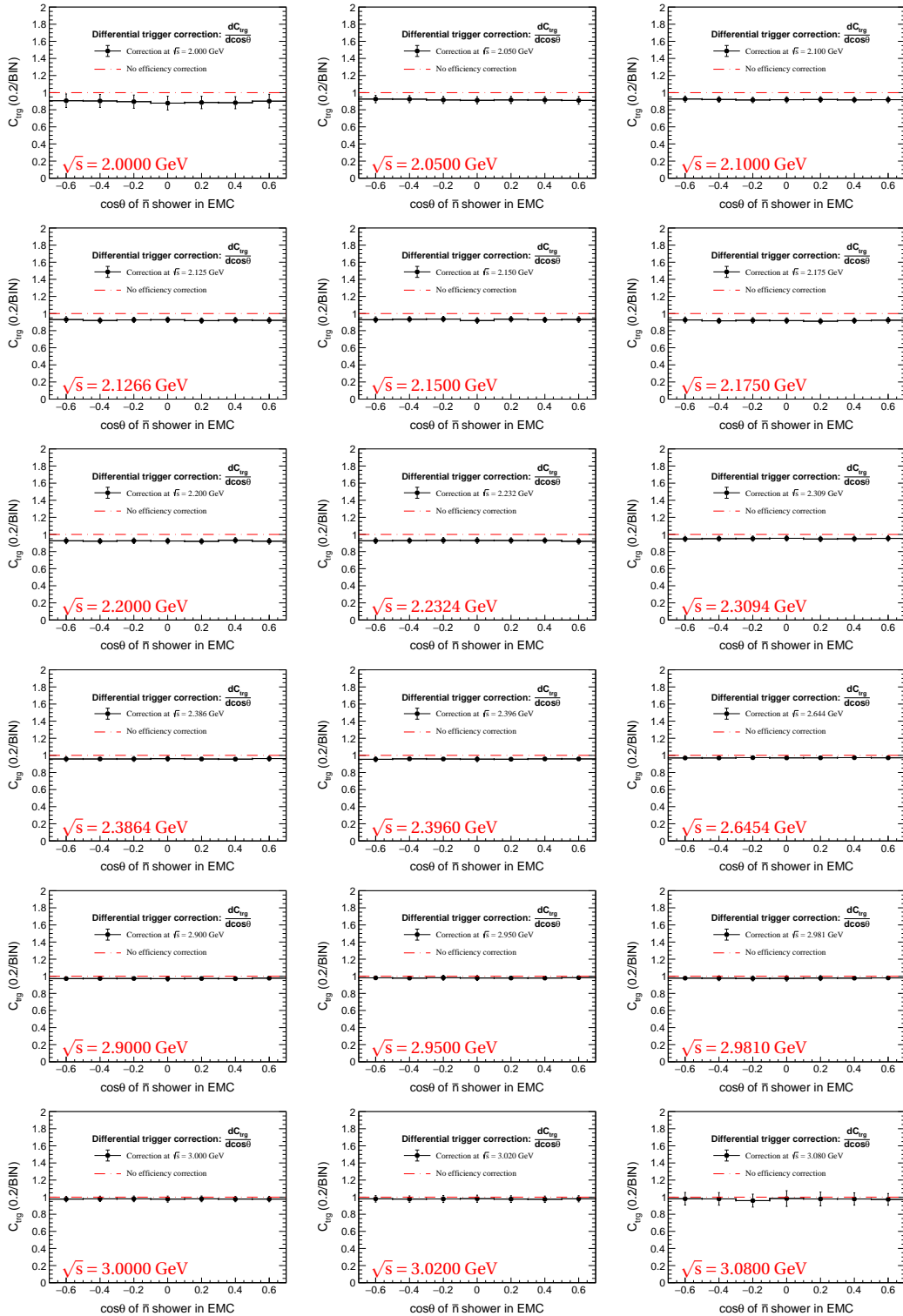


Fig. A.29: Differential correction factor $\frac{dC_{\text{trg}}}{d\cos\theta}$ determined from the signal MC simulation with Phokhara v9.1 at all analyzed center-of-mass energies \sqrt{s} according to Table 3.11. The red dotted-dashed lines indicate a differential correction of 1 (equal to no correction).

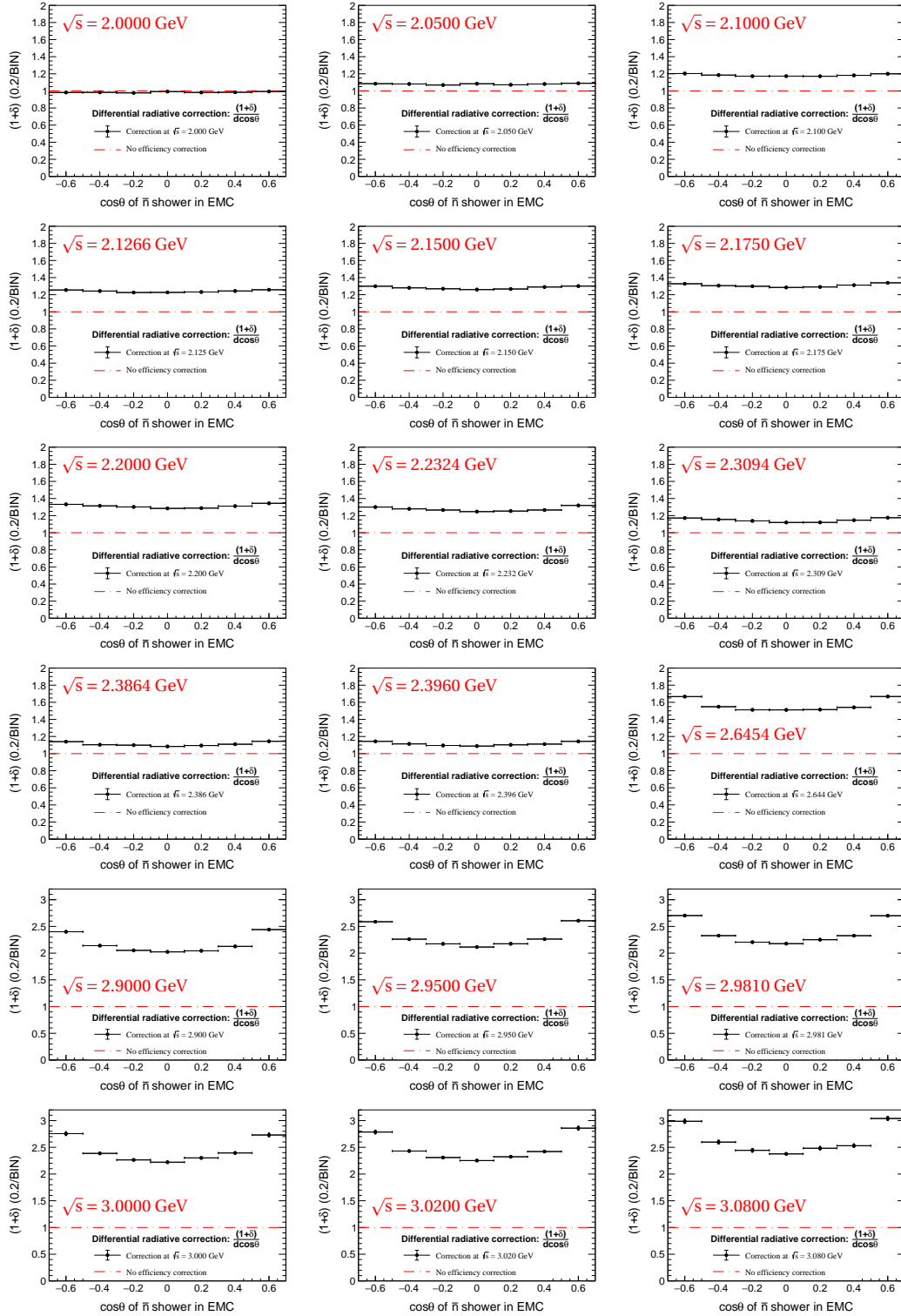


Fig. A.30: Differential correction factor $\frac{d(1+\delta)}{d\cos\theta}$ from the signal MC simulation with Phokhara v9.1 at all analyzed center-of-mass energies \sqrt{s} according to Table 3.11. The red dotted-dashed lines indicate a differential correction of 1 (equal to no correction).

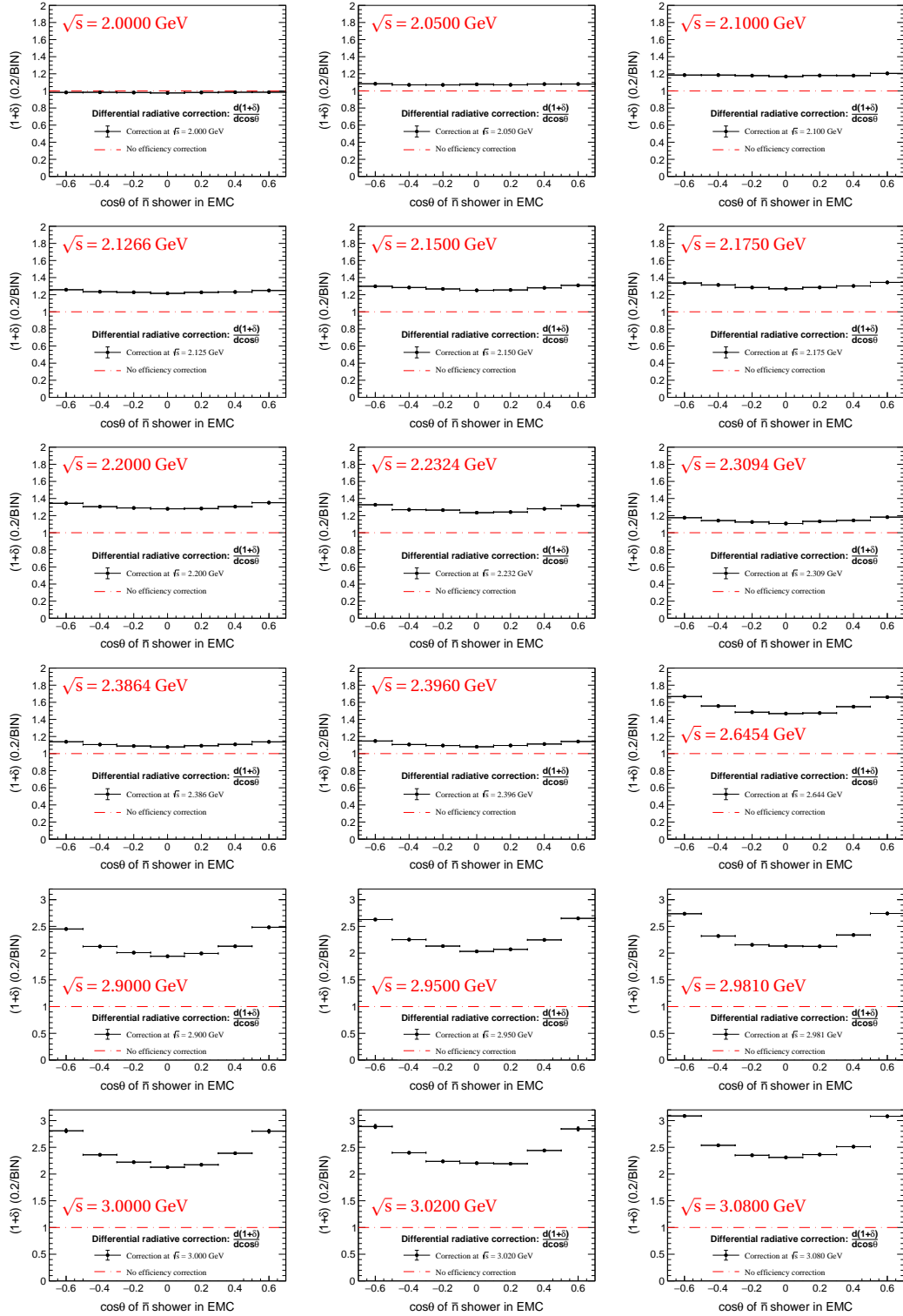


Fig. A.31: Differential correction factor $\frac{d(1+\delta)}{d\cos\theta}$ from the signal MC simulation with ConExc at all analyzed center-of-mass energies \sqrt{s} according to Table 3.11. The red dotted-dashed lines indicate a differential correction of 1 (equal to no correction).

Table A.5 shows the signal reconstruction efficiency from the signal MC and the efficiency corrections determined with the MC simulation with ConExc, in comparison with the values determined with the MC generator Phokhara v9.1, as listed in Table 8.8.

\sqrt{s} (GeV)	ϵ^{MC} (%)	C_{dm}	C_{ee}	C_{muc}	C_{trg}	$(1 + \delta)$
2.0000	0.34 ± 0.01	1.375 ± 0.034	0.750 ± 0.018	1.004 ± 0.024	0.888 ± 0.028	0.982 ± 0.001
2.0500	0.75 ± 0.01	1.267 ± 0.021	0.753 ± 0.015	1.003 ± 0.016	0.911 ± 0.015	1.076 ± 0.001
2.1000	1.15 ± 0.02	1.254 ± 0.017	0.772 ± 0.011	1.003 ± 0.013	0.921 ± 0.012	1.183 ± 0.001
2.1266	1.34 ± 0.02	1.247 ± 0.014	0.795 ± 0.009	1.004 ± 0.012	0.925 ± 0.012	1.235 ± 0.001
2.1500	1.51 ± 0.02	1.235 ± 0.014	0.825 ± 0.014	1.006 ± 0.012	0.929 ± 0.012	1.278 ± 0.001
2.1750	1.59 ± 0.02	1.234 ± 0.014	0.854 ± 0.020	1.007 ± 0.011	0.918 ± 0.012	1.305 ± 0.001
2.2000	1.74 ± 0.02	1.231 ± 0.013	0.874 ± 0.019	1.007 ± 0.011	0.923 ± 0.012	1.308 ± 0.001
2.2324	1.93 ± 0.02	1.216 ± 0.013	0.887 ± 0.021	1.006 ± 0.010	0.929 ± 0.012	1.276 ± 0.001
2.3094	1.93 ± 0.03	1.227 ± 0.013	0.892 ± 0.024	1.006 ± 0.010	0.950 ± 0.011	1.144 ± 0.001
2.3864	2.32 ± 0.02	1.167 ± 0.011	0.893 ± 0.021	1.008 ± 0.009	0.959 ± 0.010	1.107 ± 0.001
2.3960	2.36 ± 0.02	1.167 ± 0.011	0.893 ± 0.021	1.007 ± 0.009	0.958 ± 0.010	1.111 ± 0.001
2.6454	2.74 ± 0.02	1.006 ± 0.009	0.895 ± 0.027	1.007 ± 0.009	0.971 ± 0.009	1.551 ± 0.001
2.9000	2.28 ± 0.02	1.032 ± 0.010	0.898 ± 0.047	1.000 ± 0.009	0.976 ± 0.010	2.162 ± 0.001
2.9500	2.25 ± 0.02	1.046 ± 0.010	0.899 ± 0.052	0.998 ± 0.010	0.980 ± 0.010	2.287 ± 0.001
2.9810	2.16 ± 0.02	1.048 ± 0.010	0.899 ± 0.054	0.998 ± 0.010	0.977 ± 0.010	2.364 ± 0.001
3.0000	2.11 ± 0.02	1.056 ± 0.010	0.899 ± 0.056	1.011 ± 0.010	0.977 ± 0.012	2.410 ± 0.001
3.0200	2.06 ± 0.03	1.057 ± 0.010	0.899 ± 0.058	1.011 ± 0.010	0.978 ± 0.014	2.458 ± 0.001
3.0800	1.90 ± 0.02	1.059 ± 0.008	0.900 ± 0.063	1.012 ± 0.007	0.979 ± 0.027	2.605 ± 0.001

Table A.5: Summary of the signal MC reconstruction efficiency and its corrections from Tables 8.1, 8.2, 8.4, 8.5, 8.6, and 8.7 based on 500000 signal events generated with ConExc. The Born cross section input is from the final iteration of the optimization for the initial form factor parametrization.

Additional details for the systematic uncertainty study

In the following, additional details are shown for the study of the systematic uncertainty on the Born cross section and the effective form factor, as well as on the results for the magnetic form factor and the form factor ratio from the angular analysis, as discussed in Chapter 10. For the systematic uncertainty on the results from the angular analysis, the nominal values for $R_{\text{em}}^{\text{ind}}(s)$ and $G_{\text{M}}^{\text{ind}}(s)$ are slightly different from the individual results in Table 9.4, since derived with the approach 1 using the simple fit function without taking the resolution into account and not using the integral-over-the-bin-width form. The difference is around 1 %. Since the relative difference between the nominal and the varied results is taken as the systematic uncertainty, and the varied results are derived with the same approach, the small deviation of the nominal results to the values from Table 9.4 is negligible.

Systematic uncertainty on $\sigma_{\text{Born}}^{\text{ind}}(s)$ due to the signal selection

The contributions to the systematic uncertainty from the signal selection on the individual results for the Born cross section, as discussed in Section 10.1.2, are shown in Table A.6 together with the calculated values for δ_{sel} at all center-of-mass energies \sqrt{s} according to Table 3.11.

\sqrt{s} (GeV)	ΔC_{dm}	ΔC_{ee}	ΔC_{muc}	δ_{sel} (%)	\sqrt{s} (GeV)	ΔC_{dm}	ΔC_{ee}	ΔC_{muc}	δ_{sel} (%)
2.0000	3.54	1.92	2.55	4.77	2.3864	1.11	1.86	0.95	2.37
2.0500	2.09	1.61	1.65	3.11	2.3960	1.11	1.85	0.95	2.35
2.1000	1.65	1.11	1.32	2.39	2.6454	0.88	2.66	0.88	2.93
2.1266	1.55	0.90	1.24	2.18	2.9000	0.98	4.63	0.95	4.83
2.1500	1.44	1.41	1.17	2.33	2.9500	1.00	5.06	0.95	5.24
2.1750	1.41	1.92	1.15	2.65	2.9810	1.04	5.32	0.99	5.51
2.2000	1.35	1.77	1.10	2.48	3.0000	1.04	5.48	0.99	5.67
2.2324	1.29	1.92	1.06	2.54	3.0200	1.06	5.66	1.01	5.84
2.3094	1.27	2.13	1.04	2.69	3.0800	1.08	6.18	1.03	6.36

Table A.6: Summary of systematic uncertainty due to the signal selection δ_{sel} on the individual results for Born cross section at different \sqrt{s} . The values are taken from Table 8.2, 8.3, and 8.5, respectively.

Systematic uncertainty on $\sigma_{\text{Born}}(s)$ due to the signal yield extraction

Figure A.32 shows the neutron misidentification rate as described in section 10.1.3.

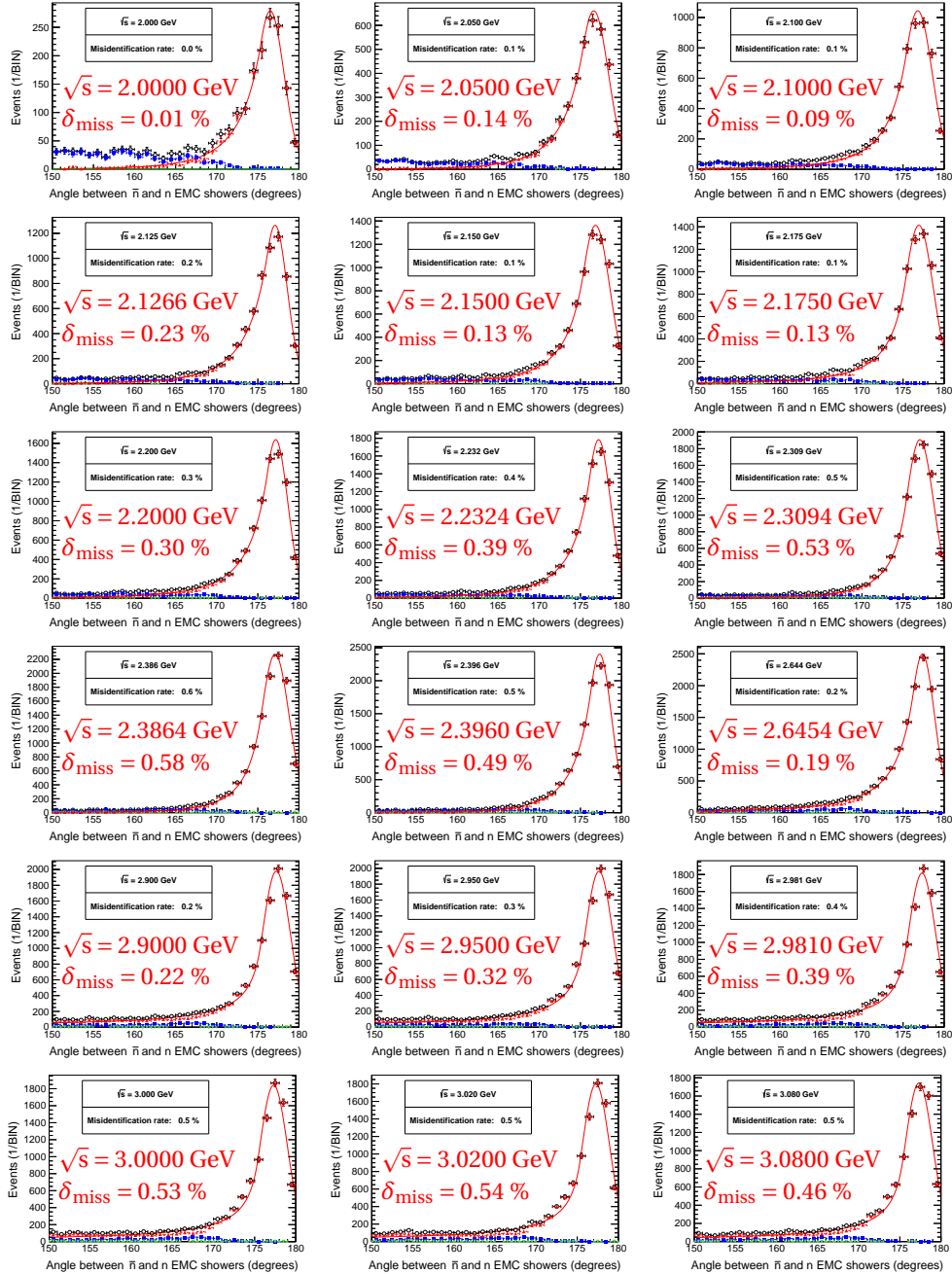


Fig. A.32: The misidentification rate of the neutron EMC shower δ_{miss} at all \sqrt{s} as defined in Section 10.1.3. The fit model is shown as the red line, taking into account only correctly identified neutron EMC showers with $\angle_{\text{shower}}^{\text{truth}} < 10^\circ$ shown as red triangles. The blue squares are the badly reconstructed neutron showers taken into account within the selection efficiency calculation in Section 8.1, the green triangles are events with misidentified neutron EMC showers, the black open circles denote all events.

The Table A.7 shows the systematic uncertainty δ_{miss} on the individual results for the Born cross section $\sigma_{\text{Born}}^{\text{ind}}$ (s) due to the neutron EMC shower misidentification, as discussed in Section 10.1.3.

\sqrt{s} (GeV)	$\epsilon_{\text{nominal}}^{\text{MC}}$ (%)	$\epsilon_{\text{w/miss}}^{\text{MC}}$ (%)	δ_{miss} (%)
2.0000	0.309	0.309	0.01
2.0500	0.738	0.739	0.14
2.1000	1.150	1.151	0.09
2.1266	1.301	1.304	0.23
2.1500	1.489	1.491	0.13
2.1750	1.540	1.542	0.13
2.2000	1.677	1.682	0.30
2.2324	1.801	1.808	0.39
2.3094	1.875	1.885	0.53
2.3864	2.247	2.260	0.58
2.3960	2.256	2.267	0.49
2.6454	2.636	2.641	0.19
2.9000	2.252	2.257	0.22
2.9500	2.214	2.221	0.32
2.9810	2.056	2.064	0.39
3.0000	2.088	2.099	0.53
3.0200	2.027	2.038	0.54
3.0800	1.951	1.960	0.46

Table A.7: Summary of the systematic uncertainty δ_{miss} on the individual results for the Born cross section due to the neutron EMC shower misidentification at different \sqrt{s} . The nominal signal MC selection efficiency $\epsilon_{\text{nominal}}^{\text{MC}}$ is taken from Table 8.1. The relative difference to the selection efficiency $\epsilon_{\text{w/miss}}^{\text{MC}}$ including the additional misidentified neutron showers with $\angle_{\text{shower}}^{\text{truth}} > 90^\circ$ is taken as the systematic uncertainty due to the neutron identification δ_{miss} .

Figure A.33 shows the fits to the opening angle distribution with the fit range from 155° to 180° for the study of the systematic uncertainty δ_{range} , as described in Section 10.1.3.

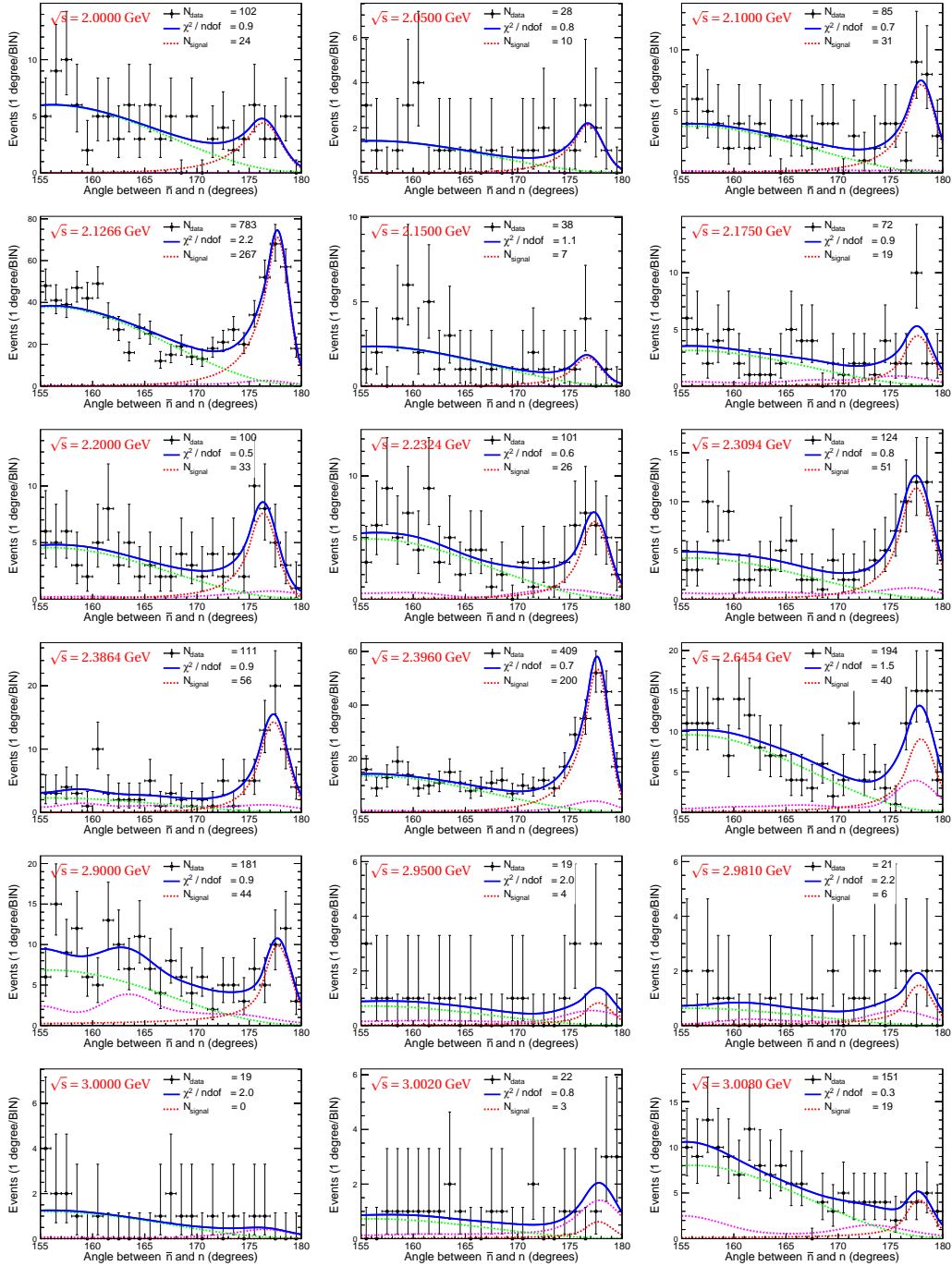


Fig. A.33: Fit to the opening angle between the neutron and antineutron EMC shower with the range of 155° for the determination of the systematic uncertainty δ_{range} on the individual results for the Born cross section at all \sqrt{s} . The notation is the same as in Figure 7.5.

Table A.8 shows the systematic uncertainty δ_{range} on the individual results for the Born cross section $\sigma_{\text{Born}}^{\text{ind}}$, as listed in Table 9.2, due to the fitting range variation from the standard value of 150° to 155° .

\sqrt{s} (GeV)	N_{155}^{fit}	$\sigma_{\text{Born}}^{\text{range}}$ (pb $^{-1}$)	$\sigma_{\text{Born}}^{\text{ind}}$ (pb $^{-1}$)	δ_{range} (%)
2.0000	24.4 ± 4.9	862.7 ± 179.3	912.7 ± 194.9	5.80
2.0500	9.6 ± 2.9	413.0 ± 126.6	424.3 ± 144.2	2.72
2.1000	31.0 ± 5.1	210.9 ± 35.5	212.6 ± 39.6	0.79
2.1266	266.9 ± 15.4	165.7 ± 10.5	172.1 ± 11.6	3.87
2.1500	7.2 ± 2.5	139.6 ± 49.2	144.1 ± 57.7	3.19
2.1750	18.5 ± 4.9	88.8 ± 26.5	94.2 ± 29.6	6.09
2.2000	32.7 ± 5.6	108.2 ± 18.9	116.5 ± 23.6	7.64
2.2324	26.0 ± 4.9	94.5 ± 18.1	99.9 ± 23.1	5.66
2.3094	51.4 ± 6.8	108.3 ± 14.7	110.2 ± 18.2	1.74
2.3864	55.7 ± 6.8	98.6 ± 12.3	100.8 ± 15.2	2.30
2.3960	200.4 ± 13.9	119.0 ± 8.9	125.8 ± 10.7	5.73
2.6454	39.8 ± 62.7	16.4 ± 25.9	18.2 ± 3.8	10.79
2.9000	44.4 ± 6.7	9.5 ± 1.5	10.3 ± 2.1	8.38
2.9500	3.7 ± 2.6	4.9 ± 3.5	8.6 ± 4.4	76.95
2.9810	6.4 ± 3.0	8.8 ± 4.2	10.3 ± 5.5	17.04
3.0000 (upper limit)	0 ± 1.9	2.5	4.0	56.66
3.0200	2.7 ± 3.1	3.3 ± 3.8	4.2 ± 2.9	24.33
3.0800	18.9 ± 5.1	3.1 ± 0.9	3.4 ± 1.1	11.10

Table A.8: Results for the Born cross section $\sigma_{\text{Born}}^{\text{range}}$ under the fitting range of 155° together with the extracted signal yield N_{155}^{fit} , the nominal Born cross section $\sigma_{\text{Born}}^{\text{ind}}$ and the resulting systematic uncertainty δ_{range} at all \sqrt{s} .

Figure A.34 shows plots with the composite fit model applied to the collider data with an alternative background shape model for the study of the systematic uncertainty δ_{bg} , as described in Section 10.1.3. For the KDE method, a smoothing parameter of $\rho = 2$ takes into account the low statistics in the collider data samples with the beam related and cosmic ray background. The mirroring is restricted to the lower limit.

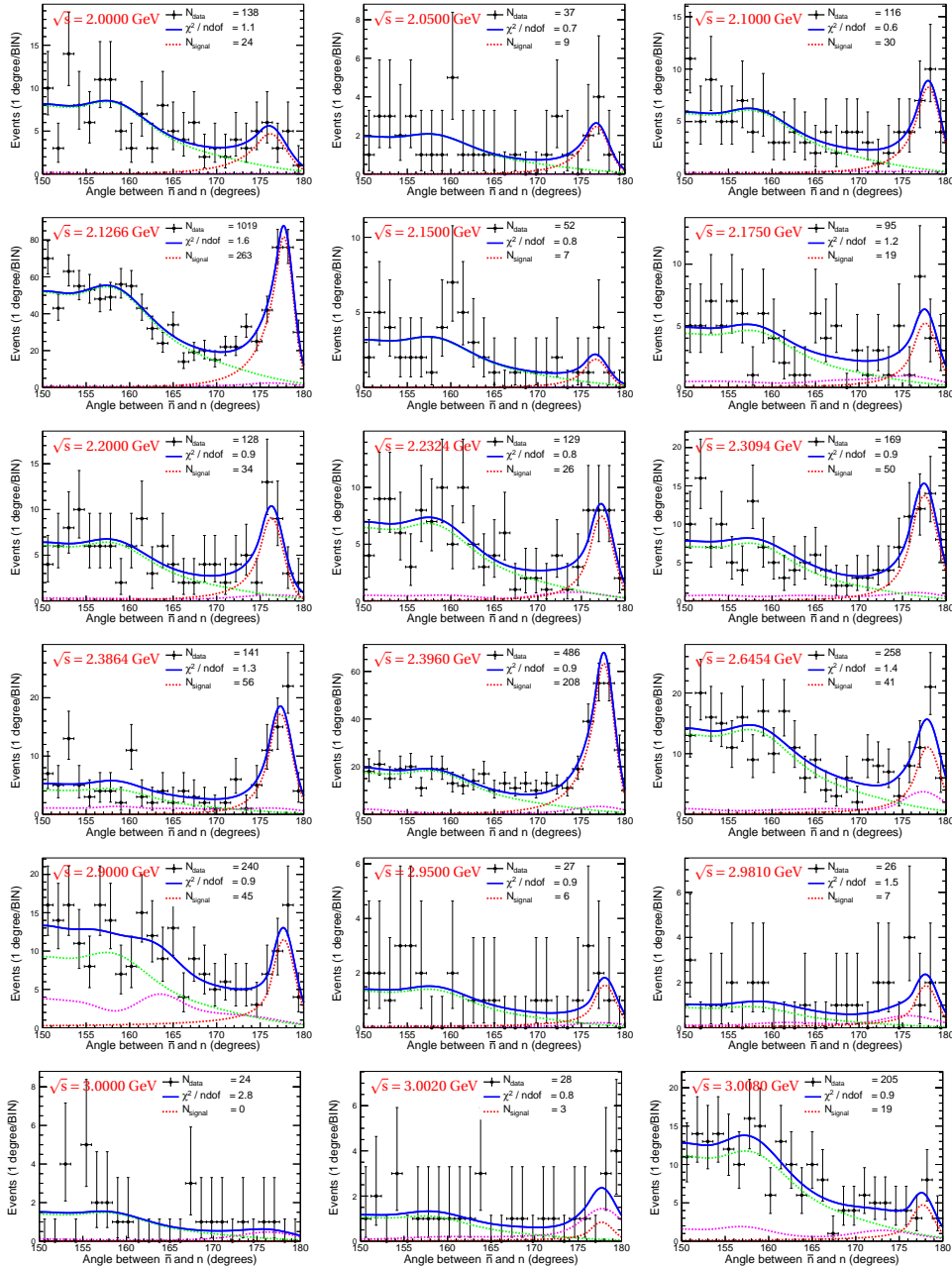


Fig. A.34: Fit to the opening angle between n and \bar{n} EMC showers with a KDE extracted background shape model for the determination of the systematic uncertainty δ_{bg} at all \sqrt{s} . The notation is the same as in Figure 7.5.

Table A.9 shows the systematic uncertainty due to the background shape model. The relative differences between the results for the Born cross section and the nominal results is taken as the systematic uncertainty δ_{bg} .

\sqrt{s} (GeV)	$N_{\text{bg}}^{\text{fit}}$	$\sigma_{\text{Born}}^{\text{bg}}$ (pb ⁻¹)	$\sigma_{\text{Born}}^{\text{ind}}$ (pb ⁻¹)	δ_{bg} (%)
2.0000	23.5 ± 5.9	832.2 ± 214.3	912.7	9.67
2.0500	9.3 ± 3.4	399.8 ± 146.4	424.3	6.06
2.1000	29.9 ± 6.1	203.1 ± 42.0	212.6	4.70
2.1266	262.7 ± 18.0	163.1 ± 12.0	172.1	5.52
2.1500	6.7 ± 3.0	129.6 ± 58.9	144.1	11.21
2.1750	18.7 ± 5.3	89.4 ± 26.5	94.2	5.43
2.2000	33.7 ± 6.8	111.7 ± 22.8	116.5	4.30
2.2324	25.8 ± 5.9	93.9 ± 21.7	99.9	6.40
2.3094	50.3 ± 7.9	106.1 ± 17.1	110.2	3.88
2.3864	56.1 ± 8.0	99.2 ± 14.5	100.8	1.67
2.3960	208.2 ± 15.8	123.6 ± 10.0	125.8	1.77
2.6454	40.8 ± 8.5	16.9 ± 3.6	18.2	8.05
2.9000	45.1 ± 8.4	9.6 ± 1.9	10.3	6.62
2.9500	6.1 ± 3.1	8.1 ± 4.1	8.6	6.79
2.9810	7.1 ± 3.7	9.8 ± 5.1	10.3	4.73
3.0000 (upper limit)	0 ± 3.2	4.2	4.0	7.07
3.0200	3.3 ± 3.7	4.0 ± 4.5	4.2	3.80
3.0800	18.7 ± 6.6	3.1 ± 1.1	3.4	12.66

Table A.9: The Born cross section $\sigma_{\text{Born}}^{\text{bg}}$ under the variation of the background shape model together with the extracted signal yield $N_{\text{bg}}^{\text{fit}}$, the nominal Born cross section $\sigma_{\text{Born}}^{\text{ind}}$ and the resulting systematic uncertainty δ_{bg} at all \sqrt{s} .

The opening angle fits with an alternative signal shape model for the study of the systematic uncertainty δ_{sig} , as described in section 10.1.3, are shown in Figure A.35. The signal shape is extracted from the signal MC simulation at each \sqrt{s} after all the selection criteria applied and additionally convoluted with a Gaussian function to take into account resolution differences between data and MC simulation.

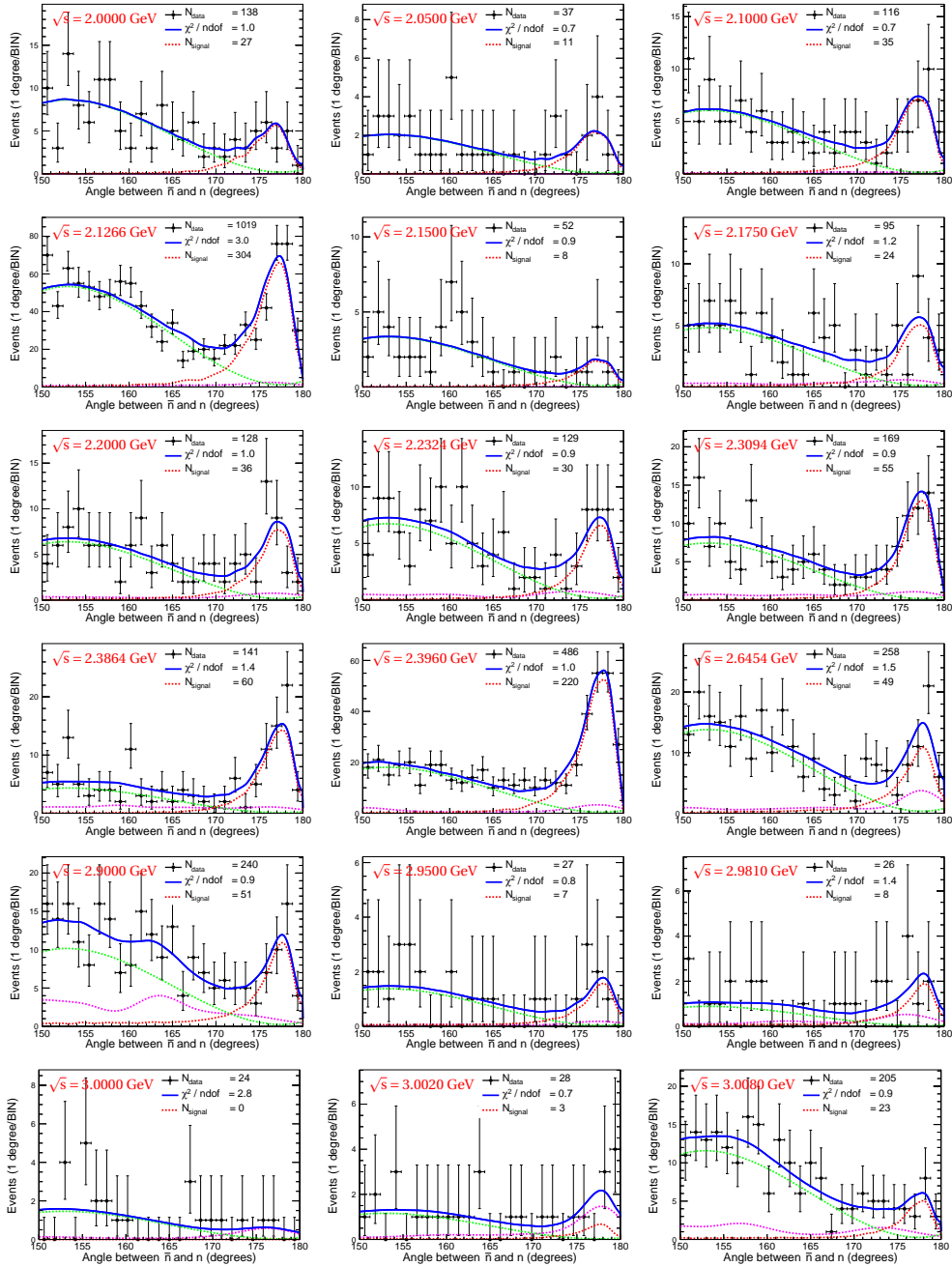


Fig. A.35: Fit to the opening angle between n and \bar{n} EMC showers with an alternative signal shape model for the determination of the systematic uncertainty δ_{sig} at all \sqrt{s} . The notation is the same as in Figure 7.5.

Table A.10 shows the systematic uncertainty due to the signal shape model for the composite fit model from Equation 7.3. The relative differences between the results for the Born cross section with a variation of the signal shape model and the nominal results is taken as the systematic uncertainty δ_{sig} .

\sqrt{s} (GeV)	$N_{\text{sig}}^{\text{fit}}$	$\sigma_{\text{Born}}^{\text{sig}}$ (pb ⁻¹)	$\sigma_{\text{Born}}^{\text{ind}}$ (pb ⁻¹)	δ_{sig} (%)
2.0000	26.7 ± 6.9	944.6 ± 248.7	912.7	3.38
2.0500	10.7 ± 3.6	461.5 ± 155.2	424.3	8.06
2.1000	34.7 ± 9.6	236.1 ± 65.4	212.6	9.95
2.1266	304.2 ± 19.6	188.8 ± 13.1	172.1	8.86
2.1500	8.3 ± 3.5	160.4 ± 68.7	144.1	10.17
2.1750	24.0 ± 10.3	114.7 ± 26.6	94.2	17.88
2.2000	35.6 ± 18.7	117.9 ± 62.1	116.5	1.19
2.2324	30.0 ± 6.4	109.3 ± 23.5	99.9	8.63
2.3094	55.0 ± 8.3	115.9 ± 17.8	110.2	4.91
2.3864	59.7 ± 8.4	105.7 ± 15.1	100.8	4.56
2.3960	220.3 ± 16.3	130.8 ± 10.4	125.8	3.81
2.6454	49.1 ± 9.4	20.3 ± 3.9	18.2	10.12
2.9000	50.6 ± 9.9	10.8 ± 2.2	10.3	5.06
2.9500	7.2 ± 3.3	9.6 ± 4.4	8.6	9.85
2.9810	8.5 ± 3.9	11.6 ± 5.4	10.3	11.34
3.0000 (upper limit)	0 ± 4.0	5.4	4.0	35.00
3.0200	3.0 ± 3.8	3.7 ± 4.7	4.2	12.69
3.0800	23.2 ± 6.8	3.8 ± 1.1	3.4	9.25

Table A.10: Born cross section $\sigma_{\text{Born}}^{\text{sig}}$ under the variation of the signal shape model together with the extracted signal yield $N_{\text{sig}}^{\text{fit}}$, the nominal Born cross section $\sigma_{\text{Born}}^{\text{ind}}$ and the resulting systematic uncertainty δ_{sig} at all \sqrt{s} .

Table A.11 shows the total systematic uncertainty due to the fit for the signal yield extraction, including the individual uncertainties δ_{miss} , δ_{range} , δ_{bg} , and δ_{sig} . The quadratic addition is taken as the systematic uncertainty from the fit procedure δ_{fit} . For the most results the uncertainty δ_{fit} fluctuates around 10% and doesn't exceed 20%. For several results at large \sqrt{s} , especially at $\sqrt{s} = 2.9500$ GeV and $\sqrt{s} = 3.0000$ GeV, the systematic uncertainty becomes very large with over 77% and 57%, respectively. This observed behavior is due to very low statistics after the signal selection and therefore strong fluctuation within the fit procedure for the signal yield extraction.

\sqrt{s} (GeV)	δ_{miss} (%)	δ_{range} (%)	δ_{bg} (%)	δ_{sig} (%)	δ_{fit} (%)
2.0000	0.01	5.80	9.67	3.38	11.77
2.0500	0.14	2.72	6.06	8.06	10.47
2.1000	0.09	0.79	4.70	9.95	11.04
2.1266	0.23	3.87	5.52	8.86	11.13
2.1500	0.13	3.19	11.21	10.17	15.47
2.1750	0.13	6.09	5.43	17.88	19.65
2.2000	0.30	7.64	4.30	1.19	8.86
2.2324	0.39	5.66	6.40	8.63	12.15
2.3094	0.53	1.74	3.88	4.91	6.52
2.3864	0.58	2.30	1.67	4.56	5.40
2.3960	0.49	5.73	1.77	3.81	7.12
2.6454	0.19	10.79	8.05	10.12	16.84
2.9000	0.22	8.38	6.62	5.06	11.82
2.9500	0.32	76.95	6.79	9.85	77.88
2.9810	0.39	17.04	4.73	11.34	21.01
3.0000 (upper limit)	0.53	56.66	7.07	35.00	57.10
3.0200	0.54	24.33	3.80	12.69	27.71
3.0800	0.46	11.10	12.66	9.25	19.21

Table A.11: Summary for the systematic uncertainty δ_{fit} on the individual results for the Born cross section due to the fit to the opening angle for signal yield extraction at all \sqrt{s} . The values for the calculation are taken from the Table A.7, A.8, A.9, and A.10. The systematic uncertainty δ_{fit} is calculated by adding the four individual contributions in quadrature.

Systematic uncertainty due to the form factor model

The angular distributions for the study of the angular distribution model dependant systematic uncertainty δ_{model} with the nominal form factor parametrization and the two extreme cases shown in Table 10.1 at the corresponding \sqrt{s} are shown in Figure A.36.

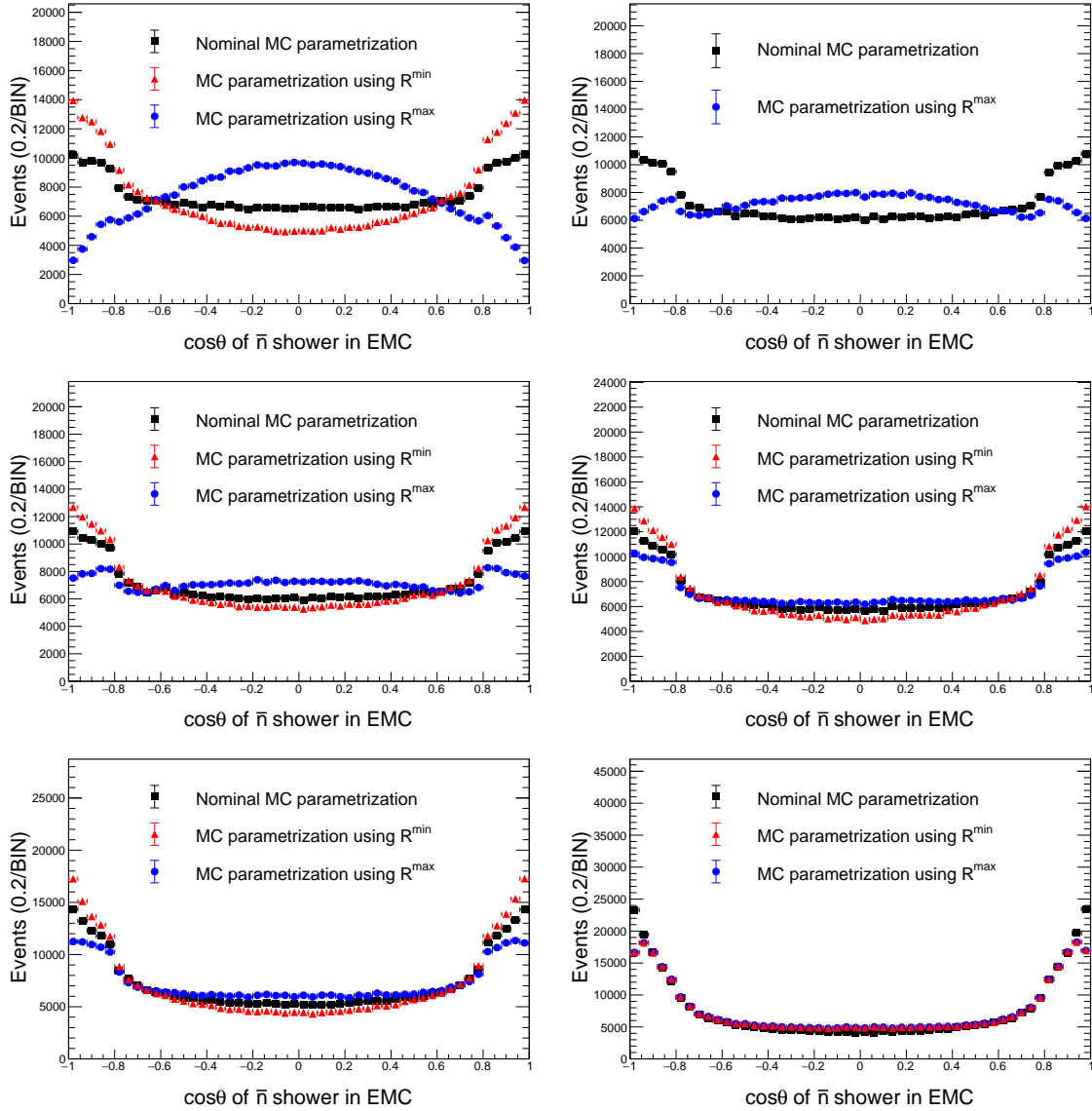


Fig. A.36: The angular distribution of the antineutron for category C classified signal events from the signal MC simulation on generator level at $\sqrt{s} = 2.0000, 2.1266, 2.1500, 2.3960, 2.6454,$ and 3.0800 GeV with the standard parametrization and with the two extreme cases under the parametrization $R_{\text{em}}^{\text{min}}$ and $R_{\text{em}}^{\text{max}}$ as listed in Table 10.1. The event generator Phokhara v9.1 is used for this study.

Table A.12 shows the nominal Born cross section $\sigma_{\text{Born}}^{\text{nominal}}$ and the two Born cross section values derived with the minimal and maximal form factor ratio parametrization as explained in Section 10.1.4. The largest relative difference is taken as the systematic uncertainty δ_{model} due to the input model dependency of the angular distribution from the form factor parametrization.

\sqrt{s} (GeV)	$\sigma_{\text{Born}}^{\text{max}}$ (pb $^{-1}$)	$\sigma_{\text{Born}}^{\text{min}}$ (pb $^{-1}$)	$\sigma_{\text{Born}}^{\text{nominal}}$ (pb $^{-1}$)	δ_{model} (%)
2.0000	974.9 \pm 208.3	741.4 \pm 157.8	912.7 \pm 194.9	18.76
2.0500	475.6 \pm 161.1	352.8 \pm 119.4	424.3 \pm 144.2	16.84
2.1000	212.6 \pm 39.6	179.4 \pm 32.4	212.6 \pm 39.6	15.61
2.1266	201.7 \pm 12.9	155.0 \pm 9.8	172.1 \pm 11.6	9.96
2.1500	154.1 \pm 55.7	130.3 \pm 47.1	144.1 \pm 57.7	9.55
2.1750	99.7 \pm 28.1	86.2 \pm 24.2	94.2 \pm 29.6	8.53
2.2000	121.1 \pm 21.0	106.9 \pm 18.5	116.5 \pm 23.6	8.25
2.2324	104.0 \pm 20.3	90.7 \pm 17.7	99.9 \pm 23.1	9.15
2.3094	117.1 \pm 16.3	101.8 \pm 14.2	110.2 \pm 18.2	7.62
2.3960	131.3 \pm 9.5	117.9 \pm 8.5	125.8 \pm 10.7	6.26
2.6454	20.0 \pm 3.5	16.9 \pm 2.9	18.2 \pm 3.8	9.81
2.9000	11.2 \pm 1.9	9.5 \pm 1.6	10.3 \pm 2.1	9.30
2.9500	9.7 \pm 4.2	8.3 \pm 3.6	8.6 \pm 4.4	12.23
2.9810	11.2 \pm 5.0	8.3 \pm 3.7	10.3 \pm 5.5	19.25
3.0000 (upper limit)	4.5	3.0	4.0	25.35
3.0200	4.7 \pm 4.6	3.5 \pm 3.4	4.2 \pm 4.9	16.95
3.0800	3.7 \pm 1.0	2.9 \pm 0.8	3.4 \pm 1.1	16.44

Table A.12: Summary of systematic uncertainty δ_{model} on the Born cross section due to the signal MC simulation input model for the form factors at different \sqrt{s} . The values for $\sigma_{\text{Born}}^{\text{min}}$ and $\sigma_{\text{Born}}^{\text{max}}$ are derived using the minimum and maximum form factor ratio from the combined results in Chapter 11, as listed in Table 10.1. The nominal Born cross section is quoted from Table 9.2. The systematic uncertainty results at $\sqrt{s} = 2.3960$ GeV is used also at $\sqrt{s} = 2.3864$ GeV.

Systematic uncertainty due to the trigger efficiency

Table A.13 shows the nominal trigger efficiency correction $C_{\text{trg}}^{\text{nominal}}$ and the trigger efficiency correction $C_{\text{trg}}^{\text{hadronic}}$ obtained with the inclusive hadronic collider data sample, as explained in Section 8.5. The relative difference is taken as the systematic uncertainty δ_{trg} .

\sqrt{s} (GeV)	$C_{\text{trg}}^{\text{nominal}}$ (%)	$C_{\text{trg}}^{\text{hadronic}}$ (%)	δ_{trg} (%)	\sqrt{s} (GeV)	$C_{\text{trg}}^{\text{nominal}}$ (%)	$C_{\text{trg}}^{\text{hadronic}}$ (%)	δ_{trg} (%)
2.0000	89.3 ± 2.8	93.3 ± 2.9	4.48	2.3864	95.8 ± 1.0	98.0 ± 1.1	2.30
2.0500	91.6 ± 1.5	95.3 ± 1.6	4.04	2.3960	95.7 ± 1.0	97.9 ± 1.1	2.30
2.1000	91.8 ± 1.2	95.3 ± 1.3	3.81	2.6454	97.2 ± 1.0	98.8 ± 1.0	1.65
2.1266	92.4 ± 1.2	95.8 ± 1.2	3.68	2.9000	97.4 ± 1.0	98.8 ± 1.0	1.44
2.1500	92.9 ± 1.2	96.2 ± 1.2	3.55	2.9500	98.0 ± 1.0	99.2 ± 1.0	1.22
2.1750	91.8 ± 1.2	95.3 ± 1.2	3.81	2.9810	97.8 ± 1.0	99.1 ± 1.1	1.33
2.2000	92.4 ± 1.2	95.7 ± 1.2	3.57	3.0000	97.8 ± 1.2	99.1 ± 1.2	1.33
2.2324	92.8 ± 1.2	96.1 ± 1.2	3.56	3.0200	97.9 ± 1.4	99.1 ± 1.4	1.23
2.3094	95.1 ± 1.1	97.6 ± 1.2	2.63	3.0800	97.8 ± 2.7	99.0 ± 2.8	1.23

Table A.13: Summary of the systematic uncertainty δ_{trg} due to the trigger efficiency correction at different \sqrt{s} . The values for $C_{\text{trg}}^{\text{nominal}}(s)$ are taken from Table 8.6.

Systematic uncertainty due to the radiative correction ($1 + \delta$)

Table A.14 shows the The products of the signal MC selection efficiency and the radiative correction factor $\epsilon^{\text{MC}} \times C_{\text{ISR}}$ for both iterations for the calculation of the systematic uncertainty δ_{ISR} , as discussed in Section 10.1.6

\sqrt{s} (GeV)	$\epsilon^{\text{MC}} \times C_{\text{ISR}}$ (%)		δ_{ISR} (%)	\sqrt{s} (GeV)	$\epsilon^{\text{MC}} \times C_{\text{ISR}}$ (%)		δ_{ISR} (%)
	2nd last tuning	final tuning			2nd last tuning	final tuning	
2.0000	0.3246 ± 0.0028	0.3194 ± 0.0028	1.60	2.3864	2.4668 ± 0.0269	2.4975 ± 0.0271	1.23
2.0500	0.7972 ± 0.0137	0.7978 ± 0.0136	0.08	2.3960	2.5375 ± 0.0274	2.5144 ± 0.0273	0.92
2.1000	1.3545 ± 0.0192	1.3625 ± 0.0192	0.55	2.6454	4.0331 ± 0.0426	4.1335 ± 0.0439	2.43
2.1266	1.6273 ± 0.0217	1.6149 ± 0.0216	0.77	2.9000	4.9881 ± 0.0572	4.9142 ± 0.0563	1.50
2.1500	1.9006 ± 0.0240	1.1907 ± 0.0243	0.36	2.9500	5.1626 ± 0.0600	5.1378 ± 0.0593	0.48
2.1750	1.9560 ± 0.0246	2.0160 ± 0.0254	2.97	2.9810	5.1175 ± 0.0606	4.9202 ± 0.0584	4.01
2.2000	2.2053 ± 0.0264	2.1984 ± 0.0268	0.31	3.0000	5.1375 ± 0.0614	5.1090 ± 0.0603	0.56
2.2324	2.2809 ± 0.0268	2.2981 ± 0.0273	0.75	3.0200	4.9727 ± 0.0607	5.0526 ± 0.0604	1.58
2.3094	2.1406 ± 0.0250	2.1518 ± 0.0251	0.52	3.0800	5.2772 ± 0.0648	5.1643 ± 0.0627	2.19

Table A.14: Summary of systematic uncertainties δ_{ISR} due to the radiative correction at different \sqrt{s} . The values for the final signal MC parametrization are taken from the Tables 8.1 and 8.7, respectively.

Uncertainty on $R_{em}^{ind}(s)$ and $G_M^{ind}(s)$ due to the signal selection

Plots for the extraction of the systematic uncertainty due to the signal selection on the individual results for the form factor ratio $R_{em}^n(s)$ and the magnetic form factor $G_M(s)$ investigated with a massive MC simulation approach as discussed in Section 10.2.1 are shown in Figure A.37 and A.38, respectively:

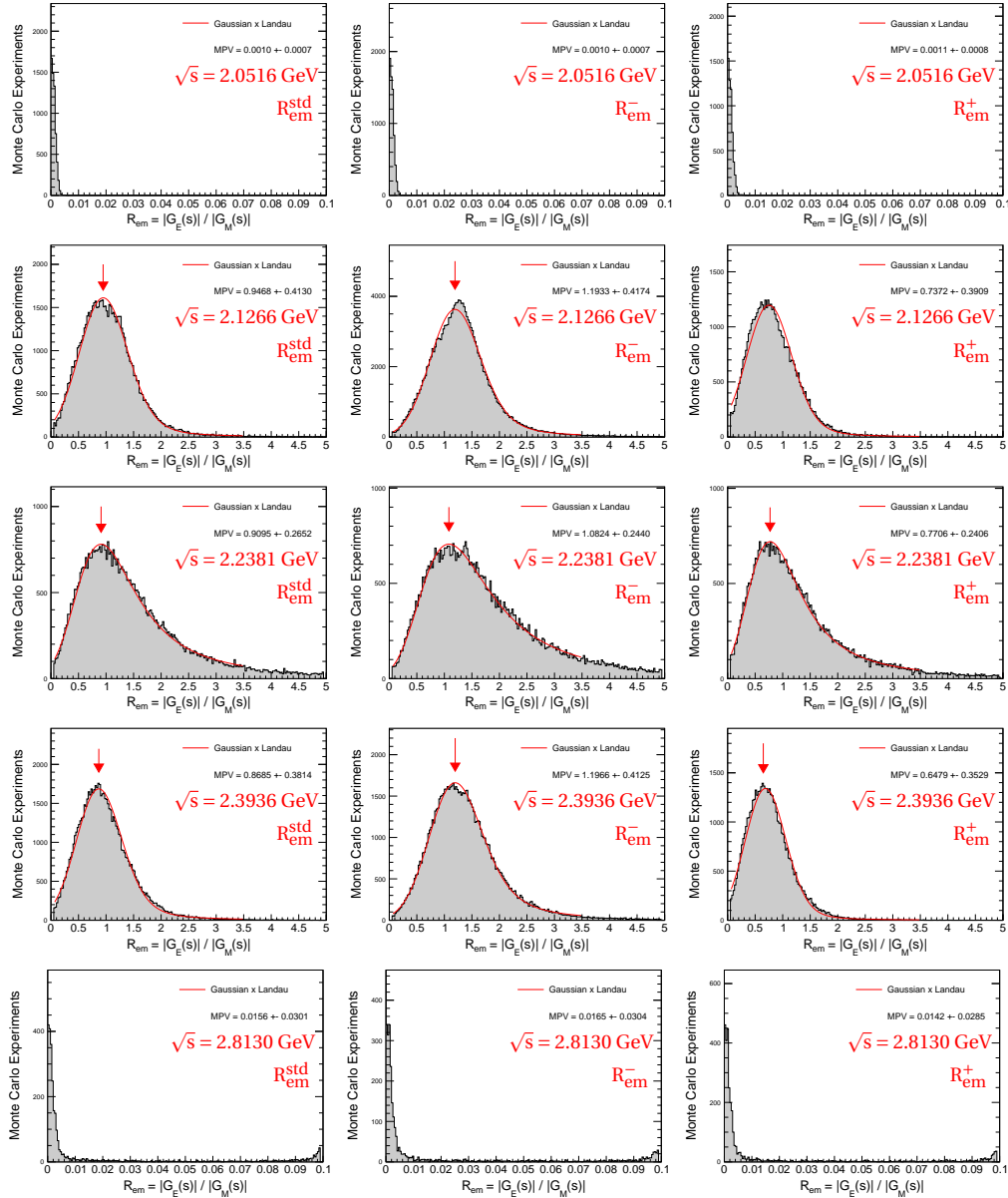


Fig. A.37: Plots for the MC simulation study for the determination of δ_{dtsel}^R and $\delta_{dtsel}^{G_M}$ as explained in Section 10.2.1. The left, middle and right rows show the results with R_{em}^{std} , R_{em}^- , and R_{em}^+ , respectively. The columns show from top to bottom the results at the corresponding \sqrt{s} in the rising order. Grey histograms represent the MC simulations, the red lines are the fits for the extraction of the mean value for R_{em}^{std} , R_{em}^- , and R_{em}^+ .

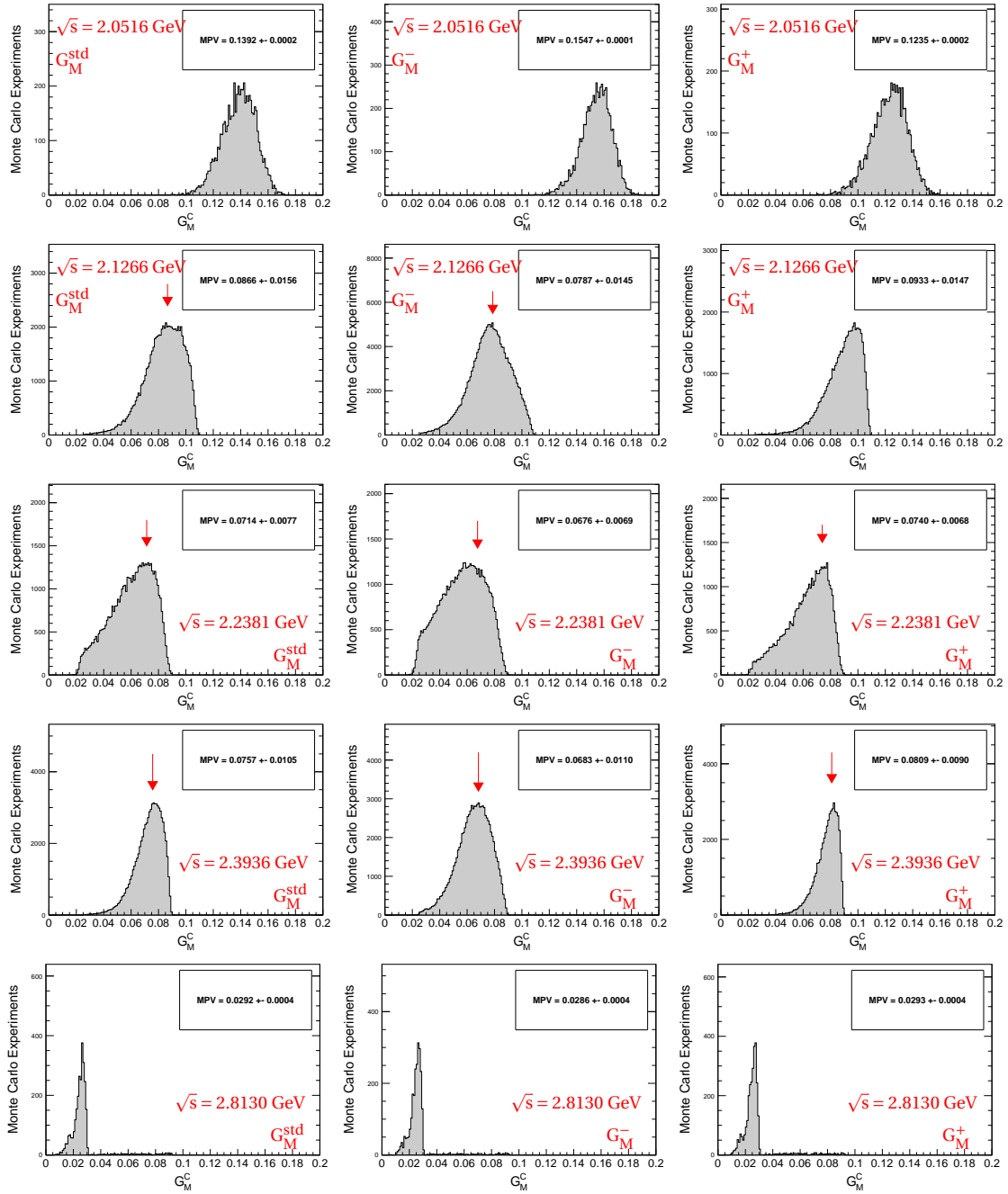


Fig. A.38: Plots for the MC simulation study for the determination of $\delta_{\text{dtsel}}^{G_M}$ as explained in Section 10.2.1. The left, middle and right rows show the results with G_M^{std} , G_M^- , and G_M^+ , respectively. The columns show from top to bottom the results at the corresponding \sqrt{s} in the rising order. Grey histograms represent the MC simulations, the red lines are the fits for the extraction of the mean value for G_M^{std} , G_M^- , and G_M^+ .

Uncertainty on $R_{em}^{ind}(s)$ and $G_M^{ind}(s)$ due to the fit range

Extraction of the form factor ratio and the magnetic form factor under the systematically varied condition of the opening angle range from 155° to 180° (instead of the nominal 150° to 180°) for the study of the systematic uncertainties δ_{drange}^R and $\delta_{drange}^{G_M}$, as described in the Section 10.2.2. The fits to the corrected angular distribution of category C classified signal events are shown in Figure A.39. Table A.15 shows the systematic uncertainty on the form factor ratio δ_{drange}^R and the magnetic form factor $\delta_{drange}^{G_M}$ due to the fitting range variation from the standard value of 150° to 155° . The relative differences between the nominal results and the results derived with the varied opening angle fit range, as discussed in Section 10.2.2, is taken as the systematic uncertainty.

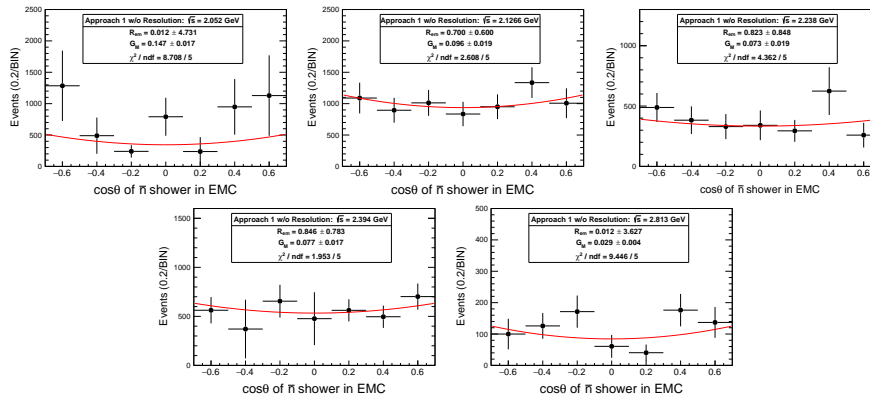


Fig. A.39: Extraction of the ratio R_{em}^{drange} and the magnetic form factor G_M^{drange} with the differential signal yield obtained under the variation of the fit range for the fit to the opening angle distribution as explained in Section 10.2.2.

\sqrt{s} (GeV)	R_{em}^{drange}	R_{em}^{ind}	δ_{drange}^R (%)	$G_M^{drange} (\times 10^2)$	$G_M^{ind} (\times 10^2)$	$\delta_{drange}^{G_M}$ (%)
2.0516	0.012 ± 4.731	0.012 ± 4.987	1.23	14.56 ± 1.81	15.13 ± 1.74	2.87
2.1266	0.700 ± 0.600	0.707 ± 0.582	1.03	9.62 ± 1.86	9.80 ± 1.85	1.86
2.2380	0.823 ± 0.848	1.009 ± 0.801	18.50	7.30 ± 1.95	7.13 ± 1.95	2.31
2.3936	0.846 ± 0.783	0.812 ± 0.713	4.20	7.66 ± 1.676	7.87 ± 1.56	2.63
2.8130	0.012 ± 3.205	0.162 ± 2.562	92.49	2.70 ± 0.22	3.04 ± 0.32	3.11

Table A.15: The form factor ratio R_{em}^{drange} and the magnetic form factor G_M^{drange} under the variation of the fit range for the fit to the opening angle together with the nominal results R_{em}^{ind} , G_M^{ind} and the resulting systematic uncertainty δ_{drange}^R , $\delta_{drange}^{G_M}$ at all \sqrt{s} .

Uncertainty on $R_{em}^{ind}(s)$ and $G_M^{ind}(s)$ due to the background model

The extraction of the ratio and magnetic form factor with the differential signal yield obtained by using an alternative background shape model for the fit to the opening angle between the antineutron and neutron EMC showers. The results are shown in Figure A.40. The relative difference to the nominal results are taken as the systematic uncertainties δ_{dbg}^R and $\delta_{dbg}^{G_M}$, respectively. For the KDE method as an alternative background shape model, a smoothening parameter of $\rho = 2$ takes into account the low statistics in the beam-related data samples. The mirroring is restricted to the lower limit. Table A.16 shows the systematic uncertainty on the form factor ratio and the magnetic form factor due to the background shape model. The relative differences between the nominal results and the results derived with the varied background shape model, as discussed in Section 10.2.2, is taken as the systematic uncertainty δ_{dbg} .

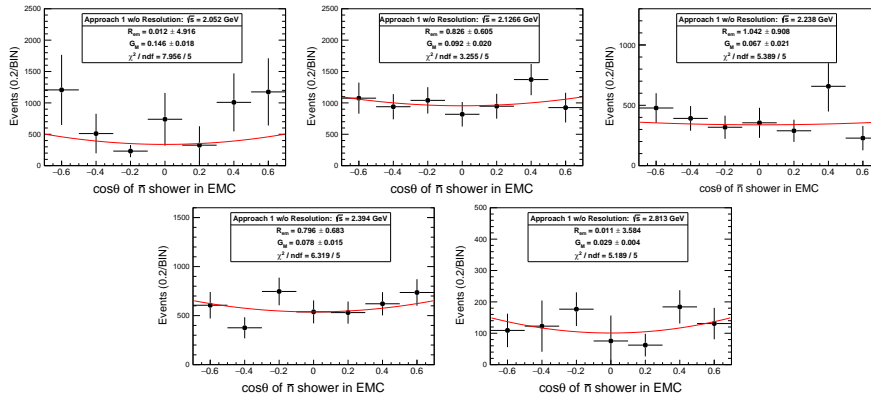


Fig. A.40: Extraction of the ratio R_{em}^{dbg} and the magnetic form factor G_M^{dbg} with the differential signal yield obtained under the variation of the background shape model for the fit to the opening angle distribution as explained in Section 10.2.2.

\sqrt{s} (GeV)	R_{em}^{dbg}	R_{em}^{ind}	δ_{dbg}^R (%)	$G_M^{dbg} (\times 10^2)$	$G_M^{ind} (\times 10^2)$	$\delta_{dbg}^{G_M}$ (%)
2.0516	0.012 ± 4.916	0.012 ± 4.987	1.55	14.56 ± 1.81	15.13 ± 1.74	3.78
2.1266	0.826 ± 0.605	0.707 ± 0.582	16.73	9.22 ± 1.95	9.80 ± 1.85	5.91
2.2380	1.042 ± 0.908	1.009 ± 0.801	3.25	6.72 ± 2.12	7.13 ± 1.95	5.78
2.3936	0.796 ± 0.683	0.812 ± 0.713	1.93	7.83 ± 1.51	7.87 ± 1.56	0.47
2.8130	0.011 ± 3.584	0.011 ± 3.587	1.33	2.95 ± 0.25	3.05 ± 0.19	3.57

Table A.16: The form factor ratio R_{em}^{dbg} and the magnetic form factor G_M^{dbg} under the variation of the background shape model together with the nominal results R_{em}^{ind} , G_M^{ind} and the resulting systematic uncertainty δ_{dbg}^R , $\delta_{dbg}^{G_M}$ at all \sqrt{s} .

Uncertainty on $R_{em}^{ind}(s)$ and $G_M^{ind}(s)$ due to the signal shape model

The extraction of the ratio and magnetic form factor with the differential signal yield obtained by using an alternative signal shape model for the fit to the opening angle between the antineutron and neutron EMC showers. The results are shown in Figure A.41. The relative difference to the nominal results are taken as the systematic uncertainties δ_{dsig}^R and $\delta_{dsig}^{G_M}$, respectively. The signal shape is extracted from the signal MC simulation and additionally convoluted with a Gaussian distribution to take into account the resolution difference between the data and the simulation. Table A.17 shows the systematic uncertainty on the form factor ratio and the magnetic form factor due to the signal shape model. The relative differences between the nominal results and the results derived with the varied signal shape model is taken as the systematic uncertainty δ_{dsig} .

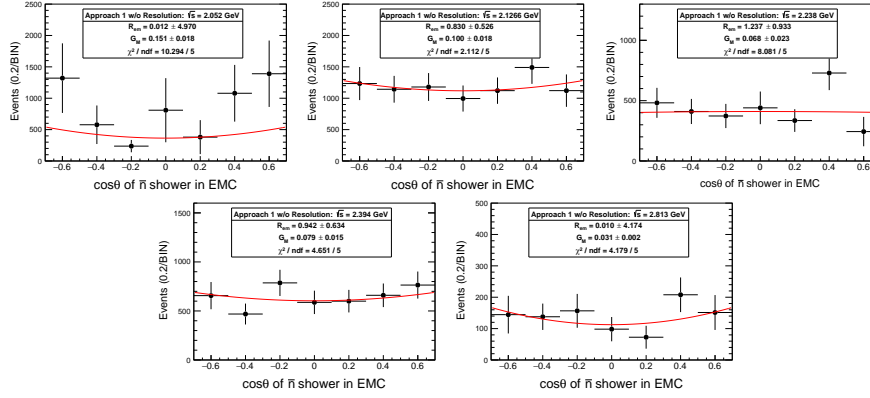


Fig. A.41: Extraction of the ratio R_{em}^{dsig} and the magnetic form factor G_M^{dsig} with the differential signal yield obtained under the variation of the signal shape model for the fit to the opening angle distribution as explained in Section 10.2.2.

\sqrt{s} (GeV)	R_{em}^{dsig}	R_{em}^{ind}	δ_{dsig}^R (%)	$G_M^{dsig} \times 10^2$	$G_M^{ind} (\times 10^2)$	$\delta_{dsig}^{G_M}$ (%)
2.0516	0.012 ± 4.970	0.012 ± 4.987	0.40	15.11 ± 1.78	15.13 ± 1.74	0.15
2.1266	0.830 ± 0.526	0.707 ± 0.582	17.30	9.97 ± 1.82	9.80 ± 1.85	1.71
2.2380	1.237 ± 0.933	1.009 ± 0.801	22.53	6.82 ± 2.30	7.13 ± 1.95	4.38
2.3936	0.924 ± 0.634	0.812 ± 0.713	16.04	7.87 ± 1.54	7.87 ± 1.56	0.01
2.8130	0.010 ± 4.174	0.011 ± 3.587	10.62	3.11 ± 0.22	3.05 ± 0.19	2.07

Table A.17: The form factor ratio R_{em}^{dsig} and the magnetic form factor G_M^{dsig} under the variation of the signal shape model together with the nominal results R_{em}^{ind} , G_M^{ind} and the resulting systematic uncertainty δ_{dsig}^R , $\delta_{dsig}^{G_M}$ at all \sqrt{s} .

Uncertainty on $R_{\text{em}}^{\text{ind}}(s)$ and $G_M^{\text{ind}}(s)$ due to neutron misidentification

Table A.18 shows the details for the calculation of the systematic uncertainty of the form factor ratio δ_{dmiss}^R and of the magnetic form factor $\delta_{\text{dmiss}}^{G_M}$ due to the misidentified neutron EMC showers, as discussed in detail in the Section 7.1. The systematic uncertainty is calculated as the luminosity weighted average of the \sqrt{s} -individual contributions, as explained in Section 10.2.2:

$$\delta_{\text{dmiss}} = \left(\sum_i \delta_{\text{dmiss}}^i \times \mathcal{L}^i \right) / \left(\sum_i \mathcal{L}^i \right) \quad (\text{A.1})$$

\sqrt{s} (GeV)	δ_{dmiss} (%)	\mathcal{L}_{int} (pb^{-1})	δ_{dmiss}^R (%)	$\text{Cor}(R_{\text{em}}, G_M)$	$\delta_{\text{dmiss}}^{G_M}$ (%)
2.0000	0.01	$10.074 \pm 0.005 \pm 0.067$	0.07	0.002	0.01
2.0500	0.14	$3.344 \pm 0.003 \pm 0.027$			
2.1000	0.09	$12.167 \pm 0.006 \pm 0.085$			
2.1266	0.23	$108.49 \pm 0.02 \pm 0.94$	0.23	0.765	0.18
2.1500	0.13	$2.841 \pm 0.003 \pm 0.024$	0.36	0.769	0.28
2.1750	0.13	$10.625 \pm 0.006 \pm 0.091$			
2.2000	0.30	$13.699 \pm 0.007 \pm 0.092$			
2.2324	0.39	$11.856 \pm 0.007 \pm 0.087$			
2.3094	0.53	$21.089 \pm 0.009 \pm 0.143$			
2.3864	0.58	$22.549 \pm 0.010 \pm 0.176$	0.52	0.820	0.43
2.3960	0.49	$66.869 \pm 0.017 \pm 0.475$			
2.6454	0.19	$67.725 \pm 0.018 \pm 0.355$	0.22	0.724	0.16
2.9000	0.22	$105.253 \pm 0.025 \pm 0.905$			
2.9500	0.32	$15.942 \pm 0.010 \pm 0.143$			
2.9810	0.39	$16.071 \pm 0.010 \pm 0.095$			
3.0000	0.53	$15.881 \pm 0.010 \pm 0.110$			
3.0200	0.54	$17.290 \pm 0.011 \pm 0.123$	not extracted		
3.0800	0.46	$126.185 \pm 0.029 \pm 0.921$			

Table A.18: The systematic uncertainty for $R_{\text{em}}^{\text{ind}}$ and G_M^{ind} due to the misidentification of the neutron showers in the EMC. The resulting systematic uncertainty $\delta_{\text{dmiss}}^{R, G_M}$ at all analyzed \sqrt{s} is calculated as the luminosity weighted average with Equation A.1. The systematic uncertainty δ_{dmiss} is quoted from Table A.7, the luminosity \mathcal{L}_{int} from Table 3.11. The factor $\text{Cor}(R_{\text{em}}, G_M)$ represents the correlation between the results for $R_{\text{em}}^{\text{ind}}$ and G_M^{ind} obtained from the fit in Equation 9.8 is used for the calculation of $\delta_{\text{dmiss}}^{G_M}$ from δ_{dmiss}^R .

Combined uncertainty on $R_{\text{em}}^{\text{n}}(s)$ and $G_{\text{M}}^{\text{n}}(s)$ due to the opening angle fit

Table A.19 lists all contribution for the systematical uncertainty $\delta_{\text{dfit}}^{\text{R}}$ and $\delta_{\text{dfit}}^{\text{G}_\text{M}}$ due to the opening angle fit procedure, including δ_{dmiss} , δ_{drange} , δ_{dbg} , and δ_{dsig} .

\sqrt{s} (GeV)	$\delta_{\text{dmiss}}^{\text{R}}$	$\delta_{\text{drange}}^{\text{R}}$	$\delta_{\text{dbg}}^{\text{R}}$	$\delta_{\text{dsig}}^{\text{R}}$	$\delta_{\text{dfit}}^{\text{R}}$	$\delta_{\text{dmiss}}^{\text{G}_\text{M}}$	$\delta_{\text{drange}}^{\text{G}_\text{M}}$	$\delta_{\text{dbg}}^{\text{G}_\text{M}}$	$\delta_{\text{dsig}}^{\text{G}_\text{M}}$	$\delta_{\text{dfit}}^{\text{G}_\text{M}}$
2.0516	0.07	1.23	1.55	0.40	2.14	0.01	2.87	3.78	0.15	4.79
2.1266	0.23	1.03	16.73	17.30	24.01	0.18	1.86	5.91	1.71	6.41
2.2380	0.36	18.50	3.25	22.53	29.34	0.28	2.31	5.78	4.38	7.62
2.3936	0.52	4.20	1.93	16.04	16.70	0.43	2.63	0.47	0.01	2.72
2.8130	0.22	92.49	1.33	10.62	14.12	0.16	0.32	3.57	2.07	5.46

Table A.19: The form factor ratio $R_{\text{em}}^{\text{dsig}}$ and the magnetic form factor $G_{\text{M}}^{\text{dsig}}$ under the variation of the signal shape model together with the nominal results $R_{\text{em}}^{\text{ind}}$, $G_{\text{M}}^{\text{ind}}$ and the resulting systematic uncertainty $\delta_{\text{dsig}}^{\text{R}}$, $\delta_{\text{dsig}}^{\text{G}_\text{M}}$ at all \sqrt{s} . All values are shown in units of %. The shown values are from the Tables A.18, A.15, A.16, and A.17.

Uncertainty on $R_{\text{em}}^{\text{ind}}(s)$ and $G_{\text{M}}^{\text{ind}}(s)$ due to the form factor model

Table A.20 shows the details for the calculation of the systematic uncertainty on the form factor ratio $\delta_{\text{drad}}^{\text{R}}$ and on the magnetic form factor $\delta_{\text{drad}}^{\text{G}_\text{M}}$ due to the form factor parametrization in the signal MC simulation, as discussed in Section 10.2.5. For this study, the angular analysis is performed for the results derived using the second last version of the signal MC simulation. The relative difference between the two sets of results is taken as the systematic uncertainty. The systematic uncertainty is shown in Figure 10.13.

\sqrt{s} (GeV)	$R_{\text{em}}^{\text{pre}}$	$R_{\text{em}}^{\text{ind}}$	$\delta_{\text{drad}}^{\text{R}}$ (%)	$G_{\text{M}}^{\text{pre}} (\times 10^2)$	$G_{\text{M}}^{\text{ind}} (\times 10^2)$	$\delta_{\text{drad}}^{\text{G}_\text{M}}$ (%)
2.0516	0.012 ± 4.983	0.012 ± 4.987	4.15	15.59 ± 1.74	15.13 ± 1.74	3.04
2.1266	0.543 ± 0.629	0.707 ± 0.582	23.20	10.29 ± 1.79	9.80 ± 1.85	4.92
2.2380	0.872 ± 0.774	1.009 ± 0.801	13.63	7.45 ± 1.89	7.13 ± 1.95	4.43
2.3936	0.916 ± 0.719	0.812 ± 0.713	12.65	7.53 ± 1.60	7.87 ± 1.56	4.29
2.8130	0.012 ± 3.600	0.011 ± 3.587	9.08	3.01 ± 0.24	3.05 ± 0.19	0.40

Table A.20: The form factor ratio $R_{\text{em}}^{\text{pre}}$ and the magnetic form factor $G_{\text{M}}^{\text{pre}}$ derived with the second last signal MC simulation form factor parametrization, together with the nominal results $R_{\text{em}}^{\text{ind}}$, $G_{\text{M}}^{\text{ind}}$ and the resulting systematic uncertainty $\delta_{\text{drad}}^{\text{R}}$, $\delta_{\text{drad}}^{\text{G}_\text{M}}$ at all \sqrt{s} .

Uncertainty on $G_M^{\text{ind}}(s)$ due to the luminosity measurement

Table A.21 shows the details for the calculation of the systematic uncertainty on the magnetic form factor $\delta_{\text{dL}}^{\text{GM}}$ due to the luminosity measurement, as discussed in the Section 10.3. The systematic uncertainty is calculated as the luminosity weighted average of the \sqrt{s} -individual contributions:

$$\delta_{\text{dL}} = \left(\sum_i \delta_L^i \times \mathcal{L}^i \right) / \left(\sum_i \mathcal{L}^i \right) \quad (\text{A.2})$$

\sqrt{s} (GeV)	\mathcal{L}_{int} (pb^{-1})	$\delta_{\text{dL}}^{\text{GM}}$ (%)
2.0000	$10.074 \pm 0.005 \pm 0.067$	0.70
2.0500	$3.344 \pm 0.003 \pm 0.027$	
2.1000	$12.167 \pm 0.006 \pm 0.085$	
2.1266	$108.49 \pm 0.02 \pm 0.94$	0.87
2.1500	$2.841 \pm 0.003 \pm 0.024$	0.73
2.1750	$10.625 \pm 0.006 \pm 0.091$	
2.2000	$13.699 \pm 0.007 \pm 0.092$	
2.2324	$11.856 \pm 0.007 \pm 0.087$	
2.3094	$21.089 \pm 0.009 \pm 0.143$	
2.3864	$22.549 \pm 0.010 \pm 0.176$	0.71
2.3960	$66.869 \pm 0.017 \pm 0.475$	
2.6454	$67.725 \pm 0.018 \pm 0.355$	0.82
2.9000	$105.253 \pm 0.025 \pm 0.905$	
2.9500	$15.942 \pm 0.010 \pm 0.143$	
2.9810	$16.071 \pm 0.010 \pm 0.095$	not extracted
3.0000	$15.881 \pm 0.010 \pm 0.110$	
3.0200	$17.290 \pm 0.011 \pm 0.123$	
3.0800	$126.185 \pm 0.029 \pm 0.921$	

Table A.21: The systematic uncertainty on G_M^{ind} due to the luminosity measurement. The resulting systematic uncertainty $\delta_{\text{dL}}^{\text{GM}}$ at all analyzed \sqrt{s} is calculated as the luminosity weighted average with Equation A.2. The luminosity \mathcal{L}_{int} with the corresponding systematic uncertainty is quoted from Table 3.11.

Uncertainty on $G_M^{\text{ind}}(s)$ due to the angular distribution model

Table A.22 shows the details for the calculation of the systematic uncertainty on the magnetic form factor $\delta_{\text{dmodel}}^{\text{GM}}$ due to the dependence of the angular distribution shape on the signal MC simulation form factor model, as discussed in the Section 10.3. The systematic uncertainty is calculated as the luminosity weighted average of the \sqrt{s} -individual contributions:

$$\delta_{\text{dmodel}} = \left(\sum_i \delta_{\text{model}}^i \times \mathcal{L}^i \right) / \left(\sum_i \mathcal{L}^i \right) \quad (\text{A.3})$$

\sqrt{s} (GeV)	δ_{model}	\mathcal{L}_{int} (pb ⁻¹)	$\delta_{\text{dmodel}}^{\text{GM}}$ (%)
2.0000	18.76	10.074 ± 0.005 ± 0.067	17.01
2.0500	16.84	3.344 ± 0.003 ± 0.027	
2.1000	15.61	12.167 ± 0.006 ± 0.085	
2.1266	9.96	108.49 ± 0.02 ± 0.94	9.96
2.1500	9.55	2.841 ± 0.003 ± 0.024	8.27
2.1750	8.53	10.625 ± 0.006 ± 0.091	
2.2000	8.25	13.699 ± 0.007 ± 0.092	
2.2324	9.15	11.856 ± 0.007 ± 0.087	
2.3094	7.62	21.089 ± 0.009 ± 0.143	
2.3864	6.26	22.549 ± 0.010 ± 0.176	6.26
2.3960	6.26	66.869 ± 0.017 ± 0.475	
2.6454	9.81	67.725 ± 0.018 ± 0.355	9.73
2.9000	9.30	105.253 ± 0.025 ± 0.905	
2.9500	12.23	15.942 ± 0.010 ± 0.143	
2.9810	19.25	16.071 ± 0.010 ± 0.095	
3.0000	25.35	15.881 ± 0.010 ± 0.110	not extracted
3.0200	16.95	17.290 ± 0.011 ± 0.123	
3.0800	16.44	126.185 ± 0.029 ± 0.921	

Table A.22: The systematic uncertainty for G_M^{ind} due to the model dependence of the angular distribution shape. The resulting systematic uncertainty $\delta_{\text{dmodel}}^{\text{GM}}$ at all analyzed \sqrt{s} is calculated as the luminosity weighted average with Equation A.3. The luminosity \mathcal{L}_{int} with the corresponding systematic uncertainty is quoted from Table 3.11. The uncertainty δ_{model} is quoted from Table A.12.

Uncertainty on $G_M^{\text{ind}}(s)$ due to the trigger efficiency correction

Table A.23 shows the details for the calculation of the systematic uncertainty on the magnetic form factor $\delta_{\text{dtrg}}^{\text{GM}}$ due to the trigger efficiency correction, as discussed in the Section 10.3. The systematic uncertainty is calculated as the luminosity weighted average of the \sqrt{s} -individual contributions:

$$\delta_{\text{dtrg}} = \left(\sum_i \delta_{\text{trg}}^i \times \mathcal{L}^i \right) / \left(\sum_i \mathcal{L}^i \right) \quad (\text{A.4})$$

\sqrt{s} (GeV)	δ_{trg}	\mathcal{L}_{int} (pb^{-1})	$\delta_{\text{trg}}^{\text{GM}}$ (%)
2.0000	4.48	$10.074 \pm 0.005 \pm 0.067$	4.10
2.0500	4.04	$3.344 \pm 0.003 \pm 0.027$	
2.1000	3.81	$12.167 \pm 0.006 \pm 0.085$	
2.1266	3.68	$108.49 \pm 0.02 \pm 0.94$	3.68
2.1500	3.55	$2.841 \pm 0.003 \pm 0.024$	3.28
2.1750	3.81	$10.625 \pm 0.006 \pm 0.091$	
2.2000	3.57	$13.699 \pm 0.007 \pm 0.092$	
2.2324	3.56	$11.856 \pm 0.007 \pm 0.087$	
2.3094	2.63	$21.089 \pm 0.009 \pm 0.143$	
2.3864	2.30	$22.549 \pm 0.010 \pm 0.176$	2.30
2.3960	2.30	$66.869 \pm 0.017 \pm 0.475$	
2.6454	1.65	$67.725 \pm 0.018 \pm 0.355$	1.50
2.9000	1.44	$105.253 \pm 0.025 \pm 0.905$	
2.9500	1.22	$15.942 \pm 0.010 \pm 0.143$	
2.9810	1.33	$16.071 \pm 0.010 \pm 0.095$	not extracted
3.0000	1.33	$15.881 \pm 0.010 \pm 0.110$	
3.0200	1.23	$17.290 \pm 0.011 \pm 0.123$	
3.0800	1.23	$126.185 \pm 0.029 \pm 0.921$	

Table A.23: The systematic uncertainty for G_M^{ind} due to the trigger efficiency correction. The resulting systematic uncertainty $\delta_{\text{dtrg}}^{\text{GM}}$ at all analyzed \sqrt{s} is calculated as the luminosity weighted average with Equation A.4. The luminosity \mathcal{L}_{int} with the corresponding systematic uncertainty is quoted from Table 3.11. The uncertainty δ_{trg} is quoted from Table A.13.

External Contributions to the Final Results from this Analysis

In the Appendix B the signal selection classifications A and B are summarized. The strategy for the signal event classification is discussed in detail in Section 5.2. The signal selection classifications denoted as A and B are not subject of this thesis and not the contribution by the author. Strategy A has been developed by Dr. Jifeng Hu and is discussed from Section B.1 and in the following. Strategy B has been developed by Dr. Xiaorong Zhou and is discussed from Section B.7 and in the following. For this analysis, an algorithm for the measurement of the time-of-flight for neutral particles has been developed, which is used in category A and B for the signal selection. This method is discussed in detail in the Appendix C. The discussion in Appendix B is based on internal communication with the BESIII collaboration and the four main authors of this analysis in the course of a future publication of the obtained results.

B1 Category A: Event classification

This category uses both EMC and TOF information to select the antineutron candidate and TOF information (EMC information optional) to select the neutron candidate.

1. S_{A0} : Events with charged tracks are rejected, events with $N_{\text{charged}} = 0$ are selected.
2. S_{A1} : The antineutron candidate's deposition energy $E_{\bar{n}}$ is measured by the EMC. To suppress beam related and cosmic background, the final cut criterion is $E_{\bar{n}} > 0.5$ GeV. Fig. B.1 (a) shows the $E_{\bar{n}}$ spectrum at $\sqrt{s} = 2.3960$ GeV. This spectrum has two bumps around 0.2 GeV and 1.2 GeV which are dominated by beam-associated background and $e^+e^- \rightarrow \gamma\gamma$ background, respectively.
3. S_{A2} : The number of hits measured by the EMC is denoted as N_{HIT}^{50} . N_{HIT}^{50} includes the number of hits from the leading shower and neighboring showers inside a 50 degree cone around the leading shower in the EMC. Fig. B.1 (b) shows the N_{HIT}^{50} distribution, indicating that the beam related and cosmic, as well as digamma events populate the lower region of the distribution. The cut value is set to be $30 < N_{\text{HIT}}^{50} < 140$. In addition, Fig. B.1 (e) and (f) show the correlations between $E_{\bar{n}}$ and N_{HIT}^{50} from collider data and from signal MC, respectively.
4. S_{A3} : Only the barrel region of EMC is used for analysis. To reject the digamma background, an optimized cut value of $|\cos\theta| < 0.7$ is applied.
5. S_{A4} and S_{A5} : The time-of-flight of the antineutron is measured by TOF counters and denoted as T_{TOF1} . The shower position is measured in the EMC and in the TOF counters and denoted as \vec{V}_{EMC1} and $\vec{V}_{\text{TOF1}'}$, respectively. Only TOF counters which are not further away than three times ϕ_c (Eqn. C.1) from the leading shower position in the EMC are used for the determination of the \bar{n} time-of-flight signal. Thus a cut value of $\theta_{\text{TOF1}',\text{EMC1}} < 0.5$ radian on the polar angle between the shower of the antineutron in the EMC and in the TOF is required, which is calculated as:

$$\theta_{\text{TOF1}',\text{EMC1}} = \arccos\left(\frac{\vec{V}_{\text{TOF1}'}\cdot\vec{V}_{\text{EMC1}}}{|\vec{V}_{\text{TOF1}'||\vec{V}_{\text{EMC1}}|}\right) \quad (\text{B.1})$$

Fig. B.1 (d) shows the $\theta_{\text{TOF1}',\text{EMC1}}$ distribution, which indicates the coincidence between EMC and TOF response.

6. S_{A6} : The time difference between the measured and expected flight time ($\Delta T_{\bar{n}}$) under the hypothesis of a photon (details are listed in C) is calculated as:

$$\Delta T_{\bar{n}} \equiv T_{\text{TOF1}} - T_0^\gamma - T_{\gamma 1} \quad (\text{B.2})$$

where T_0^γ is the event start time and $T_{\gamma 1}$ the predicted flight time from the interaction point (IP) to the TOF counters. Fig. B.1 (c) shows the $\Delta T_{\bar{n}}$ spectrum, which has a significant peak at zero. The peak is dominated by processes with photons in the final state. **This criterion is no longer used and replaced by $|\cos\theta| < 0.7$.**

7. S_{A7} : The neutron candidate is located in the recoil direction of the antineutron candidate. The position in the EMC and the position in the TOF counters are denoted as V_{EMC2} and $V_{\text{TOF2'}}$, respectively. Only TOF counters which are not further away than six times ϕ_c from the recoil direction of the leading shower in the EMC (or second leading shower position if there is a shower at the recoil direction of the leading shower in the EMC) are accounted as the neutron time-of-flight signal.
8. S_{A8} : The time measured by the TOF counters, associated to the neutron candidate, is denoted as T_{TOF2} . The time difference between the measured and expected neutron time of flight is defined as

$$\Delta T_n \equiv T_{\text{TOF2}} - T_0^n - T_n. \quad (\text{B.3})$$

where T_0^n is the event start time under the hypothesis of an neutron mass and T_n is the predicted flight time from the IP to the TOF counters. To improve the correct identification of the neutron a cut for $|\Delta T_n| < 4$ ns is required as shown in Fig. B.2 (b). The bump around -6 ns in the signal MC simulation is due to a T_0^n misalignment. The bump around -3 ns in the collider data is coming from $e^+e^- \rightarrow \gamma\gamma$ background.

9. S_{A9} : If a electromagnetic shower is found at the recoil direction of the leading shower, its deposited energy measured in the EMC and denoted as E_n , which will be set to zero if the second energetic shower is not found. Fig. B.2 (a) shows the E_n spectrum, where $E_n < 0.7$ GeV is applied to reject the $e^+e^- \rightarrow \gamma\gamma$ background ($0.06 < E_n < 0.7$ GeV is applied for data samples of $\sqrt{s} = 2.6444, 2.9000, 3.0800$ GeV (denoted as $S_{A9'}$).)

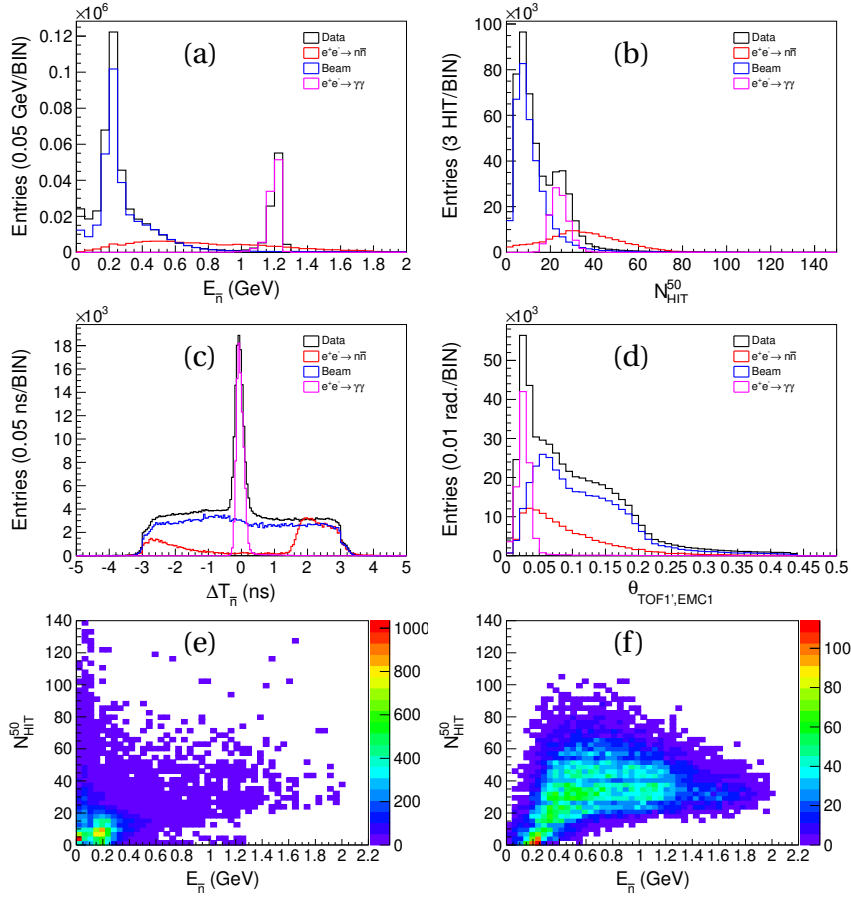


Fig. B.1: Category A: Antineutron variables at $\sqrt{s} = 2.3960$ GeV: (a) deposited energy $E_{\bar{n}}$ of the leading shower (antineutron candidate) in EMC, (b) number of hits N_{HIT}^{50} from the leading shower and its neighboring showers in EMC, (c) time difference $\Delta T_{\bar{n}}$ between the measured and expected time-of-flight of the antineutron candidate, (d) opening angle $\theta_{\text{TOF1}',\text{EMC1}}$ between EMC position and TOF position of the antineutron candidate, (e) scatter plot of $E_{\bar{n}}$ and N_{HIT}^{50} in data, (f) scatter plot of $E_{\bar{n}}$ and N_{HIT}^{50} in MC. Black histograms are collider data, red ones signal MC simulations with ConExc, blue ones separated beam data samples, magenta ones digamma MC simulations with Babayaga v3.5. The Signal MC is scaled by a factor of 360, the separated beam data samples are scaled by the data-taking time, the digamma MC simulation is scaled to the luminosity of the data.

10. S_{A10} and S_{A11} : The opening angle ($\theta_{\text{TOF2}',\text{EMC1}}$) and time difference (ΔT) between the antineutron and neutron candidates are calculated as:

$$\theta_{\text{TOF2}',\text{EMC1}} = \arccos\left(\frac{V_{\text{EMC1}} \cdot V_{\text{TOF2}'}}{|V_{\text{EMC1}}| |V_{\text{TOF2}'|}\right), \quad (\text{B.4})$$

$$\Delta T = T_{\text{TOF1}} - T_{\text{TOF2}}.$$

Fig. B.2 (c) shows the ΔT distribution for collision data and signal MC, which has three significant peaks around -6 ns, 0 ns and 6 ns in data. The peaks around -6 ns and 6 ns in data are dominated by cosmic rays and beam related background. The center peak around 0 ns is dominated by the processes $e^+e^- \rightarrow n\bar{n}$ and $e^+e^- \rightarrow \gamma\gamma$. Fig. B.2 (d) shows the $\theta_{\text{TOF2',EMC1}}$ distribution. The peak around π is expected for signal MC simulation events due to its two particle kinematics (red histogram). No peaking background in this region is observed in the separated beam data sample. Thus, $|\Delta T| < 4$ ns and $\theta_{\text{TOF2',EMC1}} > 3.0$ radian are applied to improve signal-to-background ratio.

11. S_{A12} : If a second leading shower is found at the recoil direction to the leading shower in the EMC, a cut of $\theta_{\text{EMC2,EMC1}} > 3.0$ is applied to further improve signal-to-background ratio, especially for the data samples $\sqrt{s} = 2.6444, 2.9000, 2.9500, 2.9810, 3.0000, 3.0200, 3.0800$ GeV.

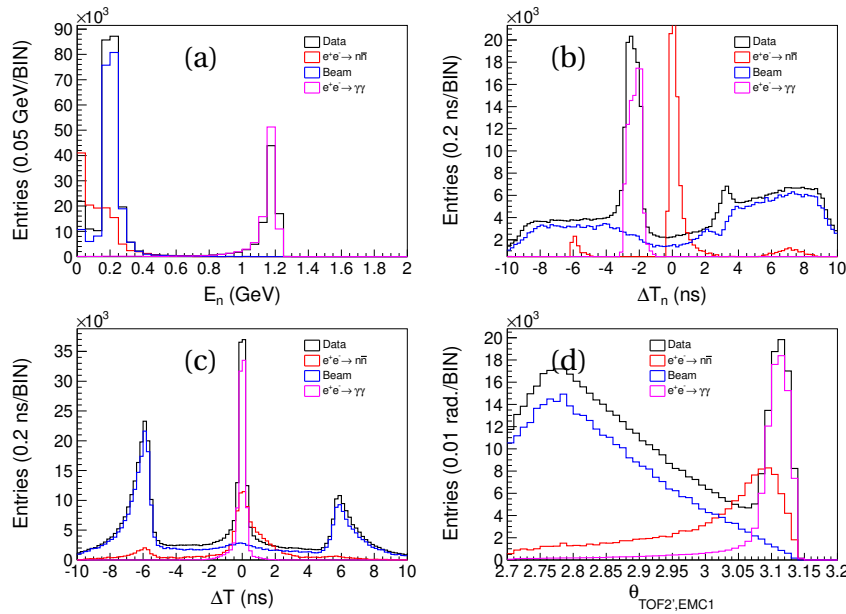


Fig. B.2: Category A: Neutron variables at $\sqrt{s} = 2.3960$ GeV: (a) deposited energy E_n of the second energetic shower (neutron candidate) in EMC, (b) time difference ΔT_n between the measured and expected time-of-flight of the neutron candidate, (c) time difference ΔT_n between the antineutron candidate and the neutron candidate, (d) opening angle $\theta_{\text{TOF2',EMC1}}$ between the antineutron candidate and the neutron candidate. Black histograms are collider data, the red ones signal MC simulations with ConExc, the blue ones separated beam data samples, magenta ones the digamma MC simulations with Babayaga v3.5. The signal MC is scaled by a factor of 360, the separated beam data samples are scaled to the data-taking time, the digamma MC simulation is scaled to the luminosity of the collider data. In the distribution of the neutron, the selection criteria related to the antineutron are not applied to the data.

All mentioned selection criteria are listed in Table B.1.

Expression	Unit	Object	Notation
$N_{\text{charged}} == 0$	-	\bar{n}, n	S_{A0}
$0.5 < E_{\bar{n}} < 2.0$ ($0.3 < E_{\bar{n}} < 2.0$)	GeV	\bar{n}	S_{A1} ($S_{A1'}$)
$30 < N_{\text{HIT}}^{50} < 140$	-	\bar{n}	S_{A2}
$ \cos\theta < 0.7$	radian	\bar{n}	S_{A3}
$ \Delta\phi_{(\text{TOF1,EMC1})} < 3\phi_c$	radian	\bar{n}	S_{A4}
$\theta_{(\text{TOF1,EMC1})} < 0.5$	radian	\bar{n}	S_{A5}
$0.5 < \Delta T_{\bar{n}} < 10$ ($ \Delta T_{\bar{n}} < 10$)	ns	\bar{n}	S_{A6} ($S_{A6'}$) (removed)
$ \Delta\phi_{(\text{TOF2,EMC1}')} < 6\phi_c$	radian	n	S_{A7}
$ \Delta T_n < 4$	ns	n	S_{A8}
$E_n < 0.7$ ($0.06 < E_n < 0.7$)	GeV	n	S_{A9} ($S_{A9'}$)
$\theta_{\text{TOF2',EMC1}} > 3.0$ ($\theta_{\text{TOF2',EMC1}} > 2.9810$)	radian	n, \bar{n}	S_{A10} ($S_{A10'}$)
$ \Delta T < 4.0$	ns	n, \bar{n}	S_{A11}
$\theta_{\text{EMC2,EMC1}} > 3.0000$	radian	n, \bar{n}	S_{A12}

Table B.1: Category A: Summary of the selection criteria for the signal events. The selection criteria are listed in the same order as applied in the analysis. For details on the matching of the time-of-flight signal to the showers in the EMC see C.

B2 Category A: Signal extraction

To extract the number of signal events (signal yield) from the collider data after the signal selection has been applied, a model for ΔT_n which combines the signal process with three kinds of background contributions is defined as shown below:

$$\text{PDF}(\Delta T_n) = N_{\text{sig}} * \text{PDF}_{n\bar{n}} + \sum N_{\text{bkg}} * \text{PDF}_{\text{bkg}}, \text{bkg} = q\bar{q}, \gamma\gamma, \text{beam}. \quad (\text{B.5})$$

The model is the probability density function of ΔT_n , consisting of four components. The PDF of the digamma component is extracted from data at each energy point, to avoid precise MC tuning. The PDF of the beam related and cosmic ray component is extracted from the separated beam collider data at $\sqrt{s} = 2.2324$ GeV and $\sqrt{s} = 2.6454$ GeV. The PDFs of the signal and hadron component are extracted from the MC simulation samples produced with the ConExc and LuArLw generator.

The discussed PDFs are implemented by RooKeysPdf, and used with a reduced dataset implemented by RooDataSet. The reduced dataset is obtained from the corresponding collider data samples after the signal selection. The number of hadron events is fixed to the predicted production in the collider according to the corresponding cross section and luminosity. The number for the digamma component is fixed in the same way. The normalization of the beam related and cosmic ray events is left free for the data samples below $\sqrt{s} = 2.6454$ GeV and set to zero above this \sqrt{s} . The selection criteria $S_{A0} - S_{A11}$ are used below $\sqrt{s} = 2.6454$ GeV. Above, the criterion S_{A9} is replaced with $S_{A9'}$ and additionally S_{A12} is applied. The motivation is to suppress more background while still keep the event efficiency high, because with high momentum neutrons can hit the TOF and EMC simultaneously, while low momentum neutrons tend to be blocked by the TOF. Table B.2 lists the construction setup in detail.

Sample at \sqrt{s} (GeV)	Selection applied	Parameters	Normalization
2.0000-2.3960	$S_0 - S_{A11}$	MirrorBoth, $\rho = 0.8$	$N_{\text{sig}}, N_{\text{beam}}$ free, $N_{q\bar{q}}, N_{\gamma\gamma}$ fixed.
2.6454-3.0800	$S_{A0} - S_{A11} + S_{A12}$	MirrorBoth, $\rho = 1.0$	$N_{\text{sig}}, N_{\gamma\gamma}$ free, $N_{\text{beam}}=0$, $N_{q\bar{q}}$ fixed.
sep. beam	$S_{A0} + S_{A3} + S_{A11}$	MirrorBoth, $\rho = 1.0$	PDF shared.

Table B.2: Category A: Setup configuration for the signal extraction.

For each \sqrt{s} , a combined PDF with four components is constructed and added to the RooSimultaneous class. Second, the collider data distribution is added to the RooSimultaneous class. The RooSimultaneous class indexes each PDF and each data set. The model and the collider data at each energy point are indexed and linked. Each model will fit to each data by seeking a global negative-logarithm-likelihood value. The solution is optimized for all energy points simultaneously, therefore individual results may be not optimized. There are no common parameters except of the shape of the separated beam sample PDF which is shared.

Finally, a simultaneous fit is performed using the maximum likelihood method which uses the global likelihood for optimization. Free parameters are determined in case of a successful fitting. The numerical results are listed in Table B.3. Plots for the above discussed survived signal and background contributions are shown in Figure B.3.

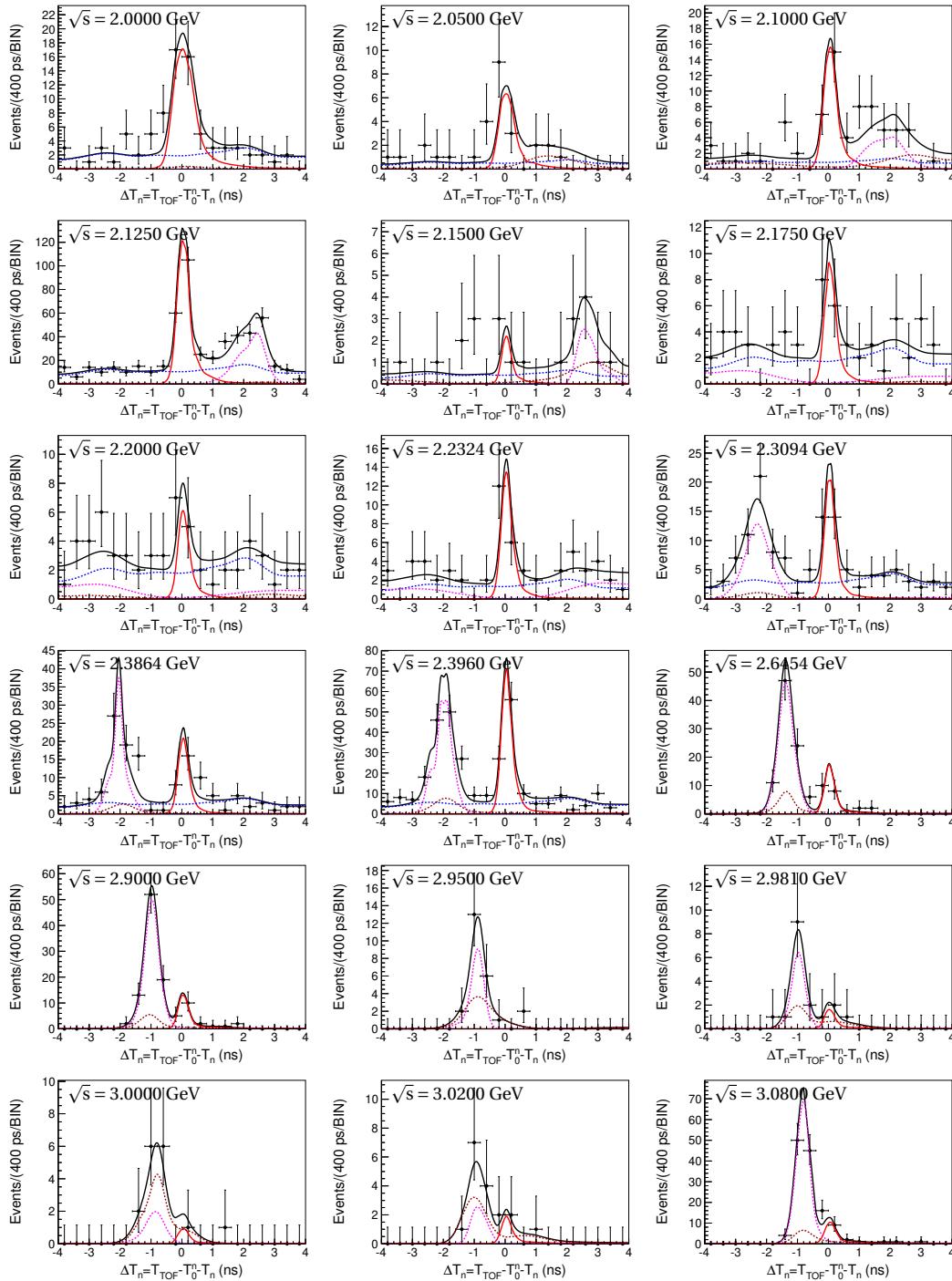


Fig. B.3: Category A: Simultaneous fit of signal and background shape in ΔT_n with Eq. B.5 at 18 energy points (2.0000 GeV - 3.0800 GeV). The black points represent the collider data, the red line represents the signal MC simulation with ConExc, the blue dotted line represents the combined beam associated and cosmic ray background at $\sqrt{s} = 2.2324 + 2.6444$ GeV, the magenta dotted-dashed line represents the digamma background extracted from collider data at the corresponding \sqrt{s} , the orange dotted-dashed line represents the hadronic background MC with ConExc and the black line is the combined fit model.

\sqrt{s} (GeV)	N_{sig}	\sqrt{s} (GeV)	N_{sig}
2.0000	39.2 ± 7.4	2.3864	23.7 ± 5.9
2.0500	12.3 ± 4.1	2.3960	82.2 ± 10.1
2.1000	24.2 ± 5.7	2.6444(+2)	20.5 ± 4.7
2.1250	174.3 ± 15.2	2.9000	16.7 ± 4.5
2.1500	3.9 ± 3.1	2.9500	0.0 ± 1.8
2.1750	11.7 ± 4.2	2.9810	2.3 ± 1.9
2.2000	7.9 ± 3.7	3.0000	1.3 ± 1.3
2.2324	16.5 ± 4.8	3.0200	2.9 ± 2.1
2.3094	24.2 ± 6.0	3.0800	14.7 ± 4.7

Table B.3: Category A: Number of reconstructed signal events in collider data. The values are obtained from the fit procedure as described in this section. The shown errors are statistical.

B3 Category A: Reconstruction efficiency

Two types of corrections are applied. The correction \mathcal{C}_{dm} for the differences between the collider data and the MC simulation, and the trigger efficiency correction \mathcal{C}_{trg} . The correction \mathcal{C}_{dm} and the frequency distribution from the signal MC w($p, \cos\theta$) are shown in Figure B.4. The absolute value for \mathcal{C}_{dm} at $\sqrt{s} = 2.3960$ GeV is:

$$\mathcal{C}_{\text{dm}}^{\text{abs}}(2.396 \text{ GeV}) = (94.5 \pm 1.7)\% \quad (\text{B.6})$$

The correction of the trigger efficiency \mathcal{C}_{trg} is applied. The distribution of the event energy spectrum after passing the final selection criteria $S_{A0} - S_{A12}$ is shown at $\sqrt{s} = 2.3960$ GeV

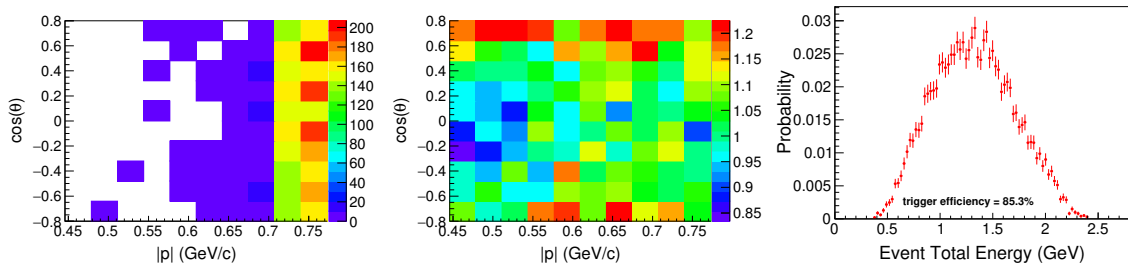


Fig. B.4: Category A: (left) The frequency distribution of signal MC simulation from ConExc before normalization at $\sqrt{s} = 2.3960$ GeV, (middle) the ratio of efficiencies from collider data over signal MC simulation at $\sqrt{s} = 2.3960$ GeV. (Right) Normalized deposited energy spectrum of the total energy deposition in an event at $\sqrt{s} = 2.3960$ GeV.

in Figure B.4 (right). After the substitution into Eq. B.7 (for details see the determination of the trigger efficiency correction in Section 8.5)

$$\mathcal{E}_{\text{trg}} = \frac{\sum_{i=0}^N f(E_{\text{total}}^i)}{N}, \quad (\text{B.7})$$

the trigger correction factor at $\sqrt{s} = 2.3960$ GeV is calculated to be:

$$\mathcal{E}_{\text{trg}}^{\text{abs}}(2.396 \text{ GeV}) = (89.2 \pm 1.1)\% \quad (\text{B.8})$$

The signal MC simulation reconstruction efficiency and its correction factors for the analyzed data samples are listed in Table B.4.

\sqrt{s} (GeV)	ϵ_{MC} (%)	\mathcal{E}_{trg} (%)	\mathcal{E}_{dm} (%)
2.0000	1.35	82.9±1.0	108.3±3.4
2.0500	1.27	83.3±1.0	104.1±2.8
2.1000	1.23	83.8±1.1	96.5±2.3
2.1250	1.19	84.6±1.1	96.3±2.2
2.1500	1.15	85.7±1.1	93.3±2.1
2.1750	1.09	83.8±1.1	94.4±2.1
2.2000	1.06	85.3±1.2	94.6±2.0
2.2324	1.08	85.1±1.1	98.8±2.1
2.3094	1.21	87.6±1.1	96.6±1.9
2.3864	1.40	89.3±1.0	95.9±1.7
2.3960	1.35	89.2±1.1	94.5±1.7
2.6454	0.64	94.7±1.6	83.8±1.2
2.9000	0.56	95.9±1.8	79.9±1.2
2.9500	0.57	96.7±1.8	77.9±1.2
2.9810	0.56	95.8±1.8	78.8±1.5
3.0000	0.57	96.0±1.7	80.2±2.2
3.0200	0.55	95.7±1.8	80.0±8.2
3.0800	0.56	96.5±1.8	95.8±1.6

Table B.4: Category A: Signal MC event selection efficiency and its corrections, based on 500000 MC simulation events with the event generator ConExc in BesEvtGen-00-03-18 for the three categories at all analyzed energy points.

B4 Category A: Angular analysis

For the angular analysis, a slightly modified event selections is used to maximize the signal yield: $S_{A0} - S_{A10}$, S_{A1} and S_{A10} are replaced with $S_{A1'}$ and $S_{A10'}$ respectively. First, a fit to the ΔT_n distribution of the total data events is performed at $\sqrt{s} = 2.1266$ GeV, as illustrated in Figure B.5 (ALL). The number of total data events is 774, the number of signal events is estimated to be 216.1 ± 17.1 at $\sqrt{s} = 2.1266$ GeV. Following, the $\cos\theta$ distribution in the range from -0.7 to 0.7 is divided into 7 bins with a width of 0.2. A series of analyses at each energy point is performed to obtain the signal yield from each bin, as listed in Table B.5.

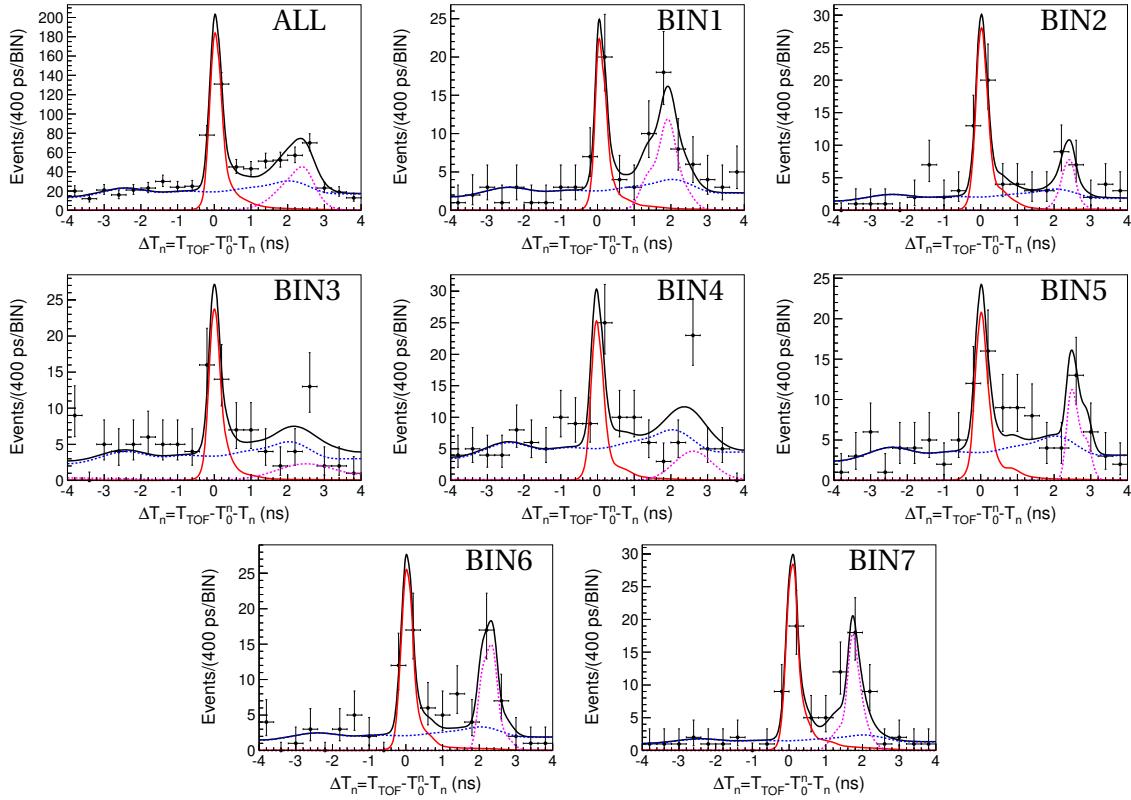


Fig. B.5: Category A: Fit to ΔT_n at each $\cos\theta$ bin at $\sqrt{s} = 2.1266$ GeV. The signal shape is represented by the red solid line, the $e^+e^- \rightarrow \gamma\gamma$ background by the magenta dashed line, the beam related and cosmic ray background the by blue dashed line.

Due to the low statistics in the collider data at $\sqrt{s} = 2.0500, 2.1500, 2.2000, 2.2324,$ and 2.9500 GeV, it is difficult to perform a stable angular analysis. Therefore, neighboring (in \sqrt{s}) data samples are combined to increase the statistics. For the combined results in Section 9.4, the groups are chosen accordingly to the category B and C.

\sqrt{s} (GeV)	$N_{\text{fit}}^{(\text{B1})}$	$N_{\text{fit}}^{(\text{B2})}$	$N_{\text{fit}}^{(\text{B3})}$	$N_{\text{fit}}^{(\text{B4})}$	$N_{\text{fit}}^{(\text{B5})}$	$N_{\text{fit}}^{(\text{B6})}$	$N_{\text{fit}}^{(\text{B7})}$
2.000	3.76±2.75	8.37±3.44	7.63±3.24	3.68±3.08	7.35±3.34	6.67±2.93	6.51±2.95
2.050	0.00±0.81	0.00±0.53	2.88±1.99	0.69±1.96	0.72±1.06	7.00±2.89	3.65±2.08
2.100	3.21±2.04	5.28±2.56	4.18±2.53	9.05±3.97	4.35±2.64	0.81±1.15	4.40±2.31
2.125	25.31±6.13	33.96±6.65	28.60±6.39	31.12±7.14	27.62±6.83	31.10±6.46	33.44±6.76
2.150	1.05±1.14	0.61±1.20	0.00±2.50	0.60±1.88	0.00±0.52	2.91±1.93	0.00±0.51
2.175	1.30±1.53	2.25±1.78	0.00±0.93	4.48±3.18	1.17±1.47	3.47±2.07	0.33±1.13
2.200	1.85±1.76	1.50±1.62	0.00±0.56	5.70±3.00	2.12±1.77	0.00±2.17	0.71±1.04
2.2324	1.89±1.64	2.02±1.71	4.48±2.54	0.77±1.61	2.75±2.02	1.88±1.70	1.75±1.83
2.3094	0.81±1.34	5.95±2.71	4.90±2.66	4.84±2.96	4.10±2.63	3.47±2.77	1.24±2.31
2.3864	4.84±2.58	4.66±2.39	1.28±1.73	4.65±2.92	2.17±2.01	6.34±3.09	2.27±2.31
2.396	16.73±4.47	16.19±4.63	11.33±4.17	17.27±5.40	10.47±4.26	15.41±4.40	15.50±4.33
2.644	3.70±2.16	1.88±1.43	0.00±0.53	5.99±2.88	3.58±2.04	1.90±1.74	4.03±2.21
2.900	3.78±2.06	2.98±1.93	2.42±1.97	1.18±1.41	1.69±3.20	3.92±2.01	5.04±2.25
2.950	0.00±0.51	0.00±0.51	0.00±0.59	0.00±0.51	0.59±1.06	0.00±8.69	0.00±0.51
3.080	3.77±2.05	2.31±2.09	2.01±1.46	2.94±1.80	0.00±0.90	3.89±2.60	6.37±2.81

Table B.5: Category A: Summary of the extracted differential signal yield $N_{\text{fit}}^{\cos\theta(\text{Bi})}$ from the collider data at different \sqrt{s} , using the independent fit method, as described in Section B.2. Bi represents the i-th bin.

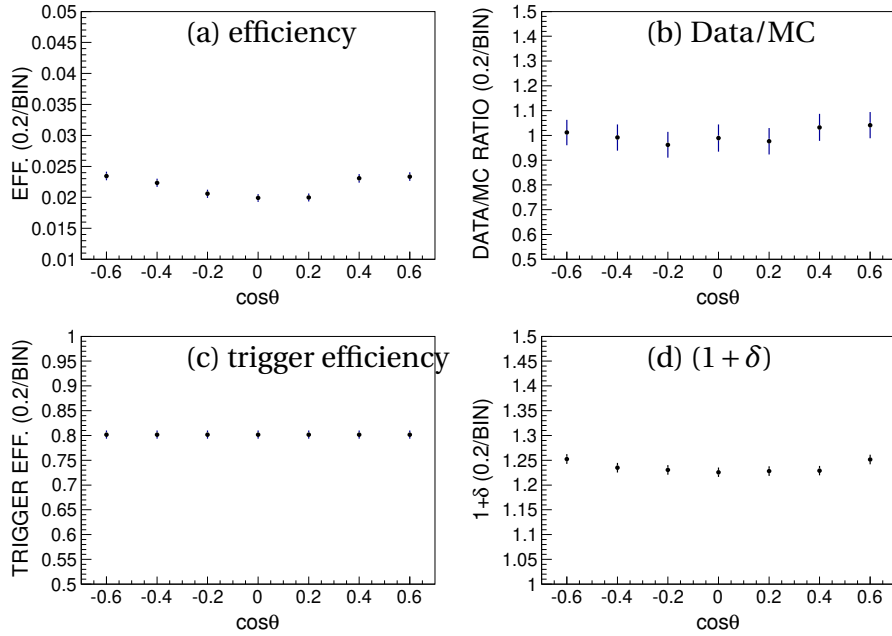


Fig. B.6: Category A: Differential efficiency corrections at $\sqrt{s} = 2.1266$ GeV. (Top left) Selection efficiency $e_{h,\bar{h}}^{\text{MC}}$ extracted from signal MC simulation with ConExc in BesEvtGen-00-03-18, (top right) correction factor \mathcal{C}_{dm} derived with control samples $J/\psi \rightarrow p\bar{n}\pi^- (\bar{p}n\pi^+)$, (bottom left) trigger efficiency correction \mathcal{C}_{trg} , (bottom right) Radiative correction factor $(1 + \delta)$.

Before performing the angular analysis, the extracted signal yield from the collider data must be corrected. Figure B.6 (a) shows the MC simulation event selection efficiency, the data to MC correction (b), the trigger efficiency correction (c), and the radiative correction (d), respectively. From Figure B.6 (c) can be seen, that the trigger efficiency correction is flat over the whole range and can be applied as an absolute correction value instead of the differential correction shown in the figure, without any changes in the results. The final results for the magnetic form factor G_M and the form factor ratio $R = |G_E|/|G_M|$ from category A are listed in Table B.6 for the case of the simple fit with Eq. 9.6, and additionally by taking into account the category- and sample-individual resolution. The corresponding plots are shown in Figure B.7.

\sqrt{s} (GeV)	Simple Fit		
	$G_M (\times 10^{-2})$	$R_{em}^n = G_E^n/G_M^n $	χ^2/ndf
2.0000	7.3 ± 17.5	3.43 ± 9.18	1.8/5
2.1250	6.5 ± 3.6	2.25 ± 1.71	0.98/5
2.1750, 2.2000	5.4 ± 5.4	0.90 ± 3.03	8.0/5
2.3864, 2.3960	8.4 ± 2.3	1.05 ± 0.89	4.4/5
2.6444 - 2.9500	4.9 ± 1.2	0.00 ± 84.1	3.2/5
\sqrt{s} (GeV)	Convolution Fit		
	$G_M (\times 10^2)$	$R_{em}^n = G_E^n/G_M^n $	χ^2/ndf
2.0000	7.3 ± 17.5	3.43 ± 9.18	1.8/5
2.1250	6.5 ± 3.6	2.25 ± 1.71	0.98/5
2.1750, 2.2000	5.4 ± 5.4	0.90 ± 3.03	8.0/5
2.3864, 2.3960	8.4 ± 2.3	1.05 ± 0.89	4.4/5
2.6444 - 2.9500	4.9 ± 1.2	0.00 ± 84.1	3.2/5

Table B.6: Category A: Magnetic form factor G_M and form factor ratio $R_{em} = |G_E/G_M|$ at $\sqrt{s} = 2.1266$ and the four combined data samples. The errors are statistical.

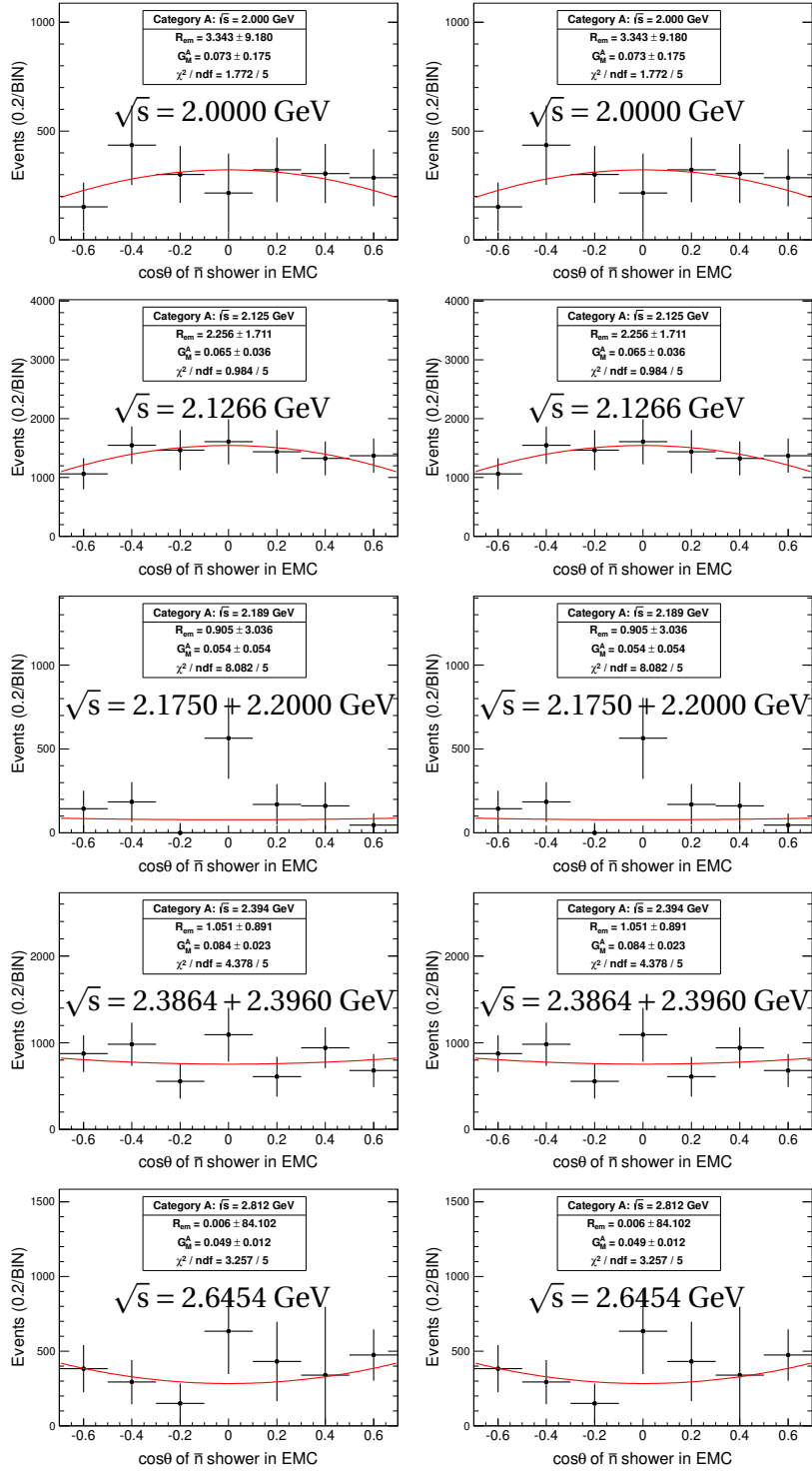


Fig. B.7: Category A: results from the angular distribution fit of the efficiency corrected angular distributions at the five data sets at $\sqrt{s} = 2.0000, 2.1266, 2.1875, 2.3936,$ and 2.6454 GeV.

B5 Category A: Systematic uncertainty

The following systematic uncertainty contributions are studied for the Born cross section and the effective form factor:

1. Luminosity (U_L^A): The uncertainty of the luminosity determination is directly taken from the publication for the measurement [27]. Then the uncertainty is propagated to the cross section calculation.
2. Antineutron selections and neutron selections ($U_{n,\bar{n}}^A$): The major difference of this selection efficiency has been corrected by studying MC simulation control sample and data control sample using $J/\psi \rightarrow p\pi^-\bar{n}(n)$. The error of the correction is taken as the systematic error.
3. T_0 and T_0^n misalignment ($U_{T_0}^A$): T_0 is used in the selection of $\Delta T_{\bar{n}} = T_{\text{TOF1}} - T_0 - T_{\gamma 1} < 10$ ns. The time window of 10 ns is large enough to cover interactions from 2 bunches. Even if T_0 is shifted one bunch interval, it does not affect the overall efficiency. Thus the uncertainty representing the misidentification of T_0 is ignored. T_0^n is used in the calculation of $\Delta T_n = T_{\text{TOF2}} - T_0^n - T_n < 4$ ns. The regression of T_0^n will affect the neutron selection efficiency. The discrepancy of the neutron selection efficiency is taken as the systematic uncertainty.
4. Angular distribution (U_{model}^A): The angular distribution affects our selection efficiency. Three MC simulation samples with different settings $G_E = 0$, $G_M = 0$ and $G_E = G_M$ respectively are produced at each energy point. Because our selection efficiency is smaller in the center $\cos\theta$ region than at the outer sides, the sample with $G_M = 0$ will result in the largest selection efficiency (ϵ_{max}) on average, while the sample with $G_E = 0$ the opposite (ϵ_{min}). We assume that the average efficiency is uniformly distributed between the minimum value and the maximum value with the variation of the G_E/G_M ratio. The variance of the selection efficiency is close to $1/\sqrt{12}(\epsilon_{\text{max}} - \epsilon_{\text{min}})$, which is taken as the systematic uncertainty U_{model}^A .
5. The antineutron and neutron misidentification (U_{mis}^A): After the final selection, the leading shower in the EMC is 99.9% coming from an antineutron, as studies with signal MC simulation and a matching algorithm show. The variation of the signal yield due to the misidentification is considered as a systematic uncertainty. Since the misidentification is extremely small, this uncertainty will be ignored.

6. Time resolution of the neutron (U_{res}^A): Discrepancy in ΔT_n between the control samples from collider data and MC simulation sample for $J/\psi \rightarrow p^- \pi^+ n$ are studied. It is found that the time resolution of the MC simulation has 0.1 ns difference to the collider data. Thus a smearing of 0.1 ns is applied to ΔT_n of the MC simulation sample. The second order difference is used to vary the PDF for ΔT_n from the MC simulation sample. The difference for the observed signal yield before and after the variation is taken as the systematic uncertainty.
7. Event level selections (U_{evt}^A): The opening angle selection and the time difference selection depend on the antineutron and the neutron information. There is no way to study the effect from both particles simultaneously using the control samples. A variation of the cut on the opening angle is performed between 2.95 to 3.0 rad, while the selection criterion on the time difference is excluded, to estimate changes in the cross section. This uncertainty is included to the next uncertainty.
8. Signal yields extraction (U_{fit}^A): The difference of the signal yield is studied under variations of the selection criteria. The nominal values are set to $E_{\bar{n}} = 0.5$ GeV, $N_{\text{HIT}} = 30$, and $\theta_{\text{EMC1}', \text{TOF2}'} = 3.0$ rad. The variations are studied one by one. For example, $E_{\bar{n}} = 0.5$ GeV is changed to 0.3 GeV while all other selection criteria are unchanged. Other variations are $N_{\text{HIT}} = 30 \rightarrow 35$ and $\theta_{\text{EMC1}', \text{TOF2}'} = 3.0 \rightarrow 2.98 \rightarrow 2.95$ rad. Attention should be paid to the selection efficiency, data/MC correction and trigger correction, which need to be re-calculated for the modified selection criteria. The cross section results with the modified selection criteria are re-calculated and compared to the nominal values. The maximum difference is taken as a systematic uncertainty U_{fit}^A .
9. The systematic uncertainty U_{tri}^A from the trigger efficiency is determined as the difference of the trigger efficiency determined with the $e^+ e^- \rightarrow \bar{p} p$ selection and the results for the trigger efficiency obtained with the $e^+ e^- \rightarrow \bar{q} q \rightarrow \text{hadrons}$ selection.

All the discussed systematic uncertainties for the results on the Born cross section and the effective form factor are summarized in Table B.7.

Following the systematic uncertainties on the form factor ratio $|G_E/G_M|$ and the magnetic form factor G_M are discussed. The systematic uncertainties for the ratio arise from the selection of the angular distribution of the antineutron, the angular efficiency determination, the fit method for the extraction of the signal yield, and correction for the radiative events.

\sqrt{s} (GeV)	U_L^A	$U_{n,\bar{n}}^A$	$U_{T_0}^A$	U_{model}^A	U_{mis}^A	U_{res}^A	U_{fit}^A	U_{tri}^A	Total (%)
2.0000	0.6	3.1	0.2	10.8	0.1	5.0	-14.5, +0.0	4.6	-19.5, +13.1
2.0500	0.6	2.6	0.2	10.3	0.1	5.0	-27.0, +1.9	4.6	-29.8, +12.8
2.1000	0.7	2.3	0.2	7.8	0.1	5.0	-2.6, +23.1	4.6	-10.9, +25.4
2.1500	0.7	2.2	0.2	9.5	0.1	5.0	-1.1, +11.7	4.6	-12.0, +16.7
2.1250	0.7	2.2	0.2	8.1	0.1	5.0	-6.3, +70.2	4.6	-12.5, +71.0
2.1750	0.8	2.2	0.2	8.8	0.1	5.0	0.0, +42.6	4.6	-11.4, +44.1
2.2000	0.6	2.1	0.2	8.0	0.1	5.0	-17.5, +22.3	4.5	-20.5, +24.7
2.2324	0.7	2.1	0.2	8.0	0.1	5.0	-22.6, +20.8	4.5	-25.0, +23.4
2.3094	0.6	1.9	0.2	8.7	0.1	5.0	-5.6, +2.8	4.2	-12.4, +11.4
2.3864	0.7	1.7	0.2	9.0	0.1	5.0	-2.8, +14.4	4.1	-11.6, +18.2
2.3960	0.7	1.7	0.2	9.0	0.1	5.0	-3.1, +8.0	4.1	-11.6, +13.8
2.6440	0.3	1.4	0.2	5.1	0.1	5.0	-11.0, +1.8	3.0	-13.5, +8.0
2.9000	0.8	1.5	0.2	1.3	0.1	5.0	-32.3, +7.0	2.6	-32.8, +9.2
2.9500	0.8	1.5	0.2	1.3	0.1	5.0	-96.0, +1.0	2.6	-96.1, +6.1
2.9800	0.8	1.9	0.2	1.3	0.1	5.0	-73.9, +0.0	2.6	-74.1, +6.1
3.0000	0.8	2.7	0.2	0.5	0.1	5.0	-100.0, +0.0	2.6	-100.0, +6.3
3.0200	0.8	10.2	0.2	0.5	0.1	5.0	-55.9, +14.9	2.6	-57.1, +18.9
3.0800	0.7	1.6	0.2	4.5	0.1	5.0	-91.5, +25.3	2.0	-91.7, +26.3

Table B.7: Category A: Summary of all systematic uncertainty sources for the Born cross section measurement.

- The uncertainty of the differential event reconstruction (δ_{dsel}) comes from the uncertainty of the correction for the differences between collider data to the signal MC simulation, the fit range, the signal- and the background shape model, and the trigger efficiency. This uncertainty is determined by varying the selection criteria for the deposition energy of the antineutron in the EMC, the number of hits in the EMC, the opening angle between antineutron and neutron, and so on. The maximum difference on the $|G_E/G_M|$ results to the nominal values is taken as the systematic uncertainty. This uncertainty is large because the angular distribution has very low statistics in many bins in most of the analyzed data samples.
- The uncertainty of the ISR effect (δ_{drad}) is determined as the difference of the results for $|G_E/G_M|$ between the different signal MC simulation versions (used during the iterative optimization of the FF model in the signal MC simulation).

Additionally to the systematic uncertainty sources as discussed for the FF ratio, the systematic uncertainty for G_M includes the luminosity, the trigger efficiency, the data to MC correction and the angular efficiency. The uncertainty from the luminosity of $\sim 1\%$ is quoted from the published luminosity measurements at BESIII. The uncertainty from the

trigger efficiency correction is taken as the relative error of the trigger efficiency. Table B.8 summarizes all discussed uncertainties on G_E/G_M and G_M , respectively.

\sqrt{s} (GeV)	δ_{dsel}^R (%)	δ_{drad}^R (%)	δ_{sys}^R (%)	$\delta_{\text{sel}}^{G_M}$ (%)	$\delta_{\text{lum}}^{G_M}$ (%)	$\delta_{\text{trig}}^{G_M}$ (%)	$\delta_{\text{drad}}^{G_M}$ (%)	$\delta_{\text{sys}}^{G_M}$ (%)
2.0516	16.8	5.0	17.5	28.0	1.4	4.6	2.3	29.0
2.125	69.8	5.0	69.9	41.3	1.4	4.6	1.5	42.0
2.2380	20.4	5.0	21.0	8.10	1.4	4.5	3.3	10.0
2.3936	55.1	5.0	55.3	44.5	1.4	4.1	4.7	45.5
2.8130	30.0	5.0	30.4	12.6	1.4	3.0	6.9	15.3

Table B.8: Category A: Summary of the systematic uncertainties on $|G_E/G_M|$ and on the $|G_M|$.

B6 Category A: Summary of the results

Table B.9 summarizes the derived Born cross sections σ_{Born} and the effective FFs $|G|$ from the signal classification approach category A.

\sqrt{s} GeV	N^{obs}	\mathcal{L}_{int} (pb $^{-1}$)	$(1+\delta)$	ϵ_{MC} (%)	C_{dm} (%)	C_{trg} (%)	σ_{Born} (pb)	$ G $ ($\times 10^2$)
2.0000	38.3 \pm 7.3	10.074	0.98	1.35	108.3 \pm 3.4	82.9 \pm 1.0	320.1 \pm 61.0 \pm 62.6	17.2 \pm 1.6 \pm 1.6
2.0500	12.8 \pm 4.1	3.343	1.08	1.27	104.1 \pm 2.8	83.3 \pm 1.0	321.9 \pm 103.1 \pm 95.9	16.5 \pm 2.6 \pm 2.4
2.1000	24.3 \pm 5.7	12.167	1.18	1.23	96.5 \pm 2.3	83.8 \pm 1.1	170.2 \pm 39.9 \pm 43.3	11.7 \pm 1.3 \pm 1.4
2.1250	172.2 \pm 14.9	108.490	1.24	1.19	96.3 \pm 2.2	84.6 \pm 1.1	132.0 \pm 11.4 \pm 22.0	10.2 \pm 0.4 \pm 0.8
2.1500	3.0 \pm 2.2	2.841	1.29	1.15	93.3 \pm 2.1	85.7 \pm 1.1	89.0 \pm 65.2 \pm 63.2	8.3 \pm 3.0 \pm 2.9
2.1750	10.9 \pm 4.1	10.625	1.31	1.09	94.4 \pm 2.1	83.8 \pm 1.1	90.8 \pm 34.1 \pm 40.0	8.4 \pm 1.5 \pm 1.8
2.2000	8.0 \pm 3.5	13.699	1.31	1.06	94.6 \pm 2.0	85.3 \pm 1.2	52.1 \pm 22.8 \pm 12.9	6.3 \pm 1.3 \pm 0.7
2.2324	10.0 \pm 3.9	11.856	1.28	1.08	98.8 \pm 2.1	85.1 \pm 1.1	72.5 \pm 28.3 \pm 18.1	7.5 \pm 1.4 \pm 0.9
2.3094	22.6 \pm 5.8	21.089	1.14	1.21	96.6 \pm 1.9	87.6 \pm 1.1	91.8 \pm 23.5 \pm 11.3	8.5 \pm 1.0 \pm 0.5
2.3864	22.5 \pm 5.8	22.549	1.11	1.40	95.9 \pm 1.7	89.3 \pm 1.0	74.9 \pm 19.3 \pm 13.6	7.7 \pm 1.0 \pm 0.7
2.3960	80.3 \pm 9.9	66.869	1.11	1.35	94.5 \pm 1.7	89.2 \pm 1.1	95.0 \pm 11.7 \pm 13.1	8.7 \pm 0.5 \pm 0.6
2.6454	19.4 \pm 4.7	67.714	1.55	0.64	83.8 \pm 1.2	94.7 \pm 1.6	36.3 \pm 8.8 \pm 4.9	5.7 \pm 0.6 \pm 0.3
2.9000	16.3 \pm 4.4	105.253	2.16	0.56	79.9 \pm 1.2	95.9 \pm 1.8	16.7 \pm 4.5 \pm 5.4	4.1 \pm 0.5 \pm 0.6
2.9500	0.0 \pm 1.3	15.942	2.29	0.57	77.9 \pm 1.2	96.7 \pm 1.8	0.0 \pm 8.2 0.0	0.0 \pm 3.0 \pm 0.0
2.9800	2.3 \pm 1.9	16.071	2.36	0.56	78.8 \pm 1.5	95.8 \pm 1.8	14.3 \pm 11.8 \pm 10.6	3.9 \pm 1.6 \pm 1.4
3.0000	1.4 \pm 1.3	15.881	2.41	0.57	80.2 \pm 2.2	96.0 \pm 1.7	8.3 \pm 7.7 \pm 8.3	3.0 \pm 1.4 \pm 1.5
3.0200	2.9 \pm 2.1	17.290	2.46	0.55	80.0 \pm 8.2	95.7 \pm 1.8	16.7 \pm 11.7 \pm 9.5	4.3 \pm 1.5 \pm 1.2
3.0800	12.1 \pm 4.3	126.185	2.61	0.56	95.8 \pm 1.6	96.5 \pm 1.8	7.1 \pm 2.5 \pm 6.5	2.8 \pm 0.5 \pm 1.3

Table B.9: Category A: Summary of the results for the Born cross section σ_{Born} and the effective FF $|G|$. The number of observed events N^{obs} is derived in Section B.2, the luminosity \mathcal{L}_{int} is quoted from [27], the signal MC simulation efficiency ϵ_{MC} , the radiative correction factor $(1+\delta)$, the data/MC efficiency correction factor C_{dm} and the trigger efficiency correction factor C_{trg} are calculated as described in Section B.3. The systematical uncertainties are calculated according to Section B.5.

B7 Category B: Event classification

In this category both, EMC and TOF information are used to select the antineutron candidate, while only EMC information are used to select the neutron candidate. Following the selection criteria are described in detail, followed by a summary in Table B.12.

1. S_{B0} : Events with charged tracks are rejected. Events with $N_{\text{charged}} = 0$ are selected.
2. S_{B1} : The most energetic shower is identified as an antineutron candidate. To guarantee more than 90% trigger efficiency, the deposition energy of the antineutron candidate is required to be larger than 0.5 GeV. Fig. B.8 (left) shows the energy comparison between the collider data and the signal MC simulation.
3. S_{B2} : A time-of-flight signal matched to the leading shower in the EMC (antineutron candidate) must be valid in the event.
4. S_{B3} : To remove digamma background, the absolute value of the difference between the measured and expected time-of-flight for antineutron candidate ($\Delta T_{\bar{n}} = T_{\text{TOF1}} - T_0^\gamma - T_{\gamma 1}$) is required to be larger than 0.5 ns as shown in Fig. B.9 (left).
5. S_{B4} : The second most energetic shower, is identified as a neutron shower. The deposition energy of the neutron candidate is shown in Fig. B.8 (right). Since the neutron shower transfers only kinetic energy during the interaction with the EMC, the low momentum neutrons deposit only a small amount of energy in the EMC. As a consequence, the deposition energy of the neutron candidate is required to be within (0.04, 0.6) GeV for the data samples below $\sqrt{s} = 2.3094$ GeV, and within (0.06, 0.6) GeV above $\sqrt{s} = 2.3094$ GeV. The time information from the EMC for the neutron candidate is required to be within the window $|t_{\text{EMC}}^{\bar{n}} - t_{\text{EMC}}^n| < 10$ (in units of 50 ns) around the antineutron EMC time value.
6. S_{B5} : No TOF counters within $\Delta\phi = 25^\circ$ around the neutron candidate position in the EMC are allowed with a signal.
7. S_{B6} : The polar angle of the neutron and the antineutron candidates are required to be within $|\cos\theta| < 0.75$. A comparison of these distributions between the collider data and the signal MC simulation is shown in Fig. B.9 (right).
8. S_{B7} : To remove cosmic ray background, the last layer with hits in the MUC is required to be smaller than 6.

9. S_{B8} : After the selection criteria discussed above, the dominant background is beam related and from cosmic rays, which will be rejected by a multivariate analysis. To further separate the signal from the background studied with the separated beam samples, the boosted decision tree (BDT) technique is used. The boosting method is chosen to be AdaBoost. Following is the detailed description for the multivariate analysis:

- $S_{B8.1}$: To prevent that the signal MC simulation differs from real data, a data-driven approach is used and clean neutron and antineutron samples are selected with the processes $J/\psi \rightarrow \bar{p}n\pi^+$ and $J/\psi \rightarrow p\bar{n}\pi^-$ from collider data as the signal input for the BDT training. A detailed selection description is shown in Section 8.2.1. Due to the dependence of the detector impact on the antineutron and neutron momentum, the momentum ranges for the clean neutron and antineutron samples are chosen to be consistent with the ones in the analyzed signal process for $e^+e^- \rightarrow \bar{n}n$. Six different momentum ranges are defined for the neutron and antineutron control samples, as shown in Table B.10. Since the S/B (signal-to-background) ratio in the collider data after the preliminary selection is expected to be extremely small, the data sample can be treated as a quasi background sample, and following as the background input for BDT training.

Energy (GeV)	[2.1, 2.125]	[2.175, 2.2324]	2.3094	[2.3864, 2.396]	2.644(+2)	[2.90, 3.08]
$\beta = \frac{p}{\sqrt{p^2c^2 + M^2c^4}}$	[0.42, 0.50]	[0.5, 0.57]	[0.55, 0.60]	[0.60, 0.65]	[0.68, 0.72]	> 0.7

Table B.10: Category B: The momentum region selected from the control samples $J/\psi \rightarrow \bar{p}n\pi^+$ and $J/\psi \rightarrow p\bar{n}\pi^-$ in collider data at $\sqrt{s} = 3.0970$ GeV as the signal input for the BDT training for the corresponding energy samples for the analysis of $e^+e^- \rightarrow \bar{n}n$.

- $S_{B8.2}$: All input variables for the antineutron or neutron are track-level based. Originally, nineteen variables for the antineutron and neutron candidate are considered. In the following, variables with a strong dependence on the antineutron/neutron momentum are removed, listed as: the energy deposition of neutron in EMC. Beside that, if two variables are strongly correlated (correlation coefficient larger than 50%), the variable with the weaker separation power is removed, listed as: the energy seed of the antineutron, the energy shape $(E5 \times 5 - E3 \times 3)/E5 \times 5$ of the antineutron, the lateral moment of antineutron, the A20 moment of antineutron, the A42 moment of antineutron, the energy seed of the neutron, the energy shape of the neutron, the second

moment of the neutron, the lateral moment of the neutron, the A20 moment of the neutron, and the A42 moment of the neutron. Finally, seven variables are used for the BDT training. The importance of each variable is derived by counting how frequently the variables are used to split the decision tree nodes. The importance values are normalized and shown in Table B.11.

1	$N_{\text{hit}}^{40}(\bar{n})$	2.400e-01	number of hits within 40° cone around \bar{n} shower in EMC
2	$\Delta T_{\bar{n}}$	1.936e-01	$T_{\text{TOF1}} - T_{\bar{n}} - T_0$
3	$E_{\bar{n}}$	1.459e-01	deposited energy of \bar{n} in EMC
4	$N_{\text{HIT}}(n)$	1.257e-01	number of hits of n shower in EMC
5	$N_{\text{HIT}}(\bar{n})$	1.074e-01	number of hits of \bar{n} shower in EMC
6	$\Delta z(\bar{n})$	9.700e-02	distance difference of \bar{n} between tof and EMC in z direction
7	2. Moment (\bar{n})	9.030e-02	second moment of \bar{n} in EMC

Table B.11: Category B: The variables used for training and evaluation of the BDT classifier, ranked by their importance, at $\sqrt{s} = 2.3960$ GeV.

- $S_{B8.3}$: The output discriminator from the BDT training is shown in Fig. B.10. The discriminator value for the BDT is evaluated by the optimization of $S/\sqrt{S+B}$ with a signal to background ratio set to 1:8. The output maximum $S/\sqrt{S+B}$ value is 0.1054, while a cut value of 0.1 is chosen for further analysis.

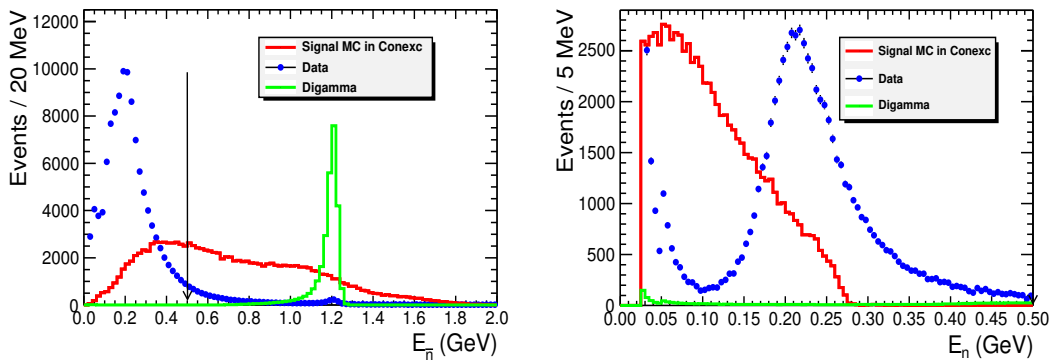


Fig. B.8: Category B: Deposited energies in the EMC at $\sqrt{s} = 2.3960$ GeV. (Left) the deposition energy $E_{\bar{n}}$ of the antineutron candidate in the EMC, (right) the deposition energy E_n of the neutron candidate in the EMC. Dots in blue represent collision data, red histograms represent the signal MC simulations with ConExc and the green lines are the MC simulation for the background process $e^+e^- \rightarrow \gamma\gamma$ with Babayaga 3.5.

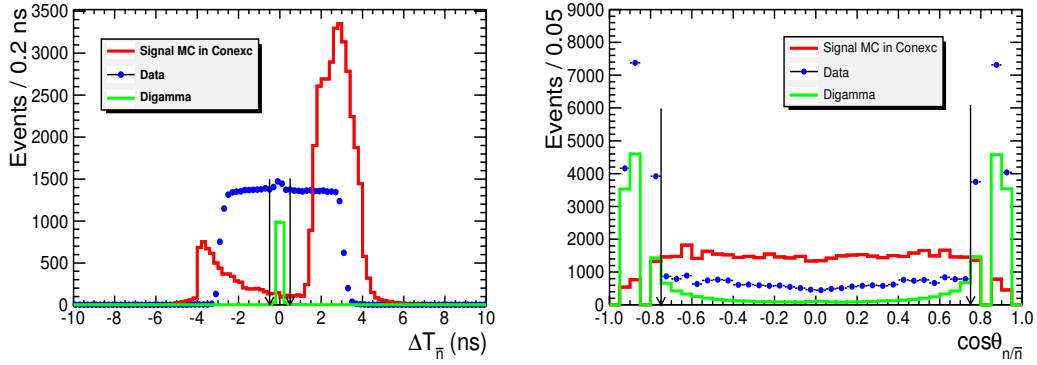


Fig. B.9: Category B at $\sqrt{s} = 2.3960$ GeV: (left) Time difference between measured and expected time-of-flight of antineutron candidate, (right) polar angle of n candidate. Dots in blue represent collision data, red histograms represent signal MC simulations by ConExc and the green lines are the MC for the background process $e^+e^- \rightarrow \gamma\gamma$ using Babayaga 3.5.

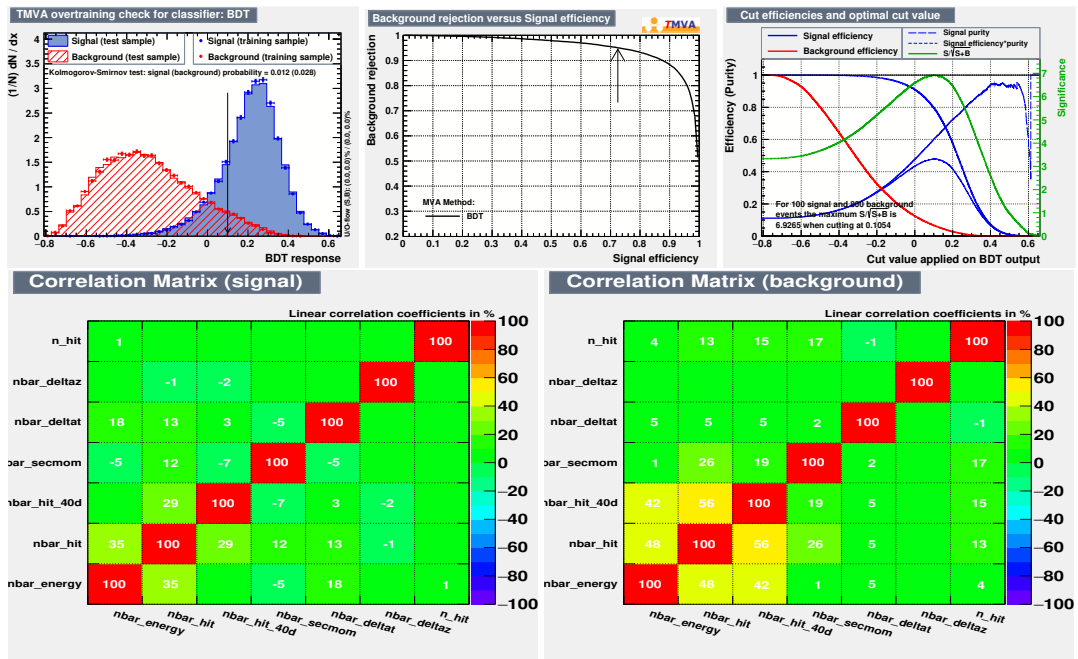


Fig. B.10: Category B at $\sqrt{s} = 2.3960$ GeV: (Top left) Output discriminator of BDT training. Blue dots are the likelihood output from signal MC training sample, the blue histogram is the likelihood output from the signal MC test sample, red dots are the likelihood output from background training sample and the red histogram is the likelihood output from the background test sample. (Top middle) The background rejection versus signal efficiency. (Top left) The figure-of-merit for BDT selection. (Bottom left) Correlation matrix for signal MC variables as listed in table B.11. (Bottom right) correlation matrix for background (collider data sample as described in $S_{B7.1}$) as listed in table B.11.

Expression	Unit	Object	Notation
$N_{\text{charged}} = 0$	-	\bar{n}, n	S_{B0}
$0.5 < E_{\bar{n}} < 2.0$	GeV	\bar{n}	S_{B1}
$T_{\bar{n}}$ valid	ns	\bar{n}	S_{B2}
$ \Delta T_{\bar{n}} > 0.5$	ns	\bar{n}	S_{B3}
$0.06 < E_n < 0.6$ ($0.04 < E_n < 0.6$)	GeV	n	S_{B4}
T_n not valid	ns	n	S_{B5}
$ \cos\theta < 0.75$	-	n, \bar{n}	S_{B6}
$l_{\text{muc}} < 6$	-	n, \bar{n}	S_{B7}
BDT discriminator > 0.1	-	n, \bar{n}	S_{B8}

Table B.12: Category B: Summary of the selection criteria. The selection criteria are listed in the same order as applied in the analysis. For the details on the matching of the time-of-flight signal to the showers in the EMC see C.

B8 Category B: Signal extraction

After the selection criteria $S_{B0} - S_{B7}$ are applied, all the physical background has been removed. The only survived background is beam related and from cosmic rays. Figure B.11 shows the distribution of the opening angle between \bar{n} and n for the remaining data events, as well as the survived background events from the separated beam data samples.

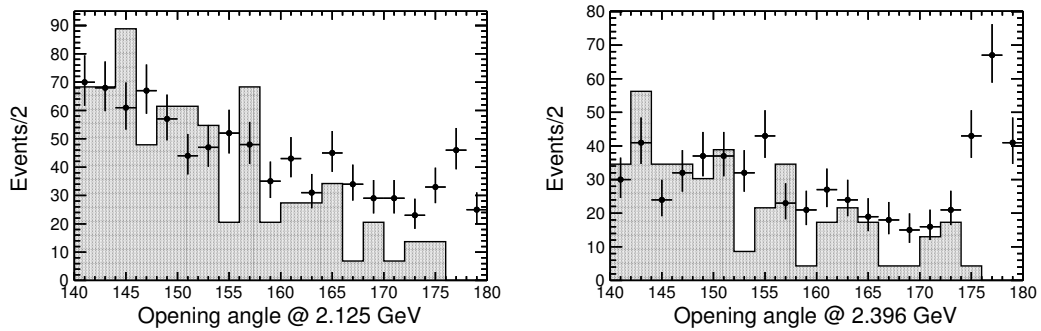


Fig. B.11: Category B: Opening angle between neutron and antineutron after selection at $\sqrt{s} = 2.1266$ and 2.3960 GeV. Black dots with error bars represent data, the grey histograms are the survived events from beam-associated background after scaling according to data-taking time. The data in the region between 170° and 180° not described by the background represents the signal region.

Figure B.12 shows the opening angle distribution between antineutron and neutron for the remaining signal MC simulation events. The flat tail represents events with misidentified neutron candidates. The signal shape is extracted from an optimized samples. A matching between the EMC showers of the selected neutron candidates and their true (generated) position is applied. This angle is restricted to 10° . The signal shape is modeled using the crystal ball function.

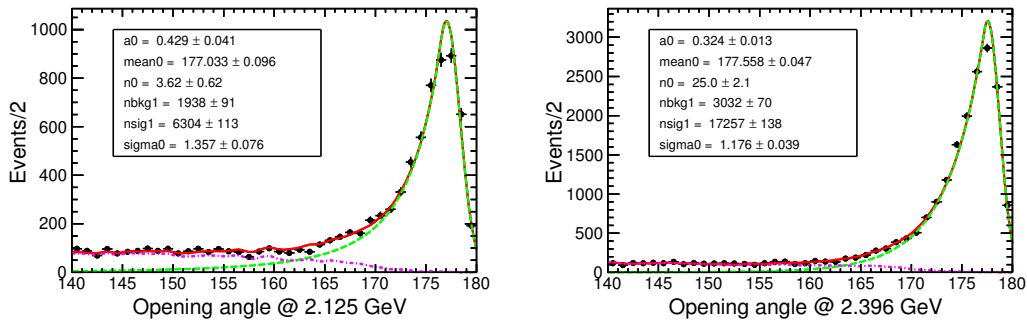


Fig. B.12: Category B: Opening angle between neutron and antineutron after selection at $\sqrt{s} = 2.1266$ GeV and 2.3960 GeV from signal MC with ConExc. Dots with error bars represent signal MC simulation, the green line is the signal shape modeled by the Crystal Ball function, the magenta dotted line represent signal MC with misidentified neutron events, the red line is the overall fit to obtain initial parameters for the Crystal Ball function for the combined signal and background shape fit to the collider data.

The initial parameters for the Crystal Ball function as obtained from the fit to the signal MC simulation are fixed to the signal shape in the collider data. A third-order polynomial is used to describe the background shape. An unbinned maximum likelihood fit is applied to the data samples at each energy with the above defined PDF to describe the data shape. The fit results are shown in Fig. B.13 and listed in Table B.13.

\sqrt{s} (GeV)	N_{sig}	\sqrt{s} (GeV)	N_{sig}	\sqrt{s} (GeV)	N_{sig}
2.0000	16.2 ± 4.5	2.0500	2.3 ± 2.1	2.1000	36.1 ± 6.6
2.1250	226.1 ± 16.6	2.1500	12.5 ± 3.8	2.1750	22.7 ± 5.2
2.2000	29.0 ± 5.8	2.2324	27.3 ± 5.9	2.3094	40.8 ± 6.8
2.3864	56.9 ± 8.0	2.3960	172.3 ± 13.7	2.6454	57.9 ± 8.2
2.9000	29.3 ± 5.8	2.9500	5.1 ± 2.6	2.9810	4.9 ± 2.5
3.0000	5.9 ± 2.6	3.0200	7.5 ± 2.8	3.0800	19.8 ± 4.9

Table B.13: Category B: Number of reconstructed signal events in collider data. The values are obtained from the fit procedure as described above. The errors are statistical.

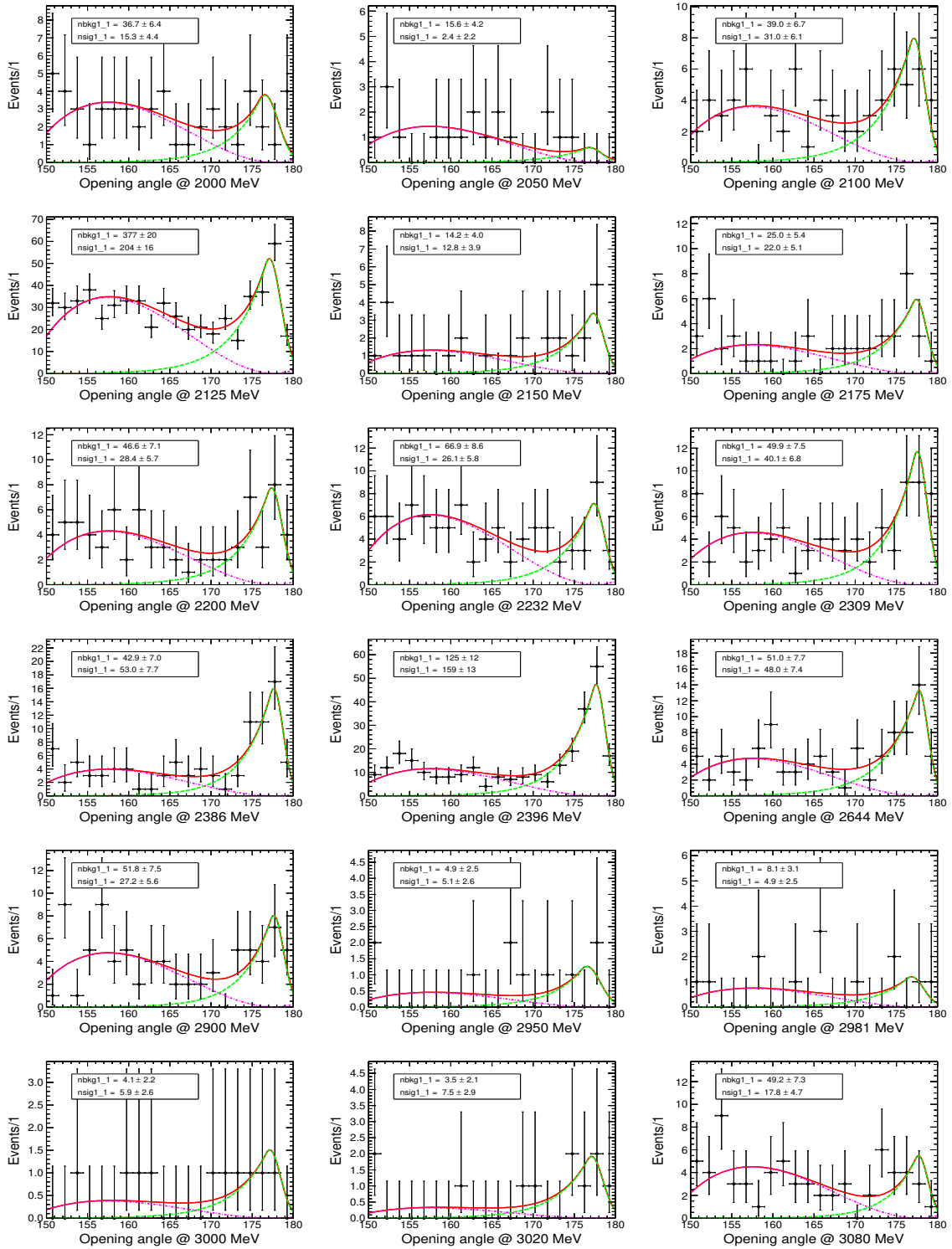


Fig. B.13: Category B: The plots show the opening angle between the neutron and the antineutron after selection at $\sqrt{s} = 2.0000 - 3.0800$ GeV. Black dots with error bars represent data, the red line is the overall fit, the green dashed line represents the signal shape modeled with the Crystal ball function with initial parameters as described in Figure B.12, the magenta dash-dotted line represents the background with the initial parameters obtained as described in Figure B.11.

B9 Category B: Reconstruction efficiency

According to the described method in Chapter B.7, there are three data to MC correction contributions for the selection strategy in category B. These cover the \bar{n} -based selection, the n -based selection and the BDT discriminator. The efficiency corrections for the \bar{n} and n selection can be obtained from the control samples $J/\psi \rightarrow \bar{p}n\pi^+$ and $J/\psi \rightarrow p\bar{n}\pi^-$ directly. The efficiency correction for the BDT cut is obtained after and before applying the BDT cut. The efficiency correction for the difference between the collider data and the corresponding MC simulation, obtained with the control samples, are shown in Figure B.14 as an example at $\sqrt{s} = 2.3864$ and 2.3960 GeV.

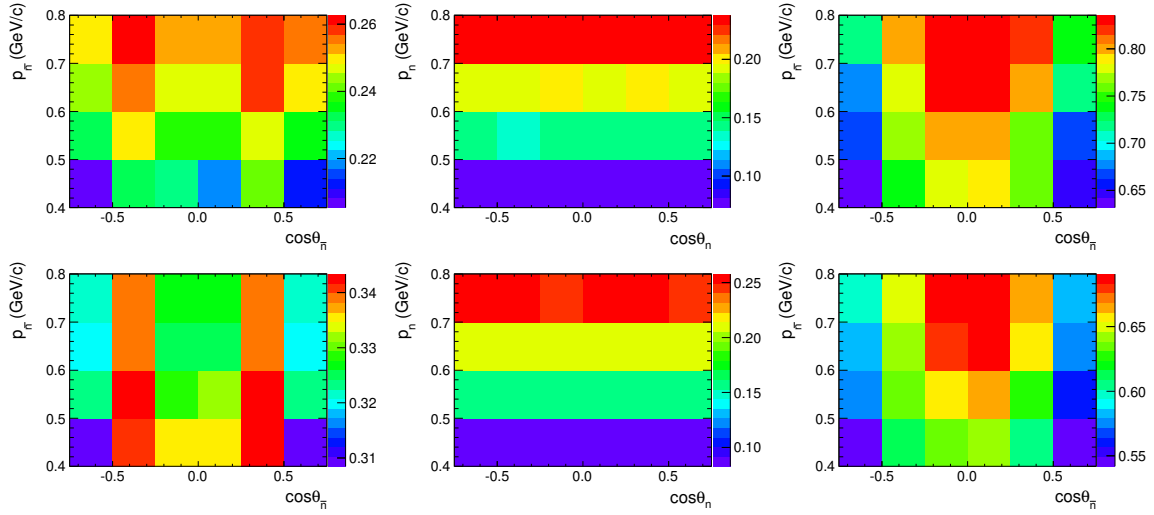


Fig. B.14: Category B: 2D Efficiency of (left) the \bar{n} selection, (middle) the n selection, and (right) the BDT cut for data and MC, the upper plots are show the efficiency curves from collider data. The bottom plots show the corresponding curves obtained from the signal MC, as an example at 2.3960 GeV.

The correction factor \mathcal{E}_{dm} for the differences between the collider data and the MC correction, obtained with a 2D efficiency weighting, is determined according to Equation 8.2.3. In Figure B.15 (left) the frequency for signal MC events after the final selection is shown. The data to MC efficiency ratio in each bin is shown in Figure B.15 (right). The efficiency correction for the differences between the collider data and the MC simulation at 2.3960 GeV is calculated to:

$$\mathcal{E}_{\text{dm}}^{\text{abs}}(2.3960 \text{ GeV}) = 0.885 \pm 0.026 \quad (\text{B.9})$$

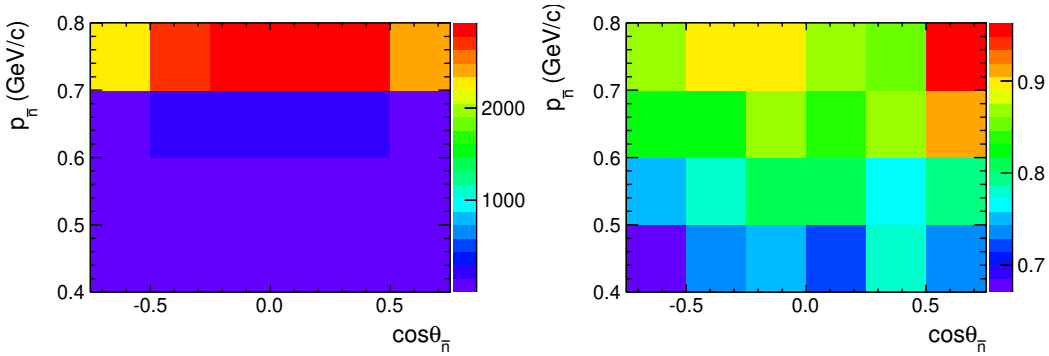


Fig. B.15: Category B: (left) The frequency distribution from signal MC simulation with ConExc in BesEvtGen-00-03-18 before normalization at $\sqrt{s} = 2.3960$ GeV, (right) the ratio of the efficiencies from collider data over the corresponding efficiencies from the MC simulation (for the control samples) at $\sqrt{s} = 2.3960$ GeV.

In this analysis, the trigger efficiency correction \mathcal{C}_{trg} is applied as shown in Section 8.5.1. The distribution of the total deposition energy in the event coming from the signal process is shown in Figure B.16 at $\sqrt{s} = 2.1266$ GeV and 2.3960 GeV, obtained from the signal MC simulation. Since the simulation of the hadronic interaction in the EMC from the neutron and antineutron is imperfect, differences exist in the deposition energy between the collider data and the signal MC simulation. Hence, the deposition energy in 40 degree cones around the neutron and the antineutron shower in the EMC is replaced by the corresponding values from the control samples $J/\psi \rightarrow \bar{p}n\pi^+$ and $J/\psi \rightarrow p\bar{n}\pi^-$. The distributions for the updated total energy deposition of a signal event is shown in Figure B.16.

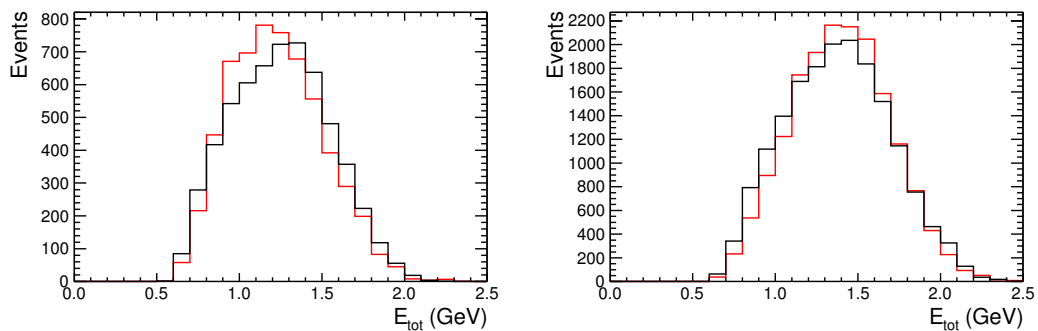


Fig. B.16: Category B: Total deposition energy of the signal process at (left) $\sqrt{s} = 2.1266$ GeV and (right) $\sqrt{s} = 2.3960$ GeV. Black histograms show the distribution from the signal MC simulation (ConExc in BesEvtGen-00-03-18), the red histograms are the updated distributions for the deposited energy of the neutron and the antineutron, with the deposited energy in a 40 degree cones around the EMC shower for the neutron (antineutron) replaced by the corresponding values from the control samples.

The updated total deposition energy is used for the calculation of the correction factor \mathcal{C}_{trg} for the trigger efficiency in Equation 8.13. The correction factor at $\sqrt{s} = 2.3960$ GeV is calculated to be:

$$\mathcal{C}_{\text{trg}}^{\text{abs}}(2.3960 \text{ GeV}) = 0.955 \pm 0.008 \quad (\text{B.10})$$

As discussed in Section 8.5.1, an alternative parametrization for the trigger efficiency curve has been extracted from an inclusive hadron selection for the process $e^+e^- \rightarrow \bar{q}q \rightarrow$ hadrons. The difference between the nominal results and the results for the trigger efficiency obtained with the alternative efficiency parametrization are used as the systematic uncertainty from the trigger efficiency. The summary of the signal reconstruction efficiency and the discussed correction factors at each center-of-mass energy is shown in Table B.14.

\sqrt{s} (GeV)	$\epsilon_{\text{MC}}(\%)$	$\mathcal{C}_{\text{trg}}(\%)$	$\mathcal{C}_{\text{dm}}(\%)$
2.0000	0.43	86.7 ± 2.5	76.8 ± 2.5
2.0500	0.86	87.2 ± 1.5	69.6 ± 1.5
2.1000	1.43	88.7 ± 1.5	76.6 ± 1.3
2.1250	1.69	89.4 ± 1.3	77.8 ± 1.3
2.1500	1.91	90.3 ± 1.3	78.0 ± 1.3
2.1750	2.04	88.6 ± 1.0	81.7 ± 1.2
2.2000	2.38	90.4 ± 1.0	81.6 ± 1.1
2.2324	2.56	90.5 ± 1.0	83.1 ± 1.1
2.3094	2.56	94.0 ± 0.9	85.9 ± 1.1
2.3864	3.20	94.8 ± 0.8	88.7 ± 1.0
2.3960	3.12	94.3 ± 0.8	88.7 ± 1.0
2.6454	3.02	96.3 ± 0.7	84.0 ± 0.7
2.9000	2.40	97.2 ± 0.7	80.7 ± 0.5
2.9500	2.34	97.7 ± 0.7	80.7 ± 0.8
2.9810	2.22	97.3 ± 0.7	80.7 ± 0.8
3.0000	2.24	97.5 ± 0.7	80.7 ± 0.8
3.0200	2.14	97.4 ± 0.7	80.7 ± 0.8
3.0800	2.08	97.8 ± 0.7	80.0 ± 1.3

Table B.14: Category B: Signal MC event selection efficiency and its corrections, based on 500000 MC simulation events with the event generator ConExc in BesEvtGen-00-03-18 for the three categories at all analyzed energies.

B10 Category B: Angular analysis

The angular distributions at each energy point are analyzed with the same strategy as described in Sec. B.8. By dividing the $\cos\theta$ distribution of \bar{n} into 7 bins from -0.7 to 0.7 with a step size of 0.2, the opening angle between the \bar{n} and n in collider data is fitted to obtain the number of the signal events in each bin, as shown in Figure B.17 at $\sqrt{s} = 2.1266$ GeV. Table B.15 shows the differential signal yield at each c.m. energy. Figure B.18 shows the signal reconstruction efficiency from the signal MC simulation and two efficiency corrections at $\sqrt{s} = 2.1266$, $\sqrt{s} = 2.3864$, and $\sqrt{s} = 2.3960$ GeV, including the ISR correction and the corrections due to data/MC differences. Figure B.19 shows the fit to the $\cos\theta_{\bar{n}}$ distributions after all corrections for the five (combined) data samples with and without considering the individual position resolution.

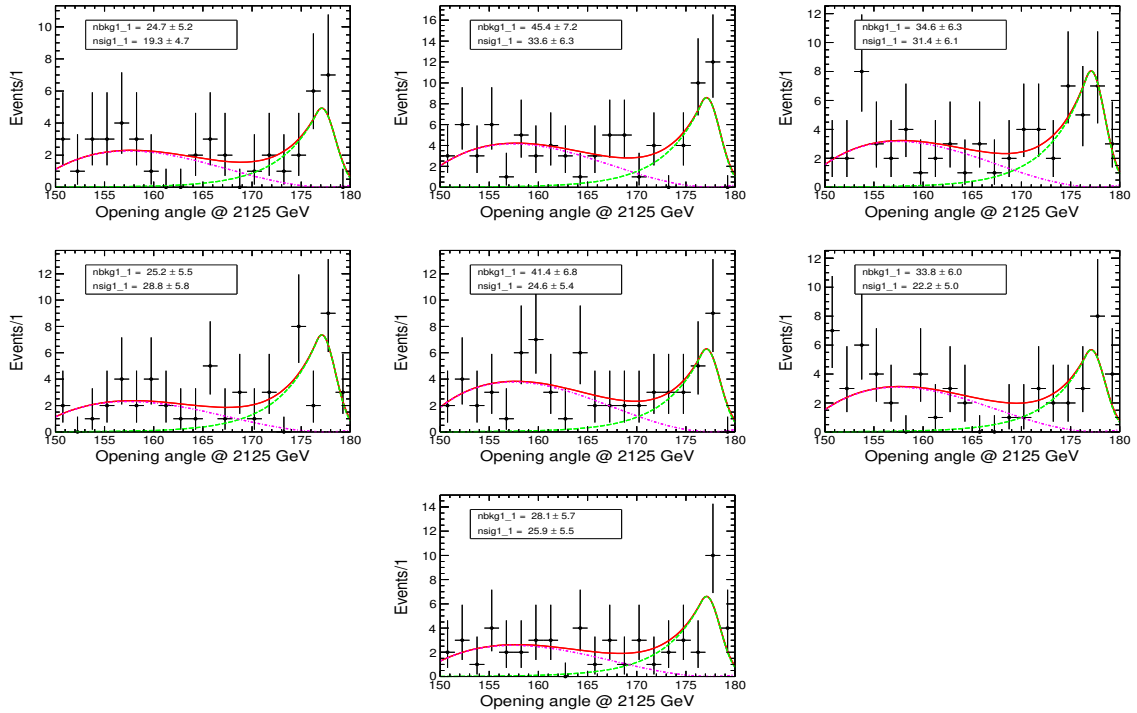


Fig. B.17: Category B: results of fits of the opening angle between \bar{n} and n for each $\cos\theta$ bin of \bar{n} at $\sqrt{s} = 2.1266$ GeV. Black dots with errors represent data, the green line the signal shape component, the magenta dashed line the background component and the red line shows the simultaneous fit. Details for the functions of each component and the total fit, as well as the fit method are described in Section B.8.

\sqrt{s}	$N_{\text{fit}}^{(\text{B1})}$	$N_{\text{fit}}^{(\text{B2})}$	$N_{\text{fit}}^{(\text{B3})}$	$N_{\text{fit}}^{(\text{B4})}$	$N_{\text{fit}}^{(\text{B5})}$	$N_{\text{fit}}^{(\text{B6})}$	$N_{\text{fit}}^{(\text{B7})}$
2.0000	1.3 ± 1.4	3.3 ± 2.0	2.0 ± 1.5	1.5 ± 1.4	2.0 ± 1.4	0.0 ± 0.5	2.5 ± 1.9
2.050	0.0 ± 0.5	1.7 ± 1.5	0.0 ± 0.5	0.0 ± 0.5	0.0 ± 0.5	0.0 ± 0.5	0.0 ± 0.5
2.100	4.7 ± 2.3	2.4 ± 1.7	6.0 ± 2.4	3.2 ± 2.0	6.5 ± 2.7	4.9 ± 2.5	3.1 ± 1.9
2.125	19.3 ± 4.7	33.6 ± 6.3	31.4 ± 6.1	28.8 ± 5.8	24.6 ± 5.4	22.2 ± 5.0	25.9 ± 5.5
2.150	1.3 ± 1.2	2.9 ± 1.7	3.0 ± 1.7	0.0 ± 0.5	1.3 ± 1.3	0.9 ± 1.1	2.6 ± 1.8
2.175	3.5 ± 2.0	2.9 ± 1.8	4.1 ± 2.1	3.2 ± 2.0	2.0 ± 1.4	2.0 ± 1.4	2.3 ± 1.6
2.200	3.0 ± 1.7	1.8 ± 1.5	2.1 ± 1.9	1.3 ± 1.4	3.3 ± 1.9	1.6 ± 1.4	7.4 ± 2.8
2.232	0.0 ± 0.5	0.2 ± 1.4	3.6 ± 2.0	6.6 ± 2.8	4.1 ± 2.2	4.3 ± 2.5	4.7 ± 2.3
2.309	2.9 ± 1.8	4.7 ± 2.4	5.1 ± 2.5	7.9 ± 3.0	9.6 ± 3.3	3.8 ± 2.0	5.2 ± 2.4
2.386	3.7 ± 2.1	10.6 ± 3.5	10.3 ± 3.6	6.1 ± 2.7	6.5 ± 2.7	13.3 ± 3.7	6.5 ± 2.8
2.396	23.7 ± 5.1	23.7 ± 5.2	22.7 ± 5.0	25.8 ± 5.3	21.7 ± 4.8	26.7 ± 5.4	26.6 ± 5.4
2.644	9.5 ± 3.3	5.9 ± 2.6	8.6 ± 3.2	9.3 ± 3.3	5.8 ± 2.6	9.0 ± 3.2	7.9 ± 3.1
2.900	6.5 ± 2.6	3.8 ± 2.2	2.9 ± 1.9	7.3 ± 2.8	3.0 ± 1.7	3.3 ± 2.1	2.0 ± 1.5
2.950	0.0 ± 0.5	1.0 ± 1.0	0.0 ± 0.5	0.0 ± 0.5	0.0 ± 2.2	1.0 ± 1.0	4.1 ± 2.5
2.988	4.8 ± 2.3	3.0 ± 1.8	1.2 ± 1.3	1.2 ± 1.3	1.3 ± 1.4	2.7 ± 1.7	6.4 ± 3.0
3.080	1.7 ± 1.5	3.3 ± 2.0	2.9 ± 1.8	2.9 ± 1.8	2.8 ± 1.9	3.0 ± 1.9	3.2 ± 2.0

Table B.15: Category B: Summary of the extracted differential signal yield $N_{\text{fit}}^{\cos\theta(\text{Bi})}$ from collider data at different \sqrt{s} , using the composite fit method, described in the previous section. Bi represents the i-th bin.

Table B.15 shows the differential signal yield for the angular analysis, extracted as described in Section B.8.

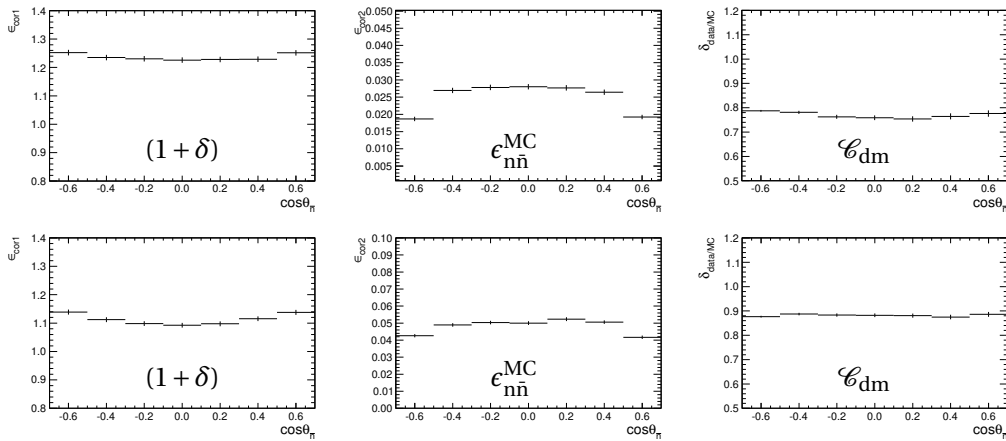


Fig. B.18: Category B: Angular corrections at $\sqrt{s} = 2.1266$ GeV (top) and the combined sample at $2.3864 + 2.3960$ GeV (bottom). (Left) Correction $(1 + \delta)$ for radiative events. (Middle) Reconstruction efficiency $\epsilon_{n,\bar{n}}^{\text{MC}}$ from signal MC simulation with ConExc. (right) Efficiency correction \mathcal{C}_{dm} from the control samples $J/\psi \rightarrow p\bar{n}\pi^- (\bar{p}n\pi^+)$.

The results for the magnetic form factor and the FF ratio from the category B signal event classification are shown in table B.16 for the case of the simple fit with Equation 9.6, as well as for the individual position resolution taken into account.

\sqrt{s} (GeV)	Simple Fit		
	$G_M (\times 10^{-2})$	$R_{em}^n = G_E^n/G_M^n $	$\chi^2/\text{d.o.f.}$
2.0000 - 2.1000	12.2 ± 10.3	1.344 ± 2.202	4.6 / 5
2.1266	10.1 ± 2.2	0.845 ± 0.626	3.5 / 5
2.1500 - 2.3094	6.9 ± 2.8	1.442 ± 1.146	6.4 / 5
2.3864 - 2.3960	8.6 ± 1.5	0.879 ± 0.581	2.0 / 5
2.6454 - 2.9500	3.3 ± 0.9	0.765 ± 1.259	3.7 / 5
\sqrt{s} (GeV)	Fit with Individual Resolution		
	$G_M (\times 10^2)$	$R_{em}^n = G_E^n/G_M^n $	$\chi^2/\text{d.o.f.}$
2.0000 - 2.1000	11.8 ± 10.3	1.427 ± 2.282	4.9 / 5
2.1266	10.1 ± 2.2	0.851 ± 0.626	3.5 / 5
2.1500 - 2.3094	7.6 ± 3.0	1.423 ± 1.112	6.4 / 5
2.3864 - 2.3960	8.7 ± 1.5	0.831 ± 0.581	3.0 / 5
2.6454 - 2.9500	3.3 ± 0.9	0.817 ± 1.224	3.7 / 5

Table B.16: Category B: Results for the magnetic form factor G_M and the form factor ratio $R_{em} = |G_E/G_M|$ at $\sqrt{s} = 2.1266$ and the four combined data samples with and without taking the individual position resolution into account. The errors are statistical.

A toy MC study for the FFs extraction has been performed to verify the results. Fit results at the c.m energies $\sqrt{s} = 2.0000 - 2.1000$ and $\sqrt{s} = 2.3864 - 2.3960$ including the resolution are not stable due to the low statistics of the angular distributions and show unphysical values for the FF ratio. The final results for the disentangled FFs are provided from an simultaneous analysis of the three categories under increased statistics. The results from the individual category B are shown for comparison. The final results from the simultaneous fit, using the corrected angular distributions from the antineutron obtained by the three classification categories, are shown in Table 9.5.

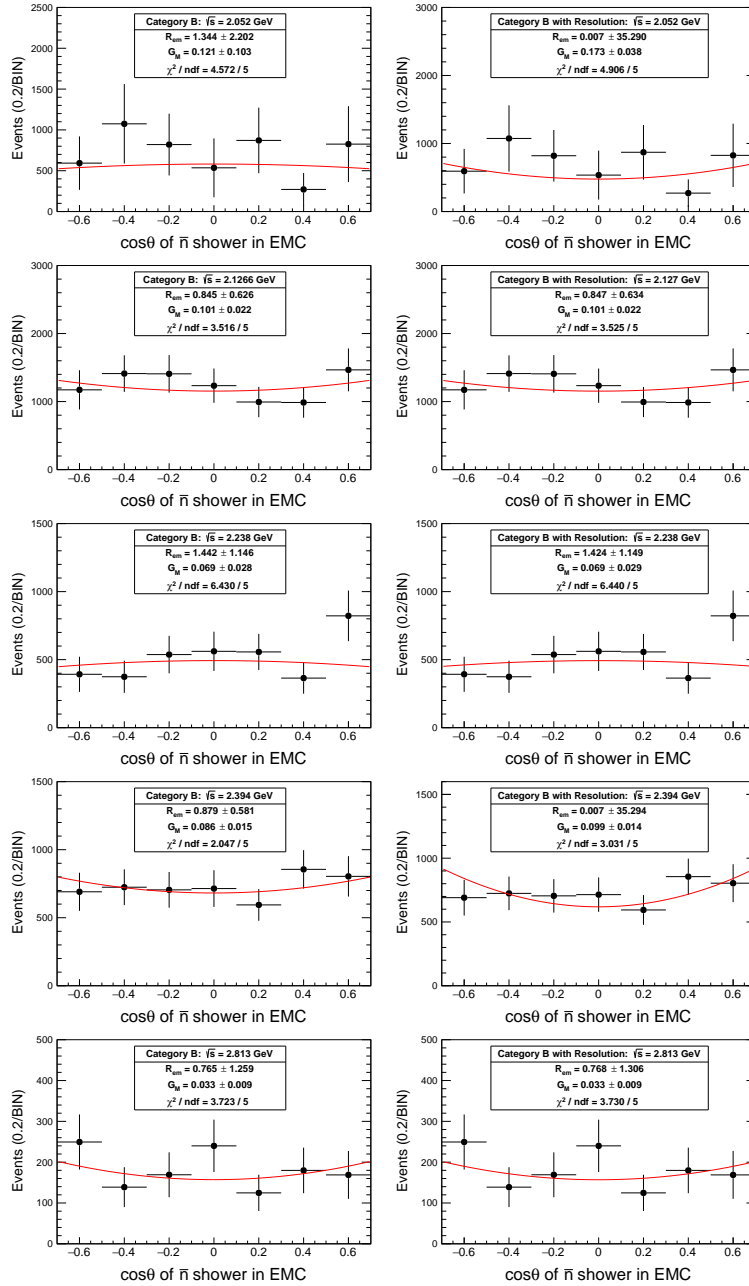


Fig. B.19: Results from the angular distribution fit of the efficiency corrected angular distributions for category B signal events at the five data sets at $\sqrt{s} = 2.0516$ GeV (top column), at 2.1266 GeV (2nd column), at 2.2383 GeV (3rd column), 2.3936 (4rd column), and 2.8130 GeV (column row). The left and right row show results with the fit from equation 9.6 and additionally including the category individual resolution, respectively. Dots represent corrected data yields, the red lines show the fit results.

B11 Category B: Systematic uncertainty

The systematic uncertainty sources in category B are coming from the uncertainty from the luminosity measurement (U_L^B), from the event selection of \bar{n} and n ($U_{n\bar{n}}^B$), from the event level selection (U_{evt}^B), from the method of Boosted Decision Tree (U_{BDT}^B), from the signal yield extraction via fit (U_{fit}^B), from the initial form factor model implemented in the signal MC simulation (U_{model}^B), from the trigger efficiency correction (U_{trg}^B), and from the iterative optimization of the signal MC simulation ($U_{\text{lineshape}}^B$).

1. Luminosity(U_L^B): The integrated luminosity is measured by analyzing large-angle Bhabha scattering process with an uncertainty of 1.0%.
2. Selection of \bar{n} and n ($U_{n\bar{n}}^B$): In the analysis, the difference of the selection between data and MC has been corrected using the control samples $J/\psi \rightarrow p\bar{n}\pi^-$. One standard error from of the correction factor is taken as the systematic uncertainty from the signal particles selection. The uncertainty is mainly due to the statistical uncertainty of the control samples.
3. Event level selection (U_{evt}^B): Apart from the selection on \bar{n} and n , there are several selection criteria on the event level (selection criteria with correlations coming from both signal particles). These are the selection criteria E_{extra} and l_{muc} . To study these uncertainty sources, we vary the selection criteria on l_{muc} and E_{extra} , to be less than 7 layers and less than 0.3 GeV (compared to 6 layers and less than 0.15 GeV as the nominal selection criteria). The difference of the calculated cross sections to the nominal values are then taken as the systematic uncertainties.
4. Uncertainty of BDT (U_{BDT}^B): Though the efficiency difference between the collider data and the signal MC simulation for the application of the Boosted Decision Tree is corrected, it is worth to study the stability of the results. In the following, several studies are discussed: First, a cut-based method is applied instead of the BDT selection criteria. Two cuts with a strong suppression power for the remaining background are introduced to replace the BDT method. The first one is the number of hits in a 40 degree cone around the \bar{n} candidate in the EMC. The second one is the amount of deposited energy outside of 40 degree cones around the \bar{n} and n candidates in the EMC. The determination of the Born cross section is performed as in the nominal approach (including all re-calculated efficiency correction). The obtained Born cross section is 95.0 ± 9.3 pb. The detailed description of the cut-based selection is shown in B.13. As a second approach, a alternative BDT-based method

with different input variables is tested to compare with the nominal results. The output results are shown in Table B.17. In the nominal results, the BDT discriminator has the optimal cut value of 0.1. For the alternative results, two cut values are applied at 0.12 and 0.08, and the largest deviation to the nominal results is taken as the systematic uncertainty coming from the BDT method. In a third attempt, instead of a BDT approach, a MLP-based method (multilayer perceptron - an artificial neural network) is used. The output results are shown in Table B.17.

Method	N^{obs}	ϵ_{mc} (%)	ϵ_{cor}
(1)	144 ± 14	2.5	0,929
(2)	232 ± 18	3.94	0.935
(3)	194 ± 16	3.35	0.943
(4)	185 ± 15	2.97	1.05

Table B.17: Category B: Study of systematic uncertainties from the BDT method at $\sqrt{s} = 2.3960$ GeV. Approach (1) use a cut-based method, approaches (2) and (3) use a different input parameter for the BDT method, and a different BDT cut value, respectively. Approach (4) uses a MLP method instead of the nominal BDT method.

5. Signal yields extraction ($U_{\text{fit}}^{\text{B}}$): The uncertainty from the fit for the signal yield extraction is estimated under three aspects: The signal shape, the background shape and the fitting range. For the uncertainty from the signal shape, the model is changed to a Crystal Ball function without considering the resolution difference between data and MC. For the uncertainty from the background shape, a forth-order polynomial is used instead of a third-order one. For the uncertainty from the fitting range, an alternative range is used and the differences in the calculated Born cross section are taken as the systematic uncertainty. The uncertainties from these three sources are assumed as uncorrelated and added in quadrature. Fig. B.20 shows the angle distribution for these three methods as an example for the data samples at $\sqrt{s} = 2.1266$ GeV and 2.3960 GeV.
6. Angular distribution (U_{model}): The uncertainty from the form factor model is studied by using modified signal MC simulation samples. The uncertainty is estimated by varying the initial $|G_E/G_M|$ ratios in the signal MC simulation within 1 standard deviation around the measured results with this analysis.
7. Uncertainty from trigger efficiency (U_{tr}^{B}): The uncertainty of the correction factor from trigger efficiency is considered by using the parameterization for the trigger efficiency obtained with the inclusive hadronic control samples as discussed in Sec. B.9. The uncertainty varies between 1.0% to 7.0% for different c.m.energies.

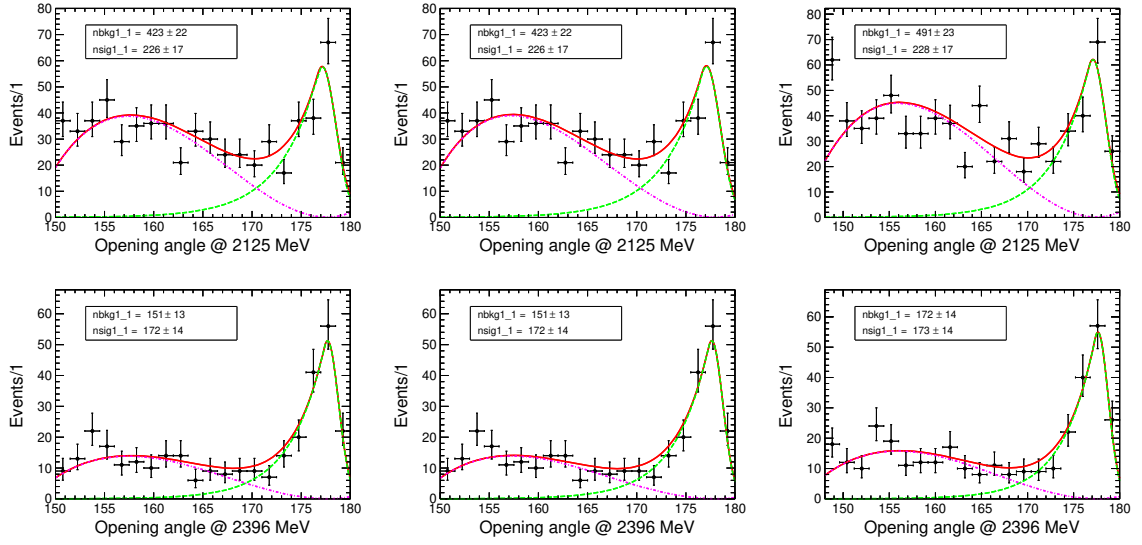


Fig. B.20: Category B: Variation of the fit to the opening angle between the neutron and antineutron for the study of the systematic uncertainty. (Left) Varying the signal shape, (middle) varying the background shape, and (right) varying the fit range. The upper plots are for the data set at $\sqrt{s} = 2.1266$ GeV, the bottom plots are at $\sqrt{s} = 2.3960$ GeV.

8. Uncertainty from the ISR correction ($U_{\text{ISR}}^{\text{B}}$): The difference between the product for the reconstruction efficiency and the ISR correction $\varepsilon \times \delta_{\text{ISR}}$ for the last two MC optimization iterations is used as the systematic uncertainty. It is in average less than 1.0% for analyzed data sample.

The uncertainties are summarized in Table B.18.

The systematic uncertainty sources on the FF ratio $|G_{\text{E}}/G_{\text{M}}|$ and on the magnetic FF $|G_{\text{M}}|$ are discussed. The systematic uncertainty for the ratio $|G_{\text{E}}/G_{\text{M}}|$ comes from the sources which affect the shape of the angular distribution. These are the uncertainties of the event selection, the fit method for the signal yield extraction, and the ISR correction factor.

- The uncertainty for the event selection $\delta_{\text{d}_{\text{sel}}}$ comes from the uncertainty of data to MC efficiency correction, by varying the individual bin content in the antineutron angular distribution within 1σ of the correction factor uncertainty, the difference on the $|G_{\text{E}}/G_{\text{M}}|$ ratio results after the angular analysis is taken as the uncertainty.
- The uncertainty from the fitting method of signal comes from three aspects, which are the fitting range, the signal shape model and the background shape model. The combined data samples show a large uncertainty which is mainly caused by

\sqrt{s} (GeV)	$U_{n\bar{n}}^B$	U_{evt}^B	U_{BDT}^B	U_{fit}^B	U_{model}^B	U_{trg}^B	$U_{\text{lineshape}}^B$	U_L^B	U_{tot}^B
2	3.26	4.42	6.0	3.1	5.2	5.1	3.1	1.0	11.8
2.05	2.11	4.42	6.0	6.4	9.2	5.0	0.1	1.0	14.5
2.1	1.64	4.42	6.0	0.4	9.6	4.6	0.1	1.0	13.1
2.125	1.61	4.42	6.0	1.0	9.6	4.5	0.5	1.0	12.1
2.15	1.57	5.94	3.8	1.6	9.6	4.3	0.8	1.0	12.9
2.175	1.49	5.94	3.8	1.1	6.5	4.6	0.3	1.0	10.8
2.2	1.39	5.94	3.8	0.8	10.3	4.2	1.6	1.0	13.4
2.232	1.37	5.94	3.8	2.4	9.7	4.2	0.9	1.0	13.1
2.309	1.24	5.94	3.8	1.4	8.5	3.2	1.1	1.0	11.7
2.386	1.10	2.68	3.6	1.6	10.4	2.8	2.9	1.0	12.2
2.396	1.11	2.68	3.6	0.6	7.1	3.1	0.8	1.0	9.1
2.644	0.83	9.44	3.9	1.7	7.3	2.1	0.2	1.0	12.9
2.9	0.61	9.44	4.8	1.5	7.3	1.7	5.0	1.0	14.0
2.95	0.99	9.44	4.8	4.3	7.3	1.4	1.3	1.0	13.8
2.981	0.99	9.44	4.8	5.2	7.8	1.6	1.4	1.0	14.4
3	0.99	9.44	4.8	2.6	10.0	1.5	1.3	1.0	15.0
3.02	0.99	9.44	4.8	2.5	9.6	1.6	1.3	1.0	14.7
3.08	1.63	9.44	7.2	1.3	10.5	1.4	0.11	1.0	16.1

Table B.18: Category B: Summary of all systematic uncertainty sources for the Born cross section measurement, in percent. The last column is the summary of the total uncertainties.

fluctuations of the collider data. However, under the current statistical situation is tolerable to use it, since the results are dominated by the statistical uncertainty.

- The uncertainty from the radiative events is studied similar as for the Born cross section measurement above. By using the values for the reconstruction efficiency and $(1 + \delta)$ from the second-to-last MC optimization iteration, the difference on the results for $|G_E/G_M|$ is taken as the uncertainty.

For the systematic uncertainty on $|G_M|$, apart from the sources discussed above for the ratio $|G_E/G_M|$, the sources which affect the absolute normalization of the angular shape must be taken into account. These are the systematic uncertainty from the luminosity measurement and the trigger efficiency correction. The uncertainty from the luminosity measurement is 1%, its effect on the final results for $|G_M|$ is less than 1%. The uncertainty from the trigger efficiency correction is studied by varying its value within the corresponding 1σ deviation. The difference to the nominal results for the magnetic FF $|G_M|$ is taken as the systematic uncertainty. Table B.19 summarizes all the uncertainty source for the angular analysis results from Category B.

\sqrt{s} (GeV)	δ_{dsel} (%)	$\delta_{\text{dfit}}^{\text{range}}$ (%)	$\delta_{\text{dfit}}^{\text{signal}}$ (%)	$\delta_{\text{dfit}}^{\text{bkg}}$ (%)	δ_{drad} (%)	δ_{lum} (%)	δ_{trig} (%)	δ_{sys} (%)
2.0516	1.7 (1.0)	42.4 (27.1)	36.1 (22.9)	52.5 (33.9)	6.1 (2.5)	0.8	2.5	76.8 (49.2)
2.125	1.2 (1.0)	19.1 (1.0)	18.8 (15.7)	17.3 (15.8)	4.4 (15.8)	1.0	1.0	32.2 (27.5)
2.2380	1.5 (1.0)	48.9 (32.9)	49.3 (32.9)	52.3 (33.5)	1.3 (1.0)	1.0	2.6	86.9 (58.6)
2.3936	0.7 (1.0)	0.1 (1.0)	0.2 (1.0)	1.5 (1.0)	8.1 (1.4)	1.0	1.2	8.3 (2.6)
2.8130	0.3 (1.0)	1.5 (1.0)	0.3 (1.0)	6.1 (3.0)	1.7 (3.0)	1.0	1.0	6.5 (4.3)

Table B.19: Category B : Summary of the systematic uncertainties on the form factor ratio $R_{\text{em}} = |G_E/G_M|$ and the magnetic form factor $|G_M|$ (in brackets) at different \sqrt{s} .

B12 Category B: Summary of the results

Table B.20 summarizes the derived Born cross sections σ_{Born} and the effective FFs $|G|$ from the signal classification approach category B.

\sqrt{s} (GeV)	N^{obs}	\mathcal{L}_{int} (pb $^{-1}$)	$(1 + \delta)$	ϵ_{mc} (%)	\mathcal{C}_{dm} (%)	\mathcal{C}_{trg} (%)	σ_{Born} (pb)	$ G $ ($\times 10^2$)
2.0000	16.2 \pm 4.54	10.074	0.98	0.432	76.8 \pm 2.51	86.7 \pm 2.5	570.4 \pm 159.8 \pm 67.3	23.1 \pm 3.2 \pm 1.4
2.0500	2.27 \pm 2.12	3.343	1.08	0.86	69.6 \pm 1.47	87.2 \pm 1.5	120.4 \pm 112.5 \pm 17.5	10.1 \pm 4.7 \pm 0.7
2.1000	36.1 \pm 6.56	12.167	1.18	1.432	76.6 \pm 1.26	88.7 \pm 1.5	258.4 \pm 46.9 \pm 33.9	14.5 \pm 1.3 \pm 1.0
2.1250	226.1 \pm 16.6	108.49	1.24	1.69	77.8 \pm 1.26	89.4 \pm 1.3	142.9 \pm 10.4 \pm 18.7	10.7 \pm 0.4 \pm 0.7
2.1500	12.5 \pm 3.82	2.841	1.28	1.906	78.0 \pm 1.227	90.3 \pm 1.3	256.0 \pm 78.2 \pm 33.0	14.2 \pm 2.2 \pm 0.9
2.1750	22.7 \pm 5.15	10.625	1.31	2.04	81.7 \pm 1.22	88.6 \pm 1.0	110.4 \pm 25.0 \pm 11.9	9.3 \pm 1.1 \pm 0.5
2.2000	29 \pm 5.81	13.699	1.31	2.38	81.6 \pm 1.14	90.4 \pm 1.0	92.0 \pm 18.4 \pm 12.3	8.5 \pm 0.9 \pm 0.6
2.2320	27.3 \pm 5.91	11.856	1.28	2.56	83.1 \pm 1.14	90.5 \pm 1.0	93.4 \pm 20.2 \pm 12.2	8.6 \pm 0.9 \pm 0.6
2.3090	40.8 \pm 6.84	21.089	1.15	2.56	85.9 \pm 1.07	94.0 \pm 0.9	81.3 \pm 13.6 \pm 9.5	8.0 \pm 0.7 \pm 0.5
2.3860	56.9 \pm 7.98	22.549	1.11	3.20	88.7 \pm 0.98	94.8 \pm 0.8	84.4 \pm 11.8 \pm 10.3	8.3 \pm 0.6 \pm 0.5
2.3960	172.3 \pm 13.7	66.869	1.11	3.12	88.7 \pm 0.99	94.3 \pm 0.7	88.9 \pm 7.0 \pm 8.1	8.5 \pm 0.3 \pm 0.4
2.6440	57.9 \pm 8.17	67.714	1.55	3.02	84.0 \pm 0.7	96.3 \pm 0.7	22.5 \pm 3.1 \pm 2.9	4.5 \pm 0.3 \pm 0.3
2.9000	29.3 \pm 5.78	105.253	2.17	2.40	80.7 \pm 0.5	97.2 \pm 0.7	6.8 \pm 1.3 \pm 0.9	2.7 \pm 0.3 \pm 0.2
2.9500	5.1 \pm 2.58	15.94	2.29	2.34	80.7 \pm 0.8	97.7 \pm 0.7	7.5 \pm 3.8 \pm 1.0	2.9 \pm 0.7 \pm 0.2
2.9810	4.92 \pm 2.52	16.07	2.36	2.22	80.7 \pm 0.8	97.3 \pm 0.7	7.4 \pm 3.8 \pm 1.0	2.9 \pm 0.7 \pm 0.2
3.0000	5.87 \pm 2.59	15.88	2.41	2.24	80.7 \pm 0.8	97.5 \pm 0.7	8.7 \pm 3.8 \pm 1.3	3.1 \pm 0.7 \pm 0.2
3.0200	7.51 \pm 2.81	17.29	2.46	2.14	80.7 \pm 0.8	97.4 \pm 0.7	10.4 \pm 3.9 \pm 1.5	3.4 \pm 0.6 \pm 0.3
3.0800	19.8 \pm 4.9	126.185	2.61	2.08	80.0 \pm 1.3	97.8 \pm 0.7	3.7 \pm 0.9 \pm 0.5	2.1 \pm 0.3 \pm 0.2

Table B.20: Category B: Summary of the results for the Born cross section σ_{Born} and the effective FF $|G|$. The number of observed events N^{obs} is derived in Section B.8, the luminosity \mathcal{L}_{int} is quoted from [27], the signal MC simulation efficiency ϵ_{mc} , the radiative correction factor $(1 + \delta)$, the data/MC efficiency correction factor \mathcal{C}_{dm} and the trigger efficiency correction factor \mathcal{C}_{trg} are calculated as described in Section B.9. The systematical uncertainties are calculated according to Section B.11.

B13 Category B: cross check of the BDT approach with a cut-based signal selection

The selection criteria based on cuts instead the BDT approach for the selection of the category B classified signal events are listed as following:

- The event is required to have no charged tracks.
- The most energetic shower is treated as the \bar{n} candidate and its deposition energy is required to be larger than 0.5 GeV.
- To remove the $e^+e^- \rightarrow \gamma\gamma$ process, the number of hits detected in a 40 degrees cone around the \bar{n} in the EMC is required to be larger than 40.
- The flight time of the \bar{n} measured with the TOF system is required to be valid, and the absolute value of time difference between the measured and expected flight time of the antineutron candidate, $\Delta T_\gamma = T_{\text{TOF}} - T_\gamma - T_0$, is required to be larger than 0.5 ns.
- The second energetic shower is treated as the n candidate, with the deposition energy to be within $E_n = (0.06, 0.5)$ GeV.
- The flight time of the n in the TOF detector is required to be not valid.
- The polar angle of the n is required to be within $|\cos\theta| < 0.75$.
- The deposition energy in the event, excluding the energy deposited in a 40 degree cone around the \bar{n} shower in the EMC and the n deposition energy, is required to be less than 0.1 GeV. This criterion removes a majority of the hadronic background.

After the above selection, the signal yield in the opening angle distribution between \bar{n} and n at $\sqrt{s} = 2.3960$ GeV is shown in Figure B.21, for signal MC simulation and the collider data, respectively. The signal shape in the signal MC simulation is described by the Crystal Ball function. The parameters for the Crystal Ball function obtained from the simulation are fixed for the fit to the collider data. In the fit to the collider data, the background parameters are shared between the collider data sample and the separated beam samples.

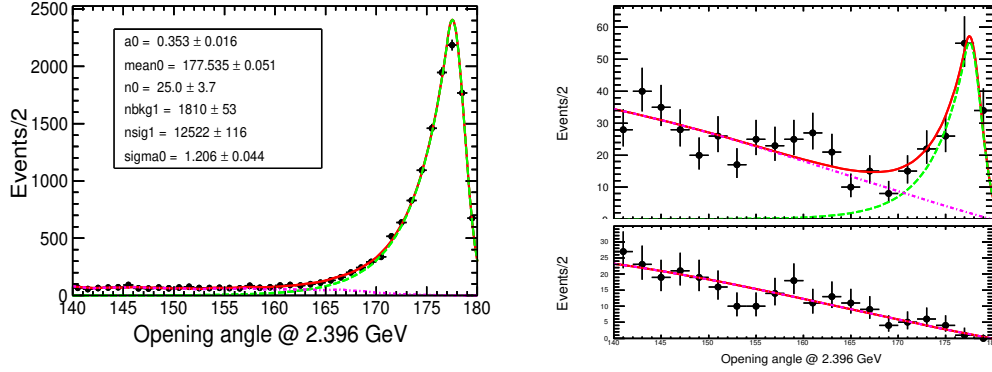


Fig. B.21: Category B: Opening angle distribution between \bar{n} and n at $\sqrt{s} = 2.3960$ GeV, for signal MC simulation and collider data after the cut-based selection.

Following, the Born Cross section of the signal process is extracted. The selection efficiency from the signal MC simulation is 2.5 %. Two correction factors are considered, a data/MC efficiency difference correction, and a trigger efficiency correction. Figure B.23 shows the selected efficiency difference of \bar{n} and n between the collider data and the signal MC simulation. The data/MC efficiency difference on E_{extra} is not considered, since this is a event level criterion and the cut value for E_{extra} is quite loose. The data/MC efficiency difference for the other selection criteria is shown in Figure B.22. The calculated weighted data/MC correction factor is 92.9 %. The trigger efficiency is calculated according to the weighted total deposition energy, to be 94.7 %. The Born cross section according to the cut-based selection is calculated to be:

$$\sigma^{\text{Born}} = \frac{N_{\text{obs}}}{L \mathcal{E}_{\text{mc}} \delta_{\text{data/MC}}^{\text{cor}} \delta_{\text{trg}}^{\text{cor}} (1 + \delta)} = \frac{144 \pm 14}{66.9 \times 0.025 \times 0.929 \times 0.947 \times 1.03} = 95.0 \pm 9.3 \text{ pb} \quad (\text{B.11})$$

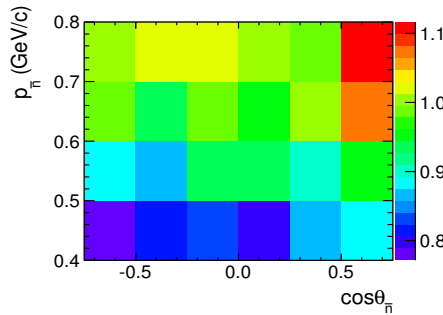


Fig. B.22: Category B: Efficiency difference for the \bar{n} and n selection between the collider data and the MC Simulation for the control samples at $\sqrt{s} = 2.3960$ GeV for the extraction of the data/MC efficiency correction factor \mathcal{C}_{dm} , as discussed in Section 8.2.

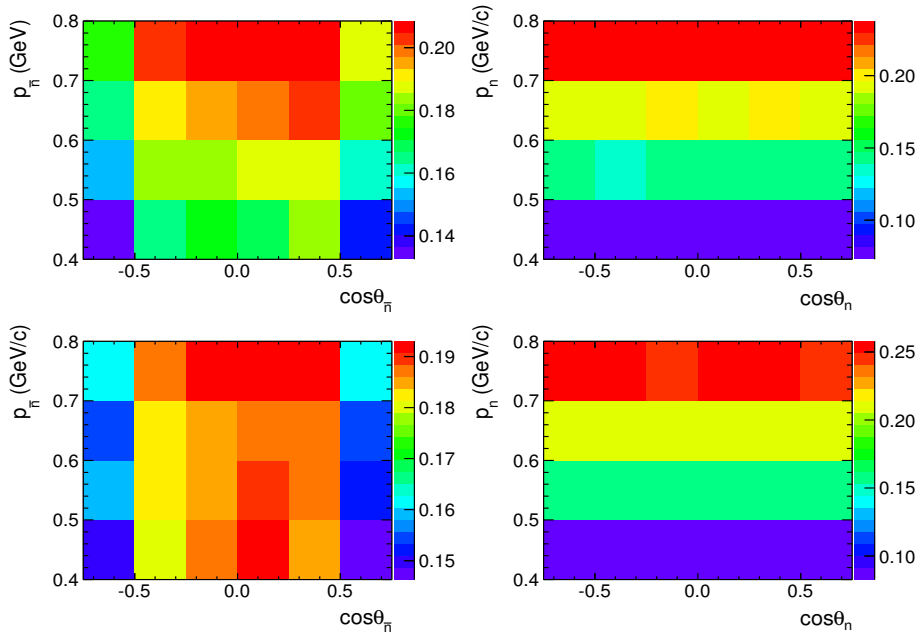


Fig. B.23: Selection efficiency for \bar{n} (left) and n (right) from the collider data at $\sqrt{s} = 2.3960$ GeV (top) and signal MC simulation with ConExc (bottom) from control samples introduced in Section 8.2, analyzed under the modified selection strategy for category B using a cut-based selection instead of the BDT discriminator.

The Time-of-Flight Measurement for Neutral Particles at BESIII

In Appendix C the algorithm for the time-of-flight measurement of the antineutron and neutron for this analysis is introduced. Initially, the time-of-flight measurement for neutral particles was not foreseen at the BESIII experiment. The BESIII experiment has been not developed and constructed with the main goal of a measurement of processes with neutral hadrons only in the final state. Therefore there was no need to discriminate between photons and neutral hadrons with the TOF system. For this analysis, an algorithm for exactly this purpose has been developed. The algorithm has been optimized especially for the analyzed signal process $e^+e^- \rightarrow \bar{n}n$ and can't be simply applied for the time-of-flight measurement in other pure neutral final state processes. Nevertheless, this first attempt to measure the flight time for neutral particles, even if optimized for this specific signal channel, is a significant improvement compared to the standard reconstruction framework of the BESIII experiment. The flight time determination for the antineutron is discussed in Section C.1, the calculation of the flight time for the neutron is shown in Section C.2. A verification study for this method, using the pure neutral $e^+e^- \rightarrow \gamma\gamma$ final state, is shown in Section C.3.

C1 Determination of the time-of-flight of the antineutron

The leading shower (EMC1), located in barrel region of the EMC, is selected as the antineutron candidate. The energy of the leading shower is denoted as $E_{\bar{n}}$. The location of the leading shower in the EMC with respect to the interaction point (IP) is denoted as V_{EMC1} . A cone for the opening angle between the leading shower and its neighbor showers with the location V_i (i is the index of the showers in the EMC) is defined and restricted to an $< 50^\circ$. A TOF signal is associated with the leading shower in the EMC, if the following condition is met: The angle between the EMC1 and the shower in the TOF system closest to the vector between the EMC1 and the IP (TOF1) is smaller than span of 3 TOF counters ($3 \times \phi_c$). If this condition is met, the TOF1 is associated to the EMC1 and assumed to be the corresponding TOF signal for the leading EMC shower. The angle between the EMC1 and TOF1 is defined as following:

$$\theta_i = \arccos\left(\frac{V_{EMC1} \cdot V_i}{|V_{EMC1}| |V_i|}\right) < \theta_{cone}$$

$$|\Delta\phi_{TOF1,EMC1}| = \begin{cases} |\phi_{EMC1} - \phi_i|, & |\phi_{EMC1} - \phi_i| \leq \pi \\ 2\pi - |\phi_{EMC1} - \phi_i|, & |\phi_{EMC1} - \phi_i| > \pi \end{cases} \quad (C.1)$$

$$\phi_c = \frac{2\pi}{88}$$

ϕ_{EMC1} is the azimuthal angle of the leading shower, ϕ_i is the azimuthal angle of a TOF counter. ϕ_c is an azimuthal span of one TOF counter. There are two layers of scintillators for the TOF system in the barrel region of the BESIII detector. Each layer consists 88 TOF counters which are arranged cylindrically. The TOF counters are associated with the leading shower (if the above conditions are met), if they have a valid double-ends readout (TDC, ADC). The TOF counter in each layer closest to the leading shower, is prior to the other TOF counters in the same layer. Each layer is used independently if only one of two layers is available. Two layers are combined if both are available. The flight time (T_{TOF1}) is calculated with the TOF calibration service given the TOF intersection (V_{TOF1}) and valid corresponding readouts (TDC, ADC). The intersection is calculated by a linear

interpolation from the EMC position (V_{EMC1}) to the interaction point (V_{IP}) as follows:

$$V_{TOF1} = V_{IP} + L \cdot \frac{V_{EMC1} - V_{IP}}{|V_{EMC1} - V_{IP}|}, \quad (C.2)$$

Here, L is the flight path from the TOF intersection point to the interaction point. T_{TOF1} is used to calculate the event start time T_0 under the hypothesis of a photon or T_0^n under the hypothesis of an antineutron. The calculation is described as follows:

$$T_{cor} \equiv T_{TOF1} - T_{\gamma 1}(T_{\bar{n}}) - T_{offset}$$

$$N = \begin{cases} \left\lceil \frac{T_{cor}}{T_b} \right\rceil, & T_{cor} - \left\lceil \frac{T_{cor}}{T_b} \right\rceil T_b \leq \frac{1}{2} T_b \\ \left\lceil \frac{T_{cor}}{T_b} \right\rceil + 1, & T_{cor} - \left\lceil \frac{T_{cor}}{T_b} \right\rceil T_b > \frac{1}{2} T_b \end{cases} \quad (C.3)$$

$$T_0^\gamma(T_0^n) = NT_b + T_{offset}$$

T_{offset} is the run-related time offset and is obtained from the BESIII offline database. T_b is the time interval between single bunches in the collider, which is ~ 6 nanoseconds for the collider data collected in 2014/15, and used for the analysis in this work. N is an integer bunch number representing the N^{th} bunch from which the current event is created. T_0 is required to be positive. $T_{\gamma 1}$ is the predicted flight time of a photon, calculated by using the flight path divided by the light speed in vacuum (c).

$$T_{\gamma 1} = \frac{L}{C} \quad (C.4)$$

The predicted flight time ($T_{\bar{n}}$) of the antineutron is calculated as:

$$T_{\bar{n}} = \frac{L}{\beta C}, \beta = \frac{\sqrt{E_{cm}^2 - m^2}}{E_{cm}} \quad (C.5)$$

E_{cm} is the beam energy, m_n is the neutron mass. Taking T_0 as the reference time, the time difference between the flight time of an antineutron and of a photon is defined as:

$$\Delta T_{\bar{n}} \equiv T_{TOF1} - T_0^\gamma - T_{\gamma 1} \quad (C.6)$$

In addition, the position (V_{TOF1}) of the antineutron impact with the TOF counter is measured. The x and y component are measured using the TOF counter identifier (TID).

The z-component is measured by the TOF calibration service given two valid TDC readouts (TDC1, TDC2). $V_{\text{TOF1}'}$ is determined to be:

$$\phi = (\text{TID} + \text{S})\phi_c$$

$$V_{\text{TOF1}'} = \begin{cases} x &= R \cos(\phi) \\ y &= R \sin(\phi) \\ z &= \text{ToFCaliSvc} :: \text{ZTDC}(\text{TDC1}, \text{TDC2}, \text{TID}) \end{cases} \quad (\text{C.7})$$

R is the radial distance from the TOF counters' center location to the origin of the BESIII detector. R is 83.85 cm for the inner layer of TOF counters and 89.55 cm for the outer layer of the TOF counters. S is 1/2 for the inner layer and 0 for the outer layer due to the small shift of the center location. The measured position is used to calculate the opening angle ($\theta_{\text{TOF1}', \text{EMC1}}$) between the leading EMC shower position V_{EMC1} and the signal position in the TOF system $V_{\text{TOF1}'}$:

$$\theta_{\text{TOF1}', \text{EMC1}} = \arccos\left(\frac{V_{\text{TOF1}'} \cdot V_{\text{EMC1}}}{|V_{\text{TOF1}'}| |V_{\text{EMC1}}|}\right). \quad (\text{C.8})$$

C2 Determination of the time-of-flight of the neutron

TOF counters (TOF2) along a specific direction, for instance, the recoiling direction of the leading shower, are selected as the neutron candidate, The recoiling direction is calculated to be:

$$V_{\text{RCL}} = -(V_{\text{EMC1}} - V_{\text{IP}}) + \Delta V, \quad (\text{C.9})$$

ΔV is a position correction due to initial-state-radiation and boost effects. This correction is extracted from the MC simulation study of $e^+e^- \rightarrow \gamma\gamma$. Only TOF counters within an azimuthal angle difference ($\Delta\phi_{\text{TOF2}, \text{RCL}}$) of 6 TOF counters span are checked for whether their double-ends readout (TDC, ADC) are valid. The TOF counter in each layer closest to the recoiling direction, is prior to the other TOF counters in the same layer. Each layer is used independently, if only one of two layers is available. Two layers are combined if both are available. The time of flight (T_{TOF2}) of the neutron is calculated with the TOF calibration service given for the TOF intersection (V_{TOF2}) and the corresponding readouts (TDC, ADC). The intersection is calculated by a linear extrapolation along the recoiling

direction:

$$V_{\text{TOF2}} = V_{\text{IP}} + L_n \cdot \frac{V_{\text{RCL}}}{|V_{\text{RCL}}|}, \quad (\text{C.10})$$

L_n is the flight path of the neutron from the IP to the TOF intersection point. The predicted flight time of the neutron (T_n) is calculated with the neutron speed as follows:

$$T_n = \frac{L_n}{\beta C}, \beta = \frac{\sqrt{E_{\text{cm}}^2 - m^2}}{E_{\text{cm}}}, \quad (\text{C.11})$$

E_{cm} is the beam energy and m_n is the neutron mass. Taking T_0^n as the reference time into account, the time difference between the measured and expected flight time of the neutron is defined as:

$$\Delta T_n \equiv T_{\text{TOF2}} - T_0^n - T_n. \quad (\text{C.12})$$

With respect to V_{TOF2} , the hitting position $V_{\text{TOF2}'}$ is measured by from TOF counters. The x-component and y-component is measured by using the TOF counter identifier (TID). The z-component is measured by the TOF calibration service given two valid TDC readouts (TDC1, TDC2). The (x,y,z) of $V_{\text{TOF2}'}$ is expressed as:

$$\begin{aligned} \phi &= (\text{TID} + \text{S})\phi_c \\ V_{\text{TOF1}'} &= \begin{cases} x &= R \cos(\phi) \\ y &= R \sin(\phi) \\ z &= \text{TofCaliSvc} :: \text{ZTDC}(\text{TDC1}, \text{TDC2}, \text{TID}) \end{cases} \end{aligned} \quad (\text{C.13})$$

R is the radial distance from TOF counters' center location to the origin of the BESIII detector. R is 83.85 cm for the inner layer TOF counters and 89.55 cm for the outer layer ones. S is 1/2 for inner layer and 0 for outer layer. Apart from TOF information of neutron, EMC information is also used to improve identification of the neutron candidate. The second energetic shower is associated as long as the shower could be found when its direction deviation from V_{EMC1} more than $\frac{1}{2}\pi$. If the second energetic shower is not found, its energy (E_n) is set to zero.

C3 Study of the photon detection efficiency with the algorithm for the neutral TOF measurement

The process of $J/\psi \rightarrow \pi^+ \pi^- \pi^0$ is used to study the photon detection efficiency. To select candidate events, two charged π , one good shower and a missing shower are subject to a five constrains kinematic fit. The five constrains are the four-momentum conservation and additionally the π^0 mass. A $\chi^2 < 50$ and $\theta > 0.45$ are required to obtain a clean photon sample. Here, θ is the opening angle between the direction of the missing photon and direction of the reconstructed photon. This selection rejects events with high momentum π^0 coming from a two photons decay with a very small angle in between. Figure C.1 shows an excellent agreement between the efficiency determined with the collider data and with the MC simulation for $J/\psi \rightarrow \pi^+ \pi^- \pi^0$ (difference: $< 1\%$).

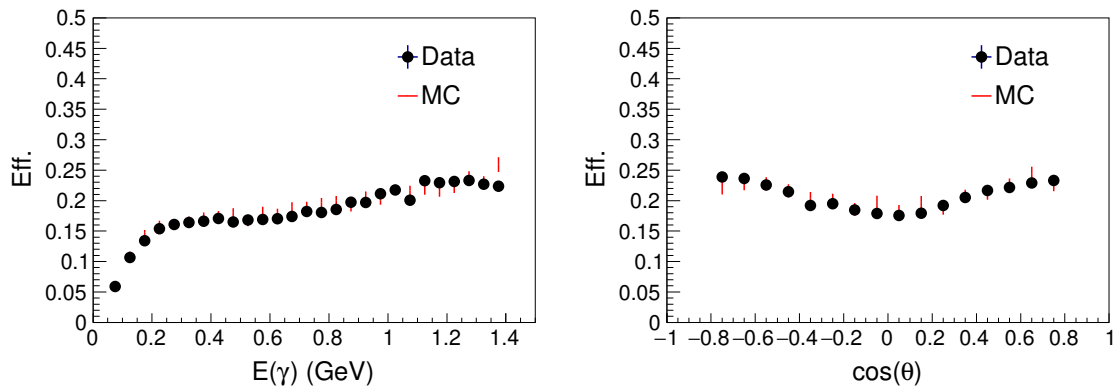


Fig. C.1: Detection efficiency of a photon in the TOF system (left) as a function of energy within the interval of $E_\gamma = (0.05, 1.40)$ GeV and $\cos(\theta) = (-0.8, 0.8)$ rad, (right) as a function of $\cos(\theta) = (-0.8, 0.8)$ rad within the interval of $E_\gamma = (0.8, 1.20)$ GeV.

C4 Performance test of the neutral TOF reconstruction and verification with $e^+e^- \rightarrow \gamma\gamma$ selection

We analyze the process $e^+e^- \rightarrow \gamma\gamma$ to test the reconstruction of the time-of-flight for neutral particle and additionally partially verify the analysis strategy of category A. The selection criteria for the process $e^+e^- \rightarrow \gamma\gamma$ are listed in Table C.1 and compared to the selection criteria for $e^+e^- \rightarrow n\bar{n}$. Attention should be paid to the fact that the event start time (rmT_0^γ) is determined under the photon hypothesis, while T_0^n is determined under

the antineutron hypothesis. The energy of the leading shower is constrained according to the beam energy.

Index	$e^+e^- \rightarrow \gamma\gamma$	$e^+e^- \rightarrow n\bar{n}$
0	$ \cos\theta < 0.8$	$ \cos\theta < 0.8$
1	$ \Delta T_{\gamma 1} \equiv T_{\text{TOF1}} - T_0^{\gamma} - T_{\gamma 1} < 1 \text{ ns}$	$0.5 < T_{\text{TOF1}} - T_0^{\gamma} - T_{\gamma 1} < 10 \text{ ns}$
2	$ \Delta T_{\gamma 2} \equiv T_{\text{TOF2}} - T_0^{\gamma} - T_{\gamma 2} < 1 \text{ ns}$	$ T_{\text{TOF2}} - T_0^n - T_n < 4 \text{ ns}$
3	$0.7E_{\text{cm}} < E_1 < 1.1E_{\text{cm}}$	$0.025 < E_1 < 2.0 \text{ GeV}$
4	$E_2 < 1.1E_{\text{cm}} \text{ GeV}$	$E_2 < 0.7 \text{ GeV}$

Table C.1: Comparison of the selection criteria for the process $e^+e^- \rightarrow \gamma\gamma$ and $e^+e^- \rightarrow n\bar{n}$.

In addition, the following corrections are applied to the MC simulation samples for $e^+e^- \rightarrow \gamma\gamma$ to reduce the discrepancy to the collider data:

1. $E_i' = G(E_i(1 + D_1), C_1)$, $i=1,2$.
2. $\Delta T_{\gamma i}' = G(\Delta T_{\gamma i} - D_2, C_2)$, $i=1,2$.

where $D_1 = 9.852 \times 10^{-3}$, $C_1 = 1.063 \times 10^{-2}$, $D_2 = 4.529 \times 10^{-2} \text{ ns}$, and $C_2 = 7.593 \times 10^{-2}$. D denotes a displace transformation, G denotes a Gaussian smear. After the above selection criteria and corrections, the number of survived digamma events $N_{\text{obs}}^{\gamma\gamma}$ is counted. After dividing by the MC simulation reconstruction efficiency ($\varepsilon_{\text{MC}}^{\gamma\gamma}$) and the luminosity of the collider data sample (L), the measured cross section is obtained and compared to the predicted cross section. The relation of $N_{\text{obs}}^{\gamma\gamma} = L\sigma\varepsilon_{\text{MC}}^{\gamma\gamma}$ is well verified as listed in Table C.2. The survived events in the collider data are compared to those survived in the MC simulation as shown in Figures C.2, C.3, and C.4.

\sqrt{s} (GeV)	L (nb $^{-1}$)	$\varepsilon_{\text{MC}}^{\gamma\gamma}$ (%)	$N_{\text{obs}}^{\gamma\gamma}$	$\sigma_{\text{obs}}^{\gamma\gamma}$ (nb)	$\sigma_{\text{gen}}^{\gamma\gamma}$ (nb)
2.000	10075 ± 5	2.033	-	87.58 ± 0.65	87.99 ± 0.85
2.125	108490 ± 30	2.029	-	76.47 ± 0.19	77.43 ± 0.34
2.175	10625 ± 6	2.035	-	73.30 ± 0.58	74.57 ± 0.32
2.200	13699 ± 7	2.041	-	71.40 ± 0.51	72.52 ± 0.32
2.2324	11856 ± 7	2.039	-	69.92 ± 0.54	70.51 ± 0.31
2.396	66869 ± 7	2.046	-	60.39 ± 0.21	61.10 ± 0.27
2.6440	33722 ± 13	2.063	-	48.69 ± 0.19	50.03 ± 0.22
2.900	105253 ± 25	2.068	-	41.35 ± 0.14	41.73 ± 0.18
3.080	126185 ± 29	2.058	-	36.97 ± 0.12	37.22 ± 0.16

Table C.2: Verification of the relation $N_{\text{obs}}^{\gamma\gamma} = L\sigma\varepsilon_{\text{MC}}^{\gamma\gamma}$ for the digamma process.

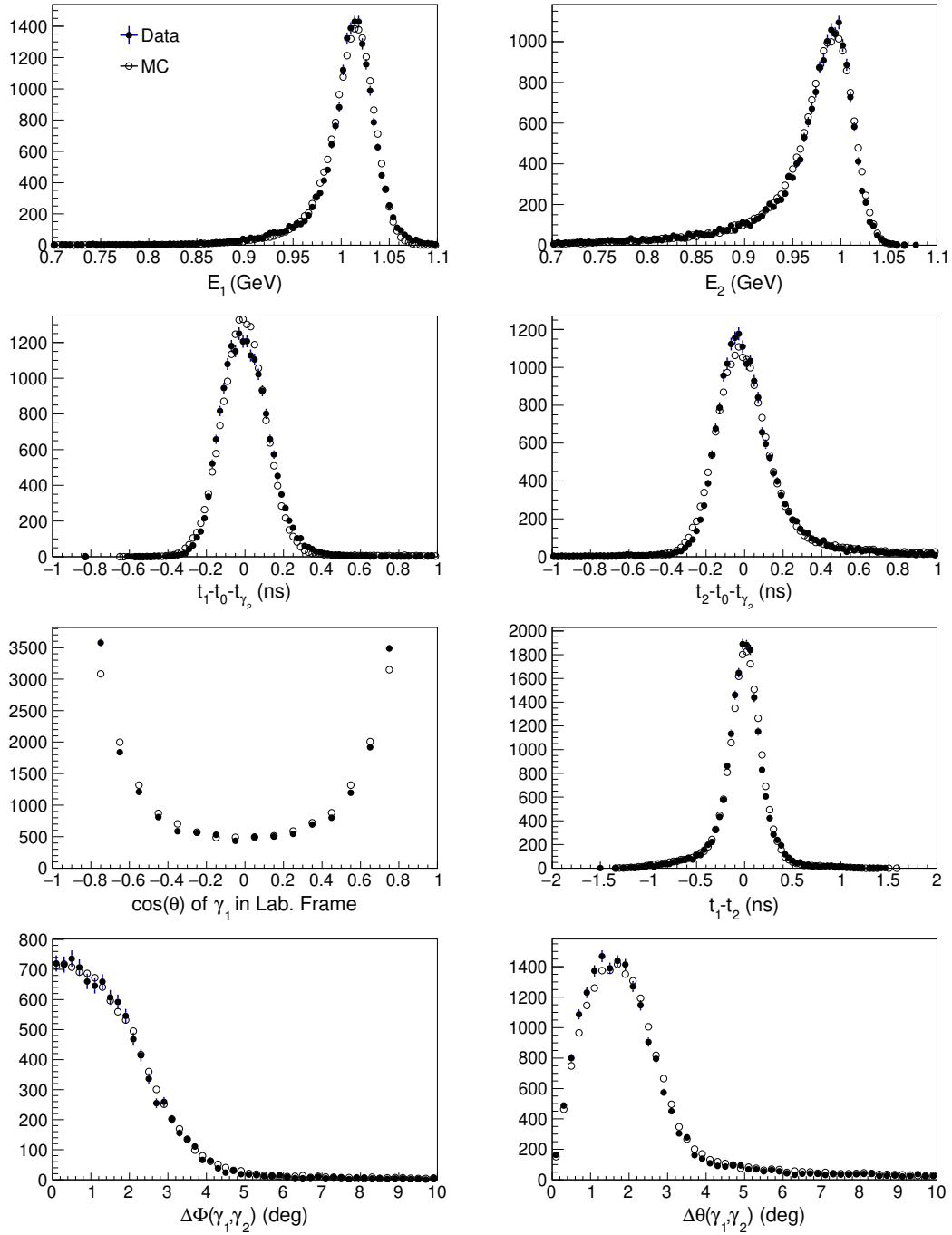


Fig. C.2: Comparison between the signal MC simulation for $e^+e^- \rightarrow \gamma\gamma$ generated with Babayaga 3.5 and the collider data at $\sqrt{s} = 2.0000$ GeV under the digamma selection. Variables from left to right, top to bottom, are the deposition energy of the most energetic and the second most energetic photon E_1 and E_2 , the difference between the expected and measured flight time of the leading (second leading) photon $\Delta T_{\gamma_1} = t_1 - t_0 - t_{\gamma_2}$ ($\Delta T_{\gamma_2} = t_2 - t_0 - t_{\gamma_2}$), the polar angle of the leading photon $\cos(\theta)_1$, the flight time difference between the two photons $t_1 - t_2$, the azimuthal angular difference $\Delta\Phi(\gamma_1, \gamma_2)$, and the solid angular difference $\Delta\theta(\gamma_1, \gamma_2)$.

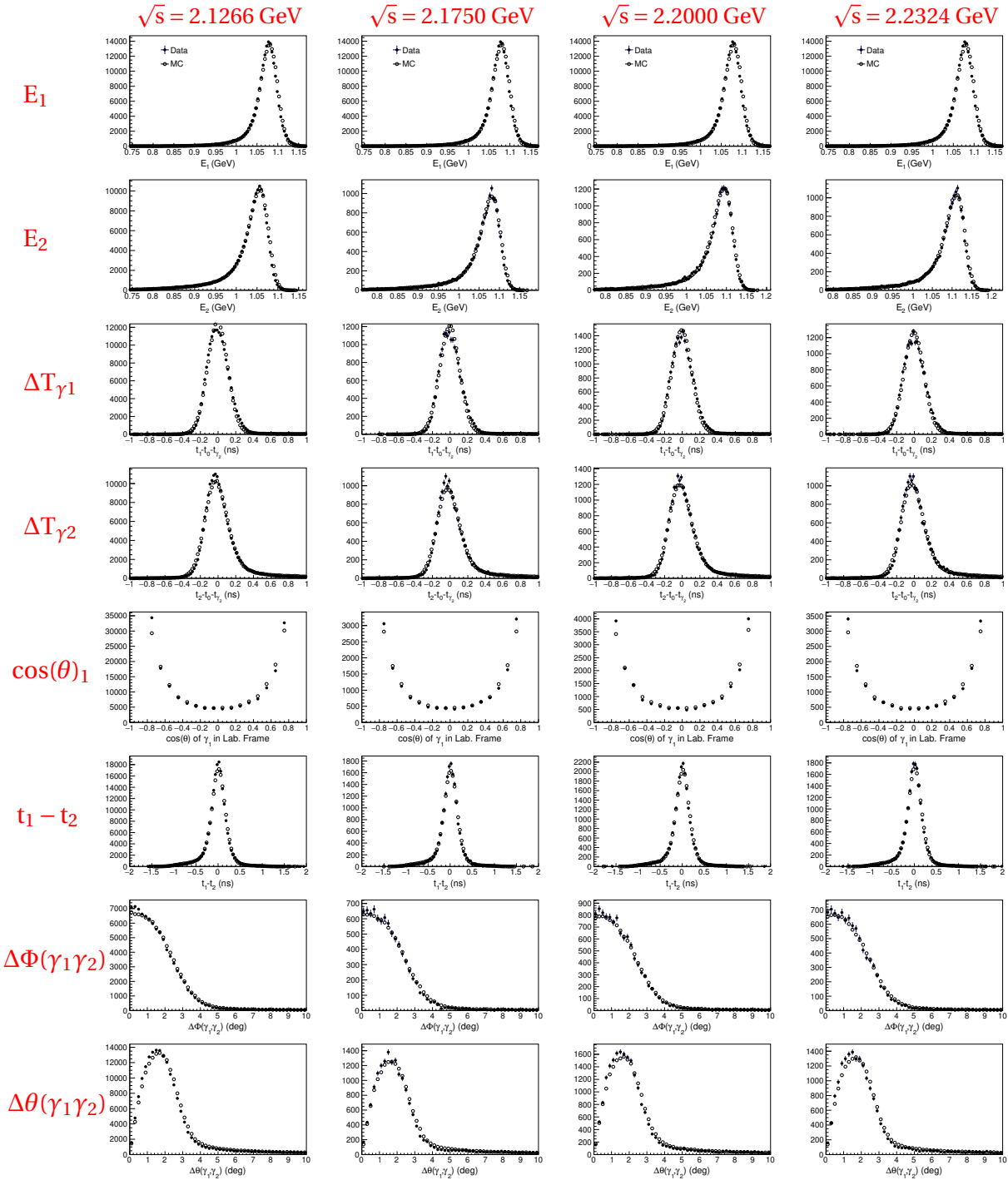


Fig. C.3: Comparisons between signal MC simulation for $e^+e^- \rightarrow \gamma\gamma$ generated with Babayaga 3.5 and collider data at $\sqrt{s} = 2.1266$ GeV, $\sqrt{s} = 2.1750$ GeV, $\sqrt{s} = 2.2000$ GeV, and $\sqrt{s} = 2.2324$ GeV under the digamma selection. Variables and notation are the same as in Figure C.2.

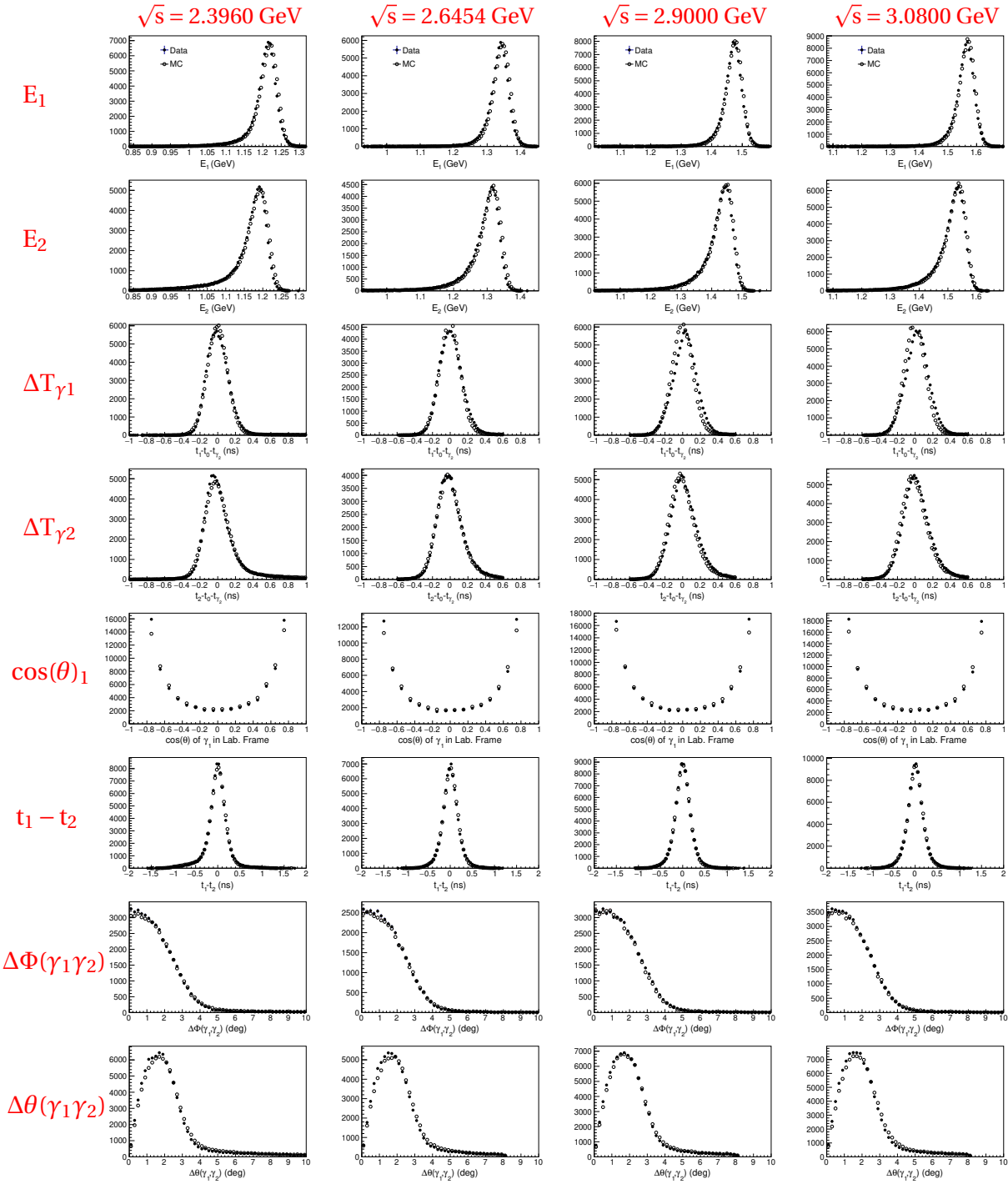


Fig. C.4: Comparisons between signal MC simulation for $e^+e^- \rightarrow \gamma\gamma$ generated with Babayaga 3.5 and collider data at $\sqrt{s} = 2.3960$ GeV, $\sqrt{s} = 2.6454$ GeV, $\sqrt{s} = 2.9000$ GeV, and $\sqrt{s} = 3.0800$ GeV under the digamma selection. Variables and notation are the same as in Figure C.2.

List of Figures

2.1	The Standard Model of particle physics.	7
2.2	Original results from Hofstadter for the "Electron-proton scattering from the proton with an incident energy of 188 Mev".	10
2.3	Feynman diagram for lepton-nucleon scattering in leading order.	11
2.4	Feynman diagram for the lepton-antilepton annihilation with a following nucleon-antinucleon production and the reversed process, both in leading order.	14
2.5	The BESIII experiment beam pipe with the interaction point.	16
2.6	Feynman diagrams for the first-order correction to $e^+e^- \rightarrow N\bar{N}$	17
2.7	The form factors $G_E^p(Q^2)$, $G_M^p(Q^2)/\mu_p$, and $G_E^p(Q^2)/G_M^p(Q^2)$ as a function of Q^2	22
2.8	Selected data on the electric and magnetic FF of the proton in the SL region.	23
2.9	Results on the ratio between the electric and magnetic proton form factor extracted with the polarization transfer method.	25
2.10	Feynman diagram for the leading-order Initial-State-Radiation process $l^+l^- \rightarrow N\bar{N}\gamma_{ISR}$	26
2.11	World data on the effective FF of the proton $ G_{eff}^p(q^2) $	27
2.12	World data on the individual magnetic FF and the FF ratio of the proton.	28
2.13	Results on the electric and magnetic FF of the neutron in the SL region.	30
2.14	Results on the ratio between the electric and magnetic neutron form factor measured in double polarization experiments in the SL region.	31
2.15	World data on the effective FF of the neutron in the TL region.	32
2.16	World data on the magnetic FF of the neutron in the TL region.	33
2.17	One possible lowest order diagram in QED for the interaction between a virtual photon with high momentum and a nucleon in the pQCD framework.	35
2.18	Parametrization of the magnetic FFs of the proton and neutron in the TL region with the DR based Mainz model.	37
2.19	Parametrization of the effective FFs of the proton and neutron in the TL region with the relativistic constituent quark model.	38

2.20	Illustration of the two different contributions for the lattice QCD calculation of the nucleon FFs.	39
2.21	TL effective FF of the proton with the χ EFT prediction.	40
2.22	Feynman diagrams for the virtual photon scattering of the proton including the hard and soft sub-process.	41
2.23	QCD contribution to the photon vacuum polarization in terms of quark-antiquark loop and the contribution through the coupling to vector mesons in the VMD model.	42
2.24	Nucleon FFs prediction for SL and TL regions with different VMD models compared to the experimental results.	44
3.1	The BEPCII facility center with the collider ring and the linac.	46
3.2	Schematic cross section of the BESIII detector.	47
3.3	Schematic cross-section of the beam pipe.	49
3.4	Mechanical structure of the multilayer drift chamber.	50
3.5	The superconducting solenoid at BESIII.	52
3.6	Schematic cross section of the TOF detector.	53
3.7	Differential K/π separation capability of TOF.	55
3.8	Architecture for the TOF readout electronics.	56
3.9	Schematic cross-section of the EMC detector.	57
3.10	Block diagram for the EMC readout.	59
3.11	Monte Carlo simulation of energy loss in the TOF counters for 1 GeV photons and the matching of the TOF signal to the EMC shower.	60
3.12	Monte Carlo simulation for the energy deposition from a 1 GeV photon and for the expected energy resolution for reconstructed showers.	61
3.13	Schematic cross-section of the MUC sub-detector.	63
3.14	Schematic representation of a RPC with the gas gap between resistive plates.	63
3.15	Data flow diagram of the L1 trigger and the block diagram of the trigger logic.	65
3.16	Open channels during data collection for 2015 collected data set.	67
3.17	Visualization of the short and long tracks in the MDC.	69
3.18	EMC trigger cell arrangement in the EMC barrel region and the end caps.	70
3.19	Efficiency of crystal trigger with respect to the energy deposition in an array of 2×2 to 4×4 trigger cells.	70
3.20	Simulation at J/ψ center-of-mass energy of energy deposition for beam related background, cosmic ray background and pure neutral final state event.	71

3.21	The overall BESIII software framework architecture and the event data flow in simulation.	73
3.22	The structure of the BESIII calibration software and the analysis software in BOSS.	73
3.23	Comparison of data sets collected by BESIII and other experiments.	76
4.1	Diagram of the standard simulation process chain in BOOST.	80
4.2	Phenomenological visualization of the different phases for the simulation of an event with a Monte Carlo event generator.	81
4.3	Original Born cross section of the process $e^+e^- \rightarrow \bar{n}n$ simulated with the generator Phokhara v9.1.	83
4.4	Simulation for the electromagnetic FFs of the neutron with Phokhara v9.1.	84
4.5	Original Born cross section of the process $e^+e^- \rightarrow \bar{n}n$ simulated with ConExc.	86
4.6	Results for the signal MC simulation optimization from the second last and final iteration.	88
5.1	Detector response for a signal event at $\sqrt{s} = 2.3960$ GeV shown in XY view of the BESIII detector.	92
5.2	Example for the development of a hadronic shower in the EMC.	97
5.3	Analysis strategy flow.	100
5.4	Angular distribution of the \bar{n} shower and the Energy deposition of the \bar{n} shower in EMC.	103
5.5	The distribution of the second moment from the \bar{n} shower and the number of hits of all EMC showers in 50° around and including the \bar{n} shower in the EMC.	104
5.6	Energy deposition of the n shower in EMC.	105
5.7	Energy deposition outside of the 50° -cone around the \bar{n} shower and of the 20° -cone around the n shower in EMC and the last layer with hits in the MUC.	107
5.8	Opening angle between the \bar{n} and the n shower in the EMC after all applied selection criteria.	108
6.1	The determination of the number for the misidentified and badly reconstructed neutron showers with the signal MC simulation at $\sqrt{s} = 2.3960$ GeV.	112
6.2	The opening angle between the \bar{n} and n EMC shower after applied selection criteria at all analyzed \sqrt{s}	113
6.3	Simulation of beam-gas induced particles in the BESIII detector including inelastic Bremsstrahlung and Coulomb scattering at $\sqrt{s} = 3.773$ GeV.	116

7.1	Fit results for the parameters of the signal shape component for the composite model fit.	122
7.2	The opening angle for data in collision and non-collision mode after the applied signal selection.	123
7.3	Beam related and cosmic ray background from the combined separated beam samples at $\sqrt{s} = 2.2324$ and 2.6444 GeV.	124
7.4	Probability density functions for the hadronic background component of the composite model fit at different \sqrt{s}	126
7.5	Results from the composite fit model applied to collider data at $\sqrt{s} = 2.3960$ GeV.	129
7.6	Results for the differential signal yield extraction with the composite fit model at different $\cos\theta_{\bar{n}}$ bins at $\sqrt{s} = 2.3960$ GeV.	130
7.7	Results for the differential signal yield extraction with the massive MC simulation approach at different $\cos\theta_{\bar{n}}$ bins at $\sqrt{s} = 2.3960$ GeV.	132
8.1	χ^2 from the 1C kinematic fit to the $J/\psi \rightarrow p\bar{n}\pi^-$ ($J/\psi \rightarrow p\bar{n}\pi^-$) collider data and MC simulation.	138
8.2	The recoil mass $m_{p\pi}^{\text{recoil}}$ of the $p\pi^-$ ($\bar{p}\pi^+$) system from collider data and MC simulation at $\sqrt{s} = 3.097$ GeV.	139
8.3	The angle between the generated position and the reconstructed EMC shower position of (left) \bar{n} and (right) n	141
8.4	Comparison of the selection variables for $e^+e^- \rightarrow \bar{n}n$ between collider data and $J/\psi \rightarrow p\bar{n}\pi^-$ ($J/\psi \rightarrow \bar{p}n\pi^+$) MC simulation at $\sqrt{s} = 3.0970$ GeV.	142
8.5	The recoil momentum of $p\pi^-$ and $\bar{p}\pi^+$ from collider data after the selection of the process $J/\psi \rightarrow p\bar{n}\pi^-$ ($\bar{p}n\pi^+$) at $\sqrt{s} = 3.097$ GeV.	143
8.6	Efficiency of the \bar{n} selection from collider data and MC simulation for $J/\psi \rightarrow p\bar{n}\pi^-$ at $\sqrt{s} = 3.097$ GeV.	144
8.7	Efficiency of the n selection from collider data and MC simulation for $J/\psi \rightarrow \bar{p}n\pi^+$ at $\sqrt{s} = 3.097$ GeV.	145
8.8	Variables for the calculation of the efficiency correction factor C_{dm} at $\sqrt{s} = 2.3960$ GeV.	147
8.9	Differential signal efficiency $\frac{d\epsilon^{\text{MC}}}{d\cos\theta}$ from the signal MC simulation with Phokhara 9.1 and the corresponding efficiency corrections $\frac{dC_{\text{dm}}}{d\cos\theta}$ at $\sqrt{s} = 2.1266$ and $\sqrt{s} = 2.3960$ GeV.	148
8.10	Born cross section for $e^+e^- \rightarrow \bar{n}n$ under variation of the cut value for the selection criterion E_{extra}	150

8.11	Comparison of the E_{extra} distribution at $\sqrt{s} = 2.396$ GeV between $e^+e^- \rightarrow \bar{p}p$ data and $e^+e^- \rightarrow \bar{n}n$ signal MC simulation.	151
8.12	Fit of the function from Equation 8.10 to the results of C_{ee}^{data}	152
8.13	The differential correction factor $\frac{dC_{\text{muc}}}{d\cos\theta}$ from signal MC simulation with Phokhara v9.1 at $\sqrt{s} = 2.1266$ and $\sqrt{s} = 2.3960$ GeV.	154
8.14	Open trigger channels at the time of the data collection for the collider data set used for this analysis.	155
8.15	Survived events from the process $e^+e^- \rightarrow \bar{p}p$ after the introduced selection with respect to the proton momentum $p_p = \vec{p} _p$ at $\sqrt{s} = 2.1266, 2.3960, 2.6444$ GeV and from the J/ψ data set.	157
8.16	Trigger efficiency with respect to the total energy deposition in the EMC from the control samples $e^+e^- \rightarrow \bar{p}p$ and from $J/\psi \rightarrow \bar{p}p$ at $\sqrt{s} = 3.0970$ GeV.	158
8.17	Trigger efficiency with respect to the total energy deposition in the EMC from the final state array $e^+e^- \rightarrow$ hadrons studied from the control samples.	159
8.18	Comparison of the trigger efficiency ϵ_{trg} (9 and 12) between RAW and DST data and under different selection requirements.	160
8.19	Fit of the EMC-based trigger efficiency ϵ_{trg} (9 and 12) with the Function 8.13.	161
8.20	Total energy deposition in the EMC from the signal MC simulation and the replaced distribution from the control channels at $\sqrt{s} = 2.1266$ and $\sqrt{s} = 2.3960$ GeV.	162
8.21	Extraction of the trigger efficiency correction C_{trg} at $\sqrt{s} = 2.1266$ and $\sqrt{s} = 2.3960$ GeV.	162
8.22	Differential correction factor $\frac{dC_{\text{trg}}}{d\cos\theta}$ from signal MC simulation at $\sqrt{s} = 2.1266$ and 2.3960 GeV.	163
8.23	Angular distribution of the antineutron at $\sqrt{s} = 2.3960$ GeV for the nominal form factor parametrization using $G_E^n(s) = G_M^n(s)$ and two extreme parametrization cases with $G_E^n(s) = 0$ and $G_M^n(s) = 0$	164
8.24	Feynman diagrams for the QED corrections to $e^+e^- \rightarrow \bar{n}n$	165
8.25	Differential radiative correction $\frac{d(1+\delta)}{d\cos\theta}$ from signal MC simulation at $\sqrt{s} = 2.1266$ and 2.3960 GeV.	166
9.1	Individual results for the Born cross section of the process $e^+e^- \rightarrow \bar{n}n$ from category C classified signal events (this work).	172
9.2	Individual results for the effective form factor of the process $e^+e^- \rightarrow \bar{n}n$ from category C classified signal events (this work).	172

9.3	Comparison of the results for the Born cross section and the effective form factor for the process $e^+e^- \rightarrow \bar{n}n$ from the three signal selection classification categories.	174
9.4	The resolution of the \bar{n} EMC shower position reconstruction at $\sqrt{s} = 2.1266$ and $\sqrt{s} = 2.3960$ GeV.	176
9.5	Differential selection efficiency and its efficiency corrections at $\sqrt{s} = 2.3960$ GeV.	177
9.6	Study for the choice of the angular fit function.	178
9.7	The extraction of the results for $G_M^{\text{ind}}(s)$ and $R_{\text{em}}^{\text{ind}}(s)$ under different fit and data sample characteristics.	179
9.8	Individual results for the magnetic form factor of the neutron $ G_M^{\text{ind}}(s) $ from category C classified signal events.	181
9.9	Individual results for the form factor ratio of the neutron $R_{\text{em}}^{\text{ind}}(s)$ from category C classified signal events.	181
9.10	Simultaneous angular analysis with the nominal: fit to the corrected angular distributions from the three categories.	183
9.11	Angular analysis with added angular distributions from the three categories.	184
9.12	Random MC angular distributions based on the corrected angular distributions of the antineutron from the three signal selection classification categories A, B, and C at $\sqrt{s} = 2.8130$ GeV.	185
9.13	Extraction of the most probable value for the ratio $R_{\text{em}}^{\text{mcbda}}$ and the corresponding statistical uncertainty ΔR^{mcbda} at $\sqrt{s} = 2.8130$	186
9.14	Results for the ratio R^{mcbda} and the corresponding statistical uncertainty ΔR^{mcbda} from the remaining four data sets.	188
9.15	The distributions of the results for the category-individual magnetic form factor $ G_M^{i,\text{mcbda}}(s) $ extracted with the MC simulation at $\sqrt{s} = 2.3936$ GeV.	189
9.16	The results for the form factor ratio and the magnetic form factor of the neutron from the three simultaneous approaches compared to the individual results.	191
10.1	Polar angle between the reconstructed neutron EMC shower position and the generated position $\angle_{\text{shower}}^{\text{truth}}$ and the signal shape model at $\sqrt{s} = 2.0000$, 2.3960, and 3.0800 GeV.	195
10.2	The angular distribution of the antineutron for category C classified signal events from MC truth at $\sqrt{s} = 2.3960$ GeV with the standard parametrization and with the two extreme cases with the corresponding Born cross sections.	197
10.3	Trigger efficiency with the nominal and the hadronic parametrization.	198

10.4	The products of the signal MC selection efficiency and the radiative correction factor $\epsilon^{\text{MC}} \times (1 + \delta)$ for the final and second last parametrization.	199
10.5	Results for the Born cross section of the process $e^+e^- \rightarrow \bar{n}n$ from category C classified signal events.	201
10.6	Results for the effective form factor of the neutron from the process $e^+e^- \rightarrow \bar{n}n$ from category C classified signal events.	201
10.7	The distribution of the reconstructed and corrected signal events from collider data D_{nominal} and a corresponding randomly generated distribution D_{random}^i at $\sqrt{s} = 2.3936$ GeV.	203
10.8	The distribution of the results for R_{random}^i and $G_{M, \text{random}}^i$ obtained from the 100k MC simulations of D_{random}^i at $\sqrt{s} = 2.3936$ GeV.	204
10.9	The distribution of the results for $R^+(s)$ and $G_M^+(s)$ as well as for $R^-(s)$ and $G_M^-(s)$ obtained from the 100k MC simulations of D_+ and D_- at $\sqrt{s} = 2.3936$ GeV.	205
10.10	The results for the systematic uncertainty on the form factor ratio and the magnetic form factor due to the signal selection.	206
10.11	MC study for the investigation of a possible systematic uncertainty of the form factor ratio due to the bin width δ_{bin} in the angular distribution.	208
10.12	MC study for the investigation of a possible systematic uncertainty of the form factor ratio due to the fit range for the fit of the angular distribution.	209
10.13	The investigation of the systematic uncertainty from the signal MC simulation model for the ISR event contribution.	210
10.14	Results for the form factor ratio of the neutron $R_{\text{em}}^{\text{ind}}$ obtained with category C classified signal events including the systematic uncertainty.	211
10.15	Results for the magnetic form factor of the neutron $G_M^{\text{ind}}(s)$ obtained with category C classified signal events including the systematic uncertainty.	213
10.16	The nominal, minimal, and maximal angular distributions from the three signal selection classification categories at $\sqrt{s} = (2.3864 - 2.3960)$ GeV and the corresponding results for the most probable value MPVs for R^{std} , R^- and R^+ for the study of the systematic uncertainties.	214
10.17	Distributions for the magnetic FF from the 100k simulations for the data set at $\sqrt{s} = 2.3936$ GeV for the study of the systematic uncertainty.	215
10.18	Results for the energy weighted average magnetic form factor $G_M^{\text{av,mc bda}}$ and the form factor ratio $R_{\text{em}}^{\text{mc bda}}$ including the systematic uncertainty at different energies \sqrt{s}	216

11.1	Comparison between the combined results for the Born cross section obtained with this analysis and existing measurements.	219
11.2	Comparison for the Born cross section for the process $e^+e^- \rightarrow \bar{n}n$ obtained with this analysis to the Born Cross section for the process $e^+e^- \rightarrow \bar{p}p$	220
11.3	The Ratio of the Born cross sections for the process $e^+e^- \rightarrow \bar{n}n$ from this analysis over $e^+e^- \rightarrow \bar{p}p$	220
11.4	Comparison of the results from this work with the effective form factors of different baryons.	221
11.5	Oscillation of the effective FF of the proton determined by the BaBar and the determination of the normalization parameter $m_a^2(n)$ for the modified dipole parametrization with the results from this work.	222
11.6	The oscillation of the effective FF of the neutron measured in this analysis after subtraction of the modified dipole parametrization with the parameter $\mathcal{A}(n)^{\text{new}} = 4.87 \text{ GeV}^{-4}$	223
11.7	Comparison of the results for the magnetic form factor from this work with different parametrizations.	227
11.8	Comparison of the electromagnetic FF ratio R_{em} of the neutron from this work with the available results for the proton and the Λ channel.	228
11.9	Comparison of the experimental results from this work with the corresponding results in the SL momentum transfer domain.	230
11.10	Comparison of the experimental results for the magnetic FF in the SL and TL region and fit for the determination of the asymptotic behavior between the SL and TL results.	232
A.1	Expected and generated $e^+e^- \rightarrow \gamma\gamma(\gamma_{\text{ISR}})$ events.	241
A.2	Expected and generated events with hadronic final states.	242
A.3	Fit to the opening angle between the \bar{n} and n of the signal MC simulation for the extraction of the signal shape parameters for the composite fit in Section 7.3.	244
A.4	Fit to the opening angle between the \bar{n} and n of the signal MC simulation for the extraction of the signal shape parameters for the composite fit in Section 7.3.	245
A.5	Signal yield extraction with the composite fit model and the corresponding Pull distribution at $\sqrt{s} = 2.0000, 2.0500, 2.1000, \text{ and } 2.1266 \text{ GeV}$	246
A.6	Signal yield extraction with the composite fit model and the corresponding Pull distribution at $\sqrt{s} = 2.1500, 2.1750, 2.2000, 2.2324, 2.3094, 2.3864, 2.3960, \text{ and } 2.6454 \text{ GeV}$	247

A.7	Signal yield extraction with the composite fit model and the corresponding Pull distribution at $\sqrt{s} = 2.9000, 2.9500, 2.9810, 3.0000, 3.0200, \text{ and } 3.0800$ GeV.	248
A.8	Differential signal yield at $\sqrt{s} = 2.0000$ GeV	250
A.9	Differential signal yield at $\sqrt{s} = 2.0500$ GeV	250
A.10	Differential signal yield at $\sqrt{s} = 2.1000$ GeV	251
A.11	Differential signal yield at $\sqrt{s} = 2.1266$ GeV	251
A.12	Differential signal yield at $\sqrt{s} = 2.1500$ GeV	252
A.13	Differential signal yield at $\sqrt{s} = 2.1750$ GeV	252
A.14	Differential signal yield at $\sqrt{s} = 2.2000$ GeV	253
A.15	Differential signal yield at $\sqrt{s} = 2.2324$ GeV	253
A.16	Differential signal yield at $\sqrt{s} = 2.3094$ GeV	254
A.17	Differential signal yield at $\sqrt{s} = 2.3864$ GeV	254
A.18	Differential signal yield at $\sqrt{s} = 2.3960$ GeV	255
A.19	Differential signal yield at $\sqrt{s} = 2.6454$ GeV	255
A.20	Differential signal yield at $\sqrt{s} = 2.9000$ GeV	256
A.21	Differential signal yield at $\sqrt{s} = 2.9500$ GeV	256
A.22	Differential signal efficiency from signal MC simulation with Phokhara v9.1.	257
A.23	Differential signal efficiency from signal MC simulation with ConExc.	258
A.24	Differential correction factor $\frac{d\mathcal{E}_{dm}}{d\cos\theta}$ determined from the signal MC simulation with Phokhara v9.1.	259
A.25	Differential correction factor $\frac{d\mathcal{E}_{dm}}{d\cos\theta}$ determined from the signal MC simulation with ConExc.	260
A.26	Differential correction factor $\frac{d\mathcal{C}_{muc}}{d\cos\theta}$ determined from the signal MC simulation with Phokhara v9.1.	261
A.27	Differential correction factor $\frac{d\mathcal{C}_{muc}}{d\cos\theta}$ determined from the signal MC simulation with ConExc.	262
A.28	Total energy deposition in the EMC from MC simulation with Phokhara v9.1 and the replaced distribution as discussed in Section 8.5 at all analyzed \sqrt{s} according to Table 3.11.	263
A.29	Differential correction factor $\frac{d\mathcal{C}_{trg}}{d\cos\theta}$ determined from the signal MC simulation with Phokhara v9.1.	264
A.30	Differential radiative correction $\frac{d(1+\delta)}{d\cos\theta}$ from signal MC simulation with Phokhara v9.1.	265
A.31	Differential radiative correction $\frac{d(1+\delta)}{d\cos\theta}$ from signal MC simulation with ConExc.	266

A.32	Plots for the determination of the systematic uncertainty on the individual results for the Born cross section due to the misidentification of the neutron shower in the EMC.	269
A.33	Plots for the determination of the systematic uncertainty δ_{range} on the individual results for the Born cross section $\sigma_{\text{Born}}^{\text{ind}}$ due to the fit range of the composite fit model from Equation 7.3.	271
A.34	Plots for the determination of the systematic uncertainty δ_{bg} on the individual results for the Born cross section $\sigma_{\text{Born}}^{\text{ind}}$ due to the background shape of the composite fit model from Equation 7.3.	273
A.35	Summary for the systematic uncertainty δ_{sig} on the individual results for the Born cross section due to the signal shape of the composite model fit to the opening angle for the signal yield extraction at all \sqrt{s}	275
A.36	Variation of the input model of the form factors in Phakhara v9.1 for the study of the model dependent systematic uncertainty δ_{model} on the Born cross section.	278
A.37	Plots for the MC simulation study for the determination of $\delta_{\text{dsel}}^{\text{R}}$ and $\delta_{\text{dsel}}^{\text{GM}}$	281
A.38	Plots for the MC simulation study for the determination of $\delta_{\text{dsel}}^{\text{GM}}$	282
A.39	Extraction of the ratio $R_{\text{em}}^{\text{dbg}}$ and the magnetic form factor $G_{\text{M}}^{\text{dbg}}$ under the variation of the fit range for the signal extraction.	283
A.40	Extraction of the ratio $R_{\text{em}}^{\text{dbg}}$ and the magnetic form factor $G_{\text{M}}^{\text{dbg}}$ under the variation of the background shape model for the signal extraction.	284
A.41	Extraction of the ratio $R_{\text{em}}^{\text{dbg}}$ and the magnetic form factor $G_{\text{M}}^{\text{dbg}}$ under the variation of the signal shape model for the signal extraction.	285
B.1	Category A: Selection variables for the signal particle \bar{n}	294
B.2	Category A: Selection variables for the signal particle n	295
B.3	Category A: Simultaneous fit of signal and background shape in ΔT_n with Eq. B.5 at 18 energy points (2.0000 GeV - 3.0800 GeV).	298
B.4	Category A: Variables for the calculation of the efficiency correction factor $\mathcal{E}_{\text{dm}}^{\text{abs}}$ at $\sqrt{s} = 2.3960$ GeV.	299
B.5	Category A: Fit to ΔT_n at each $\cos\theta$ bin at $\sqrt{s} = 2.1266$ GeV.	301
B.6	Category A: Differential efficiency corrections at $\sqrt{s} = 2.1266$ GeV.	302
B.7	Category A: results from the angular distribution fit of the efficiency corrected angular distributions.	304
B.8	Category B: Deposited energies in the EMC at $\sqrt{s} = 2.3960$ GeV of the antineutron and neutron candidate in the EMC.	311

B.9	Category B: Time difference between measured and expected time-of-flight of the antineutron candidate and the polar angle of the neutron candidate.	312
B.10	Category B: Output discriminator of BDT training at $\sqrt{s} = 2.3960$ GeV. . . .	312
B.11	Category B: Opening angle between neutron and antineutron after selection at $\sqrt{s} = 2.1266$ and 2.3960 GeV from the separated beam data samples. . . .	313
B.12	Category B: Opening angle between neutron and antineutron after selection at $\sqrt{s} = 2.1266$ GeV and 2.3960 GeV from the signal MC simulation with ConExc.	314
B.13	Category B: Plot for the opening angle between the neutron and the antineutron after selection at $\sqrt{s} = 2.0000 - 3.0800$ GeV.	315
B.14	Category B: Individual efficiency corrections for the selection of \bar{n} , of n , and for the BDT discriminator.	316
B.15	Category B: Variables for the calculation of the efficiency correction \mathcal{C}_{dm}^{abs} at $\sqrt{s} = 2.3960$ GeV	317
B.16	Category B: Total deposition energy of the signal process at $\sqrt{s} = 2.1266$ and $\sqrt{s} = 2.3960$ GeV.	317
B.17	Category B: Fit of the opening angle between \bar{n} and n in each analyzed bin of the $\cos\theta$ distribution.	319
B.18	Category B: Angular corrections at $\sqrt{s} = 2.1266$ GeV and the combined sample at $2.3864 + 2.3960$ GeV.	320
B.19	Category B: Results for the magnetic form factor G_M and the form factor ratio $R_{em} = G_E/G_M $	322
B.20	Category B: Study of systematic uncertainty due to the fit for the signal extraction.	325
B.21	Category B: Opening angle distribution between \bar{n} and n at $\sqrt{s} = 2.3960$ GeV after the cut-based selection.	329
B.22	Category B: Efficiency difference for the \bar{n} and n selection between the collider data and the MC Simulation for the control samples at $\sqrt{s} = 2.3960$ GeV.	329
B.23	Category B: Selection efficiency for \bar{n} and n from the collider data at $\sqrt{s} = 2.3960$ using a cut-based selection instead of the BDT discriminator.	330
C.1	Detection efficiency of a photon in the TOF system.	336
C.2	Performance test for the TOF reconstruction using the digamma selection at $\sqrt{s} = 2.0000$ GeV.	338
C.3	Performance test for the TOF reconstruction using the digamma selection at $\sqrt{s} = 2.1266$ GeV, $\sqrt{s} = 2.1750$ GeV, $\sqrt{s} = 2.2000$ GeV, and $\sqrt{s} = 2.2324$ GeV.	339

- C.4 Performance test for the TOF reconstruction using the digamma selection
at $\sqrt{s} = 2.3960$ GeV, $\sqrt{s} = 2.6454$ GeV, $\sqrt{s} = 2.9000$ GeV, and $\sqrt{s} = 3.0800$ GeV. 340

List of Tables

3.1	Parameters and performance of the BESIII sub-systems.	48
3.2	Parameters of the Multilayer Drift Chamber.	51
3.3	The contributions to the total TOF time resolution for a 1 GeV moun.	54
3.4	Parameters of the Time-of-Flight system.	55
3.5	Parameters of the electromagnetic calorimeter.	58
3.6	Properties of the Muon Counter system.	63
3.7	Expected event rates at the J/ψ -peak.	66
3.8	Trigger condition explanations for Figure 3.16.	68
3.9	Large luminosity data sets collected at resonances.	77
3.10	Scan data sets collected at discrete center-of-mass energies \sqrt{s}	77
3.11	Data sets used for the $e^+e^- \rightarrow \bar{n}n$ analysis in this work.	78
4.1	Input card for Phokhara v9.1 signal MC generation of the process $e^+e^- \rightarrow \bar{n}n(\gamma_{\text{ISR}}\gamma_{\text{ISR}})$	85
4.2	Input card for ConExc signal MC generation of the process $e^+e^- \rightarrow \bar{n}n(\gamma_{\text{ISR}})$	85
4.3	Fit parameter for the last two signal MC tuning iterations.	87
5.1	Summary of the selection criteria $S_1 - S_{10}$ for the signal process $e^+e^- \rightarrow \bar{n}n$	109
6.1	The change of the statistics with the application of the event selection criteria for all analyzed collider data, signal, and background samples at $\sqrt{s} = 2.3960$ GeV.	112
6.2	Summary of the event statistics at all \sqrt{s}	114
6.3	Summary of the time used for the collider data collection.	117
6.4	Topological study of the hadronic background from the inclusive MC simulation after the signal selection.	119
7.1	The number of the hadronic background events after the signal selection studied at different \sqrt{s}	125
7.2	Configuration for the composite model fit.	128

7.3	Summary of extracted signal events $N_{\text{fit}}^{\text{tot}}$ from collider data at different \sqrt{s} using the composite model fit approach.	133
7.4	Summary of extracted signal events $N_{\text{fit}}^{\text{tot}}$ from collider data at different \sqrt{s} using the massive MC simulation approach.	133
8.1	Summary of the signal reconstruction efficiency at different \sqrt{s}	136
8.2	Summary of the efficiency corrections due to differences between data and MC simulation for selection variables $S_1 - S_7$	146
8.3	Summary of the efficiency corrections C_{ee}^{data} derived by the data-driven method at different \sqrt{s}	151
8.4	Summary of the efficiency corrections C_{ee} derived from the fit at different \sqrt{s}	152
8.5	Summary of the efficiency corrections due to differences between data and MC simulation for the selection variable S_9 at different \sqrt{s}	154
8.6	Summary of efficiency corrections due to BESIII trigger system C_{trg} at different \sqrt{s}	163
8.7	Summary of efficiency corrections due to radiative correction factor $(1 + \delta)$ at different \sqrt{s}	166
8.8	Summary of signal MC reconstruction efficiency and its corrections.	167
9.1	Summary of all values for the calculation of the $e^+e^- \rightarrow \bar{n}n$ Born cross section and the effective form factor of the neutron.	170
9.2	Individual results for the Born cross section and effective form factor of the neutron, calculated with values from Table 9.1 from category C classified signal events (this work).	171
9.3	Comparison of the category-individual results for the Born cross section and effective form factor of the neutron and their error-weighted combination.	174
9.4	Summary of the individual results for $ G_M^{\text{ind}}(s) $ and $R_{\text{em}}^{\text{ind}}(s) = G_E^n(s) / G_M^n(s) $ for the category C classified signal events.	180
9.5	Results for the category-individual magnetic form factors G_M^i , their average G_M^{av} , and form factor ratio $R_{\text{em}} = G_E / G_M $ at $\sqrt{s} = 2.1266$ and the combined data samples obtained with three approaches.	190
10.1	Form factor ratio input values for signal MC produced for the evaluation of δ_{model}	196
10.2	Summary of systematic uncertainties on the Born cross section and the effective form factor for the signal event classification category C at different \sqrt{s}	200

10.3	Results from the MC simulation for the determination of $\delta_{\text{dsel}}^{\text{R}}$ and $\delta_{\text{dsel}}^{\text{GM}}$. The values for $R_{\text{em}}^{\text{std}}$ are within their errors in agreement with the nominal results for $R_{\text{em}}^{\text{ind}}$ from Table 9.4 (right). The uncertainty $\delta_{\text{dsel}}^{\text{R}}$ is shown with respect to the \sqrt{s} in Figure 10.10.	205
10.4	Summary of systematic uncertainties on the individual results for the form factor ratio $\delta_{\text{sys}}^{\text{R}}$ at different \sqrt{s}	211
10.5	Summary of systematic uncertainties on the individual results for the mag- netic form factor $\delta_{\text{sys}}^{\text{GM}}$ at different \sqrt{s}	212
10.6	Summary of systematic uncertainties on the form factor ratio $\delta^{\text{sys}} R_{\text{em}}^{\text{mcbda}}$ and on the magnetic FF $\delta^{\text{sys}} G_{\text{M}}^{\text{av,mcbda}}$ results using the combined analysis at all analyzed \sqrt{s}	216
11.1	Summary of the final results for the Born cross section, the effective FF, the magnetic FF, and the FF ratio from this work.	218
A.1	Summary of the signal MC simulation for the process $e^+e^- \rightarrow \bar{n}n(\gamma_{\text{ISR}})$ generated with Phokhara v9.1 for signal optimization and efficiency deter- mination.	240
A.2	Summary of the background MC simulation for the process $e^+e^- \rightarrow \gamma\gamma(\gamma_{\text{ISR}})$ generated with Babayaga 3.5.	241
A.3	Summary of the background MC simulation for the process $e^+e^- \rightarrow \bar{q}q(\gamma_{\text{ISR}})$ \rightarrow hadrons(γ_{ISR}) generated with BesEvtGen.	242
A.4	Summary of different MC simulations used in this analysis for the estima- tion of the background contamination and for efficiency studies.	243
A.5	Summary of the signal MC reconstruction efficiency and its corrections with ConExc.	267
A.6	Summary of systematic uncertainty due to the signal selection δ_{sel} on the individual results for the Born cross section at different \sqrt{s}	268
A.7	Summary of the systematic uncertainty due to the neutron EMC shower misidentification δ_{miss} on the individual results for the Born cross section.	270
A.8	Summary of the systematic uncertainty δ_{range} on the individual results for the Born cross section $\sigma_{\text{Born}}^{\text{ind}}$ due to the fit range of the composite fit model from Equation ref 7.3.	272
A.9	Summary for the systematic uncertainty δ_{bg} on the individual results for the Born cross section due to the background shape of the composite model fit to the opening angle for the signal yield extraction at all \sqrt{s}	274

A.10	Summary for the systematic uncertainty δ_{sig} on the individual results for the Born cross section due to the signal shape of the composite model fit to the opening angle for the signal yield extraction at all \sqrt{s}	276
A.11	Summary for the systematic uncertainty δ_{fit} on the individual results for the Born cross section due to the fit to the opening angle for signal yield extraction at all \sqrt{s}	277
A.12	Summary of systematic uncertainty δ_{model} on the individual results for the Born cross section due to the signal MC simulation input model for the form factors at different \sqrt{s}	279
A.13	Summary of the systematic uncertainty δ_{trg} on the individual results on the Born cross section due to the trigger efficiency correction at different \sqrt{s}	280
A.14	Summary of the systematic uncertainty δ_{trg} on the individual results for the Born cross section due to the radiative correction at different \sqrt{s}	280
A.15	Summary of the systematic uncertainty on the individual results on $R_{\text{em}}^{\text{ind}}$ and $G_{\text{M}}^{\text{ind}}$ due to the fit range for the signal extraction.	283
A.16	Summary of the systematic uncertainty on the individual results for $R_{\text{em}}^{\text{ind}}$ and $G_{\text{M}}^{\text{ind}}$ due to the background shape model for the signal extraction.	284
A.17	Summary of the systematic uncertainty on the individual results for $R_{\text{em}}^{\text{ind}}$ and $G_{\text{M}}^{\text{ind}}$ due to the signal shape model for the signal extraction.	285
A.18	Summary of the systematic uncertainty on the individual results for $R_{\text{em}}^{\text{ind}}$ and $G_{\text{M}}^{\text{ind}}$ due to the misidentification of the neutron showers in the EMC.	286
A.19	Summary of the systematic uncertainty on the individual results for $R_{\text{em}}^{\text{ind}}$ and $G_{\text{M}}^{\text{ind}}$ due to the differential signal yield extraction.	287
A.20	Summary of the systematic uncertainty on the individual results for $R_{\text{em}}^{\text{ind}}$ and $G_{\text{M}}^{\text{ind}}$ due to the form factor model from the signal MC simulation.	287
A.21	Summary of the systematic uncertainty on the individual results for $G_{\text{M}}^{\text{ind}}$ due to the luminosity measurement.	288
A.22	The systematic uncertainty on the individual results for $G_{\text{M}}^{\text{ind}}$ due to the model dependence of the angular distribution shape.	289
A.23	Summary of the systematic uncertainty on the individual results for $G_{\text{M}}^{\text{ind}}$ due to the trigger efficiency correction.	290
B.1	Category A: Summary of the selection criteria for the signal events.	296
B.2	Category A: Setup configuration for the signal extraction.	297
B.3	Category A: Number of reconstructed signal events in collider data.	299
B.4	Category A: Signal MC event selection efficiency and its corrections.	300

B.5	Category A: Summary of the extracted differential signal yield $N_{\text{fit}}^{\cos\theta(\text{Bi})}$ from the collider data at different \sqrt{s}	302
B.6	Category A: Magnetic form factor G_M and form factor ratio $R_{\text{em}} = G_E/G_M $ at $\sqrt{s} = 2.1266$ and the four combined data samples. The errors are statistical.	303
B.7	Category A: Summary of all systematic uncertainty sources for the Born cross section measurement.	307
B.8	Category A: Summary of the systematic uncertainties on $ G_E/G_M $ and on the $ G_M $	308
B.9	Category A: Summary of the results for the Born cross section σ_{Born} and the effective FF $ G $	308
B.10	Category B: The momentum region selected from the control samples $J/\psi \rightarrow \bar{p}n\pi^+$ and $J/\psi \rightarrow p\bar{n}\pi^-$ in collider data at $\sqrt{s} = 3.0970$ GeV.	310
B.11	Category B: The variables used for training and evaluation of the BDT classifier at $\sqrt{s} = 2.3960$ GeV.	311
B.12	Category B: Summary of the selection criteria.	313
B.13	Category B: Number of reconstructed signal events in collider data.	314
B.14	Category B: Signal MC event selection efficiency and its corrections.	318
B.15	Category B: Summary of the extracted differential signal yield $N_{\text{fit}}^{\cos\theta(\text{Bi})}$ from collider data at different \sqrt{s}	320
B.16	Category B: Results for the magnetic form factor G_M and the form factor ratio $R_{\text{em}} = G_E/G_M $	321
B.17	Category B: Study of systematic uncertainties from the BDT method at $\sqrt{s} = 2.3960$ GeV.	324
B.18	Category B: Summary of all systematic uncertainty sources for the Born cross section measurement.	326
B.19	Category B : Summary of the systematic uncertainties for the results from the angular analysis.	327
B.20	Category B: Summary of the results for the Born cross section σ_{Born} and the effective FF $ G $	327
C.1	Comparison of the selection criteria for the process $e^+e^- \rightarrow \gamma\gamma$ and $e^+e^- \rightarrow n\bar{n}$	337
C.2	Verification of the relation $N_{\text{obs}}^{\gamma\gamma} = L\sigma\varepsilon_{\text{MC}}^{\gamma\gamma}$ for the digamma process.	337

Bibliography

- [1] R. Hofstadter and R.W. McAllister, Phys. Rev. 102 (1956) 851.
- [2] Hofstadter R. and R. W. McAllister, Phys. Rev. 98, 217 (1955).
- [3] Hofstadter R., F. Bumiller and M.R. Yearian, Rev. Mod. Phys. 30, 482 (1958).
- [4] C. E. Hyde-Wright and K. de Jager, Ann. Rev. Nucl. and Part. Sci. 54, 217 (2004).
- [5] C.F. Perdrisat, V. Punjabi, and M. Vanderhaeghen, Progr. Part. Nucl. Phys. 59, 694 (2007).
- [6] V. Punjabi, C.F. Perdrisat, M.K. Jones, E.J. Brash, C.E. Carlson, "The Structure of the Nucleon: Elastic Electromagnetic Form Factors", arXiv:1503.01452v4 [nucl-ex]
- [7] C.E. Carlson, Eur. Phys. J. Special Topics 198, 65 (2011).
- [8] J. Arrington, K. de Jager, and C. F. Perdrisat, Jou. Phys. Conf. Ser. 299, 012002 (2011).
- [9] Jones M. K. et al., (Jefferson Lab Hall A Collaboration), Phys. Rev. Lett. 84, 1398, (2000).
- [10] Hyde, Charles Earl and Kees de Jager et al., "Electromagnetic form factors of the nucleon and Compton scattering", Ann.Rev.Nucl.Part.Sci. 54, 217-267, (2004).
- [11] Pohl R, et al., "The size of the proton", Nature. 466 (7303): 213–216, (2010).
- [12] R. Bijker and F. Iachello, Phys. Rev. C69, 068201 (2004).
- [13] M. A. Belushkin, H. -W. Hammer and U.-G. Meißner, Phys. Rev. C75, 035202 (2007).
- [14] A. Z. Dubnickov a, S. Dubnicka and M. Erdelyi, Prog. Part. Nucl. Phys. 61, 162 (2008).
- [15] J. P. B. C. de Melo, T. Frederico, E. Pace, S. Pisano and G. Salme, Phys. Lett. B671, 153 (2009).
- [16] Y. Yan, K. Khosonthongkee, C. Kobdaj and P. Suebka, J. Phys. G37, 075007 (2010).
- [17] E. A. Kuraev, E. Tomasi-Gustafsson and A. Dbeyssi, Phys. Lett. B712, 240 (2012).
- [18] Y. .A. Simonov, Phys. Rev. D85, 125025 (2012).
- [19] E. L. Lomon and S. Pacetti, Phys. Rev. D85, 113004 (2012).

- [20] B. Aubert et al., Phys. Rev. D73, 012005 (2006).
- [21] J.P. Lees et al., Phys. Rev. D87, 092005 (2013).
- [22] A. Antonelli et al., (FENICE Collaboration) Phys. Lett. B 334 (1994) 431.
- [23] A. Antonelli et al. (Fenice Collaboration), Phys. Lett. B 334, 431 (1994).
- [24] A. Antonelli, R. Baldini, P. Benasi, M. Bertani, M. Biagini, et al., "The first measurement of the neutron electromagnetic form-factors in the timelike region", Nuclear. Phys. B 517 (1998) 3–35.
- [25] D. Bisello, et al., "Baryon pair production in e^+e^- annihilation at $s = 2.4$ GeV", Z. Phys. C 48 (1990) 23–28.
- [26] M. N. Achasov et al., "Study of the process $e^+e^- \rightarrow n\bar{n}$ at the VEPP-200 e^+e^- collider with the SND detector", Phys. Rev. D 90, 112007, (2014)
- [27] B. X. Zhang and Z. Gao, The BESIII Collaboration 2015 Summer Meeting.
- [28] S. L. Glashow and S. Weinberg, Phys. Rev. D 15, 1958 (1977).
- [29] G. Arnison et al. [UA1 Collaboration], Phys. Lett. B 122, 103 (1983).
- [30] G. Arnison et al. [UA1 Collaboration], Phys. Lett. B 126, 398 (1983).
- [31] J. E. Augustin et al., Phys. Rev. Lett. 33, 1406 (1974).
- [32] Atlas Collaboration, Physics Letters B716, 1-29 (2012).
- [33] C. F. Perdrisat et al., Prog. Part. Nucl. Phys. 59 (2007) 694.
- [34] A. Denig and G. Salme, "Nucleon Electromagnetic Form Factors in the Timelike Region", Prog. Part. Nucl. Phys. 68, 113 (2013), doi:10.1016/j.pnpnp.2012.09.005, [arXiv:1210.4689 [hep-ex]].
- [35] A. Anotnelli et al., Nucl. Phys. B 517, (1998) 3.
- [36] Professor E. Rutherford ER.S. (2009) LXXIX. The scattering of α and β particles by matter and the structure of the atom, The London, Edinburgh, and Dublin Philosophical Magazine and Journal of Science, 21:125, 669-688, DOI: 10.1080/14786440508637080.
- [37] James Chadwick: Possible Existence of a Neutron. In: Nature. Band 129, Nr. 3252, 27. Februar 1932, S. 312, doi:10.1038/129312a0.
- [38] James Chadwick: The Existence of a Neutron. In: Proceedings of the Royal Society of London. Series A, Containing Papers of a Mathematical and Physical Character. Band 136, Nr. 830, 1. Mai 1932, S. 692–708.
- [39] O. Stern, Nature 132 (1933) 103.
- [40] L. Alvarez and F. Bloch, "A Quantitative Determination of the Neutron Moment in Absolute Nuclear Magnetons", Phys. Rev. 57 (1940) 111

-
- [41] M.N. Rosenbluth, "High energy elastic scattering of electrons on protons", Phys. Rev. 79 (1950) 615.
- [42] R. Hofstadter, H. Fechter, and J. McIntyre, Scattering of high energy electrons and the method of nuclear recoil, Phys.Rev. 91 (1953) 422.
- [43] R. Hofstadter, Rev. Mod. Phys. 28 (1956) 214.
- [44] R. D. Peccei, "Discrete and global symmetries in particle physics", Lect. Notes Phys. 521 (1999) 1. [hep-ph/9807516].
- [45] L. L. Foldy, Phys. Rev. 87 (1952) 688.
- [46] A. Zichichi, S. Berman, N. Cabibbo, R. Gatto, Proton anti-proton annihilation into electrons, muons and vector bosons, Nuovo Cim. 24 (1962) 170–180.
- [47] N. Cabibbo and R. Gatto, Phys. Rev. 124, 1557 (1961).
- [48] J. Haidenbauer, X.-W. Kang, U.-G. Meißner, Nucl. Phys. A 929, 102 (2014).
- [49] D. Lin, "Measurement of proton electromagnetic form factors using the initial-state-radiation process $e^+e^- \rightarrow \bar{p}p\gamma$ at BESIII", Dissertation Thesis, Institute of Nuclear Physics Mainz, (2017), urn:nbn:de:hebis:77-diss-1000015218.
- [50] C. Patrignani et al. (Particle Data Group), Chin. Phys. C, 40 (2016) 100001.
- [51] C. Adamuscin, E.A. Kuraev, E. Tomasi-Gustafsson, and F. Maas, Phys. Rev. C75, (2007) 045205; E.A. Kuraev, C. Adamuscin, E. Tomasi-Gustafsson, and F. Maas, Phys. Lett. B649, (2007) 400.
- [52] S. Pacetti, R. Baldini and E. Tomasi-Gustafsson, Phys. Rep. 550-551 (2015) 1.
- [53] V. Matveev, R. Muradyan, A. Tavkhelidze, Automodelity in strong interactions, Teor. Mat. Fiz. 15 (1973) 332–339.
- [54] S.J. Brodsky, G.R. Farrar, Scaling laws at large transverse momentum, Phys. Rev. Lett. 31 (1973) 1153–1156.
- [55] E. Titchmarsh, The Theory of Functions, Oxford science publications, Oxford University Press, 1939
- [56] R. Baldini, S. Pacetti, A. Zallo and A. Zichichi, "Unexpected features of $e^+e^- \rightarrow p\bar{p}$ and $e^+e^- \rightarrow \Lambda\bar{\Lambda}$ cross sections near threshold", Eur. Phys. J. A 39, (2009) 315
- [57] L.N. Hand, D.G. Miller, R. Wilson, Rev. Mod. Phys. 35, 335 (1963)
- [58] T. Janssens, R. Hofstadter, E.B. Hughes, M.R. Yearian, Phys. Rev. 142, 922 (1966).
- [59] L.E. Price et al., Phys. Rev. D 4, 45 (1971).
- [60] J. Litt et al., Phys. Lett. B 31, 40 (1970).
- [61] Ch. Berger et al., Phys. Lett. B 35, 87 (1971).

- [62] W. Bartel et al., Nucl. Phys. B 58, 429 (1973).
- [63] F. Borkowski, G.G. Simon, V.H. Walther, R.D. Wendling, Nucl. Phys. B 93, 461 (1975).
- [64] G.G. Simon, Ch. Schmitt, F. Borkowski, V.H. Walther, Nucl. Phys. A 333, 381 (1980).
- [65] R.C. Walker et al., Phys. Rev. D 49, 5671 (1994).
- [66] L. Andivahis et al., Phys. Rev. D 50, 5491 (1994).
- [67] M.E. Christy et al., Phys. Rev. C 70, 015206 (2004).
- [68] I.A. Qattan et al., Phys. Rev. Lett. 94, 142301 (2005).
- [69] P.N. Kirk, M. Breidenbach, J.I. Friedman, G.C. Hartmann, H.W. Kendall et al., Phys. Rev. D 8, 63 (1973).
- [70] A.F. Sill et al., Phys. Rev. D 48, 29 (1993).
- [71] J. C. Bernauer, PhD thesis, (2010)
wwwa1.kph.uni-mainz.de/A1/publications/doctor/bernauer.pdf
- [72] J. J. Kelly, Phys. Rev. C 70, 068202 (2004).
- [73] E.J. Brash, A. Kozlov, S. Li, G.M. Huber, Phys. Rev. C 65, 051001 (2002).
- [74] V. Punjabi, C. Perdrisat, K. Aniol, F. Baker, J. Berthot, et al., Proton elastic form-factor ratios to $Q^2 = 3.5 \text{ GeV}^2$ by polarization transfer, Phys. Rev. C 71 (2005) 055202.
- [75] A. Puckett, E. Brash, O. Gayou, M. Jones, L. Pentchev, et al., Final analysis of proton form factor ratio data at $Q^2 = 4.0, 4.8 \text{ and } 5.6 \text{ GeV}^2$, Phys. Rev. C 85 (2012) 045203.
- [76] A. Puckett, E. Brash, M. Jones, W. Luo, M. Meziane, et al., Recoil polarization measurements of the proton electromagnetic form factor ratio to $Q^2 = 8.5 \text{ GeV}^2$, Phys. Rev. Lett. 104 (2010) 242301.
- [77] L. Andivahis et al., Phys. Rev. D 50, 5491 (1994).
- [78] M.E. Christy et al., Phys. Rev. C 70, 015206 (2004).
- [79] I.A. Qattan et al., Phys. Rev. Lett. 94, 142301 (2005).
- [80] O. Gayou et al (Jefferson Lab Hall A), Phys. Rev. Lett. 88 , 092301 (2002).
- [81] M. Castellano, G. Di Giugno, J. Humphrey, E. Sassi Palmieri, G. Troise, et al., The reaction $e^+e^- \rightarrow \bar{p}p$ at a total energy of 2.1 GeV, Nuovo Cim. A 14 (1973) 1–20.
- [82] A. Antonelli et al., (FENICE Collaboration) Phys. Lett. B 313 (1993) 283.
- [83] A. Antonelli et al., (FENICE Collaboration) Nucl. Phys. B 517 (1998) 3.
- [84] B. Delcourt et al., (DM1 Collaboration), Phys. Lett. B 86 (1982) 395.
- [85] A. Antonelli et al., (DM2 Collaboration), Z. Phys. C 48 (1990) 23.

-
- [86] T. Pedlar, et al., Precision measurements of the timelike electromagnetic form-factors of pion, kaon, and proton, *Phys. Rev. Lett.* 95 (2005) 261803.
- [87] M. Ablikim, et al., Measurement of the cross section for $e^+e^- \rightarrow \bar{p}p$ at center-of-mass energies from 2.4 GeV to 3.07 GeV, *Phys. Lett. B* 630 (2005) 14–20.
- [88] M. Ablikim et al., (BESIII Collaboration), *Phys. Rev. D* 91 (2015) 112004.
- [89] R. R. Akhmetshin, et al., *Phys. Lett. B* 759 (2016) 634.
- [90] T. Armstrong, et al., Measurement of the proton electromagnetic form-factors in the timelike region at $8.9 \text{ GeV}^2 - 13 \text{ GeV}^2$, *Phys. Rev. Lett.* 70 (1993) 1212–1215.
- [91] M. Andreotti, S. Bagnasco, W. Baldini, D. Bettoni, G. Borreani, et al., Measurements of the magnetic form-factor of the proton for timelike momentum transfers, *Phys. Lett. B* 559 (2003) 20–25.
- [92] G. Bardin, G. Burgun, R. Calabrese, G. Capon, R. Carlin, et al., Determination of the electric and magnetic form-factors of the proton in the timelike region, *Nuclear. Phys. B* 411 (1994) 3–32.
- [93] J. Lees, et al., Study of $e^+e^- \rightarrow \bar{p}p$ via initial-state radiation at BABAR, *Phys. Rev. D* 87 (2013) 092005.
- [94] Lees, J.P. et al., (BaBar Collaboration), "Measurement of the $e^+e^- \rightarrow \bar{p}p$ cross section in the energy range from 3.0 to 6.5 GeV", *Phys.Rev. D* 88 (2013) no.7
- [95] A. Dbeyssi et al., "Baryon electromagnetic form factors at BESII", *EPJ Web Conf.* 138 01011 (2017), DOI: 10.1051/epjconf/201713801011
- [96] V. P. Druzhinin, S. I. Eidelman, S. I. Serednyakov, and E. P. Solodov, *Rev. Mod. Phys* 83, (2011) 1545 (2011).
- [97] A. Bianconi, E. Tomasi-Gustafsson, "Periodic interference structures in the time-like proton form factor", *Phys. Rev. Lett.* 114 (2015) no.23, 232301, DOI: 10.1103/PhysRevLett.114.232301.
- [98] M. Ambrogiani, et al., Measurements of the magnetic form-factor of the proton in the timelike region at large momentum transfer, *Phys. Rev. D* 60 (1999) 032002.
- [99] G. Bassompierre, et al., First determination of the proton electromagnetic form-factors at the threshold of the timelike region, *Phys. Lett. B* 68 (1977) 477.
- [100] A. Bravar, et al., Single spin asymmetries in inclusive charged pion production by transversely polarized anti-protons, *Phys. Rev. Lett.* 77 (1996) 2626-2629.
- [101] J. P. Lees et al., (BaBar Collaboration), *Phys. Rev. D* 73 (2006) 012005.
- [102] M. Ablikim et al. (BESIII Collaboration), "Measurement of proton electromagnetic form factors in $e^+e^- \rightarrow p\bar{p}$ in the energy region 2.00 - 3.08 GeV", arXiv:1905.09001 [hep-ex].

- [103] R.R. Akhmetshin et al., "Study of the process $e^+e^- \rightarrow p\bar{p}$ in the c.m. energy range from threshold to 2 GeV with the CMD-3 detector", Phys. Lett. B 759 (2016) 634-640, <https://doi.org/10.1016/j.physletb.2016.04.048>
- [104] S. Galster, et al., Nucl. Phys. B 32 (1971) 221.
- [105] C. Herberg, M. Ostrick, H. Andresen, J. Annand, K. Aulenbacher, et al., Determination of the neutron electric form-factor in the D(e,e' n)p reaction and the influence of nuclear binding, Eur. Phys. J. A 5 (1999) 131–135.
- [106] M. Ostrick, C. Herberg, H. Andresen, J. Annand, K. Aulenbacher, et al., Measurement of the neutron electric form-factor $G(E,n)$ in the quasifree H-2(e(pol.),e' n(pol.))p reaction, Phys. Rev. Lett. 83 (1999) 276–279.
- [107] D. Glazier, M. Seimetz, J. Annand, H. Arenhovel, M. Ases Antelo, et al., Measurement of the electric form-factor of the neutron at $Q^2 = 0.3 \text{ (GeV/c)}^2$ to 0.8 (GeV/c)^2 , Eur. Phys. J. A 24 (2005) 101–109.
- [108] G. Kubon et al., Phys. Lett. B 524, 26 (2002).
- [109] M. Meyerhoff, D. Eyl, A. Frey, H. Andresen, J. Annand, et al., First measurement of the electric form-factor of the neutron in the exclusive quasielastic scattering of polarized electrons from polarized He-3, Phys. Lett. B 327 (1994) 201–207.
- [110] K.M. Hanson, et al., Phys. Rev. D 8 (1973) 753.
- [111] D. Benaksas, D. Drikey, D. Frèrejacque, Phys. Rev. Lett. 13 (1964) 353.
- [112] J.R. Dunning, et al., Phys. Rev. 141 (1966) 1286.
- [113] H. Anklin, D. Fritschi, J. Jourdan, M. Loppacher, G. Masson, et al., Precision measurement of the neutron magnetic form-factor, Phys. Lett. B 336 (1994) 313–318.
- [114] H. Anklin, L. deBever, K. Blomqvist, W. Boeglin, R. Bohm, et al., Precise measurements of the neutron magnetic form-factor, Phys. Lett. B 428 (1998) 248–253.
- [115] G. Kubon, H. Anklin, P. Bartsch, D. Baumann, W. Boeglin, et al., Precise neutron magnetic form-factors, Phys. Lett. B 524 (2002) 26–32.
- [116] H. Gao, J. Arrington, E. Beise, B. Bray, R. Carr, et al., Measurement of the neutron magnetic form-factor from inclusive quasielastic scattering of polarized electrons from polarized He-3, Phys. Rev. C 50 (1994) 546–549.
- [117] T. Eden, R. Madey, W. Zhang, B. Anderson, H. Arenhovel, et al., Electric form-factor of the neutron from the H-2 (e (polarized), e-prime n (polarized)) H-1 reaction at $Q^2 = 0.255 \text{ (GeV/c)}^2$, Phys. Rev. C 50 (1994) 1749–1753.
- [118] Plaster B. et al. Phys. Rev. C 73, 025205 (2006).
- [119] I. Passchier, R. Alarcon, T. Bauer, D. Boersma, J. van den Brand, et al., The Charge form-factor of the neutron from the reaction polarized H-2(polarized e, e-prime n) p, Phys. Rev. Lett. 82 (1999) 4988–4991.

- [120] Zhu H. et al., Phys. Rev. Lett. 87, 081801 (2001).
- [121] Warren G. et al. [Jefferson Lab E93-026 Collaboration], Phys. Rev. Lett. 92, 042301 (2004).
- [122] J. Becker, H. Andresen, J. Annand, K. Aulenbacher, K. Beuchel, et al., Determination of the neutron electric form-factor from the reaction $\text{He-3}(e, e' n)$ at medium momentum transfer, Eur. Phys. J. A 6 (1999) 329–344.
- [123] Rohe D. et al., Phys. Rev. Lett. 83, 4257 (1999).
- [124] Bermuth J. et al., Phys. Lett. B 564, 199 (2003).
- [125] R. Schiavilla, I. Sick, Neutron charge form-factor at large q^2 , Phys. Rev. C 64 (2001) 041002.
- [126] S. Rock, R. Arnold, P.E. Bosted, B. Chertok, B. Mecking, et al., Measurement of elastic electron - neutron scattering and inelastic electron - deuteron scattering cross-sections at high momentum transfer, Phys. Rev. D 46 (1992) 24–44.
- [127] A. Lung, L. Stuart, P.E. Bosted, L. Andivahis, J. Alster, et al., Measurements of the electric and magnetic form-factors of the neutron from $Q^2 = 1.75 \text{ GeV}/c^2 \rightarrow 4 \text{ GeV}/c^2$, Phys. Rev. Lett. 70 (1993) 718–721.
- [128] P. Markowitz, J. Finn, B. Anderson, H. Arenhovel, A. Baldwin, et al., Measurement of the magnetic form-factor of the neutron, Phys. Rev. C 48 (1993) 5–9.
- [129] E. Bruins, T. Bauer, H. den Bok, C. Duif, W. van Hoek, et al., Measurement of the neutron magnetic form-factor, Phys. Rev. Lett. 75 (1995) 21–24.
- [130] W. Brooks, J. Lachniet, Precise determination of the neutron magnetic form-factor to higher Q^2 , Nuclear. Phys. A 755 (2005) 261–264.
- [131] B. Anderson, et al., Extraction of the neutron magnetic form-factor from quasi-elastic polarized-He-3(polarized-e, e-prime) at $Q^2 = 0.1 - 0.6 (\text{GeV}/c)^2$, Phys. Rev. C 75 (2007) 034003.
- [132] R. Madey et al., E93-038 Collaboration, Phys. Rev. Lett. 91, 122002 (2003).
- [133] E. Geis et al. (BLAST Collaboration), Phys. Rev. Lett. 101, 042501 (2008).
- [134] C.E. Jones-Woodward et al., Phys. Rev. C 44, 571 (1991).
- [135] A.K. Thompson et al., Phys. Rev. Lett. 68, 2901 (1992).
- [136] J. Golak, G. Ziener, H. Kamada, H. Witala, W. Gloeckle, Extraction of electromagnetic neutron form-factors through inclusive and exclusive polarized electron scattering on polarized He-3 target, Phys. Rev. C 63 (2001) 034006.
- [137] S. Riordan, S. Abrahamyan, B. Craver, A. Kelleher, A. Kolarkar et al., Phys. Rev. Lett. 105, 262302 (2010).

- [138] B. Schlimme, P. Achenbach, C. Ayerbe Gayoso, J. Bernauer, R. Bhm et al., *Phys. Rev. Lett.* 111(13), 132504 (2013).
- [139] I. Cloët, G. Eichmann, B. El-Bennich, T. Klahn, C. Roberts, *Few Body Syst.* 46, (2009) 1.
- [140] J. R. Dunning, K. W. Chen et al., *Phys. Rev.* 141 (1966) 1286.
- [141] E. Tomasi-Gustafsson and M. P. Rekalo. *Phys. Lett. B*(504) (2001) 291–295.
- [142] Brodsky S. J. and G.R. Farrar, *Phys. Rev. D* 11, (1975) 1309.
- [143] D.V. Shirkov et al. *Phys. Rev. Lett.* 79, (1997) 1209.
- [144] H.-W. Hammer, U.-G. Meißner, and D. Drechsel, *Phys. Lett. B* 385 (1996) 343.
- [145] J.P.B.C. de Melo, T. Frederico, E. Pace, S. Pisano, and G. Salmè, *Phys. Lett. B* 671 (2009) 153.
- [146] J. Green, J. Negele, A. Pochinsky, S. Syritsyn, M. Engelhardt et al., arXiv:1404.4029 (2014)
- [147] J. Haidenbauer, X.-W. Kang, U.-G. Meißner, *Nucl. Phys. A* 929 (2014) 102-118.
- [148] B. Holzenkamp, K. Holinde, J. Speth, *Nucl. Phys. A* 500 (1989) 485.
- [149] X.-W. Kang, J. Haidenbauer, U.-G. Meißner, *JHEP* 1402 (2014) 113.
- [150] D. Zhou and R. G. E. Timmermans, *Phys. Rev. C* 86, 044003 (2012).
- [151] T. Hippchen, J. Haidenbauer, K. Holinde, V. Mull, *Phys. Rev. C* 44 (1991) 1323.
- [152] G. P. Lepage and S. J. Brodsky, *Phys. Rev. D* 22 (1980) 2157, V. L. Chernyak and A. R. Zhitnitsky, *Phys. Rept.* 112,(1984) 173.
- [153] A. Duncan and A. H. Mueller, *Phys. Rev. D* 21,(1980) 1636.
- [154] Nikolai Kivel, Marc Vanderhaeghen, *Phys. Rev. D* 83 (2011) 093005.
- [155] T. Massam, A. Zichichi, A one-paramenter fit to the electromagnetic form factors of the nucleon, *Il Nuovo Cimento A Series* 10 43 (4) (1966) 1137–1148
- [156] F. Iachello, A. Jackson, A. Lande, Semiphenomenological fits to nucleon electromagnetic form-factors, *Phys. Lett. B* 43 (1973) 191–196.
- [157] F. Iachello, Q. Wan, Structure of the nucleon from electromagnetic timelike form factors, *Phys. Rev. C* 69 (2004) 055204.
- [158] R. Bijker, F. Iachello, Re-analysis of the nucleon space- and time-like electromagnetic form-factors in a two-component model, *Phys. Rev. C* 69 (2004) 068201.
- [159] Q. Wan, F. Iachello, A unified description of baryon electromagnetic form factors, *Internat. J. Modern. Phys. A* 20 (2005) 1846–1849.

- [160] E.L. Lomon, S. Pacetti, Time-like and space-like electromagnetic form factors of nucleons, a unified description, *Phys. Rev. D* 85 (2012) 113004.
- [161] Henryk Czyz, Johann H. Kuhn, and Szymon Tracz, *Phys. Rev. D* 90, 114021 (2014).
- [162] H.W.Hammer, U.G.Meissner, *Eur. Phys. J. A* 20, (2004) 469.
- [163] J. Ellis, and M. Karliner, *New J. Phys.* 4, (2002) 18.
- [164] V.L.Chernyak,I.R.Zhitnitsky, *Nucl.Phys. B*246 (1984) 52.
- [165] T.Hyer, *Phys.Rev. D*47 (1993) 3875.
- [166] A.A.Logunov,N.Van Hieu,I.T.Todorov, *Ann.Phys. (NY)* 31 (1965) 203.
- [167] P.Cesselli, M.Nigro, C.Voce, *Proc. Physics at Lear, Erice* 11, (1999) 465
- [168] L.N. Hand, D.G. Miller, R. Wilson, Electric and magnetic form factors of the nucleon, *Rev. Modern Phys.* 35 (1963) 335–349.
- [169] J. Litt, G. Buschhorn, D. Coward, H. Destaebler, L. Mo, R. Taylor, B. Barish, S. Loken, J. Pine, J. Friedman, G. Hartmann, H. Kendall, Measurement of the ratio of the proton form factors, g_e/g_m , at high momentum transfers and the question of scaling, *Phys. Lett. B* 31 (1) (1970) 40–44.
- [170] L.E. Price, J.R. Dunning, M. Goitein, K. Hanson, T. Kirk, R. Wilson, Backward-angle electron-proton elastic scattering and proton electromagnetic form factors, *Phys. Rev. D* 4 (1971) 45–53.
- [171] C. Berger, V. Burkert, G. Knop, B. Langenbeck, K. Rith, Electromagnetic form factors of the proton at squared four-momentum transfers between 10 and 50 fm^2 , *Phys. Lett. B* 35 (1) (1971) 87–89.
- [172] W. Bartel, F. Busser, W. Dix, R. Felst, D. Harms, et al., Measurement of proton and neutron electromagnetic form-factors at squared four momentum transfers up to 3 (GeV/c^2) , *Nuclear. Phys. B* 58 (1973) 429–475.
- [173] K.M. Hanson, J.R. Dunning, M. Goitein, T. Kirk, L.E. Price, R. Wilson, Large-angle quasielastic electron-deuteron scattering, *Phys. Rev. D* 8 (1973) 753–778.
- [174] F. Borkowski, G. Simon, V. Walther, R. Wendling, Electromagnetic form factors of the proton at low four-momentum transfer (ii), *Nuclear Phys. B* 93 (3) (1975) 461–478.
- [175] L. Andivahis, P.E. Bosted, A. Lung, L. Stuart, J. Alster, et al., Measurements of the electric and magnetic form-factors of the proton from $Q^2 = 1.75 \text{ GeV}/c^2$ to $8.83 \text{ GeV}/c^2$, *Phys. Rev. D* 50 (1994) 5491–5517.
- [176] R. Walker, B. Filippone, J. Jourdan, R. Milner, R. McKeown, et al., Measurements of the proton elastic form-factors for $1 \text{ GeV}/c^2 \leq Q^2 \leq 3 \text{ GeV}/c^2$ at SLAC, *Phys. Rev. D* 49 (1994) 5671–5689.
- [177] M. Christy, et al., Measurements of electron proton elastic cross-sections for $0.4 < Q^2 < 5.5 (\text{GeV}/c)^2$, *Phys. Rev. C* 70 (2004) 015206.

- [178] I. Qattan, J. Arrington, R. Segel, X. Zheng, K. Aniol, et al., Precision Rosenbluth measurement of the proton elastic form-factors, *Phys. Rev. Lett.* 94 (2005) 142301.
- [179] T. Janssens, R. Hofstadter, E.B. Hughes, M.R. Yearian, Proton form factors from elastic electron-proton scattering, *Phys. Rev.* 142 (1966) 922–931.
- [180] D.H. Coward, H. DeStaebler, R.A. Early, J. Litt, A. Minten, L.W. Mo, W.K.H. Panofsky, R.E. Taylor, M. Breidenbach, J.I. Friedman, H.W. Kendall, P.N. Kirk, B.C. Barish, J. Mar, J. Pine, Electron-proton elastic scattering at high momentum transfers, *Phys. Rev. Lett.* 20 (1968) 292–295.
- [181] A.F. Sill, R.G. Arnold, P.E. Bosted, C.C. Chang, J. Gomez, A.T. Katramatou, C.J. Martoff, G.G. Petratos, A.A. Rahbar, S.E. Rock, Z.M. Szalata, D.J. Sherden, J.M. Lambert, R.M. Lombard-Nelsen, Measurements of elastic electron-proton scattering at large momentum transfer, *Phys. Rev. D* 48 (1993) 29–55.
- [182] M. Jones, et al., G_E^p/G_M^p ratio by polarization transfer in $ep \rightarrow ep$, *Phys. Rev. Lett.* 84 (2000) 1398–1402.
- [183] O. Gayou, et al., Measurement of G_E^p/G_M^p in $ep \rightarrow ep$ to $Q^2 = 5.6 \text{ GeV}^2$, *Phys. Rev. Lett.* 88 (2002) 092301.
- [184] M. Jones, et al., Proton $G(E)/G(M)$ from beam-target asymmetry, *Phys. Rev. C* 74 (2006) 035201.
- [185] G. Ron, et al., Low Q^2 measurements of the proton form factor ratio $\mu_p G_E/G_M$, *Phys. Rev. C* 84 (2011) 055204.
- [186] C.B. Crawford, A. Sindile, T. Akdogan, R. Alarcon, W. Bertozzi, et al., Measurement of the proton electric to magnetic form factor ratio from vector H-1(vector e, e' p), *Phys. Rev. Lett.* 98 (2007) 052301.
- [187] K. T. Chao and Y. F. Wang, Physics at BESIII, *Int. J. of Mod. Phys. V24* (2009) Supplement 1.
- [188] Y. Minghan and Z. Zhipeng, *Nucl. Phys. B (Proc. Suppl.)* 1B, 207-216 (1988).
- [189] S. Fang, S. Chen: "The Beijing Electron Positron Collider", *Part. Accel.* Vol. 25, (1990) 51–61.
- [190] M. Ablikim et al., (BESIII Collaboration), *Nucl. Instr. Meth. A* 614 (2010) 345-399.
- [191] D. M. Asner, *International Journal of Modern Physics A24*, Issue 1 supp. (2008)
- [192] Superconducting Magnet Design Report, BESIII Collaboration, internal document
- [193] Bicron BC-408 data sheet, www.crystals.saint-gobain.com/sites/imdf.crystals.com/files/documents/sgc-bc400-404-408-412-416-data-sheet.pdf
- [194] Y. J. Sun and C. Li et al., *Nucl. Instrum. Meth. A* 763, 190-196 (2014)

-
- [195] Miao He, "Energy Loss Correction for BESIII EM Calorimeter" in proceedings of "XI International Workshop on Advanced Computing and Analysis Techniques in Physics Research" PoS(ACAT) 057, (2007) <https://pos.sissa.it>
- [196] Moun Counter System Design Report, BESIII Collaboration, internal document.
- [197] Shu-Jun Wei et al., Nuclear Instruments and Methods in Physics Research A598, 323-327 (2009).
- [198] M. Ablikim et al. (BESIII Collaboration), Chin. Phys. Vol. 40, No. 6 (2017) 063001.
- [199] Shu-Jun Wei et al., Nucl. Instrum. Meth. A 598, 323–327 (2009).
- [200] G. Barrand et al., Comput. Phys. Commun. 140 (2001) 45.
- [201] C. Arnault, "CMT: a Software Configuration Management Tool", Proceeding of CHEP2000, Padova, Italy, 2000.
- [202] Yutie Liang et al., Nucl. Instrum. Meth. A 603 (2009) 325.
- [203] W. Li et al., (BESIII Collaboration), "The Offline Software For The BESIII Experiment" (2018).
- [204] S. Agostinelli et al. (Geant4 Collaboration), Nucl. Instrum. Meth. A 506, (2003) 250.
- [205] J. Allison et al. (Geant4 Collaboration), IEEE Trans. Nucl. Sci. 53, (2006) 270.
- [206] Rene Brun and Fons Rademakers, Nucl. Instrum. Meth. A 389, 81-86 (1997)
- [207] https://root.cern.ch/download/docRooFit_Users_Manual_2.91-33.pdf/RooFit_Users_Manual_2.91-33.pdf
- [208] G. S. Huang, for BESIII Collaboration, arXiv:1209.4813.
- [209] M. Ablikim et al., (BESIII Collaboration), Phys. Rev. Lett. 110, (2013) 252001
- [210] arXiv:1510.02293 [hep-ex]
- [211] M. Ablikim et al., (BESIII Collaboration), Phys. Rev. D 93 (2016) 052010.
- [212] M. Ablikim et al., (BESIII Collaboration), Chin. Phys. C 37 (2013) 063001.
- [213] M. Ablikim et al., (BESIII Collaboration), Phys. Rev. D 95 (2017) 052003.
- [214] M. Ablikim et al., (BESIII Collaboration), Chin. Phys. C 37 (2013) 123001.
- [215] M. Ablikim et al., (BESIII Collaboration), Chin. Phys. C 39 (2015) 093001.
- [216] M. Ablikim et al., (BESIII Collaboration), Phys. Rev. D 91 (2015) 112004.
- [217] M. Ablikim et al., (BESIII Collaboration), "Luminosity measurements for the R scan experiment at BESIII", Chinese Physics C. 41. (2017) 063001.
- [218] Z. Y. Deng et al., HEP&NP. 30, (2006) 371.

- [219] P. Richardson, "Spin Correlations in Monte Carlo Simulations", arXiv:hep-ph/0110108v1 (2001).
- [220] R. G. Ping, Chin. Phys. Vol. 40, No. 11 (2016) 113002.
- [221] R. G. Ping, (2013) BESIII-doc-162-v18.
- [222] F. Jegerlehner, <http://www-com.physik.hu-berlin.de/~fjeger/alphaQED.uu> (the version included in PHOKHARA was taken from <http://www-zeuthen.desy.de/fjeger/alphaQED.uu> and thus it is not updated)
- [223] K. Hagiwara, A.D. Martin, D. Nomura and T. Teubner, Phys. Lett. B 649 (2007) 173 [arXiv:hep-ph/0611102].
- [224] Henryk Czyz, Johann H. Kuhn, Szymon Tracz, Phys. Rev. D 90, 114021 (2014) [arXiv:1407.7995v2]
- [225] G. Balossini, C. M. C. Calame, G. Montagna, O. N. F. Piccinini, Nucl. Phys. B 758, (2006) 227.
- [226] R. L. Yang, R. G. Ping and H. Chen, Chin. Phys. Lett. 31 (2014) 061301.
- [227] S. Jadach, B.F.L. Ward, Z. Was, The Precision Monte Carlo Event Generator KK For Two-Fermion Final States In e^+e^- Collisions, Comput. Phys. Commun. (2000) 130:260-325
- [228] Y. F. Wang, W. G. Li, G. Chen, G. Sun et al, (BESIII Collaboration), "Design and Construction of the BESIII detector", Internal report
- [229] Balashov, Vsevolod V., "Interaction of Particles and Radiation with Matter", Springer (1997) ISBN 978-3-642-64383-5
- [230] C. Grupen and B. Shwartz, Particle Detectors, 2nd ed. Cambridge University Press, (2008).
- [231] Internal study of noise in the interaction region at BESIII.
- [232] R. Fletcher, "A new approach to variable metric algorithms", Comput. J. 13 (1970) 317
- [233] BESIII Niklaus Berger and Kai Zhu, Trigger Efficiencies for 2009 Running
- [234] N. Berger et al. Chin. Phys. C 34 1779 (2010).
- [235] M. Ablikim et al., (BESIII Collaboration), e-print: arXiv:1902.00665 [hep-ex]
- [236] A. Bianconi and E. Tomasi-Gustafsson, Phys. Rev. C 93, 035201 (2016).
- [237] I. T. Lorentz, H.-W. Hammer, and U.-G. Meissner, Phys. Rev. D 92, 034018 (2015).
- [238] J. Messchendorp (PANDA Collaboration), "The PANDA Experiment at FAIR - Subatomic Physics with Antiprotons", JPS Conf. Proc., 13, 010016 (2017), doi:10.7566/JPSCP.13.010016, arXiv:1610.02804 [nucl-ex].
- [239] Z. Ye, J. Arrington, R. J. Hill, G. Lee, Phys. Lett. B 777 (2018).

Curriculum Vitae

Persönliche Daten

Name, Vorname	Larin, Paul
Anschrift	Am Rodelberg 55 • 55131 Mainz
Geburtsdatum	4. August 1986 in Kujbyschew, Russland
Angehörigkeit	Deutsch

Studium und Ausbildung

- 05.2013-07.2020 **Promotion zum Dr. rer. nat. in Physik** am Helmholtz-Institut Mainz, zwischen August 2014 und März 2015 am Institute of High Energy Physics, Chinese Academy of Science, Beijing
- *Dissertation: „Measurement of the Timelike Electromagnetic Form Factors of the Neutron at the BESIII Experiment with the Process $e^+e^- \rightarrow nn$ “ (Note: mit Auszeichnung)*
 - *Betreuer: Prof. Dr. Frank E. Maas*
- 10.2011-03.2013 **M. Sc. in Physik** an der Johannes Gutenberg-Universität Mainz
- *Master-Thesis: „Voruntersuchungen zur Messung der zeitartigen Formfaktoren des Neutrons mit dem BESIII Detektor“ (Note: 1,0)*
 - *Nebenfach: Volkswirtschaftslehre, Mikro- und Makroökonomie*
- 10.2008-09.2011 **B. Sc. in Physik** an der Johannes Gutenberg-Universität Mainz
- *Bachelor-Thesis: „Voruntersuchungen für ein neues Präzisionsexperiment zur Messung der schwachen Ladung des Protons“ (Note: 1,0)*
 - *Nebenfach: Volkswirtschaftslehre, Mikro- und Makroökonomie*
- 04.2007-09.2008 **Grundwehrdienst** mit anschließend freiwillig verlängertem Wehrdienst im Stabsdienst der Luftwaffe, Jagdbombergeschwader 33, Cochem
- 03.2007 **Abitur** Werner-Heisenberg-Gymnasium, Neuwied

Berufspraxis

- Seit 05.2013 **Wissenschaftlicher Mitarbeiter** am Helmholtz-Institut Mainz
Mitwirkung an Forschungsaktivitäten und Repräsentation der wissenschaftlichen Arbeit bei Konferenzen, Durchführung und Betreuung physikalischer Praktika für Studenten
- 12.2011-05.2013 **Wissenschaftliche Hilfskraft** am Helmholtz-Institut Mainz
Unterstützung bei Forschungsaktivitäten der Arbeitsgruppe für elektromagnetische Präzisionsexperimente

Auslandserfahrung / Teilnahme an internationalen Konferenzen

- 08.2014-03.2015 **China**, Peking: *Forschungsaufenthalt am Institute of High Energy Physics an der Chinese Academy of Science im Rahmen meiner Promotion.*
- 2012-2019 *Teilnahme an etwa zwei Dutzend diverser nationaler und internationaler Konferenzen, Kollaborationstreffen und Workshops unter anderem in Deutschland, Italien, Spanien, Schweden und China*

Außeruniversitäres Engagement und Stipendien

- Seit 05.2015 Ehrenamtlicher Mitarbeiter des Projekts **Chancengleichheit**
- 09.2014-03.2015 Stipendiat des **DAAD**
- 07.2010-09.2011 Stipendiat der **Votum-Stiftung**
- 09.2008-03.2010 **Ehrenamtlicher Betreuer** meines Vaters, Oleg Larin

Sprachkenntnisse

- Sprachen Russisch: zweite Muttersprache
 Englisch: C1
 Französisch: Schulkenntnisse (5 Jahre)